

ATOMIC AND PLASMA-MATERIAL INTERACTION DATA FOR FUSION

VOLUME 9

INTERNATIONAL ATOMIC ENERGY AGENCY, VIENNA, 2001

The volumes of ATOMIC AND PLASMA–MATERIAL INTERACTION DATA FOR FUSION are published by the International Atomic Energy normally once a year.

For these volumes, papers, letters and reviews are accepted which deal with the following topics:

- Elementary collision processes in fusion plasmas involving photons, electrons, ions, atoms and molecules;
- Collision processes of plasma particles with surfaces of fusion relevant materials;
- Plasma-material interaction phenomena, including the thermophysical response of materials.

Each submitted contribution should contain fusion relevant data and information in either of the above areas. Original contributions should provide new data, using well established methods. Review articles should give a critical analysis or evaluation of a wider range of data. They are normally prepared on the invitation by the Editor or on prior mutual consent. Each submitted contribution is assessed by two independent referees.

Every manuscript submitted must be accompanied by a *disclaimer* stating that the paper has not been published and is not being considered for publication elsewhere. If no copyright is claimed by the authors, the IAEA automatically owns the copyright of the paper.

Guidelines for the preparation of manuscripts are given on the inside back cover. Manuscripts and correspondence should be addressed to: The Editor, ATOMIC AND PLASMA–MATERIAL INTERACTION DATA FOR FUSION, International Atomic Energy Agency, Wagramer Strasse 5, P.O. Box 100, A-1400 Vienna, Austria.

Publisher: International Atomic Energy Agency, Wagramer Strasse 5, P.O. Box 100, A-1400 Vienna, Austria

Editor: R.E.H. Clark, Atomic and Molecular Data Unit, Division of Physical and Chemical Sciences

Editorial Board:

R. Behrisch (Germany)	A. Miyahara (Japan)
H.B. Gilbody (UK)	D.R. Schultz (USA)
R. Janev (Macedonia)	H.P. Summers (UK)
A. Kingston (UK)	T. Kato (Japan)
Yu. V. Martynenko (Russ. Fed.)	J. Roth (Germany)
E. Menapace (Italy)	W. Wiese (USA)

ATOMIC AND PLASMA–MATERIAL INTERACTION DATA FOR FUSION, VOLUME 9
IAEA, VIENNA, 2001
STI/PUB/023/APID/09

FOREWORD

The present volume of Atomic and Plasma–Material Interaction Data for Fusion is devoted to a critical review of the role of atomic, molecular and plasma–wall interaction processes in divertor plasmas of magnetic fusion devices.

This volume is intended to provide fusion reactor designers a detailed survey of existing, critically assessed data for the behaviour of plasma facing materials under particle impact. Volume 9 of Atomic and Plasma-Material Interaction Data for Fusion is the result of a three year Co-ordinated Research Project on Atomic and Plasma–Wall Interaction Data for Fusion Reactor Divertor Modeling, 1998–2000.

The International Atomic Energy Agency expresses its appreciation to the contributors to this volume for their dedicated effort and co-operation.

EDITORIAL NOTE

This publication has been prepared from the original material as submitted by the authors. The views expressed do not necessarily reflect those of the IAEA, the governments of the nominating Member States or the nominating organizations.

The use of particular designations of countries or territories does not imply any judgement by the publisher, the IAEA, as to the legal status of such countries or territories, of their authorities and institutions or of the delimitation of their boundaries.

The mention of names of specific companies or products (whether or not indicated as registered) does not imply any intention to infringe proprietary rights, nor should it be construed as an endorsement or recommendation on the part of the IAEA.

The authors are responsible for having obtained the necessary permission for the IAEA to reproduce, translate or use material from sources already protected by copyrights.

CONTENTS

Atomic and plasma-wall interaction issues in divertor plasma modeling	1
<i>R.K. Janev</i>	
Electron impact ionization of edge plasma constituents	11
<i>S. Matt, T. Fiegele, G. Senn, K. Becker, H. Deutsch, O. Echt, A. Stamatovic, P. Scheier, T.Märk</i>	
Electron-molecule dissociation cross-sections of H ₂ , N ₂ and O ₂ in different vibrational levels	47
<i>M. Capitelli, R. Celiberto, A. Eletskaa, A. Laricchiuta</i>	
Dynamical calculations of state to state and dissociation cross-sections for atom-molecule collision processes in hydrogen	65
<i>F. Esposito, M. Capitelli</i>	
Collision integrals of high temperature hydrogen species	75
<i>C. Gorse, M. Capitelli</i>	
Dissociative electron attachment to rovibrationally excited molecular hydrogen and its heavier isotopic variants	83
<i>J.M. Wadehra</i>	
Dissociative recombination and excitation in fusion edge plasmas	97
<i>J.B.A. Mitchell</i>	
Elastic and inelastic collision processes at low energies which involve hydrogen ion, atoms and molecules	135
<i>P.S. Krstić, D.R. Schultz</i>	
Calculations of charge transfer and ionization cross-sections in collision between multicharged ions A ^{q+} (1 ≤ q ≤ 8) and atomic hydrogen	159
<i>C. Harel, H. Jouin, B. Pons, L.F. Errea, J.D. Gorfinkiel, C. Illescas, A. Macías, L. Méndez, A. Riera</i>	
Calculations of charge transfer and ionization cross-sections for ion — H ₂ (D ₂ ,DT,T ₂) collisions	167
<i>D. Elizaga, L.F. Errea, J.D. Gorfinkiel, C. Illescas, A. Macías, L. Méndez, I. Rabadán, A. Riera, A. Rojas, P. Sanz</i>	
State-selective and total electron capture, excitation and ionization cross-sections for slow collisions of H(2s) and He ⁺ (2s) with H ⁺ , He ²⁺ , Li ³⁺ , Be ⁴⁺ , and B ⁵⁺	179
<i>E.A. Solov'ev, J.A. Stephens, R.K. Janev</i>	
Cross-sections for ion production in H ⁺ + H ₂ collisions calculated with the trajectory-surface-hopping method	193
<i>A. Ichihara, O. Iwamoto, K. Yokohama</i>	
Isotope effect on dynamics of a collinear He + H ₂ ⁺ collisions	237
<i>K. Onda</i>	
Recombination of hydrogen on a carbon surface	267
<i>M. Rutigliano, M. Cacciatore, G.D. Billing</i>	
Above surface neutralization of highly charged ions interacting with a metal surface	281
<i>M.N. Mirakhmedov, R.A. Salimova</i>	
Some features of scattering, sputtering and ion emission in hyperthermal energy range	293
<i>V.Kh. Ferleger, U.Kh. Rasulev, I.A. Wojciechowski</i>	
Nonelastic sputtering of ionic crystals under electron, cesium and multiply charged ion bombardment	307
<i>B.G. Atabaev, Sh.S. Radzhabov, R. Dzhabbarganov, N.G. Saidkhanova</i>	

Atomic physics and plasma wall interaction issues in divertor plasma modeling

R.K. Janev

National Institute for Fusion Science, Gifu, Japan
Macedonian Academy of Sciences and Arts, Skopje, Macedonia

Abstract. The role of atomic, molecular and plasma wall interaction processes in divertor plasmas of magnetic fusion devices is briefly outlined. Some critical issues in the atomic physics and plasma wall interaction databases, which determine the accuracy and predictive capabilities of divertor plasma modeling codes, are discussed in more detail.

1. Introduction

The control of plasma burn conditions in a magnetic fusion reactor (or the energy confinement of presently operating large tokamak devices) requires control of the impurity ingress from the wall into the main plasma and exhaust of the thermal reactor power and helium ash from the D-T reactor. Medium- and high-Z wall impurities, even in trace concentrations, may extinguish the thermonuclear burn (due to excessive radiative losses), while accumulated fusion-born alpha particles in the reacting D-T plasma can reduce its reactivity below the ignition threshold (fuel dilution). Thermal power exhaust is also required to avoid achieving the bremsstrahlung radiation limit (at high plasma temperatures). The poloidal divertor concept [1] is currently considered as the most effective approach to solving the impurity control and thermal power exhaust problems in the present large tokamak devices and future fusion reactors. The main idea of poloidal divertor is to convert the radial (cross-field) plasma and impurity motion in the peripheral region of the main torus into one parallel to the magnetic field lines and direct it outside the main torus into a smaller chamber (divertor) located outside the torus. This is achieved by letting the peripheral magnetic field lines to be open and strike some material boundaries (plates) in the divertor chamber. The scrape-off (peripheral) plasma, outside the last closed magnetic flux surface (separatrix), becomes subject of strong conduction forces created by the large temperature gradients existing between the separatrix and the bottom of divertor region (divertor plates). This intense conductive flow in the scrape-off plasma layer directs towards the divertor region not only the radial plasma fluxes (thus strongly reducing their impact on the tokamak wall and thereby the impurity generation on the walls), but it also diverts the radial motion of wall impurities and directs them towards the divertor (thus strongly reducing the impurity ingress in the main plasma). While providing a solution to the impurity and thermal power exhaust problems, the divertor concept creates a severe material problem. The heat and particle fluxes directed on the divertor plates are so large that the resulting thermal loads are an order of magnitude (or more) larger than those which can be withstood by any of presently available materials. Reduction of these thermal loads on divertor plates to acceptable levels (a few kW/m²) is a necessary condition for the effective operation of a divertor.

The presently followed approach to solving this problem is an active divertor plasma cooling and dispersion of directed plasma momentum over the divertor sidewalls. The divertor plasma

cooling is achieved by controlled injection (seeding) of recyclable impurities (such as Ne, Ar, Kr) in the divertor region (radiative cooling) and of cold molecular hydrogen (dissociative cooling). The hydrogen atoms from the molecule dissociation serve as an efficient medium for dissipation of directed plasma momentum by elastic (momentum transfer) and charge exchange ion-atom collisions. As a result of these atomic/molecular processes, the plasma temperature in the divertor region drops from its values of 100–200 eV at the entrance in the divertor chamber to about 1 eV near the divertor plates, and the thermal load to the plates is drastically reduced. Moreover, when the plasma temperature drops below 2–3 eV and the density of molecular hydrogen is of the order of divertor plasma density (10^{14} – 10^{15} cm⁻³), volume plasma recombination can occur, leading to its physical detachment from the plates [2, 3]. This plasma detachment phenomenon is particularly beneficial for the reduction of thermal loads on divertor plates.

Under the plasma conditions existing in the divertor (temperatures of 1–30 eV, plasma and neutral densities of 10^{14} – 10^{15} cm⁻³), an extremely large number of collision processes can occur between the plasma constituents themselves and of plasma constituents with the divertor walls. The composition of a typical divertor plasma includes, besides the plasma electrons and protons, the hydrogenic species H, H₂, H₂⁺, H⁻ (and possibly H₃⁺), generic atomic impurities such as O, C, Be, W, ... (and their low charged ions), deliberately injected impurities, such as Ne and Ar, and molecular impurities such as O₂, CO, CO₂, C_xH_y, etc. In a fusion reactor, helium atoms and its ions will also be present in the divertor region at a significant (up to 10%) concentration level. Due to several specific processes (in the gas phase and in surface collisions), hydrogen (and impurity) molecules may also exist in the plasma in excited vibrational states, which makes the plasma kinetics extremely complex.

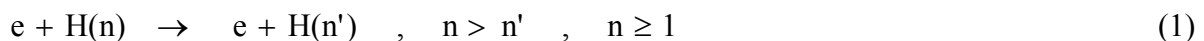
Surveys of atomic, molecular and plasma wall interaction processes in the divertor region have been published in the past [4–6], including the description of their role in the divertor plasma dynamics. Here we shall give a brief account of these processes from the point of view of divertor plasma modeling.

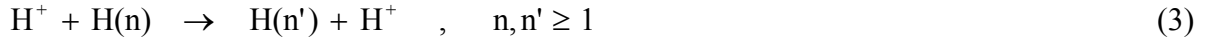
The modeling of divertor plasmas includes several aspects: plasma (particle, momentum and energy) transport, impurity transport, neutral particle transport, plasma radiative (and other energy) losses, plasma impurity radiation for diagnostic purposes, etc. All these aspects are, of course, mutually related, and for each of them specific modeling codes have been developed. The most elaborate divertor plasma transport codes (e.g. B2 code) and neutral particle transport codes (e.g. EIRENE) [7] have already been coupled in comprehensive computer modeling packages.

2. Atomic and molecular processes in a divertor plasma

2.1. Atomic and molecular hydrogen

Collision processes of plasma electrons and ions (protons in a H-plasma) with atomic and molecular hydrogen in the divertor are of fundamental importance for the plasma and neutral particle transport. The processes involving atomic hydrogen include:



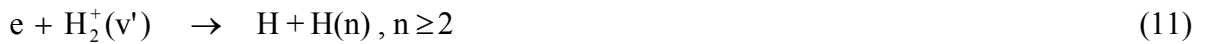
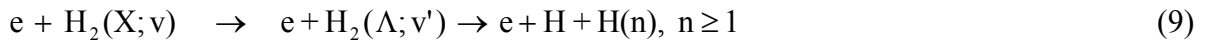
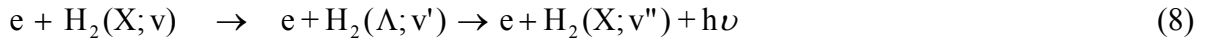
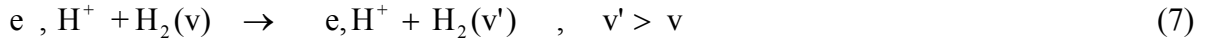


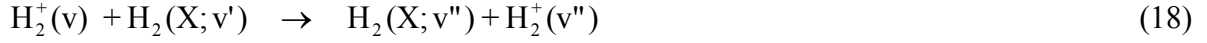
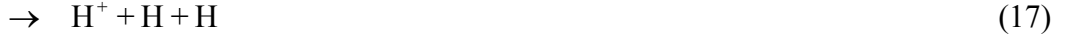
as well as the radiative recombination



which becomes important at temperatures below $\sim 0.2\text{--}0.3$ eV. The three-body recombination (the inverse reaction (2)) is important only for plasma temperatures below $0.3\text{--}0.5$ eV and plasma densities above $5 \times 10^{14} \text{ cm}^{-3}$. A radiative-collisional model for atomic hydrogen in divertor plasma, by which the plasma cooling due to atomic hydrogen in divertor plasma is calculated, requires, of course, inclusion in the kinetic scheme also the process of spontaneous emission of excited states, $\text{H}(n) \rightarrow \text{H}(n') + h\nu$, $n' < n$. The plasma cooling due to the processes involving atomic hydrogen is by far insufficient for significant reduction of divertor plasma temperature. However, the ionization processes (2) and (5), and particularly the charge exchange process (3), have a significant impact on the plasma transport.

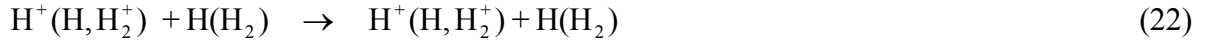
The processes involving molecular hydrogen (assumed to be also in vibrationally excited states) are much more numerous. This is not only due to the internal degrees of freedom in H_2 , but also because of the existence of dissociative (antibonding) electronic states of H_2 , as well as of resonant states in the $(e+\text{H}_2)$ system. Relevant to the plasma transport and cooling problems are the processes:





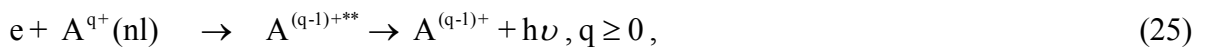
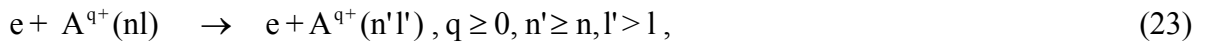
where X and Λ denote the ground and an electronically excited states of H_2 . Construction of a collisional-radiative model for the molecular hydrogen in a divertor plasma requires knowledge of the cross sections not only for the above processes but also cross section information for all similar processes when the initial state of H_2 is an excited electronic state. Such information is presently practically non-existent. Estimates of the plasma cooling capacity of molecular hydrogen show that it is insufficient for reducing divertor temperatures in a high power fusion device below 4–5 eV. As reactions (7)–(21) however show, the molecular hydrogen has a major impact on the plasma transport in the divertor. These processes also play a major role in the neutral particle transport.

From the point of view of plasma and neutral particle transport, and particularly in the context of plasma momentum dissipation and particle exhaust, besides the charge exchange processes (3) and (16), a prominent role play also the elastic (momentum transfer) processes in ion-neutral and even neutral-neutral particle collisions,



2.2. Atomic and molecular impurities

Atomic impurities (C, O, Be, W, B, ...) in the divertor region may exist in both neutral (near the walls) and ionized (in the divertor interior) form. Due to the relatively low divertor plasma temperatures (1–30 eV), the charge state (q) of ionized atomic impurities (A^{q+}) is also low ($q \leq 3-4$). The molecular impurities (CO , O_2 , CO_2 , $\text{C}_x\text{H}_y, \dots$) in the divertor region can normally be either neutral (near the walls) or singly charged, because their dissociation energy rapidly decreases with the increase of their charge. From the point of view of plasma cooling (but also from the point of view of impurity transport) the most important electron-impact processes of atomic impurities (designated by A) are:



$$e + A^{q+}(nl) \rightarrow A^{q+**} \rightarrow e + A^{(q+1)+} + e, q \geq 1, \quad (27)$$

$$\rightarrow e + A^{(q+2)+} + 2e \quad (28)$$

$$e + A^{q+}(nl) \rightarrow A^{(q-1)+} + h\nu, q \geq 1, \quad (29)$$

where two stars on A^{q+} indicate a doubly excited state. In the level population kinetics, the inverse processes of (23) and (24), as well as the spontaneous radiative decay of excited states, are also included. The above processes provide a strong cooling of the divertor plasma which increases with the increase of atomic number Z of the impurity A .

Proton-impact processes with the neutral impurities are, generally, not important, except when the conditions for a quasi-resonant (or accidental resonance) charge exchange (as in the case of $H^+ + O$) are fulfilled. However, the charge exchange processes of multiply charged impurity ions A^{q+} ($q \geq 2$) with H , H_2 and He (in fusion reactors), i.e.

$$A^{q+} + H(H_2, He) \rightarrow A^{(q-1)+} + H^+(H_2^+, He^+), \quad (30)$$

as well as other two-electron transition processes, such as double electron capture and transfer ionization,

$$A^{q+} + H_2(He) \rightarrow A^{(q-2)+} + 2H^+(He^{2+}) \quad (31)$$

$$\rightarrow A^{(q-1)+} + H_2^+(He^+) + e \quad (32)$$

may be important, particularly when q is large.

The electron-impact processes with molecular impurities are similar to those of the molecular hydrogen. However, when the molecule contains three or more atoms, the number of dissociative excitation, ionization and recombination channels increases drastically. For instance, while the electron-impact dissociative excitation of H_2 gives only two fragments, the similar process of CH_4 may produce $CH_3 + H$, $CH_2 + 2H$ (or H_2), $CH + 3H$ (or $H + H_2$), $C + 2H_2$ (or $2H + H_2$), with the atomic and molecular products both being in excited (electronic and/or vibrational) states. Similarly, the $e + H_2^+$ recombination produces only two ($H, H(n)$) fragments, while the recombination of CH_4^+ with electrons produces $CH_3 + H$, $CH_2 + 2H$, $CH_2 + H_2$ and $CH + H + H_2$. The number of dissociative channels of more complex hydrocarbon molecules (such as C_2H_6 or C_3H_8), which are always present in divertor plasmas when wall materials contain carbon (in one form or another), dramatically increases with the increase of molecular complexity. The molecular fragmentation processes lead to multiplication of molecular species in the plasma and to long reaction chains before the complete dissociation of the initial molecule is accomplished. Obviously, the molecular impurity reaction kinetics becomes very complex, even without inclusion of the vibrational states of initial molecule and molecular fragments (reaction products) into account.

The proton-impact processes with neutral molecular impurities are, in general, less important than those of electrons, except for the excitation of vibrational and rotational transitions when the opposite is true. However, if the molecule contains a large number of atoms (like the

heavier hydrocarbons) and its ionization potential is smaller than 13.6 eV (again like C_xH_y), the electron capture by slow protons from such molecule can have a quasi-resonant character, and therefore a large cross section in the eV-energy region. The quasi-resonant electron capture conditions in these systems can easily be met because of the many vibrational modes (and states) of the molecular (product) ion which are available to absorb the reaction exothermicity. Most of the C_xH_y molecules have large, quasi-resonant charge exchange cross sections with protons in the energy range pertinent to divertor plasma temperatures. In the temperature region below 1 eV, heavy particle exchange reactions (reactive collisions) start to become increasingly important with decreasing the temperature in proton-molecule collisions due to the formation of intermediary compounds in long living states.

2.3. Status of cross section databases and divertor modeling issues

The atomic and molecular processes discussed in the preceding subsections are directly related to the modeling of plasma and neutral particle transport, impurity transport and radiation, volume plasma recombination and other properties of divertor plasmas. Their inclusion in the modeling codes is essential for describing the observed properties and radiation of divertor plasmas, as well as for making reliable predictions. The predictive power of the modeling codes depends not only on the comprehensive account of all important collision processes, but also on the accuracy of the cross sections (or rate coefficients) of the processes included in the codes. We shall give here a general assessment of the data status for the above discussed processes and emphasize some critical data-related aspects of the modeling codes.

A comprehensive and sufficiently accurate (for the purposes of plasma modeling) database presently exists only for the processes of hydrogen [8], helium [9] and lithium [10] atoms colliding with electrons, protons and multiply charged ions. (Neutral lithium beams are currently being used for divertor plasma diagnostics on some tokamaks.) The database for electron-impact processes with molecular hydrogen and its ions (H_2^+ , H_3^+) is also available [11], but mainly for the ground electronic and vibrational states of H_2 . A significant extension of this database has recently been made to include the excitation, ionization and electron attachment processes, (8)–(10), (14), of vibrationally excited H_2 (or H_2^+) and their isotopes [12]. This database, however, cannot be considered complete because the important reactions (13) and (15) are still not covered. The excitation of higher electronic states of H_2 , as well as the excitation and ionization from excited electronic states of H_2 , have still not been studied, with exception of a few cases [13]. The lack of such data for the excited electronic states of H_2 , prevents to construct a reliable collision-radiative model for H_2 . Moreover, such a model would require coupling of electronic transition processes in H_2 with the full vibrational kinetics, as well as with the reaction kinetics of H_2^+ and H_3^+ ions. Having in mind that several of the processes in the reaction scheme (7)–(21) produce vibrationally excited H_2 , and that for many of the processes involving initially vibrationally excited H_2 the cross sections are still not known, one is led to the conclusion that the present modeling codes for divertor plasma and neutral particle transport are still incomplete. The cross sections and reaction rates for the important ion-conversion reaction (16) and $H^+ + H_2(v)$ dissociation (17) have only recently become available from the classical-trajectory-surface-hopping method [14, 15]. More accurate quantal calculations for these reactions in the thermal energy region would be desirable. Except for a few transitions, cross section data are presently not available also for the equally important reaction



although some calculations are underway [16].

The incompleteness of the atomic/molecular collision database for divertor plasma modeling is further emphasized by the fact that some of the molecular processes are mass-dependent (e.g. processes proceeding via formation of a $(\text{H}_2)^*$ resonance, as (13)–(15), or of a long lived intermediary compound, as H_3^+) and their cross section for the different hydrogen isotopes are not the same. From the point of view of modeling a D_2 - T_2 divertor plasma, the available cross sections for these processes related to H_2 will not be sufficient, but new cross section information for the isotopic molecules D_2 , DT and T_2 will be required for such processes.

Regarding the elastic and momentum transfer processes involving ion-neutral and neutral-neutral hydrogenic isotopomers, highly accurate and virtually complete cross section (integral and differential) information is available in the region below 100eV [17].

The collisional database for electron-impact processes (excitation, ionization, recombination) involving low-Z atomic divertor plasma impurities (Be, B, C, O) is to a large degree complete and of adequate accuracy for impurity transport and radiative cooling calculations. For the medium- (Ne, Ar) and high-Z (Kr, W) impurities, however, the database for these processes (particularly for the transitions between excited states) is still incomplete. For the collision processes of atomic impurity ions with H, He and H_2 , Eqs. (30)–(32), there is a large body of cross section information (see e.g. the collections [18–21]), but it is still rather incomplete. Particularly large gaps (and cross section uncertainties) exist for the state selective electron capture cross sections involving incompletely stripped ions, for the two-electron transition processes (31) and (32), and for the processes involving excited H and He atoms. Without completion of the database for these processes, the impurity transport and radiation in the divertor region cannot be modelled with an adequate accuracy.

A large amount of data for the collision processes of diatomic molecular impurities (e.g. CO, CH, O_2) with plasma electrons and ions is available in the literature, although no systematic compilations and critical assessments of these data for modeling purposes have been made so far. However, for the more complex molecular impurities, such as the polyatomic hydrocarbons C_xH_y , the cross sections for both electron- and proton-impact processes are very scarce (see, e.g. [22, 23]). Particularly deficient are the data for the dissociative excitation of C_xH_y molecules by electron impact, for the dissociative recombination of C_xH_y^+ ions with electrons (with identification of the many dissociation channels) and for the electron capture processes of C_xH_y with protons. The modeling of the transport and radiation of these abundant impurities in the divertor plasma presently cannot be done at any reasonable level of reliability. This also implies that the transport of carbon impurities in the divertor plasma cannot be reliably modelled. Several experimental and theoretical groups are, however, currently involved in the efforts to improve the collisional database for C_xH_y impurities, and the collection and critical assessment of first results of these efforts is underway [24].

3. Plasma wall interaction processes

The energies of plasma particles (electrons and protons), hydrogen neutrals and impurity ions and atoms in the divertor region are typically below 20–30 eV and their interaction processes with the divertor material surfaces (of the divertor side walls and divertor plates) are fairly

numerous and complex. This complexity particularly increases when the collision energy of the interacting atomic particle with the surface drops below $\sim 10\text{--}15$ eV and the quantum-mechanical features of the interaction start to manifest themselves to full extent. This energy region is below the threshold for physical sputtering for most of the solid materials so that one of the most powerful processes characterising the interaction of energetic plasma and impurity particles with the walls of the fusion device is not operating in the divertor for the medium- and high-Z wall materials. For the low-Z wall materials, (such as Be and C), physical sputtering occurs in its near threshold region and, therefore, the corresponding yields are rather small. The available experimental data, as well as those produced by the TRIM. SP code, have been collected in Ref. [25] and presented in analytic form. For graphite materials, the chemical erosion is a much more important process at plasma and impurity energies pertinent to the divertor temperatures. Chemical erosion yield data for various graphite materials, surface conditions, and projectile particles are fairly abundant in the literature, and these data have recently been compiled and critically assessed in Ref. [26]. An important issue in the field of chemical erosion, which has an impact on divertor plasma, particle and impurity transport modeling, is the flux and fluence dependence of the erosion yield. There is still not well established relationship of the yield on these parameters for all carbon materials. The lack of understanding of basic physical mechanisms underlying the chemical erosion phenomenon, limits the data for this process only to those produced by the experiment. Due to the varying experimental conditions from experiment to experiment (and sometimes, even within the same experiment), there are large uncertainties (within a factor of two, or more) in the chemical erosion data. An outstanding issue from the point of view of modeling of a $\text{H}_2\text{-D}_2$ divertor plasma is the isotope dependence of the C_xH_y erosion yield. There are strong indications provided by some experimental groups that the C_xD_y production yield on graphite bombarded by D atoms is much larger (50–100%) than the yield of C_xH_y production when the same graphite material is bombarded with H of same energy (see e.g. [26]). The chemical erosion data of this kind, produced by another experimental group, are inconclusive in this respect (due to large uncertainties) [26]. The isotope dependence of chemical erosion yield has far-reaching consequences on the operation of the divertor and, in particular, on the hydrogen recycling and maintaining the isotope mix ratio in a fusion reactor.

Related to the hydrogen recycling in divertor (and the toroidal device as well), is the problem of hydrogen (isotope) retention in and release from the divertor materials. Even for pure materials of fusion interest (such as Be, W), the parameters determining the hydrogen retention and release (such as solubility, diffusivity and recombination coefficients in the transport equation of hydrogen particles in the bulk material) have still not been established sufficiently accurately. This information is virtually completely absent for the so-called mixed materials (such as BeC, BeW, CW) which are formed on the divertor walls due to the redeposition on the surfaces of eroded material. The erosion (in particular the chemical erosion of carbon containing materials) yields of mixed materials is also virtually unknown. The absence of reliable data (or data at all) on the erosion of wall materials and hydrogen (retention and) release leaves the divertor plasma modelers with large uncertainties in the hydrogen and impurity (atomic and molecular) influxes into the divertor region, which are important source terms in the transport (particle, energy and momentum) equations.

Furthermore, since the divertor plasma modeling is presently performed on a fairly detailed quantum level (with inclusion of electronically and vibrationally excited states of atomic and molecular particles), it is obviously important to know not only the overall (hydrogen and impurity) fluxes entering the plasma from divertor walls, but also the composition of these fluxes with respect to their aggregate (atom or molecule), charge (ion or neutral) and quantum

(ground or excited) state. This level of information on the composition and charge/quantum states of particles entering the plasma from the walls requires a microscopic (quantum) treatment of the particle-surface interaction processes and detailed knowledge of the mechanisms of these processes. A brief, qualitative review of these processes is given elsewhere [27]. While the mechanisms of atom/ion surface interaction processes (such as electron capture, two- and multiple-electron transition Auger processes) are fairly well established and the methods for their theoretical description (and rate calculations) adequately well developed, the processes involving molecular break-up, formation and desorption, or particle sticking or desorption (e.g. by plasma particle impact) are still in the stage of development (see e.g. [28–30]). The molecular dynamics codes, coupled with proper description of the quantum effects, are presently the most powerful approach to the study of molecular processes on solid surfaces. Development of computer code packages which describe the particle-surface interaction properly, include the particle retention and release processes, and provide information on the aggregate, charge and quantum state of particles coming back to divertor plasma from the walls, is a challenging next step in the divertor plasma modeling. This step would allow treatment of the volume and plasma wall interaction processes at the same level of detail, as well as a self-consistent description of the plasma, neutral particle and impurity behaviour and properties in the divertor region.

4. Conclusions

The present review of atomic, molecular and plasma wall interaction processes in fusion divertor plasmas, although kept relatively brief, has shown that there are still remaining outstanding issues in the databases for these processes which prevent a detailed modeling of the dynamics and properties of divertor plasma. The lack of data is to a large degree related to the lack of appropriate experimental and theoretical methods for the study of some of these processes, and in many cases to the limited knowledge and understanding of the underlying physical mechanisms. The largest gaps in the databases are in the areas of collision processes involving molecular species (both hydrogen and molecular impurities) and plasma wall interaction processes. Since the current modeling of hydrogen behaviour in the divertor plasma requires inclusion of complete collisional-radiative models for the atomic and molecular hydrogen, the cross sections for collision processes of these species in excited (electronic and vibrational) states must be known. As we have seen, the database for the processes involving vibrationally excited hydrogen is fairly incomplete. Even more incomplete is the database for some of the important divertor molecular impurities, such as the hydrocarbons. From the point of view of fusion reactor design purposes, the information on collision processes is required not for lightest molecule (H_2), but rather for D_2 , DT and T_2 . For many types of processes, the cross section show a nontrivial mass dependence and the cross section information related to H_2 -processes cannot be used.

The databases for the plasma wall interaction processes are much more incomplete than those for the volume plasma (gas phase) processes. Here, even the basic mechanisms for many of the numerous processes are still not well understood. The description of these processes on a quantum level is required to match the level of description of atomic/molecular processes in the divertor plasma. Outstanding modeling issues in this data area are related to the information on the aggregate, charge and quantum state distribution of the hydrogen entering the plasma from divertor walls, and to the accurate composition of impurity influxes from the walls (as well as the mechanisms of their formation). A major effort is still required to reach a full quantum level of description of plasma wall interaction processes in order to achieve the necessary self-consistent modeling of divertor plasmas.

REFERENCES

- [1] JANEV, R.K., in “Atomic and Molecular Processes in Magnetic Fusion Edge Plasmas”, (JANEV, R.K., Ed.), Plenum Press, New York, 1995, 1.
- [2] HUTCHINSON, I.H. et al., *Phys. Plasmas* **1** (1994) 1511.
- [3] LIPSCHULTZ, B. et al., *J. Nucl. Mater.* **220–222** (1995) 50.
- [4] HARRISON, M.F.A., in “Atomic and Plasma-Material Interaction Processes in Controlled Thermonuclear Fusion”, (JANEV, R.K., DRAWIN, H.W., Eds.), Elsevier, Amsterdam, 1993, 285.
- [5] POST, D.E., *J. Nucl. Mater.* **220–222** (1995) 143.
- [6] JANEV, R.K., *Contrib. Plasma Phys.* **38** (1998) 307.
- [7] REITER, D., in “Atomic and Plasma-Material Interaction Processes in Controlled Thermonuclear Fusion”, (JANEV, R.K., DRAWIN, H.W., Eds.), Elsevier, Amsterdam, 1993, 243.
- [8] JANEV, R.K., SMITH, J.J., *At. Plasma-Mater. Inter. Data Fusion (Suppl. Nucl. Fusion)* **4** (1993) 1.
- [9] RALCHENKO, Yu.V. et al., Report NIFS-DATA-XX (2000, in preparation).
- [10] WUTTEE, D., *ADNDT* **65** (1997) 155; SCHWEINZER, J. et al., *ADNDT* **72** (1999) 239.
- [11] JANEV, R.K. et al., “Elementary Processes in Hydrogen-Helium Plasmas”, Springer, Berlin-Heidelberg, 1987.
- [12] CELIBERTO, R. et al., *ADNDT* (2000, in press).
- [13] CELIBEROT, R. et al., *Phys. Rev.* **A60** (1999) 2001.
- [14] ICHIHARA, A. et al., *At. Plasma-Mater. Inter. Data Fusion* **9** (2001) (this volume).
- [15] ICHIHARA, A. et al., *J. Phys.* **B33** (2000, in press).
- [16] KRSTIC, P.S., SCHULTZ, D.R. (private communication, 2000).
- [17] KRSTIC, P.S., SCHULTZ, D.R., *At. Plasma-Mater. Inter. Data Fusion* **8** (1998) 1.
- [18] PHANEUF, R.A. et al., *Atomic Data for Fusion*, **5**, (1987) ORNL-6090.
- [19] JANEV, R.K., Ed., *Physica Scripta* **T37** (1991).
- [20] JANEV, R.K., Ed. *Physica Scripta* **T62** (1996).
- [21] *At. Plasma-Mater. Inter. Data Fusion*, **3** (1992), **6** (1995).
- [22] TAWARA, H., Report NIFS-DATA-19 (1992).
- [23] TAWARA, H. et al., Report NIFS-DATA-6 (1990).
- [24] JANEV, R.K. et al., Report NIFS-DATA (in preparation).
- [25] ECKSTEIN, W. et al., *At. Plasma-Mater. Inter. Data Fusion*, **7-B** (2001) 1.
- [26] HAASZ, A.A. et al., *At. Plasma-Mater. Inter. Data Fusion*, vol. **7-A** (1998) 1.
- [27] SNOWDON, K.J., TAWARA, H., *Comm. At. Mol. Opt. Phys.* **34** (1998) 21.
- [28] RUTIGLIANO, M. et al., *At. Plasma-Mater. Inter. Data Fusion*, **9** (2001) (this volume).
- [29] MURAKHMEDOV, M.N., SALIMOVA, R.A., *At. Plasma-Mater. Inter. Data Fusion* **9** (2001) (this volume).
- [30] VERLEGER, V.Kh. et al., *At. Plasma-Mater. Inter. Data Fusion* **9** (2001) (this volume).

Electron impact ionization of edge plasma constituents

S. Matt^a, T. Fiegele^a, G. Senn^a, K. Becker^b, H. Deutsch^c, O. Echt^d,
A. Stamatovic^e, P. Scheier^a, T.D. Märk^f

^a Institut für Ionenphysik, Leopold Franzens Universität, Innsbruck, Austria

^b Department Physics, Stevens Institute Technology, Hoboken, New Jersey,
United States of America

^c Institut für Physik, Universität Greifswald, Greifswald, Germany

^d Department of Physics, University New Hampshire, Durham, New Hampshire,
United States of America

^e Faculty of Physics Beograd, Beograd, Yugoslavia

^f Dept. Plasmaphysics, Comenius Univerzita, Bratislava, Slovakia

Abstract. In order to understand and elucidate the role of the radiative and collisional processes in the plasma edge region of fusion reactors, it is essential to have available a detailed and quantitative knowledge on these elementary processes such as cross sections, reaction rate coefficients etc. Much effort has been recently devoted to the experimental determination of absolute partial and total electron impact ionization cross sections of molecules and radicals due to the ever increasing importance of these cross sections in the diagnostics of many applications such as low- and high- temperature plasma physics and chemistry, atmospheric physics and mass spectrometry. In addition supporting calculations have recently been developed in order to allow the analytic quantitative description of these cross section functions for modelling codes using a novel approach to the determination of electron induced appearance energies. In this review we will therefore discuss (i) experimental studies on electron impact ionisation of neutral molecules and electron impact ionisation of molecular ions including the measurement of ionization cross sections and appearance energies and the determination of kinetic energy release distribution for dissociative ionization and (ii) the theoretical determination of electron impact ionisation cross sections for the single ionisation of molecules and the multiple ionisation of atoms.

1. Introduction

Recent studies in the field of thermonuclear fusion based on the magnetic confinement of high temperature plasma have demonstrated that the conditions at the plasma periphery (“plasma edge”) play an important role for achieving, sustaining and controlling the thermonuclear fusion plasma [1]. In order to understand and elucidate the role of the radiative and collisional processes in this plasma edge region (in particular (i) their influence on the plasma properties and dynamics and (ii) their use for controlling the plasma conditions), it is essential to have available a detailed and quantitative knowledge on these elementary processes such as cross sections, reaction rate coefficients etc.

Because of the relatively low temperature in the plasma edge the plasma contains — besides electrons and atomic ions — a significant number of neutral hydrogen atoms and low charged atomic and molecular impurities (produced and introduced for instance via plasma/wall interactions, via diagnostics or via cooling). According to Janev [1] the most important collision processes (from a standpoint of their effects on plasma edge properties and behavior such as ionization balance, plasma energy, plasma transport etc.) are electron impact excitation/ionization reactions with plasma edge atoms, ions and molecules. In a recent book edited by Janev [1] three chapters [2–4] deal in detail with the present knowledge concerning the electron impact ionization of plasma edge atoms, plasma edge ions and plasma edge molecules. The impurities present in such an edge plasma obviously will depend on the materials used for the plasma facing components (first wall, protective tiles, divertor plates, antennas for rf heating etc.) and on the gases introduced for cooling and diagnostic purposes.

Nevertheless Janev [1] and recently Post [5] have given lists of atomic and molecular impurities to be considered in such studies including the rare gases, Li, Be, B, C, N, O, Al, Si, Mg, Ti, Cr, Fe, Ni, Cu, Mo, Nb, Ta and W and H₂, CO, O₂, N₂, CO₂, H₂O, CH₄, C₂H₂, and C_nH_m. Some of these impurities may reach levels of about 1 to several percent of the plasma density. The most important impurity generating processes are according to Janev [1] thermal and particle-induced desorption and chemical sputtering from the walls.

Whereas electron impact ionization of neutral and ionized *atomic* targets is a well studied and documented subject [2, 3] (save for a few targets and for some cases involving multiple and step-wise ionization), the situation in case of *molecular* targets is far from satisfying. A similar situation exists for the area of plasma/wall interactions [6]. According to Tawara [4], who reviewed electron impact ionization of hydrocarbon molecules many data (concerning total and partial ionization cross sections) appear to be of relatively low accuracy or have not yet been measured (see Table 10 in Ref. [4]). The latter applies in particular to hydrocarbon molecular ions, where almost no experimental (and theoretical) studies exist (see also Ref [7]). Moreover, the subject of electron impact induced ionization of molecular ions has so far received very little attention (in contrast to the field of electron impact ionization of atomic ions [8]).

Spurred by these data needs in fusion edge plasmas [1, 4] we have carried out during the past five years the following experimental and theoretical studies for edge plasma constituents of interest:

- (i) Measurements of partial (and total) cross section functions for the electron impact ionization of neutral molecules and study of the kinetic energy release for the dissociative ionization of neutral molecules
- (ii) Experimental studies of the electron induced ionization and dissociation of molecular ions (identification of reaction channels, kinetic energy release measurements, cross section measurements) and
- (iii) Theoretical studies concerning the quantitative analytic description of electron impact ionisation cross sections for the single ionisation of molecules, multiple ionization and step-wise ionization of atoms and atomic ions.

These studies constituted on the one hand a continuation of previous research in this laboratory (i.e. on the experimental determination of accurate ionization cross sections for neutral molecules and on theoretical concepts for the prediction of ionization cross sections for various targets, i.e., atoms, molecules and clusters [9]) and on the other hand an extension of recently started experiments on the inelastic interaction of electrons with molecular ions [10]. In this review we will only discuss on the one hand experimental studies on electron impact ionisation of neutral molecules (Section 2) and electron impact ionisation of molecular ions (Section 3) and on the other hand the theoretical determination of electron impact ionisation cross sections for the single ionisation of molecules (Section 4) and the multiple ionisation of atoms (Section 5).

2. Experimental determination of electron impact cross sections of molecules

The general approach to the quantitative study of electron impact ionization and dissociative ionization of molecules is that of implementing an electron beam colliding either with a stagnant gas target or with a molecular beam. Assuming single collision conditions (i.e., $N_t L \sigma$

$\ll 1$, with N_t target density, L collision interaction length and σ cross section) the total positive ion current i_t produced along the interaction volume defined by L is

$$i_t = i_e N_t L z \sigma_t \quad (1)$$

where i_e is the electron current and σ_t is the *total* ionization cross section. If the product ions are analyzed with respect to their mass to charge ratio m/ze the respective individual ion current i_p measured is given by

$$i_p = i_e N_t L z \sigma_p \quad (2)$$

where σ_p is the *partial* ionization cross section, i.e., the cross section for the production of a specific ion irrespective of its charge ze . Therefore, the total ionization cross section is related to the partial cross section via the weighted sum

$$\sigma_t = \sum z \sigma_p \quad (3)$$

Experimental determination of the partial or the total cross section therefore involves the accurate measurement of the four quantities in equ. (1) and (2). At first sight this appears to be an easy task, however, as it has been discussed in detail in [11, 12, 13] there are a number of experimental conditions which have to be fulfilled in order to arrive at reliable and accurate cross sections. In the case of absolute total cross sections the most difficult parameter to be measured accurately is the target density N_t , whereas for partial cross sections the proper measurement of the individual ion currents for the various fragment ions using mass spectrometry proves to be the crucial point.

Progress has been very slow considering the fact that (i) these cross sections have now been measured since about the 1930s [14] and that (ii) their accurate knowledge is of great importance for mass spectrometry, plasma physics, etc [1, 15, 16]. Nevertheless, there have been some advances in experimental techniques in the seventies and early eighties; the corresponding results have been summarized in [9, 16–20] (see also earlier work referenced in these reviews). Despite these experimental improvements, large discrepancies existed for even simple molecular targets such as NH_3 (see for example Fig. 1 in Ref. [21] which shows a typical situation for total cross sections in 1986 as reported by [22]). In the past ten years or so, however, major progress has been achieved in both, experiment and theory (see below), the experimental progress being mainly due to improved measuring methods for the absolute gas density. Thus for a number of target systems reliable total electron impact ionization cross sections are available, where the data sets of several groups agree within a few percent (including also total cross sections obtained by summing up the partial cross sections measured by mass spectrometry). Deutsch et al. [23] have recently made extensive comparisons between available reliable experimental cross sections and the predictions of theoretical models for 31 molecules, see below. Fig. 1 summarizes today's situation concerning the total ionization cross section for NH_3 demonstrating the enormous progress since 1985 where data sets differed by more than a factor of two. Results concerning the molecules mentioned H_2 , CO , O_2 , N_2 , CO_2 , H_2O , CH_4 , C_2H_2 , and C_nH_m in the context of edge plasma applications are given in Section 4.

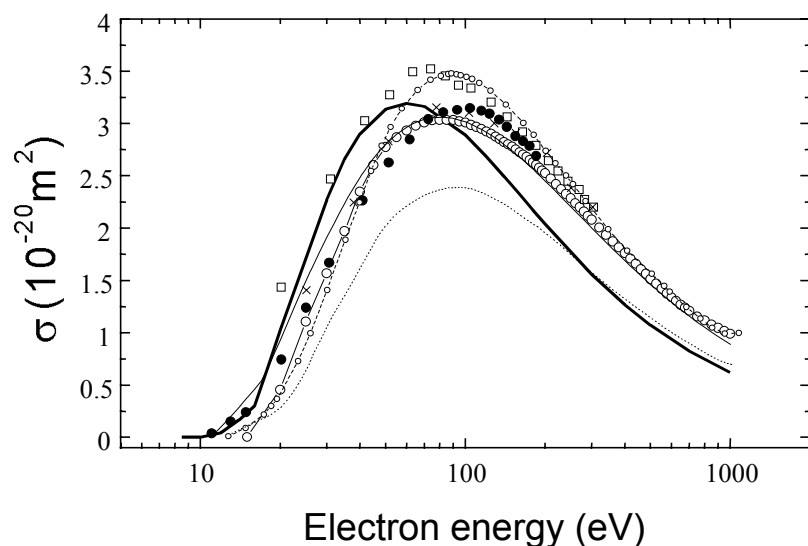


Figure 1. Total electron impact ionization cross section for NH_3 as a function of electron energy after [23]. The points denote experimental results from various groups and the lines denote calculations using the DM, BEB and JK approach (see below).

Particularly striking progress has been achieved in the field of partial ionization cross sections in the past 15 years with machines following two different philosophies. This has been achieved on the one hand by the sophisticated use of (modified) commercial machines as pioneered in Innsbruck involving the penetrating-field-extraction and ion beam-deflection method [24–26] and later on introduced in Greifswald [27] and on the other hand by the construction of dedicated experimental set-ups specifically designed for the use in this field. In each case the most important feature is the possibility to detect parent and fragment ions without discrimination by using controlled ion source extraction and mass spectrometer transmission techniques. In addition metastable decay has been taken into account quantitatively where important [26].

A detailed description of the apparatus and the experimental procedure used in our laboratory for the accurate measurement of partial ionization cross sections of atoms and of molecules has been given previously [24–26]. Briefly, the experimental set-up consists of a modified Nier-type electron impact ion source, a molecular beam source (either a Knudsen-type oven or a nozzle expansion source) and a high resolution double focussing Nier-Johnson sector field mass spectrometer (see Fig. 2). The performance and operating conditions of this apparatus have been continuously improved over the past 15 years. For instance, the introduction of the penetrating-field extraction in combination with a correction method based on ion trajectory calculations [24] allows to account for the energy dependent discrimination and the introduction of the ion beam-deflection method allows to account for discrimination at the mass spectrometer entrance slit by integration over measured ion beam profiles [25]. Today it is possible to measure with high accuracy (absolute) partial ionization cross section functions for atomic and molecular parent ions [9, 19] as well as partial ionization cross section functions for fragment ions formed with excess kinetic energy up to electron energies of 1000 eV [26].

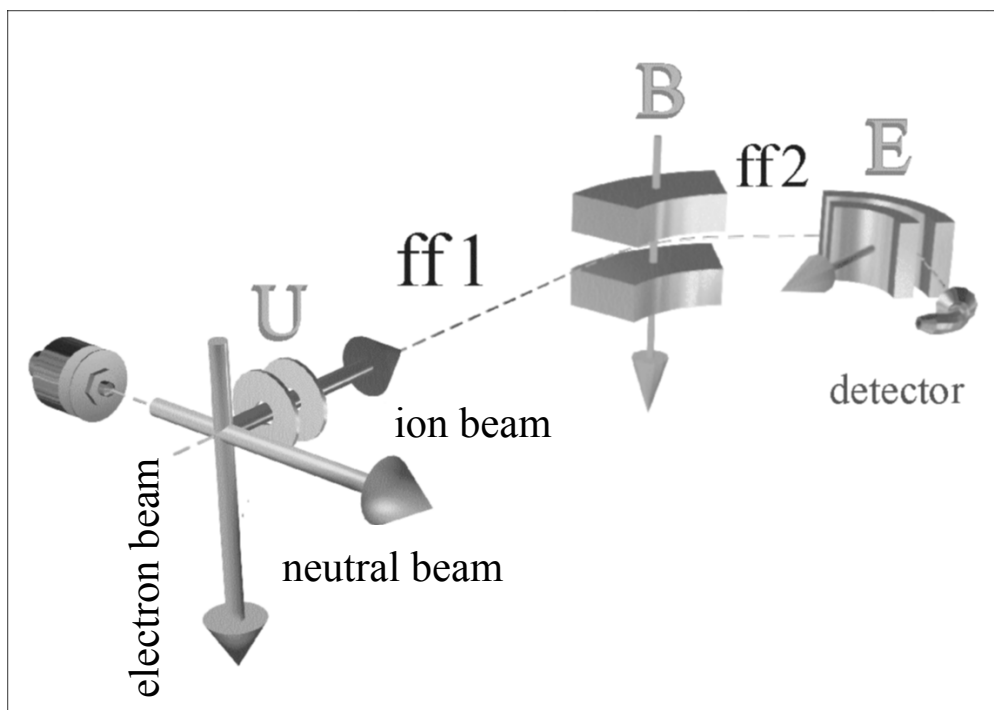


Figure 2. Schematic view of the two sector field mass spectrometer used in Innsbruck for the measurement of partial electron impact ionisation cross sections.

The performance of this improved instrument was tested recently in detail with CF_4 [24] and used then for the study of C_2H_6 [28] and C_3H_8 [25]. As shown and discussed in these papers it is necessary (in order to account quantitatively for discrimination effects in the case of fragment ions produced with excess kinetic energy in the ion source) and also possible to measure the kinetic energy distributions of the fragment ions formed by electron impact ionization in the ion source. Over the years we have developed in our laboratory two methods to measure this kinetic energy distribution, one method is based on the fact that the extracted ion beam shape contains information on the original ion kinetic distribution [29] and the other method relies on a retarding potential field method applied at the exit of the two sector field mass spectrometer [30].

Figure 3 shows as an example the production of CF^+ via electron impact ionization of CF_4 measured with this instrument (Fig. 2) designated by full squares demonstrating the importance of being able to detect also highly energetic fragment ions without discrimination, the earlier studies shown in this figure give cross sections that underestimated the corresponding ion yield. As already mentioned above an important feature in this context is the ability to determine the corresponding kinetic energy distribution of the fragment ions produced.

Figure 4 shows as an example (of current interest to the fusion community [4]) of kinetic energy distributions for the production of CH_3^+ produced by electron impact ionization of C_3H_8 measured by two different methods as described in Ref. [29, 30]. Besides thermal and quasi-thermal fragment ions this dissociative ionization channel also leads to the production of highly energetic ions with kinetic energies at around 3 eV.

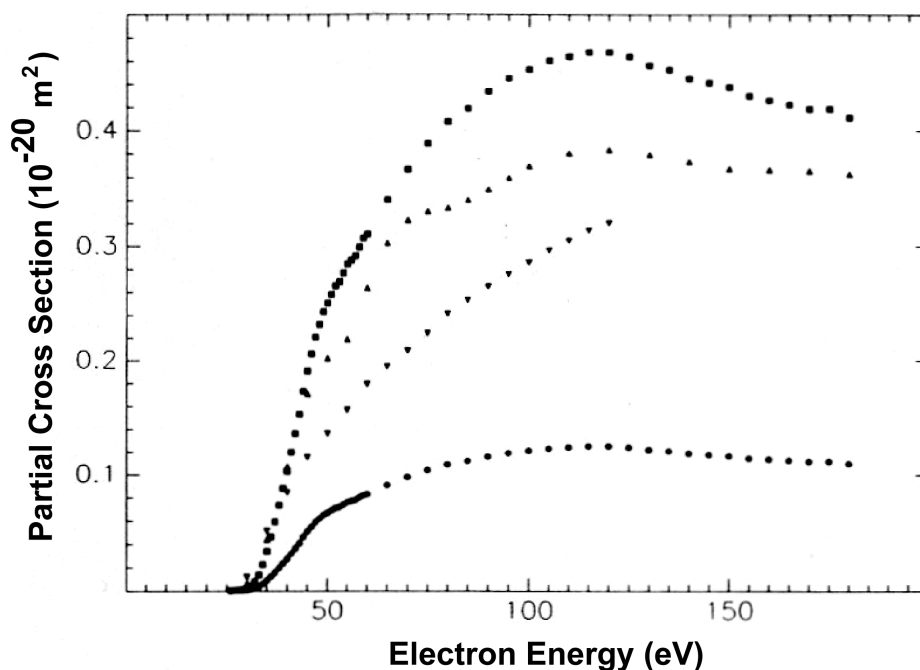


Figure 3. Partial electron impact ionization cross section for the production of CF^+ by electron impact ionization of CF_4 after [23]. Uncorrected data (see text) designated full circle: Stephan et al. [31], full inverted triangles: Poll et al. [32], full triangles: Ma et al. [33] and corrected data (see text) designated full squares: Poll et al. [24].

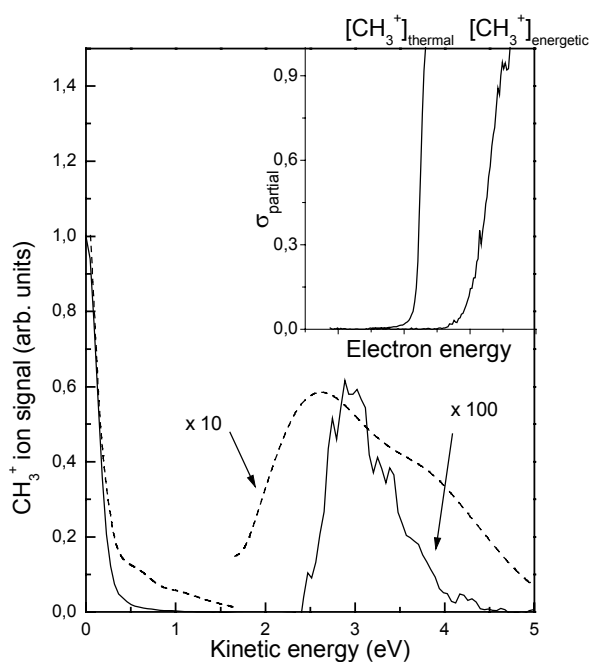


Figure 4. Kinetic energy distribution for the fragment ion CH_3^+ produced by electron impact ionization of C_3H_8 as measured with the ion beam deflection method [29] (designated by dashed line) and the mass analyzed retarding potential method [30] (designated by full line). In the inset we show the corresponding cross section threshold curves for the thermal ions and the energetic ions peaking at around 3 eV.

It is clear from the measured threshold behavior of the corresponding partial ionization cross sections (see inset in Fig. 4) for these two groups of ions that quite different reaction mechanisms are responsible for the formation of these two groups of ions. As can be seen in Fig. 5 there exists very good agreement between the total ionization cross section obtained by summation of the corrected partial ionization cross sections [20] and two sets of total ionization cross section data obtained without mass analysis [34–36]. In addition all of these experimental data sets are in agreement with two different types of calculations [37, 38].

It is appropriate to note here also some of the specifically successful instruments of the second category (see above) introduced recently, including (i) the fast-neutral-beam apparatus of Becker and co-workers [39, 40] allowing also the study of radical targets, (ii) the time of flight position sensitive detection system of Stebbings and co-workers [41, 42] and (iii) the focusing time of flight apparatus of Vidal and co-workers [43, 44] which also yields information on ion pair information. In each case several molecular systems have been measured and there is good agreement between the results of these groups and the two groups mentioned above. In addition several other groups have during the past 15 years reported valuable cross section data sets [45–52] (see also a recent book on novel aspects of electron-molecule collisions [53]).

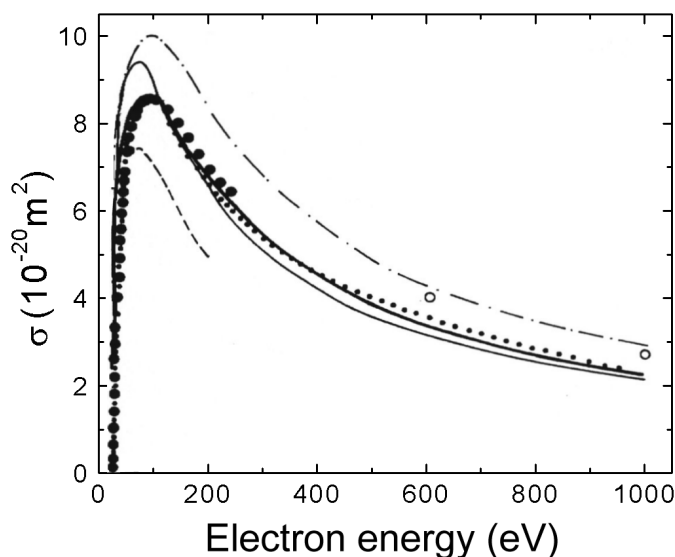


Figure 5. Total electron impact ionization cross section for propane (C_3H_8) as a function of electron energy. The experimental data are from Schram et al (1966) designated by open circles [34], Djuric et al. (1991) designated by big filled circles [35], Grill et al (1993) designated by small filled circles [35], and Nishimura and Tawara (1994) designated by dash-dot line [36]. The thick solid line represents a BEB calculation [37] and the thin solid line a DM calculation [38].

3. Electron impact ionization of molecular ions: Time dependence of the kinetic energy release of propane fragment ions — a case study

The study of dissociative collisions of electrons with molecular ions has been dominated for many years by the investigation of dissociative recombination. Dissociative excitation, dissociative ionization and direct ionization of molecular ions by electron collisions have received less attention. Nevertheless, the incentives associated with controlled thermonuclear fusion have recently led to a number of efforts since the edge plasmas contain many molecular ions. In principle, the research literature abounds with studies of dissociative reactions of mass-selected ions which are induced by photon absorption, gas-phase collisions,

or surface collisions. In some of these, the kinetic energy release (KER) was determined as well [54, 55]. In contrast, reports on electron-induced dissociative reactions of molecular ions are scarce. Most of them involved diatomic or other small ions with the goal of measuring absolute cross sections for fragmentation [56]. Cross sections for ionization and dissociation of fullerene ions were reported recently by Salzborn and coworkers [57]. Freiser and coworkers [58] explored dissociative electron capture by polyatomic ions to obtain structural information from the fragment pattern and McLafferty and coworkers [59] extended these studies to large multiply charged ions. However, except for recent work in our laboratory [60, 61], the KER released in electron-induced reactions of polyatomic ions has not been measured.

Induced reactions offer, however, the possibility of analyzing the KER for ions with very short lifetimes. There is considerable interest in the time dependence of the KER [62–64], because statistically driven decay reactions without a reverse activation energy feature a KER which increases with decreasing ion lifetime as — at the same time — the statistically distributed excitation energy in the parent ion increases [61, 65]. In contrast, decay reactions with a large reverse barrier are characterized by an essentially constant, or even decreasing, KER [66].

In previous studies on this subject, the time at which dissociation was measured (relative to the time of ion formation in the ion source) was varied by varying the acceleration voltages [64, 67]. The advent of ion traps has made it possible to greatly increase the ion lifetimes being sampled [65], but a lower limit of the order of 1 to 10 μs still exists. By recently positioning a high-performance electron gun near the intermediate slit of a double focusing magnetic mass spectrometer of reverse geometry we have been able to measure the KER for electron induced reactions occurring within less than 0.75 μs after electron-impact excitation of various propane derived ions. We observe a large fractional decrease of the average KER for decay of C_3H_8^+ into C_3H_7^+ , but a much smaller effect for decay of C_3H_7^+ into C_3H_5^+ when comparing the KER of this electron induced decay with the KER of the spontaneous decay reaction at this position of the mass spectrometer system (occurring on the time scale of about 11 to 14 μs). As will become clear below the differences are attributed to the existence of a large reverse activation energy for decay of C_3H_7^+ into C_3H_5^+ .

Details of the experimental set-up and data analysis have been published elsewhere [68, 69]. The apparatus consists of a high resolution double focusing tow sector field mass spectrometer of reversed Nier-Johnson type geometry as already shown in Fig. 2. Propane molecules are introduced via a capillary leak gas inlet system into the ion source where they are ionized by an electron beam of variable energy and current. Ensuing cations are extracted by a weak electric field and accelerated through a potential drop of $U_{\text{ac}} = 3 \text{ kV}$ into the spectrometer. They pass through the first field free region (1ff), are then momentum-analyzed by a magnetic sector field, enter a second field-free region (2ff, length 33.3 cm), pass through a 90° electric sector field and are finally detected by a channeltron-type electron multiplier operated in the single-ion counting mode.

In order to analyze the decay of mass-selected molecular ions (MIKE scan technique [63]), the parent ions are selected with the magnetic sector field and decay reactions in the 2ff are analysed by varying the voltage of the electric sector field. The decay may be either spontaneous (metastable), or it may be induced in this region of the mass spectrometer by electrons from a high-performance, home built electron gun [69]. The electron gun is mounted just before the defining aperture between the magnetic sector and the electric sector and the electrons intersect the ion beam at 90° . The gun is an order of magnitude more

powerful than the electron gun used previously for post-ionization of fullerene cat- and anions [60, 70], typically parameters used are an electron energy of 150 eV which results in an electron beam current of 7 mA. This setting is a compromise as the electron beam current would increase further with increasing energy, but the ionization cross section of propane reaches its maximum near 75 eV [18].

Mass-analyzed ion kinetic energy (MIKE) spectra are usually recorded as follows: The magnet is tuned to the mass of the parent ion, m_p , while the electric sector field voltage U is scanned (Fig. 6). Stable singly charged ions will have a kinetic energy of 3 keV and pass at the nominal sector field voltage of $U_p = 509$ V. Daughter ions (mass m_d), formed in the 2ff, will then pass at a voltage

$$U_d = \frac{m_d}{m_p} U_p \quad (4)$$

This equation relates the position of a daughter ion peak to the position of the parent ion peak in a MIKE spectrum. In practice, the parent ion peak will have a finite width and a distinct shape which will also be imposed on the daughter ion peak. Any kinetic energy release (KER) in the reaction will further modify the peak shape of the daughter. If the MIKE peak is strictly Gaussian, then the average kinetic energy release, can be extracted from its full width at half maximum, ΔU , [71]. If the peak in the MIKE spectrum is not a Gaussian, then the Kinetic Energy Release Distributions (KERD) has to be derived from its derivative with respect to the sector field voltage. Details, including the use of ion trajectory calculations to simulate MIKE peaks for our spectrometer and various corrections, have been described in detail in [68, 69]. As a MIKE scan will always sample decay reactions which occur between the magnetic and electric sector, there is an important difference in the time scale between spontaneous and induced decay reactions. A parent ion (here assumed to be $C_3H_8^+$) formed in the ion source at $t = 0$, will traverse the 2ff at a time interval $11.2 \leq t \leq 14.2$ μ s. In contrast, if the reaction is electron-induced in the 2ff, it has to occur within $t \leq 0.75$ μ s in order to contribute to the MIKE spectrum.

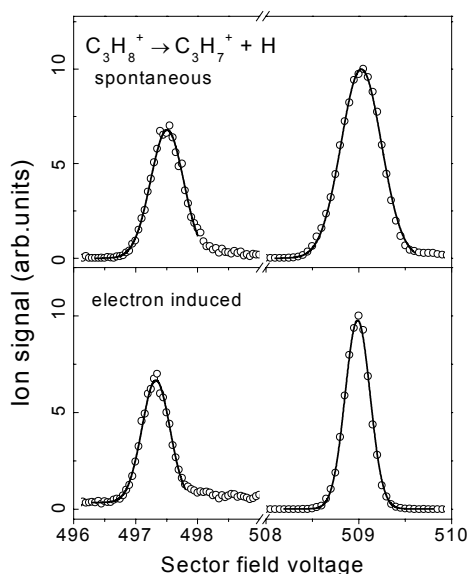
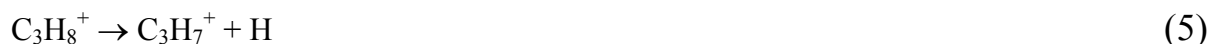


Figure 6 Top: MIKE scan for spontaneous dissociation of $C_3H_8^+$ into $C_3H_7^+ + H$ after [69]. The solid line indicates a least-squares fit of a Gaussian. Bottom: MIKE scan for the electron-induced reaction.

Figure 6 (upper part) displays the MIKE scan for the spontaneous reaction (5).



In this case the peak is Gaussian, except for a slightly enhanced background to the right of the daughter ion peak which is believed to stem from decay reactions in the electric sector field [72]. From the excellent non-linear least squares fit (solid line in Fig. 6) and after correcting for the width of the parent ion peak an average KER of 9.3 ± 1.5 meV can be derived in good agreement with an earlier values of 9.4 meV from our laboratory [68] and of 9.6 meV reported by Medved et al. [64]. In the lower part of Fig. 6 we show the MIKE spectrum for the electron-induced decay reaction (5). The corresponding average KER of 13.2 ± 1.2 meV for the electron-induced reaction (5) thus is larger than the spontaneous reaction by 3.9 ± 1.8 meV. Moreover, the corresponding KERD are readily derived from the Gaussian fits to the MIKE spectra after deconvolution with the parent ion peaks. The shift of the distribution for the electron-induced reaction is obvious from the results shown in Fig. 7.

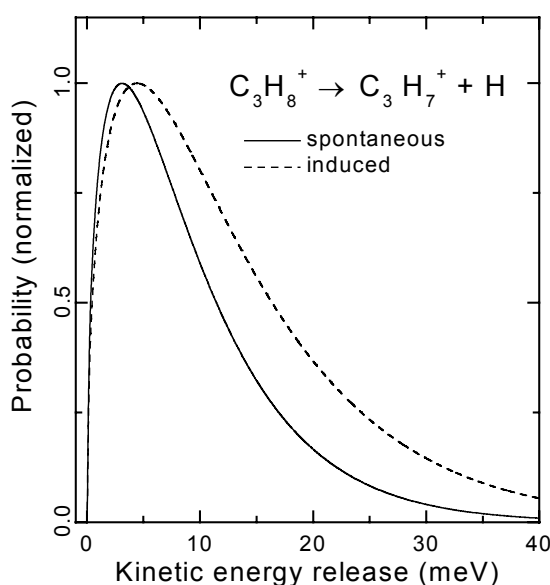


Figure 7. Kinetic energy release distributions (KERD) for spontaneous and electron-induced dissociation of C_3H_8^+ into $\text{C}_3\text{H}_7^+ + \text{H}$ after [69].

Similar studies have been carried out for the reaction



In Fig. 8 upper panel we show the corresponding MIKE spectrum for the electron-induced reaction. The daughter peak is, like in the spectrum for the spontaneous reaction, flat-topped, characteristic of a reaction which features a sizeable reverse activation energy. The KERD derived from these data is displayed in Fig. 8 lower panel. A large threshold value in the KER is immediately apparent. The average KER for the electron induced reaction is found from this distribution to be 397 meV, while the average KER for the spontaneous reaction is obtained as 386 meV. The uncertainty of these values are probably on the order of 10 meV. In a previous study [68] we had derived an average KER of 400 meV for the spontaneous reaction, while Holmes et al. [71] reported a value of 440 meV.

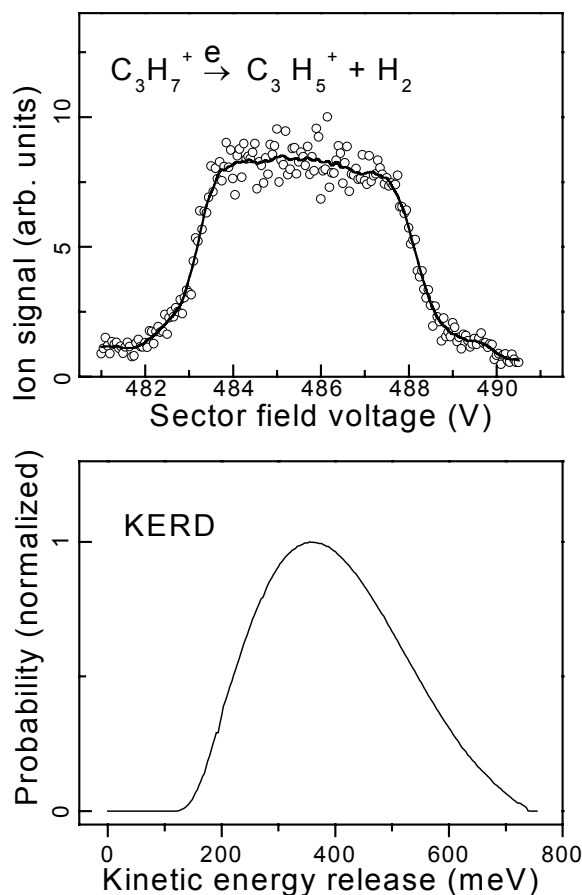


Figure 8. Top: MIKE scan for electron-induced dissociation of $C_3H_7^+$ into $C_3H_5^+ + H_2$ after [69]. The solid line results from FFT-smoothing. Bottom: The KERD distribution obtained from the smooth MIKE spectrum, after deconvolution with the parent ion peak.

Therefore, for reaction 5 we find a dramatic change of the KERD (see Fig. 6), corresponding to an increase of the average KER by 42 %, whereas the average KER for reaction 6, in contrast, is enhanced by a mere 3 %. It should be pointed out that the average KER measured for the induced reactions only represent lower limits, because the MIKE peak is actually a superposition of the spontaneous and electron induced signal. As discussed in detail in Ref. [69] the strong enhancement in the case of reaction (5) is attributed to a change in the time scale over which the reaction is monitored. Furthermore, the occurrence of only a small change for reaction (6) is attributed to the existence of a large reverse activation energy.

It is interesting to note that we have recently extended our experimental set-up by adding a third field free region with a high performance electron gun and a third analyzer (electric sector field) thus allowing us to study in more detail electron induced dissociation and ionization of mass selected molecular ions including step by step ionisation mechanisms (see Fig. 9).

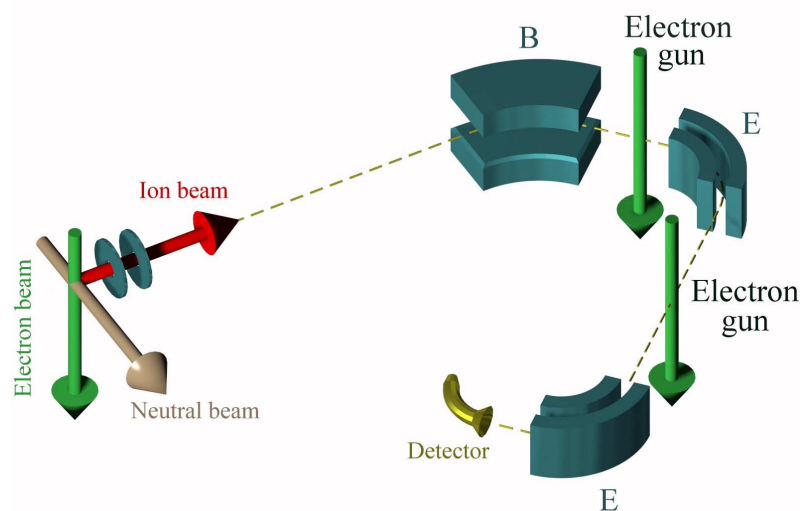


Figure 9. Schematic view of recently constructed three sector field mass spectrometer used for the study of electron induced dissociation and ionization reactions in Innsbruck.

4. Cross sections: Theoretical considerations

4.1. Single ionisation of molecules

Considerable progress in the experimental determination of cross sections for atomic and molecular targets has been achieved in the past decade as discussed above. Despite this effort only about 75 molecules have been studied so far quantitatively, well below the actual need in plasma physics and plasma chemistry and in particular also not including all of the targets important in fusion.

Unfortunately, rigorous quantum mechanical calculations of ionization cross sections for molecular targets are beyond the capability of current quantum-mechanical electron collision theory for essentially all molecules [73–75]. However the need to incorporate molecular ionization cross sections in modelling codes for various applications (e.g. in fusion edge plasmas [15] and in plasma processing [76]) has stimulated the use of ‘simplistic’ *additivity rules* to estimate molecular ionization cross sections. Many variants of the additivity rule, whose concept was first introduced by Ötvös and Stevenson [77] can be found today in the literature [78, 79] and are used for a wide range of applications. They all rely on the concept that the molecular ionization cross section is derived by adding in some fashion the ionization cross sections of the atomic constituents of the molecule with or without accounting for molecular bonding and/or weighting factors for the atomic cross sections.

The most recent variant of the additivity rule is the so-called Modified Additivity Rule (MAR) of Deutsch et al. [80, 81] which includes appropriately chosen weighting factors to account for molecular bonding. Predictions of the MAR have been compared to available experimental cross section data for many molecules with sum formulas of the form AB_x [80] and A_xB_y , $A_xB_yC_z$, and $A_pB_sC_tD_u$ [81] and reasonable agreement was found in essentially all cases. In addition to these additivity approaches, there have been other conceptually simplistic (geometric) methods such as:

- (1) the geometric approach of Kistemaker and co-workers [82] which considers different electron-molecule approach geometries and calculates the ionization cross section by averaging over all possible orientations, and
- (2) a theoretical approach by Harland and co-workers [based on the calculation of the maximum in the electron-impact ionization cross section as a function of the electron-molecule approach geometry and subsequent averaging over the different orientations [83–85].

In contrast there exist now also more rigorous methods [23, 86–94] including:

- (1) the Deutsch-Märk (DM) formalism which combines a Gryzinski-type energy dependence of the cross section with quantum mechanically calculated molecular structure information based on an additivity concept [23, 86–88],
- (2) the method of Jain, Khare (JK) and co-workers [89, 90], which combines two cross section expressions (the Mott and Bethe cross section) describing ionizing collisions which occur at large impact parameters and at small impact parameters, respectively, and
- (3) the Binary-Encounter Bethe (BEB) theory of Kim, Rudd and co-workers [91–94] which in addition to combining two cross section expressions (the binary encounter and Bethe cross section) introduces also an additivity concept with quantum mechanically calculated molecular quantities.

Deutsch et al. [23] have recently published an extensive comparison and review about the status of calculations of absolute electron-impact ionization cross sections for molecules and radicals with special emphasis on the DM formalism and the BEB formalism which are the most widely used calculation schemes among those methods that may be labeled “more rigorous” theoretical approaches. Both methods incorporate quantum mechanically calculated molecular structure information, a fact that sets them apart from the more simplistic additivity rules and the purely geometric methods. It is noteworthy to point out in this context, that both the DM formalism and the BEB formalism also make use of an additivity *concept* in the sense that the ionization cross section of a molecule is obtained by summing up the contributions arising from the ejection of an electron from the different molecular orbitals. This has sometimes led people to erroneously refer to the DM and BEB calculations as variants of the additivity *rule*. We would like to make a clear distinction between simplistic additivity rules (like the ones mentioned above [77–85]) and more rigorous methods like the DM formalism and the BEB formalism which include quantum mechanically calculated molecular structure information — even though these approaches also incorporate an additivity concept in some fashion. The method of Jain and Khare and co-workers can also be classified as a more rigorous theoretical approach, but it has only been applied to a limited number of target molecules. Extensive comparisons has been made by Deutsch et al. [23] between calculated ionization cross sections using the DM formalism and the BEB formalism (including also results from the JK formalism where available) and experimentally determined cross sections for 31 molecules and radicals. Before showing here some results pertinent to the fusion edge plasma we will shortly outline the DM approach.

The original concept of Deutsch and Märk [95] introduced in 1987, which was developed for the calculation of atomic ionization cross sections has been modified and extended several times. We begin with a brief outline of the original DM approach and the subsequent modifications which resulted in a very general formula that is now applicable to the single ionization of ground-state [95, 96] and excited-state (metastable) atoms [97, 98], the removal of a specific single outershell [99] and inner shell electron [100] of atoms as well as to the single ionization of molecules [86], radicals [87, 88], small Ag, H₂ and CO₂ clusters and C₆₀ [101–103] and atomic ions [104, 105] as well as to the multiple ionization of atoms

[106–109] (see section 4.2). In all cases, only direct ionization processes are considered in the original DM formalism (i.e. the prompt removal of a single electron from the electron shell by the incoming electron and it is, therefore, not possible to distinguish between single and multiple ionization when inner shell electron ejection occurs). Two-step ionization mechanisms such as auto ionization after inner shell excitation cannot be described by the DM formalism (nor by any of the other methods, as for instance BEB or JK, described above).

Thomson [110] was the first to derive a formula for the electron impact ionization cross section of an atom using a classical binary encounter approximation. This classical treatment was modified by several authors using different initial conditions. Gryzinski [111] introduced the concept of a continuous velocity distribution for atomic electrons, which resulted in an expression for the ionization cross section σ of the form

$$\sigma = \sum_{n,l} 4\pi(a_0)^2 \xi_n \left(\frac{R}{E_{nl}} \right)^2 \cdot f(U) \quad (7)$$

with

$$f(U) = d \frac{1}{U} \left(\frac{U-1}{U+1} \right)^a \cdot \left[b + c \left(1 - \frac{1}{2U} \right) \right] \ln(2.7 + \sqrt{U-1}) \quad (8)$$

$$\text{and } a = 3/2, b = 1, c = 2/3, \text{ and } d = 1 \quad (9)$$

Here a_0 denotes the Bohr radius, R the Rydberg energy (ionization energy E_i of the hydrogen atom), ξ_n the number of electrons in the n -th atomic sub-shell, and E_{nl} refers to the ionization energy in the n -th sub-shell and U is the reduced energy given by $U = E/E_{nl}$ where E is the energy of the incident electron. However, as has been shown and discussed in detail even this improved cross section formula fails for some rather simple atoms such as neon, nitrogen, and fluorine [95, 112].

Deutsch and Märk [95] suggested to replace the Bohr radius a_0 in equation (7) by the radius of the maximum charge density r_{nl} of the corresponding electronic sub-shell (labeled by the quantum numbers n and l) on the basis of a comparison between the classical binary encounter formula and the quantum mechanical Born-Bethe formula [113]. Support for this substitution comes from (i) the application of the Bethe formalism to the ionization cross section of an atomic electron with quantum numbers (n,l) is approximately proportional to the mean square radius $\langle r^2 \rangle$ of the (n,l) sub-shell [114, 115] and from (ii) the experimental observation of the existence of a correlation between the maximum of the atomic ionization cross section and the sum of the mean square radii of all outer electrons [116]. Subsequently, Margreiter et al. [96, 97] successfully applied the following semi-classical formula to the calculation of the absolute electron-impact ionization cross section σ of a large number of ground-state and excited-state atoms

$$\sigma = \sum_{n,l} g_{nl} \pi (r_{nl})^2 \xi_{nl} \cdot f(U) \quad (10)$$

where r_{nl}^2 is the square radius of the maximum charge density of the (n,l) sub-shell electron and g_{nl} are weighting factors which were originally introduced by Bethe [113]. These generalized weighting factors g_{nl} introduced by Margreiter et al. [96, 97] were obtained from a fitting procedure using reliable experimental ionization cross section data for the rare gases and uranium [16]. In a first approximation, these weighting factors were taken to be 3 for s-electrons and 0.5 for all other electrons [95].

Table 1. Reduced weighting factors for the different subshells.

Valence Electron (n,l), number in sub-shell	Reduced Weighting Factors $g_{nl} \cdot E_{nl}$
(1s),1	38.20
(1s),2	70.00
(2s),1	12.00
(2s),2	20.00
(2p),1	32.50
(2p), 2–6	30.00
(3s),1	9.80
(3s),2	14.00
(3p),1	31.50
(3p)2–4	25.00
(3p),5–6	22.00
(3d),1–10	13.60
(4s),1	7.40
(4s),2	10.00
(4p),1	31.00
(4p),2–4	22.40
(4p),5	18.50
(4p),6	17.50
(4d),all electrons	11.20
(4f), all electrons	20.00
(5s),1	6.35
(5s),2	7.50
(5p),1	30.50
(5p),2–4	20.00
(5p),5	16.00
(5p),6	13.00
(5d), all electrons	8.85
(5f), all electrons	1.00
(6s),1	5.40
(6s),2	6.00
(6p),1	30.00
(6p),2–4	18.00
(6p),5	14.50
(6p),6	7.50
(6d), all electrons	6.50

Subsequently, a more detailed analysis revealed that the g_{nl} are not constants, but depend on the quantum numbers n and l , and on the ionization energy E_{nl} in such a way that the product $g_{nl} E_{nl}$ (referred to as the "reduced weighting factor") is independent of the nuclear charge Z for completely filled sub-shells [97]. Table 1 summarizes the final set [117, 118] of the reduced weighting factors $g_{nl} E_{nl}$ for electrons in the various (n,l) sub-shells. Moreover, Table 2 summarizes the final values for the parameters a, b, c , and d to be used for s-, p-, d-, and f-electrons [117, 118].

Table 2. Parameters for the energy dependent function.

s-electrons:	$a = 1.06$	$b = 0.23$	$c = 1$	$d = 1.1$
p-electrons:	$a = 2$	$b = 1$	$c = 1$	$d = 1$
d-electrons:	$a = 3/2$	$b = 3$	$c = 2/3$	$d = 1$
f-electrons:	$a = 3/2$	$b = 1$	$c = 2/3$	$d = 1$

The straightforward extension of the DM-formula of equation (10) to molecular targets [86] results in an equation of the form

$$\sigma = \sum_j g_j \pi(r_j)^2 \xi_j f_j(U) \quad (11)$$

where the summation is now carried out over the molecular orbitals labeled "j". It was found advantageous [86–88] to reduce the case of a molecular ionization cross section calculation using the DM formalism to the previously derived atomic ionization cross section formula of equation (10). This requires a Mulliken population analysis [119, 120] (or an equivalent method) which expresses the molecular orbitals in terms of the atomic orbitals of the constituent atoms. As a result, each term in the above sum over "j" in equation (11) is expressed in terms of the appropriate atomic weighting factors $g_j(A, nl)$, effective occupation numbers $\xi_j(A, nl)$, atomic radii of maximum charge density $r_j(A, nl)$, and functions $f_j(A, nl, U)$ where "A" labels the various constituent atoms of the molecule under study. For more details of this method see also Ref. [23], the maximum charge density radii necessary for the calculations can be taken from Ref. [122].

It is important for the application of the DM formalism to molecular targets to realize the sensitivity of the calculations to the Mulliken representation of the molecular orbitals in terms of atomic orbitals of the constituent atoms. Figure 10 shows the calculated H₂O DM total electron impact ionization cross sections resulting from four different Mulliken representations. As one can see, there are differences in the maximum cross section value of about 25% as well as a 15 eV difference in the energetic position of the maximum depending on the particular choice of Mulliken representation.

In the following we will compare as an example in Figs. 11–19 calculated and measured total ionization cross sections for the most important plasma edge targets in tokamaks, including H₂, C₂, O₂, N₂, CO₂, H₂O, CH_{x=1-4}, and C₂H₂, the cross section for C₃H₈ is shown in Fig. 4 and cross sections for other larger hydrocarbons are given in [23].

Text cont. on page 33.

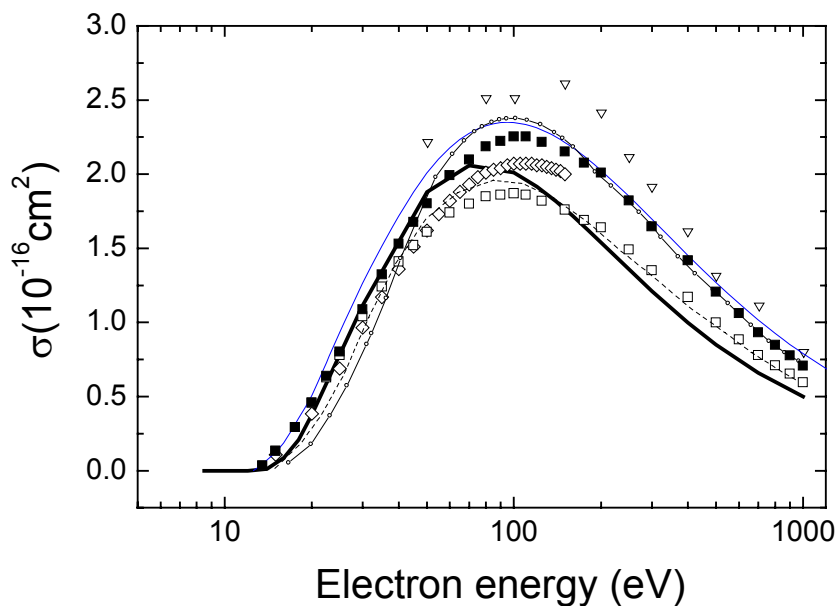


Figure 10. Calculated H_2O ionization cross sections using the DM formalism with four different atomic basis sets employed in the Mulliken population analysis (see Ref. [23] for details). The four calculated curves correspond to the following basis sets, thick solid line (ref. [121]), thin solid line (6-311g**), dash-dot line (sto-6g), and dashed line (cc-pvtz).

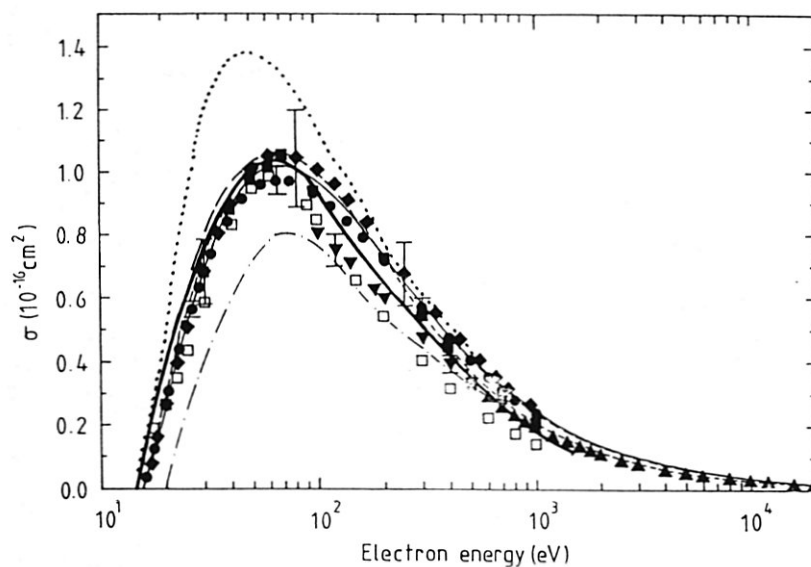


Figure 11. Electron impact ionization cross section of H_2 as a function of electron energy after [23]. The various experimental data points are taken from [23]. The open squares denote CTMC calculations of Ref. [91]. The thick solid line represents the DM calculation [23], the thin solid line and the dashed line denote respectively the BEB and BED calculation [123, 124], the dash-dot line is the calculation of Saksena et al. [123, 124], and the dotted line are results obtained with the method of Khare and co-workers as given in [123, 124].

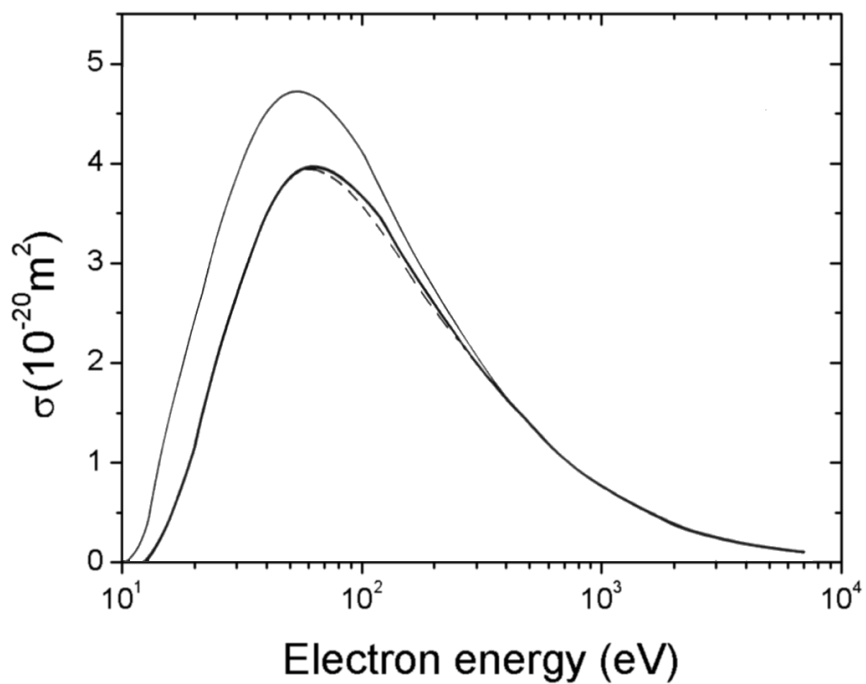


Figure 12. Electron impact ionization cross section of C_2 as a function of electron energy after [23]. The three different curves represent DM calculations using three different atomic basis sets; 6-311g (thick solid line), dashed line (cc-pvdz), thin solid line (sto-6g).

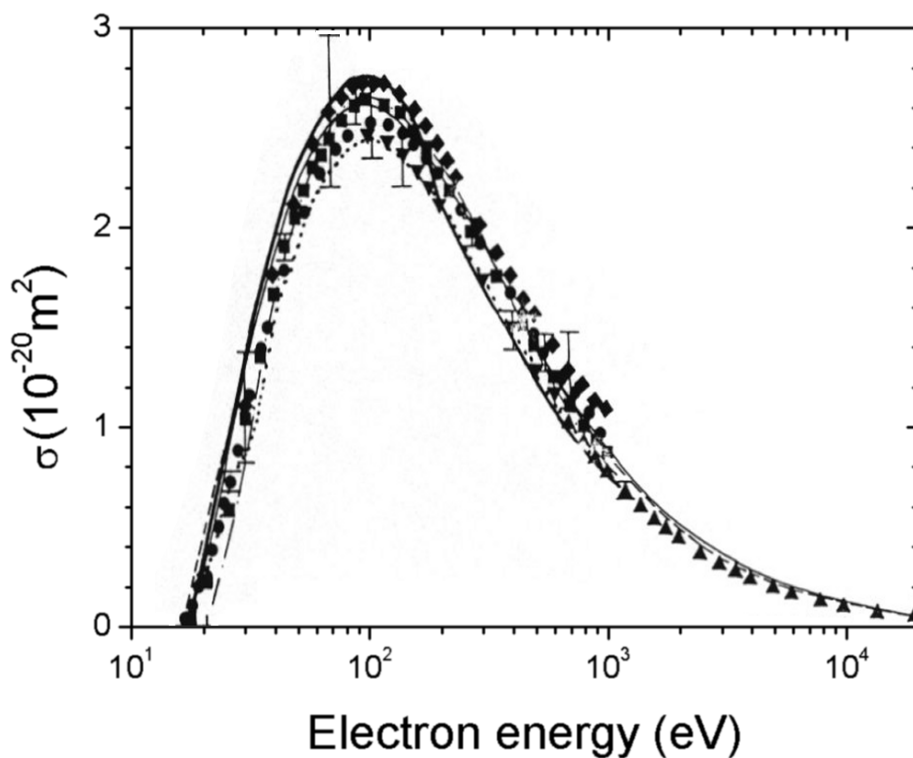


Figure 13. Electron impact ionization cross section of N_2 as a function of electron energy after [23]. The various experimental data points are taken from [23]. The thick solid line represents the DM calculation [23], the thin solid line and the dashed line denote respectively the BEB and BED calculations [92], the dash-dot line is the calculation of Saksena et al. [123, 124], and the dotted line are results obtained with the method of Khare and co-workers as given in [123, 124].

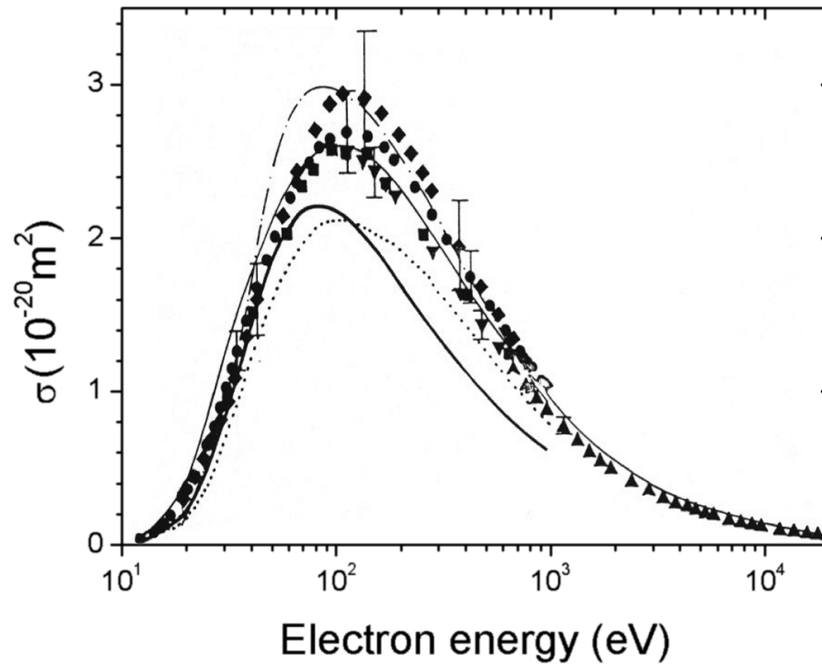


Figure 14. Electron impact ionization cross section of O_2 as a function of electron energy after [23]. The various experimental data points are taken from [23]. The thick solid line represents the DM calculation [23], the thin solid line denotes the BEB calculation [92], the dash-dot line is the calculation of Saksena et al. [123, 124], and the dotted line are the results obtained with the method of Khare and co-workers as given in [123, 124].

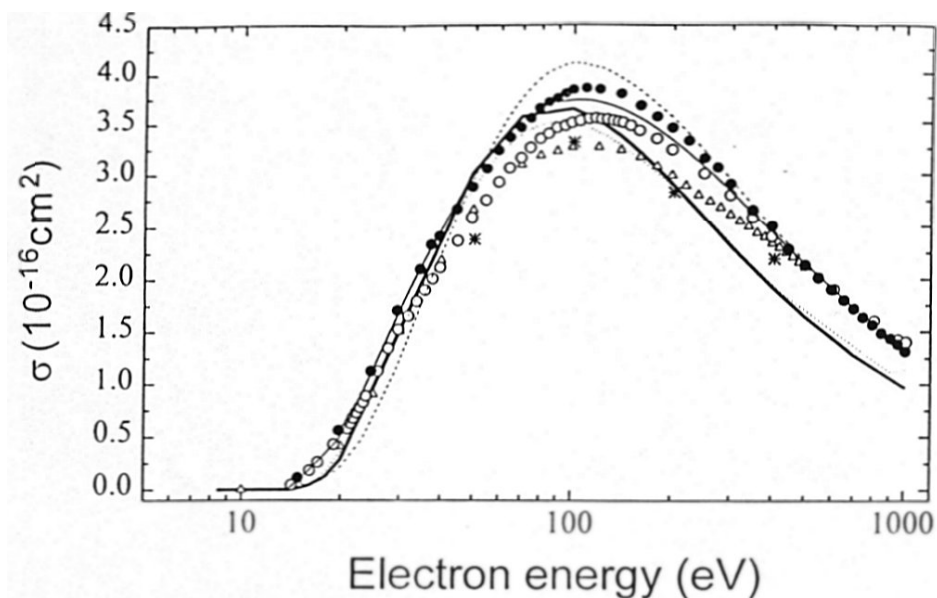


Figure 15. Electron impact ionization cross section of CO_2 as a function of electron energy after [23]. The various experimental data points are taken from [23]. The thick solid line represents the DM calculation [23], the thin solid line denotes the BEB calculation [92], the dotted line represents the calculation of Jain and Khare [89] and the dashed line denotes the calculation of Saksena et al. [123, 124].

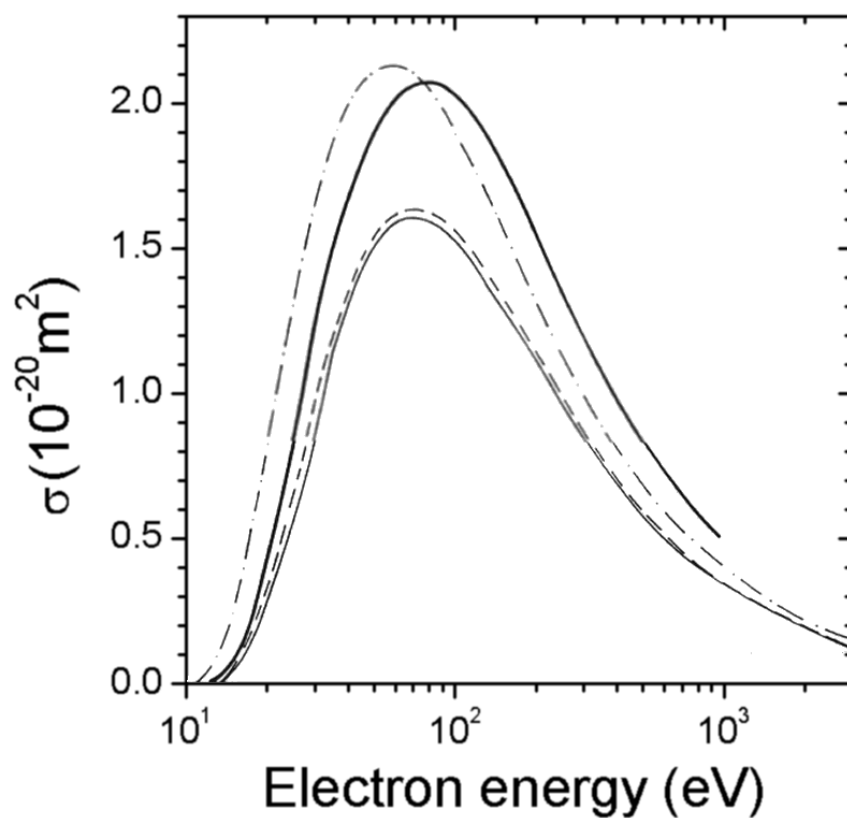


Figure 16. Electron impact ionization cross section of H_2O as a function of electron energy after [23]. The various experimental data points are taken from [23]. The thick solid line represents the DM calculation [23], the thin solid line denotes the BEB calculation [92], the dashed line refers to the calculation of Jain and Khare [89], and the open circles connected by a solid line denote the calculation of Saksena et al [123, 124].

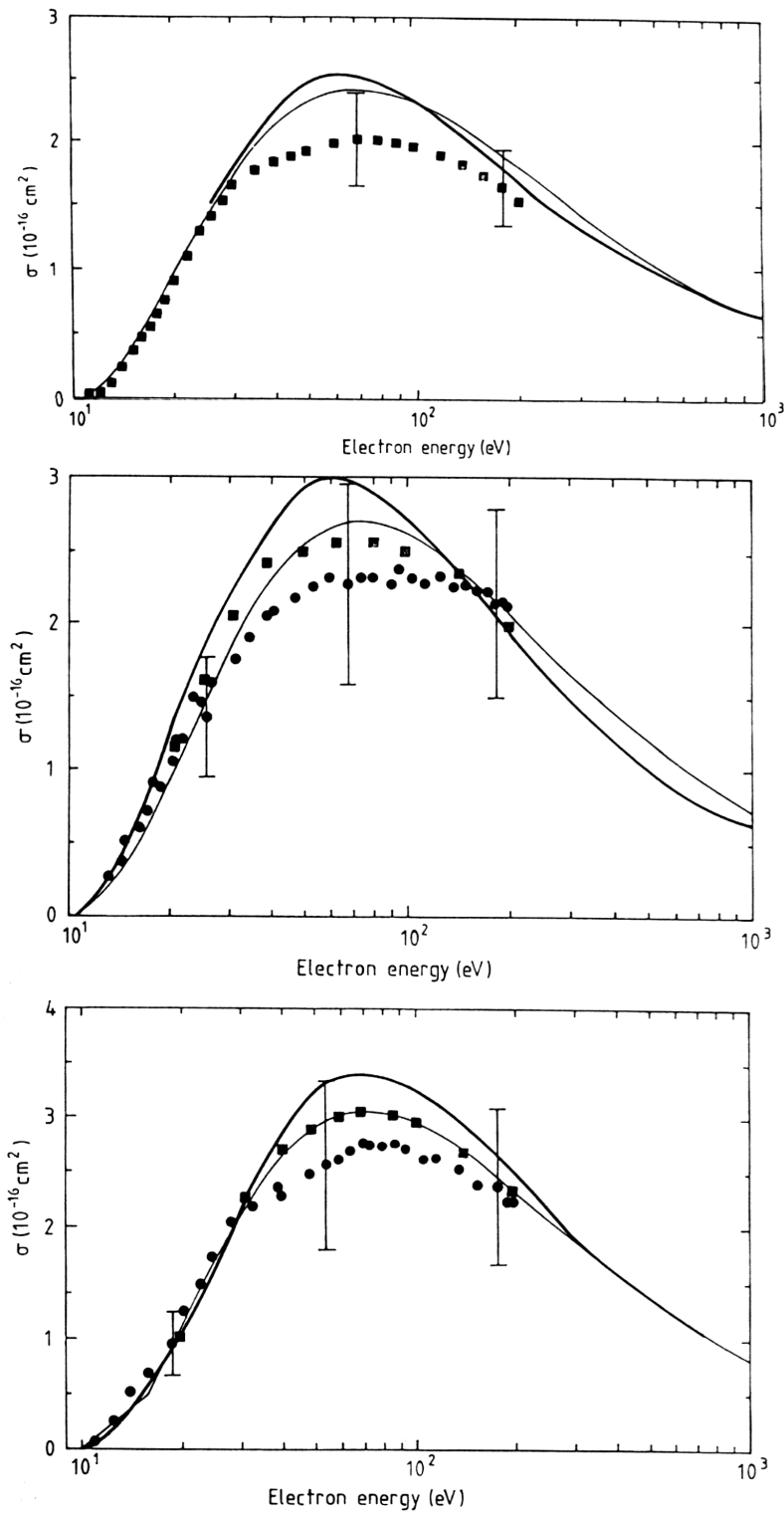


Figure 17. Electron impact ionization of the CH_x ($x=1-3$) free radicals as a function of electron energy after [23]. The thick solid line represents the DM calculation [23], the thin solid line denotes the BEB calculation [92]. The experimental data points (taken for fully deuterated species) are from Baiocchi et al. [125] (full dots) and from Tarnovsky et al. [126] (full squares). Top diagram: CH, center diagram: CH₂, and bottom diagram: CH₃.

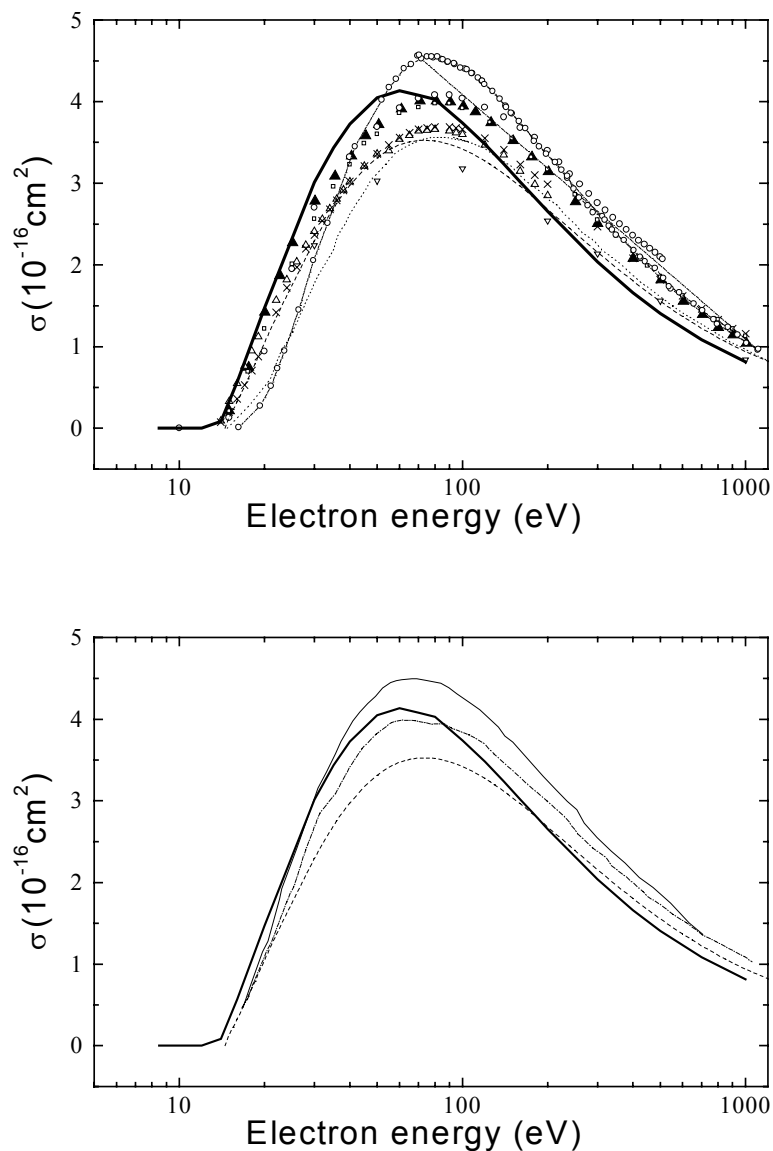


Figure 18. Electron impact ionization cross section of CH_4 as a function of electron energy after [23]. The various experimental data points are taken from [23]. The thick solid line represents the DM [23] calculation, the fine dotted line represents the calculation of Jain and Khare [89], the dash dotted line combined with open circles denote calculated values as given in [127] using the method of Saksena et al. [123, 124], and the dashed line are the BEB results from [93] using a vertical ionization energy.

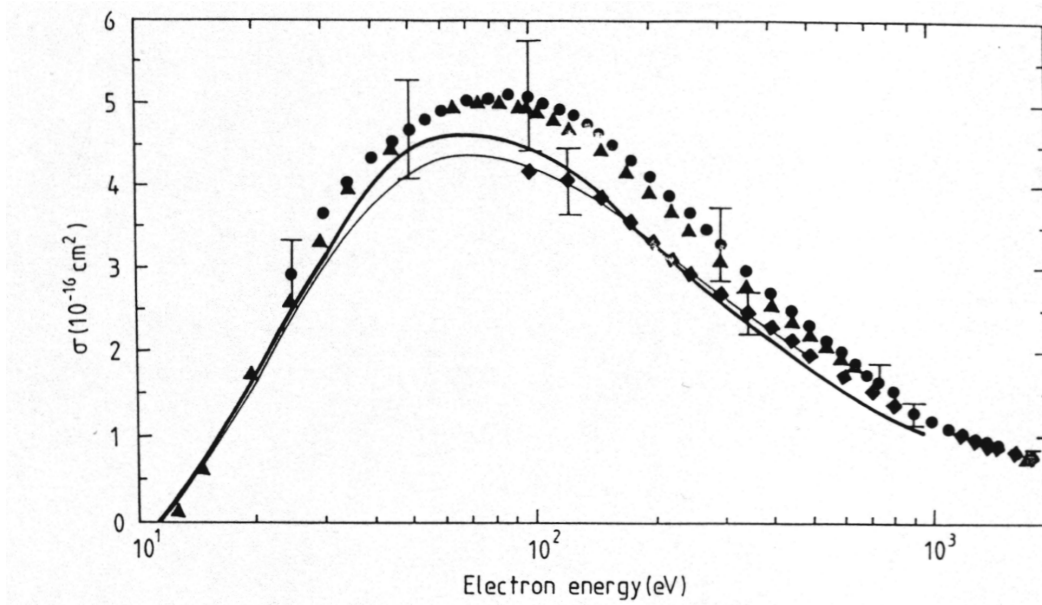


Figure 19. Electron impact ionization cross section of C_2H_2 as a function of electron energy after [23]. The various experimental data points are taken from [23]. The thick solid line represents the DM calculation [23], the thin solid line denotes the BEB calculation [92].

4.2. Multiple ionisation of atoms

The multiple ionization of a neutral atom by electron impact (single-step multiple ionization)



is a collision process of fundamental interest. The cross sections for the single-step multiple ionization of an atom are significantly smaller than cross sections for single ionization [16] and decline rapidly with the stage of ionization [108, 109, 128, 129]. Nonetheless, multiple ionization processes are important in then tokamak edge plasmas [1] and in other environments with an abundance of energetic electrons. Although electron temperatures in these plasma regions are relatively low, well below 1 keV, the high energy part of the energy distributions may after all lead to the production of more highly charged species and thus influence the plasma properties. As mentioned above the elements that need special consideration include Li, Be, B, C, N, Al, Si, Mg, Ti, Cr, Fe, Ni, Cu, Mo, Nb, Ta and W as possible impurities in the plasma edge and Ne, Ar, Kr, Xe as gases which are injected from the outside into the plasma volume for cooling the plasma scrape off layer [1, 5].

Calculations of multiple atomic ionization cross sections using rigorous quantum mechanical methods are difficult for all but the simplest atoms [16, 73–75]. This is due to — among other things — the need to consider two or more continuum electrons and their mutual interaction in the exit channel. Experimental data for the formation of highly charged ions are scarce for most atoms [108, 109, 128–130] because of among other reasons the fact that the cross sections for the single-step formation of highly-charged multiple ions are comparatively

small. Modellers and practitioners rely heavily on semi-empirical and semi-classical methods to determine multiple ionization cross sections for modelling purposes and for other applications [1, 16, 76]. A simple variant of the Deutsch-Märk (DM) formalism described above has been applied successfully to the calculation of cross sections for the formation of multiply charged ions A^{m+} for several atoms such as high- Z atoms with a nuclear charge Z of 10 and above and various stages of ionization [106–108] as well as several low- Z targets [109, 128, 129].

This simple DM variant has the following advantages over two other semi-empirical methods which have been recently proposed by Fisher et al. [131] and by Shevelko et al. [132], respectively, to calculate cross sections for multiple ionization of neutral atoms: (i) the application of the DM variant requires fewer semi-empirical parameters which, in addition, can easily be related to physical quantities and (ii) the energy-dependent function of the DM variant (derived from classical considerations, see [95, 111]) is the same for all stages of ionization. So far the following targets and respective ionization stages have been investigated with this DM variant: Be (m up to 4) [128], B (m up to 5) [128], C (m up to 6) [128], N (m up to 7) [133], O (m up to 8) [128,106], Ne (m up to 10) [106,108,109], S ($m = 2,3$) [106], Si (m up to 14) [109], Ar (m up to 18) [108, 129, 133], Kr ($m = 6-8$) [108,133], Cu ($m = 2-5$) [106,107], Fe ($m = 3-5$) [107], Ga ($m = 2,3$) [106], Ag ($m = 2$) [106], In ($m = 2,3$) [106], Pb ($m = 2,3$) [106], Ge ($m = 3$) [106], As ($m = 3$) [106], Xe ($m = 6-13$) [108] and U ($m = 4$) [107].

In the following we will shortly summarize the theoretical background for this DM variant and give some illustrative examples. Where possible, we compare the results obtained with the DM formalism with experimental data and results obtained by using the semi-empirical method (ST) of Shevelko and Tawara [132], the other semi-empirical method [131] was found to show very large deviations from the data for higher charge states, see e.g. Fig. 5 in Ref. [108]) and is, therefore, not considered in more detail here.

Starting from the DM formalism described above, which was originally developed for the calculation of cross sections for the single ionization of an atom [95, 96], the cross section σ^{m+} for the formation of an ion A^{m+} , which in principle is a product of m independent terms each describing the removal of a single electron, can be simplified to an expression of the form

$$\sigma^{m+} = g^m \sum_k \pi (r_k)^2 \xi_k f_k(U) \quad (13)$$

where the summation extends over the various atomic sub-shells with $k = 1$ referring to the outermost sub-shell, $k = 2$ to the second outermost sub-shell, etc. In the above equation, $(r_k)^2$ is the square of the maximum charge density of the atomic sub-shell labelled by k , ξ_k is the number of electrons in that sub-shell, and g^m are weighting factors (see Refs. [109, 128] for further details). The functions $f_k(U)$ describe the energy dependence of the ionization cross section and are identical to the function given in equ. (8), however U refers to the reduced impact energy, $U = E/E_m$, where E is the energy of the incident electron and E_m is the ionization energy required for the simultaneous removal of m electrons from atom A , which is larger than the binding energy E_k of electrons in the sub-shell labelled by k . We further note that for impact energies above about 10^5 eV the energy dependence has to be modified to include relativistic effects. This has been discussed in a previous paper [98]. The weighting factors g^m for equ. (13) have been determined from a fitting procedure (for details, see the

previous papers by Deutsch et al. [109, 128]) and can be approximated by an exponential function of the form:

$$g^m(Z) = a(Z)e^{-b(Z)m} \quad (14)$$

where Z is the nuclear charge and $a(Z)$ and $b(Z)$ are two empirically determined functions (see Fig. 20).

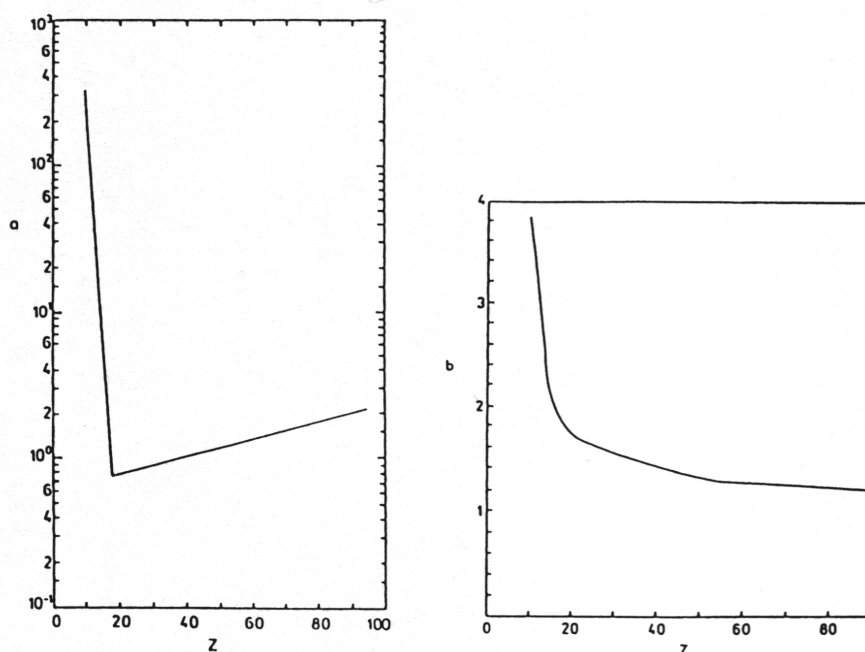


Figure 20. Parameter a from equation (14) as a function of the nuclear charge Z (left hand side) and parameter b from equation (14) as a function of nuclear charge Z (right hand side) after Ref. [109].

Experimental data for the formation of multiply charged ions A^{m+} (for $m > 3$) produced by electron impact ionisation of a neutral atom A are available for only a few atoms, primarily for the noble gases Ne, Ar, Kr, and Xe (e.g., [50, 51, 129, 134–141]). In contrast experimental data for the formation of multiply charged ions from other neutral atomic targets mentioned above (e.g., N etc.) are not available in the literature to the best of our knowledge.

The cross section for the double ionization of Ar has been measured by more groups than any other double ionization cross section. This is due to a controversy regarding the cross section ratio Ar^+/Ar^{2+} which appeared in the literature in the late 1980s [50]. As a consequence, many groups using different experimental techniques revisited the measurement of this cross section ratio, e.g., [51, 137, 142]. This resulted in a level of confidence of the experimentally determined Ar^{2+} ionization cross section by now of better than 10% which renders it perhaps the best known atomic double ionization cross section. Fig. 21 shows as an example the DM calculation for the formation of Ar^{2+} in comparison with some of the experimental data that have been reported for this cross section [134, 143, 144] and in comparison with the ST cross section [145]. It is obvious that the experimental data sets are in excellent agreement with each other (in particular those of Ref. [134] and [139]) and that the DM cross section is in good agreement with the measured data. The ST cross section lies significantly below the measured data for impact energies up to 500 eV (up to a factor of 4 near the maximum of the cross section) and approaches the measured data only in the high energy region. Fig. 22 shows as another example the calculated DM cross sections for Ar^{m+} ($m=3-5$) in comparison with selected experimental data [138, 141, 144] and with the ST cross sections. For more details on the argon case (in particular on the increasing discrepancy observed between the

calculated DM cross sections and the calculated ST cross sections as m increases) where experimental data are available up to $m=8$ see [133].

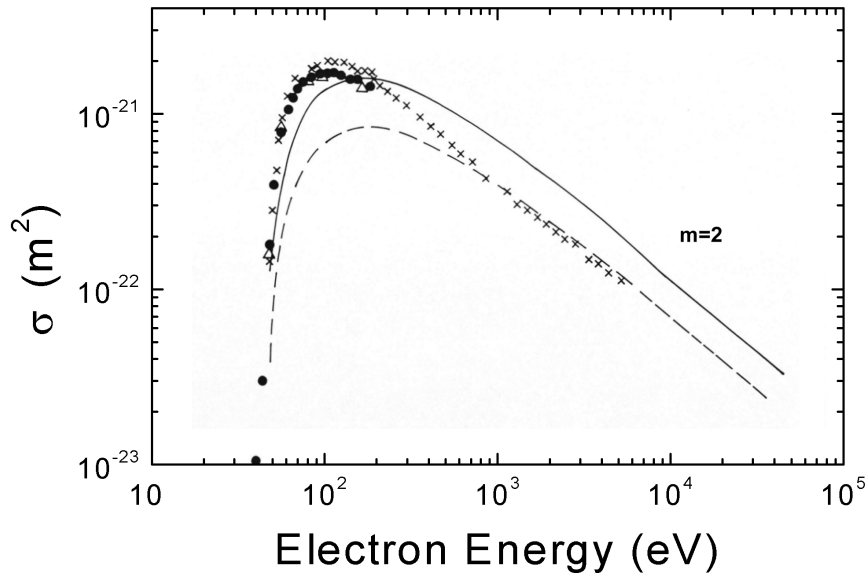


Figure 21. Cross sections for the formation of Ar^{2+} ions by electron impact ionisation of Ar after [133]. The experimental data are from Märk [142] (open triangles), Wetzel et al. [134] (filled dots), and McCallion et al. [144] (crosses). The solid line represents the DM cross section and the dashed line represents the ST cross section.

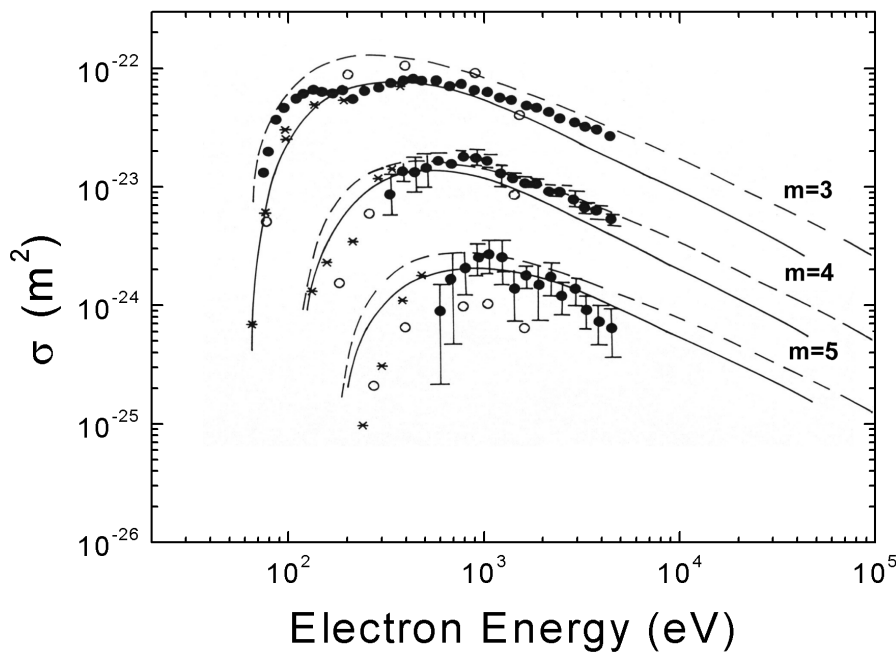


Figure 22. Cross sections for the formation of Ar^{m+} ($m=3-5$) ions by electron impact ionisation of Ar after [133]. The experimental data are from Almeida et al. [138] (open dots), Koslowski et al. [141] (stars), and McCallion et al. [144] (filled dots). The solid line represents the DM cross section and the dashed line represents the ST cross section.

In Ne, experimental data are available up to $m = 5$. Ne cross sections based on the DM formalism with m up to three have been presented and discussed in [106] and excellent agreement was observed between our calculations and experimental data of Lebius et al.

[136]. Figure 23 shows as an example a comparison between the available experimental data for the formation of Ne^{4+} and Ne^{5+} and the results of calculations based on the DM-formalism (dashed line) and the ST method (solid line). Two observations are apparent, (i) there is satisfactory agreement between the experimental data and the present predictions of the DM-formalism for Ne^{4+} over the entire range of impact energies and for Ne^{5+} in the regime of higher impact energies (above about 2 keV) and (ii) the predictions of Shevelko and Tawara [132] overestimate the experimental data in both cases and the overestimation increases with increasing stage of ionization.

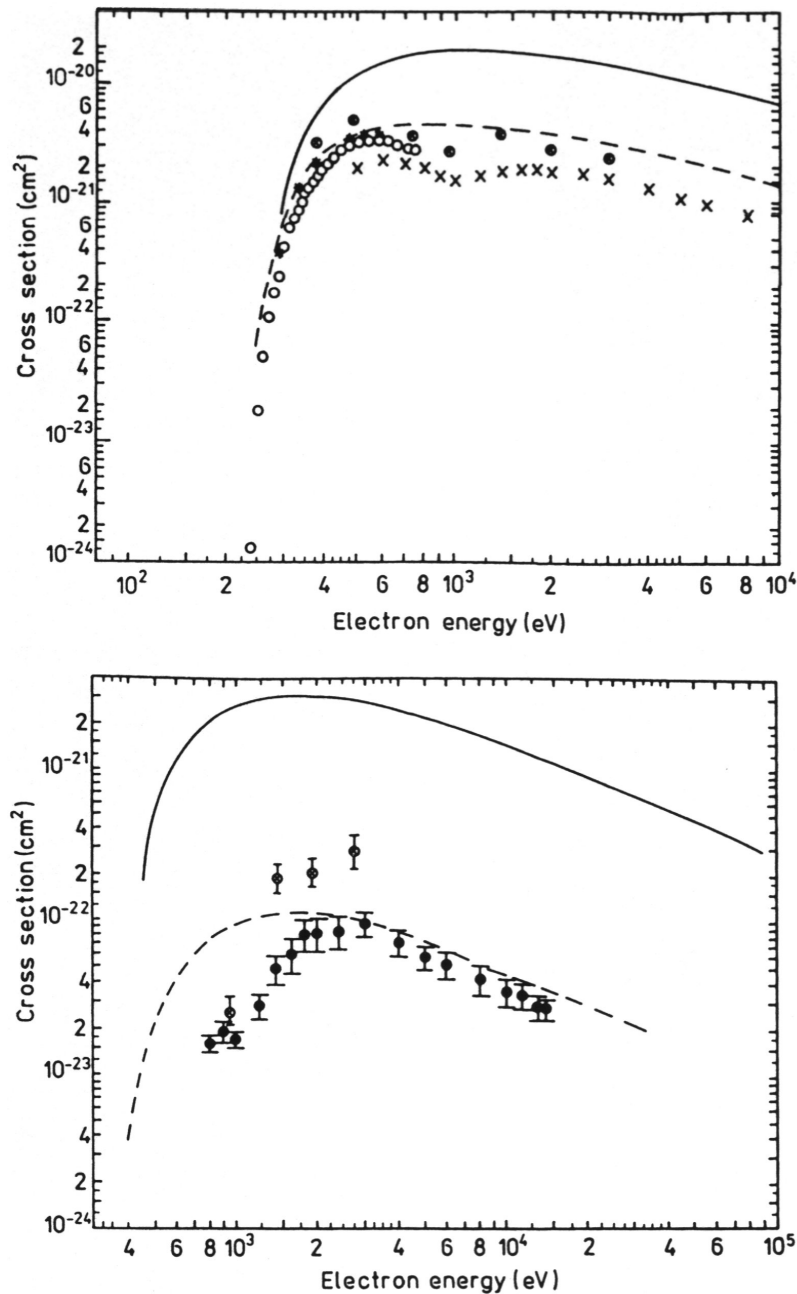


Figure 23. Upper part: Calculated cross sections after [109] for the formation of Ne^{4+} by electron impact ionisation of Ne using the DM formalism (dashed line) and the ST method (solid line) in comparison with the experimental data points designated in [109]. Lower part: Same as upper part for Ne^{5+} .

Figure 24 summarizes the results given in [109] of the calculations for the formation of Ne^{m+} ions for $m = 1-10$. It is apparent from this figure 4 that the cross sections for the formation of multiply charged ions decreases rapidly with the degree of ionization m . This is to be expected, since the probability that a collision of an atom with a single electron results in the simultaneous, single-step removal of m electrons decreases rapidly with increasing m . Moreover, the position of the maximum of the cross section curve for the formation of the multiply-charged ions shifts strongly with the degree of ionization. This again is to be expected as the threshold for ionization increases strongly with the degree of ionization and thus the cross section is shifted to higher energies. In order to understand this in a more quantitative manner it is interesting to rewrite equ. (13) in the reduced form, i.e.,

$$\frac{\sigma^{m+}(U)}{g^m} = \sum_k \pi(r_k)^2 \xi_k f_k(U) \quad (15)$$

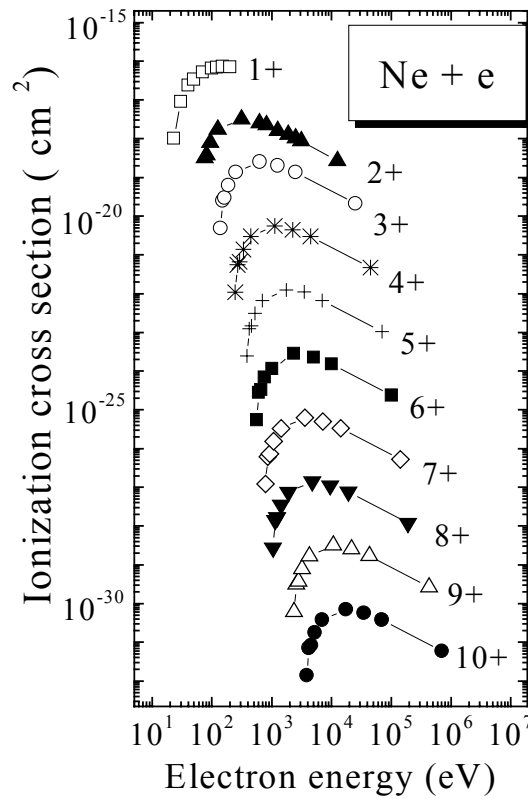


Figure 24. Calculated cross sections using the DM formalism for the formation of Ne^{m+} ($m = 1-10$) ions by electron impact ionisation of Ne as a function of electron energy after [109].

In this case the dependence of the cross section on the reduced energy is determined only by the function $f_k(U)$. For Ne ions up to $m = 8$, the cross section dependence on U is independent on m , i.e. given by

$$\sigma^{m+}(U) \propto (r_{2s})^2 \xi_{2s} f_{2s}(U) + (r_{2p})^2 \xi_{2p} f_{2p}(U) \quad (16)$$

It follows, that the position of the maximum of the cross section scales with the ionization energy E_m because $U_{\max} = E_{\max}/E_m$ is independent of m . This scaling law is also valid (to within about 5%) for the production of ninefold and tenfold charged Ne ions as the additional

term in equ.(16) representing the contribution of the 1s electrons is only of minor importance for the overall cross section.

From a standpoint of applications, in particular considering fusion plasmas, it is often quite desirable to have ionisation rate coefficients available rather than electron impact ionisation cross sections. Therefore we give here as an example four sets (Figs. 25–28) of ionisation rate coefficients for Be, B, C and O atoms as a function of electron temperature (1 eV corresponding to 11605 K in these figures).

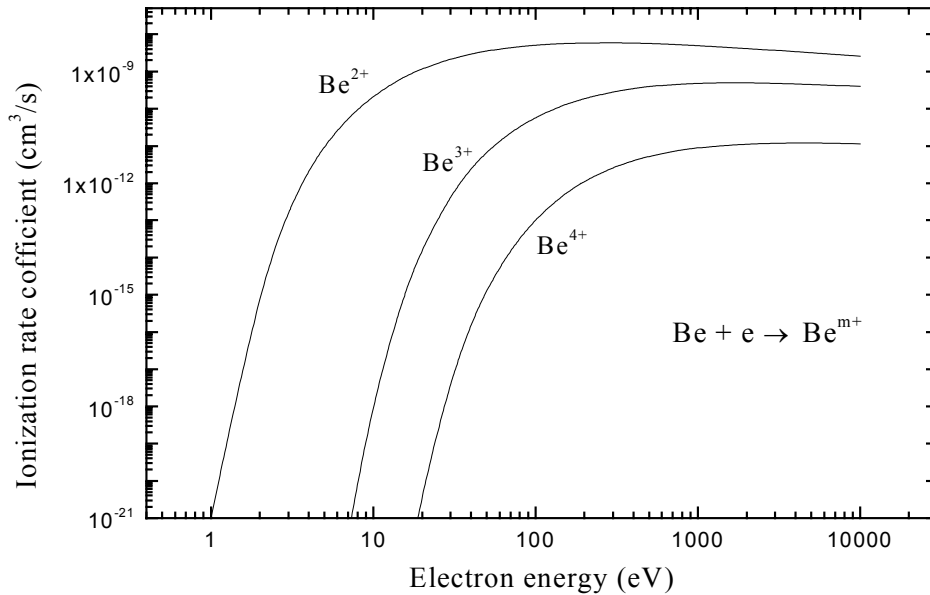


Figure 25. Ionization rate coefficients for Be as a function of the electron temperature after [128].

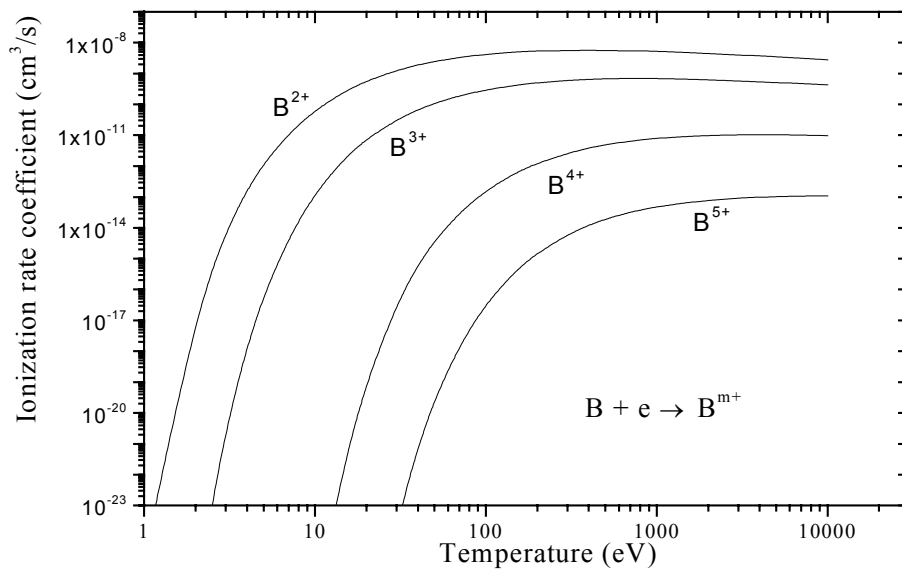


Figure 26. Ionization rate coefficients for B as a function of the electron temperature after [128].

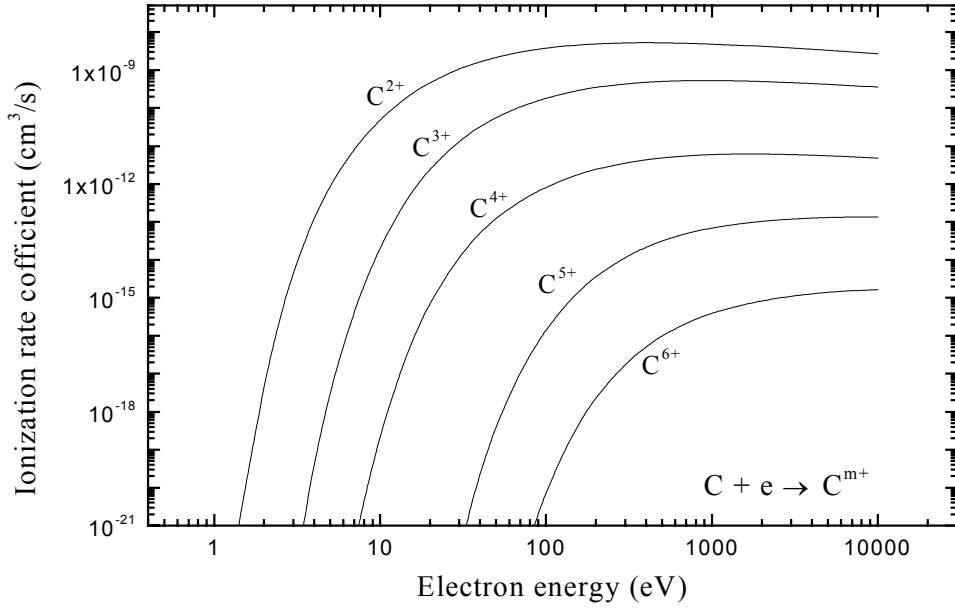


Figure 27. Ionization rate coefficients for C as a function of the electron temperature after [128].

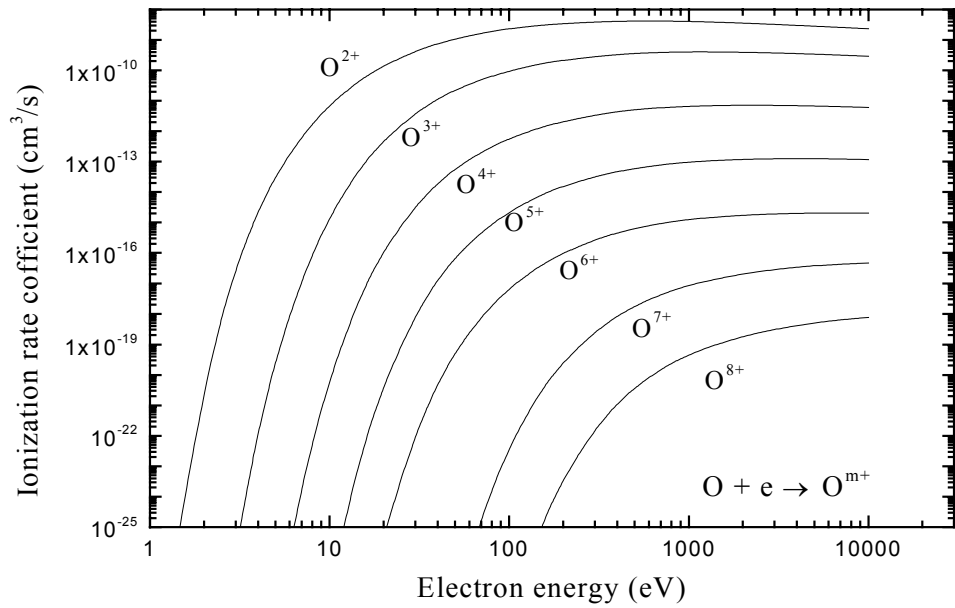


Figure 28. Ionization rate coefficients for O as a function of the electron temperature after [128].

5. Conclusions

In this paper we have reviewed the present status of our knowledge on single ionisation of molecules (and molecular ions) and on multiple ionisation of atoms by single electron impact with special reference to work performed in our Innsbruck laboratory within a IAEA

sponsored CRP. Significant progress has been made in the last decade with development of novel experimental and theoretical techniques. However our knowledge of ionisation cross sections and ionisation rate coefficients is still insufficient. The importance of electron impact ionisation in many fields of science and technology, in particular in fusion plasmas, therefore ensures that the study of electron induced ionisation will need to be continued also in the 21st century.

ACKNOWLEDGEMENTS

This work was carried out (i) within the Association EURATOM-ÖAW and (ii) within the IAEA Co-ordinated Research Project (CRP) on “Atomic and Plasma-Wall Interaction Data for Fusion Reactor Divertor Modelling” (1995–1999) and partially supported by the FWF, Wien, Austria.

REFERENCES

- [1] JANEV, R.K., Ed., Atomic and Molecular Processes in Fusion Edge Plasmas, Plenum, New York 1995.
- [2] MÄRK, T.D., Chapter 4 in Ref. [1], 59.
- [3] DEFRANCE, P., DUPONCHELLE, M., MOORES, D.L., Chapter 7 in Ref. [1] 153.
- [4] TAWARA, H., Chapter 16 in Ref. [1], 461.
- [5] POST, D.L., in Atomic and Molecular Data and their Applications (MOHR, P.J., WIESE, W.L., Eds), AIP Conference Proceedings 434, Woodbury 1998, 233.
- [6] HOFER, W.O., ROTH, P., Eds., Physical processes of the Interaction of Fusion Plasmas with Solids, Academic Press, San Diego 1996.
- [7] GREGORY, D., TAWARA, H., Book of Abstracts, 15th ICPEAC, New York, 1989, 352.
- [8] DUNN, G.H., Chapter 8 in Electron Impact Ionization (MÄRK, T.D., DUNN, G.H., Eds.), Springer, Wien 1985, 277.
- [9] MÄRK, T.D., Plasma Phys. and Controlled Fusion **34** (1992) 2083.
- [10] RAUTH, T., ECHT, O., SCHEIER, P., MÄRK, T.D., Chem. Phys. Lett. **247** (1995) 515.
- [11] KIEFFER, L. J., DUNN, G. H., Rev. Mod. Physics **38**, (1966) 1.
- [12] MÄRK, T.D., in Electron Impact Ionization (MÄRK, T.D., DUNN, G.H., Eds.), Springer, Wien 1985, 137.
- [13] DE HEER, F.J., INOKUTI, M., Electron Impact Ionization (MÄRK, T.D., DUNN, G.H., Eds.), Springer, Wien 1985, 232.
- [14] TATE, J.T., SMITH, P.T., Phys. Review **39** (1932) 270.
- [15] TARNOVSKY, V., BECKER, K., Plasma Sources Sci. Techn. **4** (1995) 307.
- [16] MÄRK, T.D., DUNN, G.H., Ed., Electron Impact Ionization, Springer, Wien 1985.
- [17] MÄRK, T.D., in Electron Molecule Interactions And Their Applications (CHRISTOPHOROU, L.G., Ed.), Academic Press, New York 1984, 251.
- [18] FREUND, R.S., in Swarm Studies And Inelastic Electron Molecule Collisions (PITCHFORD, L.C., MC.KOY, B.V., CHUTJIAN, A., TRAJMAR, S., Eds.) Springer, New York 1987, 329.
- [19] MÄRK, T.D., in Atomic And Molecular Processes In Fusion Edge Plasmas (JANEV, R.K, Ed.) Plenum Press, New York 1995, 59.
- [20] MÄRK, T.D., in Linking The Gaseous And The Condensed Phases Of Matter (CHRISTOPHOROU, L.G., ILLENBERGER, E., SCHMIDT, W.F., Eds.) Plenum Press, New York 1994, 155.

- [21] MATT, S., FIEGELE, T., HANEL, G., MUIGG, D., DENIFL, G., BECKER, K., DEUTSCH, H., ECHT, O., MASON, N., STAMATOVIC, A., SCHEIER, P., MÄRK, T.D., Proceedings of 2nd Intern. Conference on Atomic and Molecular Data and their Applications, Oxford, AIP Conference Proceedings, 2000, in print.
- [22] MÄRK, T.D., Invited review lecture , XIIIth Summer school on the physics of ionized gases (SPIG), Sibenik 1986.
- [23] DEUTSCH, H., BECKER, K., MATT, S., MÄRK, T.D., Int. J. Mass Spectrometry **197** (2000) 37.
- [24] POLL, H. U., WINKLER, C., MARGREITER, D., GRILL, V., MÄRK, T.D., Int. J. Mass Spectrometry Ion Processes **112** (1993) 1.
- [25] GRILL, V., WALDER, G., MARGREITER, D., RAUTH, T., POLL, H. U., SCHEIER, P., MÄRK, T.D., Z. Physik **D25** (1993) 217.
- [26] FOLTIN, V., FOLTIN, M., MATT, S., SCHEIER, P., BECKER, K., DEUTSCH, H., MÄRK, T.D., Chem. Phys. Letters **289** (1998) 181.
- [27] BASNER, R., SCHMIDT, M., BECKER, K., DEUTSCH, H., Adv. Atomic Molecular Optical Physics **43** (2000) 147.
- [28] GRILL, V., WALDER, G., SCHEIER, P., KURDEL, M., MÄRK, T.D., Int. J. Mass Spectrom. Ion Proc. **129** (1993) 31.
- [29] POLL, H.U., GRILL, V., MATT, S., ABRAMZON, N., BECKER, K., SCHEIER, P., MÄRK, T.D., Int. J. Mass Spectrometry Ion Processes **177** (1998) 143.
- [30] MAIR, C., FIEGELE, T., BIASIOLI, F., WÖRGÖTTER, R., GRILL, V., LEZIUS, M., MÄRK, T.D., Plasma Sources Sci. Technology **8** (1999) 191.
- [31] STEPHAN, K., DEUTSCH, H., MÄRK, T.D., J. Chem. Physics **83** (1985) 5712.
- [32] POLL, H.U., MEICHSNER, J., Contribution Plasma Physics **27** (1987) 359.
- [33] MA, C., SPORLEDER, C.H., BONHAM, R.A., Phys. Review **A44** (1991) 2921.
- [34] SCHRAM, B.L., VAN DER WIEL, M.J., DE HEER, F.J., MOUSTAFA, H.R., J. Chem. Phys. **44** (1966) 49.
- [35] DJURIC, N., CADEZ, I., KUREPA, M., Int. J. Mass Spectrom. Ion Proc. **108** (1991) R1.
- [36] NISHIMURA, H., TAWARA, H., J. Phys. B. **27** (1994) 2063.
- [37] IRIKURA, K.K., KIM, Y-K., private communication 2000.
- [38] DEUTSCH, H., BECKER, K., PROBST, M., MÄRK, T.D., J. Phys. **B** submitted (2000).
- [39] FREUND, R.R., WETZEL, R.C., SHUL, R.J., HAYES, T.R., Phys.Review A **41** (1990) 3575.
- [40] TARNOVSKY, V., BECKER, K., J. Chem. Phys. **98** (1992) 7868.
- [41] STRAUB, H.C., RENAULT, P., LINDSAY, B.G., SMITH, K.A., STEBBINGS, R.F., Phys. Review **A52** (1995) 1115.
- [42] STRAUB, H.C., LINDSAY, B.G., SMITH, K.A., STEBBINGS, R.F., J. Chem. Physics **108** (1998) 109.
- [43] TIAN, C., VIDAL, C.R., J. Chem. Physics **108** (1998) 927.
- [44] TIAN, C., VIDAL, C.R., Phys. Review **A59** (1999) 1955.
- [45] ALMEIDA, D.P., Int. J. Mass Spectrometry **184** (1999) 49.
- [46] BRUCE, M.R., MA, C., BONHAM, R.A., Chem. Phys. Letters **190** (1992) 285.
- [47] THOMPSON, W.R., SHAH, M.B., GILBODY, H.B., J. Phys. B **28** (1995) 3121.
- [48] JIAO, C.Q., GARSCADDEN, A., HAALAND, P.D., Int. J. Mass Spectrometry **184** (1999) 83.
- [49] O'CONNOR, C.S.S., PRICE, S.D., Int. J. Mass Spectrometry **184** (1999) 11.
- [50] KRISNAKUMAR, E., SRIVASTAVA, S.K., Int. J. Mass Spectrometry and Ion Processes **113** (1992) 1.
- [51] SYAGE, J.A., Phys. Review **A46** (1992) 5666.

- [52] JOHNSTON, M., FUJII, K., NICKEL, J., TRAJMAR, S., *J. Phys.* **B29** (1995) 531.
- [53] BECKER, K. (Ed.), *Novel Aspects Of Electron-Molecule Collisions*, World Scientific, Singapore 1998.
- [54] JARROLD, M.F., ILLIES, J., BOWERS, M.T., *J. Chem. Phys.* **79** (1983) 6086.
- [55] GOTTS, N.G., STACE, J., *Phys. Rev. Lett.* **66** (1991) 21.
- [56] DUNN, G.H., DJURIC, N., in *Novel Aspects of Electron-Molecule Collisions* (BECKER, K., Ed.) World Scientific, Singapore 1998, 241.
- [57] VÖLPEL, R., HOFMANN, G., STEIDL, M., STENKE, M., SCHLAPP, M., TRASSL, R., SALZBORN, E., *Phys. Rev. Lett.* **71** (1993) 3439.
- [58] CODY, R.B., FREISER, B.S., *Analytical Chemistry* **51** (1979) 547.
- [59] KRUGER, N.A., ZUBAREV, R.A., HORN, D.M., McLAFFERTY, F.W., *Int. J. Mass Spectrom. Ion Proc.* **185/186/187** (1999) 787.
- [60] RAUTH, T., ECHT, O., SCHEIER, P., MÄRK, T.D., *Chem. Phys. Lett.* **247** (1995) 515.
- [61] MATT, S., PARAJULI, R., STAMATOVIC, A., SCHEIER, P., MÄRK, T.D., LASKIN, J., LIFSHITZ, C., *Eur. Mass Spectrom.* **5** (1999) 477.
- [62] LEVSEN, K., *Fundamental Aspects of Organic Mass Spectrometry*, Verlag Chemie, Weinheim, 1978.
- [63] COOKS, R.G., BEYNON, J.H., CAPRIOLI, R., LESTER, G.R., *Metastable Ions*, Elsevier, Amsterdam, 1973.
- [64] MEDVED, M., COOKS, R.G., BEYNON, J.H., *Int. J. Mass Spectrom. Ion Proc.* **19** (1976) 179.
- [65] LIFSHITZ, C., GEFEN, S., ARAKAWA, R., *J. Phys. Chem.* **88** (1984) 4242.
- [66] LASKIN, J., WEICKHARDT, C., LIFSHITZ, C., *Int. J. Mass Spectrom. Ion Proc.* **161** (1997) L7.
- [67] JI, Y., FOLTIN, M., LIAO, C., MÄRK, T.D., *J. Chem. Phys.* **96** (1992) 3624.
- [68] MATT, S., SONDEREGGER, DAVID, R., ECHT, O., SCHEIER, P., LASKIN, J., LIFSHITZ, C., MÄRK, T.D., *Int. J. Mass Spectrom. Ion Proc.* **185/186/187** (1999) 813.
- [69] MATT, S., ECHT, O., STAMATOVIC, A., MÄRK, T.D., *J. Chem. Phys.* **113** (2000) in print.
- [70] MATT, S., ECHT, O., RAUTH, T., DÜNSER, B., LEZIUS, M., STAMATOVIC, A., SCHEIER, P., MÄRK, T.D., *Z. Phys.* **D40** (1997) 389.
- [71] HOLMES, J.L., OSBORNE, A. D., *Int. J. Mass Spectrom. Ion Proc.* **23** (1977) 189.
- [72] RUMPF, B.A., DERRICK, P. J., *Int. J. Mass Spectrom. Ion Proc.* **82** (1988) 239.
- [73] RUDGE, M.R.H., *Rev. Mod. Physics* **40** (1968) 564.
- [74] YOUNGER, S.M., in *Electron Impact Ionization* (MÄRK, T.D., DUNN, G.H. Eds.), Springer Verlag, Wien 1985, 1.
- [75] YOUNGER, S.M., MÄRK, T.D., in *Electron Impact Ionization* (MÄRK, T.D., DUNN, G.H., Eds.), Springer Verlag, Wien 1985, 24.
- [76] TARNOVSKY, V., BECKER, K., *Plasma Sources Sci. Technol.* **4** (1995) 307.
- [77] ÖTVOS, J.W., STEVENSON, D.P., *J. Am. Chem. Soc.* **78** (1956) 546.
- [78] FITCH, W.L., SAUTER, A.D., *Anal. Chem.* **55** (1983) 832.
- [79] DEUTSCH, H., SCHMIDT, M., *Beitr. Plasmaphysik* **24** (1984) 475.
- [80] DEUTSCH, H., BECKER, K., MÄRK, T.D., *Int. J. Mass Spectrometry Ion Processes* **167/168** (1997) 503.
- [81] DEUTSCH, H., BECKER, K., BASNER, R., SCHMIDT, M., MÄRK, T.D., *J. Phys. Chemistry* **106** (1998) 8819.
- [82] BOBELDIJK, M., VAN DER ZANDE, W.J., KISTEMAKER, P.G., *Chem. Phys.* **179** (1994) 125.
- [83] AITKEN, C.G., BLUNT, D.A., HARLAND, P.W., *J. Chem. Physics* **101** (1994) 11074.

- [84] AITKEN, C.G., BLUNT, D.A., HARLAND, P.W., *Int. J. Mass Spectrometry Ion Processes* **149/150** (1995) 279.
- [85] VALLANCE, A., HARLAND, P.W., MacLAGAN, R.G.A.R., *J. Phys. Chemistry* **100** (1996) 15021.
- [86] MARGREITER, D., DEUTSCH, H., SCHMIDT, M., MÄRK, T.D., *Int. J. Mass Spectrometry Ion Processes* **100** (1990) 157.
- [87] DEUTSCH, H., CORNELISSEN, C., CESPIVA, L., BONACIC-KOUTECKY, V., MARGREITER, D., MÄRK, T.D., *Int. J. Mass Spectrometry Ion Processes* **129** (1993) 43.
- [88] DEUTSCH, H., MÄRK, T.D., TARNOVSKY, V., BECKER, K., CORNELISSEN, C., CESPIVA, L., BONACIC-KOUTECKY, V., *Int. J. Mass Spectrometry Ion Processes* **137** (1994) 77.
- [89] JAIN, D.K., KHARE, S.P., *J. Phys.* **B9** (1976) 1429.
- [90] KHARE, S.P., MEATH, W.J., *J. Phys.* **B20** (1987) 2101.
- [91] KIM, Y.K., RUDD, M.E., *Phys. Rev.* **A50** (1994) 3954.
- [92] HWANG, W., KIM, Y.K., RUDD, M.E., *J. Chem. Physics* **104** (1996) 2965.
- [93] KIM, Y.K., HWANG, W., WEINBERGER, N.M., ALI, M.A., RUDD, M.E., *J. Chem. Physics* **106** (1997) 1026.
- [94] HUO, W.M., KIM, Y.K., *IEEE Trans. Plasma Science* **27** (1999) 1225.
- [95] DEUTSCH, H., MÄRK T.D., *Int. J. Mass Spectrom. Ion Proc.* **79** (1987) R1.
- [96] MARGREITER, D., DEUTSCH, H., MÄRK, T.D., *Int. J. Mass Spectrom. Ion Proc.* **139** (1994) 127.
- [97] MARGREITER, D., DEUTSCH, H., MÄRK, T.D., *Contrib. Plasma Phys.* **30** (1990) 487.
- [98] DEUTSCH, H., MARGREITER, D., MÄRK, T.D., *Z. Phys.* **D29** (1994) 31.
- [99] DEUTSCH, H., MÄRK, T.D., *Contrib. Plasma Phys.* **34** (1994) 19.
- [100] DEUTSCH, H., BECKER, K., MATT, S., MÄRK, T.D., *J. Phys.* **B32** (1999) 4249.
- [101] DEUTSCH, H., BECKER, K., PITTNER, J., BONACIC-KOUTECKY, V., MATT, S., MÄRK, T.D., *J. Phys.* **B29** (1996) 5175.
- [102] DEUTSCH, H., BECKER, K., MÄRK, T.D., *Int. J. Mass Spectrom. Ion Proc.* **144** (1995) L9.
- [103] DEUTSCH, H., BECKER, K., MATT, S., MÄRK, T.D., *J. Chem. Phys.* **111** (1999) 1964.
- [104] DEUTSCH, H., MÄRK T.D., *Nucl. Instrum. Meth. Phys. Res.* **B98** (1995) 135.
- [105] DEUTSCH, H., BECKER, K., MÄRK, T.D., *Int. J. Mass Spectrom. Ion Proc.* **151** (1995) 207.
- [106] DEUTSCH, H., BECKER, K., MÄRK, T.D., *Contrib. Plasma Phys.* **35** (1995) 421.
- [107] DEUTSCH, H., BECKER, K., MÄRK, T.D., *J. Phys.* **B29** (1996) L497.
- [108] DEUTSCH, H., BECKER, K., ALMEIDA, D.P., MÄRK, T.D., *Int. J. Mass Spectrom. Ion Proc.* **171** (1997) 115.
- [109] DEUTSCH, H., BECKER, K., MATT, S., MÄRK, T.D., *Plasma Phys. Control. Fusion* **40** (1998) 1721.
- [110] THOMSON, J.J., *Phil. Mag.* **23** (1912) 449.
- [111] GRYSSINSKI, M., *Phys. Rev.* **A138** (1965) 305.
- [112] MARGREITER, D., PhD Thesis 1992, Universität Innsbruck.
- [113] BETHE, H, *Ann. Phys.* **5** (1930) 325.
- [114] MOTT, M.S., MASSEY, H.S.W., *The Theory of Atomic Collisions*, Oxford University Press, Oxford 1943, 243.
- [115] MANN, J.S., *J. Chem. Phys.* **46** (1967) 1646.
- [116] TIWARI, P., RAI, D.K., RUSTGI, M.L., *J. Chem. Phys.* **73** (1980) 3040.

- [117] DEUTSCH, H., BECKER, K., MÄRK, T.D., *Int. J. Mass Spectrom. Ion Proc.* **177** (1998) 47.
- [118] DEUTSCH, H., BECKER, K., MÄRK, T.D., *Int. J. Mass Spectrom. Ion Proc.* **185/186/187** (1999) 319.
- [119] MULLIKAN, R.S., *J. Chim. Phys.* **46** (1949) 675.
- [120] TANG, R., CALLAWAY, J., *J. Chem. Phys.* **84** (1986) 6858.
- [121] TERISSOL, M., BORDAGE, M.C., CAUDREKIER, V., SEGUR, P., in *Atomic and Molecular Data for Radiotherapy*, IAEA-TECDOC-506, International Atomic Energy Agency, Vienna, 1989.
- [122] DESCLAUX, J.P., *Atom. Data Nucl. Data Tables* **12** (1973) 325.
- [123] SAKSENA, V., KUSHWAHA, M.S., KHARE, S.P., *Physica* **B233** (1997) 201.
- [124] SALKSENA, V., KUSHWAHA, M.S., KHARE, S.P., *Int. J. Mass Spectr. Ion Proc.* **171** (1997) L1.
- [125] BAIOCCHI, F.A., WETZEL, R.C., FREUND, R.S., *Phys. Rev. Lett.* **53** (1984) 771.
- [126] TARNOVSKI, V., LEVIN, A., DEUTSCH, H., BECKER, K., *J. Phys.* **B29** (1996) 139.
- [127] KHARE, S. P., SHARMA, M. K., TORMAR, S., *J. Phys.* **B32** (1999) 3147.
- [128] DEUTSCH, H., BECKER, K., SENN, G., MATT, S., MÄRK, T.D., *Int. J. Mass Spectrom.* **192** (1999) 1.
- [129] ALMEIDA, D.P., BECKER, K., DEUTSCH, H., *Int. J. Mass Spectrom. Ion Proc.* **163** (1997) 39.
- [130] GEROM, K., PUERTA, J., WIESEMANN, K., *J. Phys.* **B27** (1994) 747.
- [131] FISHER, V., RALCHENKO, Y., GOLDGIRSH, A., FISHER, D., MARON, Y., *J. Phys.* **B28** (1995) 3027.
- [132] SHEVELKO, V.P., TAWARA, H., *J. Phys.* **B28** (1995) L589.
- [133] DEUTSCH, H., BECKER, K., MÄRK, T.D., *Plasma Phys. Controlled Fusion* **42** (2000) 489.
- [134] WETZEL, R.C., BIAOCCHI, F.A., HAYES, T.R., FREUND, R.S., *Phys. Rev.* **A39** (1987) 559.
- [135] STEPHAN, K., HELM, H., MÄRK, T.D., *J. Chem. Phys.* **73** (1980) 3763.
- [136] LEBIUS, H., BINDER, J., KOSLOWSKI, H.R., WIESEMANN, K., HUBER, B.A., *J. Phys.* **B22** (1992) 83.
- [137] SYAGE, J.A., *J. Phys.* **B24** (1991) L527.
- [138] ALMEIDA, D.P., FONTES, A.C., MATTOS, I.S., GOGHINO, C.F.L., *J. Electron. Spectr. Relat. Phenom.* **67** (1994) 503.
- [139] SCHRAM, B.L., BOERBOOM, A.J.H., KISTEMAKER, J., *Physica* **32** (1966) 185.
- [140] SCHRAM, B.L., *Physica* **32** (1966) 197.
- [141] KOSLOWSKI, H.R., BINDER, J., HUBER, B.A., WIESEMANN, K., *J. Phys.* **B20** (1987) 5903.
- [142] TARNOVSKY, V., BECKER, K., *Z. Phys.* **22** (1992) 603.
- [143] MÄRK, T.D., *Beitr. Plasmaphys.* **22** (1982) 257.
- [144] McCALLION, P., SHAH, M.B., GILBODY, H.B., *J. Phys.* **B25** (1992) 1061.
- [145] BELENGER, C., DEFRANCE, P., SALZBORN, E., SHEVELKO, V.P., TAWARA, H., USKOV, D.B., *J. Phys.* **B30** (1997) 2667.

Electron-molecule dissociation cross-sections of H₂, N₂ and O₂ in different vibrational levels

M. Capitelli^{a,b}, R. Celiberto^c, A. Eletsii^d, A. Laricchiuta^a

^aDepartment of Chemistry, University of Bari, Italy

^bResearch Center of Plasma-Chemistry, CNR, Italy

^cPolitecnico of Bari, Italy

^dRussian Research Center “Kurchatov Institute”, Moscow, Russian Federation

Abstract. Cross section data of relevant processes for collisional radiative models of H₂ plasma systems are reviewed, focusing on main dissociative and ion-formation channels. Rate coefficients, in a wide temperature range, are presented, emphasising the role of vibrationally excited targets. Furthermore an attempt is made to explain the formation of negative hydrogen ions from Rydberg states. Dissociation of N₂ and O₂ molecules are also considered.

1. Introduction

The construction of collisional radiative models for molecular and atomic hydrogen needs a lot of cross sections which, despite the large use of hydrogen plasmas, are only known when the target is in his ground state.

The knowledge of electron-molecule, atom-molecule and atom/molecule surface interaction when the molecule is in a vibrationally or electronically excited state is on the contrary very poor.

In these last years our group reported several studies on these topics which we will try to summarize in this paper. In particular we will update recent review papers [1-5] including, in some cases, unpublished work.

We focus our attention on the dissociation channels of H₂ including dissociative ionization and dissociative attachment from H₂ Rydberg states.

Dissociative cross sections are also presented for N₂ and O₂.

In a companion paper we will discuss in detail the excitation and dissociation in the H-H₂(v,j) system [6], while the collision integrals (transport cross sections) of the different interactions existing in hydrogen plasmas will be reported in ref. [7] (see also ref. [8] for the collision integrals of electronically excited H(n)).

On the other hand the paper of Billing et al. [9] summarizes the effort made in the calculation of deactivation of vibrationally excited states and recombination of atomic hydrogen on different metallic surfaces.

2. State to state electron molecule excitation-dissociation cross sections

We report calculations performed by using semiclassical and classical approximations on electron-molecule inelastic collisions. Complete sets of excitation and dissociation cross sections involving the whole vibrational ladder of ground state and electronically excited molecules have been obtained.

In some cases cross sections for different isotopes have been obtained by using the impact parameter method and appropriate scaling laws.

A list of cross sections is reported in table 1. Tables of these cross sections have been reported in ref. [5].

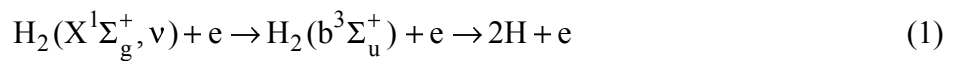
Here we want to discuss the dissociation of vibrationally excited H_2 through different channels:

- (i) repulsive $b^3\Sigma_u^+$
- (ii) repulsive portion of singlet states
- (iii) bound triplet states
- (iv) dissociative ionization

Table 1. List of H_2 processes and channels considered in the paper

PROCESS	CHANNEL
DISSOCIATION	$H_2(X^1\Sigma_g^+, v) + e \rightarrow H_2(b^3\Sigma_u^+) + e \rightarrow 2H + e$
DIRECT DISSOCIATION THROUGH EXCITED STATES	$H_2(X^1\Sigma_g^+, v) + e \rightarrow H_2(B^1\Sigma_u^+) + e \rightarrow 2H + e$ $H_2(X^1\Sigma_g^+, v) + e \rightarrow H_2(C^1\Pi_u) + e \rightarrow 2H + e$ $H_2(X^1\Sigma_g^+, v) + e \rightarrow H_2(B'^1\Sigma_u^+) + e \rightarrow 2H + e$ $H_2(X^1\Sigma_g^+, v) + e \rightarrow H_2(D^1\Pi_u) + e \rightarrow 2H + e$ $H_2(X^1\Sigma_g^+, v) + e \rightarrow H_2(B''^1\Sigma_u^+) + e \rightarrow 2H + e$ $H_2(X^1\Sigma_g^+, v) + e \rightarrow H_2(D'^1\Pi_u) + e \rightarrow 2H + e$
BOUND-BOUND EXCITATION FOLLOWED BY DISSOCIATION	$H_2(X^1\Sigma_g^+, v) + e \rightarrow H_2(a^3\Sigma_g^+) + e \rightarrow 2H + e$ $H_2(X^1\Sigma_g^+, v) + e \rightarrow H_2(c^3\Pi_u) + e \rightarrow 2H + e$
DISSOCIATIVE IONIZATION	$H_2(X^1\Sigma_g^+, v) + e \rightarrow H_2^+(^2\Sigma_g^+) + 2e \rightarrow H + H^+ + 2e$ $H_2(X^1\Sigma_g^+, v) + e \rightarrow H_2^+(^2\Sigma_u^+) + 2e \rightarrow H + H^+ + 2e$

Figure 1 reports the dissociation cross section of the process:



as a function of energy for different vibrational levels. These cross sections have been obtained by using the classical Gryzinski approximation [5]. The major effect of vibrational excitation is to decrease the threshold energy of the process having however a minor effect on the magnitude of the maximum of cross section. Table 2 reports a comparison of our cross sections and those obtained by Rescigno and Schneider [10] by using the complex Kohn method for electron energy larger than 12 eV. The agreement can be considered satisfactory.

On the other hand the recent ab-initio calculations of Stibbe and Tennyson [11], while confirming the general trend of cross sections, show a shift of their maximum toward lower energies (see figure 2). This shift is reflected on the rate coefficients calculated according to a Maxwell distribution function of electron energy. Inspection of figure 3 shows in fact that rate coefficients which use Stibbe and Tennyson cross sections are, at low temperature, up to an order of magnitude higher than those obtained by using Gryzinski cross sections.

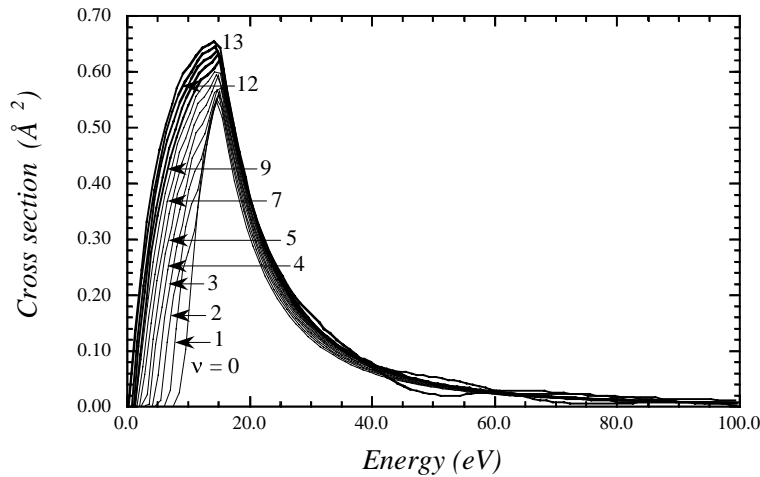


Figure 1 Dissociative cross sections, as a function of impact energy, for the process:
 $H_2(X^1\Sigma_g^+, v = 0, 13) + e \rightarrow H_2(b^3\Sigma_u^+) + e \rightarrow 2H + e$

Table 2. Cross section (a_0^2) for the process $H_2(X^1\Sigma_g^+, v) + e \rightarrow H_2(b^3\Sigma_u^+) + e \rightarrow 2H + e$.
 Comparison with results of rescigno et al.[10]

v	energy = 12eV		energy = 15 eV		energy = 18 eV		energy = 20 eV		energy = 25 eV		energy = 30 eV	
	[5]	[10]	[5]	[10]	[5]	[10]	[5]	[10]	[5]	[10]	[5]	[10]
0	1.420	1.991	1.908	2.227	1.375	1.923	1.095	1.671	0.663	1.139	0.433	0.752
1	1.374	2.176	1.986	2.296	1.414	1.959	1.128	1.695	0.685	1.152	0.448	0.768
2	1.460	2.400	1.942	2.357	1.452	1.996	1.161	1.725	0.707	1.166	0.463	0.785
3	1.571	2.631	2.004	2.428	1.484	2.036	1.189	1.757	0.725	1.185	0.476	0.803
4	1.691	2.831	1.998	2.496	1.514	2.076	1.216	1.788	0.743	1.206	0.488	0.821
5	1.788	3.011	2.028	2.565	1.540	2.116	1.239	1.820	0.759	1.228	0.499	0.840
6	1.881	3.178	2.108	2.638	1.563	2.157	1.259	1.852	0.772	1.252	0.508	0.859
7	1.956	3.340	2.090	2.722	1.587	2.202	1.280	1.888	0.786	1.279	0.518	0.880
8	2.025	3.507	2.135	2.822	1.607	2.254	1.297	1.928	0.797	1.308	0.526	0.903
9	2.092	3.678	2.226	2.942	1.623	2.313	1.310	1.975	0.807	1.341	0.532	0.927

Figure 4 reports the sum of dissociation cross sections on the repulsive part of several singlet states of H_2 as a function of energy for different vibrational levels [5, 12–15]. The intricate behaviour of cross sections for different v is the result of Franck Condon densities linking the different vibrational levels of ground state to the electronic states as well as the behaviour of integrated dipole moment as a function of internuclear distance. These cross sections have been calculated by using the semiclassical impact parameter approximation with CI electronic wavefunctions of both target and final states. Inspection of the figure shows that the increase of vibrational quantum number not only decreases the threshold energy of the process but also substantially increase their maximum. Passing from $v=0$ to $v=10$ the maximum of cross

section increases by a factor 10 much higher than the corresponding increase of cross sections for the excitation of $b^3\Sigma_u^+$ state. The decrease of cross section for $v>10$ is due, as already pointed out, to the form of Franck Condon densities or better to the integrated dipole moment.

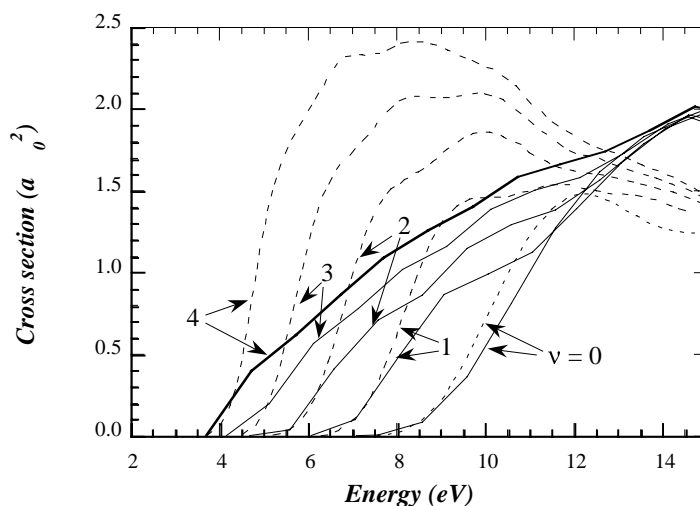


Figure 2 Dissociative cross sections, as a function of impact energy, for the process: $H_2(X^1\Sigma_g^+, v=0,4) + e \rightarrow H_2(b^3\Sigma_u^+) + e \rightarrow 2H + e$. Full line: Celiberto et al. [5]; dotted line: Stibbe and Tennyson [11].

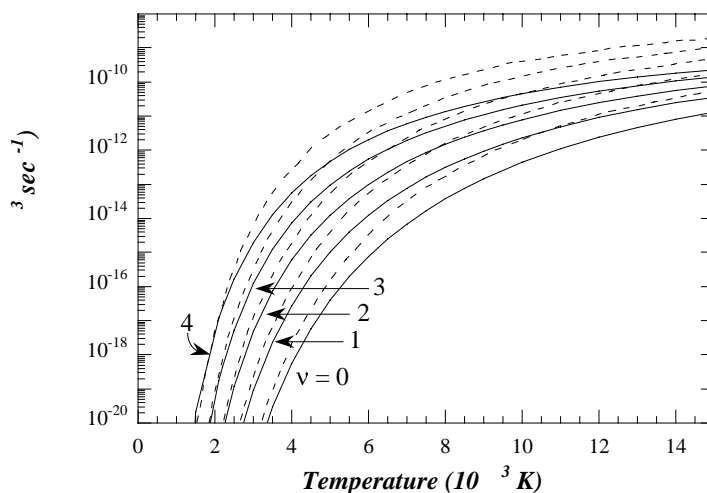


Figure 3 Dissociation rates, as a function of temperature, for different vibrational levels, for the process: $H_2(X^1\Sigma_g^+, v=0,4) + e \rightarrow H_2(b^3\Sigma_u^+) + e \rightarrow 2H + e$, obtained using cross sections of Celiberto et al. (full line)[5] and Stibbe and Tennyson (dashed line) [11].

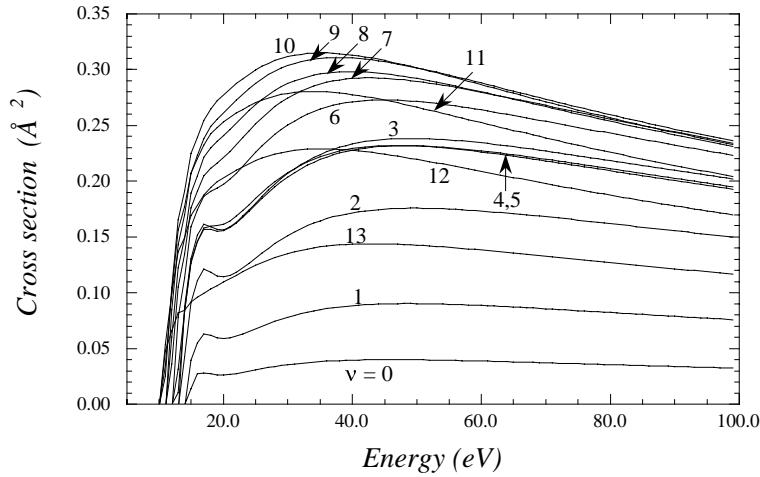
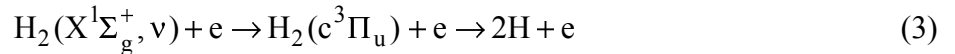
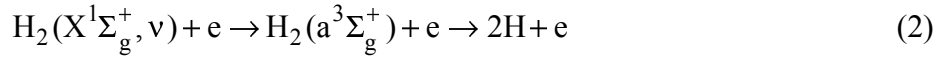


Figure 4 Dissociative cross sections, as a function of impact energy, for the process:
 $H_2(X^1\Sigma_g^+, v=0,14) + e \rightarrow H_2(B^1\Sigma_u^+, B^1\Sigma_u^+, B''^1\Sigma_u^+, C^1\Pi_u, D^1\Pi_u, D'^1\Pi_u) + e \rightarrow 2H + e$

The dissociation through the singlet states becomes important at high energies when the corresponding cross section involving the $b^3\Sigma_u^+$ loses its importance. An important role is played by the high lying vibrational levels. These cross sections are in any case important for creating excited atomic hydrogen atoms with principal quantum number larger than 2.

Figures 5 and 6 report the cross sections for the excitation of the triplet states of H_2



calculated several years ago by using the Gryzinski approximation [16]. In the same figure we have reported the corresponding cross sections calculated by Buckman and Phelps [17] by a refinement of cross sections through a Boltzmann analysis of transport coefficients.

In general these cross sections are considered dissociative [18] even though the two excited states are bound. However the $H_2(a^3\Sigma_g^+)$ state is radiatively linked to the repulsive $b^3\Sigma_u^+$ by an allowed electric dipole transition. The behaviour of $H_2(c^3\Pi_u)$ is less clear. The lowest vibrational level $v=0$ lies below to the $a^3\Sigma_g^+$ state and is metastable. It can predissociate to the $b^3\Sigma_u^+$ state by magnetic dipole and it can decay to the $b^3\Sigma_u^+$ by magnetic dipole and quadrupole radiation at a rate of about 10^5 s^{-1} . The higher vibrational levels can radiate to the $a^3\Sigma_g^+$ then cascading on $b^3\Sigma_u^+$. The history of the $c^3\Pi_u$ depends on the gas density and in dense gases it can be deactivated before radiating. The concentrations of this state is in any case important in determining the electron energy distribution function in molecular hydrogen plasmas [19].

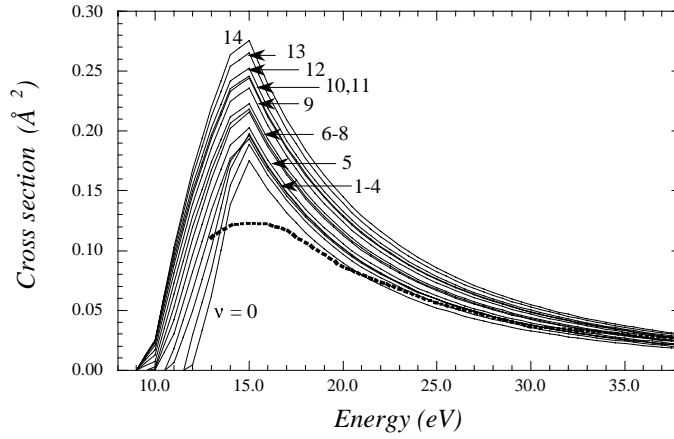


Figure 5 Dissociative cross sections, as a function of impact energy, for the process: $H_2(X^1\Sigma_g^+, v=0,14) + e \rightarrow H_2(a^3\Sigma_g^+) + e \rightarrow 2H + e$. In the figure, comparison for $v=0$ with results of Buckman and Phelps (dotted line) [17].

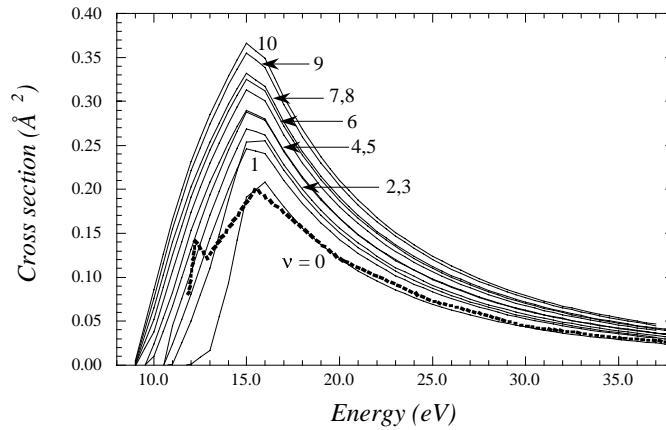


Figure 6 Dissociative cross sections, as a function of impact energy, for the process: $H_2(X^1\Sigma_g^+, v=0,10) + e \rightarrow H_2(c^3\Pi_u) + e \rightarrow 2H + e$. In the figure, comparison for $v=0$ with results of Buckman and Phelps (dotted line) [17].

We observe that the increase of vibrational quantum level has an effect similar to that one discussed for the repulsive $b^3\Sigma_u^+$ state.

Figure 7 reports the dissociation rates of H_2 calculated by inserting the above reported contributions; rates were fitted, in the temperature range $[1 \cdot 10^3, 200 \cdot 10^3 \text{ K}]$, according to the following expression:

$$\ln(\text{rate}) = c_1(T')^{-c_2} + c_3(T')^{-c_4} + c_5 \exp(-c_6 \ln(T')^2); \quad T' = \frac{T}{10^3}, \quad (4)$$

corresponding fitting coefficients are reported in table 3.

We see that the effect of vibrational quantum number in enhancing the rate is dramatic at low temperature becoming less important at high temperature.

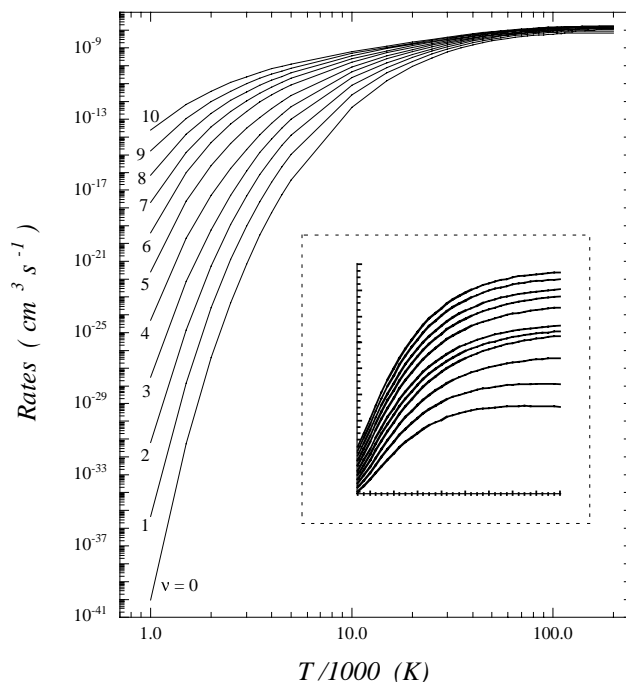


Figure 7 Dissociative rates, as a function of temperature, for different vibrational levels, for the process: $H_2(X^1\Sigma_g^+, v=0,10) + e \rightarrow H_2^* + e \rightarrow 2H + e$. The temperature region $[4 \times 10^4 - 2 \times 10^5 \text{ K}]$ is enlarged in the figure, in a linear scale.

Table 3. Fitting coefficients for H_2 dissociation rates

v	c_1	c_2	c_3	c_4	c_5	c_6
0	-11.565	-0.076012	-78.433	0.74960	-2.2126	0.22006
1	-12.035	-0.066082	-67.806	0.72403	-1.5419	1.5195
2	-13.566	-0.043737	-55.933	0.72286	-2.3103	1.5844
3	-46.664	0.74122	-15.297	-0.022384	-1.3674	1.3621
4	-37.463	0.81763	-0.40374	-0.45851	-18.093	0.011460
5	-28.283	0.99053	-10.377	-0.085590	-11.053	0.067271
6	-23.724	1.0112	-2.9905	-0.24791	-17.931	0.034376
7	-19.547	1.0224	-1.7489	-0.31413	-19.408	0.028643
8	-15.936	1.0213	-1.0175	-0.38040	-20.240	0.024170
9	-12.712	1.0212	-0.60400	-0.44572	-20.766	0.021159
10	-0.40557	-0.49721	-9.9025	1.0212	-21.031	0.019383

Figure 8 reports a comparison of the present rates, for $v=0$, with those recently reported by Martin et al. [20]. Discrepancies are found at low temperatures $[1 \times 10^3 - 8 \times 10^3 \text{ K}]$, due to differences in the threshold region of the cross section sets employed, however, at higher temperatures, the agreement is satisfactory, with errors of $\sim 10\%$.

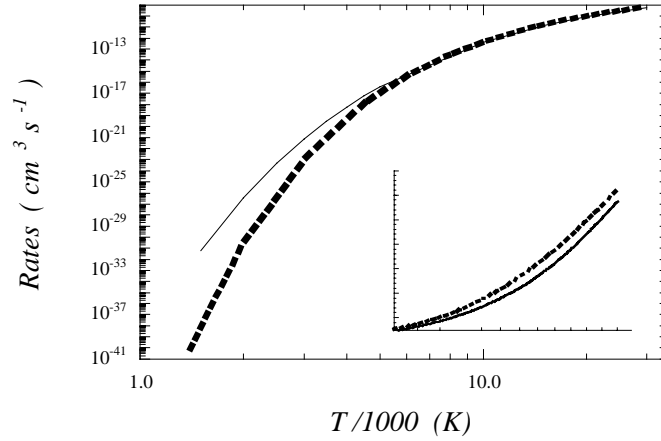
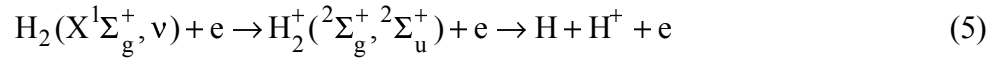


Figure 8 Comparison of total dissociative rates of H_2 for $v=0$, as a function of temperature, (dotted line) results of Martin et al. [20]; (full line) present work. (high temperature region is enlarged, in linear scale).

Let us now introduce other channels contributing to the dissociation of molecular H_2 merely dissociative ionization and dissociative attachment.

Figure 9a reports the behaviour of the sum of cross sections relative to the processes



as a function of energy for different initial vibrational quantum number [5].

Also in this case the vibrational quantum number decreases the threshold energy of the process increasing at the same time the maximum of cross section. The reported cross sections are too high compared with the experimental results [21] so that a normalization factor (0.1732) should be applied to the values reported in [5](see figure 9b).

Maxwell rate coefficients are reported, as a function of temperature, in figure 10 showing the possible importance of this process specially at high temperature. Dissociative ionization rates were fitted, between 3×10^3 and 200×10^3 K, with the analytical expression:

$$\ln(\text{rate}) = c_1(T')^{-c_2} + c_3 + c_4(\exp(-c_5 T'))^{c_4}; \quad T' = \frac{T}{10^3} \quad (6)$$

and fitting coefficients are reported in table 4.

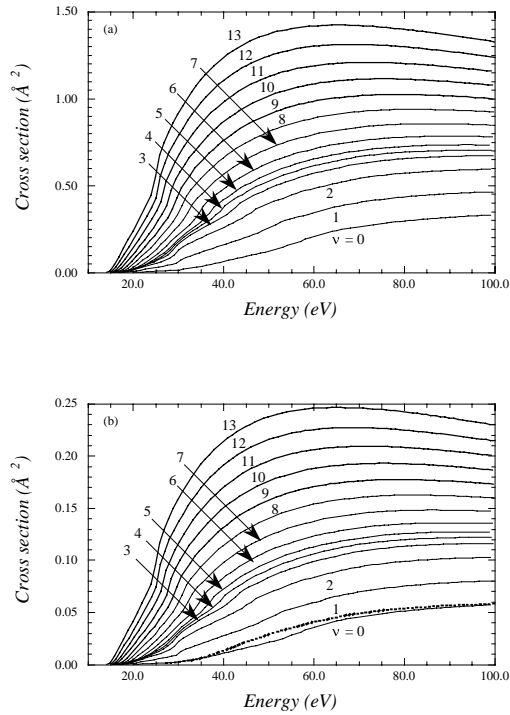


Figure 9 process:

Dissociative ionization cross sections, as a function of impact energy, for the process:
 $H_2(X^1\Sigma_g^+, v=0,13) + e \rightarrow H_2^+(^2\Sigma_g^+, ^2\Sigma_u^+) + e \rightarrow H^+ + H + e$. (a) from ref.[5];
 (b) normalized to experimental cross sections of Rapp et al.(dotted line) [21].

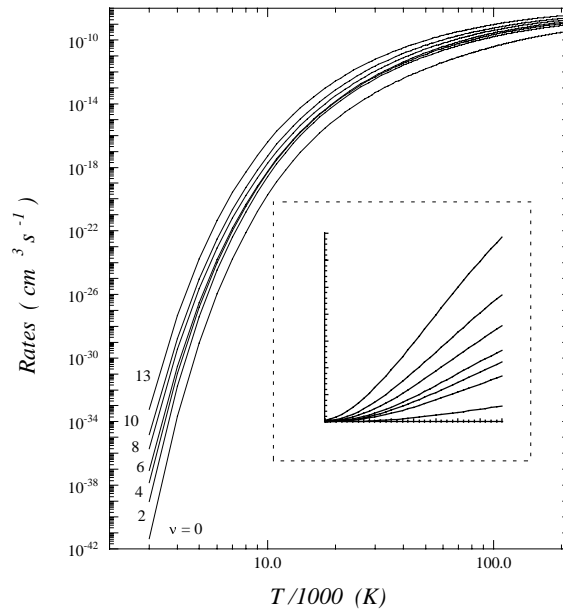


Figure 10

Dissociative ionization rates, as a function of temperature, for different vibrational levels, for the process:
 $H_2(X^1\Sigma_g^+, v=0,13) + e \rightarrow H_2^+(^2\Sigma_g^+, ^2\Sigma_u^+) + e \rightarrow H^+ + H + e$. The region of $4 \times 10^4 - 2 \times 10^5$ K is enlarged in the figure, in a linear scale.

Table 4. Fitting coefficients for H₂ dissociative ionization rates

v	c ₁	c ₂	c ₃	c ₄	c ₅
0	-211.96	1.0022	-20.350	-4.5201	-0.0023834
1	-205.18	0.99226	-19.905	-3.3364	-0.0035142
2	-199.36	0.98837	-19.600	-3.0891	-0.0041558
3	-193.98	0.98421	-19.457	-3.1386	-0.0043830
4	-188.93	0.97647	-19.397	-3.2807	-0.0045212
5	-184.22	0.96189	-19.310	-3.2609	-0.0049158
6	-179.03	0.94593	-19.170	-3.0592	-0.0056404
7	-173.64	0.93986	-19.052	-2.9880	-0.0061932
8	-169.60	0.93507	-18.908	-2.7334	-0.0068815
9	-166.64	0.92602	-18.723	-2.2024	-0.0081979
10	-165.21	0.92124	-18.549	-1.6895	-0.0096154
11	-165.69	0.93366	-18.479	-1.6311	-0.0093150
12	-164.64	0.94682	-18.440	-1.7259	-0.0088671
13	-160.71	0.95533	-18.405	-1.8938	-0.0085829

3. Dissociative attachment

Mechanisms of hydrogen atom negative ion formation in a low temperature plasma attract a great attention of researchers due to perspectives to use intense negative ion beams in both plasma technology and thermonuclear fusion research. In this connection considerable efforts performed in last years were addressed to understand the processes resulting in negative ion formation in low temperature hydrogen plasma (see e.g. [22–29]). The main mechanism for hydrogen negative ion formation is assigned to the dissociative attachment process the rate constant of which k_a drastically increases with the increase of the vibrational excitation of hydrogen molecule. According to refs. [30, 31], the maximum value of k_a occurs at $v=8$ reaching a value k_a of the order of 10^{-8} cm³/s. Dissociative attachment cross sections for hydrogen molecule and its isotopes, calculated by Wadhwa using the *resonance model*, have been extensively reported in a recent report [5].

Larger dissociative attachment rates of the order $k_a \sim 6 \times 10^{-5}$ cm³/s were estimated for the conditions of the experiment [6], where the negative hydrogen ions were produced irradiating the molecular hydrogen gas with high power ArF excimer laser ($\lambda=193$ nm). This extraordinary high magnitude was assigned to high Rydberg (HR) states of hydrogen molecule as an effective source of negative ions via the dissociative attachment process [26–27]



(here n is the effective principal quantum number for HR molecular state, v is its vibrational quantum number and n' is the principal quantum number of one of the product atoms). However until now the initial state of hydrogen molecule involved into the dissociative attachment process and the way for formation of this state via multi-quantum laser excitation have not been identified.

An attempt to explain the extraordinary high magnitude of the process (7) was performed in [27] through a classical description of polarization capture of incident electron by the HR molecule. However this mechanism does not explain the observed high sensitivity of the negative ion production rate constant to the initial electronic and vibrational state of the

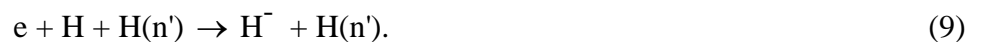
hydrogen molecule. Thus the question about the specific state of HR hydrogen molecules as well as the origin of the extraordinary high magnitude of the observed dissociative attachment rate constant for these molecules is still open.

An alternative mechanism for dissociative attachment of an electron to a highly vibrationally excited hydrogen Rydberg molecule is analyzed. The comparison between the rate constant of this process measured in [26] and that estimated using the calculated data obtained recently [32,33] provides an indication to possible initial and final states involved into the high effective process of negative ion production. Moreover a possible way for formation of highly vibrationally excited hydrogen Rydberg molecule providing the negative ion formation through the high effective dissociative attachment mechanism in conditions of the experiment [26] is analyzed.

Our approach to estimate the cross section of the dissociative attachment of the electron to HR hydrogen molecule is based on the physical consideration that an HR hydrogen molecule can be considered as a small-size hydrogen molecular ion H_2^+ surrounded with a “cloud” of the weakly bound electron having the average radius of an orbit (in atomic units) as large as n^2 (n is the effective principal quantum number of a Rydberg molecule). For this reason the interaction of an incident electron with H_2^+ and the weakly bound electron can be considered almost independently, so that one of possible channels of electron evolution should be ascribed to the dissociative recombination process



According to the proposed mechanism one of products can be in an excited state with the principal quantum number n' . Therefore the ground state hydrogen atom formed as a result of process (8) is surrounded with the “cloud” of weakly bound electron belonging to the HR molecule. If the binding energy of the weakly bound electron in the HR molecule is close to the electron affinity of hydrogen atom (0.76 eV), one can suppose that the dissociative recombination (8) is followed by the negative ion formation. The small deficiency in energy of the weakly bound electron can be recovered due to interaction with the excited hydrogen atom:



Therefore the cross section of the dissociative attachment (7) should be proportional (or equal) to that for dissociative recombination (8). As is known, the latter dramatically depends on the vibrational state of the molecular ion, in particular it increases with increasing the vibrational quantum number v [32,33]. According to quantum calculations of ref.[33], which has been performed on the basis of the super-dissociative recombination mechanism introduced by D.Bates [34], the maximum magnitude of cross section for process (8) is reached at $v=16$ for the electron energy near 0.01 eV and at $v=15$ for 0.07 – 0.1 eV. This maximum value in the indicated electron energy interval ranges between $8 \times 10^{-12} \text{ cm}^2$ and $4 \times 10^{-13} \text{ cm}^2$, decreasing smoothly with electron energy. The calculated cross section for neighbouring vibrational quantum numbers (e.g. $v=17,18$) decrease by factor 10 compared with the previous values. Thereby the dissociative recombination process results in the formation of Rydberg states of hydrogen atom with $n'=10-21$, these levels being energetically allowed for initial vibrational state with $v=16$.

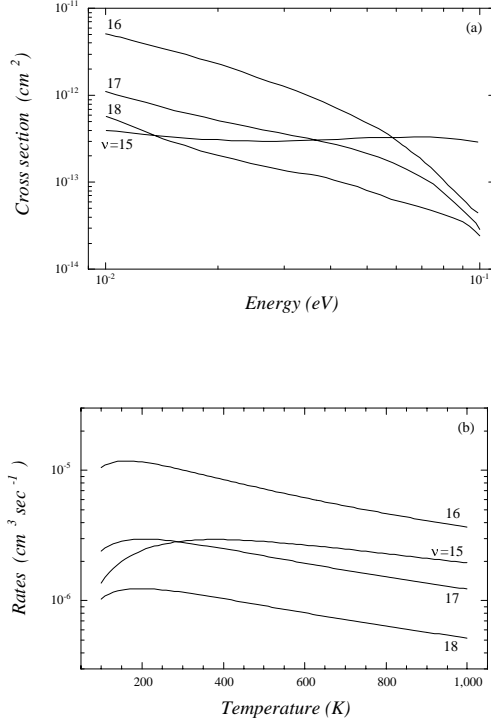


Figure 11 (a) Dissociative recombination cross sections, for different vibrational levels, from ref. [33]; (b) corresponding dissociative recombination rates.

The extraordinary high magnitude of the rate constant of negative ion production observed in [26] can be explained supposing that the Rydberg molecules in the experiment [26] are formed presumably in the vibrationally excited state $v=16$. The presence of the weakly bound electron does not affect practically the potential energy curve for the hydrogen molecular ion H_2^+ , so that one can believe that the processes (8), (9) involving the HR state molecule occur independently from each other. We can therefore suppose that the maximum probability for the negative ion formation via processes (8), (9) is realized when the binding energy of a weakly bound electron in the hydrogen Rydberg molecule is close to that of the negative hydrogen ion (0.76 eV). This provides therefore the estimated effective principal quantum number of the Rydberg hydrogen molecule $n=4$.

Apparently the process of negative ion formation (7) involves the vibrationally excited Rydberg hydrogen molecule with $v \cong 16$ and $n \cong 4$. In accordance with calculation results of [33] the final states of Rydberg atom formed in result of this process range between $n' \cong 10$ and $n' \cong 21$.

We have calculated the electron temperature dependence of the rate constant of the dissociative recombination process (8) for different vibrational quantum numbers of the hydrogen molecular ion v using the cross sections of the process evaluated in [33] and Maxwell electron energy distribution function. This calculation gives a maximum magnitude of the rate constant for $v=16$ exceeding 10^{-5} cm³/s, i.e. the same order of magnitude as the dissociative attachment coefficient reported in [26].

Special attention should be devoted to the origin of the highly vibrationally excited Rydberg hydrogen molecules in an ArF laser-irradiated hydrogen gas. The hydrogen molecule potential curves involved into the considered mechanism of population of the set of levels are shown on figure 12.

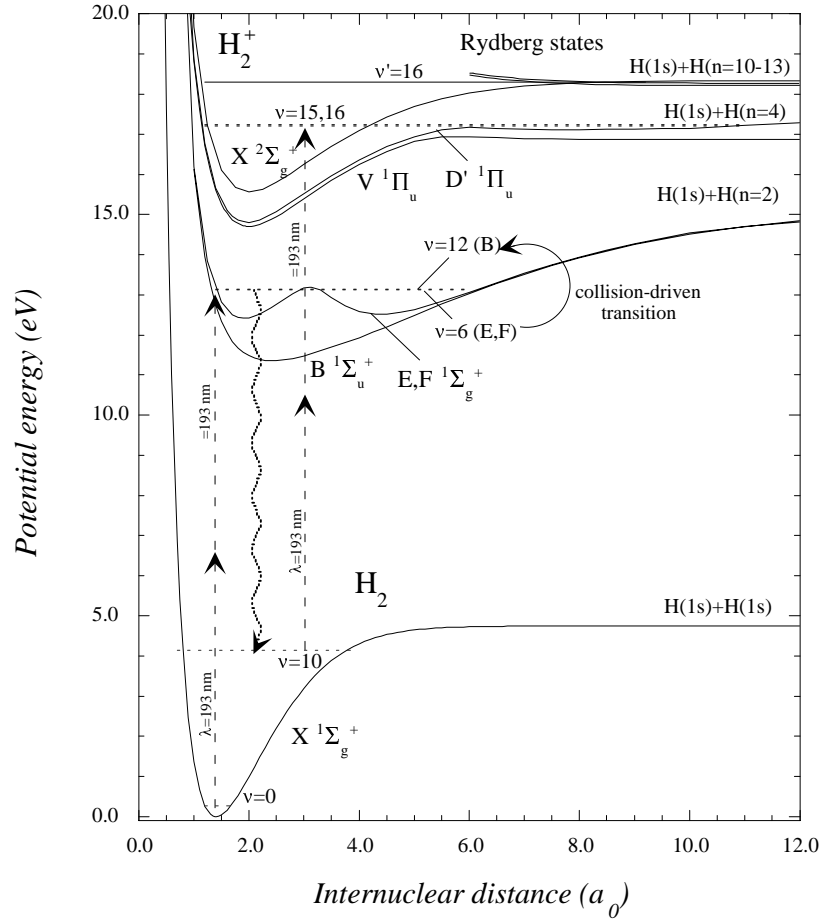
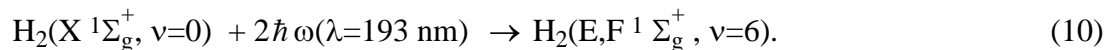
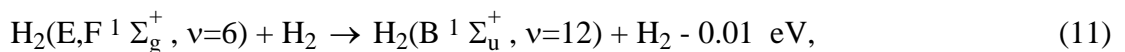


Figure 12 Pictorial view of the proposed mechanism for negative ion formation in H_2 system irradiated by ArF excimer laser.

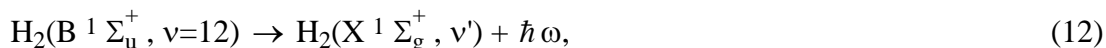
The energy of three-quantum populated super-excited states proposed in the work [26] as a source of such molecules exceeds considerably the dissociation limit of the molecular ion H_2^+ , so that rather high energy release at the collisionless transition can result in destroying Rydberg molecule. As an alternative way one can suppose a sequence of radiation and collision processes the first of which is two-photon absorption of laser radiation by the ground state hydrogen molecule [6]



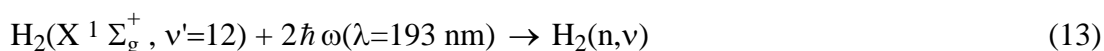
The double well state $H_2(E,F^1\Sigma_g^+)$ is not subjected to the inverted spontaneous radiation decay, because single quantum transition (10) is forbidden. However it is possible the collision-driven transition



which does not require almost for a small additional energy supply and therefore should be characterized by a large cross section. This transition is followed by the fast spontaneous radiation decay of B state characterized by the time constant of about 2 ns which results in formation of vibrationally excited molecules:



the vibrational quantum number of which v' is distributed within a rather wide range of values $0 < v' < 14$ [35]. Lifetime of these vibrationally excited molecules in relation to the collisional quenching in the conditions of the experiments [26,27] (H_2 pressure ranges in 5-50 Torr) is much longer than the laser pulse duration. So it is possible the two-quantum excitation of these molecules under the action of the high intense laser irradiation, for example



resulting in the formation of a state with the energy 17.38 eV, as accounted from the bottom of the ground state term. This state lies about 0.97 eV below the dissociation limit of the molecular ion H_2^+ , which is close to the vibrationally excited Rydberg molecules $\text{H}_2(n=4, v=15)$. The energy of this state accounted from the dissociation limit of the molecular ion H_2^+ , is amounted as 0.955 eV, supposing the similarity between the potential curves of the molecular ion H_2^+ and Rydberg molecule $\text{H}_2(n \gg 1)$ established in the work [36].

It should be noted that the exact coincidence in the energy of two laser quanta and relevant energy difference in accord to (13) is hardly attainable. It is caused by the number of molecular terms related to the asymptotic atomic states $\text{H}(1s)+\text{H}(n=4)$, differed in the electronic moment and its projection (see for example ref. [37] for the case $\text{H}(1s)+\text{H}(n=3)$). The difference in energy of these terms is in the range of accuracy of existing calculations, so that the specific term involved into the process (13) can not be surely shown in the frame of the used approach.

Therefore the dissociative attachment of these molecules can have very high values of rate constant comparable to that experimentally estimated in ref.[26].

4. Dissociation cross sections for N_2 and O_2

Recently Cosby [38] reported an accurate experimental determination of N_2 dissociation cross section which is up to a factor 3 lower than the well known experimental values of Winters [39]. Many excited states contribute to this cross section including triplet and single states with given dissociation fractions. Extending the branching ratios, η_{dis} , reported by Cosby for $v=0$ to higher vibrational states we have calculated the dissociation cross section of N_2 by using the Gryzinski method [3]. The results for the total dissociation cross section is reported in figure 13 as a function of energy for the first 36 levels of N_2 . The behaviour of cross sections and the relevant rates reported in figure 14 are in line with the other cross sections. Note also that the dissociation cross section from $v=0$ is in satisfactory agreement with the experimental results of Cosby.

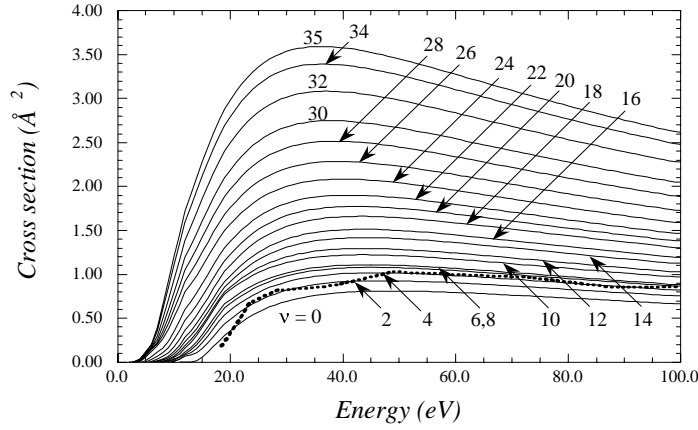


Figure 13 Dissociative cross sections, as a function of impact energy, for the process: $N_2(X^1\Sigma_g^+, v=0,35) + e \rightarrow N_2^* + e \rightarrow 2N + e$. $N_2^* \equiv (B^3\Pi_g, v_f > 12; C^3\Pi_u, v_f > 4; a^1\Pi_g, v_f > 6; b, c, o^1\Pi_u; b', c'^1\Sigma_u^+)$. Dotted line represents the experimental $v=0$ values of Cosby [38].

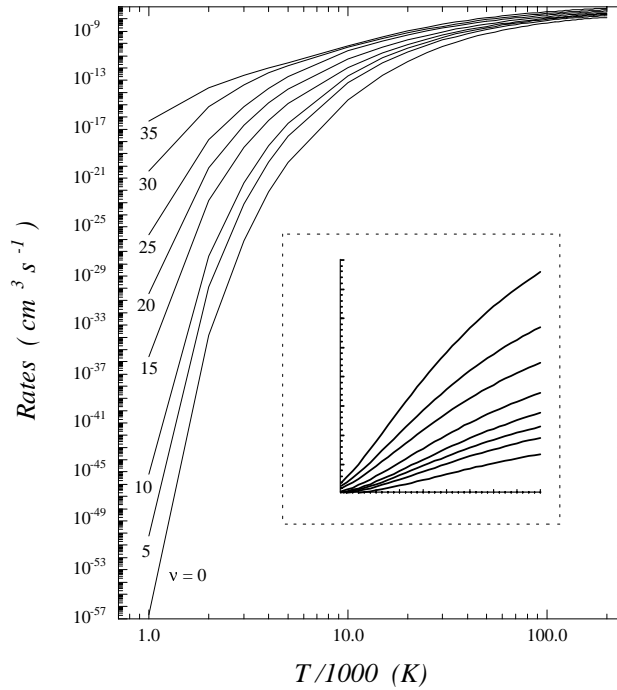


Figure 14 Dissociation rates, as a function of temperature, for different vibrational levels, for the process: $N_2(X^1\Sigma_g^+, v=0,35) + e \rightarrow N_2^* + e \rightarrow 2N + e$. The region of 4×10^4 – 2×10^5 K is enlarged in the figure, in a linear scale.

In order to fit dissociation rates of N_2 , the same analytical expression employed for H_2 dissociation was adopted in the temperature range $[1 \cdot 10^3 - 200 \cdot 10^3$ K]; the relevant c_i coefficients are reported in table 5.

Table 5. Fitting coefficients for n_2 dissociation rates

ν	c_1	c_2	c_3	c_4	c_5	c_6
0	-127.43	0.81133	-14.434	-0.024030	11.320	0.39694
1	-122.93	0.83734	-16.013	-0.0061574	11.207	0.31008
2	-116.68	0.88452	-17.755	0.010074	7.7672	0.31261
3	-102.77	0.89045	-18.579	0.017775	3.6988	0.50266
4	-90.502	1.0466	-13.658	-0.032702	-11.972	0.081030
5	-91.861	1.0322	-10.732	-0.066474	-13.087	0.064609
6	-92.261	1.0263	-10.503	-0.068859	-12.831	0.062411
7	-13.706	-0.032747	-78.352	1.0619	-13.275	0.086240
8	-11.500	-0.057301	-79.799	1.0424	-13.428	0.071214
9	-15.810	-0.0095259	-78.874	1.0448	-10.476	0.095836
10	-9.9761	-0.075727	-80.425	1.0350	-13.603	0.062290
11	-11.581	-0.056277	-67.156	1.0716	-14.600	0.075999
12	-11.872	-0.051574	-67.755	1.0574	-13.648	0.074354
13	-11.350	-0.055951	-68.864	1.0353	-12.780	0.067030
14	-7.5048	-0.11251	-69.195	1.0361	-15.847	0.053297
15	-10.761	-0.063812	-56.784	1.0552	-14.409	0.068401
16	-13.085	-0.034956	-56.696	1.0485	-12.424	0.077555
17	-5.6057	-0.14924	-57.914	1.0358	-17.483	0.046591
18	-5.3496	-0.15394	-58.143	1.0299	-17.408	0.044880
19	-13.423	-0.029100	-46.790	1.0053	-11.049	0.075185
20	-16.416	0.0047850	-60.861	0.74813	7.2409	0.35316
21	-16.621	0.0069911	-60.121	0.75494	6.4579	0.36122
22	-4.1620	-0.18205	-46.934	1.0243	-17.867	0.039009
23	-0.86980	-0.36774	-46.511	1.0252	-20.816	0.023584
24	-12.671	-0.035120	-34.731	1.0343	-10.767	0.068619
25	-13.415	-0.025410	-36.838	0.94886	-8.7046	0.067075
26	-13.467	-0.025543	-35.086	1.0141	-9.7057	0.071843
27	-11.537	-0.047473	-35.009	1.0293	-11.328	0.064623
28	-10.383	-0.062155	-34.852	1.0422	-12.356	0.061339
29	-13.063	-0.023374	-40.846	0.57638	6.8483	0.40518
30	-12.809	-0.025982	-41.076	0.57279	6.9552	0.39388
31	-12.600	-0.027974	-41.257	0.57108	7.0834	0.38945
32	-17.157	0.012623	-22.810	1.0042	-8.7990	0.11117
33	-17.322	0.014128	-20.702	1.1436	-10.012	0.11588
34	-6.4944	-0.10689	-35.817	0.37082	3.2775	1.0258
35	-36.288	0.36814	-6.1249	-0.11472	4.7795	0.68103

The impact parameter method has been used to estimate the dissociation cross sections of O_2 in the Schumann-Runge channel [40].

The relevant dissociation cross sections are reported in figure 15. Note that due to the position of potential energy curves the dissociation cross sections from $\nu=0$ is much higher than the corresponding results for $\nu>0$.

4. Conclusions

In this paper we have presented our efforts in the calculation of dissociative cross sections of diatomic molecules by electron impact. Special attention has been devoted to understand the role of vibrational excitation in affecting cross sections and rate coefficients. The main result

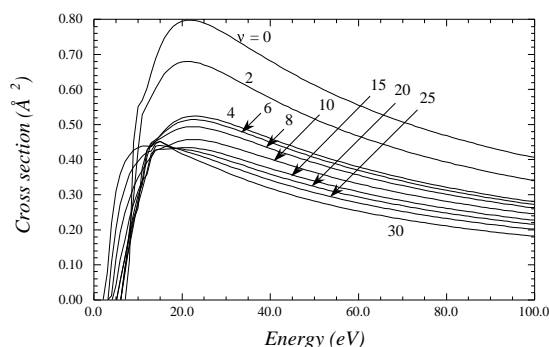


Figure 15 Dissociative cross sections, as a function of incident energy, for the process:
 $O_2(X^3\Sigma_g^-, v=0,30) + e \rightarrow O_2^*(B^3\Sigma_u^-) + e \rightarrow 2O + e.$

of this calculations is that vibrational excitation of the target decreases the threshold energy of the process increasing cross sections maximum. As a result the rate coefficients strongly increase with v especially at low temperatures.

Interesting results have been also reported on the role of Rydberg states in enhancing the dissociative attachment of molecular H_2 . This point indicates the importance of characterizing electronically excited states [41] at the same level as that presented for vibrationally excited states.

ACKNOWLEDGEMENTS

One of the authors (A. Eletskii) thanks Landau-Volta Center for providing Fellowship in the Bari University. Support from the MURST project (9703109065006) and ASI (contract on "Termodinamica, trasporto e cinetica di plasmii H_2 ") is acknowledged.

REFERENCES

- [1] CAPITELLI, M., CELIBERTO, R., CACCIATORE, M., *Adv. At. Mol. Opt. Phys.* **33** (1994) 321.
- [2] CAPITELLI, M., CELIBERTO, R., "The Dependence of Electron Impact Excitation and Ionization Cross Sections of H_2 and D_2 Molecules on Vibrational Quantum Number", in "Atomic and Molecular Processes in fusion Edge Plasmas", edited by R.K.Janev, PLENUM PRESS NEW YORK and LONDON (1995) 95.
- [3] CAPITELLI, M., CELIBERTO, R., "Electron-Molecule Cross Sections for Plasma Applications: The Role of Internal Energy of the Target", in "Novel Aspects of Electron-Molecule Collisions", edited by K.H. Becker, published by World Scientific Publishing Co. Pte. Ltd. (1998) 283.
- [4] CAPITELLI, M., CACCIATORE, M., CELIBERTO, R., ESPOSITO, F., GORSE, C., and LARICCHIUTA, A., *Plasma Phys. Rep.* **25** (1999) 3.
- [5] CELIBERTO, R., LARICCHIUTA, A., CAPITELLI, M., JANEV, R.K., WADEHRA, J.M. and ATEMS, D.E., "Cross Section Data for Electron-Impact Inelastic Processes of Vibrationally Excited Hydrogen Molecules and their Isotopes", International Nuclear Data Committee, INDC(NDS)-397, IAEA, June 1999, Vienna-Austria.

- [6] ESPOSITO, F., CAPITELLI, M., this book.
- [7] GORSE, C., CAPITELLI, M., this book.
- [8] CELIBERTO, R., LAMANNA, U.T., and CAPITELLI, M., Phys. Rev. **A58** (1998) 2106.
- [9] BILLING, G.D., CACCIATORE, M., and RUTIGLIANO, M., this book; see also BILLING, G.D., Plasma Phys. Rep. **25** (1999) 32.
- [10] RESCIGNO, T.N., and SCHNEIDER, B.I., UCRL-9921 (1988).
- [11] STIBBE, D.T., and TENNYSON, J., New J. Phys. **1** (1998).
- [12] CELIBERTO, R., and RESCIGNO, T.N., Phys. Rev. **A47** (1993) 1939.
- [13] CELIBERTO, R., LAMANNA, U.T., and CAPITELLI, M., Phys. Rev **A50** (1994) 4778.
- [14] CELIBERTO, R., CAPITELLI, M., LAMANNA, U.T., Chem. Phys. **183** (1994) 101.
- [15] CELIBERTO, R., LARICCHIUTA, A., LAMANNA, U.T., JANEV, R.K., and CAPITELLI, M., Phys. Rev **A60** (1999) 2091.
- [16] CACCIATORE, M., CAPITELLI, M., Chem. Phys. **55** (1981) 67.
- [17] BUCKMAN, S.J., PHELPS, A.V., JILA Information Center Report **27** (1985).
- [18] CRAVENS, T.E., VICTOR, G.A., DALGARNO, A., Plan. Space Sci. **23** (1975) 1059.
- [19] CAPITELLI, M., COLONNA, G., HASSOUNI, K., and GICQUEL, A., Plasma Chem. Plasma Process. **16** (1996) 153; HASSOUNI, K., GICQUEL, A., CAPITELLI, M., Phys. Rev. **E59** (1999) 3741.
- [20] MARTIN, P.G., KEOGH, W.J., MANDY, M.E., Astrophys. J. **499** (1998) 793.
- [21] RAPP, D., ENGLANDER-GOLDEN, P., and BRIGLIA, D.D., J. Chem. Phys. **42** (1965) 4081.
- [22] GORSE, C., CELIBERTO, R., CACCIATORE, M., LAGANÀ, A., CAPITELLI, M., Chem. Phys. **161** (1992) 211.
- [23] BERLEMONT, P., SKINNER, D.A., BACAL, M., Rev. Sci. Instrum. **64** (1993) 2721.
- [24] EENSHUISTRA, P.J., GOCHITASHVILI, M., BECKER, R., KLEYN, A.W., HOPMAN, H.J., J. Appl. Phys. **67** (1990) 85.
- [25] YOUNG, A.T., CHEN, P., LEUNG, K.N., STUTZIN, G.C., Rev. Sci. Instrum. **65** (1994) 1416.
- [26] DATSKOS, P.G., PINNADUWAGE, L.A., KIELKOPF, J.F., Phys. Rev. **A55** (1997) 4131.
- [27] PINNADUWAGE, L.A., DING, W.X., MCCORCLE, D.L., LIN, S.H., MEBEL, A.M., GARSCADDEN, A., J. Appl. Phys. **85** (1999) 7064 .
- [28] HASSOUNI, K., GICQUEL, A., CAPITELLI, M., Chem. Phys. Lett. **290** (1998) 502.
- [29] HISKES, J.R., Appl. Phys. Lett. **69** (1996) 755.
- [30] WADEHRA, J.M., Phys. Rev. **A29** (1994) 106.
- [31] HICKMAN, A.P., Phys. Rev. **A43** (1991) 3495.
- [32] MITCHELL, J.B.A., YOUSIF, F.B., VAN DER DONK, P.J.T., MORGAN, T.J., CHIBISOV, M.I., Int. J. Mass Spectrom. Ion Proc. **149/150** (1995) 153.
- [33] CHIBISOV, M.I., MITCHELL, J.B.A., VAN DER DONK, P.J.T., YOUSIF, F.B., MORGAN, T.J., Phys. Rev. **A56** (1997) 443.
- [34] BATES, D.R., J. Phys. **B24** (1991) 695.
- [35] SPINDLER, R.J., JR., J. Quant. Spectr. Radiat. Transfer. **9** (1969) 597.
- [36] STEPHENS, J.A., MCKOY, V., J. Chem. Phys. **97** (1992) 8060.
- [37] CAPITELLI, M., GUIDOTTI, C., LAMANNA, U., J. Phys. **B7** (1974) 1683.
- [38] COSBY, P.C., J. Chem. Phys. **98** (1993) 9544.
- [39] WINTERS, H.F., J. Chem. Phys. **44** (1966) 1472.
- [40] LARICCHIUTA, A., CELIBERTO, R., and CAPITELLI, M., work in preparation.
- [41] CELIBERTO, R., CAPITELLI, M., DURANTE, N., and LAMANNA, U.T., Phys. Rev. **A54** (1996) 432.

Dynamical calculations of state to state and dissociation cross-sections for atom-molecule collision processes in hydrogen

F. Esposito, M. Capitelli

Centro di Studio per la Chimica dei Plasmi del CNR,
Dipartimento di Chimica, Universita' degli Studi,
Bari, Italy

Abstract. Complete sets of vibrational deexcitation and dissociation cross sections for atom-diatom collision processes in hydrogen have been calculated. These results are required in kinetic codes in which translational and vibrational strong non-equilibrium conditions are studied. Good agreement is found in comparisons with experimental and theoretical data.

1. Introduction

Vibrational kinetics under strong non-equilibrium conditions are of large interest nowadays in different research fields like plasma physics, plasma chemistry, lasers and hypersonic flows [1, 2]. Kinetic models including vibrational state to state and dissociation data of simple molecules have been developed, demonstrating the large importance of vibrational kinetics in non-equilibrium conditions, like those present in rapidly expanding gas flows [1, 2]. In order to study this kind of conditions, cross sections could be inserted in fluiddynamic codes, to obtain atomic populations and vibrational distributions. However, for this kind of project there is the need of complete sets of state to state and dissociation cross sections. Also for the most studied system, the collision of atomic hydrogen with rovibrationally excited molecular hydrogen $H+H_2(v,j)$, v,j = vibrational and rotational quantum numbers, there are various sets of dynamical calculations [3–9], but the results are generally either in the form of rate coefficients, that is averaged over equilibrium distributions at specified temperatures, or they are far from being complete (i.e. many possible initial states are not considered). We have performed extensive dynamical calculations of both state to state and dissociation cross sections from any rovibrational state of H_2 in collision with atomic hydrogen. For simplifying kinetic studies, we have averaged cross sections depending on v,j on the rotational degree of freedom. In this manner, our data are of interest in any condition of rotational quasi-equilibrium, while strong non-equilibrium is allowed on both translation and vibration, which are the most useful cases to be studied. This averaging process contributes significantly to decrease the computational effort, and to obtain more reliable results, as discussed in the following section.

2. Computational details

Dynamical calculations have been performed on the LSTH (Liu-Siegbahn-Truhlar-Horowitz [10]) PES (potential energy surface), which is known to be accurate within few hundredths of eV. No interaction with electronic states different from the ground one is considered. This is a limitation that could affect results of total energy larger than 3 eV [11]. However in this context, in which complete sets of cross sections are needed, it is extremely difficult to refine dynamical calculations, because of the very large computational effort required also in relatively simple computations. As a consequence, the dynamical method chosen is the QCT (quasiclassical trajectory method [12]), in which the nuclear motion on the PES is totally

classical, including rotations and vibrations, with some pseudo-quantization rules. The method has generally a sufficient reliability, especially when averaged quantities are required, in which quantal behaviour is to some extent less important (in this sense is surely much safer to obtain cross sections rotationally averaged, as discussed in the preceding paragraph). An important limitation is represented by treating vibration as a classical motion: in other semiclassical methods this is overcome by introducing a Schroedinger equation only for vibration, with remaining degrees of freedom treated classically [13].

All the rovibrational states (348) of H₂ supported by the PES have been calculated using the WKB method [14]. Really only about one half of these states are bound: those higher in energy with respect to dissociation limit are "quasibound", that is classically bound, because of the presence of the rotational barrier, but with non-zero quantal escaping probabilities. These states are of interest in recombination kinetic schemes in which orbiting resonance theory is applied [15]. We modified the standard procedure of pseudoquantization of initial states, by allowing classical rovibrational actions not to be discretized, but distributed in the neighbourhood of each initial state of interest, that is:

$$V \in [V_0-h/2, V_0+h/2], L \in [J_0-h/4\pi, J_0+h/4\pi],$$

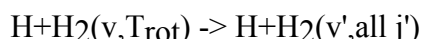
assuming the pseudoquantization of initial states given by:

$$V_0=(v+1/2)h, J_0=(j+1/2)h/2\pi.,$$

in which v and j are quantum numbers, V_0 and J_0 are pseudoquantized classical actions. Really our code allows to choose the distribution around the pseudoquantized states (i.e., a trajectory is assigned to a certain state as a function of its "distance" from the nearer pseudoquantized). We have used for this work a simple "square window" function centered in the state of interest. Analogously, also the products are analyzed with the same weight function. A continuous distribution is assigned to translational energy, which ranges from 10^{-3} eV to 6 eV. There are limitations in reliability of QCT results for both the extrema of this energy interval, because De Broglie wavelength is not negligible at very low translational energies, especially for hydrogen, in comparison with typical interaction distances, while for high energies interactions with other potential energy surfaces should be considered, for example with surface hopping method [16]. Cross section dependence on translational energy is performed by using a large number of bins (150) and averaging with a simple smoothing technique, which calculates the mean value over three or five bins around that one of interest. Integration of motion is performed by a variable time step Runge-Kutta fourth order method, with total energy check ($6 \cdot 10^{-4}$ eV) and 1 in ten back-integration check. Stratified sampling was applied to impact parameter. Not less than 50 000 trajectories were calculated for each initial rovibrational state.

3. Results

Some cross section results for vibrational deexcitation:



are displayed in fig.1, for rotational temperatures of 300K, 5000K and 20 000K. These data include both reactive and non-reactive collision processes, because there is no interest in separating the two cases in kinetic studies for which these data are calculated. At 300K results show relevant statistical fluctuations (about 0.5 \AA^2 root mean square error), due to the fact that

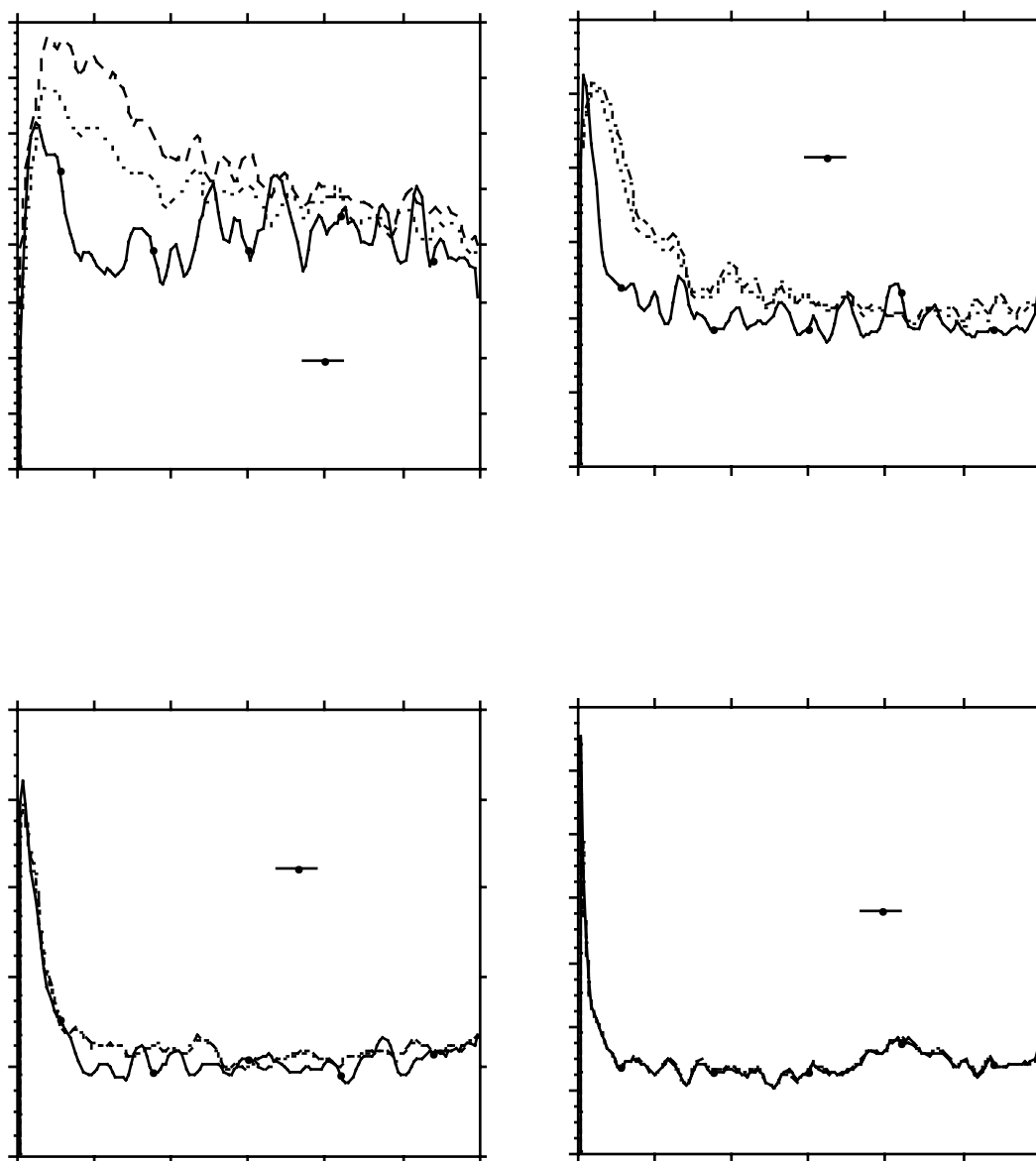


Figure 1. Some vibrational deexcitation cross sections as a function of translational energy, averaged on the rotational temperatures indicated in the figure. (a) initial $v=5$, final $v'=4$; (b) $v=9$, $v'=8$; (c) $v=12$, $v'=11$; (d) $v=14$, $v'=13$.

in this case the thermal average is made over few rotational states relatively noisy. In fact, fluctuations are much smaller for higher temperatures. Actually this does not seem a serious problem: rate coefficients obtained from these results are in good agreement with other data of both experimental and computational origin, as will be shown.

The general trend shown in fig.1 is a rapid increasing of cross section for very low translational energy values up to a maximum, followed by a decreasing down to an

approximately flat trend (in the limit of statistical fluctuations). For increasing initial vibrational quantum number v the peak increases in value and decreases in energy. Peak position is comparable with the energy interval between adjacent vibrational states. Rotational temperature is more important (roughly 30% of maximum difference in cross section value between 300K and 5000K within 1–2 eV of translational energy) for low initial v than for high one, simply because there is a wide ladder of rotational states in the first case, and consequently a large contribution to the cross section for sufficiently high rotational temperature, being true the opposite for the last vibrational levels. The general trend of dissociation cross sections:



are quite different. In that case (fig.2) there is a clear threshold to the process (of course, in this classical computational scheme no tunneling is allowed). Thresholds show a strong dependency from rotational temperature, decreasing with an increasing of this last. For higher energy values there is an increasing section, and the maximum value, reached at the end of the energy interval, is strongly dependent on rotational temperature, increasing with this last. Dissociation cross section maximum is also much higher for high initial v than for low one.

Comparison with other results in literature is possible for a small number of vibrational deexcitation [17–22] and dissociation [23] cross sections, while it is easier to compare rate coefficients obtained from those data. In fig.3 there are state to state rate coefficients from [6] (directly calculated, not via cross sections, see [6]) and those calculated by us using cross sections and the following relation:

$$k_{v,v'}(T_{\text{tr}}, T_{\text{rot}}) = \frac{Q_{\text{r}}^{-1}(v) \sum_j g_j (2j+1) \exp(-E_{v,j} / kT_{\text{rot}})}{(k^3 T_{\text{tr}}^3 \pi \mu / 8)^{1/2}} \cdot \int dE E \exp(-E / kT_{\text{tr}}) \sigma_{v,j,v'}(E)$$

with

$$Q_{\text{r}}^{-1}(v) = \sum_j g_j (2j+1) \exp(-E_{v,j} / kT_{\text{rot}})$$

$\sigma_{v,j,v'}$ is the state to state cross section summed over final j' values. The comparison generally good at 2000K and 4000K of ro-translational temperature, while our results are one order of magnitude lower at 500K (it might be an effect of our distributed actions in the reactants, probably more important for low j values). Concerning dissociation cross sections, a good agreement is found with data in [23]. Moreover the global experimental rate quoted in [24] is in good agreement with the corresponding theoretical kinetic quantity based on the present cross sections [25]. As a consequence, fluctuations in cross section results should not be considered very relevant, especially when cross sections are used in kinetic calculations, because any kinetic study is generally performed on a relatively large translational energy interval, so results are in any case averaged on this interval.

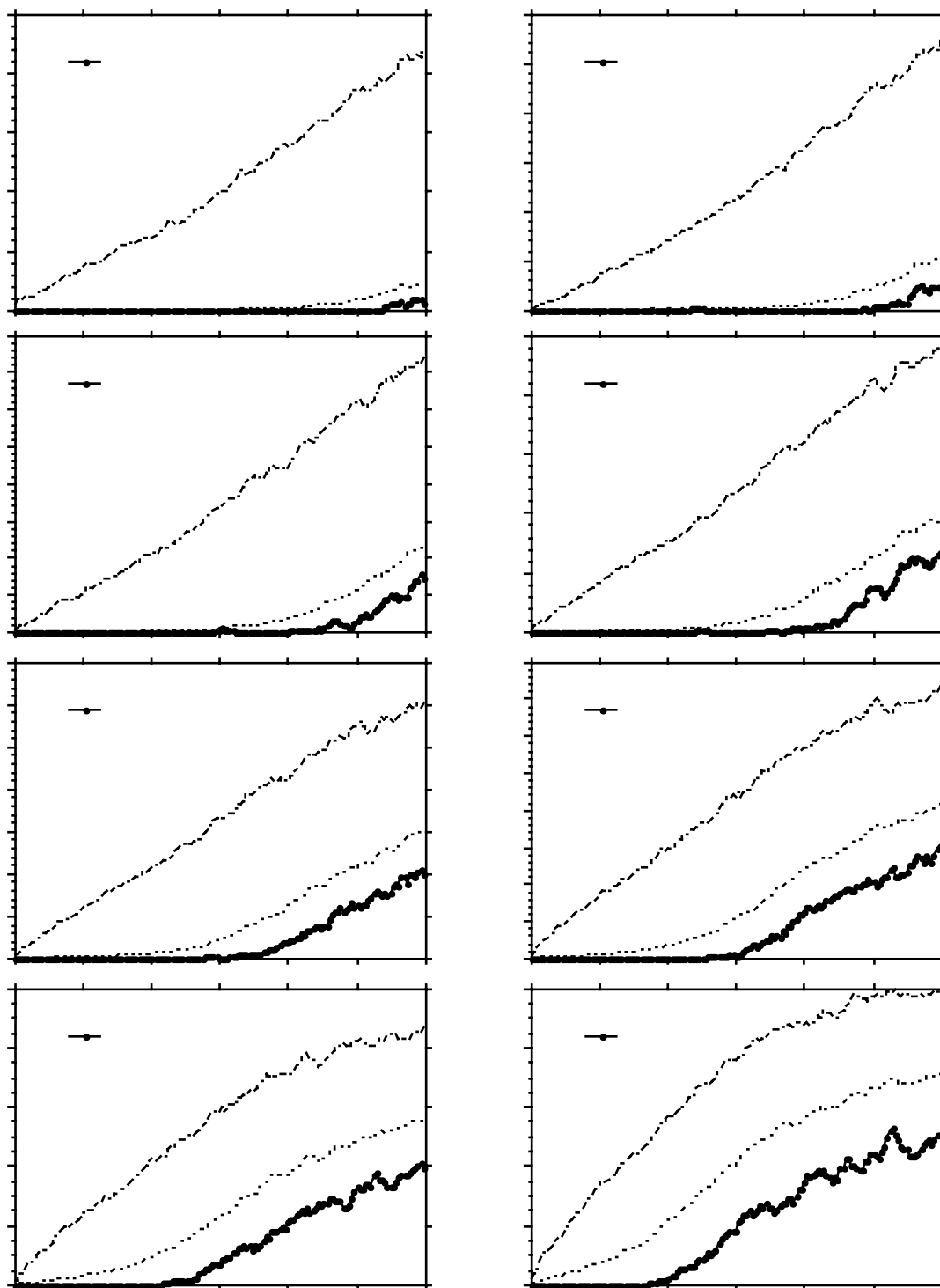


Figure 2 (a–h). Dissociation cross sections as a function of translational energy from a given vibrational state, averaged on a rotational distribution at the temperatures indicated in the figures. (a) $v=0$, (b) $v=1$, (c) $v=2$, (d) $v=3$, (e) $v=4$, (f) $v=5$, (g) $v=6$, (h) $v=7$.

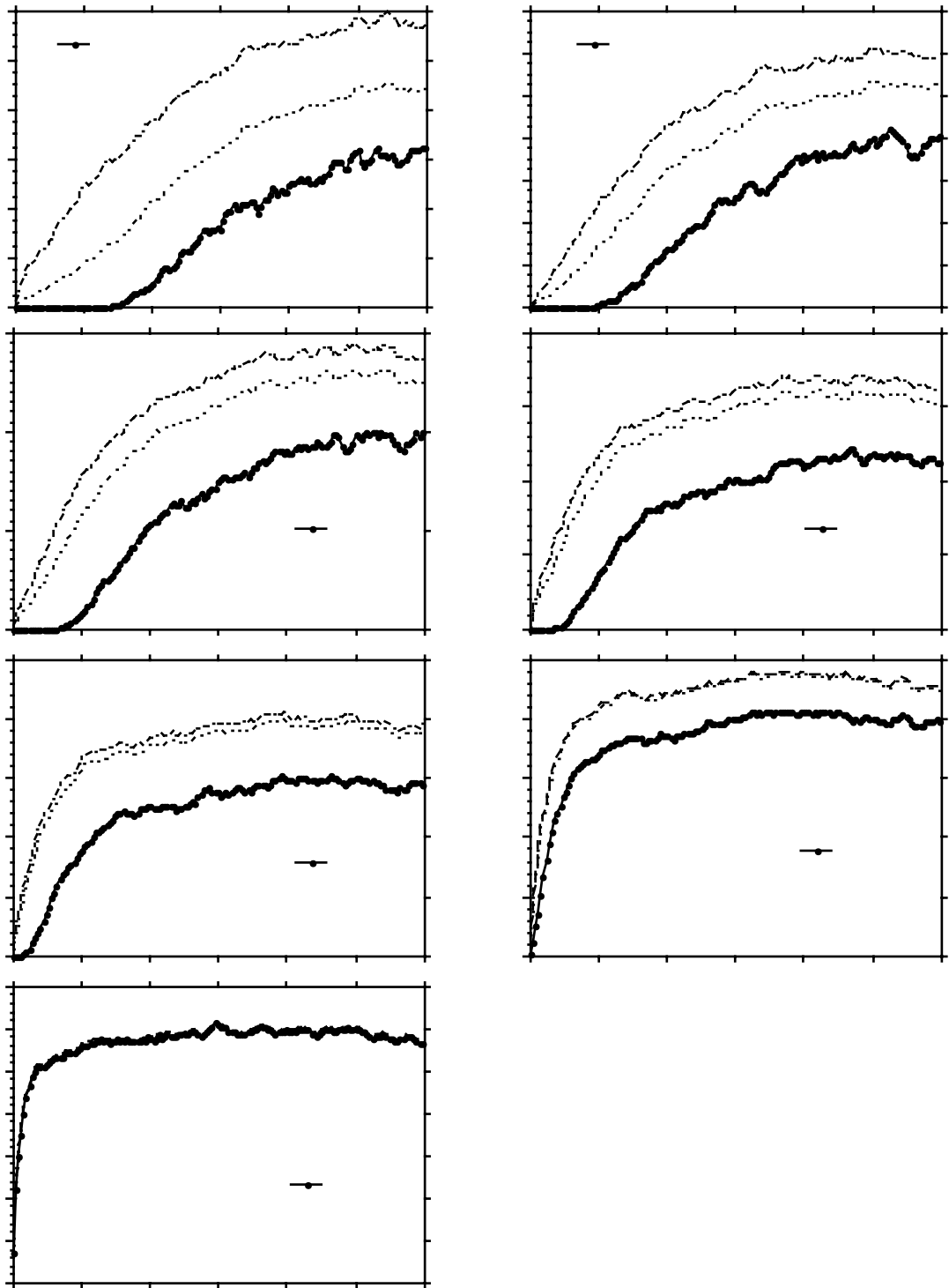


Figure 2 (i–o). (i) $\nu=8$, (j) $\nu=9$, (k) $\nu=10$, (l) $\nu=11$, (m) $\nu=12$, (n) $\nu=13$, (o) $\nu=14$.

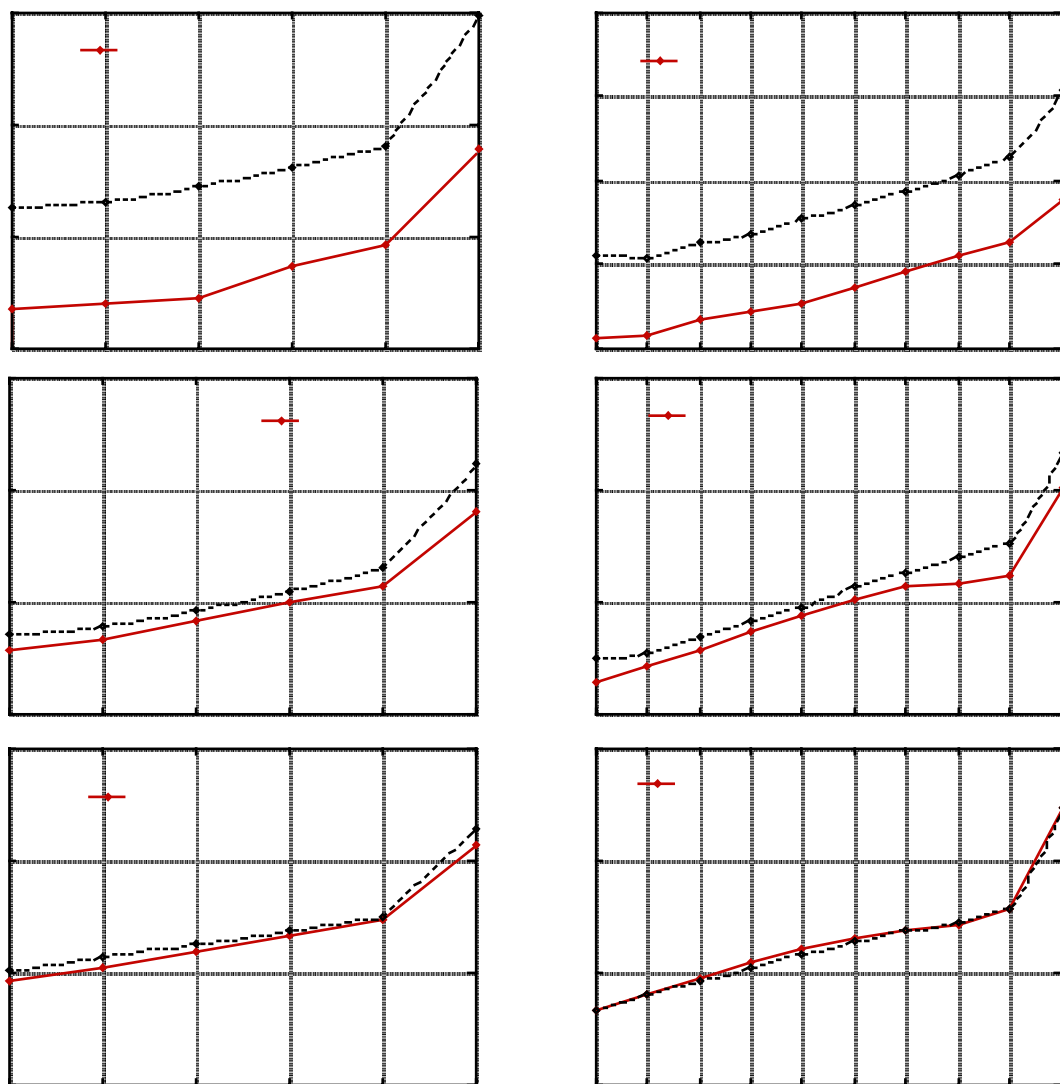


Figure 3. Comparison of vibrational deexcitation rate coefficient, averaged on a rotational distribution, calculated in this work and from ref.[6]. (a,d) $T_{rot}=500K$, (b,e) $T_{rot}=2000K$, (c,f) $T_{rot}=4000K$, (a,b,c) $v=5$, (d,e,f) $v=9$.

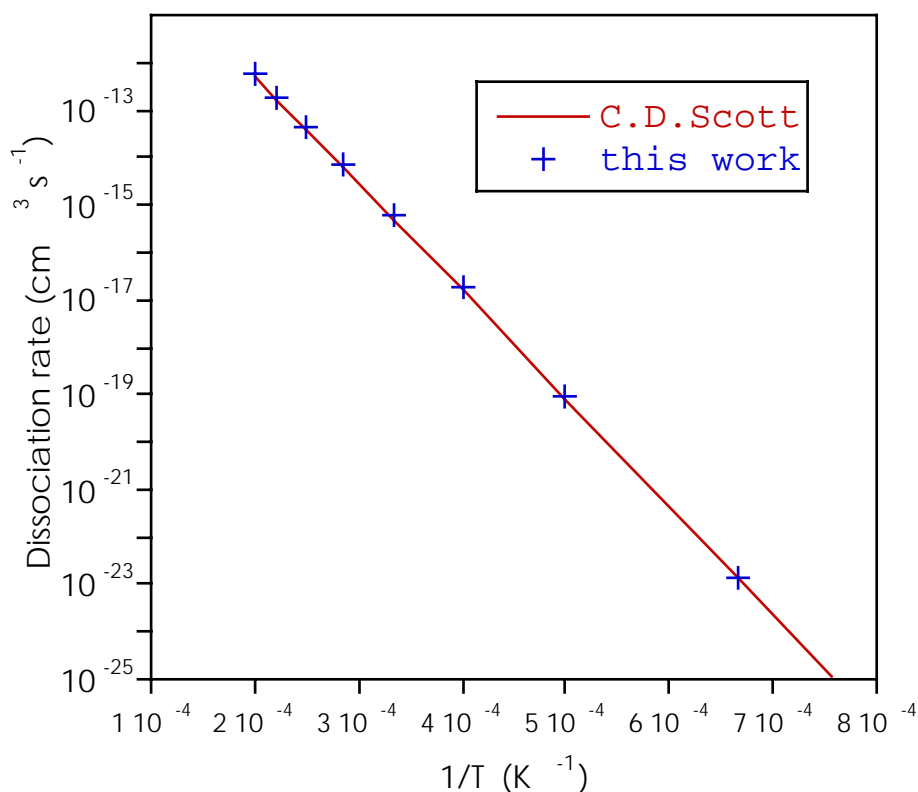


Figure 4. Comparison of global dissociation rate coefficient calculated in this work and obtained experimentally in ref. [24].

4. Conclusions

In this work the complete set of vibrational deexcitation and dissociation cross sections for reactive and non-reactive atom-molecule collisions in hydrogen has been calculated, from any initial rotational state. Data have been then averaged on rotation by using a Boltzmann rotational distribution. The results, which are of large applicability in kinetic codes in which translational-vibrational non-equilibrium is studied, have been compared with different data of experimental and computational origin, with a good agreement on averaged quantities (rate coefficients), confirming a good reliability of the dynamical method (QCT with continuous distributions of rovibrational actions) used for this kind of massive computations. However there are some problems if a larger accuracy is required. First of all, using the same computational scheme, a larger number of trajectories could be useful for low value cross sections. At least low lying vibrational states should be treated quantally with a semiclassical method, translation for very low energy values is not reliable when treated classically, and for total energies larger than about 3eV interaction with other potential energy surfaces should be considered. However, the present results can be considered among the most complete sets of cross sections in the literature.

ACKNOWLEDGEMENTS

This work was supported by MURST (9903102919-004) and by ASI (progetto termodinamica, trasporto e cinetica di plasm₂ per propulsione spaziale).

REFERENCES

- [1] CAPITELLI, M. ed. "Non Equilibrium Vibrational Kinetics", Topics in Current Physics (1986) Springer Verlag Berlin.
- [2] CAPITELLI, M. ed. "Molecular Physics and Hypersonic Flows", Kluwer Dordrecht (1997); CAPITELLI, M., FERREIRA, C.M., GORDIETS, B.F., and OSIPOV, A.I., "Plasma kinetics in atmospheric gases", Springer-Verlag 2000 (in press).
- [3] MAYNE, H.R., Chem.Phys.Lett. **66** (1979) 487.
- [4] GARCIA, E., and LAGANA', A., Chem.Phys.Lett. **123** (1986) 365.
- [5] LAGANA', A. in "Non-equilibrium processes in partially ionized gases", M. Capitelli and J.N.Bardsley eds.Plenum Press, New York, (1990) 105.
- [6] LAGANA', A. and GARCIA, E., "Quasiclassical rate coefficients for the H+H₂ reaction", University of Perugia, Italy (1996).
- [7] LAGANA, A., and GARCIA, E., Plasma Sources: Science and Technology 7 (1998) 359–362.
- [8] GORSE, C, CAPITELLI, M., BACAL, M., BRETAGNE, J. and LAGANA', A., Chem.Phys.**117** (1992) 177.
- [9] SCHWENKE, D., J.Chem.Phys.**92** (1990) 7267.
- [10] TRUHLAR, D.G. and HOROWITZ, C.J., J.Chem.Phys. **68** (1978) 2466–2476 ; **71** (1979) 1514.
- [11] VARANDAS, A.J.C., BROWN, F.B., ALDEN MEAD, C., TRUHLAR, D.G. AND BLAIS, N.C., J.Chem.Phys.86 (1987) 6258.
- [12] PATTENGILL, M.D., "Rotational Excitation III: Classical Trajectory Methods"; TRUHLAR, D.G. AND MUCKERMAN, J.T., "Reactive Scattering Cross Sections III: Quasiclassical and Semiclassical Methods", in Atom-Molecule Collision Theory, edited by R.B.Bernstein, 1979 Plenum Press, New York.
- [13] LEVINE, R.D, BERNSTEIN, R.B., Molecular Reaction Dynamics, Oxford University Press (1974), 155–159.
- [14] BLAIS, N.C., TRUHLAR, D.G., J.Chem.Phys, **65** (1976) 5335–5356.
- [15] ROBERTS, R.E., BERNSTEIN, R.B. AND CURTISS, C.F., J.Chem.Phys. **50** (1969) 5163.
- [16] TULLY, J.C., PRESTON, R.K., J.Chem.Phys, **55** (1971) 562.
- [17] MAYNE, H.R., J. Chem. Phys., **73** (1980) 217.
- [18] BARG, G.D., MAYNE, H.R., TOENNIES, J.P., J.Chem.Phys.,**74** (1981) 1017.
- [19] MAYNE, H.R., TOENNIES, J.P., J. Chem. Phys., **75** (1981) 1794.
- [20] TRUHLAR, D.G., J. Am. Chem. Soc., **111** (1989) 852.
- [21] SCHATZ, G., KUPPERMANN, A., J. Chem. Phys., **65** (1976) 4668.
- [22] ZHANG, J., MILLER, W.H., Chem. Phys. Lett., **153** (1988) 465.
- [23] DOVE, J.E. AND MANDY, M.E., Int.J.Chem.Kin.18 (1986) 893.
- [24] SCOTT, C.D., FAHRAT, S., GICQUEL, A., HASSOUNI, K. AND LEFEBVRE, M., J.Thermophysics and Heat Transfer 10 (1996) 426.
- [25] ESPOSITO, F., GORSE, C., CAPITELLI, M., *Chem. Phys. Letters*, **303** (1999) 636–640.

Collision integrals of high temperature hydrogen species

C. Gorse, M. Capitelli

Dipartimento di Chimica and Centro di Studio per
la Chimica dei Plasmi,
Bari, Italy

Abstract. Collision integrals of hydrogen species existing in a thermal plasma (H_2 , H , H^+ , e) have been calculated in the temperature range $50 \div 100\ 000K$ using theoretical and experimental informations on cross sections and potential energy curves. The calculated values, which are in satisfactory agreement with existing values, have been fitted with suitable expressions.

1. Introduction

Transport properties of high-temperature hydrogen plasmas are of paramount importance for understanding non-equilibrium plasma flows. The key point for getting reliable transport properties (viscosity, thermal and electrical conductivity) is the availability of transport cross sections (collision integrals). These data are continuously updated following the corresponding progress in cross sections and intermolecular potentials [1]. In this paper we report recent calculations performed by our group.

2. Collision integrals in hydrogen plasmas

Transport cross sections can be calculated as a function of the gas temperature (T) according to the following equation [2]:

$$\Omega^{(l,s)}(T) = \frac{4(l+1)}{(s+1)!(2l+1-(-1)^l)} \frac{1}{2kT} \int_0^{\infty} d\varepsilon e^{-\varepsilon/kT} \left(\frac{\varepsilon}{kT}\right)^{s+1} \sigma^{(l)}(\varepsilon) \quad 1)$$

where $\sigma^{(l)}(\varepsilon)$ is the gas-kinetic cross-section of order l that can be derived from measurements or computed from the intermolecular potential $V(r)$. In the last case the collision integrals are tabulated for different forms of the intermolecular potential (exponential repulsive, Morse, Lennard-Jones potential) [2]. Simple interpolations among tabulated data furnish the needed collision integrals once known the parameters entering the potential.

The considered interactions include neutral-neutral (H_2 - H_2 , H_2 - H , H - H), ion-neutral (H^+ - H_2 , H^+ - H), electron-neutral (e - H , e - H_2) and charged-charged (H^+ - e , H^+ - H^+ , e - e) types.

2.1. H_2 - H_2 interaction

In the temperature range $50 \div 1000K$ we utilized a Lennard-Jones potential [2]

$$\varphi(r) = 4 \varphi_0 \left(\left(\frac{\sigma}{r}\right)^{12} - \left(\frac{\sigma}{r}\right)^6 \right) \quad 2)$$

where $\varphi_0 = 0.0028696$ eV and $\sigma = 2.968$ Å.

In the temperature range $2,000 \div 100\ 000K$ we have used the experimental exponential repulsive potential reported in ref. [3]

$$\varphi(r) = \varphi_0 \exp(-r / \rho) \quad 3)$$

where $\varphi_0 = 246 \text{ eV}$ and $\rho = 0.3106 \text{ \AA}$.

Results for $1000\text{K} < T < 2000\text{K}$ are obtained by smoothly linking the two sets of data. A comparison between the present results and those recently reported in ref. [4] shows a satisfactory agreement, the differences not exceeding 12% in the temperature range where $\text{H}_2\text{-H}_2$ interactions are important (see figure 1).

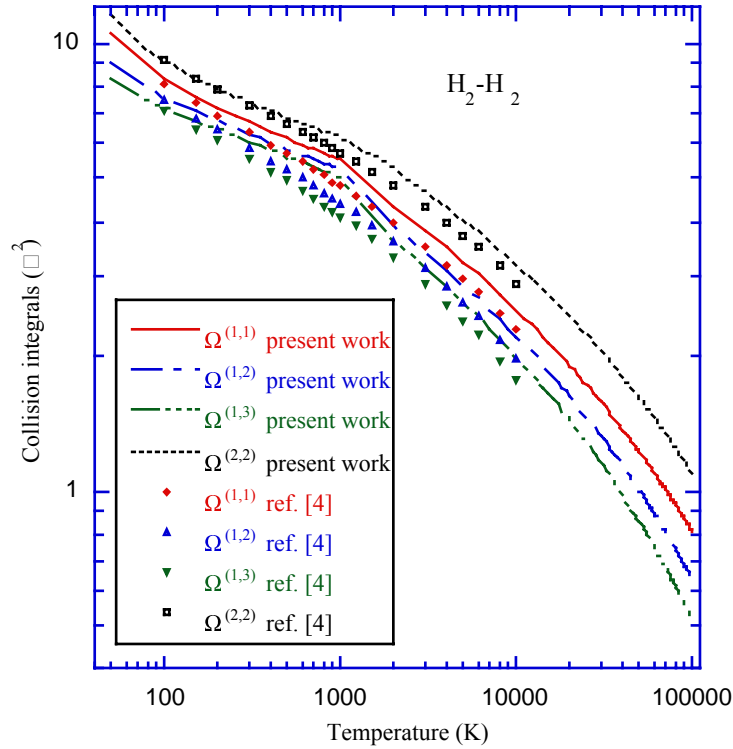


Figure 1. Comparison between collision integrals for $\text{H}_2\text{-H}_2$ interaction calculated in this work (lines) and reported in ref. [4] (symbols).

2.2. $\text{H}_2\text{-H}$ interaction

In the temperature range $50 \div 1000\text{K}$ we have used a Morse potential based on the results of ref. [5]

$$\varphi(r) = \varphi_0 \left\{ \exp\left[-2\frac{C}{\sigma}(r - r_e)\right] - 2\exp\left[-\frac{C}{\sigma}(r - r_e)\right] \right\} \quad \text{with } C = \text{Ln}2 \quad \sigma / (r_e - \sigma) \quad 4)$$

where $\varphi_0 = 0.0018 \text{ eV}$, $\sigma = 3.0528 \text{ \AA}$ and $C = 4.512$.

In the temperature range $2000 \div 100\,000\text{K}$ we have used an exponential repulsive potential derived from ref. [6] with $\varphi_0 = 22.978 \text{ eV}$ and $\rho = 0.3792 \text{ \AA}$.

Again results for $1000\text{K} < T < 2000\text{K}$ are obtained by smoothly linking the two sets of data. A good agreement between the values of the collision integrals calculated in the present work and those from ref. [5] is found as can be appreciated by figure 2.

2.3. H-H interaction

For this multi-potential interaction collision integrals are obtained as the average of the integrals derived for the interactions along the two states $^1\Sigma$ and $^3\Sigma$ over their respective statistical weights ($p_1 = 1$ for $^1\Sigma$ and $p_2 = 3$ for $^3\Sigma$ state).

$$\langle \Omega^{(l,s)} \rangle = \frac{\sum_n p_n \Omega_n^{(l,s)}}{\sum_n p_n} \quad (5)$$

In the temperature range $75 \div 100\,000\text{K}$ we used, for state $^3\Sigma$, an exponential repulsive potential [8] where $\varphi_0 = 60.42\text{ eV}$ and $\sigma = 0.3319\text{ \AA}$, and, for state $^1\Sigma$, a Morse potential [9] where $\varphi_0 = 4.84\text{ eV}$, $\sigma = 0.42093\text{ \AA}$ and $C = 0.9206$.

Again a good agreement has been found between the present results and those reported in ref. [4, 6] (see figure 3).

2.4. H^+ -H interaction

Two processes have to be considered for resonant ion-neutral interactions: purely elastic collisions and charge transfer between the two colliders. The usual approximation on the diffusion (odd l) cross section dominated by charge transfer [10] is introduced:

$$\sigma^{(l)}(\varepsilon) = 2 Q_{\text{ex}} (Q_{\text{ex}} \text{ is the total charge transfer cross section for process } H^+ + H, H + H^+)$$

$$Q_{\text{ex}} = (A - B \ln(\frac{\varepsilon}{kT})^{1/2}) / 2 \quad (6)$$

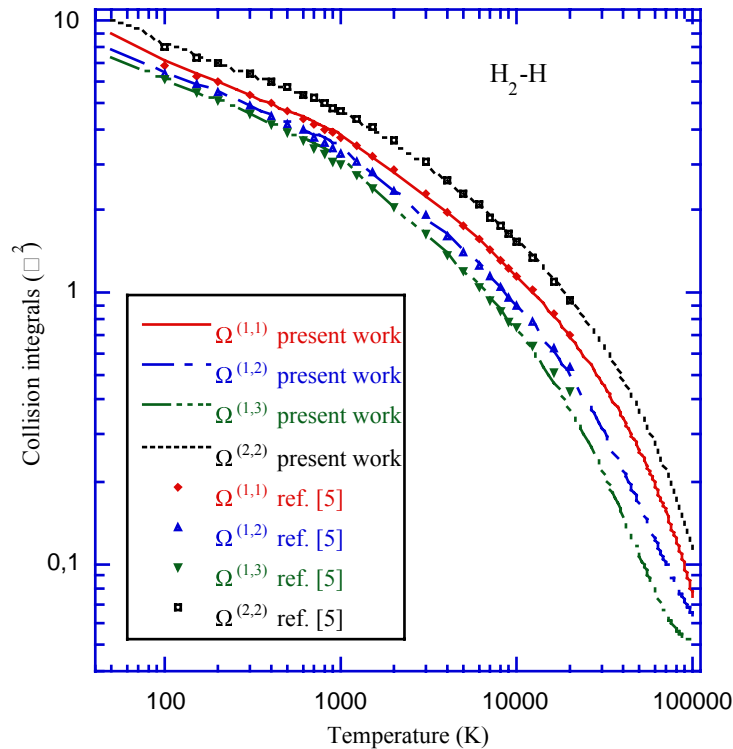


Figure 2. Comparison between collision integrals for H_2 -H interaction calculated in this work (lines) and reported in ref. [5] (symbols).

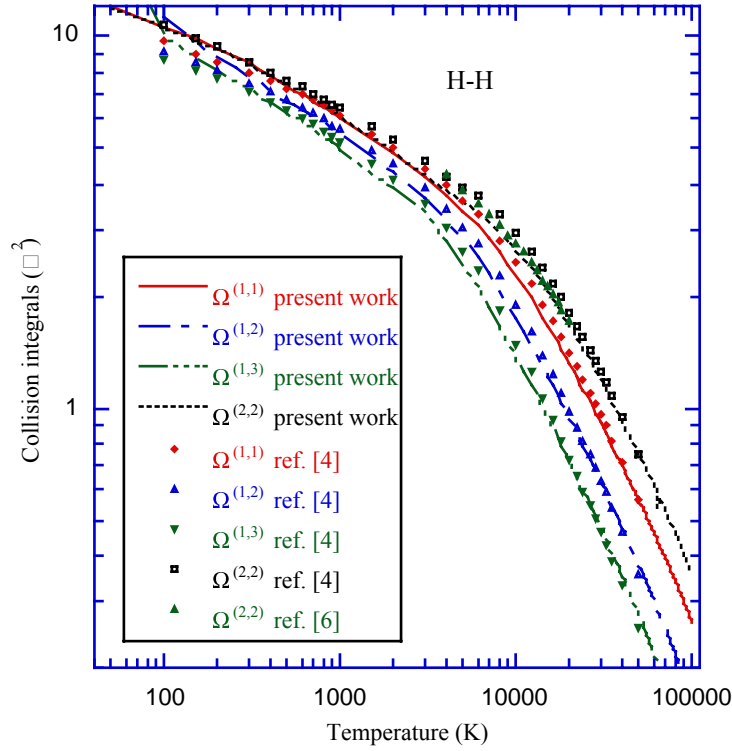


Figure 3. Comparison between collision integrals for H-H interaction calculated in this work (lines) and reported in refs. [4, 6] (symbols).

From the experimental data reported in ref. [11] we obtain $A = 28.909 \text{ \AA}^2$ and $B = 1.3427 \text{ \AA}^2$. The viscosity type (even l) collision integrals that are not altered by the charge transfer process are obtained as the average of the integrals calculated for interactions along the two states ${}^2\Sigma_g$ and ${}^2\Sigma_u$ of H_2^+ [12] over their respective statistical weights as well as in the case of neutral-neutral interactions.

In the temperature range $50 \div 100\,000 \text{ K}$ we used, for state ${}^2\Sigma_g$, a Morse potential with $\varphi_0 = 2.8607 \text{ eV}$, $\sigma = 0.57989 \text{ \AA}$ and $C = 0.80614$, and for state ${}^2\Sigma_u$, an exponential repulsive potential with $\varphi_0 = 82.029 \text{ eV}$ and $\sigma = 0.46956 \text{ \AA}$.

2.5. H^+-H_2 interaction

This process has only a weak importance on the transport coefficients of thermal plasmas. We have used a polarization potential and calculate the collision integrals as

$$\begin{aligned}
 \Omega^{(1,1)}(T) &= 425.4 \sqrt{\alpha/T} \\
 \Omega^{(1,2)}(T) &= 0.8333 \Omega^{(1,1)}(T) \\
 \Omega^{(1,3)}(T) &= 0.7292 \Omega^{(1,1)}(T) \\
 \Omega^{(2,2)}(T) &= 0.8710 \Omega^{(1,1)}(T)
 \end{aligned} \tag{7}$$

where the polarizability α of molecular hydrogen has been taken 0.79 \AA^3 .

2.6. $e\text{-H}_2$ and $e\text{-H}$ interactions

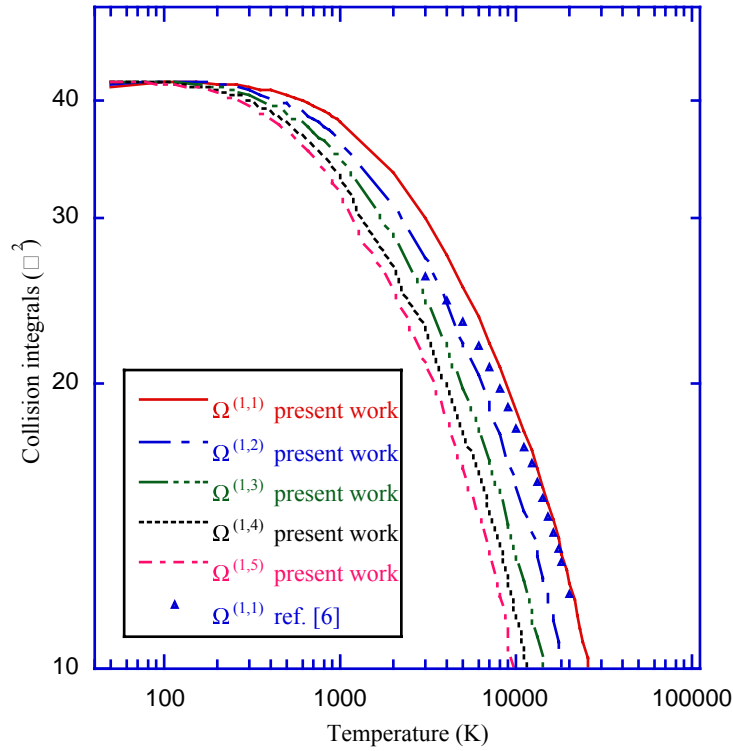


Figure 4. Comparison between collision integrals for $e\text{-H}$ interaction calculated in this work (lines) and reported in refs. [6] (symbols).

The momentum transfer cross section for H_2 and H are respectively fitted as

$$\sigma_{e\text{-H}_2} = (9619.9 + 29876 \varepsilon^{0.49331}) \exp\left(-\frac{(\varepsilon + 57.205)^2}{20.766^2}\right) + \exp(-0.26741 \varepsilon) + \exp(-0.12698 \varepsilon) \varepsilon \quad (8)$$

from the works of refs. [13–15] and as

$$\sigma_{e\text{-H}} = \ln(4.038510^8 \varepsilon) \left(\frac{1}{0.93857 \exp(1.5595\varepsilon)}\right) + 4.533910^6 \exp\left(-\frac{(\varepsilon + 13831)^2}{39.773^2}\right) \quad (9)$$

from the works of refs. [13, 16]

Then the previous expressions are introduced in equation 1) that, after a numerical integration, furnishes the different collision integrals.

2.7. Charged-charged interactions

In this case to avoid the problem due to the divergence of $\sigma^{(1)}(\varepsilon)$ cross sections at long interaction range we use the screened Coulomb potential

$$V(r) = \frac{e^2}{r} \exp\left(-\frac{r}{d}\right) \quad (10)$$

where d is the Debye length ($d = \frac{kT}{\sum_i \sqrt{4\pi(z_i e)^2 n_i}}$) 11)

Collision integrals for these interactions are approximated with closed forms [17]

$$\Omega^{(1,s)} = \frac{4}{s(s+1)} b_0^2 \left[\text{Ln}\Lambda - \frac{1}{2} - 2\gamma + \psi(s) \right] \quad 12)$$

$$\Omega^{(2,s)} = \frac{12}{s(s+1)} b_0^2 \left[\text{Ln}\Lambda - 1 - 2\gamma + \psi(s) \right] \quad 13)$$

where $\Lambda = \frac{2d}{b_0}$ is the ratio between the Debye length and the average closest impact

parameter b_0 ($b_0 = \frac{e^2}{2kT}$), $\psi(s) = \sum_{n=1}^{s-1} \frac{1}{n}$ with $\psi(1) = 0$ and γ is the Euler constant

Charge transfer between ions is disregarded as elastic cross sections are dominant when a screened potential is applied [18].

The charged-charged collision integrals calculated with Liboff equations are within 20% of the numerical integrated values reported by Hahn et al.[19].

3. Conclusions

We have reported in this paper the transport cross sections for the different interactions existing in hydrogen plasmas. These quantities can be used in the Chapman-Enskog formalism for getting transport properties for one or two temperature Hydrogen plasmas. In doing so one must be aware in the calculation of the internal conductivity due to electronically excited states of atomic hydrogen. Cross sections for this case are very peculiar as shown in ref. [20] and more recently in refs. [21].

4. Appendix

The following formula has been used to fit the collision integrals between heavy particles and between electron and heavy particles. The relevant coefficients have been reported in tables 1 and 2.

$$\Omega^{(i,j)} = \frac{a1 + a2 T^{a3}}{a4 + a5 T^{a6}} \quad 14)$$

Table 1. Parameters used to fit the collision integrals for interactions between heavy particles

	$\Omega(i,j)$	a1	a2	a3	a4	a5	a6
H ₂ -H ₂	$\Omega(1,1)$	2.4380e-05	2.4809e-03	-1.4327e+00	2.8742e-06	3.0371e-08	5.8695e-01
	$\Omega(1,2)$	1.4259e-05	3.1682e-03	-1.7833e+00	1.6998e-06	1.7595e-08	6.0928e-01
	$\Omega(1,3)$	1.3024e-05	6.1786e-03	-2.0795e+00	1.5977e-06	1.4555e-08	6.3543e-01
	$\Omega(2,2)$	3.5186e-05	2.1763e-03	-1.2460e+00	4.2223e-06	2.3015e-08	6.1530e-01
H-H	$\Omega(1,1)$	-6.1188e-01	5.8769e+00	-1.6199e-01	2.0103e-01	1.9714e-05	9.4241e-01
	$\Omega(1,2)$	2.1894e-01	2.9561e+01	-1.1279e+00	3.2253e-02	7.2245e-06	1.0328e+00
	$\Omega(1,3)$	2.2687e-13	1.0585e-11	-8.5177e-01	4.2389e-14	2.7995e-18	1.1622e+00
	$\Omega(2,2)$	-7.1447e-01	5.6502e+00	-1.5535e-01	1.9172e-01	6.8913e-06	9.7344e-01
H-H ⁺	$\Omega(1,1)$	-2.6921e-04	1.0116e-03	-6.0386e-02	9.6685e-06	4.8683e-07	1.7952e-01
	$\Omega(1,2)$	-5.9688e-04	1.2398e-03	-3.7367e-02	7.5926e-06	1.5134e-06	1.0723e-01
	$\Omega(1,3)$	-3.1526e-04	9.9045e-04	-5.5954e-02	9.1316e-06	6.2584e-07	1.6085e-01
	$\Omega(2,2)$	-8.6263e-06	2.5247e-04	-1.9289e-01	3.8546e-06	4.8342e-10	9.3162e-01
H ₂ -H	$\Omega(1,1)$	-2.7945e-02	2.3506e-01	-1.7072e-01	1.0823e-02	5.5119e-06	7.7910e-01
	$\Omega(1,2)$	-2.7078e-02	2.3563e-01	-1.6828e-01	1.2109e-02	6.3457e-06	8.3537e-01
	$\Omega(1,3)$	-5.1748e-02	2.0271e-01	-1.1051e-01	1.1034e-02	1.2671e-05	7.9727e-01
	$\Omega(2,2)$	-3.9495e-02	2.0221e-01	-1.3140e-01	8.5270e-03	2.6427e-06	8.1394e-01
H ₂ -H ⁺	$\Omega(1,1)$	4.5892e+04	4.9584e+03	-1.4372e+00	1.0000e+00	1.2123e+02	5.0011e-01
	$\Omega(1,2)$	1.9783e+03	-3.4928e+02	-5.5197e-01	-1.0000e+00	6.2983e+00	4.9974e-01
	$\Omega(1,3)$	2.8804e+04	2.8959e+06	-3.2327e+00	1.0000e+00	1.0430e+02	5.0017e-01
	$\Omega(2,2)$	3.4026e+04	8.0691e+27	-1.5844e+01	1.0000e+00	1.0315e+02	5.0016e-01

Table 2. Parameters used to fit the collision integrals for interactions between electrons and molecules or atoms (in this case the collision integrals include the factor π)

	$\Omega(i,j)$	a1	a2	a3	a4	a5	a6
e-H ₂	$\Omega(1,1)$	5.5649e+03	1.5522e+03	3.0297e-01	1.4350e+03	2.3699e-04	1.5661e+00
	$\Omega(1,2)$	4.0513e+03	1.8174e+03	2.8221e-01	1.2425e+03	1.1950e-04	1.6658e+00
	$\Omega(1,3)$	5.7662e+03	2.3715e+03	2.9381e-01	1.6721e+03	1.1851e-04	1.7411e+00
	$\Omega(1,4)$	5.3137e+03	1.9668e+03	3.0419e-01	1.4440e+03	7.6575e-05	1.8073e+00
	$\Omega(1,5)$	3.7217e+03	1.4950e+03	3.0106e-01	1.0255e+03	4.1958e-05	1.8627e+00
e-H	$\Omega(1,1)$	-3.2951e+06	2.0039e-01	1.4010e+00	-7.6684e+04	-1.6610e+01	9.3828e-01
	$\Omega(1,2)$	-1.4463e+05	5.4312e+00	8.7502e-01	-3.3497e+03	-1.0000e+00	9.2282e-01
	$\Omega(1,3)$	2.8670e+02	-1.8505e-01	6.4060e-01	6.5908e+00	1.8616e-03	9.3740e-01
	$\Omega(1,4)$	2.0304e+05	-6.8524e+02	5.0233e-01	4.5878e+03	1.0000e+00	9.7133e-01
	$\Omega(1,5)$	4.0765e-10	-3.9284e-12	4.1381e-01	8.9666e-12	1.4327e-15	1.0115e+00

ACKNOWLEDGEMENTS

This work has been partially supported by Agenzia Spaziale Italiana (contratto Termodinamica, trasporto e cinetica di plasmi di H₂ per propulsione spaziale).

REFERENCES

- [1] CAPITELLI, M., CELIBERTO, R., GORSE, C. and GIORDANO, D., Plasma Chem. Plasma Process., **16** (1996) 267S.
- [2] HIRSCHFELDER, L.J., Curtiss C.F. and Bird R.B., in "Molecular Theory of Gases and Liquids", Wiley, New York 1966.
- [3] LEONAS, V.B., Sov. Phys. Uspekhi, **15**, (1973) 266.
- [4] STALLCOP, J. R., LEVIN E, PARTRIDGE H., J. Thermophysics Heat Transf., **12** (1998) 514.
- [5] STALLCOP, J. R., PARTRIDGE H., LEVIN E, Chem. Phys. lett., **254** (1996) 25.
- [6] DEVOTO, R.S., J. Plasma Phys., **2** (1968) 617.
- [7] PARTRIDGE, H., BAUSCHLICHER JR, C.W., STALLCOP, J. R., J. Chem. Phys., **99** (1993) 5951.
- [8] VANDERSLICE, J.T., WEISSMANN, S., MASON, E.A., FALLON, R.J., Phys. fluids, **5** (1962) 155.
- [9] KOLOS, W., WOLNIEWICZ, L., J. Chem. Phys., **46** (1965) 2429.
- [10] MASON, E.A., VANDERSLICE, J.T., YOS, J.M., Phys. Fluids, **6** (1959) 688.
- [11] BELYAEV, V.A., BREZHNEV, B.G., YERASTOV, Y.M., JETP, **52** (1967) 1170.
- [12] SHARP, T.E., Atomic Data, **2** (1971) 119.
- [13] ITIKAWA, Y., Atom. Data and Nucl. Data Tables, **14** (1974) 1.
- [14] SHYN, T.W., SHARP, W.E., Phys. Rev, A **2** (1981) 1734.
- [15] SRIVASTAVA, S.K., CHUTJIAN, A., TRAJMAR, S., J. Chem. Phys., **63** (1975) 2659.
- [16] TRAJMAR, S., KANIK, I., in "Atomic and Molecular Processes in Fusion Edge Plasmas", ed. R.K. Janev, (1995) 31.
- [17] LIBOFF, R.L., Phys. Fluids, **2** (1959) 40.
- [18] MASON, E.A., SHERMAN, M.P., Phys. Fluids, **9** (1966) 1989.
- [19] HAHN H.S., MASON E.A. AND SMITH F.J., Phys.Fluids 14(1971)278.
- [20] CAPITELLI, M, LAMANNA, U, J. Plasma Phys., **12** (1974) 17.
- [21] CELIBERTO, R., LAMANNA ,U.T. AND CAPITELLI, M., Phys.Rev.A58 (1998) 2106.

Dissociative electron attachment to rovibrationally excited molecular hydrogen and its heavier isotopic variants

J.M. Wadehra

Department of Physics and Astronomy,
Wayne State University,
Detroit, Michigan, United States of America

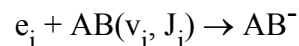
Abstract. Theoretical cross sections for dissociative electron attachment to H_2 and its five heavier isotopic variants (HD, HT, D_2 , DT, T_2) are presented. The dependence of these cross sections on the initial rovibrational excitation of the molecule is investigated. Various cross sections are fitted to simple analytical functions. These functions can be used to include the electron attachment processes in the divertor modeling computer codes conveniently.

1. Introduction

Atomic and molecular collision processes play an important role in modeling and understanding of the divertor edge plasma [1]. In the divertor plasma, the dominant molecular species are hydrogen and its heavier isotopic variants which typically are in vibrationally excited form. Dissociative attachment of low energy electrons to these molecules provides an important sink for vibrationally excited species and a significant source of low energy negative ions. In fact, in a hydrogen plasma the amount of negative ions formed is known to be anomalously large [2]. Previous theoretical as well as experimental investigations revealed [3, 4] that low energy electrons can attach themselves very efficiently to molecular hydrogen to cause dissociative attachment and, furthermore, the cross section for this process is significantly enhanced, by orders of magnitude, if the molecular hydrogen is initially in a vibrationally excited state. In this paper we present the cross sections for dissociative electron attachment to H_2 and its five heavier isotopic variants, HD, HT, D_2 , DT, T_2 . The dependence of these cross sections on the initial vibrational state of the molecule is also calculated and shown. For the convenience of using these data in the modeling of the divertor plasma, the cross sections are fitted to simple analytical functions that can be easily included in the computer codes.

2. The resonance model

The physics of the process of dissociative electron attachment to a general molecule AB is best described by the resonance model. In this model the process of dissociative attachment occurs via the formation of a temporary bound state of the electron-molecule system [5, 6]. The electron in this molecular anion state AB^- (also called the resonance state) can autodetach with a finite lifetime (related to the width, Γ , of the resonance), leaving behind a rovibrationally excited neutral molecule. On the other hand, if the lifetime of the resonance is long enough, the anion AB^- can dissociate into $A + B^-$, leading to the process of dissociative electron attachment. Thus, in a schematic sense one has



The final level with quantum numbers v_f and J_f can be either discrete (corresponding to rovibrational excitation of the molecule) or could lie in the continuum (corresponding to pure dissociation of the molecule).

A possible scenario of the resonance model is depicted in Figure 1 [7, 8]. Shown schematically in this Figure are the potential curves of the neutral molecule AB (labeled V_0) and of the resonant state AB^- (labeled V^-). The two potential curves cross at an internuclear separation $R = R_s$ such that, for $R \geq R_s$, the autodetachment of the electron is energetically not permitted and the resonance turns into a stable bound state of AB^- . R_s is referred to as the

stabilization radius. Before the incident electron, with energy ϵ , is captured, the nuclei are rovibrating in the level (v_i, J_i) under the influence of the potential $V_0(R)$. After electron capture, the nuclei of the anion move under the influence of $V^-(R)$. The probability of electron capture to form the resonant molecular anion state depends on the internuclear separation and this probability is maximum at an internuclear separation (labeled R_c in the Figure and referred to as the capture radius) at which the energy separation between the two potential curves is equal to the energy of the incident electron. If the potential curve V^- is repulsive in nature, then as the nuclei in the anion state begin to separate out the electronic potential energy gets converted into nuclear kinetic energy. Now, if the autodetachment of the electron occurs at some specific internuclear separation, labeled R in the Figure, the neutral molecule is left in a rovibrationally excited level due to the gain in the nuclear kinetic energy (indicated by a vertical dotted line in the Figure). The exact rovibrationally excited level (v_f, J_f) achieved by the molecule depends on the gain in the kinetic energy of the nuclei as well as on the relevant selection rules. Depending upon the lifetime of the resonance the nuclei in the anion state may separate to an internuclear separation larger than R_s beyond which the autodetachment of the electron is energetically not possible and dissociative attachment occurs resulting in the formation of a stable negative ion.

A few important features of the resonance model should be noted. First, the processes of dissociative electron attachment and of vibrational excitation by electron impact are treated on an equal footing so that the investigation of one of these processes leads, in a natural way, to the information related to the other process. In fact, the optical theorem (which essentially is a conservation of flux statement) relates the cross sections for these two processes within the resonance model. Also, it is tacitly assumed that the transition between the resonant state and the electronic state of the neutral molecule is a spontaneous one without any corresponding change in the nuclear positions or velocities (a Franck-Condon transition). This *local* description of the resonance model is valid when the energy of the incident electron is much larger than the spacing of vibrational levels or when the incident electron energy is much above the threshold energy. When the incident electron energy is sufficiently small such that

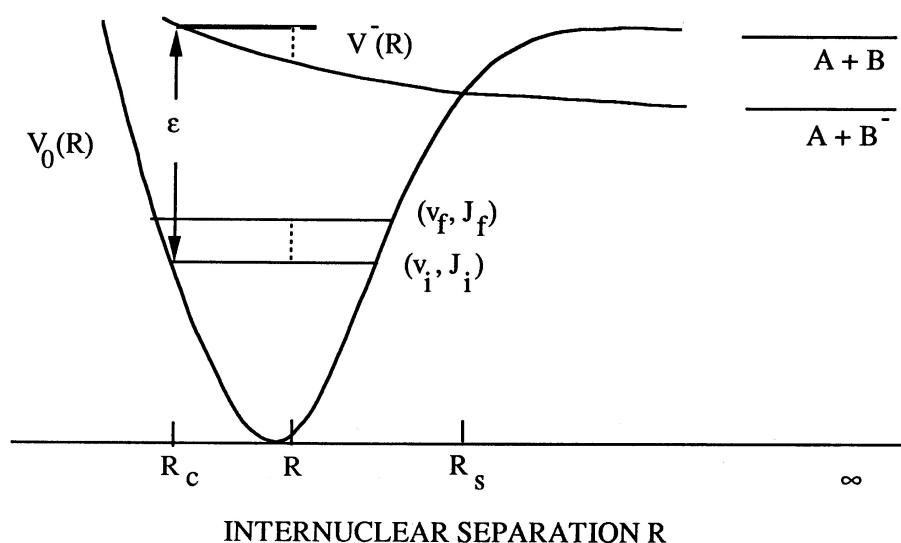
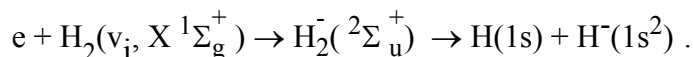


Figure 1. A schematic presentation of the potential curves of a molecule AB and of its anion state AB^- relevant to the resonance model for dissociative electron attachment.

these conditions are not met, a proper description of the resonance model is a *nonlocal* one involving, in its mathematical formulation, an integrodifferential equation with nonlocal complex potential [9].

Specifically, for molecular hydrogen (and its heavier isotopic variants) the lowest resonant state is the $^2\Sigma_u$ state of H_2 . This is a shape resonance, with the $X^1\Sigma_g$ state of H_2 as its parent, for internuclear separations less than 3 a.u. The next higher resonant state of H_2 is the $^2\Sigma_g$ state [3, 10]. In the present calculations we have used the local version of the resonance

model and have considered only the ${}^2\Sigma_u^+$ resonant state of H_2^- . Thus, in the present work we have,



Use of nonlocal version of the resonance model as well as inclusion of higher resonant states of H_2^- will be the topics of future investigations.

3. Results

3.1. Dissociative attachment to H_2 and its isotopic variants

The relative masses of the six isotopic variants of molecular hydrogen range from 1 to 3 (in units of the mass of H_2). Specifically, the relative masses of the molecules H_2 , HD, HT, D_2 , DT and T_2 are 1.00, 1.33, 1.50, 2.00, 2.40 and 3.00, respectively. We have calculated cross sections for the dissociative electron attachment to all six isotopic variants of H_2 . These cross sections, which show quite significant isotope effect, are also fitted to useful analytical forms.

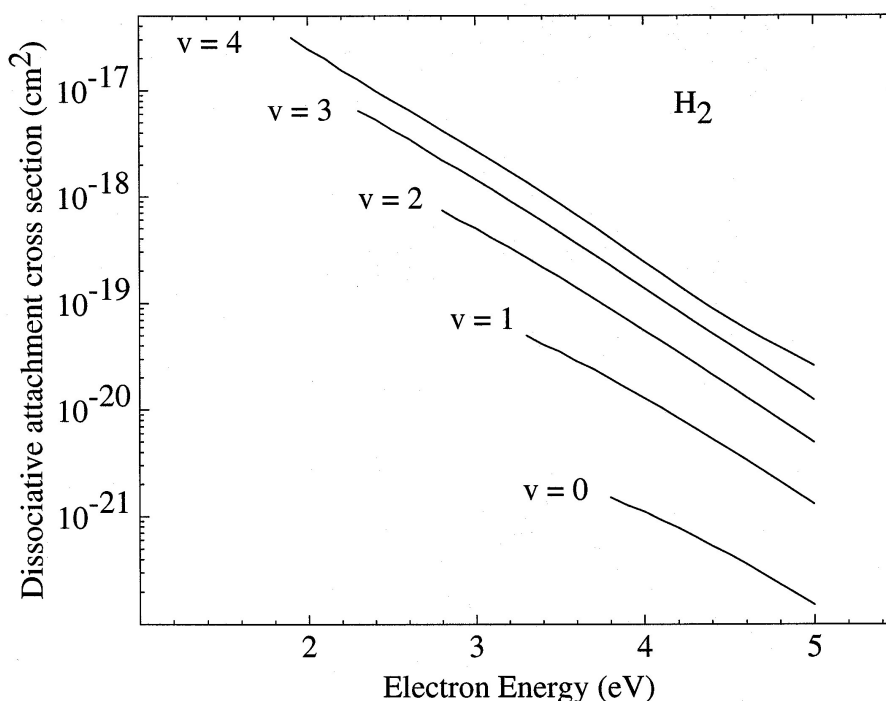


Figure 2. Cross sections for dissociative electron attachment to vibrationally excited H_2 .

Figure 2 shows the cross sections for dissociative electron attachment to H_2 which has its initial vibrational level ranging from $v = 0$ to $v = 4$. Note that the attachment cross section is dramatically enhanced if the attaching molecule H_2 is vibrationally excited. This strong enhancement of the attachment cross section (and, therefore, the attachment rate) on increasing the internal vibrational energy of the molecule is attributed to an increase in the range of internuclear separations over which the electron capture can occur. This increase occurs because of the larger amplitude of vibration for a vibrationally excited molecule. Also note that the cross section shows its peak value at the threshold and it reduces rapidly as the incident electron energy is increased above the threshold. Table 1 provides the threshold energy, E_{th} , and the peak value of the cross sections, σ_{peak} , for dissociative electron attachment to vibrationally excited H_2 . v is the initial vibrational quantum number of the vibrationally excited molecule.

Table 1. Threshold energy and the peak cross sections for dissociative electron attachment to vibrationally excited H₂. The initial vibrational quantum number is v .

v	E_{th} (eV)	σ_{peak} (au)
0	3.73	0.591(-4)
1	3.21	0.198(-2)
2	2.73	0.283(-1)
3	2.27	0.226
4	1.84	0.115(+1)
5	1.44	0.413(+1)

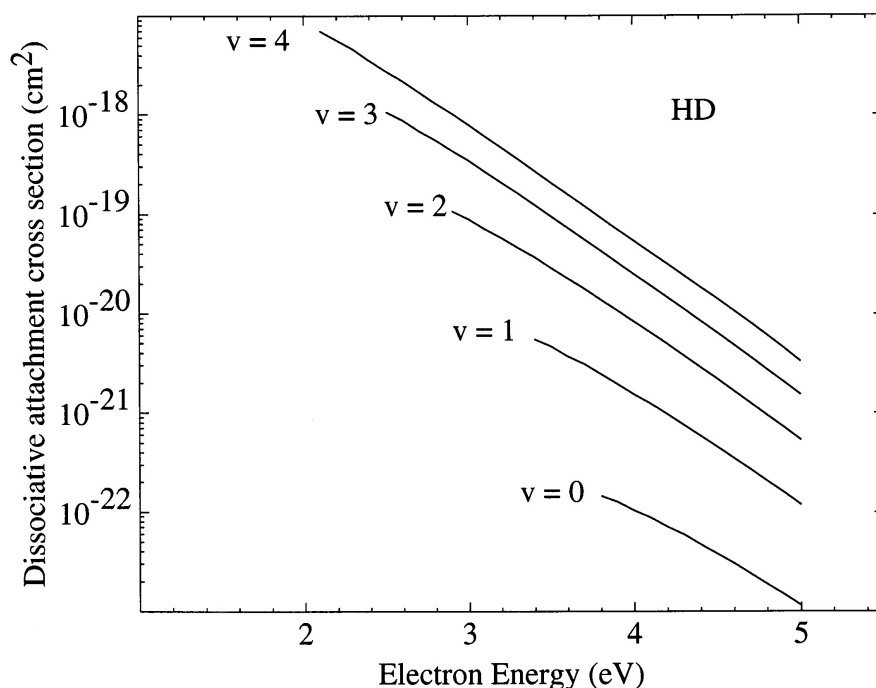


Figure 3. Cross sections for dissociative electron attachment to vibrationally excited HD.

Figures 3 to 7 show the cross sections for dissociative electron attachment to the heavier molecules HD, HT, D₂, DT and T₂ which, depending on the isotope, have their initial vibrational levels ranging from $v = 0$ or 1 to $v = 4$. Once again, note that the attachment cross sections are dramatically enhanced if the attaching molecule is initially vibrationally excited. Also note that, once again, the cross sections show their peak value at the threshold and they reduce rapidly as the incident electron energy is increased above the threshold. However, the magnitude of the attachment cross sections for heavier isotopic variants is much smaller than the magnitude of the corresponding cross sections for H₂; in fact, the attachment cross section systematically decreases as the isotope mass increases. It can be qualitatively understood by referring to the resonance model (see Figure 1).

Simple kinematic considerations show that the time taken for the separation of the nuclei to increase from the capture radius R_c to the stabilization radius R_s is proportional to $M^{1/2}$ (M is the reduced mass of the nuclei). Thus, nuclei of D₂, taking longer than the nuclei of H₂ to separate out to R_s , experience a stronger competition from electron autodetachment which, in turn, reduces the probability of dissociative attachment.

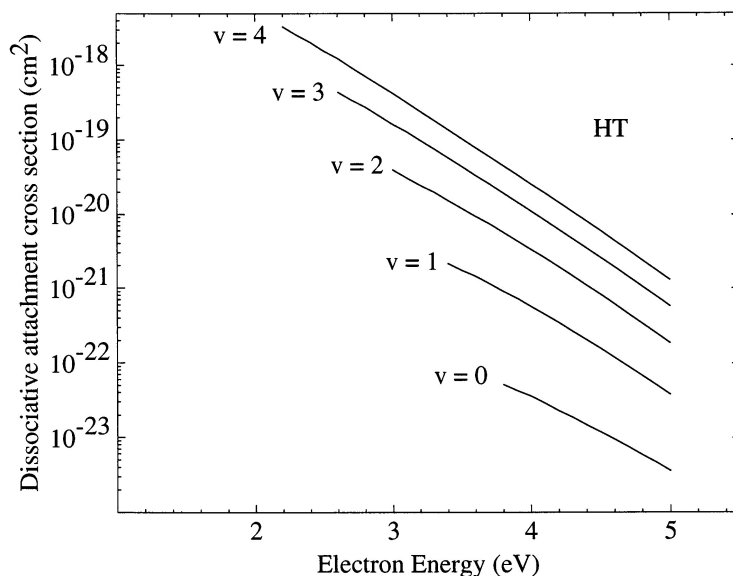


Figure 4. Cross sections for dissociative electron attachment to vibrationally excited HT.

In Tables 2 through 6 are shown the threshold energy, E_{th} , and the peak value of the cross sections, σ_{peak} , for dissociative electron attachment to vibrationally excited molecules HD, HT, D₂, DT and T₂. Again, v is the initial vibrational quantum number of the vibrationally excited molecule.

Table 2. Threshold energy and the peak cross sections for dissociative electron attachment to vibrationally excited HD. The initial vibrational quantum number is v .

v	E_{th} (eV)	σ_{peak} (au)
0	3.76	0.562(-5)
1	3.31	0.233(-3)
2	2.88	0.402(-2)
3	2.48	0.416(-1)
4	2.09	0.270
5	1.73	0.120(+1)

Table 3. Threshold energy and the peak cross sections for dissociative electron attachment to vibrationally excited HT. The initial vibrational quantum number is v .

v	E_{th} (eV)	σ_{peak} (au)
0	3.78	0.191(-5)
1	3.35	0.821(-4)
2	2.95	0.155(-2)
3	2.56	0.170(-1)
4	2.19	0.121
5	1.84	0.594

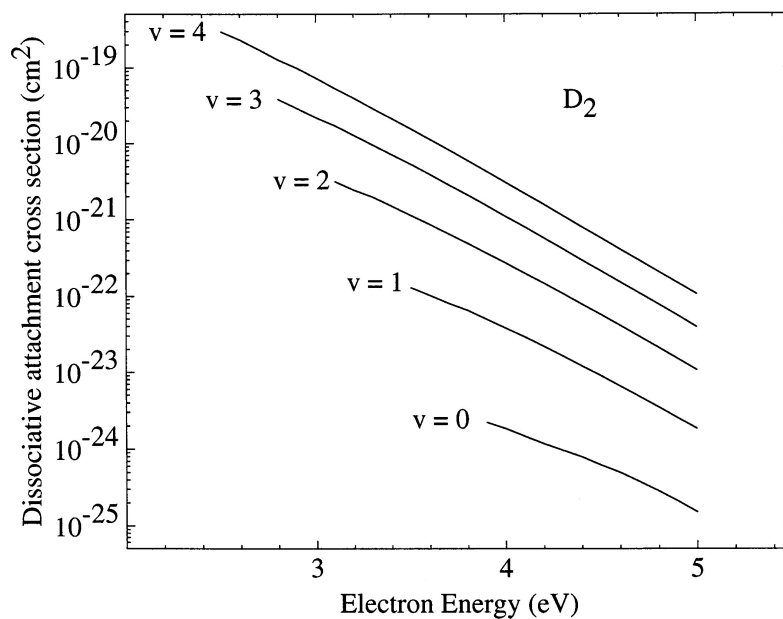


Figure 5. Cross sections for dissociative electron attachment to vibrationally excited D_2 .

Table 4. Threshold energy and the peak cross sections for dissociative electron attachment to vibrationally excited D_2 . The initial vibrational quantum number is v .

v	E_{th} (eV)	σ_{peak} (au)
0	3.81	0.111(-6)
1	3.44	0.543(-5)
2	3.08	0.119(-3)
3	2.74	0.153(-2)
4	2.41	0.132(-1)
5	2.10	0.846(-1)
6	1.80	0.387

Table 5. Threshold energy and the peak cross sections for dissociative electron attachment to vibrationally excited DT. The initial vibrational quantum number is v .

v	E_{th} (eV)	σ_{peak} (au)
0	3.82	0.120(-7)
1	3.48	0.729(-6)
2	3.16	0.181(-4)
3	2.84	0.274(-3)
4	2.54	0.273(-2)
5	2.25	0.195(-1)
6	1.97	0.104

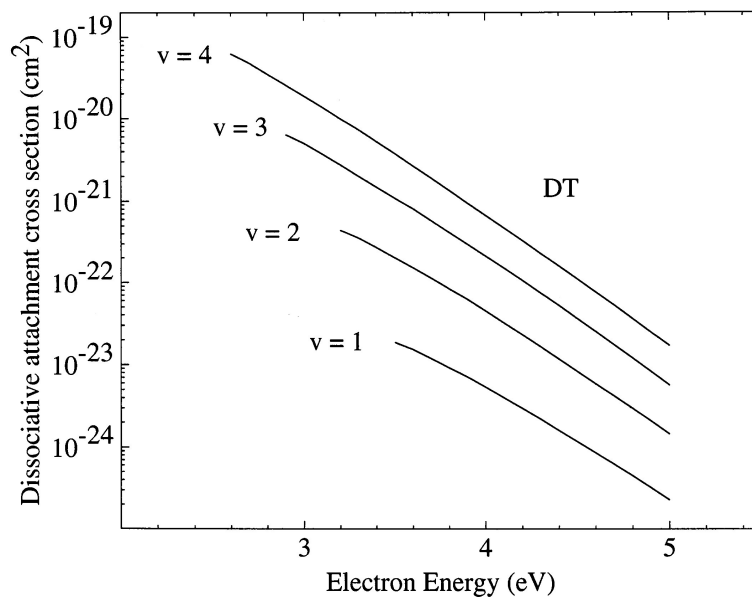


Figure 6. Cross sections for dissociative electron attachment to vibrationally excited DT.

Table 6. Threshold energy and the peak cross sections for dissociative electron attachment to vibrationally excited T₂. The initial vibrational quantum number is v.

v	E _{th} (eV)	σ _{peak} (au)
1	3.54	0.495(-7)
2	3.25	0.139(-5)
3	2.96	0.236(-4)
4	2.68	0.278(-3)
5	2.41	0.238(-2)
6	2.16	0.149(-1)
7	1.91	0.746(-1)

3.2. Simple analytical fits

For all six isotopic variants of H₂ the attachment cross sections show a peak at the threshold and a rapid reduction in magnitude as the electron energy is increased above the threshold. It is thus quite suggestive to fit the attachment cross sections just above the threshold by an expression of the form:

$$\sigma(E) = \sigma_{\text{peak}} \cdot \exp [-(E - E_{\text{th}})/E_0] \quad .$$

The validity and merit of this simple fit can be seen by plotting the ratio $\sigma/\sigma_{\text{peak}}$ for H₂ and its five heavier isotopic variants as a function of the electron energy above the threshold, $E - E_{\text{th}}$.

This type of plot is shown in figures 8 to 13 for all six isotopic variants of H₂. Since the attachment cross sections show their peak value at the threshold, the ratio $\sigma/\sigma_{\text{peak}}$ has the unit value at threshold and it decreases rapidly as the electron energy is increased above the threshold for attachment. A least squares fit of all the calculated data to an expression of the above form yields the value of the fitting parameter E₀.

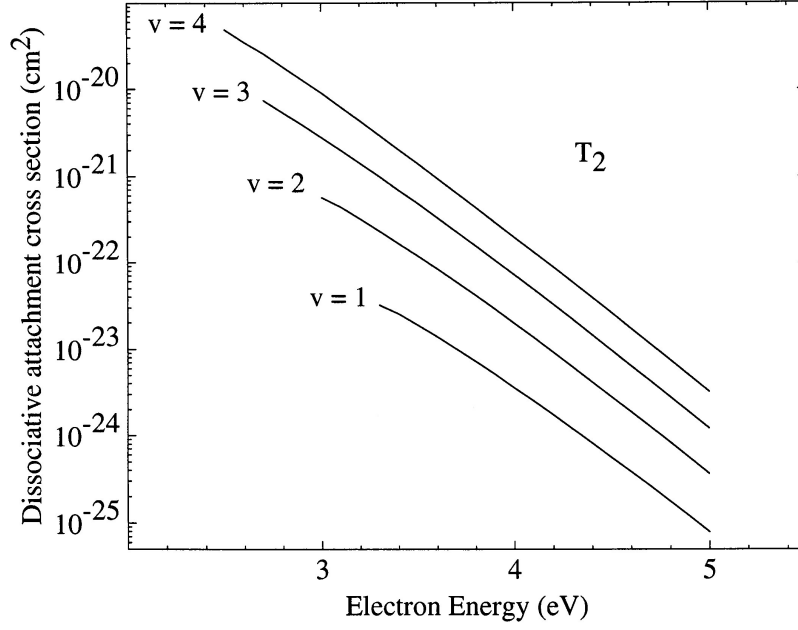


Figure 7. Cross sections for dissociative electron attachment to vibrationally excited T_2 .

This parameter E_0 has the value, in eV, 0.45, 0.39, 0.36, 0.32, 0.30 and 0.28 for the six isotopes H_2 , HD, HT, D_2 , DT and T_2 , respectively. We note in passing that the parameter E_0 depends on the isotope mass; it varies inversely as the square root of the isotope mass. This numerical observation is not yet analytically understood.

Assuming a Maxwellian distribution for electron energies, the rate of electron attachment can be written in the form of an analytical expression of the form,

$$k(\langle E \rangle) = \left(\frac{27 \langle E \rangle}{\pi m} \right)^{1/2} \sigma_{\text{peak}} \exp \left(- \frac{3 E_{\text{th}}}{2 \langle E \rangle} \right) \left[\left(\frac{3}{2} + \frac{\langle E \rangle}{E_0} \right)^{-2} + \frac{E_{\text{th}}}{\langle E \rangle} \left(\frac{3}{2} + \frac{\langle E \rangle}{E_0} \right)^{-1} \right],$$

where $\langle E \rangle = 3 kT/2$ and T is the electron temperature. This analytical expression can be conveniently used to obtain the attachment rates since σ_{peak} , E_{th} , and E_0 are provided, in the present work, for all six isotopic variants of H_2 .

3.3. Isotope effect of cross section enhancement

The results of calculations shown in Tables 1 through 6 clearly indicate that the cross sections and rates for dissociative electron attachment to H_2 and its isotopic variants are significantly enhanced if the molecule is initially rovibrationally excited. However, the factor by which the cross sections are enhanced varies from isotope to isotope.

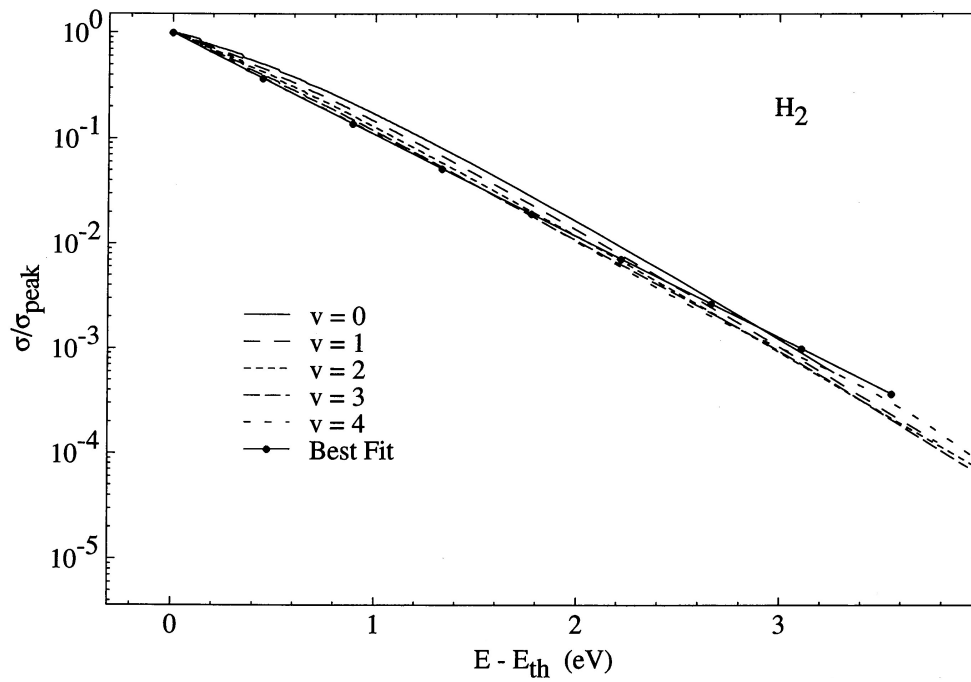


Figure 8. Ratio σ/σ_{peak} as a function of the electron energy above threshold, $E - E_{th}$, for H_2 .

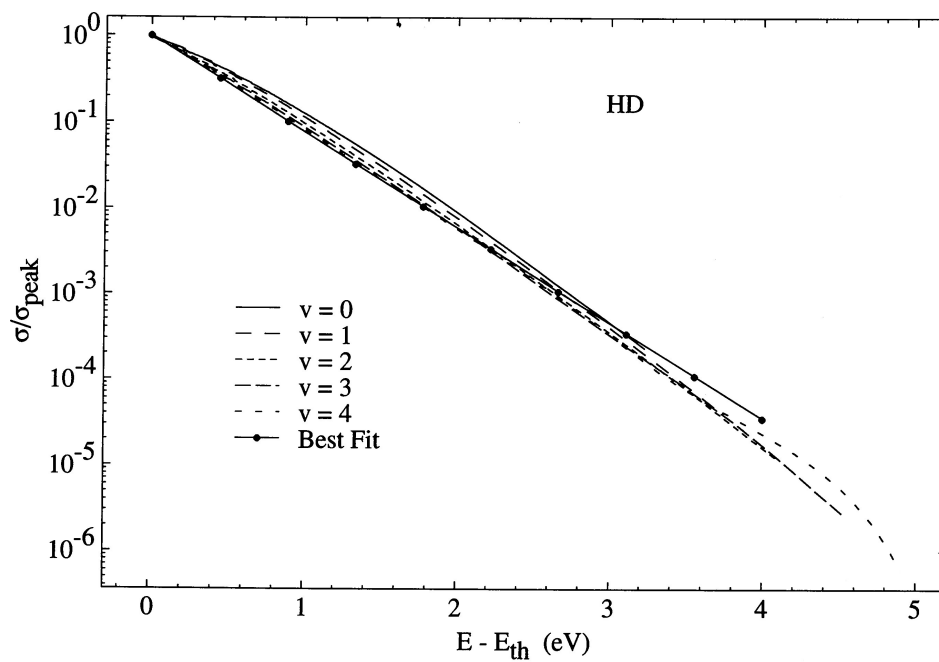


Figure 9. Ratio σ/σ_{peak} as a function of the electron energy above threshold, $E - E_{th}$, for HD.

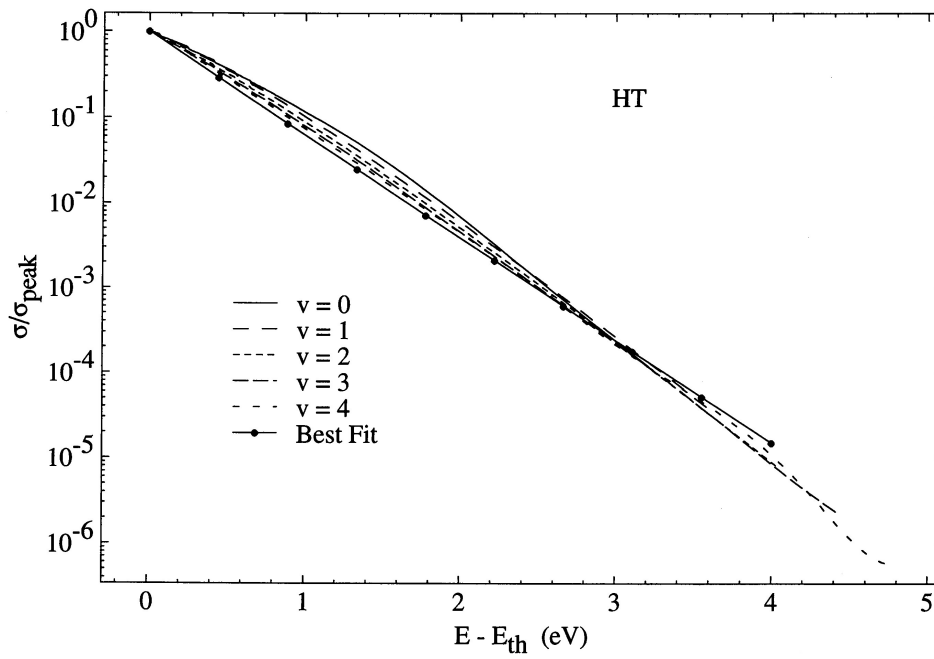


Figure 10. Ratio σ/σ_{peak} as a function of the electron energy above threshold, $E - E_{th}$, for HT.

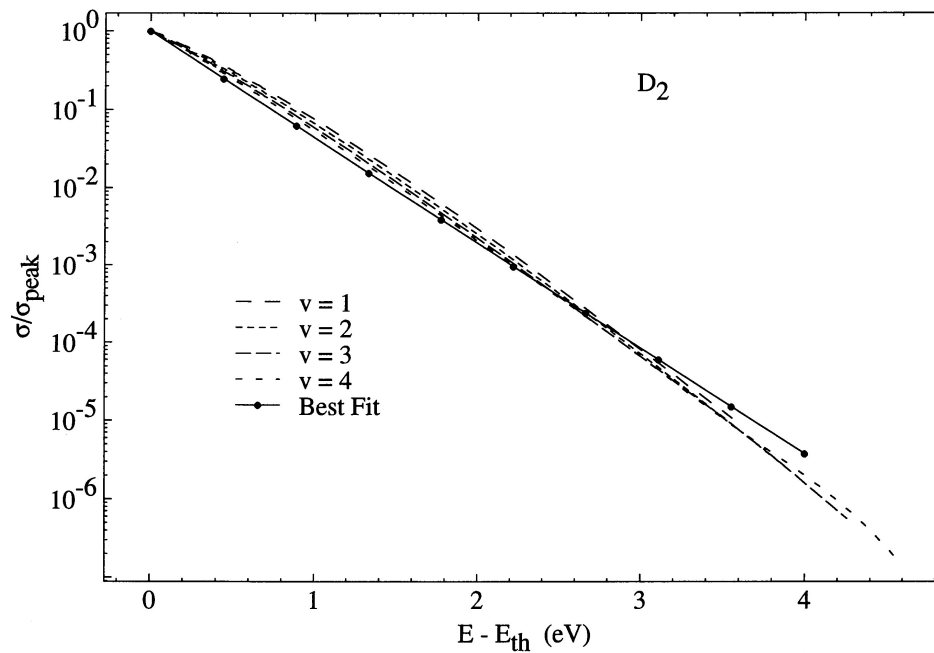


Figure 11. Ratio σ/σ_{peak} as a function of the electron energy above threshold, $E - E_{th}$, for D_2 .

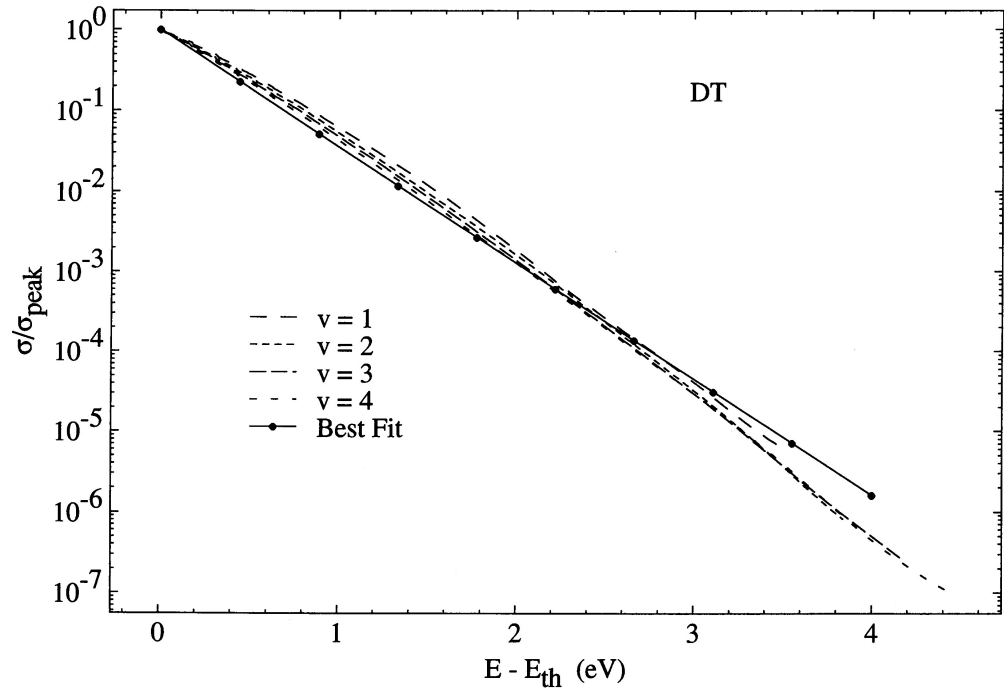


Figure 12. Ratio σ/σ_{peak} as a function of the electron energy above threshold, $E - E_{th}$, for DT.

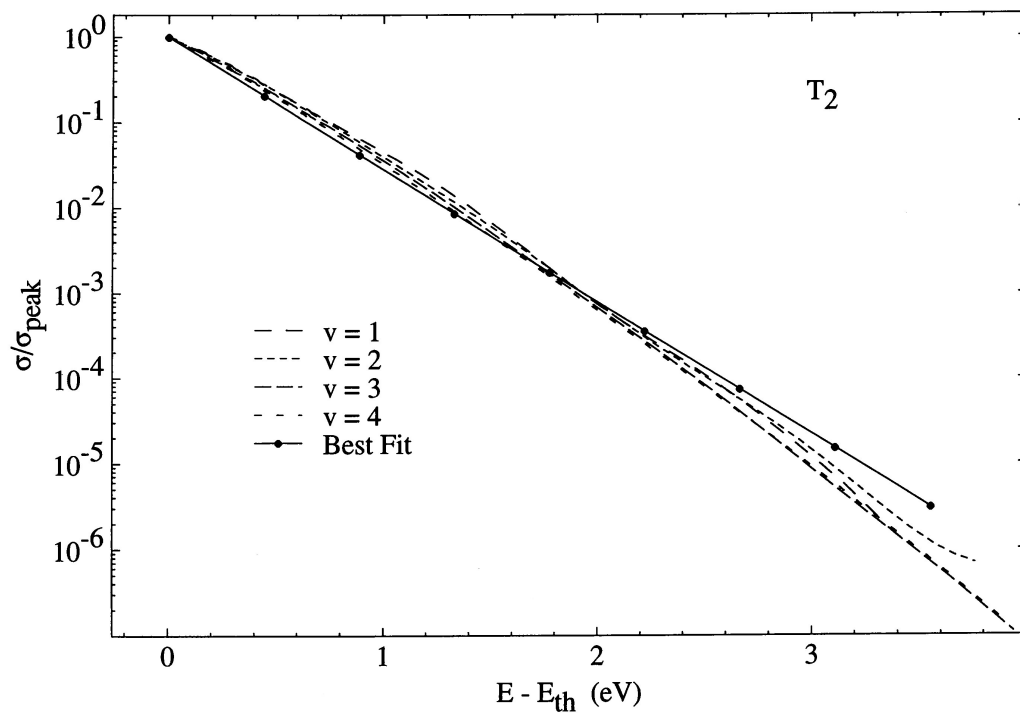


Figure 13. Ratio σ/σ_{peak} as a function of the electron energy above threshold, $E - E_{th}$, for T_2 .

Furthermore, this enhancement factor for vibrationally excited molecule is different than that for rotationally excited molecule. In order to investigate the isotope dependence of the cross section enhancement, we calculate and observe three ratios, R_I , R_V and R_J , defined as follows:

(i) For a given rovibrational level, the factor R_I by which the peak attachment cross section σ_{peak} is altered on replacing H_2 by one of its isotopic variants X ,

$$R_I = \sigma_{\text{peak}}(\text{H}^-, v = 0, J = 0) / \sigma_{\text{peak}}(X^-, v = 0, J = 0) \quad .$$

(ii) For a given isotopic variant X , the factor R_V by which the peak attachment cross section σ_{peak} is altered on exciting the molecule vibrationally from $v = 0$ to $v = 1$,

$$R_V = \sigma_{\text{peak}}(X^-, v = 1, J = 0) / \sigma_{\text{peak}}(X^-, v = 0, J = 0) \quad .$$

(iii) For a given isotopic variant X , the factor R_J by which the peak attachment cross section σ_{peak} is altered on exciting the molecule rotationally from $J = 0$ to $J = 10$,

$$R_J = \sigma_{\text{peak}}(X^-, v = 0, J = 10) / \sigma_{\text{peak}}(X^-, v = 0, J = 0) \quad .$$

Numerical values of these three ratios for all six isotopic variants of H_2 are given in Table 7. Obviously the factors R_I , R_V and R_J depend on the isotope and the dependence of these ratios on isotope mass M , obtained by a simple fitting procedure, is determined to be approximately,

$$\begin{aligned} R_I &\propto \exp(-\text{constant} \cdot M^{1/2}) & , \\ R_V &\propto M^{1/2} & , \\ R_J &\propto M^{-1} & . \end{aligned}$$

Table 7. Various factors indicating the enhancement of the peak cross section for attachment to rovibrationally excited H_2 and its isotopic variants.

Isotope	R_I	R_V	R_J
H_2	1.0	33.5	15.9
HD	10.5	41.5	11.8
HT	30.9	43.0	10.5
D_2	532	48.9	8.04
D $\bar{\text{T}}$	4925	54.2	6.89
T_2	65217	60.9	5.72

It would be interesting to understand the mass dependence of R_V and R_J analytically in the future. However, the mass dependence of R_I is well understood analytically using a semiclassical analysis of the cross section for dissociative electron attachment [11]. In such analysis the attachment cross section can be approximated by a product of the form $\sigma = \sigma_{\text{cap}} S$, where σ_{cap} is interpreted as the cross section for the formation of resonance by electron capture and the second factor (survival probability), given by

$$S = \exp \left(- \int_{R_c}^{R_s} \frac{\Gamma(R)}{\hbar} \frac{dR}{v(R)} \right) \quad ,$$

is the probability that the nuclei in the resonant state separate from the capture radius R_c to the stabilization radius R_s without any electron autodetachment having occurred. This survival probability can be approximated by $S \approx \exp(-\langle \Gamma \rangle \tau / \hbar)$, where τ is the time taken by the nuclei to separate from R_c to R_s . Now we can understand the isotope dependence of R_I since the time τ , based on simple kinematics considerations, is proportional to $M^{1/2}$. Thus the attachment cross section can be written in the following approximate form:

$$\sigma = \sigma_{\text{cap}} \exp(-\text{constant} \cdot M^{1/2})$$

As an example of this mass dependence of the cross section, we note that the value of the ratio

$$r = \frac{\ln [\sigma_{\text{peak}}(\text{T}_2) / \sigma_{\text{peak}}(\text{H}_2)]}{\ln [\sigma_{\text{peak}}(\text{D}_2) / \sigma_{\text{peak}}(\text{H}_2)]}$$

using the numerical values in Table 7, is $\ln(65217) / \ln(532) = 1.766$. On the other hand, if the mass dependence of the attachment cross section shown above is valid, then this ratio r should be

$$\frac{\sqrt{M(\text{T}_2)} - \sqrt{M(\text{H}_2)}}{\sqrt{M(\text{D}_2)} - \sqrt{M(\text{H}_2)}} = \frac{\sqrt{3} - 1}{\sqrt{2} - 1} = 1.767$$

Closeness in the two values of the ratio r attests to the validity of the isotope effect given by factor R_I .

4. Summary

In this work, which was carried out as a part of the Coordinated Research Project on Atomic and Plasma wall Interaction Data for Fusion Reactor Divertor Modeling [12], we have calculated the cross sections for dissociative electron attachment to vibrationally excited H_2 molecule and its five heavier isotopic variants, HD, HT, D_2 , DT, T_2 . In these calculations we have used a local version of the resonance model and have included only the lowest resonance of H_2^- . Calculations indicate that the cross section for dissociative electron attachment is significantly enhanced if the molecule is initially rovibrationally excited and, furthermore, the factor by which the cross section is enhanced depends on the mass of the particular isotopic variant. Finally, we have fitted various cross sections by simple analytical functions which can be very conveniently included in the modeling computer codes.

I thank my colleague, Professor W. E. Kauppila, for his kind assistance.

REFERENCES

- [1] JANEV, R. K., Atomic and Molecular Processes in Fusion Edge Plasmas, Plenum Press, New York, 1995.
- [2] HOPKINS, M. B., BACAL, M. AND GRAHAM, W. G., J. Appl. Phys. **70** (1991) 2009.
- [3] WADEHRA, J. M. AND BARDSLEY, J. N., Phys. Rev. Letts. **41** (1978) 1795.
- [4] ALLAN, M. AND WONG, S. F., Phys. Rev. Letts. **41** (1978) 1791.
- [5] O'MALLEY, T. F., Phys. Rev. **150** (1966) 14.
- [6] BARDSLEY, J. N., J. Phys. **B1** (1968) 349.
- [7] WADEHRA, J. M. in Nonequilibrium Vibrational Kinetics (CAPITELLI, M., Ed), Springer-Verlag, New York (1986) 191.
- [8] CHUTJIAN, A., GARSCADDEN, A. AND WADEHRA, J. M., Phys. Repts. **264** (1996) 393.
- [9] ATEMS, D. E. AND WADEHRA, J. M., Phys. Rev. **A42** (1990) 5201.
- [10] WADEHRA, J. M., Phys. Rev. **A29** (1984) 106.
- [11] BARDSLEY, J. N., HERZENBERG, A. AND MANDL, F., in Proc. Third Int. Conf. Atomic Collisions, North-Holland, Amsterdam (1964) 415.
- [12] JANEV, R. K., International Atomic Energy Agency Report, INDC(NDS)-402 (1999).

Dissociative recombination and excitation in fusion edge plasmas

J.B.A. Mitchell

Physique des Atomes, Lasers,
Molécules et Surfaces, Université de Rennes I,
Rennes Cedex, France

Abstract. There has been a tremendous increase in interest in the study of dissociative recombination and excitation processes following the implementation of the multi-pass merged beams technique at heavy ion storage rings in Europe and Japan. Recent developments in this field, of particular relevance to fusion reactor divertor plasmas, are described. Absolute cross sections, over wide energy ranges, the identity and internal energy of final channel products have been measured for a wide range of ions and these data are presented. The experimental measurements have prompted considerable interest from theoreticians and their progress in this field is also outlined.

1. Introduction

As molecular chemistry in hydrogen plasmas rises to importance in the cooler environment of the fusion edge and in divertor plasmas, a fuller understanding of the complex processes involved in electron-molecular ion collisions becomes essential. Volume processes such as dissociative recombination and dissociative excitation which serve to produce neutral species, can have a very practical value in preventing the surface neutralization of impacting ion species on divertor walls, a phenomenon in which the recombination energy will be deposited directly into the solid material. A number of reviews [1, 2, 3, 4] have been written concerning the importance of electron-ion recombination and excitation in fusion edge plasmas and the state of our knowledge concerning these processes at the time of their publication and the need for further research was addressed in these publications. The last few years has seen a dramatic growth in our knowledge of dissociative recombination and excitation processes and the current article will deal specifically with recent material. It is meant to read in conjunction with ref. 1 which dealt with the state of electron ion recombination and excitation processes relevant to divertor plasmas, up to 1995. Dissociative recombination is the subject of a conference series, the meetings occurring with a frequency of one every four years or so. The papers presented at these conferences are published and the reader can find them in the following publications [5, 6, 7, 8].

While molecular hydrogen is likely to be the dominant molecular species at the fusion edge, with helium ash as the next most important ingredient, other trace gases may be present such as nitrogen, oxygen, and hydrocarbon vapors caused by interaction of the hydrogenic plasma with carbon covered walls. Other species such as beryllium and boron hydrides and perhaps lithium hydrides may also be found in a practical device so information on these molecular ions is also needed. At the outset of this paper it must be said that in current and future fusion machines, tritium and deuterium are the primary fill gases as opposed to conventional hydrogen but in the following review, the bulk of the material presented will refer to conventional hydrogen containing molecules. While this fact has not been of importance to the atomic physics of plasma modeling up to now, with the advent of molecular processes whose reaction rates are critically dependent upon internal vibrational and rotational motion, it must be recognized that our reliance on conventional «light» hydrogen data is dangerous for isotopic substitution can lead to differences in molecular reaction rates of orders of magnitude in some cases. A way to compensate for this problem is for theoreticians involved in calculations of recombination and excitation problems to routinely use their codes to solve for

the corresponding reaction rates for deuterated and tritiated isotopomers. While this is now generally the case for deuterated species for which experimental data is easily obtained, the same is not true for tritiated species for which absolutely no experimental data is available. This latter lamentable fact is a consequence partly of the inherent dangers in handling radioactive tritium gas during normal operations of collision experiments but more particularly to the subsequent contamination of apparatus due to the formation of hard-cracked tritiated hydrocarbon surfaces on vacuum lines which render them radioactively contaminated and thus subject to replacement and subsequent disposal. Tritium molecular ion chemistry is specific to nuclear fusion research and since fusion related budgets for fundamental Atomic and Molecular research have essentially evaporated, it is not likely that such experiments will be performed in the foreseeable future. We must rely therefore on data for conventional hydrogenated species which have applications in other areas, recognizing that the values that we use are merely estimates of the real problem.

A number of significant events have occurred since the publication of references [1, 2, 3]. Perhaps the most spectacular is the tremendous growth of heavy ion storage ring experiments aimed at electron-molecular ion recombination and excitation measurements. This technology has allowed us to perform measurements of total collision cross sections for these processes with unprecedented accuracy over wider energy ranges but more importantly, linked with modern detector developments, they have permitted the determination of branching ratios for final product channels to be performed. The excitation state of final products arising from diatomic ion recombination and the identity of products arising from polyatomic ion recombination can now routinely be determined using 3-dimensional and grid-transmission detector techniques. Such techniques were pioneered using conventional crossed and merged beam apparatuses but the greater particle densities and lower backgrounds encountered in storage ring experiments have made what was once «just possible», now almost a routine task.

While storage rings are the prime workhorses of electron-molecular ion collision experimentation nowadays, modifications to more conventional techniques have played an important role in advancing our knowledge in this exciting and important area. Molecular ion excitation, which was for many years a neglected research area, languishing in the shadow of atomic ion excitation measurements needed for high temperature plasma modeling, has seen a rebirth with the recent studies by Dunn, Djuric and co-workers [9, 10]. Flowing Afterglow Langmuir Probe-Mass Spectrometer (FALP-MS) experiments at the University of Rennes have provided us with a wide array of measurements concerning the recombination of hydrocarbon species [11–14] and the coupling of optical diagnostic techniques to conventional afterglow apparatuses by Adams coworkers [15] and by Johnsen and co-workers [16] have extended our knowledge of final product states in the recombination of a number of systems. New methods for final state determination for the recombination of heavier species have been developed [17, 18] and while not perhaps directly related to the current topic, they serve to illustrate the enthusiasm for this subject that continues to be displayed, more than fifty years after it was first postulated [19].

Molecular ion recombination is of course also the subject of great theoretical interest and a number of practitioners have made critical advances in our understanding of what is probably the most complex of atomic and molecular collision processes. Some of these advances will be discussed in the following. While most of the theoretical effort to date has concentrated on the recombination of diatomic species, a number of brave sorties have been made into the realm of polyatomic ion recombination. This is a subject, fraught with difficulty but it must be said that already quantum chemical based models can be of great value in helping us to

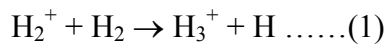
interpret final branching channels for triatomic systems. We can look forward hopefully to similar forays into the unexplored regions of complex molecular ion recombination.

A subject that must also play an important role in fusion edge and divertor plasmas is electron impact excitation of vibrational and rotational states and this is an area that has begun to attract the interest of theoreticians. Recent results on this subject will also be reviewed.

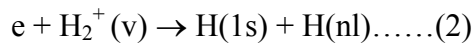
2. Dissociative recombination and excitation

2.1. H_2^+

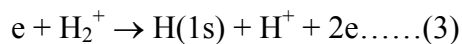
This is an ion that will be formed in the molecular regions in divertors and if the molecular hydrogen density is sufficiently high, it will be rapidly converted to H_3^+ via the ion molecule reaction:



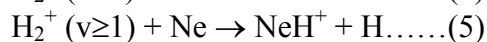
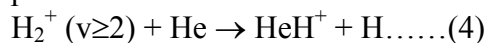
If the H_2 density is not sufficient for reaction (1) to dominate the H_2^+ chemistry, then it can react with electrons via dissociative recombination:



and dissociative excitation:



The cross sections for both these processes depend critically upon the initial vibrational state of the molecular ions. If formed via the ionisation of ground vibrational state molecular hydrogen, the vibrational population of H_2^+ ions is found to have a vibrational distribution very close to that predicted from a Franck-Condon (vertical transition) analysis [20, 21] with states with $v=1-3$ being most populated. If the hydrogen molecules in the divertor region are formed from the surface recombination of atomic hydrogen atoms, it may in fact be vibrationally excited and this would mean that the H_2^+ ions would be even more excited. While the radiative lifetimes of H_2^+ [D_2^+ , T_2^+] ions are exceedingly long ($\approx 10^6$ secs) a number of collision processes can lead to de-excitation of the ions and these include endothermic reactive collisions with helium (formed as ash in the reactor) and neon (a possible candidate as a radiative cooling agent that might be introduced into the divertor):



Because of its structural simplicity and its technological importance, H_2^+ recombination has received a great deal of attention both theoretically and experimentally. The fact that it does not have a dipole moment and therefore its vibrational states have very long radiative lifetimes, however, complicates its experimental examination. Strenuous efforts were made during the single pass merged beam experimental programme [22, 23] to produce ions having only the $v=0$ state populated, using ion trap source technology to produce cold ions. The storage ring approach to ion cooling involves waiting for a sufficient time after ion injection for higher vibrational states to radiatively decay but this is not feasible for H_2^+ . Efforts have been made to use a laser to photodissociate higher vibrational levels [24, 25] but more recent studies have indicated that in fact higher vibrational levels are removed from the stored beams via dynamic collisional processes

Merged beam [26, 27] and storage ring studies of H_2^+ [28–30] recombination have shown that highly vibrationally excited ions can be very rapidly removed via super-dissociative

recombination collisions leading to hydrogen atoms in high n states (which can be field ionized by motional electric fields in the apparatus) and lower states can be de-excited through super-elastic collisions [31] where the internal energy of the molecular ion is transferred to kinetic energy of the electron. Thus it can be seen that a clear understanding of the effects of H_2^+ recombination requires an analysis of the formation and subsequent life history of the H_2^+ ion prior to its subsequent reaction.

Many theoretical studies of H_2^+ recombination have been performed in recent years but these will be discussed in the next section concerning HD^+ where more experiments on $v=0$ state ions have been performed.

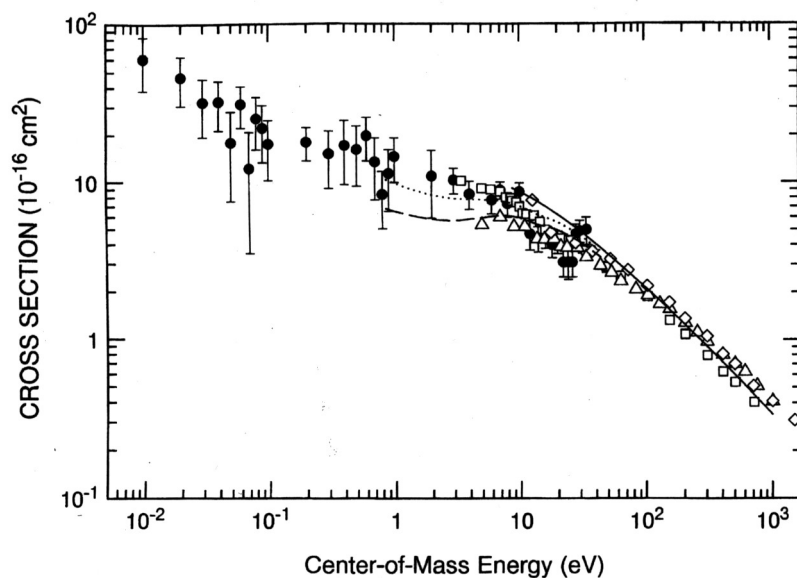


Fig. 1. Experimental cross sections for the dissociative recombination of H_2^+ in a Franck-Condon [20] or Von-Busch Dunn [21] distribution of vibrational states. Results taken using the MEIBE I merged beam apparatus {•} [32]. Other data points taken using crossed beams apparatuses [See ref 32 for details]. Theoretical data from [34, 35] {—},. Unpublished data from Peek for a Franck-Condon {...} and a Von-Busch and Dunn distribution {---}.

Dissociative excitation of vibrationally excited H_2^+ has been measured by a number of workers and the results are discussed in ref [32]. This is a very important process since it depends very strongly upon the initial state of excitation of the ion and also since it dominates over recombination for energies greater than about 5 eV. These results are displayed in figure 1. Andersen et al. [25], using the ASTRID storage ring, have also measured the DE of H_2^+ ions in vibrationally excited states. Contrary to the results of Yousif and Mitchell however, who found a cross section that increased continually with decreasing energy, achieving values of $10^{-14} \text{ cm}^2 - 10^{-15} \text{ cm}^2$, the ASTRID group found that their measured cross sections displayed a threshold at around 1 eV and reached a maximum value of less than $3 \times 10^{-16} \text{ cm}^2$. This apparent discrepancy can be understood from the studies of Van der Zande et al. [30] and Mitchell et al. [26] who found that high vibrational states of H_2^+ have very large recombination rates. They will therefore be rapidly removed via recombination collisions as the circulating ion beam makes multiple passes through the electron beam prior to the dissociative excitation experiment being performed. These high vibrational states also have

very large dissociative excitation cross sections as shown in figure 2. The single pass merged beam used in ref. 32 could directly sample these high vibrational states while multi-pass experiments cannot unless experiments are performed very rapidly following ion injection into the storage ring.

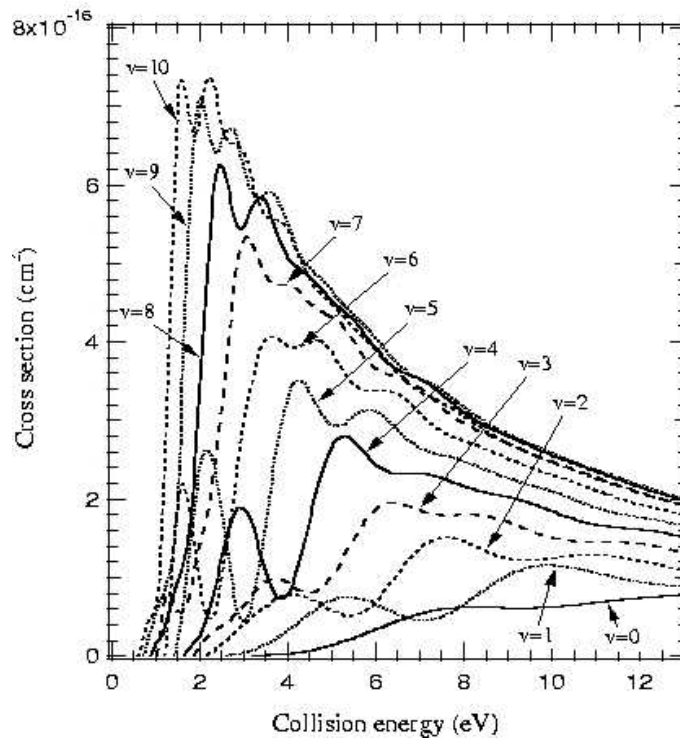


Fig.2. Theoretical cross sections for the dissociative excitation of H_2^+ as a function of initial vibrational state. [From ref. 33].

Calculations of the DE of H_2^+ in various vibrational levels have been performed recently by Takagi [33] who has found the results, shown in figure 2. These are somewhat different from those of Peek [34, 35] who used a Born-Approximation method, which of course is not applicable for threshold energies. Experimental measurement of DE to ground state ions will be discussed in the next section since the cross sections for ground vibrational state H_2^+ are predicted to be similar to that for $HD^+(v=0)$ and cleaner experiments have been done for that ion.

2.2. HD^+

This ion has been the subject of intense study since the advent of the storage ring method for recombination studies [25, 36–43]. The reason for this is that, having a dipole moment, it is infrared active and so can relax vibrationally down to the $v=0$ ground state in a time compatible with experimental measurement [44]. In addition to the experimental studies, theoretical calculations of the cross section at both high [39] and low energies [23, 43, 45–51] have progressed to the point that very good agreement is found with experiment. Theory had been crucial to our understanding of this process since it has shown the need to take account of rotational excitation of the recombining ions but also rotational coupling to neutral Rydberg states lying below the ion curve. With these corrections, the fit between experimentally observed resonances and those predicted theoretically is quite satisfactory.

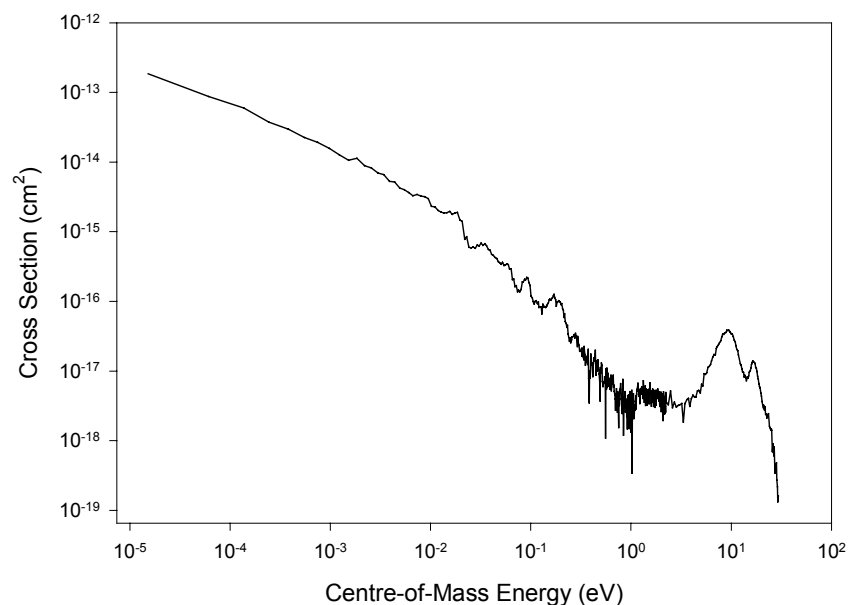


Fig. 3. Cross sections for the dissociative recombination of HD^+ measured at the TSR {—} storage ring.

This ion has been examined at four different storage rings (TSR, CRYRING, TARN II and ASTRID), and has essentially been considered as the benchmark case for the fine tuning of the techniques employed for its study. It has been found that differences have been seen in the results from these different machines, particularly in the energy region from 0.2 to 5 eV and this has been explained as being due to end effects in the collision regions. In these experiments, the electron beam is merged with the ion beam by means of magnetic deflection and since the angle between the beams is changing during this period, the collision energy is not well defined over the merging and de-merging regions¹. Care must be taken to account for this effect during the analysis of data from the storage ring method. Dissociative recombination cross sections measured at TSR are presented in figure 3 for HD^+ ions in their $v=0$ level.

HD^+ was the first ion for which the presence of a high energy peak in the recombination cross section was demonstrated [36, 37]. This peak is due to the direct recombination proceeding through doubly excited states that intersect the ion curve higher up on the potential well outer wall. Such peaks have been seen for a number of other ions such as H_3^+ and HeH^+ . Since the recombination process involves a direct excitation, the modeling of the reaction is simplified and generally good agreement is achieved between theory and experiment, though experience has shown that even in this case, the effects of underlying Rydberg states must be taken into account [39]. In a recent measurement involving complementary storage ring and Coulomb explosion measurements [51], cross sections were obtained for the recombination of individual vibrational levels of HD^+ for $v=0$ up to $v=10$. These results are displayed in figure

¹ The potential for this problem was recognized during the early development of the MEIBE I single pass merged beams apparatus and trochoidal analyzers were chosen as a means of producing an abrupt merging of the electron and ion beams, thus minimizing end effects. This method has been used successfully in other single pass machine designs. [9]

4 along with theoretical data all calculated using the Multi-Channel Quantum Defect (MQDT) approach. It can be seen that the cross section increases greatly as the initial vibrational state of the recombining ion is increased. The reason for the discrepancies between the experimental results and the theory for levels $v=3$ and $v=5$ is not understood nor why these values should be so low.

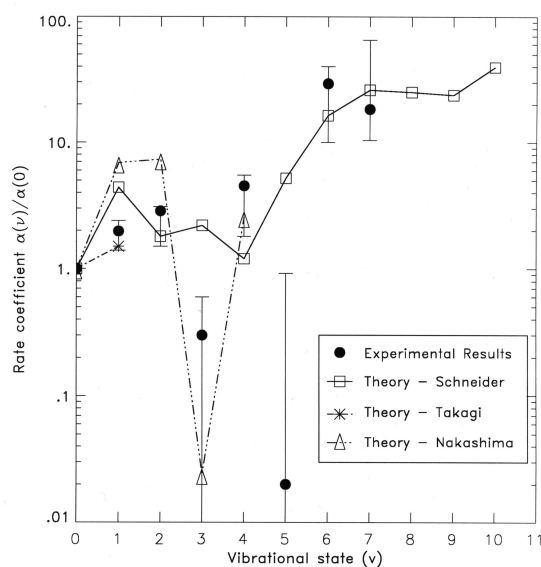


Fig. 4. Rate coefficients for the dissociative recombination of HD^+ ions in specified vibrational states. (From ref. 43.) MQDT used to derive theory points.

In addition to absolute cross section measurements, branching ratios for the decay channels following HD^+ recombination has been examined [40–42] and the results are shown in figure 5. At very low energies, only one decay channel, involving excited products is energetically allowed: $H(1s) + D(n=2)$ {or $D(1s) + H(n=2)$ } and this is seen to account for all of the recombination, no contribution going to the ground state $H(1s) + D(1s)$ { $D(1s) + H(1s)$ } channel. As the collision energy is increased, new channels $H(1s) + D(n>2)$ { $D(1s) + H(n>2)$ } open up sequentially and as they do, the more excited available channel is found to become dominant. This is in good accord with the findings for H_2^+ recombination where cross sections to more excited channels are found to be much higher than for lower energy channels. In that case however, the effect has been seen as a function of internal vibrational excitation. In both cases, (which are of course electronically similar), the effect is due to the recombination proceeding through higher lying dissociating states.

Figure 6 shows calculated cross sections for the dissociative recombination and dissociative excitation of both H_2^+ and HD^+ in their $v=0$ levels [33]. It is interesting to note that for energies between 4 and 8 eV, the two processes effectively compete with each other while the excitation dominates at higher energies. Measurements of the dissociative excitation of HD^+ ($v=0$) have been performed [22, 25, 37] and are shown in figure 7. The experimental results agree

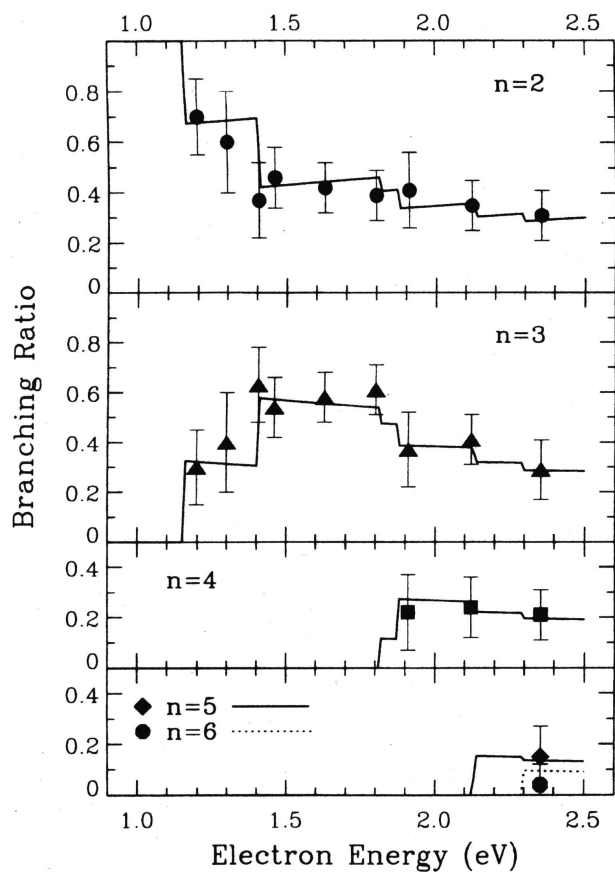


Fig. 5. Branching ratios for final channel states $H(1s) + D(n)$ $\{D(1s) + H(n)\}$ following the dissociative recombination of HD^+ [41].

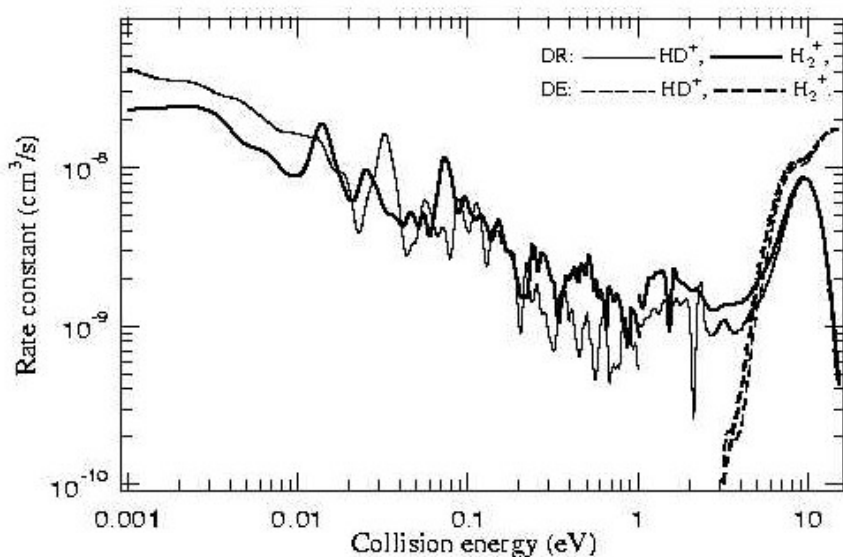


Fig. 6. Theoretical rate coefficients for the dissociative recombination and dissociative excitation of H_2^+ and HD^+ [33].

well with the calculation of Takagi in the region up to 10 eV. Above this, the cross section increases steeply after that up to a value of about $1.3 \times 10^{-15} \text{ cm}^2$ though Takagi's calculations did not extend that far in energy. The higher energy results agrees well with the Born Approximation calculation of Peek [34, 35].

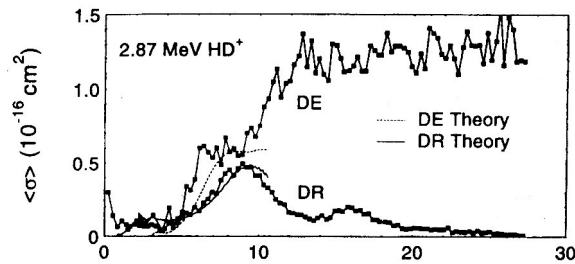


Fig. 7. Cross sections for the dissociative excitation of HD^+ ($\nu=0$) measured at the ASTRID ring. The abscissa is centre-of-mass collision energy in electron-volts [25].

In a recent measurement, the cross section for Resonant Ion Pair formation (RIP) following the recombination of electrons with HD^+ ($\nu=0$) has been measured [52] and it was found that the channel leading to $H^+ + D^-$ exhibited a sharp threshold at 1.92 eV with a maximum value of $3 \times 10^{-19} \text{ cm}^2$ falling off thereafter in an oscillatory fashion to essentially zero at an energy of around 14 eV. The channel $H^- + D^+$ could not be observed for technical reasons but it is estimated that it could have a value, perhaps three times that for the $H^+ + D^-$.

2.3. H_3^+

If the molecular hydrogen density is sufficient in the plasma, reaction (1) can dominate over H_2^+ recombination and so H_3^+ recombination will be a major ion loss process. H_3^+ is a subject of great controversy for its mechanism is not known. It cannot recombine directly in the same way as, for example, H_2^+ or O_2^+ , for the dissociating state which crosses the ion state, does so far from the $\nu=0$ state. [53, 54] Potential energy curves for H_3^+ are shown in figure 8. Experimental evidence shows, however, that in its ground state, this ion recombines with a rate that has been found by various groups to lie between $2 \times 10^{-8} \text{ cm}^3 \text{ s}^{-1}$ and $1.5 \times 10^{-7} \text{ cm}^3 \text{ s}^{-1}$ [55].

Recent theoretical studies [56] have failed to reproduce such a fast rate by orders of magnitude. Because of its importance in astrophysics, [57–59], this constitutes a major controversy for which no clear means of resolution are currently in sight. H_3^+ does display an isotope effect in some experiments [60–62] though in others the rate for D_3^+ recombination has been measured to be about equal to that found for H_3^+ ions [55, 63]. It would appear that there are experimental influences at play here that have not been clearly identified, though a number of authors [62–66] have made suggestions as to the possible influence of electric and magnetic fields and have investigated their effects. It would certainly seem that Rydberg state formation plays an important role in H_3^+ recombination and the different conditions with regard to electric and magnetic fields and the collisional environment in the various experiments seem to influence the direction of the recombination mechanism.

While this discussion is critical for astrophysics where the ions are expected to be in their ground vibrational states, it is perhaps less important in laboratory plasmas where the ions are probably in excited vibrational states prior to recombination. In this case, the reaction proceeds via a direct mechanism with a rate of about $2.3 \times 10^{-7} \text{ cm}^3 \text{ s}^{-1}$ for H_3^+ and $1.85 \times 10^{-7} \text{ cm}^3 \text{ s}^{-1}$ for D_3^+ [60]. It is nevertheless interesting to briefly review the current state of our knowledge regarding the recombination of cold triatomic hydrogen ions.

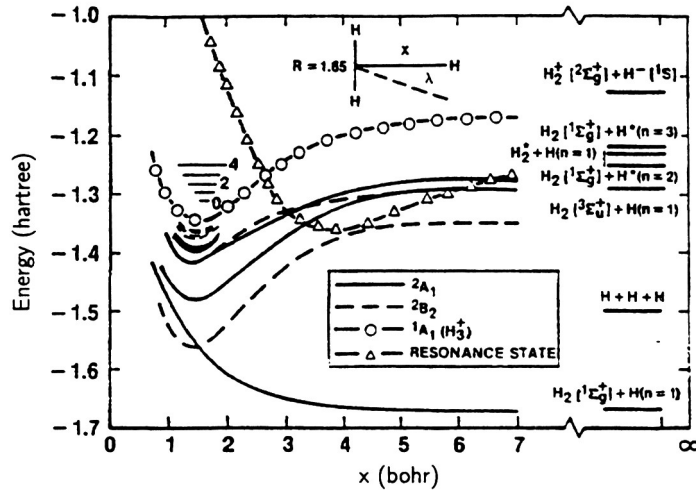


Fig. 8. Potential energy curves for H_3^+ and H_3^* (From ref. 53,54).

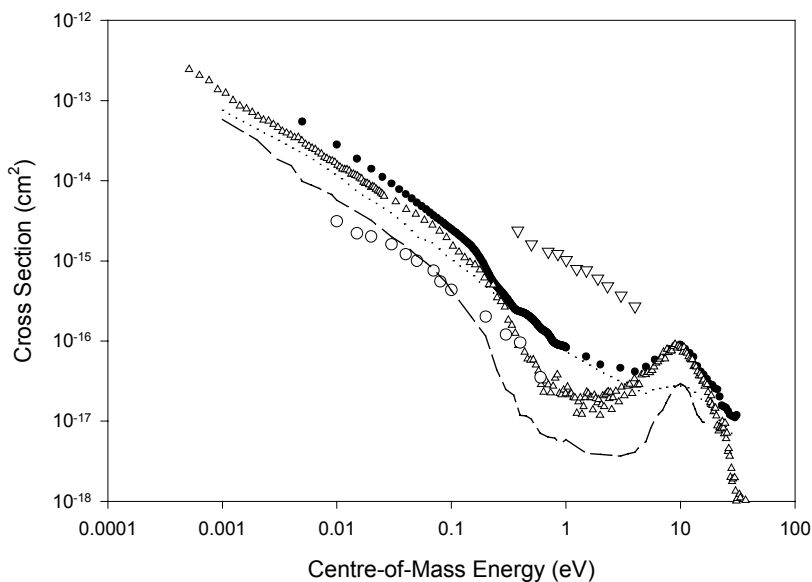


Fig. 9. Dissociative recombination cross sections for H_3^+ measured using the CRYRING [67] $\{\bullet\}$ and TARN II [68] $\{\Delta\}$ storage rings: the MEIBE merged beams apparatus [69] $\{\circ\}$ and using an inclined beams method [72] $\{\nabla\}$. Also shown are cross sections for the dissociative recombination of H_2D^+ [70] $\{\dots\}$ and D_3^+ [61] $\{--\}$ measured at CRYRING.

Figure 9 shows a compilation of cross section measurements for H_3^+ ($v=0$) taken using the CRYRING [67] and TARN [68] storage rings and using the single pass merged beams apparatus, MEIBE I [69]. A number of interesting features are seen in this figure. It is seen that there is very good agreement between the CRYRING and TARN data below about 0.3 eV while in this region, the MEIBE data is consistently lower, by about a factor of five at thermal energies. Above 0.3 eV, however, the TARN data are lower than the CRYRING results while the MEIBE results are in agreement. One of the characteristics of polyatomic ion recombination is that often the cross section is observed to present a steeper energy dependence above about 0.1 eV and this is clearly seen here.² In this case it is seen that the TARN results are steeper than the CRYRING results resulting in a much deeper minimum in the cross section at 2 eV. The maximum observed at 10 eV is similar in height. Also shown in the figure are the inclined beam results of Peart and Dolder [72] which are larger by nearly two orders of magnitude in this region. This is a striking point since results for negative ion formation following H_3^+ recombination [73] and DR results for H_2^+ [74] taken using the same apparatus are in very good agreement with the MEIBE results for these processes [75, 76].

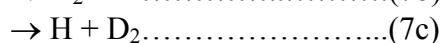
Theoretical efforts [77–81] have been made to model the recombination of H_3^+ and while calculations [77] have been successful in reproducing the maximum at 10 eV which arises due to a direct transition from the ground state to the intersecting neutral state, attempts [56] to reproduce the low energy data, based upon direct capture into the intersecting dissociative neutral state, shown in figure 8 have failed, indicating that this cannot be the mechanism for the process. Clearly indirect recombination, i.e via the formation of intermediate Rydberg states, must dominate this process³ and a number of models have been suggested that incorporate this feature though none at this time have been tested quantitatively.

The situation is rather different for D_3^+ for there the storage ring and MEIBE experiments are in agreement as seen in figure 9. While the values for D_3^+ are smaller than the storage ring values for H_3^+ , they are essentially the same as the MEIBE results for H_3^+ . A recent Flowing Afterglow Langmuir Probe study [55] of H_3^+ and D_3^+ recombination also found these ions to have equal rate coefficients ($8 \times 10^{-7} \text{ cm}^3 \text{ s}^{-1}$) at 300 K though the experiment of Johnsen and co-workers [63] indicated that the rate for D_3^+ was smaller than for H_3^+ . Clearly this is a subject that will continue to challenge recombination researchers for the foreseeable future.

Branching ratios for the dissociative recombination of H_3^+ [86–88] and H_2D^+ [70] have been measured and the CRYRING results are shown in figure 10. The possible dissociation pathways for H_3^+ are:



and for H_2D^+ :



² Notable exceptions are H_2D^+ [70], and CH_2^+ [71] which display a continuous E^{-1} energy dependence up to several electron volts.

³ Indirect recombination has been determined to be important for other polyatomic ions such as HCN^+ [82-84] and HCO^+ [85].

No indications of channels 6c or 7d were found in CRYRING experiments [88, 70]. Results [86] taken using the MEIBE technique for an excited distribution of ions found similar values to those found for the $v=0$ ions in the storage ring measurement though corresponding measurements taken with cold ions indicated that channels 6a and 6b had similar magnitudes. Channel 6c was found to account for 8% of the total reaction [87].

The dissociative excitation of H_3^+ has been measured experimentally using the inclined beams [89, 90] and single pass merged beams [91] technique. The dissociative excitation of D_3^+ has recently been measured [61] using the storage ring method and these results are displayed in figure 11. This process was also examined using the single pass merged beam method [92] and as for the case of H_3^+ , sharp resonant structures were found in the measured cross section. Orel [93] modeled this process theoretically but found that these structures were washed out when vibrational motion was taken into account. The storage ring results also failed to show any evidence for such sharp structures. A very similar situation arose in studies of the dissociative excitation of HeH^+ and this will be discussed in the next section. It should be noted in figure 11 that there is a peak appearing at 4 eV which cannot be due to direct dissociative excitation but that is probably the result of *resonant enhanced dissociative excitation*. This is actually due to direct recombination to a dissociative state that autoionizes before it can dissociatively stabilize.

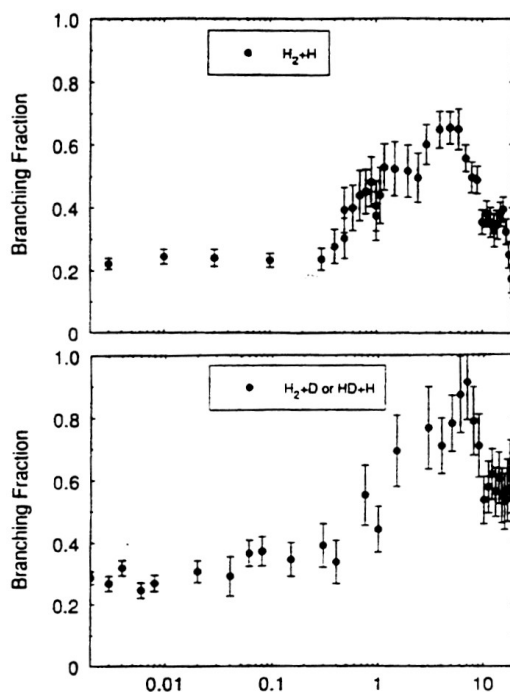


Fig. 10. Branching ratios for the dissociative recombination of H_3^+ to form $H_2 + H$ [88] and H_2D^+ to form $H_2 + D$ or $HD + H$ [70]. The abscissa is the centre-of-mass collision energy in electron-volts.

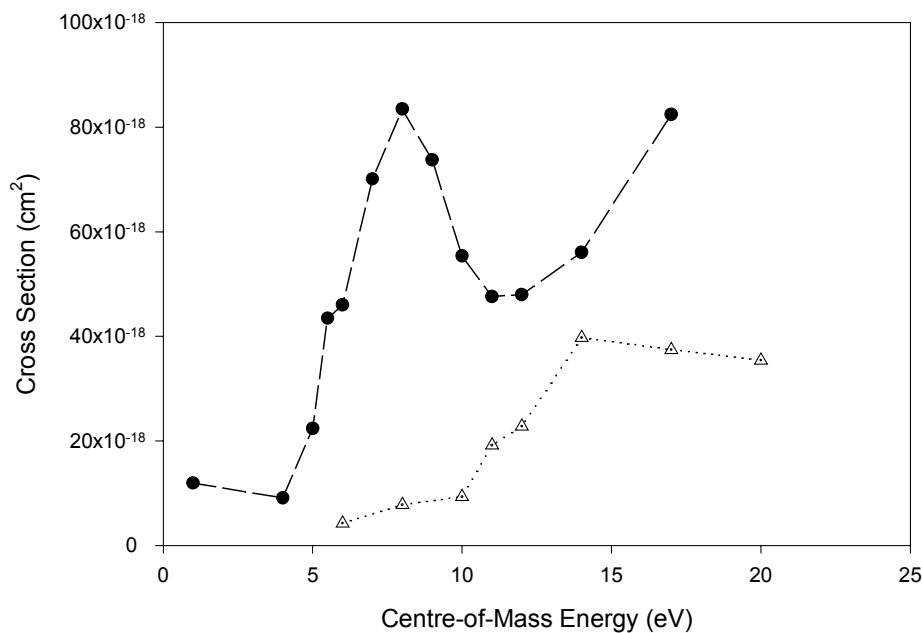


Fig. 11. Cross sections for the dissociative excitation of D_3^+ . {●} $2D + D^+$ channel, {Δ} $D + D_2^+$ channel [61].

2.4. HeH^+

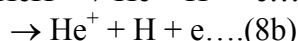
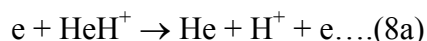
Helium atoms are formed during the course of thermonuclear fusion and one can expect that HeH^+ will be an important component of the molecular plasma in the divertor, one mechanism for its formation being reaction (4). While for many years, the recombination of HeH^+ was dismissed [94] due to its lack of a curve crossing with a suitable dissociating neutral state, experimental [95–102] and subsequent theoretical [102–105] studies have shown that indeed HeH^+ does undergo dissociative recombination with a rate of around $5 \times 10^{-9} \text{ cm}^3\text{s}^{-1}$ at 300K. The recombination proceeds via the non-adiabatic radial coupling between the ion ground state and the dissociative Rydberg states which lie adjacent to the ions state at smaller internuclear separation.

A number of merged beam and storage ring measurements have been performed on this reaction. Recent theoretical results [102] for $^4HeH^+$ recombination are shown in figure 12 along with absolute experimental data taken using the merged beams method [96]. Both the experimental and theoretical rates are absolute and it is seen that the theory is capable of reproducing the experimental results very well both in magnitude and in overall form. Differences in the structure can probably be accounted for as being due to differing internal energy states for the ions. The theoretical results apply to $v=0$ ions with a rotational temperature of 800 K. The experimental results may contain a contribution from the excited a $^3\Sigma^+$ state which has recently been shown experimentally to have a lifetime of ≈ 36 ms and to be present in HeH^+ ion beams [106]. Attempts to quench this state by modifying the ion source chemistry, [96, 107] led to a smaller cross section than could be measured with that apparatus but in fact one that is probably not incompatible with the values predicted theoretically. Figure 13 shows corresponding comparisons between theoretical calculations and relative experimental data taken at the TARN storage ring (scaled to agree in magnitude with the theoretical results). It is clear that the general agreement, at least with the gross

structure of the data, is very good indicating that the assumption of the non-radial coupling mechanism is sound and that while the direct recombination of electrons with metastable excited HeH^+ ions may contribute to the experimental results shown in figure 12, recombination involving ground state ions is also important.

Measurements of the product state distributions have been made [97, 100] and it is found that the dominant decay channel is one that leads to H atoms in the $n=2$ level. This indicates that the $\text{C}^3\Sigma^+$ state is the main state through which the recombination proceeds. An R matrix calculation of Sarpal et al. [103] had found that the ground state $\text{X}^2\Sigma^+$ state drove the recombination but this would have produced H atoms in the $n=1$ level. The experiment found that as the collision energy increased so that recombination to form H($n=3$) atoms became energetically possible, this became the major decay channel with that going to H($n=2$) disappearing. Similar results were found for HeD^+ .

Cross sections for the dissociative excitation of HeH^+ , namely:



and measured by Stromholm et al. [99], are shown in figure 14. It is evident that this is a process that has a rather small cross section compared to that for other ions. Previous measurements by Yousif and Mitchell [95] found a cross section that was dominated by sharp peaks though theoretical efforts [108] to reproduce these found that such structures should be

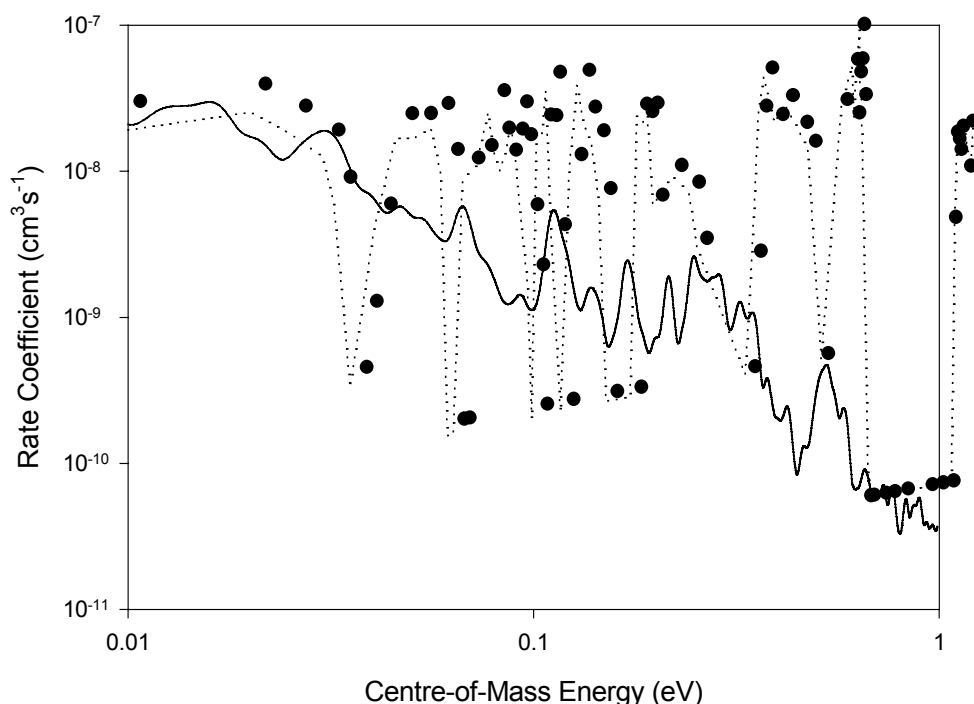


Fig. 12. Theoretical cross sections {—} for the dissociative recombination of $^4\text{HeH}^+$ [97]. Also shown are experimental cross sections {•} measured using the MEIBE I single-pass apparatus [96].

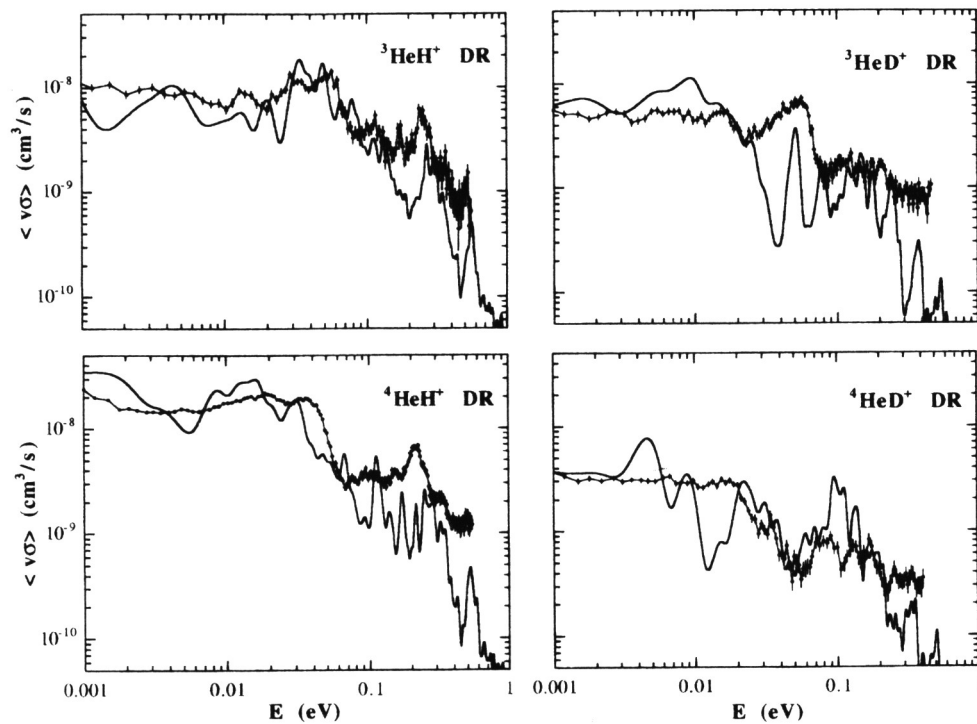


Fig. 13. Experimental $\{\diamond\}$ and theoretical $\{\text{---}\}$ rate coefficients for the dissociative recombination of ${}^3\text{HeH}^+$, ${}^4\text{HeH}^+$, ${}^3\text{HeD}^+$ and ${}^4\text{HeD}^+$ [97].

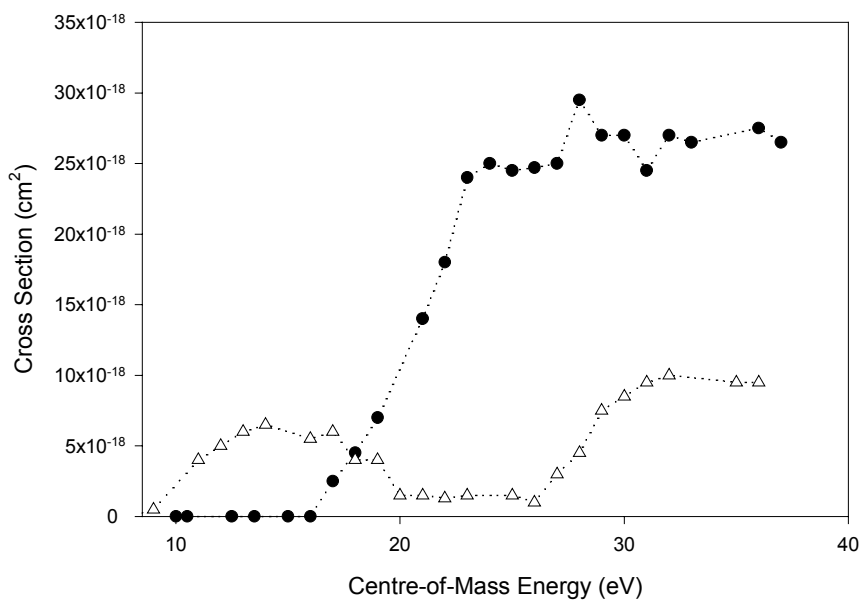


Fig. 14. Cross sections for the dissociative excitation of HeH^+ measured using CRYRING storage ring [100] leading to $\text{He}+\text{H}^+$ $\{\blacktriangle\}$ and $\text{H}+\text{He}^+$ $\{\bullet\}$.

washed out when account is taken of vibrational motion. It should be noted however, that the cross sections measured by Yousif and Mitchell were an order of magnitude larger than those measured by Stromholm et al. The threshold for reaction 8b should lie at about 30 eV while the experimental evidence indicates a threshold at about 17 eV. The reason for this has been found from theoretical studies by Orel et al. [109] who have shown that dissociative recombination to form highly excited states of He* which subsequently autoionize can contribute to this channel. This phenomenon is called *resonant enhanced dissociative excitation* [110].

2.5. N_2^+

This is an ion that has been studied experimentally and theoretically (111 and refs. therein) by many investigators. The rate coefficient has been measured using afterglow and shock tube methods and there is general agreement that it has a value between 1.8 and $2.6 \times 10^{-7} \text{ cm}^3\text{s}^{-1}$ at 300 K. This has been recently confirmed by a storage ring measurement [111], the results of which are displayed in figure 15. N_2^+ is initially formed with a number of vibrational states populated but since it does not have a dipole moment, these states do not radiatively decay during the storage time. In an attempt to obtain cooler ions, the CRYRING team used a hollow cathode ion source to form the N_2^+ . By an analysis of their imaging detector data, they were able to demonstrate that their beam had a population of 46%, 27%, 10% and 16% respectively for the states $v=0, 1, 2$ and 3.

In its ground state, N_2^+ can recombine into several different exit channels thus:

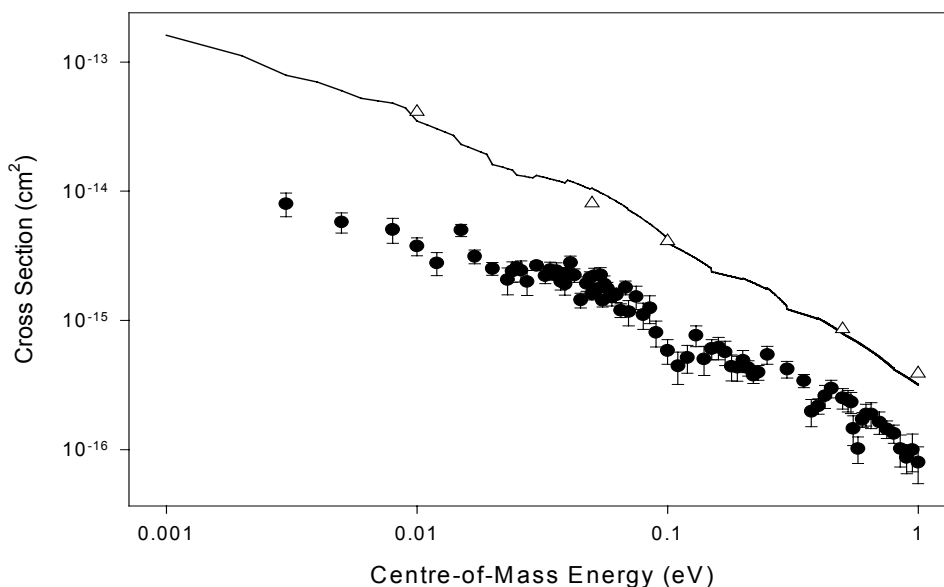
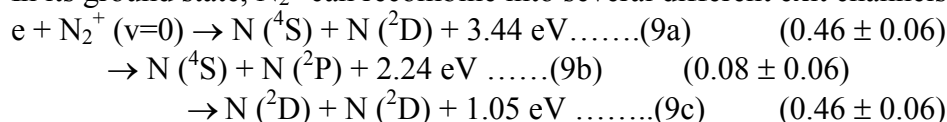


Fig. 15. Cross sections for the dissociative recombination of N_2^+ measured using CRYRING [111] {—}. Also shown are recent merged beam data { Δ } taken using the MEIBE I apparatus, the ions being produced in an r.f. source [114], along with data of Noren et al. { \bullet } [113] taken with N_2^+ ions produced in a storage trap ion source.

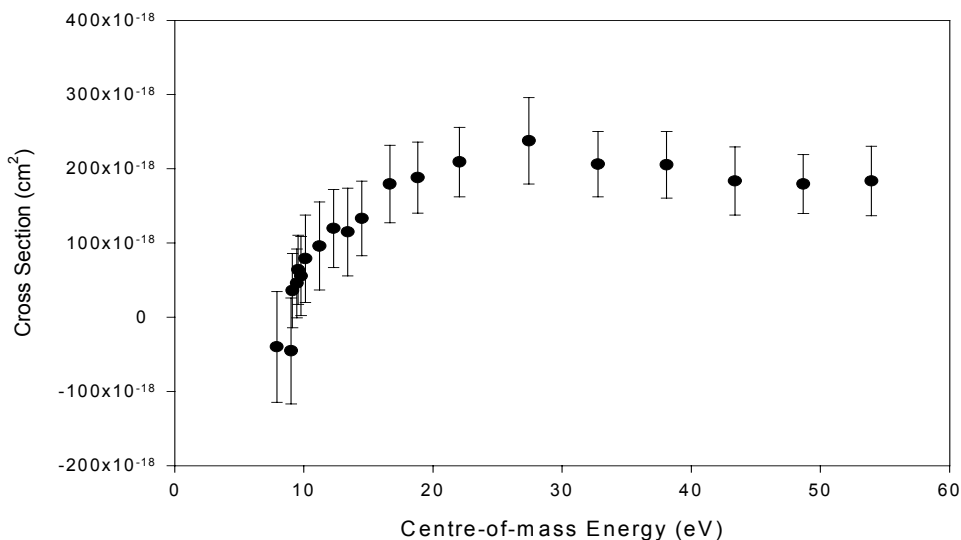


Fig. 16. Cross sections for the dissociative excitation of N_2^+ , measured at CRYRING [111].

The branching ratios for these channels have been measured [111, 112] using a time and spatially sensitive (3-D) imaging detector and the percentages indicated above have been found. In this case, it was possible to extract the branching ratios specifically for the $v=0$ state of the ion, as described in ref. [111].

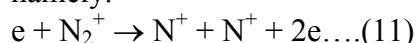
Previous merged beam measurements [113] of the recombination of N_2^+ ions that had been formed in an ion trap ion source, had found cross sections that were about a factor of five lower than expected from rate coefficient measurements and the recent storage ring data though the energy dependence was very similar. Extensive studies [114] have failed to identify a calibration error in the MEIBE measurements and the reason for this discrepancy is not well understood. Given the arguments in [115], it is likely that the conclusions of ref. [113] are not valid. The storage ring results are in general agreement with previous measurements.

Also shown in figure 15 are recent measurements of N_2^+ recombination taken using ions prepared in an R.F. source and these are in perfect agreement with the storage ring data. (These data are also in agreement with earlier merged beam results of Mul and McGowan [116]).

Cross sections for the dissociative excitation of N_2^+

$$e + N_2^+ \rightarrow N + N^+ + e \dots(10)$$

taken at CRYRING are shown in figure 16. The threshold appears at about 8.7 eV which corresponds to the dissociation energy of N_2^+ . Unlike other ions discussed in this report, this process does not proceed via the direct excitation of a repulsive excited states. Instead it proceeds via the excitation of the $C^2\Sigma_u^+$ state which is then pre-dissociated. Cross sections for the formation of N^+ ions in electron- N_2^+ collisions had previously been measured in a crossed beams experiment by Van Zyl and Dunn [117] and by subtraction of the results in figure 16 from their data, one can determine the cross section for the dissociative ionization of N_2^+ , namely:



Results of this analysis are shown in figure 17.

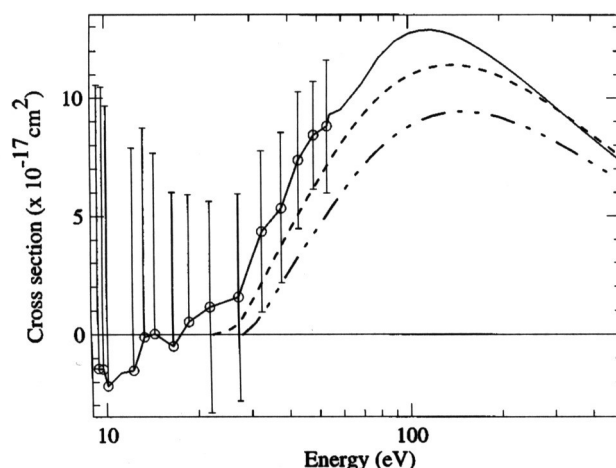
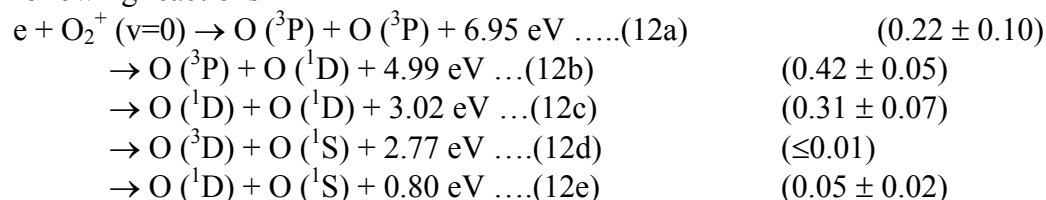


Fig. 17. Cross sections for the dissociative ionization of N_2^+ deduced from the DE measurements at CRYRING [111] and the results of Van Zyl and Dunn [117] for the formation of N^+ following electron impact on N_2^+ . {— and o} experimental data. The other lines are theoretical calculations [see 111 for details].

2.6. O_2^+

O_2^+ recombination is one of the most studied recombination processes due to its importance in the upper atmosphere. Results of a recent CRYRING experiment [118] are shown in figure 18. As in the case of N_2^+ , O_2^+ does not have a dipole moment. It is formed in a range of vibrational states [1] which have long radiative decay lifetimes and therefore the results apply to vibrationally excited ions. In experiments performed at ASTRID, [119] isotopically mixed $^{18}O^{16}O^+$ was used but even with this it was estimated that the ion beam had states with v up to 5 populated. Despite this, the recombination cross section appears to show little or no vibrational effects and the consistency of this value as determined by many different experimental methods, makes O_2^+ an ideal ion for verifying the good functioning of apparatus prior to making other recombination measurements. The room temperature rate for O_2^+ recombination is generally agreed to be $2 \times 10^{-7} \text{ cm}^3 \text{ s}^{-1}$ [120]. Figure 18 also shows cross sections measured by Mul and McGowan [116] using the MEIBE merged beams apparatus, results from a recent re-measurement using the same apparatus by Sheehan [114] and cross sections obtained by Walls and Dunn [121] using the ion trap technique. It is seen that there is good agreement between all these data.

Branching ratios for the formation of oxygen atoms in a variety of excited states via the following reactions



have been determined [119] by measuring the kinetic energies of the products as they fly apart from each other. Intense theoretical efforts [122, 123] have been made to reproduce these branching ratios and much progress has been made in understanding the mechanism for this reaction.

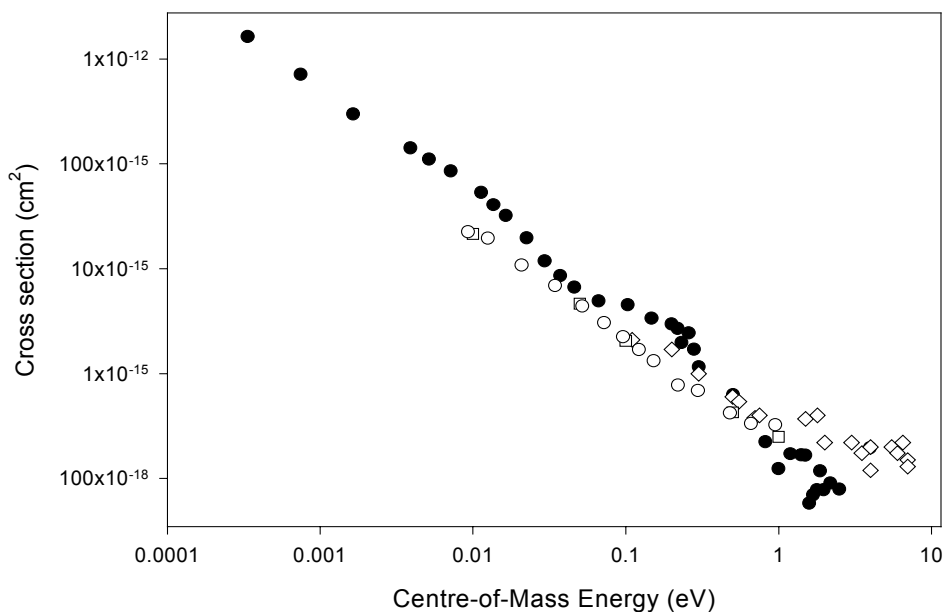
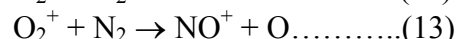
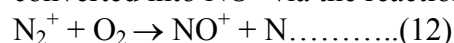


Fig. 18. Cross sections for the dissociative recombination of O_2^+ measured using CRYRING [118] {•}. Also shown are data taken using the MEIBE I merged beam experiment {□}, [114], {o} [116] and using an ion trap apparatus {◇}[121].

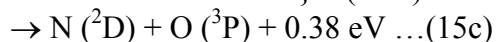
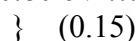
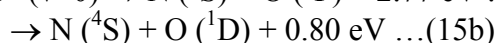
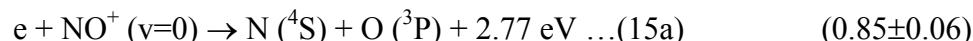
Cross sections for O^+ production in electron- O_2^+ collisions have been measured by Van Zyl and Dunn [117] and this data has been previously presented in [1].

2.7. NO^+

The NO molecule has an ionization potential of 9.26 eV which is therefore less than that of O_2 {12.07 eV} and N_2 {15.58 eV} so that when N_2^+ and O_2^+ are formed in air, they are rapidly converted into NO^+ via the reactions:



The recombination cross section for NO^+ has been the subject of many experimental and theoretical studies and has recently been examined using the storage ring technique. [124]. These results are displayed in figure 19 together with data taken using the MEIBE merged beams apparatus [116, 114] and an ion trap [121]. In the storage ring and the ion trap cases, the results refer to ions primarily in their $v=0$ level. NO^+ can recombine into the following channels:



The branching ratios have been measured [124] and are as shown.

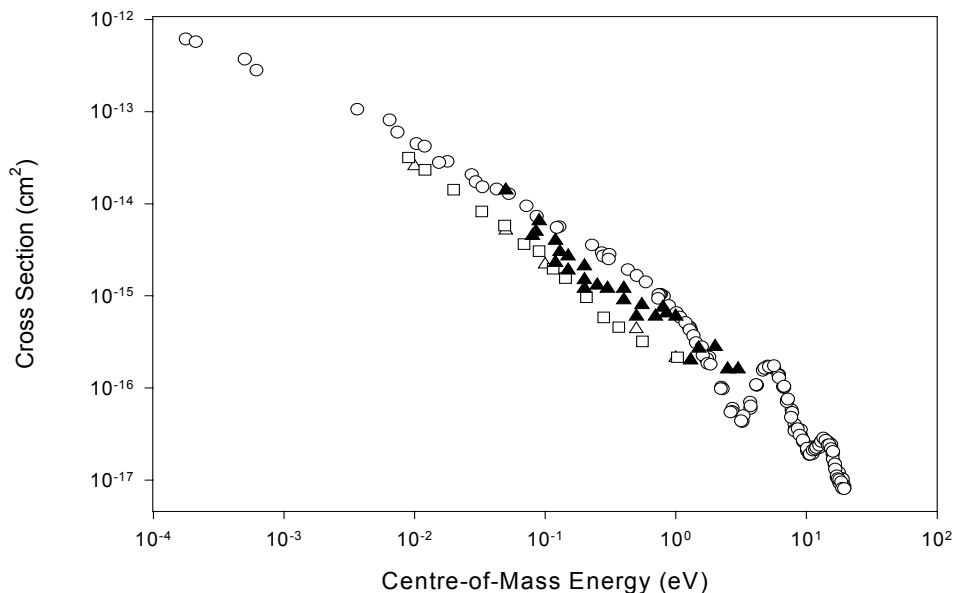


Fig. 19. Cross sections for the dissociative recombination of NO^+ , measured using the ASTRID storage ring {o}[124]. Also shown are merged beam results of Mul and McGowan {□} [116] and of Sheehan {Δ} [114]. Ion trap results of Walls and Dunn {▲} [121].

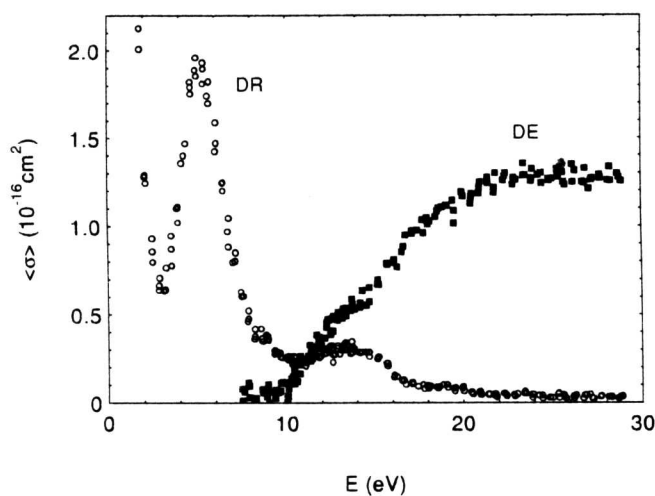


Fig. 20. Cross sections for the dissociative excitation {■} and dissociative recombination {o} of NO^+ , measured using ASTRID [124].

This reaction has recently been re-examined using an afterglow technique [125] which allowed not only ground state ions (formed from nitric oxide as parent gas and de-excited by charge exchange) to be measured but also ions, formed from an oxygen/nitrogen mixture which will have a wide range of vibrational states populated. The latter case is more typical of

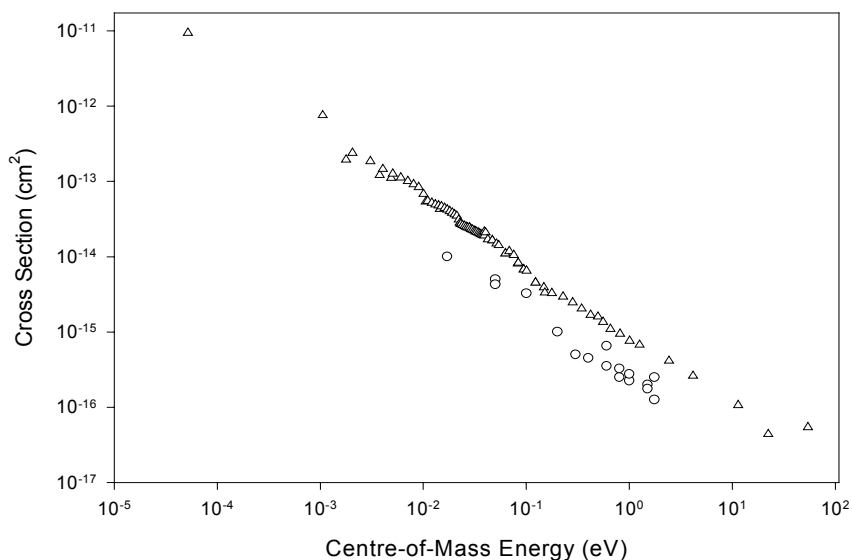


Fig. 21. Cross sections for the dissociative recombination of CO^+ measured using the CRYRING storage ring [127] $\{\Delta\}$ and the MEIBE merged beams apparatus [126] $\{o\}$.

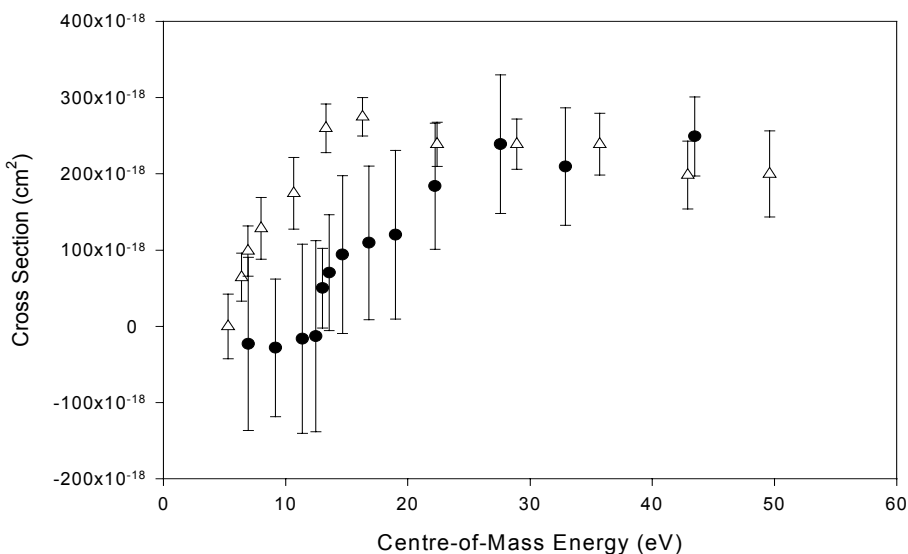
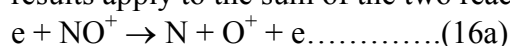


Fig. 22. Cross sections for the dissociative excitation of CO^+ measured using CRYRING $\{\bullet\}$ [127]. Also shown are results measured using the MEIBE apparatus $\{\Delta\}$ [126].

the state of NO^+ ions recombining in a laboratory plasma containing these gases. It was found that at 300 K, the rate coefficient for the excited ions ($1.6 \times 10^{-7} \text{ cm}^3 \text{ s}^{-1}$) was about a factor of three lower than for the ground state ions ($4 \times 10^{-7} \text{ cm}^3 \text{ s}^{-1}$). Branching ratios for this case were not measured.

Cross sections for the dissociative excitation [124] of NO^+ are shown in figure 20. Since it was not possible to distinguish between N-atoms and O-atoms with the detector used, the results apply to the sum of the two reactions:

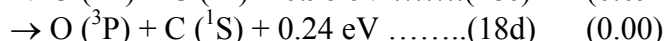
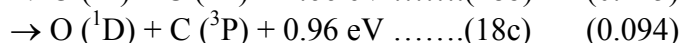
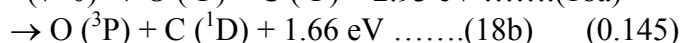
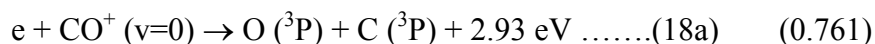


It can be seen that above 12 eV this process dominates over dissociative recombination.

2.8. CO^+

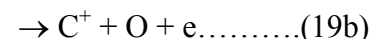
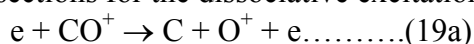
First measured by Mitchell and Hus [126] using the MEIBE merged beams apparatus, the cross section for this ion (in the $v=0$ level) has since been examined at CRYRING using the storage ring technique [127] and values for the following branching ratios have been determined and are shown in figure 21 along with the MEIBE results (which apply to ions having several vibrational states populated). A recent FALP-MS measurement [128] found a 300 K value of $1.85 \times 10^{-7} \text{ cm}^3 \text{ s}^{-1}$ which is somewhat smaller than the value obtained using the storage ring ($2.75 \times 10^{-7} \text{ cm}^3 \text{ s}^{-1}$).

Branching ratios for the possible decay channels:



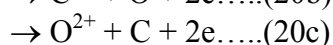
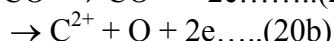
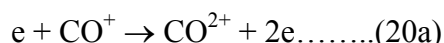
have been measured [127] and these are as shown.

Cross sections for the dissociative excitation reaction



measured using CRYRING and the MEIBE apparatus are shown in figure 22. It is interesting to note the difference in the thresholds for these two measurements though their magnitudes are similar at higher energies. For $v=0$ ground state ions, one might expect a threshold at around 9.2 eV and so the low threshold found in the MEIBE experiment (6 eV) was attributed to the presence of vibrational excitation in the CO^+ ions. The fact that the CRYRING results display a threshold at 12 eV would seem to rule this out and so it may be that some of the CO^+ ions in the MEIBE experiment were in the $\text{A}^2\Pi$ state. This has a lifetime of $\approx 3 \mu\text{s}$ which is similar to the transit time of the ions to go from the source to the interaction region in the single pass experiment though this implies that the ions are excited just as they exit the ion source, their residence time in the source being around $30 \mu\text{s}$. This could explain the fact that the recombination cross sections are found to be smaller in the MEIBE experiment than in the CRYRING experiment.

Dissociative and non-dissociative ionization of CO^+ :



has been studied using a crossed beams apparatus by Belic et al. [129]. These results are displayed in figure 23.

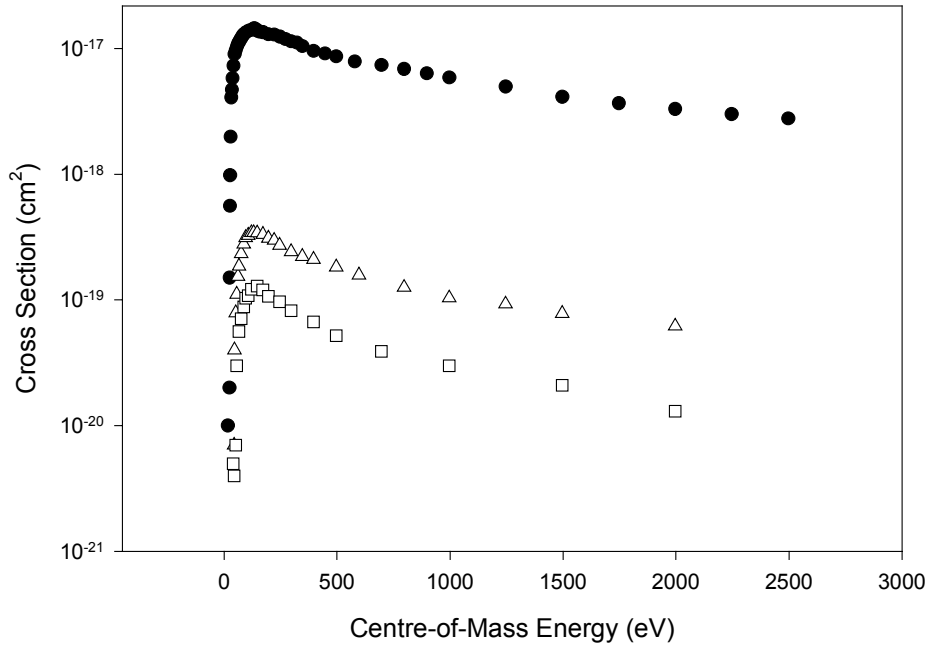
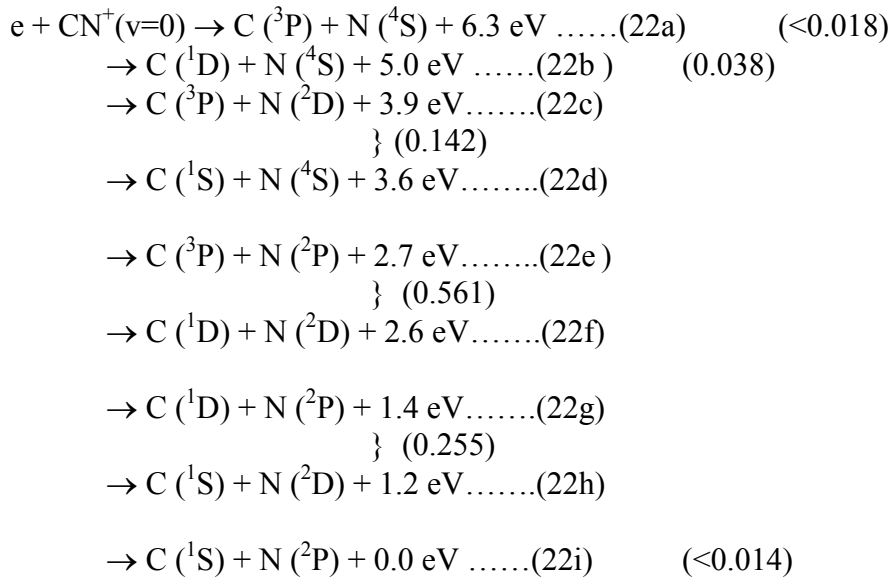


Fig. 23. Cross sections for the dissociative ionization of CO^+ to form CO^{2+} {●}, C^{2+} {△} and O^{2+} {□} [129].

2.9. CN^+

Another diatomic ion that has recently received attention from experimentalists [130, 131] is CN^+ which could conceivably appear in divertor plasmas. Its cross section is shown in figure 24. This is another case where the value found using the single pass merged beams apparatus is smaller than that found at the storage ring. The reason for this is not clear though calibration problems have been ruled out. [114]. Branching ratios for the possible recombination pathways have been measured [131] for ground state ions and are as follows:



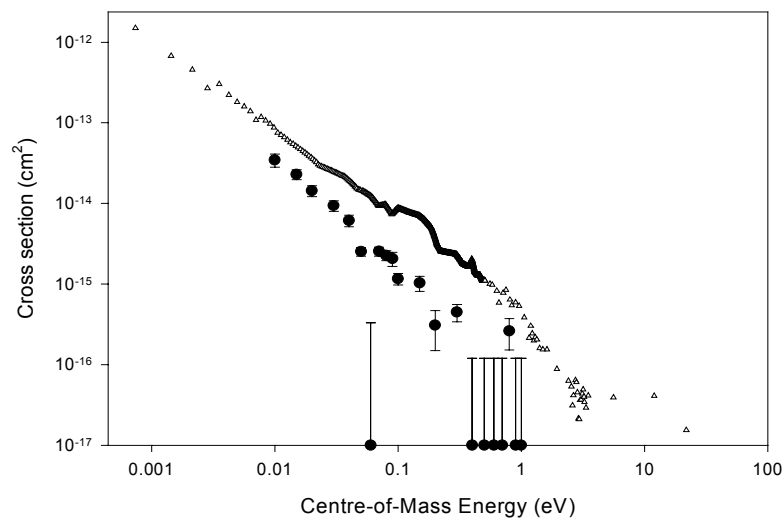


Fig. 24. Cross sections for the dissociative recombination of CN^+ measured using the CRYRING $\{\Delta\}$ [131] and the MEIBE single pass merged beams apparatus $\{\bullet\}$ [130].

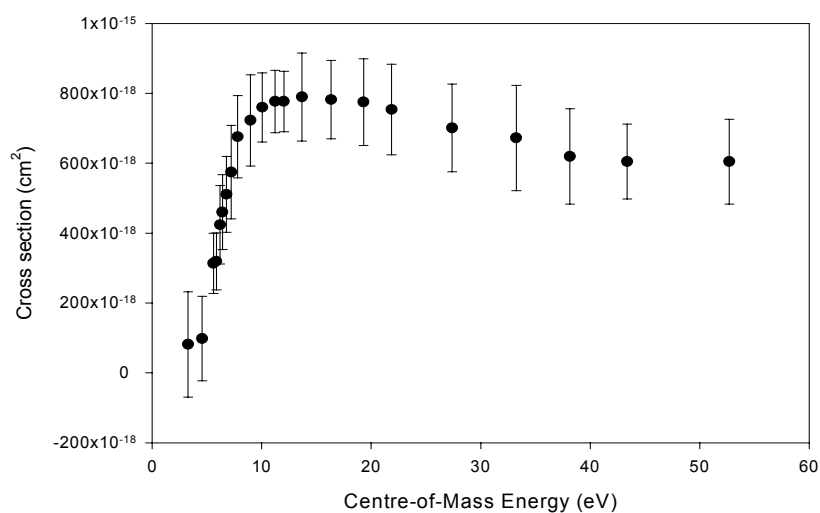
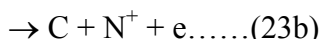
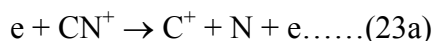


Fig. 25. Cross sections for the dissociative excitation of CN^+ measured using CRYRING $\{\bullet\}$ [131].

Measured cross sections for the dissociative excitation of CN^+ ,



are shown in figure 25. This process dominates for energies above about 3 eV.

2.10. $\text{HCN}^+/\text{HNC}^+$ and HCO^+

The ions $\text{HCN}^+/\text{HNC}^+$ [82] and HCO^+ [85] have recently been examined using the single pass merged beam technique and the results obtained are shown in figures 26. For the HCO^+ case, the figure shows low energy data that was not available at the time of the original publication and it is seen that the steep energy dependence quoted in that paper does not in fact continue down below 0.01 eV. This has a significant impact on the rate coefficient which at 300 K is found to be about $0.7 \times 10^{-7} \text{ cm}^3 \text{ s}^{-1}$ and not $1.7 \times 10^{-7} \text{ cm}^3 \text{ s}^{-1}$ as quoted in ref. [85]. The revised value for the 300 K rate coefficient is lower than that found in afterglow experiments [55, 132–137] for the same molecular ion. Unfortunately storage ring measurements are not currently available for this species.

Cross sections have been measured for a mixture of HCN^+ and its isotopomer HNC^+ , the ions being prepared from a source gas mixture of methane and nitrogen. These results are shown in figure 26. By adding a high percentage of carbon dioxide to the ion source, it was possible to produce a beam that consisted predominantly of HNC^+ ions and it is seen that in this case, the cross section is reduced by a factor of 2. Theoretical and modeling studies [83, 84] have shown that in fact neither HCN^+ nor HNC^+ have a neutral crossing state in the vicinity of their electronic and vibrational ground states and so both these ions must recombine through an indirect mechanism. Kinetic modeling of the ion source chemistry has shown that while indeed HNC^+ is almost the sole isomer present in the results taken with the carbon dioxide addition, in fact HNC^+ is also the predominant ion in the case where a mixture of HCN^+ and HNC^+ was studied. (87.5% HNC^+ compared to 12.5% HCN^+). Theoretical analysis indicates that in fact there is a suitable curve crossing for the metastable excited $\text{A } ^2\Sigma$ state of HCN^+ is also the predominant ion in the case where a mixture of HCN^+ and HNC^+ was studied. (87.5% HNC^+ compared to 12.5% HCN^+). Theoretical analysis indicates that in fact there is a suitable curve crossing for the metastable excited $\text{A } ^2\Sigma$ state of HCN^+ and given the difference between the two measurements, shown in figure 24, the deduced recombination rate for HCN^+ (it being a mixture of ground state and metastable $\text{A } ^2\Sigma$ state) is about $25 \times 10^{-7} \text{ cm}^3 \text{ s}^{-1}$ at 300K!

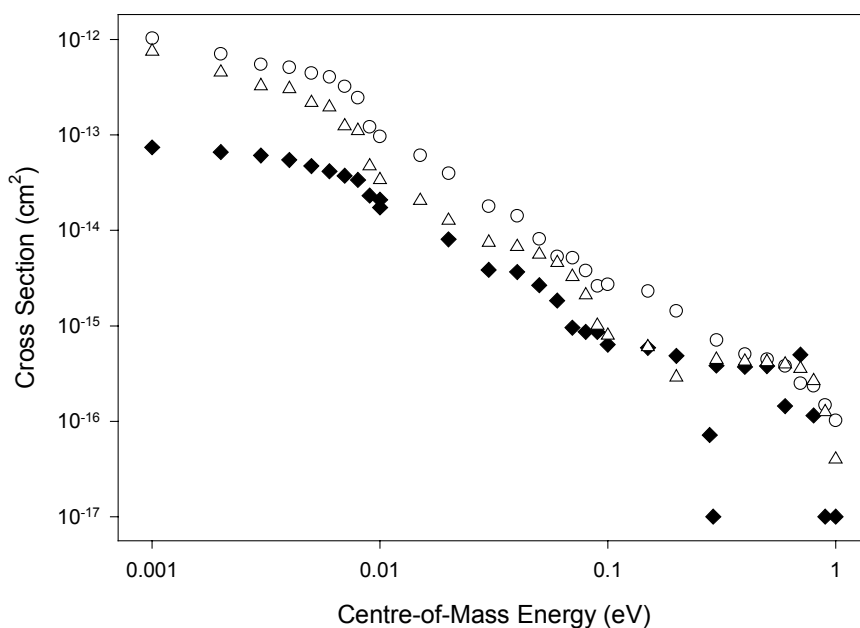


Fig. 26. Dissociative recombination cross sections for a mixture of $\text{HCN}^+/\text{HNC}^+$ ions {o}, for HNC^+ { Δ } [82] and for HCO^+ [85] { \blacklozenge } measured using the MEIBE I apparatus.

2.11. Hydrocarbon molecular ions

Cross sections for the dissociative recombination of the hydrocarbon ions CH_n^+ ($n=1-5$) [138, 139] and C_xH_y^+ ($x=1-2$, $y=0-3$) [140] were first measured in the 1970's using the MEIBE technique. The discovery of an error in the analysis of this experimental technique indicated that cross sections measured prior to 1985 had to be revised down by a factor of 2 and these values are listed in ref [141]. Since this meant that, for example, the data for CH_5^+ , which had been in agreement with Flowing Afterglow measurements for that ion, no longer agreed, there was therefore some concern that the merged beam data suffered from another, unidentified calibration error. This concern was compounded by the finding of a cross section for the recombination of N_2^+ which was much smaller than previously accepted [113]. In recent years, storage ring measurements of the cross sections for CH_5^+ have been performed [142] and in fact cross section values very similar to the corrected MEIBE values were found. These are shown in figure 27. CH_2^+ , cross sections measured at CRYRING [71] were found to be in less good agreement with the MEIBE data [139, 114] and these are shown in figure 28. Storage ring [143] and MEIBE [138, 139] results for CH^+ are also in good agreement fig. 29. The ions CH_n^+ ($n=1-5$) have been recently re-measured using the MEIBE apparatus [114] and these experiments have reconfirmed the earlier (corrected) data [138, 139].

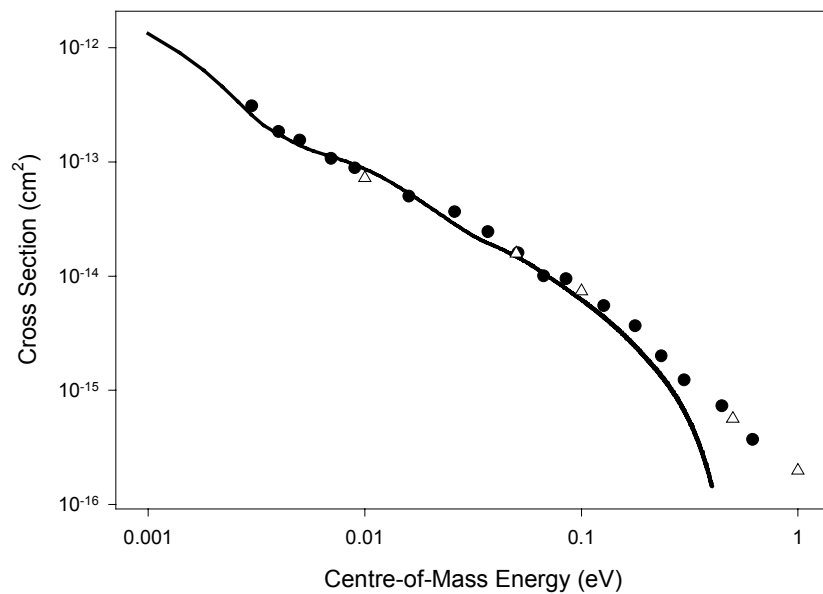


Fig. 27. Cross sections for the dissociative recombination of CH_5^+ measured using the CRYRING storage ring {—} [142] and the MEIBE apparatus {•} [139] and {Δ} [114].

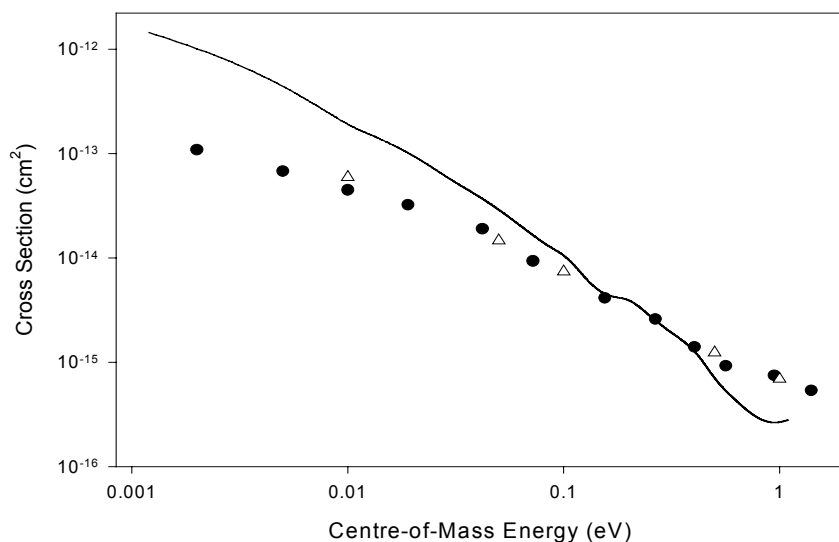


Fig. 28. Cross sections for the dissociative recombination of CH_2^+ measured using the CRYRING storage ring {—} [71] and the MEIBE apparatus {•} [139] and {Δ} [114].

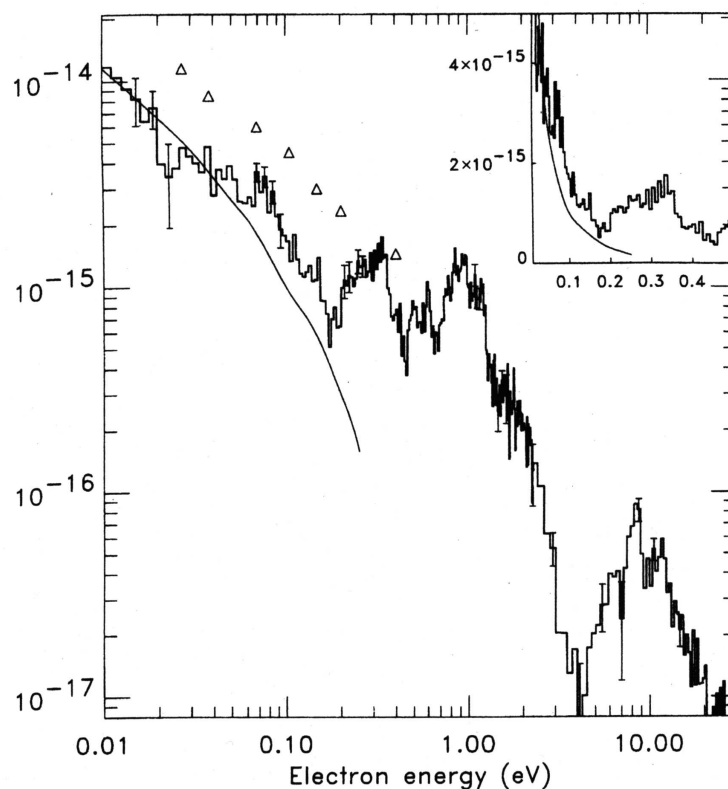
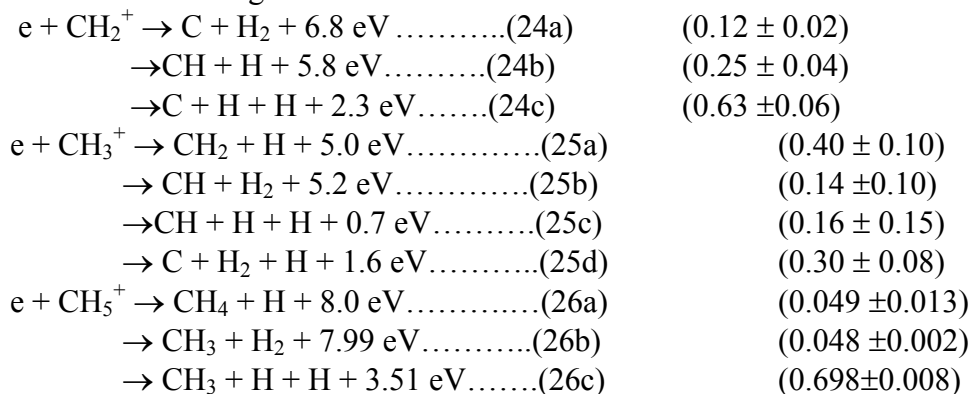


Fig. 29. Cross sections for the dissociative recombination of CH^+ measured at the TSR storage ring $\{\text{---}\}$ [143]. Also shown are measurements taken using the MEIBE apparatus $\{\Delta\}$ [138, 139] and theoretical results of Takagi et al $\{\text{---}\}$ [144].

It does seem that there is a real discrepancy between beam measured results and afterglow results for CH_5^+ . Recent measurements have found values of $(1.1 \times 10^{-6} \text{ cm}^3 \text{ s}^{-1}$ [135]), $(1.4 \times 10^{-6} \text{ cm}^3 \text{ s}^{-1}$ [136]) $(9 \times 10^{-7} \text{ cm}^3 \text{ s}^{-1}$ [137]) and $(7 \times 10^{-7} \text{ cm}^3 \text{ s}^{-1}$ [12]) while the beam results [139, 114, 142] indicate a rate coefficient of $3 \times 10^{-7} \text{ cm}^3 \text{ s}^{-1}$. Given the lack of theoretical analyses of the recombination of such ions, it is not possible at this time to identify the source of this discrepancy.

Very significant progress has been made regarding the recombination of hydrocarbon ions and branching ratios have been measured for CH_2^+ [71], CH_3^+ [145], CH_5^+ [142] and C_2H_2^+ [146] with the values being listed below.



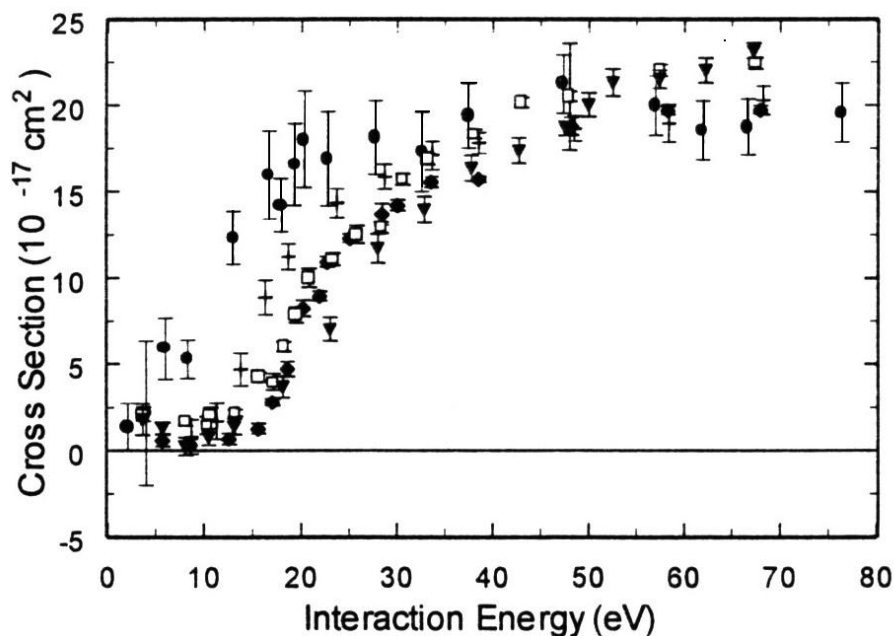
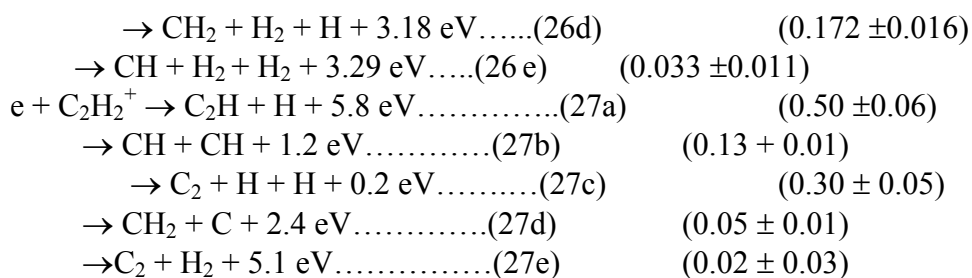


Fig. 30. Cross sections for the formation of D^+ in electron collisions with CD_n^+ taken using a crossed beams apparatus [147, 148, 10]. $\{\bullet\}$ CD^+ , $\{+\}$ CD_2^+ , $\{\blacklozenge\}$ CD_3^+ , $\{\square\}$ CD_4^+ and $\{\blacktriangledown\}$ CD_5^+ .

Experiments [147, 148, 10] have been performed to measure the dissociative collisions between electrons and CD_n^+ ions and cross sections for the formation of D^+ are shown in figure 30 and for the formation of D_2^+ in figure 31. These data were gathered using a crossed beams apparatus and refer to ions with an undetermined vibrational state population. It is interesting to note in the former case that these cross sections have essentially very similar magnitudes, i.e. they are independent of the number of hydrogen atoms in the target, at least once the threshold has been broached and on up to 70 eV. This is not the case for the formation of D_2^+ , at least in so far that the cross section for CD_2^+ is about a factor of 2 lower than for CD_5^+ though that of CD_4^+ is close to that of CD_5^+ . Dissociative excitation cross sections have been measured for CD^+ at TSR [149] and for CH_2^+ and CH_5^+ at CRYRING [71, 142]. Since the neutral products were measured in these experiments, rather than the ion, there is a fundamental difference between the measurements as the crossed beam data contains contributions from dissociative ionization, once this channel is open. Thus by subtracting these data, it is possible to obtain cross sections for the dissociative ionization reaction. Examples of this are shown in figures 32 and 33 for CD^+ and CH_5^+ respectively.

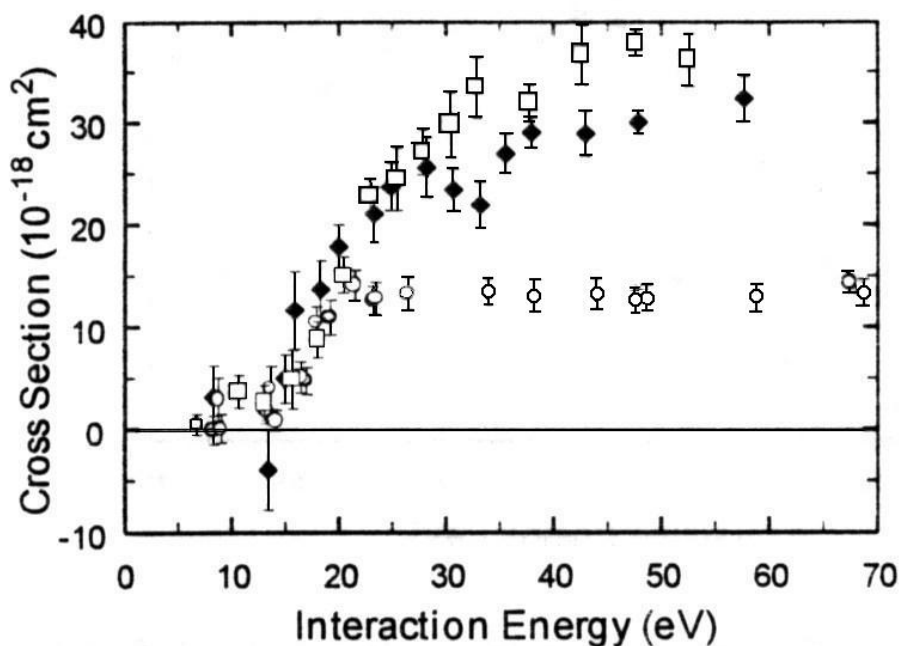


Fig. 31. Cross sections for the formation of D_2^+ in electron collisions with CD_n^+ measured using a crossed beams apparatus [148, 10]. {o} CD_2^+ , {♦} CD_4^+ and {□} CD_5^+ .

Recombination rate coefficients for more complex hydrocarbon ions formed from alkanes, alkenes, alkynes and aromatic and polyaromatic hydrocarbons have been studied using the Flowing Afterglow Langmuir Probe Mass Spectrometer (FALP-MS) apparatus at the University of Rennes in France and the data are discussed in references 11–14. Neither temperature dependences nor branching ratios are available for these species but it is interesting to note that while minor differences exist between rate coefficients for different complex ions, these differences cannot be correlated with either the size or the aromaticity of the species. This is clearly a subject that needs attention from quantum chemists.

4. Electron impact excitation of rovibrational states

While in most of the previous discussion, theory has followed upon the successes of experimental studies, an area which is for now, the sole domain of theory is that of vibrational and rotational excitation of ions following electron impact. Calculations of these processes have been made for NO^+ and for HeH^+ by Tennyson and co-workers [150, 151]. Results for rotational excitation are shown in figure 34 and it is seen that these cross sections can have very large values. This may be one of the reasons why in certain recombination experiments performed at storage rings, rotational temperatures higher than ambient have been found.

Figure 35 shows cross sections for the vibrational excitation of NO^+ as a function of electron energy and it is seen that these are considerably smaller than the rotational cross sections shown in figure 31 but are still sizeable and should be taken into account when considering the design of multi-pass storage ring experiments and plasmas with temperatures exceeding 1000 K.

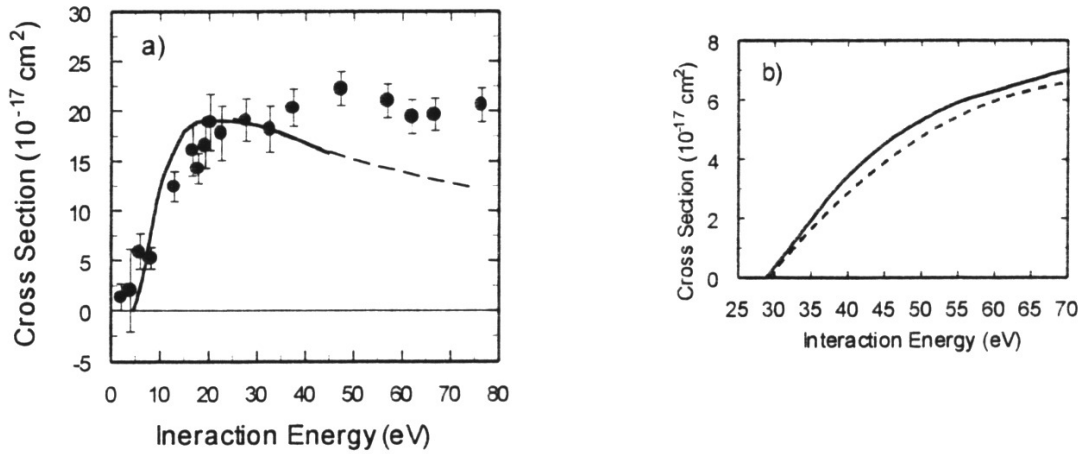


Fig. 32. (a) Cross sections for the formation of D^+ from electron collisions with CD^+ taken using a crossed beams apparatus $\{\bullet\}$ [147]. $\{—\}$ storage ring dissociative excitation measurement [149]. (b) Dissociative ionization cross sections for CD^+ $\{—\}$. Dashed line is theoretical calculation of Kim [private communication].

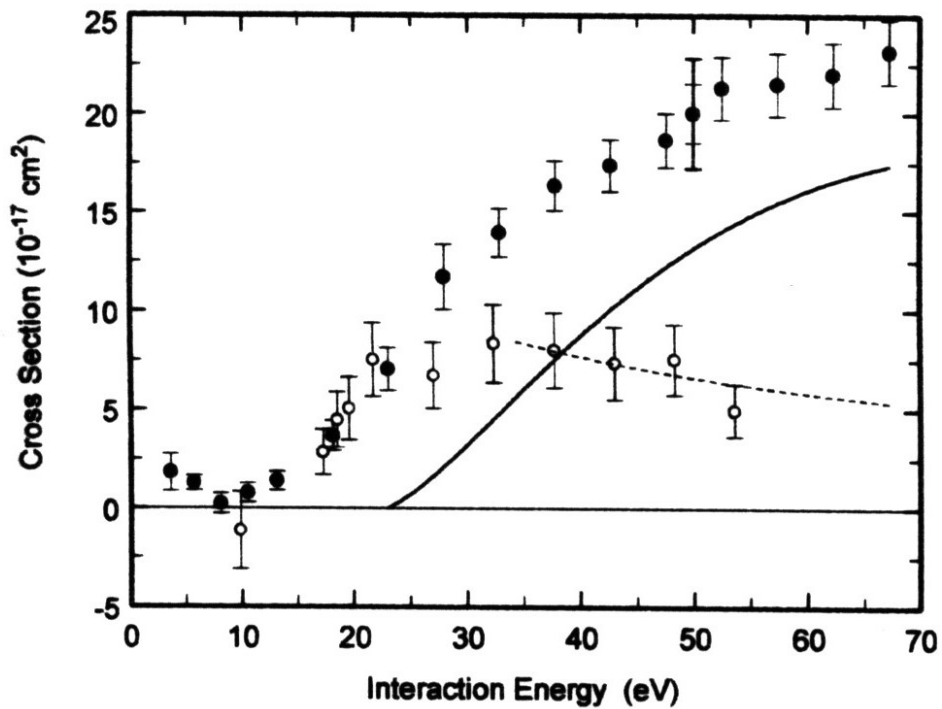


Fig. 33. Cross sections for the formation of D^+ in electron- CD_5^+ collisions measured using a crossed beams apparatus $\{\bullet\}$ [148]. Data for the dissociative excitation of CH_5^+ to form CH_4 taken using CRYRING [142] are also shown $\{o\}$. The solid curve represents the difference between these two data sets and therefore the cross section for dissociative ionization. The dashed curve is an extension of the storage ring data.

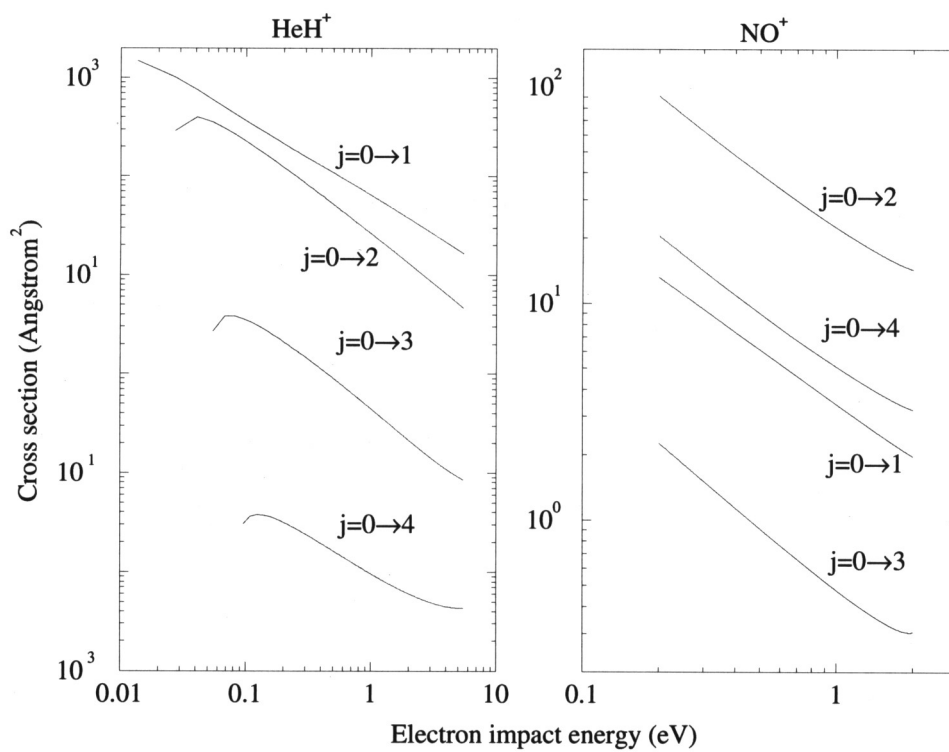


Fig. 34. Theoretical cross sections for the rotational excitation of HeH^+ and NO^+ by electron impact [150].

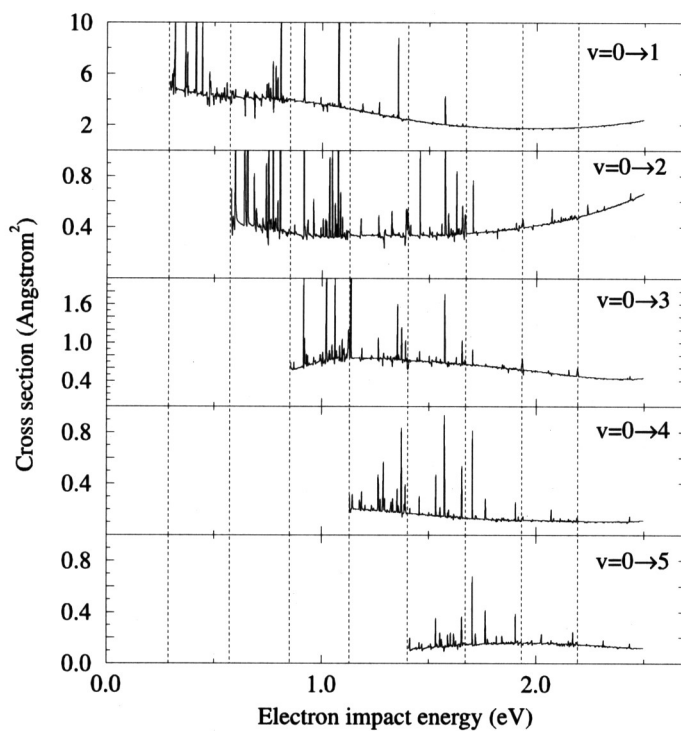


Fig. 35. Theoretical cross sections for the vibrational excitation of NO^+ by electron impact [151].

REFERENCES

- [1] J.B.A. Mitchell in *Atomic and Molecular Physics and Fusion Edge Plasmas* (editor R. K. Janev) Plenum Press, N.Y. 1994, p. 225.
- [2] G.H. Dunn in *Atomic and Plasma –Material Interaction Data for Fusion Vol 2.* (editor R. K. Janev) I.A.E.A., Vienna, Austria, 1992, p. 25.
- [3] J.B.A. Mitchell in *Dissociative Recombination: Theory, Experiment and Application III* (editors D. Zajfman, J.B.A. Mitchell and D.C. Schram) World Scientific, Singapore, 1995.
- [4] R.K. Janev in *Dissociative Recombination: Theory, Experiment and Application IV* (editors M. Larsson, I. Schneider and J.B.A. Mitchell) World Scientific, Singapore, 2000.
- [5] J.B.A. Mitchell and S.L. Guberman, *Dissociative Recombination: Theory, Experiment and Application*, World Scientific, Singapore, 1989
- [6] B.R. Rowe, J.B.A. Mitchell and A. Canosa, *Dissociative Recombination: Theory, Experiment and Application*, Plenum Press, New York, 1993.
- [7] D. Zajfman, J.B.A. Mitchell and D.C. Schwalm, *Dissociative Recombination: Theory, Experiment and Application*, World Scientific, Singapore, 1995.
- [8] M. Larsson, I. Schneider and J.B.A. Mitchell, *Dissociative Recombination: Theory, Experiment and Application*, World Scientific, Singapore, 2000.
- [9] G.H. Dunn and N. Djuric, *Novel Aspects of Electron-Molecule Scattering*, (ed. K. Becker) World Scientific, Singapore, 1998, p. 241.
- [10] N. Djuric, W. Zong, C.H. Greene, G.H. Dunn, A. Al Khalili, H. Danared, A.M. Derkatch, M. Larsson, A. Le Padellec, A. Neau, S. Rosen, W. Shi, L. Viktor and M. af Ugglas in ref. 8.
- [11] H. Abouelaziz, J.C. Gomet, D. Pasquerault, B.R. Rowe and J.B.A. Mitchell, *J. Chem. Phys.* **99**, 237, 1993.
- [12] L. Lehfaoui, C. Rebrion-Rowe, S. Laubé, J.B.A. Mitchell and B.R. Rowe, *J. Chem. Phys.* **106**, 5406, 1997.
- [13] C. Rebrion-Rowe, L. Lehfaoui, B.R. Rowe and J.B.A. Mitchell, *J. Chem. Phys.* **108**, 7185, 1998.
- [14] C. Rebrion-Rowe, T. Mostefaoui, S. Laubé and J.B.A. Mitchell, (Submitted to *J. Chem. Phys.* 2000).
- [15] N.G. Adams in ref. 8.
- [16] R. Johnsen in ref. 8.
- [17] X. Hu, J.B.A. Mitchell and R.H. Lipson (Submitted to *Phys. Rev. A* 2000).
- [18] G.B. Ramos, M. Schlamkowitz, J. Sheldon, K.A. Hardy and J.R. Peterson, *Phys. Rev. A* **51**, 2945, 1995.
- [19] D.R. Bates, *Phys. Rev.* **78**, 492, 1950.
- [20] D. Villarejo, *J. Chem. Phys.* **49**, 2523, 1968.
- [21] F. Von Busch and G.H. Dunn *Phys. Rev. A* **5**, 1726, 1972.
- [22] H. Hus, F.B. Yousif, C. Noren, A. Sen, and J.B.A. Mitchell, *Phys. Rev. Lett.* **60**, 1006, 1988.
- [23] P. Van der Donk, F.B. Yousif, J.B.A. Mitchell and P.J. Hickman, *Phys. Rev. Lett.* **67**, 42, 1991.
- [24] H.T. Schmidt, L. Vejby-Christensen, H.B. Pedesen, D. Kella, N. Bjerre and L.H. Andersen, *J. Phys. B* **29**, 2485, 1996.
- [25] L.H. Andersen, P.J. Johnson, D. Kella, H.B. Pedersen, and L. Vejby-Christensen, *Phys. Rev. A* **55**, 2799, 1997.
- [26] J.B.A. Mitchell, F.B. Yousif, P.J.T. Van der Donk, T.J. Morgan and M.I. Chibisov *Int. J. Mass Spec. Ion Proc.* **149/150**, 153, 1995.

- [27] M.I. Chibisov, J.B.A. Mitchell, P.J.T. Van der Donk, F.B. Yousif and T.J. Morgan, *Phys. Rev. A* **56**, 443, 1997.
- [28] M. Larsson, L. Brostrom, M. Carlson, H. Danared, S. Datz, S. Mannervik and G. Sundstrom, *Physica Scripta* **51**, 354, 1995.
- [29] M. Larsson, M. Carlson, H. Danared, L. Brostrom, S. Mannervik and G. Sundstrom, *J. Phys. B* **27**, 1397, 1994.
- [30] W. J. Van der Zande, J. Semaniuk, V. Zengin, G. Sundstrom, S. Rosen, C. Stromholm, S. Datz, H. Danared and M. Larsson, *Phys. Rev. A* **54**, 5010, 1996.
- [31] T. Tanabe, H. Takagi, I. Katayama, K. Chida, T. Watanabe, Y. Arakaki, M. Saito, Y. Haruyama, T. Honma, K. Noda and K. Hosono, *Phys. Rev. Lett.* **83**, 2163, 1999.
- [32] F.B. Yousif and J.B.A. Mitchell, *Z. Phys. D* **34**, 195, 1997.
- [33] H. Takagi, 21th ICPEAC abstracts of contributed papers, p407, 1999.
- [34] J.M. Peek, *Phys. Rev.* **140**, A11, 1965.
- [35] J.M. Peek, *Phys. Rev.* **154**, 52, 1967.
- [36] P. Forck, M. Greiser, D. Habs, A. Lampert, R. Repnow, D. Schwalm, A. Wolf, D. Zajfman, *Phys. Rev. Lett.* **70**, 426, 1993.
- [37] P. Forck, M. Greiser, D. Habs, A. Lampert, R. Repnow, D. Schwalm, A. Wolf and D. Zajfman *Nucl. Inst. Meth. B* **79**, 273, 1993.
- [38] T. Tanabe, I. Katayama, H. Kamegaya, K. Chida, Y. Arakaki, T. Watanabe, M. Yoshizawa, M. Saito, Y. Haruyama, T. Honma, K. Noda, S. Ohtani and H. Takagi, *Phys. Rev. Lett.* **75**, 1066, 1995.
- [39] C. Stromholm, I.F. Schneider, G. Sundstrom, L. Carata, H. Danared, S. Datz, O. Dulieu, A. Kalberg, M. af Ugglas, X. Urbain, V. Zengin, A. Suzor-Weiner and M. Larsson, *Phys. Rev. A* **52**, R4320, 1995.
- [40] D. Zajfman, Z. Amitay, C. Broude, P. Forck, B. Seidel, M. Greiser, D. Habs, D. Schwalm and A. Wolf, *Phys. Rev. Lett.* **75**, 814, 1995.
- [41] D. Zajfman, Z. Amitay, M. Lange, U. Hechtfisher, L. Knoll, D. Schwalm, R. Wester, A. Wolf and X. Urbain *Phys. Rev. Lett.* **79**, 1829, 1997.
- [42] M. Lange, J. Levin, G. Gwinner, U. Hechtfisher, L. Knoll, D. Schwalm, R. Wester, A. Wolf, X. Urbain and D. Zajfman *Phys. Rev. Lett.* **83**, 4979, 1999.
- [43] Z. Amitay, A. Baer, M. Dahan, J. Levin, Z. Vager, D. Zajfman, L. Knoll, M. Lange, D. Schwalm, R. Wester, A. Wolf, I.F. Schneider and A. Suzor-Weiner *Phys. Rev. A* **60**, 3769, 1999.
- [44] Z. Amitay, D. Zajfman and P. Forck, *Phys. Rev. A* **50**, 2304, 1994.
- [45] H. Takagi in refs. 6,7 and 8.
- [46] I.F. Schneider, O. Dulieu and A. Giusti-Suzor, *J. Phys. B* **24**, L289, 1991
- [47] H. Takagi, *J. Phys. B* **26**, 4815, 1993
- [48] I.F. Schneider, O. Dulieu, A. Giusti-Suzor and E. Roueff, *Astrophys. J.* **424**, 983, 1994.
- [49] M.G. Golubkov, G.V. Golubkov and G.K. Ivanov *J. Phys. B* **30**, 5511, 1997.
- [50] B. Valcu, I.F. Schneider, M. Raoult, C. Stromholm, M. Larsson and A. Suzor-Weiner, *Eur. Phys. D* **1**, 71, 1998.
- [51] I.F. Schneider, C. Stromholm, L. Carata, X. Urbain, M. Larsson and A. Suzor-Weiner, *J. Phys. B* **30**, 2687, 1997.
- [52] W. Zong, G.H. Dunn, N. Djuric, M. Larsson, A. Al-Khalili, A. Neau, A.M. Derkatch, L. Viktor, W. Shi, A. Le Padellec, S. Rosen, H. Danared and M. af Ugglas, *Phys. Rev. Lett.* **83**, 951, 1999.
- [53] K.C. Kulander and M.F. Guest *J. Phys. B* **12**, L501, 1979.
- [54] H.H. Michels and R.H. Hobbs *Astrophys. J.* **286**, 27, 1984.
- [55] S. Laubé, A. Le Padellec, O. Sidko, C. Rebrion-Rowe, J.B.A. Mitchell and B.R. Rowe *J. Phys. B* **31**, 2111, 1998.
- [56] I. Schneider in ref. 8.

- [57] A. Dalgarno *Adv. At. Mol. Phys.* **32**, 57, 1994.
- [58] E. Roueff in ref. 7
- [59] T. Oka in ref. 8.
- [60] J.B.A. Mitchell, C.T. Ng, L. Forand, R. Janssen and J. Wm. McGowan, *J. Phys. B* **17**, L909, 1984.
- [61] A. Le Padellec, M. Larsson, H. Danared, A. Larson, J.R. Peterson, S. Rosen, J. Semaniuk and C. Stromholm *Physica Scripta* **57**, 215, 1998.
- [62] M. Larsson, H. Danared, A. Larson, A. Le Padellec, J.R. Peterson, S. Rosen, J. Semaniuk and C. Stromholm, *Phys. Rev. Lett.* **79**, 395, 1997.
- [63] T. Gougousi, R. Johnsen and M.F. Golde *Int. J. Mass Spec. Ion Proc.* **149/150**, 131, 1993.
- [64] P. Van der Donk, F.B. Yousif and J.B.A. Mitchell *Phys. Rev. A* **43**, 5971, 1991.
- [65] F.B. Yousif, M. Rogelstad and J.B.A. Mitchell in *Proceedings of Fourth US/Mexico Symposium on Atomic and Molecular Physics*, San Juan del Rio, Mexico 1994, (eds. I. Alvarez, C. Cisneros and T.J. Morgan) World Scientific, Singapore, 1995, p. 343
- [66] R. Johnsen and J.B.A. Mitchell in *Advances in Gas-Phase Ion Chemistry* (eds. N.G. Adams and L.M. Babcock) JAI Press, (Greenwich, CT, USA), 1998, p. 49.
- [67] M. Larsson, H. Danared, J.R. Mowat, P. Sigray, G. Sundstrom, L. Brostrom, A. Filevich, A. Kalberg, S. Mannervik, K.G. Rensfelt and S. Datz *Phys. Rev. Lett.* **70**, 430, 1993.
- [68] T. Tanabe in ref. 7.
- [69] H. Hus, F.B. Yousif, A. Sen and J.B.A. Mitchell *Phys. Rev. A* **38**, 658, 1988.
- [70] S. Datz, M. Larsson, C. Stromholm, G. Sundstrom, V. Zengin, H. Danared, A. Kalberg and M. af Ugglas, *Phys. Rev. A* **52**, 2901, 1994.
- [71] A. Larson, A. Le Padellec, J. Semaniuk, C. Stromholm, M. Larsson, S. Rosen, R. Peverall, H. Danared, N. Djuric, G.H. Dunn and S. Datz, *Astrophys. J.* **505**, 459, 1998.
- [72] B. Peart and K.T. Dolder *J. Phys. B* **7**, 1948, 1974.
- [73] B. Peart, R.A. Forrest and K.T. Dolder *J. Phys. B* **12**, 3441, 1979.
- [74] B. Peart and K.T. Dolder *J. Phys. B* **7**, 236, 1974.
- [75] F.B. Yousif, P. Van der Donk and J.B.A. Mitchell *J. Phys. B* **26**, 4249, 1993.
- [76] D. Auerbach, D., R. Cacak, R. Caudano, T.D. Gaily, C.J. Keyser, J. Wm. McGowan, J.B.A. Mitchell and S.F.J. Wilk *J. Phys. B.* **10**: 3797, 1977
- [77] A.E. Orel and K.C. Kulander *Phys. Rev. Lett.* **71**, 4315, 1993.
- [78] D.R. Bates, M.F. Guest, and R.A. Kendall *Planet. Space Sci.* **41**, 9, 1993.
- [79] M.R. Flannery, *Int. J. Mass Spec. Ion Proc.* **149/150**, 597, 1995.
- [80] D.R. Bates *Adv. At. Mol. Phys.* **32**, 427, 1994.
- [81] J.B.A. Mitchell and B.R. Rowe in *Proceedings of the Third US/Mexico Symposium on Atomic and Molecular Physics* (eds. C. Cisneros, T.J. Morgan and I. Alvarez), World Scientific, Singapore, 1991, p. 16.
- [82] C. Sheehan, A. Le Padellec, W.N. Lennard, D. Talbi and J.B.A. Mitchell *J. Phys. B* **32**, 3347, 1999.
- [83] D. Talbi in ref. 8.
- [84] D. Talbi, A. Le Padellec and J.B.A. Mitchell (Submitted to *J. Phys. B* 2000)
- [85] A. Le Padellec, C. Sheehan, D. Talbi and J.B.A. Mitchell, *J. Phys. B.* **30**, 319, 1997.
- [86] J.B.A. Mitchell, J.L. Forand, C.T. Ng, D.P. Levac, R.E. Mitchell, P.M. Mul, W. Claeys, A. Sen, and J.Wm. McGowan *Phys. Rev. Lett.* **51**, 885, 1983.
- [87] J.B.A. Mitchell and F.B. Yousif in *Microwave and Particle Beam Sources and Directed Energy Concepts*, (ed. H.E. Brand) Optical Soc. America, Washington, DC, 1989, Vol. 1061, p.61.
- [88] S. Datz, G. Sundstrom, Ch. Biedermann, L. Brostrom, H. Danared, S. Mannervik, J.R. Mowat and M. Larsson, *Phys. Rev. Lett.* **74**, 896, 1995.

- [89] B. Peart and K.T. Dolder, *J. Phys. B* **7**, 1567, 1974.
- [90] B. Peart and K.T. Dolder, *J. Phys. B* **8**, L143, 1975.
- [91] F.B. Yousif, P.J.T. Van der Donk, M. Orakzai and J.B.A. Mitchell, *Phys. Rev A* **44**, 5653, 1991.
- [92] P. VanderDonk, F.B. Yousif and J.B.A. Mitchell, *Phys. Rev. A.* **43**,5971–5974, 1991
- [93] A.E. Orel, *Phys. Rev. A* **46**, 1333, 1992.
- [94] W. Roberge and A. Dalgarno, *Astrophys. J.* **255**, 489, 1982.
- [95] F.B. Yousif and J.B.A. Mitchell, *Phys. Rev A* **40**, 4318, 1989.
- [96] F.B. Yousif, J.B.A. Mitchell, M. Rogelstad, A. Le Padellec, A. Canosa and M.I.Chibisov. *Phys. Rev. A* **49**, 4610, 1994.
- [97] T. Tanabe, I. Katayama, N. Inoue, K. Chida, Y Arakaki, T. Watanabe, M. Yoshizawa, M. Saito, Y. Haruyama, K. Hosono, T. Honma, K. Noda, S. Ohtani and H. Takagi, *Phys. Rev. A* **49**, R1531, 1994.
- [98] J.R. Mowat, H. Danared, G. Sundstrom, M. Carlson, L.H. Andersen, L.Vejby-Christensen, M. af Uglaas and M. Larsson, *Phys. Rev. Lett.* **74**, 50, 1995.
- [99] C. Stromholm, J. Semaniuk, S. Rosen, H. Danared, S. Datz, W. van der Zande and M. Larsson, *Phys. Rev. A* **54**, 3086, 1996.
- [100] J. Semaniuk, S. Rosen, G. Sundstrom, C. Stromholm, S. Datz, H. Danared, M. af Ugglas, M. Larsson, W.J. Van der Zande, Z. Amitay, U. Hechtfisher, M. Grieser, R. Repnow, M. Schmidt, D. Schwalm, R. Wester, A. Wolf and D. Zajfman, *Phys. Rev. A* **54**, R4617, 1996.
- [101] A. Al-Khalili, H. Danared, M. Larsson, A. Le Padellec, R. Peverall, S. Rosen, J. Semaniuk, M. af Ugglas, L. Viktor, and W.J. Van der Zande *Hyperfine Interactions* **114**, 281, 1998.
- [102] T. Tanabe, I. Katayama, S. Ono, K. Chida, T. Watanabe, Y. Arakaki, Y. Haruyama, M. Saito, T. Odagiri, K. Hosono, K. Noda, T. Honma and H. Takagi, *J. Phys. B* **31**, L297, 1998. *Corrigendum J. Phys B*.
- [103] B.K. Sarpal, J. Tennyson and L.A. Morgan, *J. Phys. B* **27**, 5943, 1994.
- [104] S.L. Guberman *Phys. Rev. A* **49**, R4277, 1994.
- [105] W.P. Kraemer and P-A. Malmqvist, *Theor. Chem. Acc.* **100**, 65, 1998.
- [106] D. Strasser, K.G. Bhusan, H.B. Pedersen, R. Wester, O. Heber, A. Lafosse, M.L. Rappaport, N. Alstein and D. Zajfman, *Phys. Rev. Lett.* (in press) 2000.
- [107] C. Sheehan, MSc Thesis, University of Western Ontario, 1996.
- [108] A.E.Orel, T.N. Rescigno and B.H. Lengsfeld III, *Phys. Rev. A* **44**, 4328, 1991.
- [109] A.E. Orel, K.C. Kulander and T.N. Rescigno, *Phys. Rev. Lett.* **74**, 4807, 1995.
- [110] A.E. Orel and K.C. Kulander *Phys. Rev. A* **54**, 4992, 1996.
- [111] J.R. Peterson, A. Le Padellec, H. Danared, G.H. Dunn, M. Larsson, A. Larson, R. Peverall, C. Stromholm, S. Rosen, M. af Ugglas and W.J. Van der Zande, *J. Chem. Phys.* **108**, 1978, 1998.
- [112] D. Kella, P.J. Johnson, H.B. Pedersen, L. Vejby-Christensen and L.H. Andersen, *Phys. Rev. Lett.* **77**, 2432, 1996.
- [113] C. Noren, F.B. Yousif, and J.B.A. Mitchell, *J. Chem. Soc. Faraday Trans.* **85**, 1697, 1989.
- [114] C. Sheehan, PhD Thesis, University of Western Ontario, 2000.
- [115] D.R. Bates and J.B.A. Mitchell, *Planet. Space Sci.* **9**, 1297, 1991.
- [116] P.M. Mul and J.Wm. McGowan, *J. Phys. B* **12**, 1591, 1979.
- [117] B. van Zyl and G.H. Dunn, *Phys. Rev.* **163**, 43, 1967.
- [118] W. Van der Zande et al. (To be published)
- [119] D. Kella, L. Vejby-Christensen, P.J. Johnson, H.B. Pedersen and L.H. Andersen, *Science* **276**, 1530, 1997.
- [120] F.J. Mehr and M.A. Biondi, *Phys. Rev.* **181**, 264, 1969.

- [121] F.L. Walls and G.H. Dunn, *J. Geophys. Res.* **79**, 1911, 1974.
- [122] S.L. Guberman, *Science* **278**, 1276, 1977.
- [123] S.L. Guberman in ref. 8.
- [124] L. Vejby-Christensen, D. Kella, H.B. Pedersen and L.H. Andersen *Phys. Rev. A* **57**, 3627, 1998.
- [125] T. Mostefaoui, S. Laubé, G. Gautier, C. Rebrion-Rowe, B.R. Rowe and J.B.A. Mitchell *J. Phys. B* **32**, 5247, 1999.
- [126] J.B.A. Mitchell and H. Hus *J. Phys. B* **18**, 542, 1985.
- [127] S. Rosen, R. Peverall, M. Larsson, A. Le Padellec, J. Semaniuk, A. Larson, C. Stromholm and W.J. Van der Zande and G.H. Dunn *Phys. Rev A* **57**, 4462, 1998.
- [128] S. Laubé, L. Lefaoui, B.R. Rowe and J.B.A. Mitchell *J. Phys. B* **31**, 4181, 1998.
- [129] D.S. Belic, D.J. Yu, A. Siari and P. Defrance, *J. Phys. B* **30**, 5535, 1997.
- [130] A. Le Padellec, C. Sheehan and J.B.A. Mitchell *J. Phys. B* **31**, 1725, 1998.
- [131] A. Le Padellec, J.B.A. Mitchell, A. Al-Khalili, H. Danared, A. Kalberg, A. Larson, S. Rosen, M. af Ugglas, L. Vikor and M. Larsson *J. Chem. Phys.* **110**, 890, 1999.
- [132] M.T. Leu, M.A. Biondi and R. Johnsen, *Phys. Rev. A* **8**, 420, 1973.
- [133] B. Ganguli, M.A. Biondi, R. Johnsen and J.L. Dulaney, *Phys. Rev.* **37**, 2543, 1988.
- [134] B.R. Rowe, J.C. Gomet, A. Canosa, C. Rebrion and J.B.A. Mitchell, *J. Chem. Phys.* **96**, 1105, 1992.
- [135] N.G. Adams, D. Smith and E. Alge, *J. Chem. Phys.* **81**, 1778, 1984.
- [136] D. Smith and P. Spanel, *Int. J. Mass Spec. Ion Proc.* **129**, 163, 1993.
- [137] T. Gougousi, M.F. Golde and R. Johnsen, *Chem. Phys. Lett.* **265**, 399, 1997.
- [138] J.B.A. Mitchell and J. Wm. McGowan, *Astrophys. J.* **222**, L77, 1978.
- [139] P.M. Mul, J.B.A. Mitchell, V.S. D'Angelo, P. Defrance, J. Wm. McGowan and H.R. Froelich, *J. Phys. B* **14**, 1353–1361, 1981
- [140] P.M. Mul and J. Wm. McGowan, *Astrophys. J.* **237**, 749, 1980.
- [141] J.B.A. Mitchell, *Phys. Reports* **186**, 215, 1990.
- [142] J. Semaniuk, A. Larson, A. Le Padellec, C. Stromholm, M. Larsson, S. Rosen, R. Peverall, H. Danared, N. Djuric, G.H. Dunn and S. Datz, *Astrophys. J.* **498**, 886, 1998.
- [143] Z. Amitay, D. Zajfman, P. Forck, U. Hechtfisher, B. Seidel, M. Greiser, D. Habs, R. Repnow, D. Schwalm and A. Wolf, *Phys. Rev. A* **54**, 4032, 1996.
- [144] H. Takagi, N. Kosugi and M. Le Dourneuf, *J. Phys. B* **24**, 711, 1991.
- [145] L. Vejby-Christensen, L.H. Andersen, O. Heber, D. Kella, H.B. Pedersen, H.T. Schmidt and D. Zajfman, *Astrophys. J.* **483**, 531, 1997.
- [146] A.M. Derkatch, A. Al-Khalili, L. Vikor, A. Neau, W. Shi, H. Danared, M. af Ugglas and M. Larsson, *J. Phys. B* **32**, 3391, 1999.
- [147] N. Djuric, Y.-S., Chung, B. Wallbank and G.H. Dunn, *Phys. Rev. A* **56**, 2887, 1997.
- [148] N. Djuric, S. Zhou, G.H. Dunn and M.E. Bannister, *Phys. Rev. A* **58**, 304, 1998.
- [149] P. Forck, PhD Thesis, Ruprech-Karls-Universitat Heidelberg, 1994.
- [150] I. Rabadan, B.K. Sarpal and J. Tennyson, *J. Phys. B* **31**, 2077, 1998.
- [151] I. Rabadan and J. Tennyson, *J. Phys. B* **32**, 4753, 1999.

Elastic and inelastic collision processes at low energies which involve hydrogen ion, atoms, and molecules

P.S. Krstić, D.R. Schultz

Physics Division, Oak Ridge National Laboratory,
Oak Ridge, Tennessee, United States of America

Abstract. This report describes a comprehensive study of scattering of hydrogen ions and atoms principally on hydrogen molecules in the range of center-of-mass energies 0.1-100 eV and in all isotopic variants. In addition to elastic scattering among these species, the study includes vibrational excitations on the ground H_2 electronic surface. Differential and integral elastic cross sections, the related transport cross sections, and vibrationally inelastic cross sections starting from both ground and excited vibrational states, are calculated using a fully-quantal, coupled-channel approach in a truncated vibrational basis set, while the rotational dynamics of H_2 is treated with the Infinite Order Sudden Approximation (IOSA) prescription. Work was also carried out for scattering of H^+ and H on hydrogen and helium atoms, and comparisons were made between different collision systems. A comprehensive set of data has been produced varying all isotopic combinations of H in ions, atoms, and molecules, and relevant mass-dependent scaling is reported for the integral cross sections.

1. Introduction

Transport and charge balance in the boundary of tokamak plasmas, such as in the divertor and edge plasma regions of fusion reactors, has been of growing interest for plasma modeling and engineering of fusion devices [1, 2]. For example, heat exhaust, recycling hydrogen, and removing the helium ash and impurities are basic functions of the divertor while the edge plasma should suppress the inflow of deleterious impurities into the plasma core. These regions are characterized by relatively low plasma temperatures (10–500 eV in the former and 1–50 eV in the latter) with high densities (in comparison to the core), thus providing conditions for numerous interparticle collisions involving both atomic and molecular particles. Elastic processes play the dominant role in neutral particle transport and overall momentum balance and particle transport due its correspondingly large cross sections in comparison to inelastic ones [1].

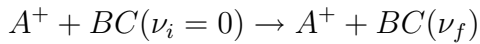
However, calculation and measurement of these processes have been overshadowed by the production of data for charge exchange and other inelastic processes. In addition to the integral and differential elastic cross sections needed to model these processes, rate coefficients (cross sections averaged over the Maxwellian temperature distributions) are needed, so we consider the somewhat extended center-of-mass energy region of 0.1–100 eV in what follows, and utilize atomic units except where explicitly noted.

Thus, the goal of this work has been to produce and tabulate the scattering data for the most abundant particles of the divertor and edge plasmas, relevant for transport processes, the data which almost without exception cannot be found in literature. These include the elastic cross sections, as well as those for resonant charge transfer and vibrational excitation of molecular targets. The existing, published data typically cover only a limited collision energy and/or angular scattering range, and are not tabulated or fitted for use in

plasma modeling codes. Earlier work [3–5], which sought to partially ameliorate this lack, provided limited comprehensive compilations based on classical [4] and semi-classical [5] approaches, and on literature surveys [3].

The particular species considered include hydrogen in all isotopic atomic (H, D, T), ionic (H^+ , D^+ , T^+), and molecular (H_2 , D_2 , T_2 , HD, HT, DT) forms, and helium. We performed fully quantal calculations of the differential and integral cross sections and its transport moments (i.e. the momentum transfer and viscosity cross sections) for all these systems. The complete database of results covering all of these studies is available through the web site of the ORNL Controlled Fusion Atomic Data Center (CFADC) (www-cfadc.phy.ornl.gov). As a further aid to plasma modeling, convenient analytical fitting coefficients to describe the differential and integral cross sections were also tabulated [7].

In the present review we summarize these results and consider in particular collisions of the type [6]



where A , B , and C are any of the hydrogen isotopes (H, D, and T). Although these are among the simplest and most fundamental of all ion/atom-molecule collisions (involving only two and three electrons, respectively), there exist no comprehensive data for these processes, especially in the energy range below 100 eV. The particular reason for this is that the number of degrees of freedom in the scattering from molecules is significantly increased in comparison to those present in ion-atom and atom-atom collisions. *Ab initio* numerical solution of the collision problem, with simultaneous inclusion of all degrees of freedom, is an extremely difficult computational task. The choice of approximations that can be reasonably applied to make computations for the processes in Eq. (1) tractable depends on the process to be considered as well as on the collision energy range. For example, in the range above a few hundred eV, the projectile is so fast that both the internuclear diatomic coordinate and its direction in space may be considered as frozen during the collision. This significantly simplifies the treatment of the collision dynamics of the electronic transitions, resulting in methods similar to those employed to treat ion-atom collisions.

In contrast, consideration of the energy range below about 100 eV, down to the order of 1 eV, requires simultaneous coupling of the electronic and vibrational motions. In particular, the excitation energy of the first vibrational state of H_2 is ~ 0.5 eV corresponding to a characteristic vibration time exceeding 50 a.u. which is comparable to the collision time. Vibrational excitations from the ground, $\nu = 0$, vibrational state to the states $\nu \leq 9$ on the ground electronic surface were calculated due to the strength of these inelastic channels. This was enough to provide the convergence of the cross sections for elastic channel and excitation channels for $\nu \leq 3$. The relevant data for $\nu \leq 3$ are also available at the CFADC web site (www-cfadc.phy.ornl.gov). The $H^+ + H_2$ charge transfer reaction, although endoergic, has a low threshold energy (1.83 eV) and is strongly coupled to the mechanism of vibrational excitation to states that are high enough ($\nu \geq 4$) to overcome

the barrier. Thus, this reaction is a second-order process with an integral cross section that is more than ten times lower than the cross section for excitation to the first excited state of H_2 for energies < 200 eV [3]. On the other hand, in order for the electron to make a transition to the excited surface ($\text{H}+\text{H}_2^+$) the H_2 bond must stretch while the projectile is still close enough to the H_2 molecule. Collisions that involve nuclear rearrangements will almost always lead to scattering at larger angles which will not significantly contribute to the considered elastic cross section results, but could influence to some extent the transport cross sections below about 1 eV due to their emphasis of large angle scattering. Thus, in the energy range considered here, it is satisfactory to treat elastic scattering and vibrational excitations with inclusion of only the ground electronic energy surface with the appropriate caution (i.e. using the transformation to the diabatic surface in the H^++H_2 case). This is the first assumption made in the present calculations. Moreover, the energy gap for any reaction that involves an electronic transition is much larger for neutral-neutral molecule collisions, which allows greater certainty in the results obtained with only one electronic surface.

The collision time is still short enough on the scale of molecular rotations (excitation energy < 0.01 eV, i.e. the characteristic time ~ 300 a.u.), to enable one to treat the direction of the diatomic internuclear axis as fixed, which is the second simplifying approximation adopted here, often called the Infinite Order Sudden Approximation (IOSA) [9]. When the rotational motion is adiabatic with respect to the relative translational motion of the molecule and a colliding particle, the projectile effectively interacts with a molecule that has no rotational angular momentum. Such a physical situation allows the complete decoupling of the diatomic rotational and projectile orbital angular momenta in the scattering system and leads to an enormous simplification in the equations of motion. Hence, the rotationally summed cross sections only depend on the initial ground rotational state. The Hamiltonian contains only a vibrational kinetic energy operator as a “signature” of the molecular target, but also depends parametrically on the molecular orientation which is fixed during the collision. The pertinent angle, γ , is defined as the angle between the reaction coordinate R (from the center of mass of the diatom to the projectile nucleus) with the diatomic internuclear axis. But since the adiabatic triatomic molecular surfaces, on which the collision dynamic evolves at these energies, are not isotropic with respect to γ , especially at small internuclear distances, one needs to calculate the observables for different angles γ and then average them for the full solid angle. For a particular initial and final vibrational state this is equivalent to the summation of all final excited rotational states and the average of initial rotational states. The calculations need to be repeated for a range of orientations and the resulting cross sections averaged. It has been shown to be strictly valid only for systems with short range rotational coupling. Thus the sudden approximation is most applicable to the neutral-neutral system ($\text{H}+\text{H}_2$) where the anisotropy of the interaction is short-ranged. However, for ion-molecule systems [10, 11] additional caution is needed since the sudden approximation is expected to be valid for the H^++H_2 system above a collision energy of about 3 eV [12, 13], while for lower energies its validity remains undetermined due to the lack of more elaborate calculations or measurements [14, 15]. Nevertheless, since typical rotational energies for H_2 are of the order of 0.01 eV or less, the classical argument of freezing molecular rotations for the duration of the collision for $E > 0.1$ eV indicates that acceptable results may be obtained as long as rotationally averaged cross sections are calculated. This is the approach that we adopt in

this work, on the whole energy range considered, and which we describe in some detail in Section 2.

Some of the existing calculations for H^+H_2 collisions utilize the “time-dependent” or “impact parameter” formalism which assumes a classical or often straight-line motion of the projectile [13]. While the straight-line trajectory method could be an acceptable approximation for small scattering angles, it poorly describes the scattering at larger angles. As demonstrated below, the scattering angles following vibrational excitation for both proton and neutral atom impact are shifted significantly toward larger values in comparison to the behavior displayed by elastic scattering. Thus we chose a fully quantal approach for both the projectile and diatomic vibrational motion, the details of which are given in Section 2.

We present and discuss the results of these calculations in Section 3. In particular, differential and integral elastic and transport cross sections are shown for $\text{H}+\text{H}_2$ and H^+H_2 collisions, for both ground and vibrationally excited states, and compared with relevant existing data. The cross sections for vibrational excitation of several low-lying excited states are also shown. It turns out that the principal mechanism for this process in the H^+H_2 system is well understood [10] and is mainly an effect of “bond dilution” – the temporary depletion of electron density from the molecular bond by the passing proton. The vibrational excitation is caused by the stretching force which acts simultaneously on both of the nuclei of H_2 . This becomes significant at small distances, thus causing the largest contribution to the cross section for large scattering angles. This mechanism is apparently weaker in $\text{H}+\text{H}_2$ scattering and the incident atom interacts predominantly with the nearest atom of the molecule. This is elucidated below through comparison with the elastic cross sections in the $\text{H}+\text{H}$ system, as well as with the dependence on the molecular orientation. The conclusions regarding the present systems are given in Section 5. For clarity, we note here that all collision energies and scattering angles used are given in the center-of-mass system.

Included in this work are both differential and total cross sections, generally computed for ten points per energy decade at $E_{CM} = 10^{0.1j-1}$ eV, $j=0, 20$, and for $E_{CM} > 10$ eV $j=23, 27, 30$, i.e. for the three energies, $E_{CM} \approx 20, 50$, and 100 eV. The differential cross sections are obtained for 768 values of the CM scattering angle $\theta_j = \frac{\pi}{2}(1 + x_j)$ radians, $j=1, 768$, where x_j is the j^{th} zero of the Legendre polynomial $P_{768}(x)$ in the interval $[-1, 1]$. Thus θ_j constitute the set of abscissas for a Gauss-Legendre integration in the interval $[0, \pi]$, used in calculation of the integral cross sections. Concerning different isotopic forms of the constituents of a collision system, we have found that no scaling of differential elastic cross sections can be discovered in the range of energies considered, thus requiring isotope specific calculations.

For the elastic channel, besides the integral cross section $\sigma_{el}^{\nu_i}(E) \equiv \sigma^{\nu_i, \nu_i}(E)$, where ν_j denotes a vibrational quantum statenum, we also calculate the first two moments which are of interest for plasma modelers (see e.g. Ref. [16]). These are the momentum transfer (diffusion) cross section

$$\sigma_{mt}^{\nu_i} = \int d\Omega \frac{d\sigma_{el}^{\nu_i}(E, \theta)}{d\Omega} (1 - \cos \theta) \quad (2)$$

and viscosity cross section

$$\sigma_{vi}^{\nu_i} = \int d\Omega \frac{d\sigma_{el}^{\nu_i}(E, \theta)}{d\Omega} \sin^2 \theta, \quad (3)$$

where $d\sigma_{el}^{\nu_i}(E, \theta)/d\Omega$ is the differential elastic cross section. The main contribution to the integral elastic cross section comes from the forward scattering angles. In contrast, $\sigma_{mt}^{\nu_i}$ is dominated by the backscattering part of the differential cross section, since the weighting factor $(1 - \cos \theta)$ is maximum at $\theta = \pi$. The weighting factor $\sin^2 \theta$ in the viscosity cross section definition, which is maximum at $\theta = \pi/2$ and goes to zero for $\theta \rightarrow 0$ or π , emphasizes the median region of the scattering angles.

No consistent scaling was found in varying isotopic mass of either projectile or a target for differential cross sections. On the other hand, a mass-dependent scaling is found for integral cross section and its moments in both varying isotopic constitution of H_2 molecule and a projectile. This is described in Section 4 of this report.

2. Theoretical framework

As discussed in the Introduction, an *ab initio* numerical solution of the problem is an extremely difficult computational task. This is mainly due to the difficulty in handling the large manifold of ro-vibrational degrees of freedom in the target molecule as well as in accounting for the presence of reactions with interchange of particles. We reduce these difficulties by freezing the diatomic rotations during the collision and truncating the resulting vibrational basis on the ground electronic surface. The analysis that follows gives a further insight into the approximations made and the method used.

The total Hamiltonian of the problem can be written in terms of the nuclear kinetic energy operator T_N and electronic energy operator \mathcal{H}_e

$$\mathcal{H} = T_N + \mathcal{H}_e. \quad (4)$$

Using the Born-Oppenheimer prescription for separation of the fast electronic and slow nuclear motions, one expands the wavefunction in terms of a complete set of eigenfunctions $\Phi_k(\vec{r}, \{\vec{R}_N\})$ of the electronic Hamiltonian for fixed $\{\vec{R}_N\}$ as

$$\Psi = \sum_k f_k(\{\vec{R}_N\}) \Phi_k(\{\vec{r}\}, \{\vec{R}_N\}) \quad (5)$$

where $\{\vec{r}\}$ and $\{\vec{R}_N\}$ are the sets of electronic and nuclear coordinates, respectively, and summation also implies integration over the electronic continuum. Substituting Eq. (5) into the Schrödinger equation for the problem yields a set of coupled partial integro-differential equations for the “nuclear” amplitudes f_k

$$\sum_k H_{jk} f_k + [T_N + E_j(\{\vec{R}_N\}) - E] f_j = 0 \quad (6)$$

where E_j are eigenenergies of the electronic Hamiltonian, E is the total (conserved) energy of the colliding system and H_{jk} are matrix elements of the dynamic (nonadiabatic)

interaction having the structure

$$H_{jk} = -\frac{1}{2} \sum_{N_i} \left\langle \Phi_j \left| \frac{\nabla_{N_i}^2}{m_{N_i}} \right| \Phi_k \right\rangle - \sum_{N_i} \left\langle \Phi_j \left| \frac{\vec{\nabla}_{N_i}}{m_{N_i}} \right| \Phi_k \right\rangle \cdot \vec{\nabla}_{N_i}, \quad (7)$$

and where summation is taken over the set of nuclei $\{N_i\}$ with masses m_{N_i} and $\vec{\nabla}_{N_i}$, $\nabla_{N_i}^2$ are the gradient and Laplacian operator for a nuclear coordinate \vec{R}_{N_i} .

For an ion (or atom) scattering from a diatomic molecule the set of nuclear coordinates may be chosen in terms of the diatomic internuclear separation ρ , the internuclear separation of the ion (or atom) and the diatomic center of the mass, \vec{R} , and the angle γ between \vec{R} and $\vec{\rho}$. For a fixed γ (IOSA) T_N simplifies significantly. That is, this yields for the kinetic energy part of the radial equation the form [8]

$$T_N^{(\ell)} = -\frac{1}{2M} \frac{\partial^2}{\partial R^2} - \frac{1}{2\mu} \frac{\partial^2}{\partial \rho^2} + \frac{1}{2M} \frac{\ell(\ell+1)}{R^2}. \quad (8)$$

where M and μ are the reduced masses of the three-atom and diatomic molecule, respectively, and ℓ is the angular momentum quantum number of the relative projectile-molecule motion. The absence of a diatomic centrifugal energy term is one of the peculiarities of the IOSA.

In order to solve the problem defined above we expand in partial waves the amplitudes $f_k^{(\ell)}$ of the nuclear wavefunctions for each electronic state k in the full set of vibronic wavefunctions $\lambda_\nu^{(k)}(\rho)$, (with $\varepsilon_\nu^{(k)}$ the corresponding eigenvalue); i.e.

$$\left(-\frac{1}{2\mu} \frac{\partial^2}{\partial \rho^2} + E_k(R \rightarrow \infty, \rho) \right) \lambda_\nu^{(k)}(\rho) = \varepsilon_\nu^{(k)} \lambda_\nu^{(k)}(\rho). \quad (9)$$

We note that $E_k(R, \rho, \gamma)$ for finite R does not depend on γ when the projectile is far enough from the diatom, that is, the adiabatic potential is isotropic in that limit. Therefore, with the ansatz

$$f_k^{(\ell)}(R, \rho, \gamma) = \sum_\nu a_\nu^{(k, \ell)}(R, \gamma) \lambda_\nu^{(k)}(\rho) \quad (10)$$

and using Eq. (8) and Eq. (6) yields

$$\left[-\frac{1}{2M} \frac{\partial^2}{\partial R^2} + \frac{1}{2M} \frac{\ell(\ell+1)}{R^2} - (E - \varepsilon_\nu^{(j)}) \right] a_\nu^{(j, \ell)} + \sum_\mu W_{\nu\mu}^{(j)}(R, \gamma) a_\mu^{(j, \ell)} + \sum_{\mu, k} H_{jk}^{(\nu, \mu)}(R, \gamma) a_\mu^{(k, \ell)} = 0 \quad (11)$$

where

$$W_{\nu\mu}^{(j)}(R) = \langle \nu | E_j(R, \rho, \gamma) - E_j(R \rightarrow \infty, \rho) | \mu \rangle \quad (12)$$

and

$$H_{jk}^{(\nu, \mu)}(R, \gamma) = \langle \nu | H_{jk}(R, \gamma, \rho) | \mu \rangle \quad (13)$$

for all electronic states j , and all vibrational states ν and μ . This system of ordinary differential equations is extremely difficult to solve, not so much because of its size, but

rather due to the difficulties in accurately determining all of its matrix elements. Besides, it has to be solved for each orientation angle γ , since the cross sections are to be averaged over it.

With the single electronic surface and IOSA prescriptions the final form of the system of coupled, second order differential equations follows as

$$\left[-\frac{1}{2M} \frac{\partial^2}{\partial R^2} + \frac{1}{2M} \frac{\ell(\ell+1)}{R^2} - (E - \varepsilon_\nu) \right] a_\nu^{(\ell)} + \sum_\mu W_{\nu\mu}(R, \gamma) a_\mu^{(\ell)} = 0 \quad (14)$$

where we omit the index of the electronic surface. This system of equations was solved numerically using Johnson's algorithm [17] of logarithmic derivatives for each angular quantum number ℓ and using the standard plane wave boundary conditions to construct the K-matrix and from it, the S-matrix.

Once the S-matrix is found, the differential cross section for a transition into vibrational state (ν_f) is [8]

$$\frac{d\sigma^{\nu_f, \nu_i}(E, \theta)}{d\Omega} = \frac{1}{8K^2} \sum_\ell \sum_{\ell'} (2\ell+1)(2\ell'+1) P_\ell(\cos\theta) P_{\ell'}(\cos\theta) \int_0^\pi d\gamma \sin\gamma (\delta_{\nu_f, \nu_i} - S_{\nu_f, \nu_i}^{(\ell)}(\gamma)) (\delta_{\nu_f, \nu_i} - S_{\nu_f, \nu_i}^{(\ell')*}(\gamma)) \quad (15)$$

where \vec{K} is the initial projectile momentum, $\delta_{i,j}$ is the Kronecker symbol, $S_{\nu_f, \nu_i}^{(\ell)}$ is the ℓ^{th} angular momentum component of the S-matrix for the transition from the initial (ν_i) to final (ν_f) vibrational state, and θ is the center-of-mass scattering angle. Finally, the total cross section is obtained by integration over the full scattering solid angle Ω , which yields

$$\sigma^{\nu_f, \nu_i}(E) = \frac{\pi}{2K^2} \sum_\ell (2\ell+1) \int_0^\pi d\gamma \sin\gamma \left| (\delta_{\nu_f, \nu_i} - S_{\nu_f, \nu_i}^{(\ell)}(\infty, \gamma)) \right|^2. \quad (16)$$

For the elastic channel (ground vibrational $\nu = 0$, and ground electronic $k = 0$) we also calculate the momentum transfer and viscosity cross sections, integrating numerically the differential cross sections over Ω , weighted with relevant θ -dependent functions (Eqs (2-3)).

3. Results

Specifically, we solved the coupled equations in Eq. (11) for the ground electronic potential surface ($k = 0$) within a truncated set of vibrational states $0 \leq \nu \leq 9$.

Checking the convergence as a function of the number of partial waves ℓ_{max} required consideration of two principal criteria. All nine inelastic (vibrationally excited) channels were included in the calculation until the elastic channel probability stably reached a value of 0.99999 (if it is repeated 10 times for a succession of ℓ -values), defining the quantity $\ell_{\text{max}}^{\text{inel}}$. Except for the highest energies treated, this was far below the convergence in ℓ needed for the elastic channel: the elastic amplitude $S_0^{(\ell)}$ oscillates for a range of large

values of ℓ until it reaches our adopted convergence criteria ($1 - \text{Re}\{S_0^{(\ell)}\} \leq 10^{-5}$, repeated 10 times in succession). The value of ℓ_{max}^{el} depends on collision energy and on the reduced mass of the system. We show typical variations of these quantities in Table I for the mass extremes of the ion-molecule and atom-molecule hydrogen systems. We also note that there is a weak dependence of ℓ_{max} on the molecular orientation (γ).

Table 1. Typical values of the maximum angular momentum quantum number required to reach numerical convergence of the elastic and inelastic scattering amplitude at $\gamma = 60^\circ$.

System	$\text{H}^+ + \text{H}_2$		$\text{T}^+ + \text{H}_2$		$\text{H} + \text{H}_2$		$\text{T} + \text{T}_2$	
E(eV)	ℓ_{max}^{inel}	ℓ_{max}^{el}	ℓ_{max}^{inel}	ℓ_{max}^{el}	ℓ_{max}^{inel}	ℓ_{max}^{el}	ℓ_{max}^{inel}	ℓ_{max}^{el}
0.1		56		90		42		68
1	41	153	80	257	17	98	38	183
5	152	326	277	561	144	191	255	358
10	251	455	443	787	209	216	367	472
100	1189	1314	2168	2406	649	649	1132	1132

Three additional numerical convergence parameters are important in the calculation. These are the minimum and maximum values of the reaction coordinate R , and the step size of the numerical mesh. In all cases $R_{\text{min}} = 0.05$ a.u., while $R_{\text{max}} = 40$ and 15 a.u. for the ion-molecule and atom-molecule cases, respectively. The step size was varied between 0.0001 and 0.001 a.u., depending on the energy and the reduced mass of the system considered.

Significant attention was paid to obtain reliable potential surfaces $E_j(R, \rho, \gamma)$. For the atom-molecule systems, only the ground (lowest in energy) potential surface was needed, which is not the case for the ion-molecule systems. In the latter, there is a strong avoided crossing between the two lowest potential surfaces at $\rho \simeq 2.6$ a.u., for all $R > \sim 4.5$ a.u. This is a consequence of the fact that when $\rho > 2.6$ the $\text{H}^+ + \text{H}_2$ surface is above the charge transfer surface $\text{H} + \text{H}_2^+$ when $R \rightarrow \infty$. When $R \rightarrow \infty$ the $\text{H}^+ + \text{H}_2$ surface becomes a function of only the diatomic coordinate ρ , i.e. $(\text{H}^+ + \text{H}_2)(R \rightarrow \infty, \rho, \gamma) \rightarrow \text{H}_2(\rho)$. On the other hand, $(\text{H} + \text{H}_2^+)(R \rightarrow \infty, \rho, \gamma) \rightarrow \text{H}(1s) + \text{H}_2^+(\rho)$. Thus if the neutral molecule is in a high enough ($\nu \geq 4$) vibrational state, then upon the approach of the projectile H^+ to the H_2 target, a diabatic transition is made to the lower adiabatic surface. To account for the effect of this curve ‘‘crossing,’’ we performed the calculation with the adiabatic surfaces transformed to the diabatic representation with the correct boundary conditions [9].

We have calculated the adiabatic surfaces for the ground state and the first excited state of H_3^+ utilizing a 54-state (11s,6p) Gaussian basis in the Unrestricted-Hartree-Fock-(full)-Configuration-Interaction (UHF-CI) approach using GAMESS [18]. The calculation was performed on a numerical mesh with a 0.1 a.u. steps in ρ between 0.2 and 6 a.u. and in R between 0 and 15 a.u., and for diatomic orientation angles $\gamma = 0, 10, 20, 30, 40, 50, 60, 70, 80, 90^\circ$, and taking advantage of the symmetry about $\gamma=90^\circ$. At larger R we approximated the potential with dipole and polarization corrections. The surfaces were

compared with the calculations of Ichihara [19] (who used a larger basis but in a narrower range of coordinates), and agreement was found to within 1.5% for the ground state (lower) surface. The adiabatic-diabatic transformation was performed using the nonadiabatic radial matrix elements determined by the Diatom-In-Molecule (DIM) method (see e.g. Ref. [9, 8]). This approach is quite accurate for values of R larger than 2 a.u. (i.e. for R even smaller than value for which the “seam” of avoided crossings occurs).

The vibrational wavefunctions of all vibrational states were found by numerical solution of the radial Schrödinger equation, Eq. (9), for vibrational quantum numbers $0 \leq \nu \leq 9$, for all relevant molecules (H_2 , HD, D_2 , HT, DT, and T_2). Although we included as many as nine excited vibrational states in order to compute the elastic cross section correctly, and since for $\nu \geq 4$ excited states of the ground electronic surface are in some instances quasis resonant (and in most cases, exothermic) with some of the vibrational states of H_2^+ , our differential cross sections for vibrational excitation for $\nu \geq 4$ might not be very accurate at the higher collision energies. Nevertheless, the elastic (ground) vibrational state is relaxed with the presence of these excited states enough to produce accurate elastic cross sections, which are the principle subject of this work.

This problem of charge transfer is not present in the collisions of the molecule with neutral projectiles although other serious problems emerge in these cases due to the high degree of symmetry present in the $\text{H}+\text{H}_2$ system. This is reflected in difficulties in calculating even the ground adiabatic potential surface accurately as well as in a strong particle interchange channel present in the dynamic regime. We used the same basis as in the H^++H_2 case to calculate the ground potential surface for $R, \rho \leq 1$ a.u., for various γ using the UHF-CI method. This is then smoothly continued to the excellent analytical surface fit of Boothroyd [20], for $R \leq 10$ a.u., and continued for large R with the analytic asymptotic potential of the van der Waals type [10, 11].

Figure 1 shows our results for the integral elastic, momentum transfer, and viscosity cross sections for scattering of H^+ and H on the ground vibrational state of H_2 . For elastic cross sections we present both results for scattering on the ground vibrational state and summed over the vibrational excitation (i.e. $\sum_{\nu_f=1}^9 \sigma_{el}^{\nu_f,0}$). For H^++H_2 we find an excellent agreement with the values given by Baer [8] at 20 eV. He calculated these cross sections by solving the Schrödinger equation numerically within the IOSA with full inclusion of vibrational motion on both the H_2 and H_2^+ surfaces, thus including charge transfer. The major approximation made by Baer is the DIM approximation for both ground and excited potential surfaces of H_3^+ as well as for the nonadiabatic couplings. Nevertheless, comparison of his differential cross sections for vibrational excitation and for vibrationally resolved charge transfer with experimental results [15] indicates that the DIM approximation at 20 eV collision energy describes correctly the important parts of the potential surfaces and interactions. No data in the energy range considered are available for comparison with our results for $\text{H}+\text{H}_2$. We note that the vibrationally summed cross section does not deviate more than 10% from the one on the ground vibrational state.

In the energy range considered, since the elastic differential cross section is strongly peaked in the forward direction, the momentum transfer cross section is always significantly smaller than the integral elastic cross section. For $\text{H}+\text{H}_2$ the data available for comparison with our results are those recommended by Phelps [3] for the momentum transfer

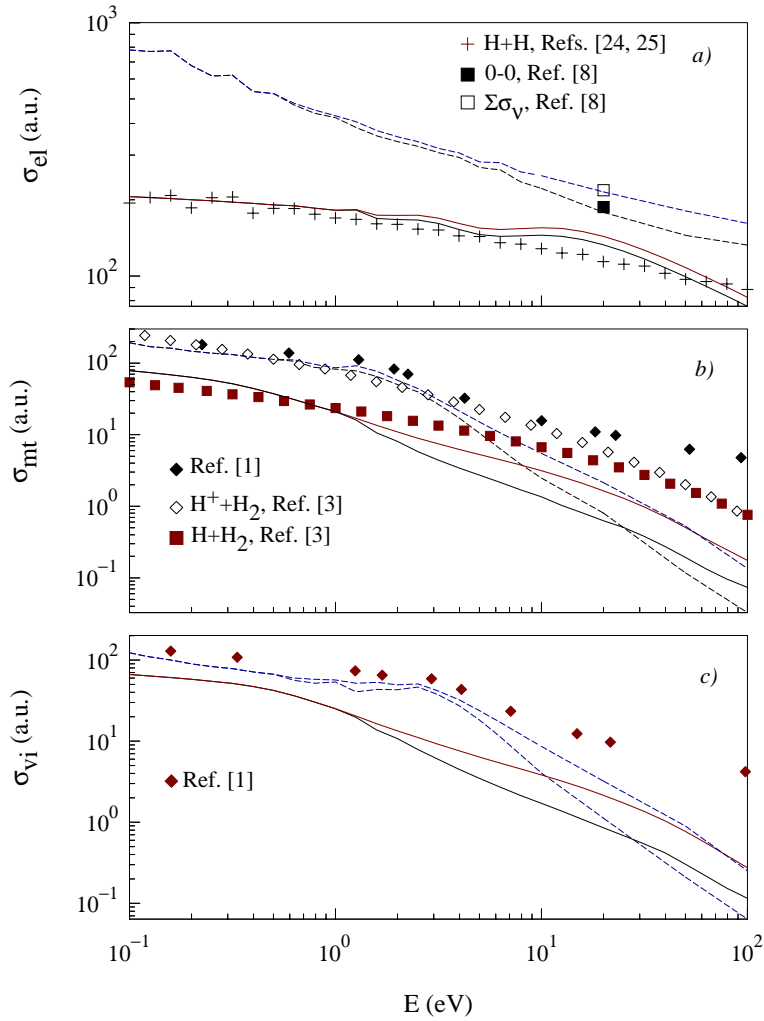


FIG. 1. Scattering of H^+ (dashed curve) and H (solid curve) on H_2 in the ground vibrational state: a) Elastic, b) momentum transfer, and c) viscosity integral cross sections. Lower curves are obtained from the elastic differential cross section ($\nu_f = \nu_i = 0$). The upper curves are obtained from sums over the elastic and final excited vibrational differential cross sections (“scattering on the ground electronic state”). Comparison with existing results from the literature is noted in the figure.

cross section, obtained by interpolation of the measured data of Lynch and Michael [21] at about 0.1 eV and theoretical data of Newman *et al.* [22] for energies above 500 eV. For collision energies below 1 eV the Phelps data are in good agreement with ours (within 20%). At higher energies, where vibrational excitations become important, depleting the ground state, the Phelps data overestimate ours by up to one order of magnitude. Somewhat improved agreement is obtained if we sum momentum transfer cross sections over all vibrational states, thus defining the cross section for scattering on the ground electronic surface.

Phelps also derived a recommended curve for the momentum transfer cross section for H^++H_2 collisions in the range of energies $0.067 \leq E \leq 6670$ eV. The only data contributing to that recommendation that were obtained from experiments (on ion mobility) are for $E < 2.3$ eV. These data were then interpolated up to the cross sections of Smith

et al. [23], obtained for energies above 330 eV. As discussed by Phelps, the resulting curve is about an order of magnitude above the quantum mechanical calculations of Giese and Gentry [10] for energies of a few tens of eV. Our curve for scattering on the ground vibrational state is in good agreement with that of Phelps in the range of the measured data (below 3 eV). At the lowest energies, below 0.2 eV, this curve slightly diverges from our result. At high energies the Phelps curve is more than an order of magnitude above our results and about 5 times above our momentum transfer cross section summed over vibrationally excited states. The classical calculations of Bachmann and Reiter [1], which do not take into account the vibrational structure of H₂, overestimate the Phelps curve at high energies by almost an order of magnitude, but agree with both Phelps and our curve at lower energies, where vibrational excitation is negligible.

We expect that in the gap between the data used by Phelps there is a steeper decline of the momentum transfer cross section, caused by the regime of strong and resolvable vibrational excitations. The fact that we have not taken into account the vibrational states of the charge transfer channel does not influence the conclusion. This would effectively increase the number of excited vibrational states and thus make the minimum even deeper. Phelps also drew several qualitative conclusions regarding the behavior of the momentum transfer cross section that are consistent with our results. For example, he noted that at high energies (about 100 eV), the cross sections for both H and H⁺ scattering on the ground electronic surface of H₂ approach each other, reflecting simply the size of the target H₂ molecule, averaged and appropriately weighted over all excited vibrational states.

Figure 1*c*) displays our results for the viscosity cross section compared with the classical results of Bachmann and Reiter [1]. Unlike the elastic cross section (not shown in this figure), the momentum transfer and viscosity cross sections in classical calculations are not dependent on the choice of an arbitrary cutoff parameter that is required to make the cross section finite. Thus, the cross sections are in reasonable agreement with our results up to several eV. Beyond this energy, they remain too large, similar to the behavior of the classical momentum transfer cross section since, among other differences, the classical calculation does not take into account any vibrational structure of the molecular target. As for the momentum transfer cross section, the viscosity cross sections summed over ν_f for both H⁺ and H projectiles almost coincide at the high end of the energy range.

We note that in general both the elastic cross section and its transport moments are larger for H⁺ than H projectiles at lower energies. This is especially pronounced for the elastic cross section since it is dominated by the small scattering angles and thus, large impact parameters, where the differences between the polarization (for H⁺) and van der Waals potentials (for H) are strong. The differences are smaller in the momentum transfer and viscosity cross sections, since these are dominated by the behavior at large scattering angles, where the target properties dominate the character of the scattering during the close approach of the projectile.

It is also very interesting to note the striking similarity of the elastic cross sections for H+H₂ and H+H [24–26], also shown in Figure 1*a*). This implies that the basic physical mechanism in scattering of H on H₂ is the interaction of the incident atom with the nearest atom of the molecule. In contrast, the well established mechanism for excitation, and thereby for the intimately connected elastic scattering of H⁺ on H₂, is the effect of “bond dilution,” as discussed in the Introduction. Due to the long range polarization

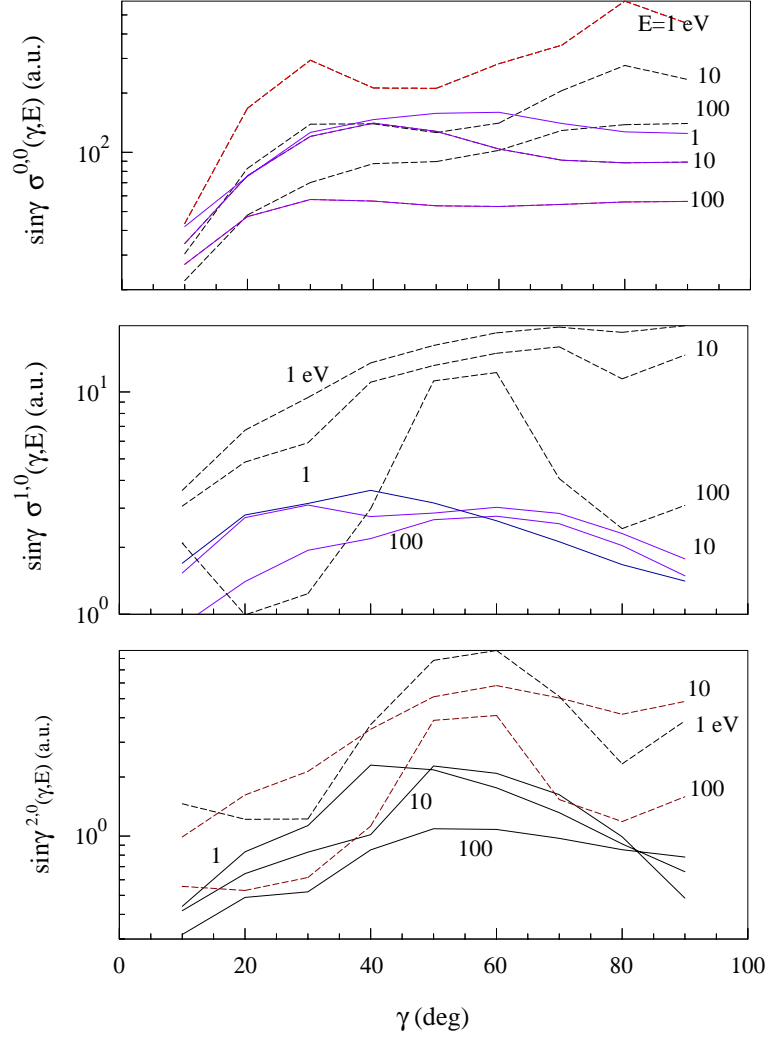


FIG. 2. Integral a) elastic, b) excitation into the the first excited vibrational state, $\nu_f = 1$, and c) excitation into $\nu_f = 2$ cross sections for scattering of H^+ (dashed curve) and H (solid curve) on $H_2(\nu_i = 0)$ as functions of the target orientation angle γ , for various center-of-mass collision energies.

forces, absent in the $H+H_2$ case, the proton acts simultaneously with both atoms in the molecule, causing a maximal contribution from scattering when the molecular orientation is almost perpendicular to the incident direction. To support this conclusion, we show in Figure 2 the integral cross sections weighted by the factor $\sin \gamma$ that is used to average over molecular orientations (see Eq. (14)), for both the elastic and first two vibrational excitations of H_2 . These are shown as functions of γ , for various collision energies. For H^++H_2 , the maximum contribution to the averaged cross section indeed tends to come from large values of γ , for both the elastic and inelastic cross sections. In contrast, for the $H+H_2$ case, contributions to the cross section tend to minimize at the largest values of γ . It comes predominantly from the nearly collinear geometries.

A comparison between our differential cross sections for elastic scattering of H and H^+ on the ground vibrational state of H_2 is shown in Figure 3 for several collision energies. The other available theoretical data for H^++H_2 , that of Schinke *et al.* [12, 11] and Baer *et al.* [8], and the experimental data of Hermann *et al.* [14] and Niedner *et al.* [15], show

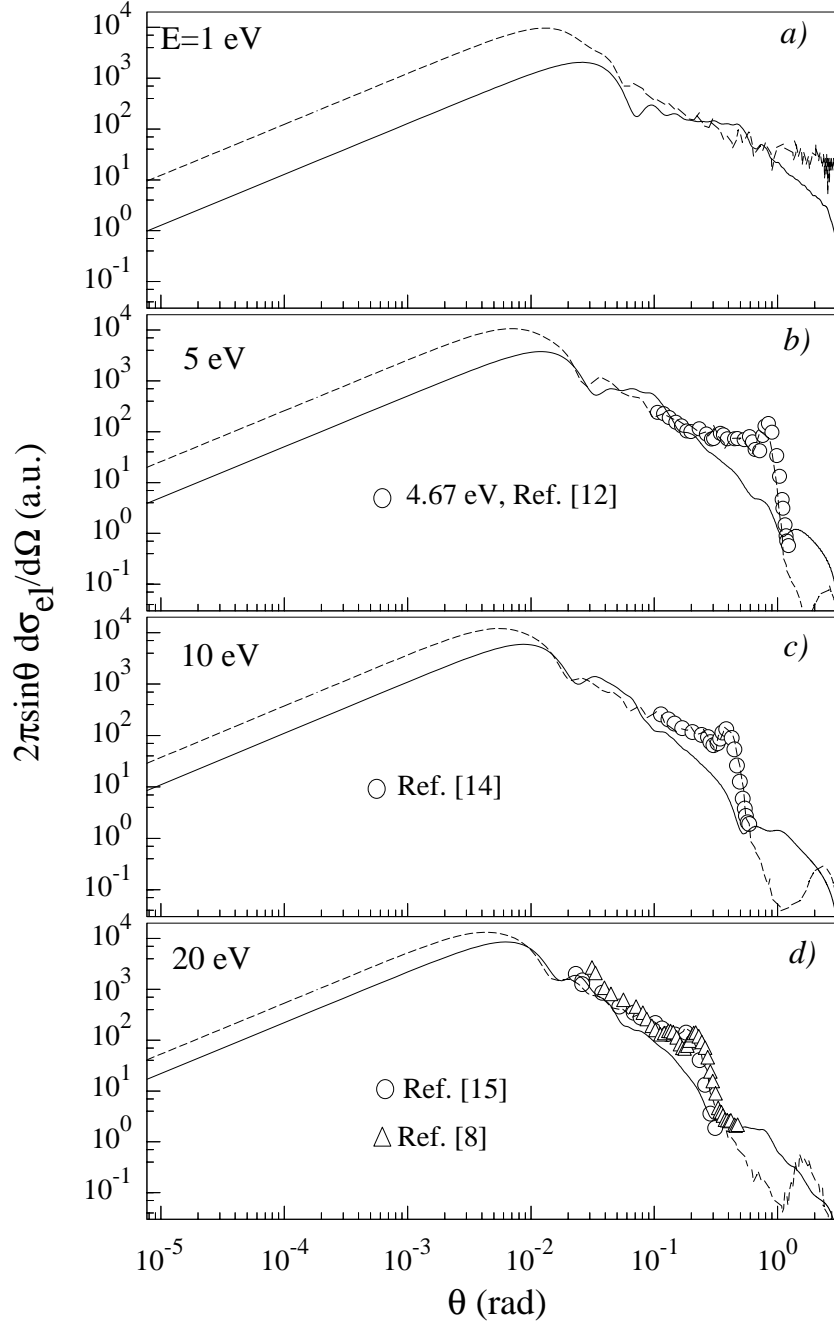


FIG. 3. Differential elastic cross section for scattering of H^+ (dashed curves) and H (solid curves) on the $H_2(v_i = 0)$ for various collision energies. Comparison with the existing results from the literature is noted in the figure.

good agreement with our fully quantal calculations. Both the Schinke *et al.* and Baer *et al.* calculations were performed using the IOSA approximation. Some deviations from our results toward small scattering angles in the Baer calculation can be explained by the insufficient number of angular momenta Baer used (about 250 compared to about 600 that we found to be needed for convergence of the elastic amplitudes at a collision energy of 20 eV). The deviations at larger scattering angles might be attributed to inaccuracy of the DIM potentials at small internuclear distances. The pronounced rainbow in the $H^+ + H_2$ cross sections is not present in the $H + H_2$ cases. A small structure is present in

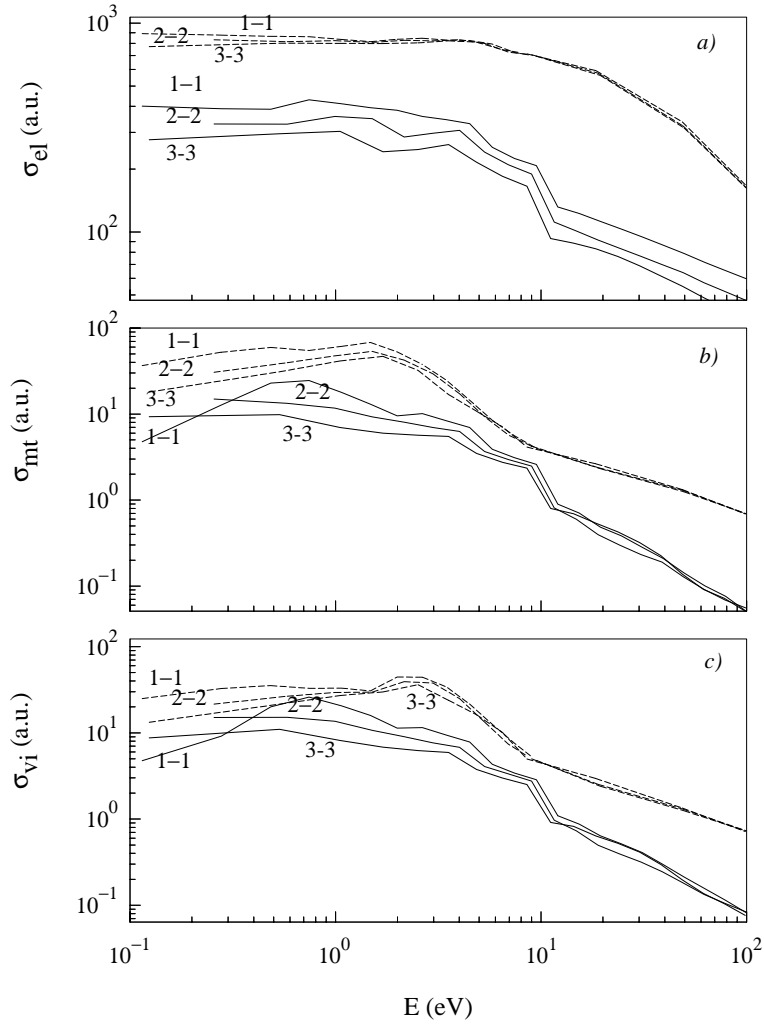


FIG. 4. Scattering of H^+ (dashed curves) and H (solid curves) on $H_2(\nu_i)$, for the first three initially excited vibrational states, $\nu_i = 1, 2, 3$. Integral a) elastic, b) momentum transfer, and c) viscosity cross sections.

the latter case, for smaller angles. In both cases the rainbow flattens and moves toward smaller angles with increase of the collision energy, as expected. At the smallest scattering angles, the H^+ scattering has a larger cross section compared to that for H scattering, due to the presence of the polarization potential in the former case.

The elastic, momentum transfer, and viscosity cross sections for scattering of H and H^+ on the three lowest vibrationally excited states of $H_2(\nu_i)$, $\nu_i=1,2,3$ are shown in Figure 4. A general characteristic of the elastic cross sections for $\nu_i > 0$ is that they are somewhat larger than the one on the ground state and that they show a sudden drop in the region in which vibrational excitation becomes significant. The momentum transfer and viscosity cross sections are somewhat smaller than the corresponding quantities for $\nu_i=0$. In most of the cases, the largest cross sections are those for $\nu_i=1$, and there is continuous decrease with increase of ν_i . All these features are a consequence of the competition between the varying size of the target (i.e. the spatial size of the electronic wavefunction increases with increasing ν_i) and the change in the “bond dilution” effect on one hand, and of the role and degree of vibrational excitation and deexcitation on the other.

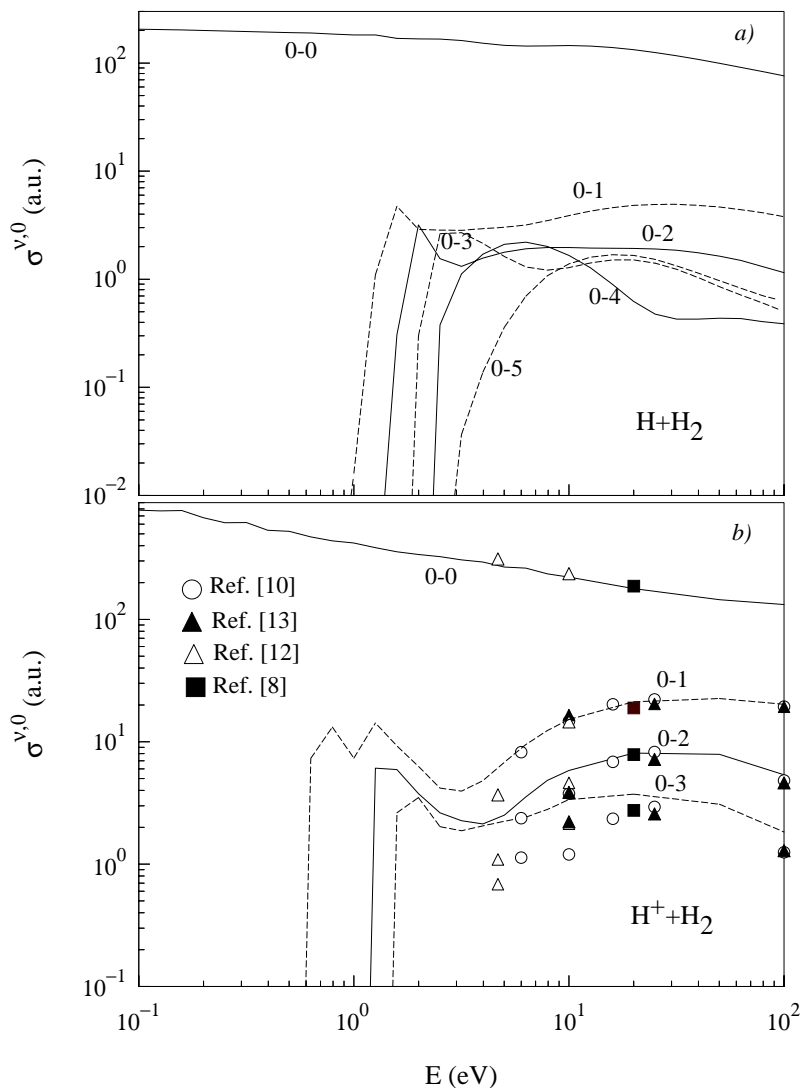


FIG. 5. Integral cross sections for vibrational excitation in scattering of a) H^+ , and b) H on H_2 in the ground vibrational state. Dashed and solid curves alternate in the figure for clarity. Comparison with existing data in the literature is noted in the figure.

Figure 5 illustrates the behavior of the integral cross sections as a function of collision energy for vibrational excitation in $H+H_2$ and H^++H_2 collisions, starting from the ground vibrational state ($\nu_i = 0$). In the former case, although the elastic cross section is almost two orders of magnitude larger, the inelastic cross sections for various ν_f are closer to one another at higher energies, with the obvious dominance of the $\nu_f=1$ case. For each ν_f , the cross section has its maximum for energies above its respective threshold, but decreases after the next ν_f -channel is open, resulting in a local minimum of the $(\nu_f - 1)$ -channel. Qualitatively, a similar behavior of the excitation cross sections is displayed by the results for the H^++H_2 system, the differences being attributed to the varying basic mechanisms of excitation in the two systems. That is, the principal excitation mechanism for ion impact is the perturbation of the electronic distribution of the molecule by the proton, which may extend to large values of the reaction coordinate, while for atom impact, the direct collision of the projectile with the closest atom in the molecule is mainly responsible for the reaction. As a consequence, for H^++H_2 in the threshold region, the cross sections

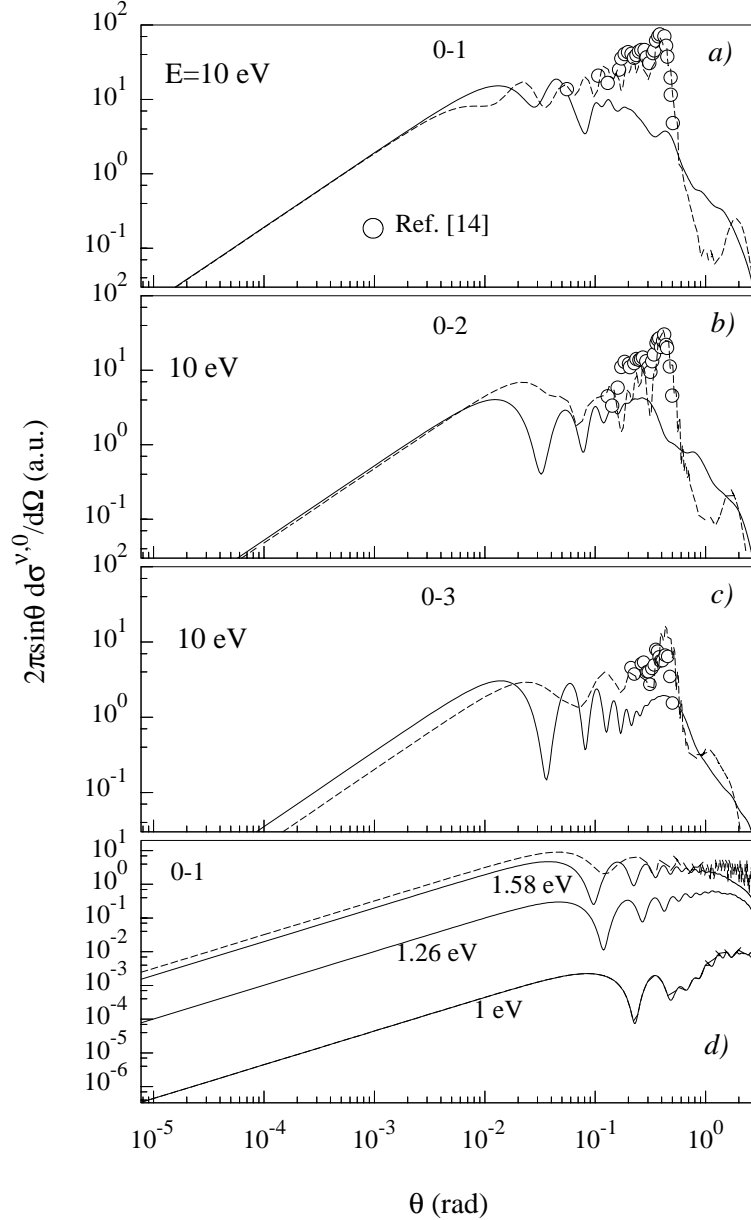


FIG. 6. Differential cross sections for vibrational excitation of $H_2(\nu_i = 0)$ in collision with H^+ (dashed line) and H (solid line). Comparison with the experimental data of Hermann *et al.*[14] is indicated in the figure. a) $\nu_f = 1$, 10 eV, b) $\nu_f = 2$, 10 eV, c) $\nu_f = 3$, 10 eV, and d) $\nu_f = 1$, 1 eV, 1.26 eV and 1.58 eV.

reach their maxima much faster and obtain somewhat larger values. Also regarding the $H^+ + H_2$ system, the differences between the cross sections for different ν_f 's are also larger, but with obvious dominance of the $\nu_f=1$ case at larger energies.

Also in Figure 5, we compare our results for $H^+ + H_2$ elastic and inelastic collisions with those available in the literature and note that we are not aware of any available data for $H + H_2$. The agreement of our fully quantal calculations with the other data is good at all energies for the elastic and first excited state, but deteriorates with decreasing collision energy and increasing values of ν_f . Since all of the results displayed, including the present one, have been performed using the IOSA, the disagreement might be attributed to the

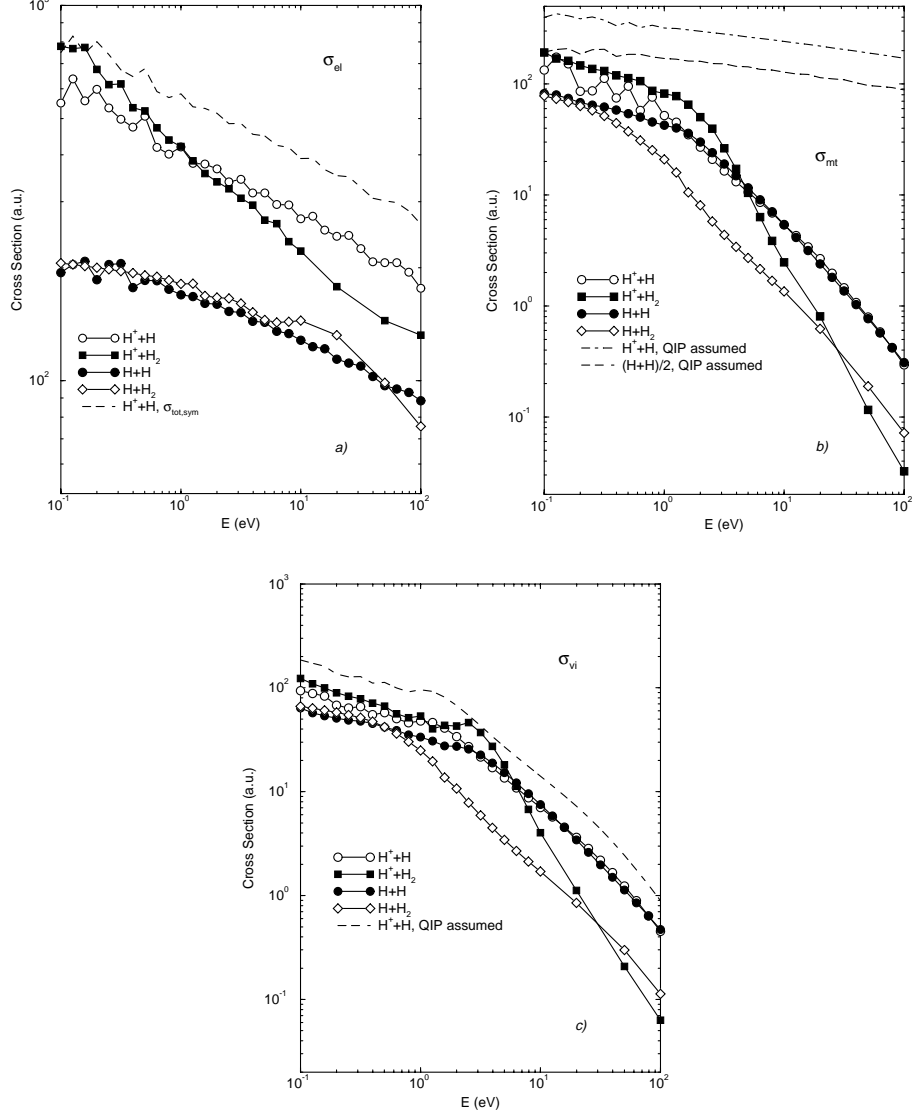


FIG. 7. Integral elastic, momentum transfer and viscosity cross sections for scattering of H^+ and H on H_2 in the ground vibrational state, compared with relevant quantities of other collision systems as noted. Cross sections denoted with “QIP” (quantum indistinguishability of particles) are for symmetric systems [25, 24], and include charge transfer (for $H^+ + H$) or recoil of the target (for $H + H$).

absence of H_2^+ vibrational states in our calculations which might influence the distribution of excited states at higher energies. It might also be attributed to the use of imprecise analytically fitted electronic surfaces [10] in the works of Giese and Gentry [10] and Schinke *et al.* [12, 13], in the use of the classical DECENT approach defined by and used by Giese and Gentry [10], in the use of the straight-line trajectory method by Schinke *et al.* [13], and in the inadequacy of the DIM electronic surfaces at small internuclear distances [8].

Comparison among our differential cross sections for vibrational excitation from $H_2(\nu_i=0)$ to $H_2(\nu_f=1,2,3)$ by H and H^+ impact at a collision energy of 10 eV is presented in Figure 6. Also shown is that the present $H^+ + H_2$ results are in good agreement with the absolute experimental data of Hermann *et al.* [14] for various ν_f . This occurs despite the poor agreement for $\nu_f=2,3$ with other theoretical integral vibrational excitation cross sections

at lower energies (Figure 5b). An obvious characteristic of the inelastic cross sections displayed in comparison to the elastic cross section is the dominance of the large scattering angles, reflecting the role of the small impact parameters in vibrational excitation. The pronounced rainbow at $\theta \sim 0.4$ rad for the $H^+ + H_2$ system is mainly responsible for the larger values of the excitation cross sections in comparison to the $H + H_2$ case. Figure 6 also shows the behavior of the differential cross sections for $H + H_2$ for several energies close to but above the first excitation threshold ($\nu_f=1$). For $E \sim 1.58$ eV we note that the differential cross section almost coincides with the corresponding cross section for the $H^+ + H_2$ case. For lower energies, the curves representing the differential cross section shift in a parallel fashion toward larger values with increase of energy.

Figure 7 shows comparison of our data [25, 24, 6, 7] for the integral elastic (σ_{el}), momentum transfer (σ_{mt}) and viscosity (σ_{vi}) cross sections for various cases considered (ion-atom, ion-molecule, atom-atom and atom-molecule hydrogen systems). Besides high extent of similarity in $H + H$ and $H + H_2$ elastic cross sections in the whole energy range, similarity to the lesser extent is evident also for $H^+ + H$ and $H^+ + H_2$.

Most of the momentum transfer cross sections for various system types do not deviate from each other by more than a factor of 2.

Viscosity cross sections are very similar for energies lower than 1 eV. At higher energies, when the vibrational excitation channels open, the cases with molecular targets deviate from the ion-atom and atom-atom systems. Finally, at higher energies, well above 100 eV, when the vibrational structure of the molecule plays a lesser role in the collision dynamics, the viscosity cross sections with like projectiles are expected to become similar.

4. Scaling relations

The scaling of the integral elastic cross section and its higher moments for H_2 targets show similar scaling with collision energy and reduced mass as in cases of ion-atom and atom-atom systems, except to account for differences in the vibrational couplings and energies. Surprisingly, after averaging over the diatomic orientations, the elastic cross sections scale well with the system's reduced mass if only the projectile is varied. For a fixed projectile mass the cross section does not depend significantly on the details of the isotopic composition of the molecular target, and no scaling is needed, especially if the collision energy is above 0.3 eV. Figure 8a illustrates these behaviors, combining various projectiles with all six isotopic combinations of H_2 . Thus, for variation of the projectile isotope and for variation of the target isotopomers, respectively, we have

$$\begin{aligned}\sigma_{el}^{A^+ + BC}(E) &= \sigma_{el}^{H^+ + H_2}\left(\frac{\mu_0}{\mu_{ABC}}E\right), A \neq H \\ \sigma_{el}^{A^+ + BC}(E) &= \sigma_{el}^{A^+ + H_2}(E)\end{aligned}\tag{17}$$

where μ_0 is the reduced mass of $H^+ + H_2$. The deviations from the $H^+ + H_2$ curve do not exceed 20% over the whole energy range. These drop to less than 5% for energies close to 100 eV, when the collision time becomes short in comparison to the characteristic vibration time of the target.

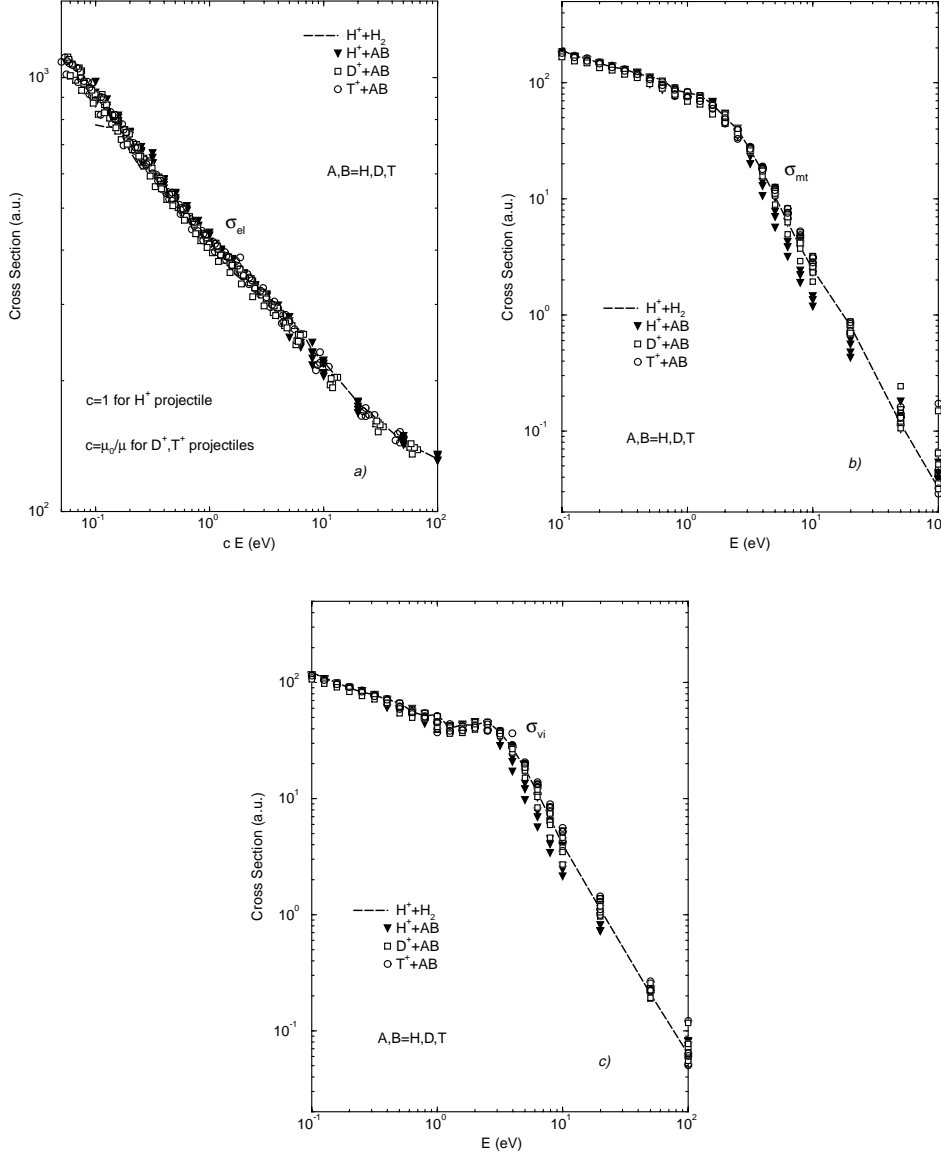


FIG. 8. Scaling of integral a) elastic, b) momentum transfer, and c) viscosity cross sections in collisions of hydrogen ions with hydrogen molecules in the ground vibrational state, varying isotopes in both projectile and target.

All the momentum transfer cross sections almost coincide at energies lower than 2 eV (Figure 8b). The curves deviate up to a factor of 3 for energies about 10 eV, where the vibrational transitions are most active. This deviation decreases toward higher energies, as with the elastic cross sections, when the momentum transfer cross section becomes very small and population of the vibrational excited states high. The dispersion in that range may also be attributed to possible convergence errors caused by the implemented truncation of the sum over vibrational states which produces the most pronounced uncertainty for large scattering angles that affect most the momentum transfer cross section. Thus

$$\sigma_{mt}^{A^++BC}(E) = \sigma_{mt}^{H^++H_2}(E) \quad (18)$$

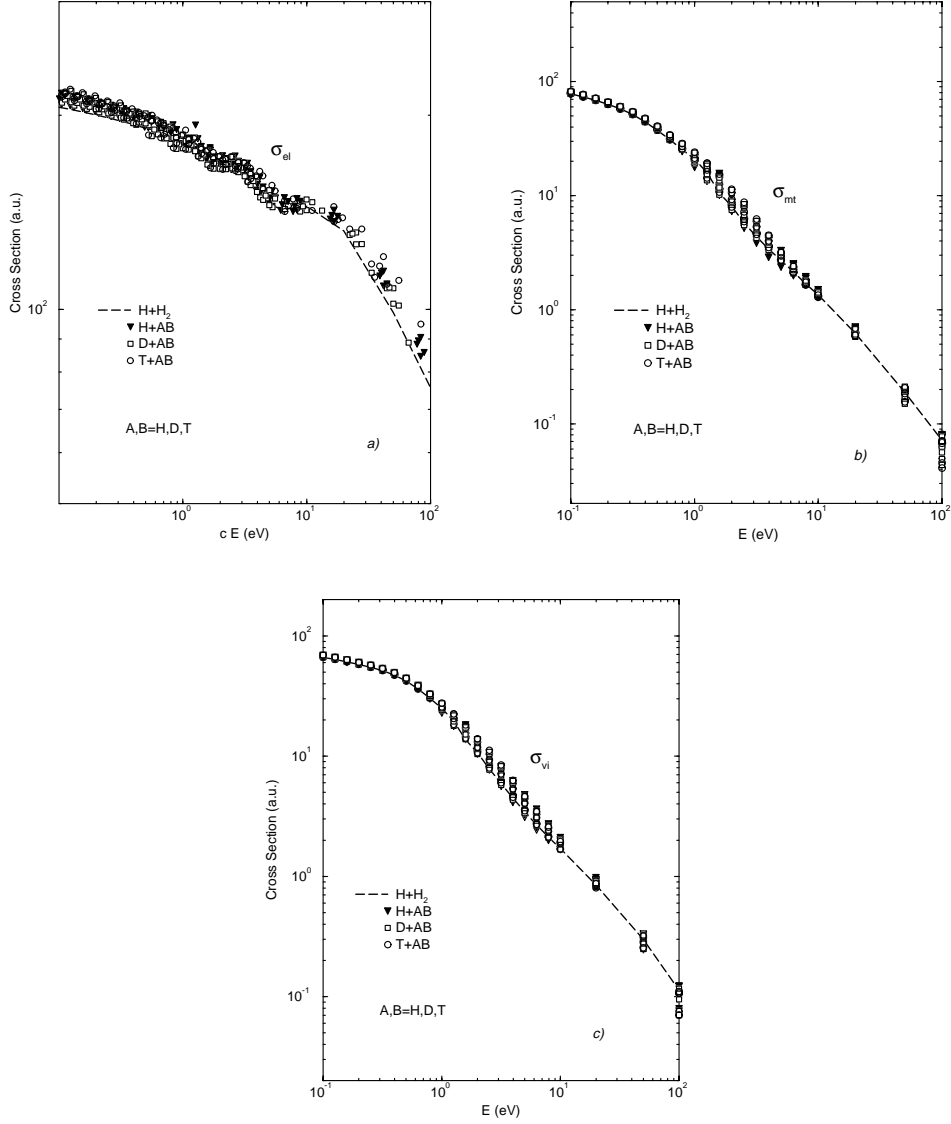


FIG. 9. Scaling of integral a) elastic, b) momentum transfer, and c) viscosity cross sections in collisions of hydrogen atoms with hydrogen molecules in the ground vibrational state, varying isotopes in both projectile and target.

for all A, B , and C .

Figure 8c shows the viscosity cross sections for all of the isotopic variants. Similar to the momentum transfer case, the curves start to deviate above 2 eV, where the details of vibrational excitations are reflected in the mid-range and backward part of the differential cross sections. The deviation decreases toward higher energies. Thus we have

$$\sigma_{vi}^{A^++BC}(E) = \sigma_{vi}^{H^++H_2}(E) \quad (19)$$

for all A, B , and C .

The collisions of neutral atoms with neutral molecules retain the properties similar to cases of ion-molecule systems. Unlike the ion-molecule case, the best scaling is reached for the elastic cross sections if it is performed using the reduced masses for all cases,

irrespective of the projectile. This is illustrated in Figure 9a. In this case

$$\sigma_{el}^{A+BC}(E) = \sigma_{el}^{H+H_2}\left(\frac{\mu_0}{\mu_{ABC}}E\right) \quad (20)$$

for all A, B , and C .

The momentum transfer and viscosity cross sections coincide, and no scaling is needed, as shown in Figures 9b and 9c. Thus

$$\begin{aligned} \sigma_{mt}^{A+BC}(E) &= \sigma_{mt}^{H+H_2}(E) \\ \sigma_{vi}^{A+BC}(E) &= \sigma_{vi}^{H+H_2}(E). \end{aligned} \quad (21)$$

We note that the dispersion of the results is smaller than in the ion-molecule case, and does not exceed 30% in the vibrationally active region of collision energies (except at 100 eV) for both momentum transfer and viscosity cross sections. For the elastic cross section, the deviations are quantitatively similar to the ion-molecule cases.

5. Conclusions

We have presented the first comprehensive study of elastic scattering of H on H₂ in the range of center of mass collision energies of 0.1-100 eV, based on fully quantal calculations and with the inclusion of vibrational excitation only, while rotational dynamics is treated within the IOSA. In the absence of pre-existing, benchmarking calculations, we have also treated the elastic and vibrationally inelastic scattering of H⁺ on H₂, favorably comparing with the data available in literature for this system. In addition, due to their utility for plasma modeling, transport cross sections as well as scattering on excited vibrational states have also been calculated. We have found that the vibrational excitation cross sections for the H+H₂ system display features not present for H⁺+H₂ collisions. The dominant scattering mechanism for H+H₂ is identified as scattering of the projectile on the closest atom in molecule, in contrast to the H⁺+H₂ system, where both elastic scattering and vibrational excitations are governed by perturbation of the electronic distribution of the molecule by the passing proton.

We note that an analysis and description of the relevant scaling of the integral cross sections for scattering of H⁺ and H on H and He in various isotopic combinations is presented elsewhere [25, 24] as are fitting coefficients for all of the differential and integral cross sections for ease of use in plasma modeling applications [7]. The calculated data for differential and integral cross sections discussed in the present work as well as those for the various isotopic combinations can be viewed and downloaded from the web site of the Controlled Fusion Atomic Data Center at Oak Ridge National Laboratory, www-cfadc.phy.ornl.gov.

The establishment of the detached plasma regimes in the divertor, which is essential for minimization of plasma-divertor plate interaction and the associated material erosion and material properties degradation effects, can be facilitated by inclusion of certain fast volume plasma recombination mechanism. One of the reaction schemes proposed is the so-called ‘‘ion conversion’’ scheme[27], which involves capture of electron by proton from a vibrationally excited H₂, followed by dissociative recombination of H₂⁺ with a plasma electron. Lack of cross sections for this and many other processes involving excited molecular states does not presently allow one to construct the collision-radiative model for the

H₂/H gas. Therefore, these processes should be a central focus in future research in atomic physics for fusion.

This work has been supported by the U.S. Department of Energy, Office of Fusion Energy Sciences, at Oak Ridge National Laboratory which is managed by UT-Battelle, LLC under contract DE-AC05-00OR22725, and performed in conjunction with the IAEA Co-ordinated Research Project (CRP) on “Atomic and Plasma-Wall Interaction Data for Divertor Modeling”.

REFERENCES

- [1] BACHMANN, P., REITER, D., *Contr. Plasma Phys.* **35**, 45 (1995).
- [2] JANEV, R.K., editor, *Atomic and Molecular Processes in Fusion Edge Plasmas* (Plenum, New York, 1995).
- [3] PHELPS, A.V., *J. Phys. Chem. Ref. Data* **19**, 653 (1990).
- [4] BACHMANN, P., BELITZ, H.J., Max Planck Institut für Plasmaphysik Report IPP 8/2 (1993).
- [5] SCHULTZ, D.R., OVCHINNIKOV, S.YU., PASSOVETS, S.V., *Atomic and Molecular Processes in Fusion Edge Plasmas*, JANEV, R.K., editor (Plenum, New York, 1995), p. 279.
- [6] KRSTIĆ, P.S., SCHULTZ, D.R., *J. Phys. B* **32**, 2415 (1999).
- [7] KRSTIĆ, P.S., SCHULTZ, D.R., Atomic and Plasma-Material Interaction Data for Fusion (Supplement to the journal *Nuclear Fusion*) **8** (1998).
- [8] BAER, M., NIEDNER-SCHATTEBURG, G., TOENNIES, J.P., *J. Chem. Phys.* **91**, 4169 (1989).
- [9] BAER, M., NIEDNER, G., TOENNIES, J.P., *J. Chem. Phys.* **88**, 1461 (1988); BAER, M., *State-Selected and State-to-State Ion-Molecule Reaction Dynamics, Part 2: Theory*, BAER, M., NG, C.-Y., editors, in *Advances in Chemical Physics* **LXXXII**, 187 (1992); BAER, M., NAKAMURA, H., *J. Chem. Phys.* **66**, 1363 (1987); MONCHICK, L., MASON, E.A., *J. Chem. Phys.* **35**, 1676 (1961); KOURI, D.J., in *Atom Molecule Collision Theory*, BERNSTEIN, R.B., editor (Plenum Press, New York, 1979).
- [10] GIESE, C.F., GENTRY, W.R., *Phys. Rev. A* **10**, 2156 (1974).
- [11] SCHINKE, R., DUPUIS, M., LESTER, JR., A., *J. Chem. Phys.* **72**, 3909 (1980), and references therein.
- [12] SCHINKE, R., McGUIRE, P., *Chem. Phys.* **31**, 391 (1978).
- [13] SCHINKE, R., *Chemical Physics* **24**, 379 (1977).
- [14] HERMAN, V., SCHMIDT, H., LINDER, F., *J. Phys. B* **11**, 493 (1978).
- [15] NIEDNER, G., NOLL, N., TOENNIES, J.P., *J. Chem. Phys.* **87**, 2685 (1987).
- [16] McDANIEL, E.W., *Collision Phenomena in Ionized Gases* (John Wiley & Sons, New York, 1964); *Atomic Collisions: Heavy Particle Projectiles* (John Wiley & Sons, New York, 1993).
- [17] JOHNSON, B.R., *J. Comp. Phys.* **13**, 445 (1973).
- [18] SCHMIDT, M.W., BALDRIDGE, K.K., BOATZ, J.A., ELBERT, S.T., GORDON, M.S., JENSEN, J.H., KOSEKI, S., MATSUNAGA, N., NGUYEN, K.A., SU, S.J., WINDUS, T.L., DUPUIS, M., MONTGOMERY, J.A., *J. Comput. Chem.* **14**, 1347 (1993).

- [19] ICHIKARA, A., YOKOYAMA, K., J. Chem. Phys. **103**, 2109 (1995).
- [20] BOOTHROYD, A.I., KEOGH, W.J., MARTIN, P.G., PETERSON, M.R., J. Chem. Phys. **95**, 4343 (1991).
- [21] LYNCH, K.P., MICHAEL, J.V., Int. J. Chem. Kinetics **10**, 233 (1978).
- [22] NEWMAN, J.H., CHEN, Y.S., SMITH, K.A., STEBBINGS, R.F., J. Geophys. Res. **91**, 8947 (19856); NEWMAN, J.H., CHEN, Y.S., SMITH, K.A., STEBBINGS, R.F., J. Geophys. Res. **94**, 7019 (1989).
- [23] SMITH, K.A., JOHNSON, L.K., GAO, R.S., STEBBINGS, R.F., in *Abstracts of Contributed Papers for the International Conference on the Physics of Electronic and Atomic Collisions*, edited by GEDDES, J., GILBODY, H.B., KINGSTON, A.E., LATIMER, C.J., WALTERS, H.R.J., (North-Holland, Amsterdam, 1987), p. 681.
- [24] KRSTIĆ, P.S., SCHULTZ, D.R., Phys. Rev. A **60**, 2118 (1999).
- [25] KRSTIĆ, P.S., SCHULTZ, D.R., J. Phys. B **32**, 3485 (1999).
- [26] JAMIESON, M.J., DALGARNO, A., ZIGELMAN, B., KRSTIĆ, P.S., SCHULTZ, D.R., Phys. Rev. A **61**, 014701 (2000).
- [27] JANEV, R.K., Contrib. Plasma Phys. **38**, 307 (1998).

Calculations of charge transfer and ionization cross-sections in collisions between multicharged ions and atomic hydrogen

C. Harel^a, H. Jouin^a, B. Pons^a, L.F. Errea^b, J.D. Gorfinkiel^b, C. Illescas^b, A. Macías^{b,c}, L. Méndez^b, A. Riera^b

^aCentre Lasers Intenses et Applications, Université Bordeaux I, Cours de la Libération, Talence, France

^bDepartamento de Química C9, Univeritad Autónoma de Madrid, Madrid, Spain

^cInstituto de Estructura de la Materia, CSIC, Madrid, Spain

1. Introduction

Currently, chemical species with nuclear charges $Z < 8$ are found in the plasmas of operating tokamak devices, at temperatures depending on their location: in the plasma core, ion temperatures up to a few keV/amu are observed whereas close to the walls they are much lower (down to energies of a few eV/amu). As is well known, charge transfer between these impurities and hydrogen leads to the formation of excited states of the residual ions whose decays contribute significantly to cooling of plasma.

We have performed molecular close coupling calculations for total and state selective electron capture cross sections in collisions between bare nuclei with charges $Z \leq 8$ and atomic hydrogen- H(1s) and H(2s)- for the nuclear projectile energy range $62.5 \text{ eV/amu} < E < 25 \text{ keV/amu}$. In the same impact energy range, we have also started a systematic study of collisions between He-like projectiles and ground atomic hydrogen.

In addition, CTMC calculations have been carried out for the same systems for impact energies up to 2.5 MeV/amu for ionisation and for impact energies up to 625 keV/amu for charge transfer.

2. Theory

We have used a molecular close coupling treatment which is known to provide reliable total and state selective electron capture cross sections for ion atom collisions in the low impact energy range (Harel and Jouin, *J.Phys.B*.**21**, 859, 1988). A full quantal treatment has been used for lower impact energies ($E < 0.1 \text{ keV/amu}$); at higher impact energies, a semiclassical treatment with rectilinear trajectories for nuclear motion has been found accurate. A common reaction coordinate formalism (quantal treatment) or a common translation factor (semiclassical treatment) are used to account for the electron momentum transfer during the collision. A detailed presentation of the present theoretical approach can be found in Errea *etal* (*J.Phys.B***31**, 3527, 1998) (see also L.F.Errea *etal*, *J.Phys.B***27**, 3603, 1994). At very high impact energies ($E > 25 \text{ keV/amu}$) we have employed an impact parameter CTMC formalism with a hydrogenic initial distribution (see for details, Illescas and Riera, *J.Phys.B***31** 2777, 1998).

Energies and couplings of the quasi-molecules are calculated using a One Electron Diatomic Molecule basis set. In the case of non bare nuclei (He-like ions) the effect of the $1s^2$ electronic

core on the active electron is taken into account using a model potential approach as proposed in Harel and Jouin (J.Phys.B.21 (1988) 859), and compact gaussians orbitals are added to the molecular expansions to improve the accuracy of the molecular data that is required at low impact velocities ($v < 0.2$ a.u.) (see L.F. Errea *et al.*, J.Phys.B32, L673, 1999). For $C^{2+} + H$ collisions the molecular wavefunctions have been obtained using a self-consistent-field multireference configuration-interaction method.

3. Results

3.1. Ion-atom molecular close coupling calculations

All the results obtained for total and partial (n and state selective) cross sections for electron capture by fully stripped ions colliding with atomic hydrogen have been tabulated and published in Atomic Data and Nuclear Data Tables **68**, 279, 1998. Sufficiently large basis sets have been used to insure a very good accuracy of the results. Also, some fundamental aspects have been discussed in various publications as the use of common coulombic trajectories for the nuclear motion and the limit of validity of the semiclassical approach at low impact energies or the use of H_2^+ -like orbitals together with a model potential description for the effect of an $1s^2$ core on the active electron in the case of He-like multicharged impinging projectiles.

As an illustration of our calculations we present, for each collisional system, a figure showing variations of total and n-partial cross sections as a function of the impact velocity.

H^+ -H(1s) collisions

The molecular basis includes all states correlating to excitation and capture channels up to $n=6$, (112 states); n-partial and state selective cross sections have been calculated for $n=1-4$

He^{2+} -H(1s) collisions

The molecular basis includes all states correlating to excitation and capture channels up to $n=3$ and 6 respectively (66 states). n-partial and state selective cross sections have been calculated for $n=1-4$.

C^{2+} -H(1s) collisions

We have calculated charge transfer and spin-change cross sections in $C^{2+}(^1S, ^3P)+H(1s)$ reaction. Cross sections calculated with a basis of 30 molecular states are tabulated in (Errea *et al.* J. Phys. B **33**, 1369 2000). The main conclusion of our calculation is that the effect of contamination of ground state beams by metastable species would only be important for $E < 1$ keV.

Li^{3+} -H(1s) collisions

The molecular basis includes all states correlating to excitation and capture channels up to $n=2$ and 7 respectively (88 states); n-partial and state selective cross sections have been calculated for $n=2-5$.

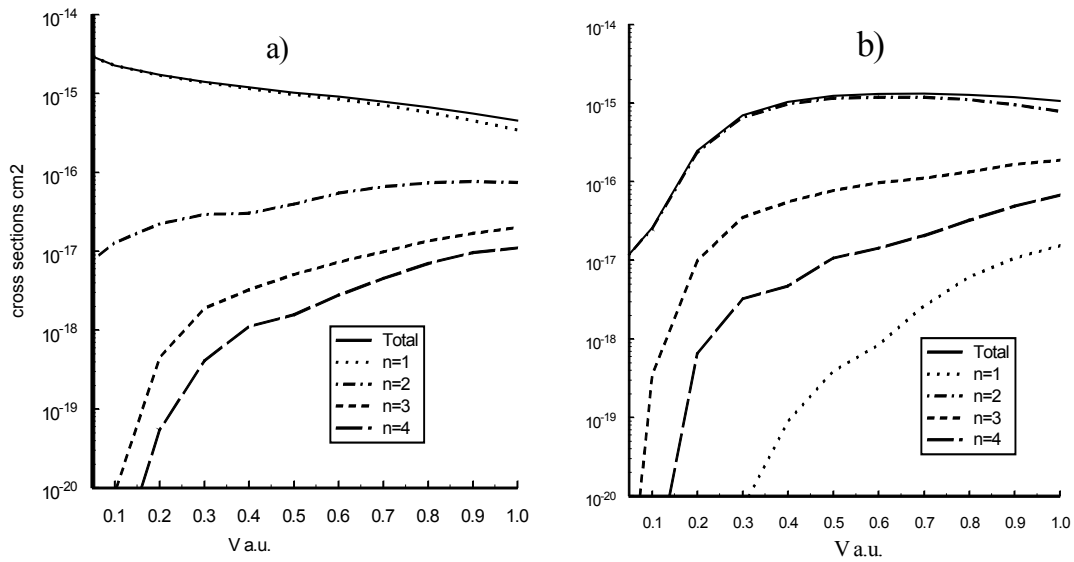


Figure 1. Total and n -partial cross sections as a function of impact velocity: a) $H^+ - H$, b) $He^{2+} - H$.

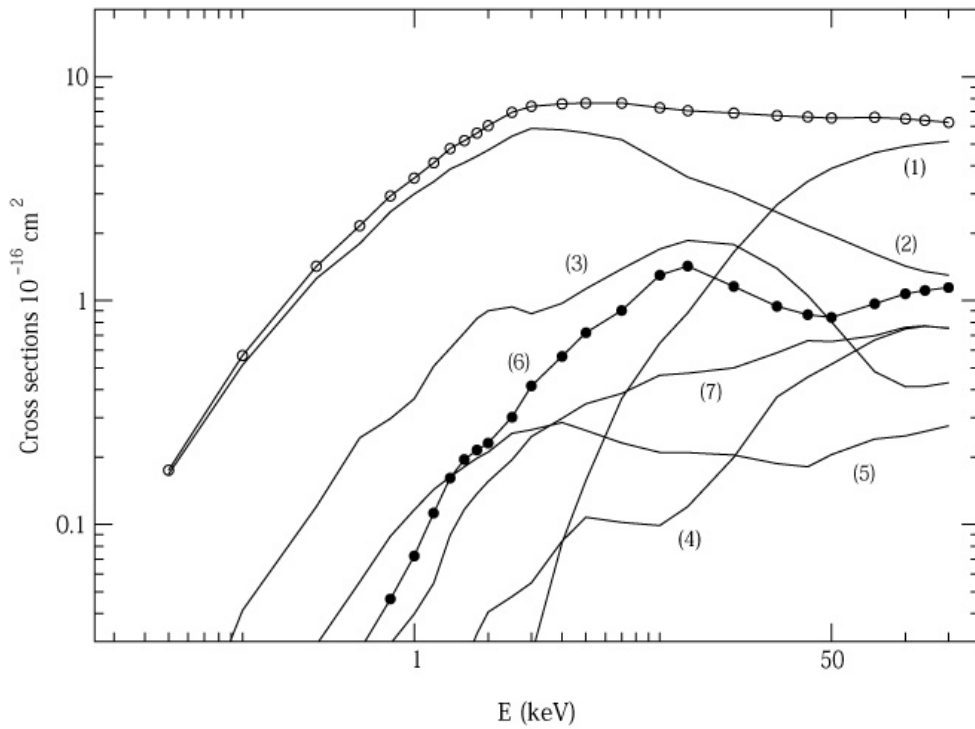


Figure 2. Total cross sections for charge transfer in $C^{2+}(^1S) + H(1s)$ collisions ---o---, and partial cross section to channels (1) $^2P(2s^22p)$, (2) $^2D(2s2p^2)$, (3) $^2S(2s2p^2)$, (4) $^2P(2s2p^2)$, (5) $^2S(2s^23s)$, (6) ---●--- excitation to $^3P(2s2p)$, (7) $^2P(2s^23p)$.

Be⁴⁺ -H (1s), H(2s) collisions

The molecular basis includes all states correlating to excitation and capture channels up to n=2 and 7 respectively (*88 states*). Cross sections are tabulated for n=2-5.

A comparison between quantal and semi-classical calculations has shown that for $v < 0.03$ a.u. ($E < 22.5$ eV/amu) a full quantal treatment was necessary; moreover, the use of a common coulombic trajectory for the nuclear motion doesn't improve the semiclassical results: a better agreement has been found between the quantal results and the rectilinear trajectories ones than with the results from a Coulomb trajectory calculation.

C⁴⁺ -H (1s) collisions

Total and partial cross sections for capture onto n=3,4 have been calculated for impact energies from 10 eV to 25 keV. An improvement of the model potential description of the effect of the 1s² core on the active electron using an OEDM basis set has allowed very accurate calculations of total and state selective cross sections, even at very low impact energies (L.F. Errea *et al* *J.Phys.B***32**, L673, 1999).

B⁵⁺ -H (1s) collisions

The molecular basis includes all states correlating to excitation and capture channels up to n=2 and 7 respectively (*88 states*); n-partial and state selective cross sections have been calculated for n=3-6.

C⁶⁺ -H(1s) collision

The molecular basis includes all states correlating to capture channels up to n=8 (121 states); n-partial and state selective cross sections have been calculated for n=3-6.

N⁷⁺, O⁸⁺ -H(1s) collisions

The molecular basis includes all states correlating to capture channels from n=4 to n=7 and the states of symmetry m=0, 1 and 2 correlating to n=8 and 9 capture channels (*129 states*); n-partial and state selective cross sections have been calculated for n=4-7.

3.2. Ion-atom CTMC calculations:

Total and n-partial electron capture cross sections as well as ionisation cross sections have been calculated for bare ions (H⁺, He²⁺, Li³⁺, Be⁴⁺, B⁵⁺, C⁶⁺, N⁷⁺ and O⁸⁺)-H(1s) collisions using the improved impact parameter CTMC treatment developed by Illescas and Riera and are tabulated in (Phys.Rev.A**60**, 4546, 1999). As an illustration of our results figure 5 shows variations of total capture cross sections for charges of the incident ion $1 \leq q \leq 8$.

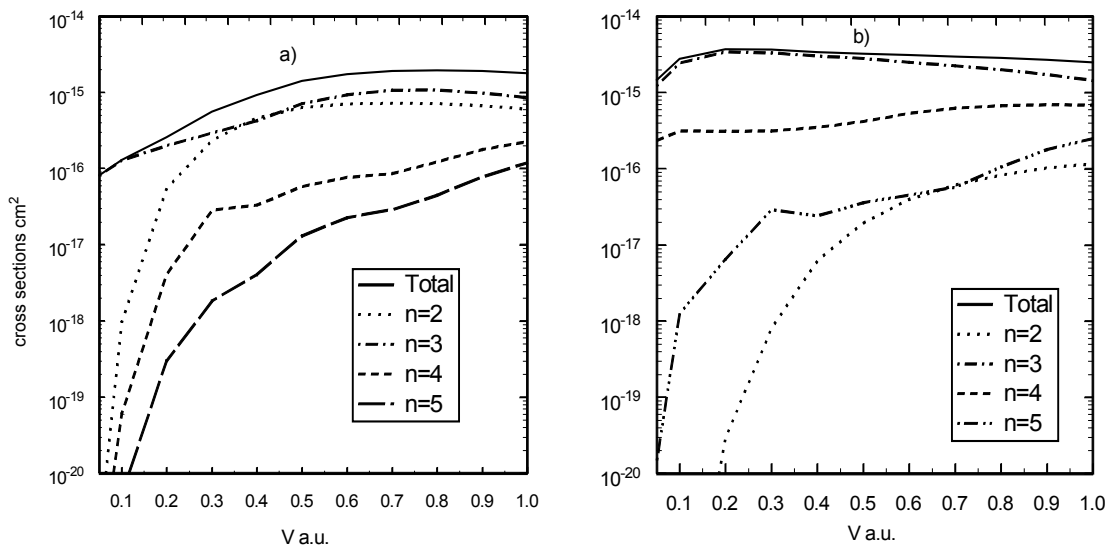


Figure 3. Same as figure 1: a) $\text{Li}^{3+}\text{-H}$; b) $\text{Be}^{4+}\text{-H}$.

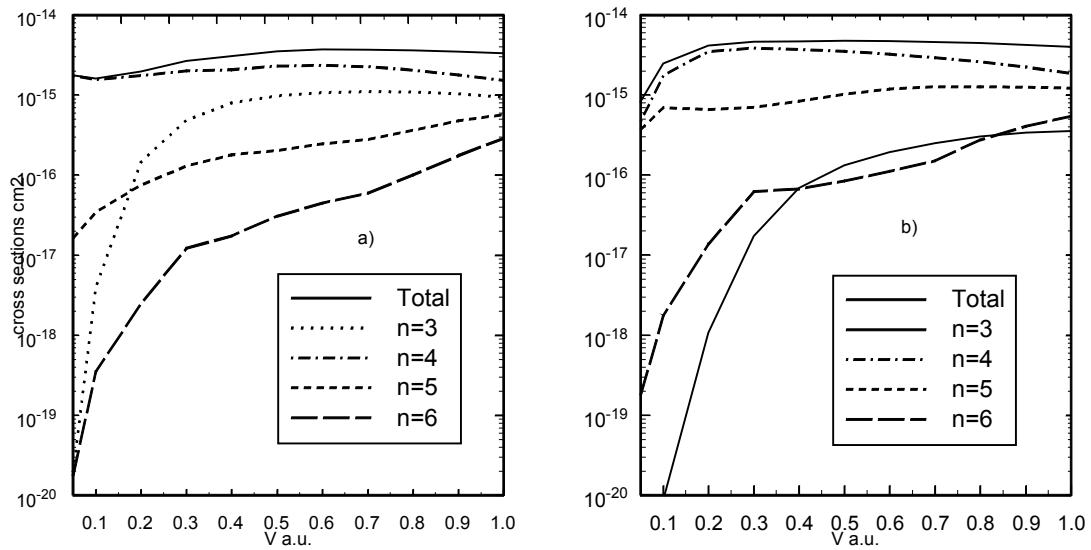


Figure 4. Same as figure 1: a) $\text{B}^{5+}\text{-H}$; b) $\text{C}^{6+}\text{-H}$.

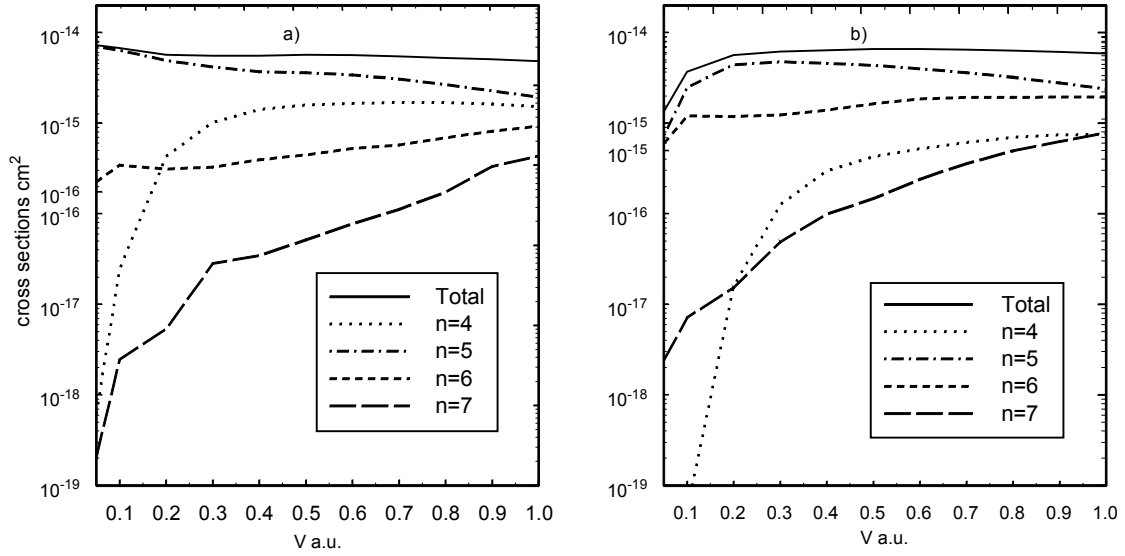


Figure 5. Same as figure 1: a) N^{7+} -H; b) O^{8+} -H.

This work has allowed to obtain scaling law for capture and ionisation cross sections as a function of the charge q of projectile for an impact velocity v :

$$\sigma_{ion}(q, v) = \sigma_{ion}(1, v) q^{2[1 - e^{(-1.4(v - 0.76 - 0.04q))}]}$$

$$\sigma_c(q, v') = \sigma_c(2, v) \left(\frac{q}{2}\right)^{1.15} \quad \text{with} \quad v' = v \left(\frac{q}{2}\right)^{0.175}$$

Moreover, we have shown that these laws allow to calculate cross sections in the case of dressed projectiles carrying a charge q : for ionisation the previous law has been found valid for $v > v_{max}$ (velocity for which the ionisation cross section present a maximum) whereas for capture the corresponding scaling is valid on the whole range investigated by the CTMC approach ($0.6 \text{ a.u.} < v < 8 \text{ a.u.}$) for $q > 1$.

4. Conclusion

Calculations involving non bare Helium-like nuclei are now in progress according with our plans for the CRP.

In parallel, during the last few years we have extended our field of research in two directions:

- (i) study of ion-atom collisions at intermediate impact energies and treatment of the ionisation process by inclusion of pseudostates in the molecular close coupling approach.
- (ii) neutralisation of slow highly charged ions at metallic surfaces.

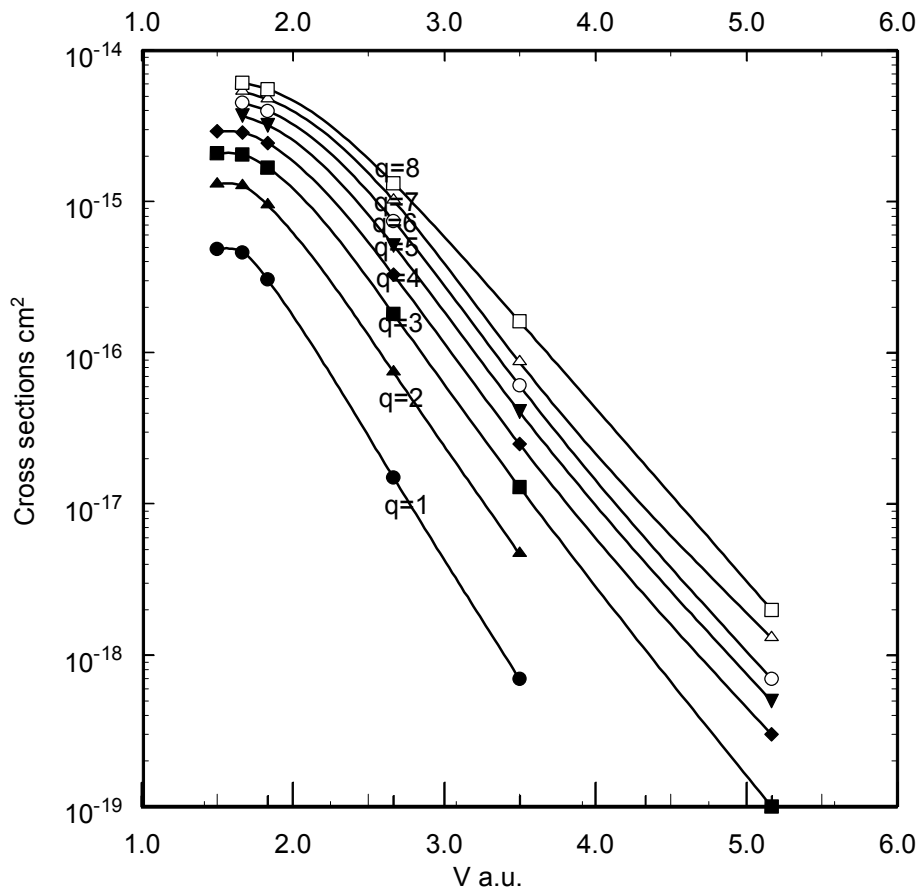


Figure 6. Improved CTMC total capture cross sections as a function of the impact velocity.

Both allow future studies of interest for other aspects of the controlled fusion as, for instance, heating by neutral injection and ions/walls interactions.

BIBLIOGRAPHY

L.F.Errea, J.D.Gorfinkiel, C.Harel, H.Jouin, A. Macías, L.Méndez, B.Pons and A.Riera, *Physica Scripta* **T62**, 27 (1996).

C.Harel, H.Jouin and B.Pons, *Atomic Data and Nuclear Tables* **68**, 279 (1998).

L.F.Errea, C.Harel, H.Jouin, L.Méndez, B. Pons and A.Riera . *J. Phys. B*, 31, 3527 (1998).

L.F.Errea, C.Harel, C. Illescas, H.Jouin, A.Macias, L.Méndez, B. Pons and A.Riera, *J. Phys. B*, 31, 3199 (1998).

C.Illescas and A.Riera, *Phys.RevA*, 60, 4546 (1999).

J.D.Gorfinkiel, C.Harel, H.Jouin, A.Macias, L.Méndez, B.Pons and A.Riera, *J.Phys B*.32, L673 (1999).

L.F.Errea, A.Macias, L.Méndez and A. Riera, *J. Phys. B*, 33, 1369 (2000).

Calculations of charge transfer and ionisation cross sections for ion-H₂(D₂, DT, T₂) collisions

D. Elizaga, L.F. Errea, J.D. Gorfinkiel, C. Illescas, A. Macías,
L. Méndez, I. Rabadán, A. Riera, A. Rojas, P. Sanz

Departamento de Química, Universidad Autónoma de Madrid,
Madrid, Spain

Abstract. Theoretical (*ab initio* and CMTc) cross sections for charge transfer and ionization in ion-H₂ collisions are presented. Vibrationally resolved cross sections are obtained for certain ions.

1. Introduction

Charge transfer cross sections in collisions of multicharged ions with molecules are of interest in the outer regions of the plasma in fusion devices, particularly near divertors. In this paper we summarize calculated cross sections for collisions of ions with H₂ (also D₂, DT and T₂) for energies above 40 eV/amu.

Our methods are based on the sudden approximation for the treatment of the rovibrational motion of the diatom. In some cases, we have used the additional familiar Franck-Condon (FC) approximation and the cross sections have been obtained from calculations at only the target equilibrium distance ρ_0 . Partial vibrational cross sections can be obtained by multiplying the FC ones by the FC factors of Table 1 [1]. At low velocities, we have employed a close-coupling expansion for the electronic wavefunction in terms of *ab initio* molecular functions (see [2]). In each case, the characteristics of the calculation, such as the basis set, were chosen from consideration of the energy and coupling diagrams [2]–[9]. At high impact energies (9–625 keV/amu for charge transfer and 9 keV/amu–2.5 MeV/amu for ionisation) classical trajectory calculations have been carried out [3].

Comparison with experimental results and other calculations (not shown here) are included in the published papers [2]–[9].

Cross sections are tabulated as a function of the relative impact velocity, v (in a.u.), and the corresponding energies are $E = 24.982 v^2$ keV/amu.

2. H⁺+H₂(X¹Σ_g⁺, ν=0,1)

We have obtained single electron capture (SEC) vibrationally resolved cross section using the sudden approximation. The basis set includes the lowest two states of H₃⁺. SEC cross sections from ν=0 and ν=1 of H₂(X¹Σ_g⁺) are given in Table 2 and plotted in Figure 1.

¹ Also at Instituto de Estructura de la Materia CSIC, Serrano 113 bis, 28006 Madrid, Spain.

State-to-state vibrational cross sections are published in [1], as well as results for D_2 , DT , and T_2 targets.

3. $Li^+ + H_2$

A 5-electronic-state calculation for the system LiH_2^+ was performed [1] in the framework of the FC approximation. Orientation averaged cross sections for SEC and excitation to $H_2(B\ ^1\Sigma_u^+)$ are given in Table 3 and plotted in Figure 2.

4. $C^{2+} + H_2$

13- and 16-state calculations were performed for the ground ($2s^2;^1S$) and metastable ($2s2p;^3P$) states of C^{2+} respectively. The collinear geometry and the FC approximation were employed [5]. Results are shown in Figure 3 and Table 4. More accurate calculations, using the sudden approximation, have been also carried out for collisions with the metastable projectile [6]. In this case, cross sections to individual vibrational states of H_2^+ have been obtained.

5. $C^{3+} + H_2$

Calculations have been carried out using the FC approximation, collinear geometry and a basis of 8 electronic states. Double electron capture (DEC) leading to Coulomb explosion of the diatom is competitive with SEC and the corresponding cross sections are listed in Table 5 and plotted in Figure 4. Preliminary results with a smaller basis were published in [7].

6. $C^{4+} + H_2$

Calculations using the sudden approximation and a basis of 8 electronic states were reported in [8]. Our results include state-selected (vibrational and electronic) cross sections in SEC, as well as cross sections for transfer dissociation and vibrational excitation in collisions with H_2 , D_2 and DT . We give cross sections for SEC into the main exit electronic channels in Table 6 and Figure 5.

7. $N^{5+} + H_2$

A model potential treatment has been used to evaluate the molecular wavefunctions. The Hamiltonian matrix elements between the two-electron wavefunction have been calculated by using the equivalent-electron approximation, as explained in [9]. The dynamical basis includes the entrance channel and 7 SEC channels. Total charge transfer cross sections are given in Table 7 and plotted in Figure 6. Preliminary results and comparison with experimental data were reported in [4].

8. CTMC calculations

We have calculated SEC and single ionisation (SI) cross sections for H^+ , He^{2+} , Li^{3+} , Be^{4+} , B^{5+} , C^{6+} , N^{7+} and O^{8+} in collisions with H_2 , using the improved impact parameter CTMC treatment (see [3]). The calculation employs the FC approximation and a model potential for the H_2 target. Results for SI are plotted in Figure 7 and tabulated in Table 8. The corresponding SEC results are given in Figure 8 and Table 9. As shown in [3], these cross sections can be used at energies beyond the peak values for collisions of dressed ions with H_2 .

Analogously to the ion-atom case, we have obtained scaling laws of the SEC and SI cross sections as functions of the charge q of the projectile and velocity v .

$$\sigma_{SEC}^{scaled}(q, vq^{0.11}) = \sigma_{SEC}(1, v)q \quad (1)$$

$$\sigma_{SI}^{scaled}(q, v) = \sigma_{SI}(1, v)q^2 \{0.92 - \exp[-0.57(v-0.01q)] - \exp[-1.8(v^2-0.08q)]\} \quad (2)$$

9. Concluding remarks

In the last few years, we have developed new methods to treat ion- H_2 collisions with a similar accuracy to those of ion-atom. These methods have been applied to several ions. We plan to extend our calculations to lower velocities of interest in cold regions of fusion plasma. A more detailed treatment of the anisotropy in the ion-target interaction will also be considered. Calculations involving projectiles in both ground and metastable states are being carried out where experimental uncertainties in the composition of the initial beams exist. Collisions with complex, heteronuclear targets is also planned.

Acknowledgements

This research has been partially supported by the DGICYT Project PB96-0056. IR acknowledges MEC for a Contrato de Incorporación de doctores. CI acknowledges MEC for a postdoctoral grant under the program SGPDE.

Table 1. Franck-Condon factors for H₂, D₂, DT and T₂

ν'	H ₂	D ₂	DT	T ₂
0	0.088088	0.032798	0.023775	0.015375
1	0.163359	0.086461	0.068723	0.049741
2	0.181715	0.129654	0.111744	0.089406
3	0.159648	0.146563	0.135583	0.118563
4	0.123301	0.139736	0.137472	0.130021
5	0.088460	0.119268	0.123728	0.125349
6	0.060893	0.094501	0.102574	0.110319
7	0.041047	0.071197	0.080280	0.090900
8	0.027458	0.051864	0.060352	0.071390
9	0.018389	0.036974	0.044134	0.054148
10	0.012398	0.026026	0.031692	0.040062
11	0.008440	0.018211	0.022508	0.029137
12	0.005807	0.012731	0.015899	0.020957
13	0.004033	0.008925	0.011218	0.014979
14	0.002816	0.006293	0.007932	0.010679
15	0.001961	0.004470	0.005635	0.007618
16	0.001342	0.003204	0.004030	0.005450
17	0.000873	0.002318	0.002905	0.003919
18		0.001693	0.002112	0.002835
19		0.001247	0.001550	0.002067
20		0.000925	0.001147	0.001519
21		0.000689	0.000857	0.001125
22		0.000513	0.000644	0.000841
23		0.000378	0.000486	0.000634
24		0.000273	0.000368	0.000481
25		0.000189	0.000277	0.000368
26			0.000206	0.000282
27			0.000148	0.000217
28				0.000167
29				0.000127

Table 2. Cross sections (in units of 10^{-16} cm²) for the reactions $\text{H}^+ + \text{H}_2(\text{X } ^1\Sigma_g^+, \nu = 0, 1) \longrightarrow \text{H} + \text{H}_2^+(\text{X } ^2\Sigma_g^+)$

$v(\text{a.u.})$	$\nu=0$	$\nu=1$
0.045	0.02	0.19
0.063	0.11	0.64
0.089	0.45	1.68
0.100	0.69	2.20
0.141	2.07	4.47
0.200	4.79	7.00
0.300	8.10	9.24
0.400	8.99	9.15

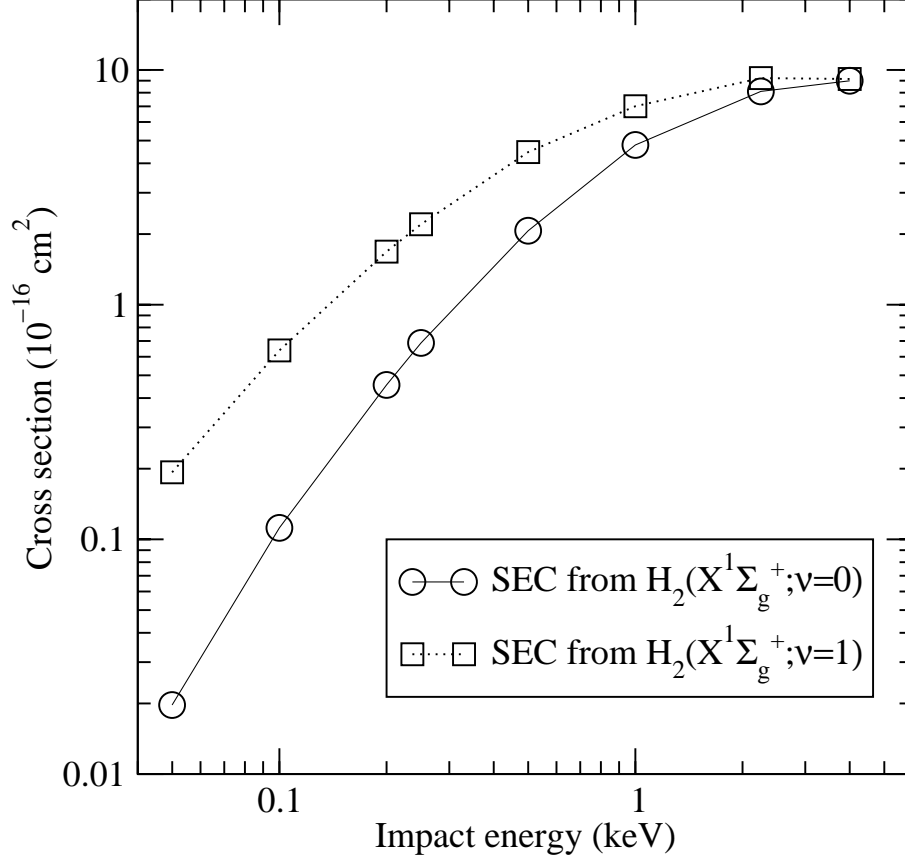


FIG. 1. Cross sections for the reactions $\text{H}^+ + \text{H}_2(\text{X}^1\Sigma_g^+; \nu = 0, 1) \rightarrow \text{H} + \text{H}_2^+(\text{X}^2\Sigma_g^+)$.

Table 3. Cross sections (in units of 10^{-16} cm^2) for the SEC reactions $\text{Li}^+ + \text{H}_2 \rightarrow \text{Li}(2s) + \text{H}_2^+$ and $\text{Li}^+ + \text{H}_2 \rightarrow \text{Li}(2l) + \text{H}_2^+$, and the excitation reaction $\text{Li}^+ + \text{H}_2(\text{X}^1\Sigma_g^+) \rightarrow \text{Li}^+ + \text{H}_2(\text{B}^1\Sigma_u^+)$

$v(\text{a.u.})$	Li(2s)	Li(2l)	H ₂ (B ¹ Σ _u ⁺)
0.063	0.02	0.03	0.04
0.089	0.04	0.10	0.05
0.100	0.07	0.13	0.06
0.141	0.06	0.21	0.06
0.200	0.18	0.48	0.15
0.250	0.29	0.53	0.23
0.300	0.31	0.63	0.27
0.350	0.31	0.79	0.30
0.400	0.41	0.99	0.29
0.500	0.74	1.46	0.23

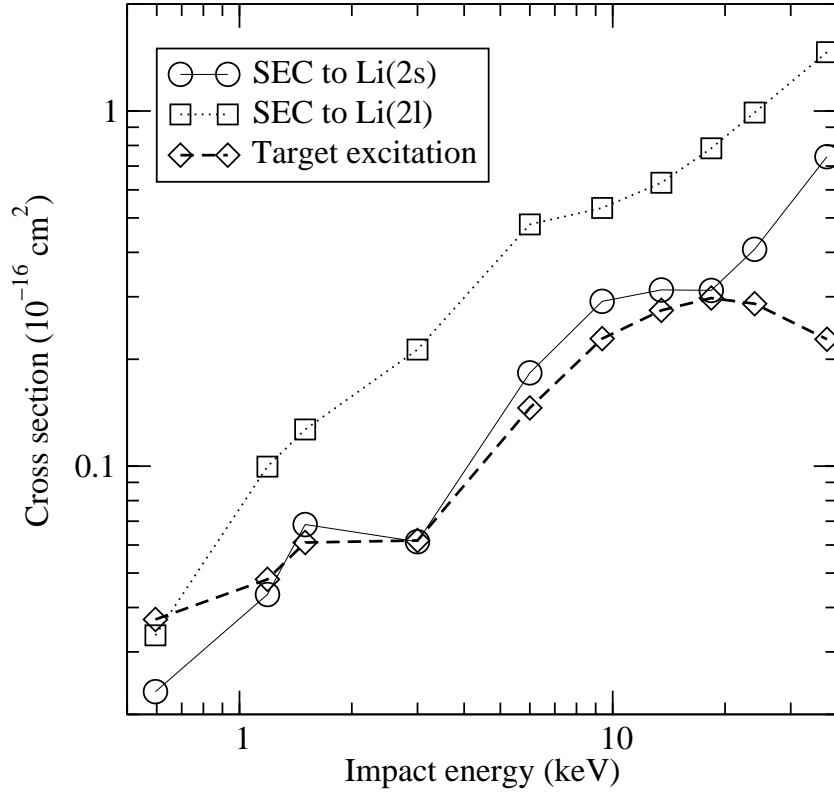


FIG. 2. Cross sections for the SEC reactions $\text{Li}^+ + \text{H}_2 \rightarrow \text{Li}(2s) + \text{H}_2^+$ and $\text{Li}^+ + \text{H}_2 \rightarrow \text{Li}(2l) + \text{H}_2^+$, and the excitation reaction $\text{Li}^+ + \text{H}_2(X \ ^1\Sigma_g^+) \rightarrow \text{Li}^+ + \text{H}_2(B \ ^1\Sigma_u^+)$.

Table 4. FC SEC cross sections (in units of 10^{-16} cm^2) for $\text{C}^{2+} + \text{H}_2(X \ ^1\Sigma_g^+)$ collisions

v (a.u.)	$\text{C}^{2+}(^1\text{S})$	$\text{C}^{2+}(^3\text{P})$
0.045	6.053	17.514
0.048	5.808	18.083
0.052	5.490	18.067
0.055	5.309	18.517
0.058	5.140	18.862
0.060	5.102	18.894
0.080	5.460	19.875
0.100	6.143	19.461
0.115	6.763	18.499
0.120	6.828	18.143
0.140	7.379	16.926
0.160	8.165	16.092
0.180	8.952	15.113
0.200	9.302	13.956
0.220	9.587	12.773
0.240	9.873	11.671
0.260	10.130	10.716

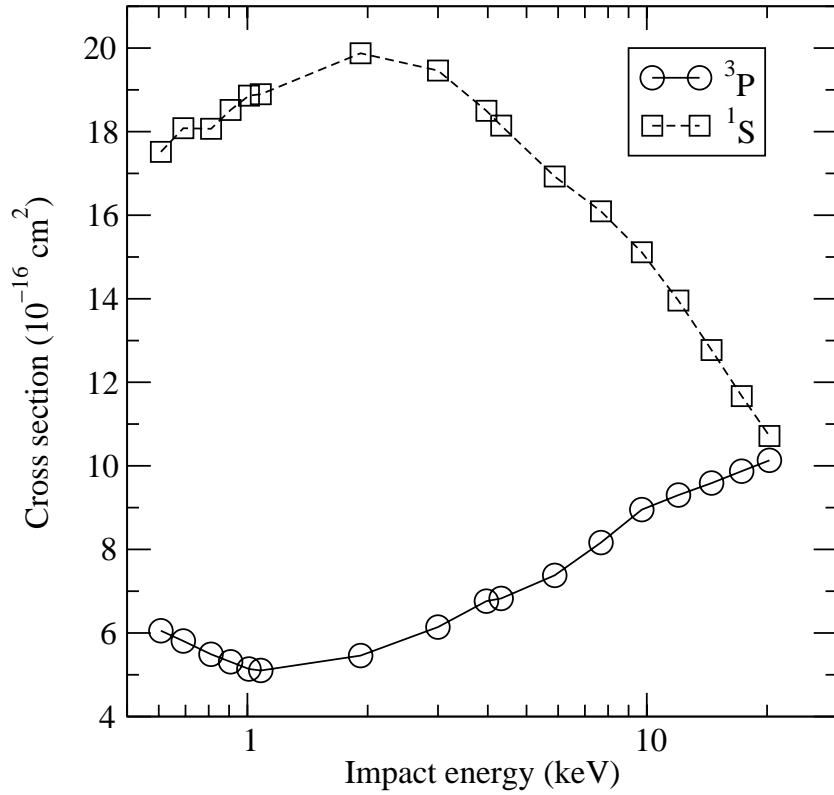


FIG. 3. FC cross sections for the reactions $\text{C}^{2+}(^1\text{S}, ^3\text{P}) + \text{H}_2(\text{X } ^1\Sigma_g^+, \nu = 0) \rightarrow \text{C}^+ + \text{H}_2^+(\text{X } ^2\Sigma_g^+)$.

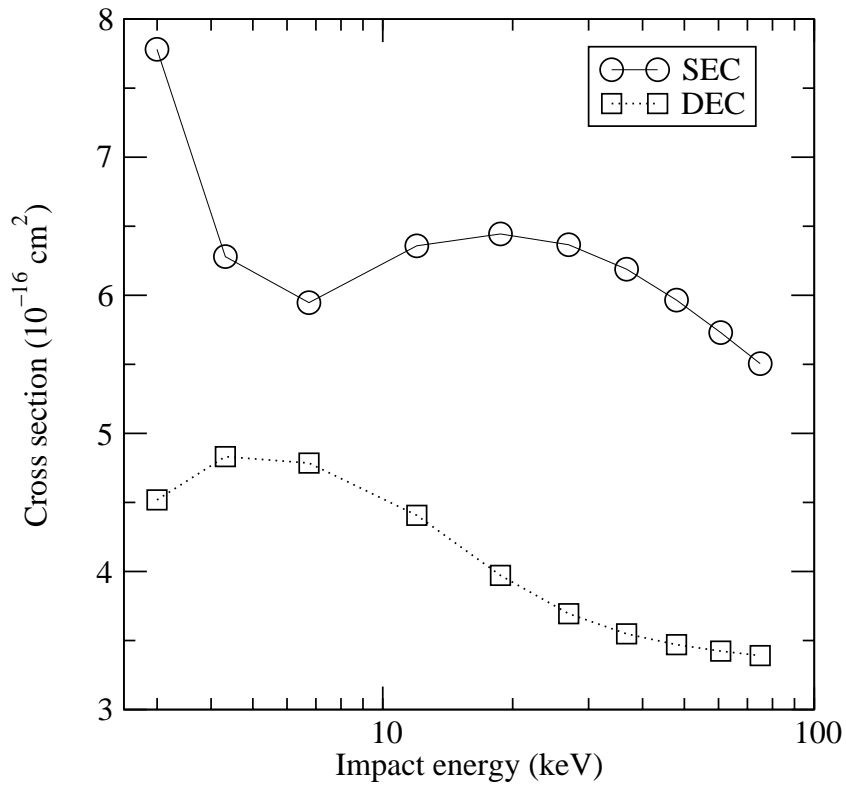


FIG. 4. FC SEC and DEC cross sections for the collision $\text{C}^{3+} + \text{H}_2$.

Table 5. FC SEC and DEC cross sections (in units of 10^{-16} cm²) for C³⁺+H₂ collisions

v (a.u.)	SEC	DEC
0.100	7.781	4.518
0.120	6.280	4.832
0.150	5.947	4.785
0.200	6.358	4.407
0.250	6.444	3.972
0.300	6.366	3.694
0.350	6.189	3.548
0.400	5.965	3.470
0.450	5.730	3.423
0.500	5.505	3.391

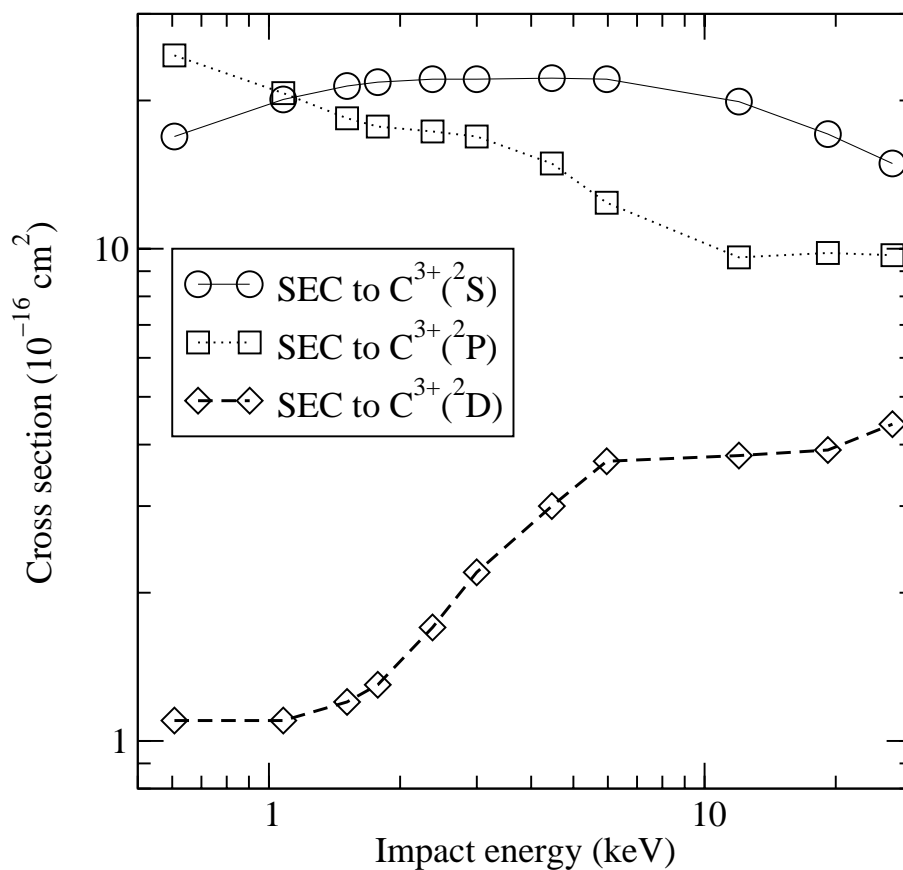


FIG. 5. Sudden cross sections for the reaction $C^{4+}+H_2 \rightarrow C^{3+}(1s^2 3l)+H_2^+(X^2 \Sigma_g^+)$

Table 6. Sudden cross sections (in units of 10^{-16} cm^2) for the reaction $\text{C}^{4+} + \text{H}_2 \longrightarrow \text{C}^{3+}(1s^2 3l) + \text{H}_2^+(\text{X } ^2\Sigma_g^+)$

$v(\text{a.u.})$	$l=0$	$l=1$	$l=2$	Total
0.045	16.9	24.7	1.1	42.8
0.060	20.1	20.7	1.1	42.0
0.071	21.4	18.4	1.2	40.9
0.077	21.8	17.7	1.3	40.8
0.089	22.1	17.3	1.7	41.1
0.100	22.1	16.9	2.2	41.3
0.122	22.2	14.9	3.0	40.0
0.141	22.1	12.4	3.7	38.1
0.200	19.9	9.6	3.8	33.3
0.253	17.1	9.8	3.9	30.8
0.300	14.9	9.7	4.4	29.1

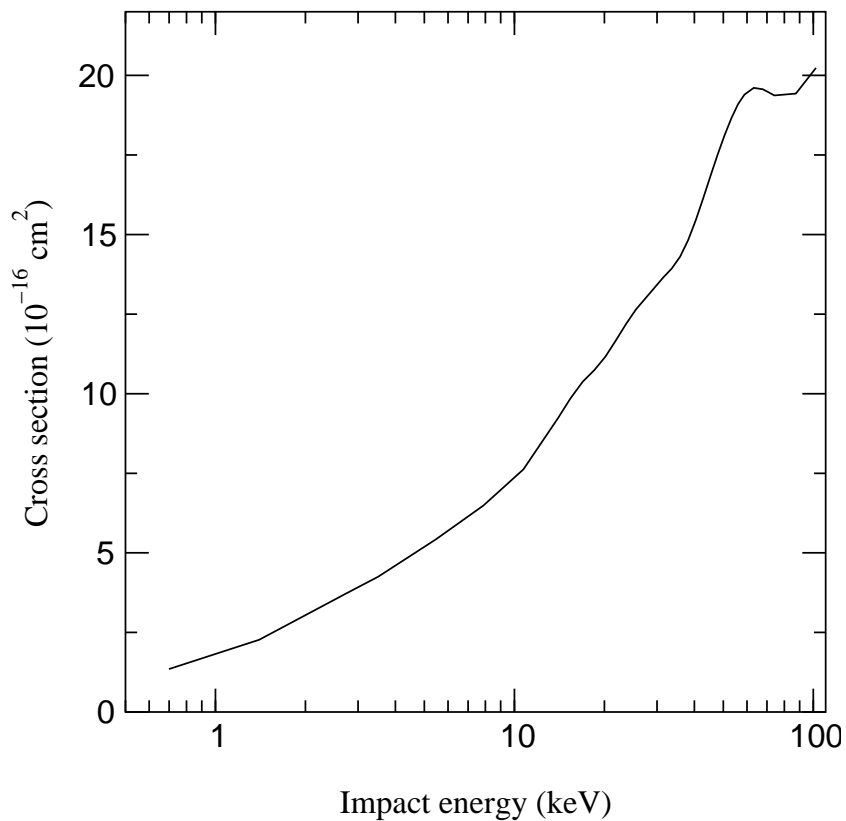


FIG. 6. Total charge transfer cross section for the collision $\text{N}^{5+} + \text{H}_2$.

Table 7. Total charge transfer cross sections (in units of 10^{-16} cm²) for the collision $N^{5+}+H_2$

v (a.u.)	σ	v (a.u.)	σ
0.0447	1.350	0.320	14.308
0.0632	2.271	0.330	14.819
0.089	3.752	0.340	15.453
0.100	4.250	0.350	16.155
0.125	5.427	0.360	16.864
0.150	6.486	0.370	17.532
0.175	7.623	0.380	18.131
0.200	9.236	0.390	18.662
0.210	9.861	0.400	19.095
0.220	10.380	0.410	19.397
0.230	10.743	0.425	19.610
0.240	11.162	0.440	19.565
0.250	11.680	0.450	19.469
0.260	12.200	0.460	19.370
0.270	12.649	0.500	19.428
0.300	13.656	0.540	20.238
0.310	13.938		

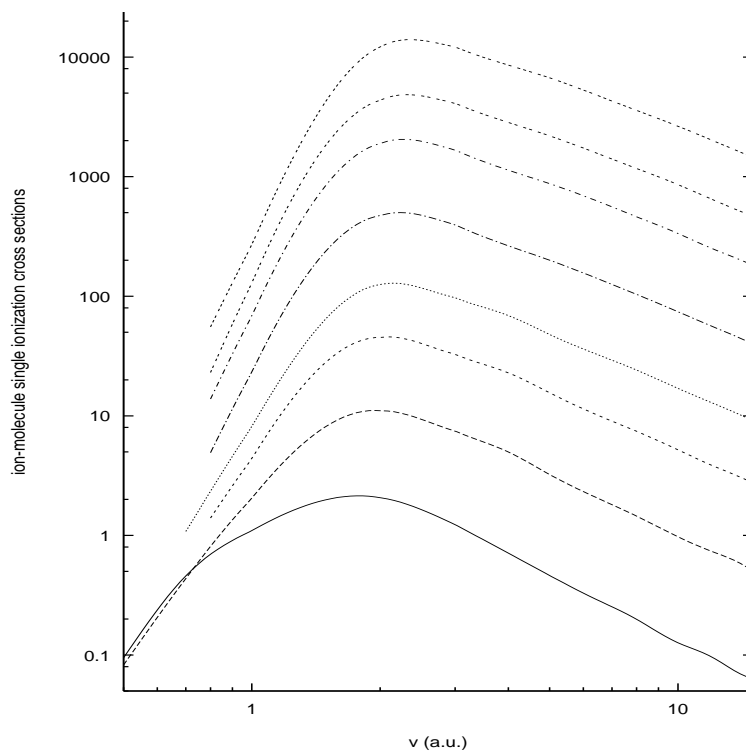


FIG. 7. SI cross sections as functions of the relative velocity v , for $A^{q+}+H_2$ collisions (in units of 10^{-16} cm² and scaled as stated below). From below to above, lines correspond to collisions with different projectiles: H^+ , He^{2+} (data $\times 2$), Li^{3+} (data $\times 5$), Be^{4+} (data $\times 10$), B^{5+} (data $\times 30$), C^{6+} (data $\times 100$), N^{7+} (data $\times 200$), and O^{8+} (data $\times 500$).

Table 8. SI cross sections (in units of 10^{-16} cm²) for $A^{q+} + H_2$ collisions, as functions of the relative velocity

v (a.u.)	H ⁺	He ²⁺	Li ³⁺	Be ⁴⁺	B ⁵⁺	C ⁶⁺	N ⁷⁺	O ⁸⁺
0.6	0.235	0.112		0.019				
0.8	0.697	0.405	0.279	0.237	0.164	0.138		
1.0	1.095	1.023	0.877	0.814	0.773	0.684	0.642	0.538
2.0	2.069	5.511	9.036	12.502	15.724	18.893	21.735	24.304
3.0	1.232	3.732	6.549	9.741	13.191	16.697	20.511	24.295
5.0	0.301	1.615	3.119	4.786	6.677	8.750	10.978	13.410
8.0	0.199	0.725	1.486	2.413	3.454	4.613	5.8485	7.163
10.0	0.127	0.488	1.040	1.699	2.475	3.354	4.293	5.282
12.0	0.096	0.368	0.772	1.289	1.874	2.514	3.241	4.044
14.0	0.070	0.292	0.615	1.019	1.487	2.018	2.569	3.212
16.0	0.058	0.214	0.491	0.814	1.195	1.626	2.115	2.615

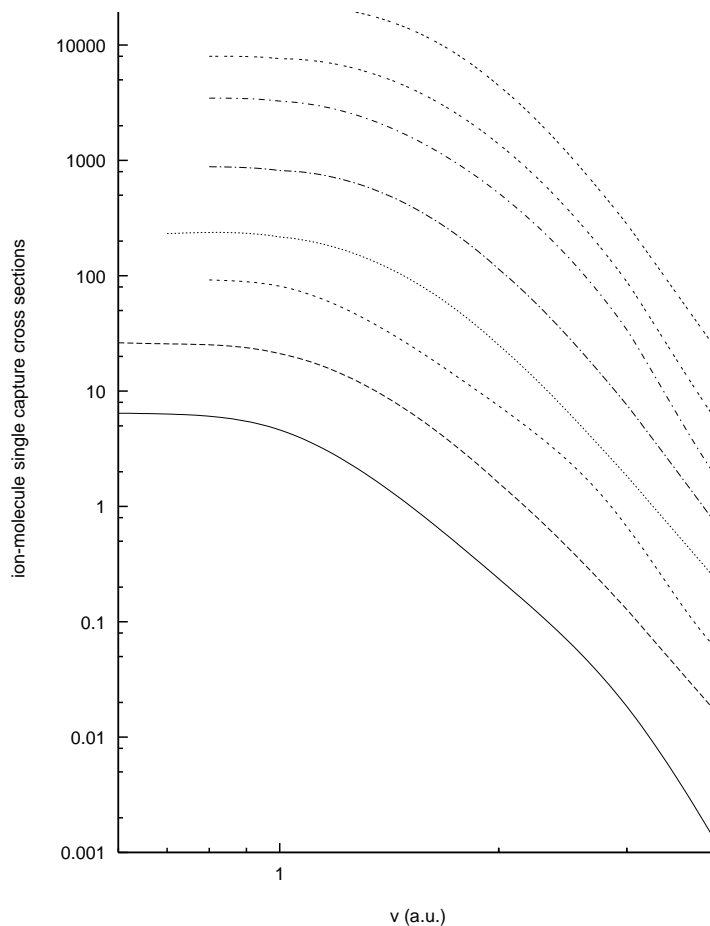


FIG. 8. SEC cross sections, as functions of the relative velocity v , for $A^{q+} + H_2$ collisions (in units of 10^{-16} cm² and scaled as stated below). From below to above, lines correspond to collisions with different projectiles: H⁺, He²⁺ (data \times 2), Li³⁺ (data \times 5), Be⁴⁺ (data \times 10), B⁵⁺ (data \times 30), C⁶⁺ (data \times 100), N⁷⁺ (data \times 200), and O⁸⁺ (data \times 500).

Table 9. SEC cross sections (in units of 10^{-16} cm²) for $A^{q+}+H_2$ collisions, as functions of the relative velocity

$v(\text{a.u.})$	H ⁺	He ²⁺	Li ³⁺	Be ⁴⁺	B ⁵⁺	C ⁶⁺	N ⁷⁺	O ⁸⁺
0.6	6.451	13.214						
0.8	5.932	12.286	18.396	22.872	29.422	34.684	39.955	45.012
1.0	4.608	10.557	16.251	21.724	27.234	32.679	38.133	43.432
2.0	0.237	0.799	1.491	2.503	3.812	5.210	6.937	8.910
3.0	0.018	0.063	0.133	0.184	0.253	0.341	0.444	0.563
5.0		0.002	0.004	0.004	0.004	0.004	0.005	0.007

REFERENCES

- [1] D. Elizaga, L.F. Errea, J.D. Gorfinkiel, A. Macías, L. Méndez, A. Riera, A. Rojas, J. Phys. B: At. Mol. Opt. Phys., **33** 2037–56, 2000.
- [2] L.F. Errea, J.D. Gorfinkiel, A. Macías, L. Méndez, A. Riera, J. Phys. B: At. Mol. Opt. Phys., **30** 3855–72, 1997.
- [3] C. Illescas, A. Riera, Phys. Rev. A, **A60** 4546, 1999.
- [4] D. Elizaga, L.F. Errea, A. Macías, L. Méndez, A. Riera, A. Rojas, Physica Scripta, **T80** 187–9, 1999.
- [5] L.F. Errea, A. Macías, L. Méndez, I. Rabadán, A. Riera, J. Phys. B: At. Mol. Opt. Phys., in press, 2000.
- [6] L.F. Errea, A. Macías, L. Méndez, A. Riera, J. Phys. B: At. Mol. Opt. Phys., **32** 4065–77, 1999.
- [7] L.F. Errea, J.D. Gorfinkiel, A. Macías, L. Méndez, A. Riera, Physica Scripta, **T80** 185–6, 1999.
- [8] L.F. Errea, J.D. Gorfinkiel, A. Macías, L. Méndez, A. Riera, J. Phys. B: At. Mol. Opt. Phys., **32** 1705–21, 1999.
- [9] D. Elizaga, L.F. Errea, J.D. Gorfinkiel, C. Illescas, L. Méndez, A. Macías, A. Riera, A. Rojas, O.J. Kroneisen, T. Kirchner, H.J. Lüdde, A. Henne, R.M. Dreizler, J. Phys. B: At. Mol. Opt. Phys., **32** 857, 1999.

State-selective and total electron capture, excitation and ionization cross-sections in slow collisions of H(2s) and He⁺(2s) with H⁺, He²⁺, Li³⁺, Be⁴⁺ and B⁵⁺

E.A. Solov'ev^a, J.A. Stephens^b, R.K. Janev^b

^aCenter for Energy Research and Informatics, Macedonian Academy of Sciences and Arts, Skopje, Macedonia

^bInternational Atomic Energy Agency, Vienna, Austria

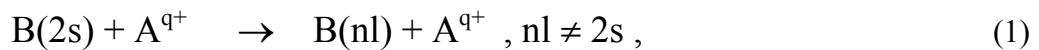
Abstract. The results of systematic calculations by the hidden crossing method for the state-selective and total cross sections for electron capture, excitation (de-excitation) and ionization processes in slow collisions of H(2s) and He⁺(2s) with H⁺, He²⁺, Li³⁺, Be⁴⁺ and B⁵⁺ ions are presented. The data for selected energies in the overall range of 0.05-20 keV/amu are presented in tabular form. The total and n-selective cross sections are also shown in graphical form.

1. Introduction

Atomic and ion species in metastable excited states are known to have significant effects on the kinetics of partially ionized plasmas. In the edge and divertor plasmas of magnetic confinement fusion devices the existence of H(2s) and He⁺(2s) metastables is expected to result from the complex collisional physics of these plasmas [1]. Radial fluxes of multiply charged impurity ions coming from the hot plasma regions travels towards the edge plasma and thereby undergo inelastic collisions with the H(2s) and He⁺(2s) metastables. The most prominent of the collision processes involving H(2s), He⁺(2s) and plasma impurity ions are those leading to collisional excitation or de-excitation of the metastables, or to the removal (i.e. electron capture or ionization) of the electron from the metastable target. In the case of H(2s), these processes are also important in the context of neutral hydrogen beam penetration in fusion plasmas [2].

In this report we present the results of cross section calculations for the excitation, de-excitation, electron transfer (or capture) and ionization processes in collisions of H(2s) and He⁺(2s) metastables with fully stripped ions of the elements with atomic number $Z \leq 5$. The calculations were performed by using the advanced adiabatic (or hidden crossing) method [3,4] which provides an adequate description of the collision dynamics of one-electron ion-atom/ion) systems in the adiabatic energy region.

The processes considered in the present report include:



where $B = H, He^+$ and $A^{q+} = H^+, He^{2+}, Li^{3+}, Be^{4+}$ and B^{5+} . Some of these processes have previously been investigated within the framework of hidden crossing theory. For instance, the processes (1)-(3) for $H(2s)$ were studied in Refs. [5] (for H^+), [6] (for He^{2+}) and [7] (for Li^{3+}) with a varying number of states included in the basis.

In the present work the cross section calculation for processes (1)-(3) were carried out in a systematic manner with a fixed basis containing all the adiabatic states having united atom principal quantum number $N \leq 10$. This ensures uniformity of the accuracy of obtained cross sections, at least for low-lying inelastic channels. The present work also reports a complete set of l -resolved electron capture cross sections for the considered collision systems.

2. Brief description of computational method

The advanced adiabatic (or hidden crossing) method applied in the present calculations is described elsewhere [4-7]. The method is based on the analytic continuation of adiabatic electron energies of the one-electron — two-Coulomb centre system in the complex plane of internuclear distance R , where the potential energy surfaces (for the states of a given symmetry) are connected with a square-root branching point (hidden crossing). These branching points sequentially and pairwise couple all potential energy surfaces (of a given symmetry) and form series along which the system evolves during the collision. Each of the hidden crossings represents a point at which the system may smoothly pass from one surface to another by just going around that point. This signifies that the system has made a transition between the two adiabatic states represented by the crossing potential surfaces. The transition probability between two adiabatic electronic states $|\alpha\rangle$ and $|\beta\rangle$ having a hidden crossing at $R_c = R_{\alpha\beta}$ in the complex R -plane is give by [4] (in atomic units)

$$p_{\alpha\beta} = \exp\left(-\frac{2}{v} \Delta_{\alpha\beta}\right) \quad (4)$$

where v is the collision velocity and $\Delta_{\alpha\beta}$ is the generalized Massey parameter defined by

$$\Delta_{\alpha\beta} = \left| \text{Im} \int_{\text{Re } X(R_c)}^{X(R_c)} \Delta E_{\alpha\beta}(R(x)) dx \right| \quad (5)$$

where

$$\Delta E_{\alpha\beta} = E_{\beta}(R) - E_{\alpha}(R) \quad (6)$$

is the difference of the considered adiabatic surfaces and $x = vt$. In the straight-line approximation for the classical trajectory, $x=(R^2-b^2)^{1/2}$, where b is the impact parameter.

The knowledge of the distribution of the hidden crossings in the complex R -plane allows following the complete dynamical evolution of a one-electron — two-Coulomb centre collision system. All series of hidden crossings end up at the continuum edge, which allows

the description of the ionization process as well. Apart from the (radial) couplings of adiabatic states at the hidden crossings, the states with different m within the same (N,l) -manifold (N,l,m are the united atom spherical quantum numbers) are rotationally coupled in the united atom region, and these couplings should also be included in the construction of the evolution matrix. Finally, at large internuclear distances, there are also rotational couplings between the states caused by the long-range dipole interaction. These couplings control the population of l -sublevels in the exit channels. The combination of all these types of couplings allows construction of the evolution (or the S -) matrix for the collision system for a given trajectory (or impact parameter value). In practical calculations one has to make a truncation of the basis at certain value N_0 . In the present calculations N_0 was taken to be 10. Transitions to states with N higher than N_0 ($=10$) were treated in the present calculations as ionization. (This introduces an error in the ionization cross sections for the considered systems of not larger than 5%).

3. Collisions of H(2s) with H^+ , He^{2+} , Li^{3+} , Be^{4+} and B^{5+}

The cross sections for the processes (1)-(3) for the H(2s) - H^+ , He^{2+} , Li^{3+} , Be^{4+} and B^{5+} collision systems in the energy range (in general) 0.1-10 keV/amu are given in Tables 1-5 and Figs. [1a,b]-[5a,b]. The specific energy range for each collision system in which the calculations have been performed was determined on the basis of the expected validity of the hidden crossing method.

In the case of charge-symmetric system $H(2s) + H^+$, there is a strong interference of the excitation and electron transfer channels, the description of which requires inclusion of dynamical and topological phases in the treatment. Since the existing codes do not allow for inclusion of phase interference effects, the cross sections for excitation and electron transfer to a given nl -state are given in Table 1 as a sum. (Exception from this interpretation are the data for $nl=1s$ (de-exc+ct) and $nl=2s$ (only ct). In the considered energy range, the contribution of each of these processes to their total cross section amounts to approximately 50%.

The summed excitation and electron capture cross sections for production of a product atom in a shell n are given in Fig. [1a], from where it is apparent that the production of a neutral atom in the $n=2$ state is dominant. The ionization cross section for this collision system is given in Fig. [1b]. For the charge - asymmetric systems $H(2s) + Z$ ($2 \leq Z \leq 5$). Tables 2-5 contain state-selective and total electron capture cross section data, cross section data for the de-excitation ($n=1$) and excitation ($n > 2$) processes, and cross section data for ionization. Figures 2a-5a show the n -selective electron capture cross sections, while Figs. 2b-5b show the total excitation, de-excitation and ionization cross sections. (For Li^{3+} and Be^{4+} , the excitation cross sections are not shown because of their high uncertainties.

4. Collisions of $\text{He}^+(2s)$ with He^{2+} , Li^{3+} , Be^{4+} and B^{5+}

The cross section data for the processes (1)-(3) in $\text{He}^+(2s) + \text{He}^{2+}$, Li^{3+} , Be^{4+} , B^{5+} collision system are given in Tables 6-9 and Figures 6a,b - 9a,b. The method of data presentation is the same as in the preceding case for $\text{H}(2s)$. The $\text{He}^+(2s) + \text{He}^{2+}$ system is charge-symmetric and the data for excitation (de-excitation) and electron transfer are given as a sum, for the same reason as discussed in the $\text{H}(2s) + \text{H}^+$ case.

REFERENCES

- [1] JANEV, R.K., in: "Atomic and Molecular Processes in Fusion Edge Plasmas", R.K. Janev, ed., (Plenum Press, New York, 1995), p.1.
- [2] JANEV, R.K., BOLEY, C.D., POST, D.E. Nucl. Fusion **29** (1989) 2125.
- [3] SOLOV'EV, E.A., Sov. Phys.-JETP **54** (1981) 893.
- [4] SOLOV'EV, E.A., Sov. Phys.-Uspekhi **32** (1989) 228.
- [5] JANEV, R.K., KRSTIC, P.S., Phys. Rev. A **46** (1992) 5554.
- [6] KRSTIC, P.S., JANEV, R.K., Phys. Rev. A **47** (1993) 3894.
- [7] JANEV, R.K., E.A. SOLOV'EV, E.A., WANG, Y., J. Phys. B **29** (1996) 2497.

Table 1: Cross sections (in units of 10^{-16} cm²) for state-specific and total charge transfer+excitation and for ionization in $H(2s) + H^+$ collisions as a function of energy (in units of keV/u).

E(keV/u)	.10	.20	.50	.70	1.00	2.00	3.00	5.00
σ_{ct+ex}								
n= 1	3.86E-21	1.80E-20	5.10E-20	7.03E-20	1.00E-19	3.15E-19	8.69E-19	2.85E-18
l= 0	3.86E-21	1.80E-20	5.10E-20	7.03E-20	1.00E-19	3.15E-19	8.69E-19	2.85E-18
n= 2	1.71E-15	1.88E-15	2.08E-15	2.26E-15	2.56E-15	3.72E-15	4.79E-15	6.53E-15
l= 0	7.93E-16	8.51E-16	9.09E-16	9.61E-16	1.05E-15	1.46E-15	1.96E-15	3.03E-15
l= 1	9.18E-16	1.03E-15	1.18E-15	1.29E-15	1.51E-15	2.26E-15	2.83E-15	3.50E-15
n= 3	1.04E-15	1.08E-15	1.09E-15	1.18E-15	1.35E-15	1.99E-15	2.49E-15	3.17E-15
l= 0	2.36E-17	3.10E-17	6.50E-17	9.45E-17	1.40E-16	2.71E-16	3.80E-16	5.47E-16
l= 1	2.08E-16	2.13E-16	2.21E-16	2.57E-16	3.25E-16	5.46E-16	7.08E-16	9.62E-16
l= 2	8.05E-16	8.32E-16	8.07E-16	8.27E-16	8.88E-16	1.17E-15	1.40E-15	1.66E-15
n= 4	4.36E-16	4.42E-16	4.52E-16	4.67E-16	5.01E-16	6.67E-16	8.40E-16	1.11E-15
l= 0	4.04E-19	1.73E-18	7.40E-18	1.16E-17	1.87E-17	4.23E-17	6.28E-17	9.57E-17
l= 1	5.36E-18	1.03E-17	2.43E-17	3.33E-17	4.76E-17	1.00E-16	1.47E-16	2.21E-16
l= 2	3.55E-18	1.38E-17	4.58E-17	6.47E-17	9.15E-17	1.73E-16	2.33E-16	2.94E-16
l= 3	4.27E-16	4.16E-16	3.75E-16	3.58E-16	3.43E-16	3.52E-16	3.97E-16	4.96E-16
n= 5	1.54E-17	4.54E-17	1.12E-16	1.44E-16	1.86E-16	3.55E-16	5.69E-16	1.03E-15
l= 0	3.32E-20	1.89E-19	1.32E-18	2.57E-18	5.17E-18	1.82E-17	3.43E-17	6.89E-17
l= 1	3.29E-19	1.44E-18	5.82E-18	9.19E-18	1.53E-17	4.63E-17	8.50E-17	1.64E-16
l= 2	2.19E-19	1.36E-18	7.93E-18	1.38E-17	2.42E-17	7.21E-17	1.27E-16	2.20E-16
l= 3	7.34E-18	2.10E-17	4.74E-17	5.76E-17	6.93E-17	1.13E-16	1.72E-16	2.96E-16
l= 4	7.48E-18	2.14E-17	4.92E-17	6.04E-17	7.25E-17	1.05E-16	1.50E-16	2.82E-16
n= 6	1.62E-18	9.40E-18	4.00E-17	5.80E-17	8.02E-17	1.29E-16	1.57E-16	1.88E-16
l= 0	7.61E-21	5.19E-20	4.56E-19	8.54E-19	1.51E-18	3.59E-18	5.27E-18	7.72E-18
l= 1	5.24E-20	3.67E-19	2.04E-18	3.22E-18	4.74E-18	8.06E-18	9.92E-18	1.20E-17
l= 2	4.11E-20	3.20E-19	2.27E-18	3.98E-18	6.59E-18	1.37E-17	1.85E-17	2.41E-17
l= 3	4.72E-19	2.71E-18	1.08E-17	1.50E-17	1.98E-17	2.93E-17	3.48E-17	4.09E-17
l= 4	5.82E-19	3.23E-18	1.31E-17	1.86E-17	2.52E-17	3.88E-17	4.60E-17	5.34E-17
l= 5	4.66E-19	2.72E-18	1.14E-17	1.64E-17	2.24E-17	3.52E-17	4.24E-17	5.00E-17
n= 7	2.36E-19	2.27E-18	1.53E-17	2.51E-17	3.88E-17	7.44E-17	9.83E-17	1.26E-16
l= 0	2.58E-21	1.86E-20	1.78E-19	3.28E-19	5.67E-19	1.31E-18	1.94E-18	2.86E-18
l= 1	1.30E-20	1.14E-19	7.25E-19	1.13E-18	1.64E-18	2.72E-18	3.29E-18	3.87E-18
l= 2	1.07E-20	9.25E-20	7.29E-19	1.31E-18	2.22E-18	4.99E-18	7.10E-18	9.94E-18
l= 3	5.69E-20	5.55E-19	3.64E-18	5.74E-18	8.38E-18	1.38E-17	1.65E-17	1.86E-17
l= 4	4.23E-20	3.89E-19	2.50E-18	4.11E-18	6.45E-18	1.30E-17	1.76E-17	2.31E-17
l= 5	4.77E-20	4.53E-19	3.00E-18	4.97E-18	7.90E-18	1.64E-17	2.25E-17	2.99E-17
l= 6	6.31E-20	6.50E-19	4.56E-18	7.51E-18	1.16E-17	2.23E-17	2.94E-17	3.79E-17
n= 8	5.80E-20	6.14E-19	4.49E-18	7.48E-18	1.17E-17	2.27E-17	3.00E-17	3.88E-17
l= 0	9.77E-22	6.07E-21	5.82E-20	1.06E-19	1.79E-19	3.95E-19	5.66E-19	8.24E-19
l= 1	3.86E-21	2.93E-20	1.90E-19	3.02E-19	4.45E-19	7.42E-19	8.93E-19	1.03E-18
l= 2	4.51E-21	3.47E-20	2.18E-19	3.59E-19	5.67E-19	1.18E-18	1.65E-18	2.31E-18
l= 3	9.12E-21	9.65E-20	7.32E-19	1.21E-18	1.86E-18	3.28E-18	3.98E-18	4.50E-18
l= 4	1.17E-20	1.28E-19	9.34E-19	1.55E-18	2.41E-18	4.60E-18	5.95E-18	7.27E-18
l= 5	9.87E-21	1.06E-19	7.06E-19	1.15E-18	1.79E-18	3.64E-18	5.12E-18	7.26E-18
l= 6	1.18E-20	1.38E-19	1.03E-18	1.72E-18	2.67E-18	5.00E-18	6.43E-18	8.00E-18
l= 7	6.15E-21	7.51E-20	6.19E-19	1.08E-18	1.77E-18	3.83E-18	5.44E-18	7.60E-18
n= 9	1.24E-20	1.50E-19	1.15E-18	1.97E-18	3.16E-18	6.36E-18	8.60E-18	1.13E-17
l= 0	5.60E-24	1.78E-22	3.56E-21	8.00E-21	1.66E-20	5.01E-20	8.24E-20	1.37E-19
l= 1	3.54E-22	3.86E-21	2.37E-20	3.92E-20	6.16E-20	1.22E-19	1.64E-19	2.20E-19
l= 2	9.34E-22	9.49E-21	4.71E-20	7.28E-20	1.10E-19	2.14E-19	2.96E-19	4.09E-19
l= 3	1.66E-21	1.80E-20	1.09E-19	1.78E-19	2.77E-19	5.49E-19	7.45E-19	1.01E-18
l= 4	2.84E-21	3.42E-20	2.57E-19	4.32E-19	6.75E-19	1.25E-18	1.57E-18	1.85E-18
l= 5	3.38E-21	4.25E-20	3.48E-19	5.96E-19	9.47E-19	1.82E-18	2.34E-18	2.83E-18
l= 6	2.32E-21	2.97E-20	2.55E-19	4.44E-19	7.28E-19	1.54E-18	2.14E-18	2.90E-18
l= 7	8.35E-22	1.08E-20	9.59E-20	1.72E-19	2.93E-19	6.94E-19	1.05E-18	1.62E-18
l= 8	1.23E-22	1.61E-21	1.48E-20	2.72E-20	4.85E-20	1.30E-19	2.14E-19	3.72E-19
$\sigma_{ct+ex;tot}$	3.20E-15	3.46E-15	3.79E-15	4.14E-15	4.73E-15	6.96E-15	8.98E-15	1.22E-14
σ_{ion}	2.76E-19	3.22E-18	3.18E-17	6.01E-17	1.08E-16	2.87E-16	4.70E-16	

Table 2: Cross sections (in units of 10^{-16} cm²) for state-specific and total charge transfer, excitation and de-excitation, and ionization for the $H(2s) + He^{+2}$ collision system as a function of energy (in units of keV/u).

E(keV/u)	.05	.10	.20	.50	1.00	2.00	5.00	10.00
σ_{ct}								
n= 2	3.40E-22	1.26E-20	1.08E-19	6.67E-19	1.97E-18	5.61E-18	2.28E-17	4.94E-17
l= 0	1.70E-22	6.25E-21	5.35E-20	3.24E-19	9.04E-19	2.13E-18	7.57E-18	2.08E-17
l= 1	1.70E-22	6.30E-21	5.45E-20	3.43E-19	1.07E-18	3.48E-18	1.53E-17	2.87E-17
n= 3	1.15E-16	4.58E-16	1.27E-15	2.96E-15	3.97E-15	4.19E-15	3.41E-15	2.51E-15
l= 0	3.23E-17	1.18E-16	2.83E-16	5.31E-16	6.96E-16	7.92E-16	6.37E-16	3.90E-16
l= 1	1.54E-17	1.04E-16	3.86E-16	1.01E-15	1.32E-15	1.44E-15	1.53E-15	1.43E-15
l= 2	6.70E-17	2.36E-16	6.05E-16	1.42E-15	1.95E-15	1.96E-15	1.25E-15	6.82E-16
n= 4	4.27E-16	5.48E-16	9.67E-16	2.62E-15	4.54E-15	6.16E-15	6.65E-15	5.79E-15
l= 0	3.86E-18	2.02E-17	7.50E-17	2.35E-16	4.29E-16	5.52E-16	3.96E-16	2.14E-16
l= 1	1.29E-16	1.52E-16	2.65E-16	6.54E-16	1.12E-15	1.63E-15	1.66E-15	1.15E-15
l= 2	1.90E-16	2.28E-16	3.66E-16	8.35E-16	1.13E-15	1.42E-15	2.46E-15	3.08E-15
l= 3	1.04E-16	1.47E-16	2.61E-16	9.01E-16	1.87E-15	2.56E-15	2.14E-15	1.34E-15
n= 5	8.34E-16	9.60E-16	9.29E-16	8.17E-16	7.87E-16	8.34E-16	8.77E-16	8.21E-16
l= 0	8.69E-18	7.38E-18	8.07E-18	1.21E-17	2.21E-17	3.93E-17	4.54E-17	3.23E-17
l= 1	8.36E-18	1.01E-17	1.33E-17	2.95E-17	5.52E-17	8.21E-17	9.60E-17	8.84E-17
l= 2	4.54E-17	4.01E-17	4.30E-17	6.19E-17	9.93E-17	1.43E-16	1.82E-16	1.80E-16
l= 3	2.26E-16	2.67E-16	2.54E-16	2.11E-16	1.95E-16	1.88E-16	2.11E-16	2.59E-16
l= 4	5.45E-16	6.35E-16	6.11E-16	5.02E-16	4.15E-16	3.81E-16	3.43E-16	2.61E-16
n= 6	1.21E-18	1.31E-17	6.41E-17	2.25E-16	4.15E-16	7.09E-16	1.18E-15	1.36E-15
l= 0	2.15E-20	2.06E-19	1.10E-18	4.26E-18	9.88E-18	2.08E-17	2.80E-17	2.20E-17
l= 1	1.62E-20	1.91E-19	1.12E-18	6.99E-18	2.14E-17	4.66E-17	7.38E-17	6.30E-17
l= 2	8.28E-20	8.00E-19	4.28E-18	1.76E-17	4.36E-17	9.20E-17	1.52E-16	1.45E-16
l= 3	2.25E-19	2.45E-18	1.10E-17	3.46E-17	6.58E-17	1.17E-16	2.17E-16	2.80E-16
l= 4	3.83E-19	4.01E-18	1.88E-17	6.20E-17	1.09E-16	1.79E-16	2.50E-16	2.97E-16
l= 5	4.79E-19	5.47E-18	2.78E-17	9.94E-17	1.66E-16	2.54E-16	4.62E-16	5.51E-16
n= 7	3.37E-20	1.02E-18	1.07E-17	7.52E-17	1.93E-16	4.48E-16	1.39E-15	2.70E-15
l= 0	8.35E-22	2.01E-20	2.23E-19	1.67E-18	5.25E-18	1.74E-17	4.65E-17	4.84E-17
l= 1	8.82E-22	2.61E-20	2.86E-19	2.42E-18	1.02E-17	4.10E-17	1.21E-16	1.39E-16
l= 2	2.12E-21	5.47E-20	6.18E-19	5.23E-18	1.87E-17	6.35E-17	2.03E-16	2.74E-16
l= 3	5.72E-21	1.67E-19	1.69E-18	1.09E-17	2.63E-17	6.25E-17	2.65E-16	5.03E-16
l= 4	9.94E-21	2.90E-19	2.89E-18	1.81E-17	3.90E-17	6.02E-17	1.87E-16	6.16E-16
l= 5	8.35E-21	2.55E-19	2.64E-18	1.88E-17	4.73E-17	9.43E-17	1.36E-16	2.24E-16
l= 6	5.88E-21	2.02E-19	2.36E-18	1.81E-17	4.64E-17	1.09E-16	4.32E-16	8.95E-16
n= 8	1.39E-21	8.96E-20	1.73E-18	2.20E-17	7.16E-17	1.47E-16	2.38E-16	2.69E-16
l= 0	3.56E-23	1.44E-21	2.48E-20	2.93E-19	1.28E-18	4.09E-18	4.46E-18	1.08E-17
l= 1	3.84E-23	2.34E-21	4.40E-20	7.07E-19	2.30E-18	3.65E-18	1.77E-17	1.11E-17
l= 2	9.98E-23	4.54E-21	8.34E-20	1.02E-18	4.06E-18	1.21E-17	1.30E-17	3.00E-17
l= 3	1.42E-22	9.07E-21	1.66E-19	2.12E-18	6.90E-18	1.31E-17	3.02E-17	3.41E-17
l= 4	2.06E-22	1.66E-20	3.26E-19	3.82E-18	1.11E-17	2.14E-17	3.44E-17	4.75E-17
l= 5	2.84E-22	1.94E-20	3.76E-19	4.75E-18	1.48E-17	2.80E-17	4.54E-17	5.04E-17
l= 6	3.19E-22	1.92E-20	3.56E-19	4.55E-18	1.55E-17	3.40E-17	5.05E-17	4.47E-17
l= 7	2.69E-22	1.71E-20	3.52E-19	4.76E-18	1.57E-17	3.10E-17	4.20E-17	4.04E-17
$\sigma_{ct,tot}$	1.38E-15	1.98E-15	3.25E-15	6.75E-15	1.01E-14	1.28E-14	1.46E-14	1.46E-14
$\sigma_{ex,de-ex}$								
n= 1	8.20E-30	2.12E-26	3.27E-24	3.09E-22	6.66E-21	1.58E-19	2.62E-18	7.95E-18
l= 0	8.20E-30	2.12E-26	3.27E-24	3.09E-22	6.66E-21	1.58E-19	2.62E-18	7.95E-18
n= 3	1.71E-19	1.65E-18	9.06E-18	4.36E-17	1.56E-16	5.04E-16	1.30E-15	1.71E-15
l= 0	8.47E-21	1.17E-19	8.02E-19	6.64E-18	3.16E-17	9.53E-17	1.87E-16	2.10E-16
l= 1	5.35E-21	1.12E-19	9.56E-19	1.06E-17	5.71E-17	2.05E-16	4.90E-16	5.72E-16
l= 2	1.57E-19	1.42E-18	7.31E-18	2.63E-17	6.76E-17	2.04E-16	6.24E-16	9.26E-16
σ_{ion}	2.81E-21	1.62E-19	3.41E-18	6.91E-17	3.70E-16	1.26E-15	3.52E-15	5.46E-15

Table 3: Cross sections (in units of 10^{-16} cm²) for state-specific and total charge transfer, de-excitation, and ionization for the $H(2s) + Li^{+3}$ collision system as a function of energy (in units of keV/u).

E(keV/u)	.10	.20	.50	.70	1.00	2.00	3.00	5.00
σ_{ct}								
n= 1	1.82E-80	5.54E-62	1.03E-45	2.10E-41	1.54E-37	1.04E-31	4.01E-29	1.54E-26
l= 0	1.82E-80	5.54E-62	1.03E-45	2.10E-41	1.54E-37	1.04E-31	4.01E-29	1.54E-26
n= 2	6.77E-29	1.72E-25	1.58E-22	7.66E-22	3.26E-21	3.24E-20	9.77E-20	3.38E-19
l= 0	3.37E-29	8.48E-26	7.58E-23	3.63E-22	1.51E-21	1.40E-20	3.86E-20	1.10E-19
l= 1	3.41E-29	8.70E-26	8.17E-23	4.03E-22	1.75E-21	1.84E-20	5.91E-20	2.28E-19
n= 3	3.64E-20	3.96E-19	3.65E-18	7.11E-18	1.39E-17	4.53E-17	7.93E-17	1.34E-16
l= 0	1.18E-20	1.24E-19	9.99E-19	1.75E-18	3.02E-18	8.05E-18	1.33E-17	2.16E-17
l= 1	1.81E-20	1.88E-19	1.48E-18	2.69E-18	4.99E-18	1.56E-17	2.75E-17	4.93E-17
l= 2	6.49E-21	8.27E-20	1.18E-18	2.67E-18	5.89E-18	2.16E-17	3.85E-17	6.37E-17
n= 4	4.12E-16	1.18E-15	2.82E-15	3.39E-15	3.82E-15	3.95E-15	3.63E-15	3.00E-15
l= 0	5.65E-17	1.29E-16	2.66E-16	3.16E-16	3.49E-16	3.13E-16	2.44E-16	1.50E-16
l= 1	8.78E-17	3.12E-16	7.82E-16	9.22E-16	1.01E-15	9.83E-16	8.52E-16	6.26E-16
l= 2	1.17E-16	3.37E-16	7.53E-16	8.63E-16	9.36E-16	1.03E-15	1.08E-15	1.11E-15
l= 3	1.51E-16	4.00E-16	1.02E-15	1.29E-15	1.52E-15	1.62E-15	1.45E-15	1.11E-15
n= 5	4.95E-15	6.06E-15	1.10E-14	1.30E-14	1.47E-14	1.59E-14	1.52E-14	1.32E-14
l= 0	3.86E-16	5.24E-16	9.04E-16	9.24E-16	8.37E-16	4.96E-16	3.12E-16	1.61E-16
l= 1	1.04E-15	1.29E-15	2.49E-15	2.74E-15	2.71E-15	1.93E-15	1.33E-15	7.33E-16
l= 2	1.35E-15	1.25E-15	2.53E-15	3.38E-15	4.21E-15	4.69E-15	4.15E-15	3.04E-15
l= 3	1.33E-15	1.34E-15	1.13E-15	1.27E-15	1.85E-15	4.19E-15	5.63E-15	6.71E-15
l= 4	8.34E-16	1.66E-15	3.91E-15	4.69E-15	5.13E-15	4.61E-15	3.72E-15	2.52E-15
n= 6	1.54E-15	1.66E-15	1.69E-15	1.74E-15	1.84E-15	2.19E-15	2.39E-15	2.52E-15
l= 0	1.98E-17	2.23E-17	3.28E-17	4.18E-17	5.31E-17	6.17E-17	5.58E-17	4.88E-17
l= 1	2.46E-17	3.23E-17	6.76E-17	9.19E-17	1.19E-16	1.43E-16	1.33E-16	1.06E-16
l= 2	7.07E-17	8.02E-17	1.34E-16	1.74E-16	2.25E-16	3.06E-16	3.13E-16	2.79E-16
l= 3	2.31E-16	2.54E-16	2.49E-16	2.56E-16	2.96E-16	4.78E-16	5.80E-16	6.17E-16
l= 4	4.75E-16	5.22E-16	4.74E-16	4.34E-16	3.87E-16	3.82E-16	5.02E-16	7.62E-16
l= 5	7.23E-16	7.51E-16	7.34E-16	7.39E-16	7.63E-16	8.22E-16	8.07E-16	7.07E-16
n= 7	1.40E-16	1.36E-16	2.10E-16	2.56E-16	3.09E-16	3.99E-16	4.36E-16	4.63E-16
l= 0	8.34E-19	1.39E-18	3.64E-18	5.21E-18	7.35E-18	1.04E-17	1.06E-17	1.07E-17
l= 1	1.22E-18	2.12E-18	6.47E-18	8.84E-18	1.10E-17	1.40E-17	1.54E-17	1.59E-17
l= 2	3.37E-18	5.15E-18	1.36E-17	1.91E-17	2.57E-17	3.54E-17	3.74E-17	3.76E-17
l= 3	9.35E-18	1.19E-17	2.19E-17	2.73E-17	3.48E-17	5.29E-17	5.95E-17	6.00E-17
l= 4	2.23E-17	2.32E-17	3.69E-17	4.50E-17	5.31E-17	6.95E-17	8.18E-17	9.63E-17
l= 5	4.30E-17	3.87E-17	5.22E-17	6.13E-17	7.06E-17	8.23E-17	8.84E-17	1.03E-16
l= 6	5.98E-17	5.35E-17	7.51E-17	8.97E-17	1.06E-16	1.34E-16	1.43E-16	1.40E-16
n= 8	5.16E-17	9.03E-17	1.92E-16	2.28E-16	2.60E-16	2.97E-16	3.04E-16	3.05E-16
l= 0	2.13E-18	3.53E-18	7.08E-18	8.07E-18	8.75E-18	8.64E-18	8.20E-18	8.27E-18
l= 1	2.68E-18	4.73E-18	9.95E-18	1.17E-17	1.31E-17	1.45E-17	1.45E-17	1.41E-17
l= 2	2.87E-18	5.29E-18	1.16E-17	1.37E-17	1.55E-17	1.85E-17	2.03E-17	2.09E-17
l= 3	9.68E-18	1.55E-17	2.92E-17	3.25E-17	3.46E-17	3.43E-17	3.28E-17	3.16E-17
l= 4	1.54E-17	2.47E-17	4.65E-17	5.26E-17	5.73E-17	6.03E-17	5.73E-17	4.96E-17
l= 5	1.21E-17	2.11E-17	4.32E-17	5.03E-17	5.60E-17	6.23E-17	6.45E-17	6.55E-17
l= 6	5.19E-18	1.08E-17	2.81E-17	3.57E-17	4.32E-17	5.30E-17	5.59E-17	5.92E-17
l= 7	1.51E-18	4.53E-18	1.67E-17	2.37E-17	3.16E-17	4.52E-17	5.09E-17	5.62E-17
$\sigma_{ct;tot}$	7.10E-15	9.13E-15	1.59E-14	1.86E-14	2.10E-14	2.28E-14	2.20E-14	1.96E-14
σ_{de-ex}								
n= 1	2.82E-30	5.19E-27	8.07E-24	1.24E-22	1.79E-21	1.12E-19	6.88E-19	4.00E-18
l= 0	2.82E-30	5.19E-27	8.07E-24	1.24E-22	1.79E-21	1.12E-19	6.88E-19	4.00E-18
σ_{ion}	2.35E-16	1.05E-15	8.51E-15	1.73E-14	3.39E-14	9.70E-14	1.54E-13	2.39E-13

Table 4: Cross sections (in units of 10^{-16} cm²) for state-specific and total charge transfer, de-excitation and ionization for the $H(2s) + Be^{+4}$ collision system as a function of energy (in units of keV/u).

E(keV/u)	.10	.15	.20	.30	.50	.70	1.00	1.50
σ_{ct}								
n= 2	4.95E-51	1.45E-44	9.70E-41	2.93E-36	1.10E-31	2.62E-29	3.38E-27	3.16E-25
l= 0	2.43E-51	7.04E-45	4.68E-41	1.38E-36	5.01E-32	1.14E-29	1.40E-27	1.22E-25
l= 1	2.52E-51	7.42E-45	5.01E-41	1.55E-36	5.99E-32	1.47E-29	1.98E-27	1.94E-25
n= 3	6.94E-27	5.62E-25	3.17E-24	8.14E-23	2.88E-21	1.23E-20	4.47E-20	1.63E-19
l= 0	2.29E-27	1.82E-25	1.02E-24	2.53E-23	8.39E-22	3.41E-21	1.17E-20	3.89E-20
l= 1	3.47E-27	2.81E-25	1.58E-24	4.06E-23	1.43E-21	6.07E-21	2.19E-20	7.70E-20
l= 2	1.18E-27	9.91E-26	5.61E-25	1.55E-23	6.06E-22	2.77E-21	1.11E-20	4.66E-20
n= 4	2.73E-20	1.91E-19	2.44E-19	1.31E-18	6.93E-18	1.64E-17	4.12E-17	1.07E-16
l= 0	6.57E-21	4.40E-20	5.46E-20	2.66E-19	1.25E-18	2.79E-18	6.56E-18	1.51E-17
l= 1	1.21E-20	8.34E-20	1.04E-19	5.19E-19	2.40E-18	5.15E-18	1.23E-17	3.26E-17
l= 2	7.07E-21	5.16E-20	6.69E-20	3.78E-19	1.94E-18	4.00E-18	8.23E-18	1.88E-17
l= 3	1.52E-21	1.23E-20	1.92E-20	1.51E-19	1.34E-18	4.49E-18	1.41E-17	4.09E-17
n= 5	1.48E-16	4.07E-16	7.32E-16	1.47E-15	2.83E-15	3.90E-15	5.06E-15	6.22E-15
l= 0	1.74E-17	4.69E-17	8.15E-17	1.52E-16	2.42E-16	2.75E-16	2.71E-16	2.28E-16
l= 1	3.63E-17	9.45E-17	1.64E-16	3.21E-16	5.97E-16	7.81E-16	9.15E-16	9.37E-16
l= 2	3.86E-17	9.46E-17	1.54E-16	2.80E-16	5.47E-16	8.31E-16	1.23E-15	1.70E-15
l= 3	3.68E-17	1.03E-16	1.83E-16	3.34E-16	5.09E-16	5.87E-16	6.90E-16	9.72E-16
l= 4	1.88E-17	6.81E-17	1.50E-16	3.83E-16	9.37E-16	1.43E-15	1.96E-15	2.38E-15
n= 6	1.80E-14	1.63E-14	1.49E-14	1.30E-14	1.07E-14	9.40E-15	8.22E-15	7.05E-15
l= 0	1.13E-15	8.41E-16	6.55E-16	4.41E-16	2.58E-16	1.85E-16	1.34E-16	9.54E-17
l= 1	3.00E-15	2.34E-15	1.93E-15	1.42E-15	9.00E-16	6.48E-16	4.59E-16	3.13E-16
l= 2	3.98E-15	3.22E-15	2.80E-15	2.32E-15	1.78E-15	1.44E-15	1.10E-15	7.87E-16
l= 3	4.27E-15	3.56E-15	3.05E-15	2.51E-15	2.20E-15	2.12E-15	2.00E-15	1.76E-15
l= 4	3.80E-15	3.78E-15	3.49E-15	2.81E-15	1.93E-15	1.61E-15	1.55E-15	1.72E-15
l= 5	1.86E-15	2.54E-15	3.00E-15	3.48E-15	3.62E-15	3.41E-15	2.98E-15	2.37E-15
n= 7	1.42E-15	1.67E-15	1.75E-15	1.93E-15	2.12E-15	2.18E-15	2.17E-15	2.02E-15
l= 0	2.06E-17	3.12E-17	2.90E-17	3.70E-17	3.90E-17	3.67E-17	3.40E-17	3.12E-17
l= 1	4.26E-17	5.28E-17	4.92E-17	5.90E-17	5.95E-17	5.64E-17	5.21E-17	4.59E-17
l= 2	7.82E-17	8.59E-17	8.55E-17	9.38E-17	1.01E-16	1.02E-16	9.99E-17	9.35E-17
l= 3	1.63E-16	1.84E-16	1.84E-16	2.03E-16	2.26E-16	2.22E-16	2.04E-16	1.75E-16
l= 4	2.59E-16	3.06E-16	3.21E-16	3.60E-16	3.98E-16	3.94E-16	3.64E-16	3.03E-16
l= 5	3.59E-16	4.46E-16	4.84E-16	5.38E-16	5.99E-16	6.25E-16	6.19E-16	5.55E-16
l= 6	4.97E-16	5.65E-16	5.95E-16	6.37E-16	6.98E-16	7.47E-16	7.98E-16	8.21E-16
n= 8	4.34E-15	4.72E-15	4.82E-15	4.83E-15	4.42E-15	3.90E-15	3.26E-15	2.54E-15
l= 0	5.86E-17	1.04E-16	1.33E-16	1.69E-16	1.59E-16	1.25E-16	8.42E-17	4.86E-17
l= 1	1.32E-16	2.06E-16	2.69E-16	3.40E-16	3.32E-16	2.70E-16	1.90E-16	1.15E-16
l= 2	2.55E-16	3.30E-16	3.62E-16	3.95E-16	4.15E-16	3.88E-16	3.22E-16	2.30E-16
l= 3	3.66E-16	4.41E-16	4.50E-16	4.33E-16	3.97E-16	3.87E-16	3.70E-16	3.13E-16
l= 4	4.25E-16	4.95E-16	5.46E-16	5.82E-16	5.01E-16	4.12E-16	3.44E-16	3.05E-16
l= 5	6.74E-16	6.79E-16	6.45E-16	6.29E-16	6.42E-16	5.97E-16	4.90E-16	3.52E-16
l= 6	1.07E-15	1.07E-15	1.01E-15	8.70E-16	6.72E-16	5.88E-16	5.46E-16	5.08E-16
l= 7	1.36E-15	1.39E-15	1.41E-15	1.41E-15	1.30E-15	1.13E-15	9.12E-16	6.62E-16
$\sigma_{ct,tot}$	2.39E-14	2.31E-14	2.22E-14	2.12E-14	2.01E-14	1.94E-14	1.88E-14	1.79E-14
$\sigma_{ex,de-ex}$								
n= 1	3.51E-28	1.87E-26	8.04E-26	1.49E-24	3.69E-23	1.44E-22	7.87E-22	8.53E-21
l= 0	3.51E-28	1.87E-26	8.04E-26	1.49E-24	3.69E-23	1.44E-22	7.87E-22	8.53E-21
σ_{ion}	4.96E-16	9.99E-16	1.48E-15	2.45E-15	3.80E-15	4.59E-15	5.19E-15	5.51E-15

Table 5: Cross sections (in units of 10^{-16} cm²) for state-specific and total charge transfer, excitation, de-excitation and ionization for the $H(2s) + B^{+5}$ as a function of energy (in units of keV/u).

E(keV/u)	.05	.10	.20	.50	1.00	2.00	5.00	10.00
σ_{ct}								
n= 2	1.05E-61	4.94E-49	4.52E-40	3.58E-32	3.86E-28	4.23E-25	2.05E-22	3.70E-21
l= 0	5.27E-62	2.47E-49	2.26E-40	1.52E-32	1.07E-28	1.62E-25	8.80E-23	1.51E-21
l= 1	5.27E-62	2.47E-49	2.26E-40	2.05E-32	2.79E-28	2.61E-25	1.16E-22	2.18E-21
n= 3	1.29E-19	5.70E-19	1.60E-18	4.46E-18	8.91E-18	2.29E-17	6.11E-17	8.04E-17
l= 0	4.28E-20	1.88E-19	5.20E-19	1.38E-18	2.42E-18	4.40E-18	5.94E-18	4.61E-18
l= 1	6.44E-20	2.85E-19	8.00E-19	2.23E-18	4.36E-18	1.02E-17	2.09E-17	2.08E-17
l= 2	2.16E-20	9.68E-20	2.80E-19	8.58E-19	2.12E-18	8.24E-18	3.42E-17	5.50E-17
n= 4	2.43E-21	8.15E-21	5.60E-20	1.84E-18	1.23E-17	4.80E-17	1.72E-16	3.20E-16
l= 0	6.06E-22	1.99E-21	1.12E-20	2.92E-19	1.61E-18	5.66E-18	2.23E-17	3.74E-17
l= 1	1.09E-21	3.45E-21	1.13E-20	2.88E-19	2.50E-18	1.24E-17	5.48E-17	1.08E-16
l= 2	6.09E-22	2.08E-21	1.55E-20	5.13E-19	3.28E-18	1.13E-17	2.84E-17	5.96E-17
l= 3	1.23E-22	6.30E-22	1.80E-20	7.48E-19	4.87E-18	1.87E-17	6.69E-17	1.16E-16
n= 5	1.36E-16	2.00E-16	2.51E-16	4.09E-16	7.53E-16	1.19E-15	1.51E-15	1.40E-15
l= 0	3.12E-19	2.79E-18	6.24E-18	2.10E-17	4.37E-17	7.51E-17	8.68E-17	5.64E-17
l= 1	2.72E-17	3.62E-17	4.07E-17	7.21E-17	1.49E-16	2.34E-16	2.51E-16	1.74E-16
l= 2	5.78E-17	7.11E-17	7.12E-17	1.02E-16	1.83E-16	2.71E-16	3.61E-16	3.59E-16
l= 3	4.09E-17	5.15E-17	7.26E-17	1.10E-16	1.82E-16	2.39E-16	2.37E-16	3.01E-16
l= 4	9.91E-18	3.81E-17	6.04E-17	1.04E-16	1.95E-16	3.73E-16	5.75E-16	5.12E-16
n= 6	2.65E-16	4.31E-16	5.20E-16	5.92E-16	6.14E-16	6.14E-16	5.53E-16	4.69E-16
l= 0	4.81E-18	6.00E-18	6.67E-18	8.98E-18	1.12E-17	1.41E-17	1.86E-17	1.58E-17
l= 1	5.43E-18	6.53E-18	7.45E-18	1.13E-17	1.78E-17	2.65E-17	3.36E-17	3.16E-17
l= 2	1.50E-17	1.95E-17	2.29E-17	3.05E-17	4.05E-17	5.17E-17	5.49E-17	5.48E-17
l= 3	6.68E-17	7.73E-17	8.25E-17	9.94E-17	1.03E-16	1.01E-16	9.39E-17	8.32E-17
l= 4	1.12E-16	1.41E-16	1.68E-16	1.88E-16	1.86E-16	1.74E-16	1.34E-16	1.07E-16
l= 5	6.18E-17	1.81E-16	2.33E-16	2.54E-16	2.55E-16	2.46E-16	2.18E-16	1.76E-16
n= 7	1.46E-21	8.84E-20	1.55E-18	2.07E-17	8.06E-17	2.21E-16	5.66E-16	8.29E-16
l= 0	2.20E-23	1.24E-21	2.41E-20	4.19E-19	1.91E-18	5.95E-18	1.45E-17	1.38E-17
l= 1	7.30E-23	3.43E-21	5.44E-20	7.17E-19	3.82E-18	1.35E-17	3.26E-17	3.59E-17
l= 2	1.34E-22	6.55E-21	1.12E-19	1.49E-18	6.45E-18	1.99E-17	5.71E-17	7.78E-17
l= 3	1.61E-22	8.62E-21	1.50E-19	2.36E-18	9.96E-18	2.90E-17	7.69E-17	1.20E-16
l= 4	2.67E-22	1.31E-20	2.56E-19	3.45E-18	1.42E-17	4.15E-17	9.64E-17	1.35E-16
l= 5	3.30E-22	2.43E-20	4.02E-19	5.25E-18	1.94E-17	5.09E-17	1.31E-16	1.67E-16
l= 6	4.69E-22	3.11E-20	5.53E-19	7.01E-18	2.49E-17	5.98E-17	1.57E-16	2.79E-16
n= 8	9.95E-25	5.26E-22	4.08E-20	1.88E-18	1.29E-17	5.14E-17	2.17E-16	5.28E-16
l= 0	2.47E-26	1.20E-23	9.04E-22	3.92E-20	2.66E-19	1.43E-18	7.45E-18	1.01E-17
l= 1	3.60E-26	1.78E-23	1.54E-21	7.92E-20	6.62E-19	3.32E-18	1.66E-17	2.91E-17
l= 2	8.07E-26	3.67E-23	3.02E-21	1.40E-19	9.55E-19	4.26E-18	2.65E-17	5.63E-17
l= 3	8.42E-26	4.44E-23	3.46E-21	1.67E-19	1.21E-18	5.02E-18	2.63E-17	8.02E-17
l= 4	1.43E-25	5.99E-23	4.91E-21	2.30E-19	1.64E-18	6.17E-18	2.27E-17	8.16E-17
l= 5	1.23E-25	7.69E-23	5.92E-21	2.83E-19	1.99E-18	8.12E-18	2.52E-17	5.06E-17
l= 6	1.65E-25	1.15E-22	8.68E-21	3.80E-19	2.55E-18	1.01E-17	4.33E-17	7.39E-17
l= 7	3.38E-25	1.63E-22	1.23E-20	5.57E-19	3.67E-18	1.30E-17	4.90E-17	1.46E-16
$\sigma_{ct,tot}$	4.02E-16	6.31E-16	7.75E-16	1.04E-15	1.54E-15	2.39E-15	3.66E-15	4.33E-15
$\sigma_{ex,de-ex}$								
n= 1	0.00E+00	3.96E-34	8.23E-30	5.74E-26	4.28E-24	1.92E-22	4.57E-21	2.21E-20
l= 0	0.00E+00	3.96E-34	8.23E-30	5.74E-26	4.28E-24	1.92E-22	4.57E-21	2.21E-20
n= 3	5.77E-19	3.54E-18	1.69E-17	1.03E-16	2.95E-16	5.88E-16	1.01E-15	1.25E-15
l= 0	3.42E-21	1.52E-19	2.26E-18	2.40E-17	7.24E-17	1.42E-16	2.12E-16	2.31E-16
l= 1	2.83E-19	1.52E-18	4.76E-18	1.29E-17	3.18E-17	7.07E-17	1.92E-16	3.34E-16
l= 2	2.91E-19	1.87E-18	9.89E-18	6.65E-17	1.91E-16	3.75E-16	6.03E-16	6.87E-16
σ_{ion}	2.97E-25	4.13E-22	6.78E-20	5.88E-18	4.92E-17	1.83E-16	3.84E-16	3.70E-16

Table 6: Cross sections (in units of 10^{-16} cm²) for state-specific and total charge transfer+excitation, and ionization for the $He^+(2s) + He^{+2}$ collision system as a function of energy (in units of keV/u).

E(keV/u)	.10	.20	.50	1.00	2.00	5.00	10.00	20.00
σ_{ct+ex}								
n= 1	7.02E-51	3.38E-22	2.69E-21	6.15E-21	1.24E-20	3.23E-20	1.36E-19	7.12E-19
l= 0	7.02E-51	3.38E-22	2.69E-21	6.15E-21	1.24E-20	3.23E-20	1.36E-19	7.12E-19
n= 3	2.01E-16	2.59E-16	2.71E-16	2.67E-16	2.77E-16	3.79E-16	5.64E-16	7.93E-16
l= 0	3.15E-18	4.90E-18	6.20E-18	8.73E-18	1.63E-17	4.39E-17	8.20E-17	1.37E-16
l= 1	5.11E-17	5.58E-17	5.64E-17	5.41E-17	5.77E-17	9.64E-17	1.58E-16	2.40E-16
l= 2	1.47E-16	1.98E-16	2.08E-16	2.04E-16	2.03E-16	2.39E-16	3.24E-16	4.16E-16
n= 4	8.40E-17	1.00E-16	1.08E-16	1.10E-16	1.13E-16	1.34E-16	1.89E-16	2.77E-16
l= 0	1.56E-21	1.42E-20	1.58E-19	6.41E-19	1.82E-18	6.22E-18	1.33E-17	2.40E-17
l= 1	7.13E-19	9.16E-19	1.66E-18	3.28E-18	6.26E-18	1.51E-17	3.12E-17	5.53E-17
l= 2	2.80E-20	1.85E-19	1.51E-18	4.83E-18	1.15E-17	2.83E-17	5.16E-17	7.35E-17
l= 3	8.32E-17	9.90E-17	1.04E-16	1.01E-16	9.37E-17	8.46E-17	9.30E-17	1.24E-16
n= 5	7.25E-20	7.59E-19	5.63E-18	1.47E-17	2.82E-17	5.60E-17	1.15E-16	2.58E-16
l= 0	3.42E-23	6.28E-22	1.28E-20	8.26E-20	3.51E-19	2.01E-18	6.52E-18	1.72E-17
l= 1	1.02E-21	1.25E-20	1.41E-19	5.44E-19	1.53E-18	5.44E-18	1.63E-17	4.10E-17
l= 2	2.97E-22	6.13E-21	1.10E-19	5.52E-19	2.04E-18	8.66E-18	2.50E-17	5.49E-17
l= 3	3.52E-20	3.66E-19	2.66E-18	6.69E-18	1.19E-17	1.97E-17	3.53E-17	7.41E-17
l= 4	3.59E-20	3.73E-19	2.71E-18	6.86E-18	1.24E-17	2.02E-17	3.14E-17	7.05E-17
n= 6	6.62E-22	2.97E-20	7.65E-19	3.60E-18	1.01E-17	2.39E-17	3.62E-17	4.71E-17
l= 0	6.56E-24	1.19E-22	2.84E-21	2.47E-20	1.20E-19	5.27E-19	1.13E-18	1.94E-18
l= 1	2.41E-23	9.05E-22	2.65E-20	1.53E-19	5.28E-19	1.45E-18	2.28E-18	2.99E-18
l= 2	1.69E-23	7.73E-22	2.22E-20	1.38E-19	5.75E-19	2.17E-18	4.10E-18	6.03E-18
l= 3	1.84E-22	8.56E-21	2.22E-19	1.02E-18	2.71E-18	5.71E-18	8.10E-18	1.02E-17
l= 4	2.57E-22	1.11E-20	2.70E-19	1.22E-18	3.28E-18	7.39E-18	1.07E-17	1.34E-17
l= 5	1.73E-22	8.21E-21	2.20E-19	1.04E-18	2.88E-18	6.63E-18	9.82E-18	1.25E-17
n= 7	2.71E-23	2.36E-21	1.35E-19	9.88E-19	3.82E-18	1.23E-17	2.19E-17	3.16E-17
l= 0	2.01E-24	3.78E-23	9.15E-22	9.16E-21	4.58E-20	1.93E-19	4.13E-19	7.15E-19
l= 1	4.80E-24	1.75E-22	7.05E-21	4.96E-20	1.80E-19	4.95E-19	7.60E-19	9.70E-19
l= 2	4.30E-24	1.84E-22	5.92E-21	4.09E-20	1.80E-19	7.41E-19	1.53E-18	2.48E-18
l= 3	5.42E-24	5.47E-22	3.26E-20	2.41E-19	9.06E-19	2.53E-18	3.84E-18	4.66E-18
l= 4	3.65E-24	4.35E-22	2.42E-20	1.66E-19	6.24E-19	2.07E-18	3.88E-18	5.78E-18
l= 5	3.34E-24	4.55E-22	2.75E-20	1.95E-19	7.47E-19	2.56E-18	4.92E-18	7.48E-18
l= 6	3.62E-24	5.23E-22	3.70E-20	2.86E-19	1.13E-18	3.67E-18	6.53E-18	9.47E-18
n= 8	7.74E-24	5.80E-22	3.47E-20	2.72E-19	1.11E-18	3.71E-18	6.66E-18	9.69E-18
l= 0	7.88E-25	1.53E-23	2.82E-22	2.99E-21	1.48E-20	5.95E-20	1.21E-19	2.06E-19
l= 1	1.87E-24	5.95E-23	1.83E-21	1.28E-20	4.76E-20	1.35E-19	2.07E-19	2.57E-19
l= 2	1.87E-24	7.81E-23	2.39E-21	1.47E-20	5.40E-20	1.82E-19	3.57E-19	5.77E-19
l= 3	1.37E-24	9.53E-23	5.31E-21	4.32E-20	1.82E-19	5.77E-19	9.21E-19	1.12E-18
l= 4	8.43E-25	1.07E-22	7.20E-21	5.68E-20	2.32E-19	7.62E-19	1.34E-18	1.82E-18
l= 5	4.55E-25	9.43E-23	6.36E-21	4.56E-20	1.74E-19	5.71E-19	1.10E-18	1.81E-18
l= 6	3.72E-25	8.94E-23	7.46E-21	6.16E-20	2.57E-19	8.39E-19	1.45E-18	2.00E-18
l= 7	1.76E-25	4.06E-23	3.84E-21	3.44E-20	1.54E-19	5.81E-19	1.17E-18	1.90E-18
n= 9	2.07E-25	1.29E-22	8.63E-21	6.66E-20	2.86E-19	1.01E-18	1.89E-18	2.83E-18
l= 0	7.82E-30	1.06E-26	4.84E-24	1.01E-22	8.76E-22	6.13E-21	1.66E-20	3.43E-20
l= 1	2.66E-27	5.94E-24	2.79E-22	1.56E-21	5.76E-21	1.95E-20	3.60E-20	5.49E-20
l= 2	4.31E-27	1.79E-23	7.63E-22	3.61E-21	1.13E-20	3.42E-20	6.41E-20	1.02E-19
l= 3	1.40E-26	2.70E-23	1.29E-21	7.27E-21	2.65E-20	8.77E-20	1.63E-19	2.52E-19
l= 4	4.59E-26	3.05E-23	1.98E-21	1.51E-20	6.35E-20	2.12E-19	3.57E-19	4.63E-19
l= 5	6.82E-26	2.65E-23	2.22E-21	1.94E-20	8.66E-20	3.01E-19	5.27E-19	7.06E-19
l= 6	5.05E-26	1.54E-23	1.48E-21	1.38E-20	6.34E-20	2.38E-19	4.65E-19	7.25E-19
l= 7	1.88E-26	5.14E-24	5.29E-22	5.06E-21	2.39E-20	9.87E-20	2.20E-19	4.05E-19
l= 8	2.81E-27	7.28E-25	7.78E-23	7.58E-22	3.69E-21	1.69E-20	4.30E-20	9.29E-20
$\sigma_{ct+ex;tot}$	2.85E-16	3.60E-16	3.86E-16	3.93E-16	4.34E-16	6.10E-16	9.35E-16	1.42E-15
σ_{ion}	2.87E-23	2.24E-21	1.58E-19	1.55E-18	8.04E-18	3.79E-17	9.48E-17	2.03E-16

Table 7: Cross sections (in units of 10^{-16} cm²) for state-specific and total charge transfer, excitation, de-excitation and ionization for the $He^+(2s) + Li^{+3}$ collision system as a function of energy (in units of keV/u).

E(keV/u)	.05	.10	.20	.50	1.00	2.00	5.00	10.00
σ_{ct}								
n= 2	3.36E-27	1.63E-20	6.05E-20	2.29E-19	1.16E-18	5.92E-18	2.78E-17	5.35E-17
l= 0	1.68E-27	8.12E-21	3.02E-20	1.13E-19	5.38E-19	2.43E-18	9.24E-18	1.66E-17
l= 1	1.68E-27	8.13E-21	3.03E-20	1.16E-19	6.20E-19	3.50E-18	1.85E-17	3.69E-17
n= 3	6.84E-17	9.28E-17	1.91E-16	6.92E-16	1.33E-15	1.96E-15	2.31E-15	2.14E-15
l= 0	5.10E-19	6.43E-18	3.78E-17	1.56E-16	2.67E-16	3.39E-16	4.05E-16	4.07E-16
l= 1	3.41E-17	4.53E-17	8.73E-17	2.98E-16	5.42E-16	7.24E-16	7.57E-16	7.61E-16
l= 2	3.38E-17	4.11E-17	6.54E-17	2.38E-16	5.26E-16	8.94E-16	1.14E-15	9.70E-16
n= 4	2.09E-17	6.73E-17	9.31E-17	1.00E-16	1.06E-16	1.20E-16	1.52E-16	1.66E-16
l= 0	9.38E-19	1.48E-18	1.50E-18	1.66E-18	2.51E-18	4.71E-18	8.38E-18	1.07E-17
l= 1	1.97E-19	6.65E-19	1.14E-18	2.30E-18	4.40E-18	9.02E-18	2.03E-17	2.75E-17
l= 2	9.27E-18	1.47E-17	1.51E-17	1.66E-17	2.02E-17	2.76E-17	3.93E-17	4.24E-17
l= 3	1.05E-17	5.05E-17	7.54E-17	7.95E-17	7.86E-17	7.83E-17	8.36E-17	8.56E-17
n= 5	1.83E-20	4.13E-19	3.04E-18	1.57E-17	3.45E-17	5.71E-17	8.74E-17	1.10E-16
l= 0	2.56E-24	1.61E-22	2.80E-21	4.88E-20	2.32E-19	7.88E-19	2.50E-18	4.54E-18
l= 1	1.83E-22	2.66E-21	2.08E-20	1.45E-19	5.35E-19	1.67E-18	6.00E-18	1.10E-17
l= 2	1.08E-22	4.03E-21	3.91E-20	4.10E-19	1.54E-18	4.18E-18	1.08E-17	1.72E-17
l= 3	6.85E-21	9.79E-20	7.21E-19	3.36E-18	7.04E-18	1.15E-17	1.93E-17	2.58E-17
l= 4	1.12E-20	3.08E-19	2.25E-18	1.17E-17	2.52E-17	3.90E-17	4.88E-17	5.15E-17
n= 6	1.58E-24	4.41E-22	2.73E-20	9.35E-19	5.25E-18	1.62E-17	4.15E-17	7.88E-17
l= 0	2.20E-27	8.42E-25	7.96E-23	5.80E-21	5.32E-20	2.54E-19	1.21E-18	3.72E-18
l= 1	2.36E-26	5.92E-24	3.67E-22	1.60E-20	1.22E-19	5.31E-19	2.82E-18	9.67E-18
l= 2	1.65E-26	6.29E-24	5.45E-22	3.40E-20	2.72E-19	1.16E-18	4.60E-18	1.25E-17
l= 3	4.07E-25	9.98E-23	5.84E-21	1.78E-19	9.38E-19	2.80E-18	7.16E-18	1.17E-17
l= 4	7.37E-25	1.96E-22	1.14E-20	3.63E-19	1.94E-18	5.64E-18	1.27E-17	1.92E-17
l= 5	3.91E-25	1.33E-22	9.05E-21	3.38E-19	1.93E-18	5.77E-18	1.30E-17	2.19E-17
n= 7	2.99E-27	3.53E-24	8.51E-22	1.10E-19	1.17E-18	5.49E-18	1.74E-17	2.58E-17
l= 0	2.34E-28	1.12E-25	1.20E-23	1.28E-21	1.67E-20	9.78E-20	4.19E-19	7.58E-19
l= 1	2.27E-28	1.21E-25	1.73E-23	2.38E-21	3.10E-20	1.77E-19	6.68E-19	1.05E-18
l= 2	1.34E-28	1.43E-25	3.56E-23	5.81E-21	6.97E-20	3.74E-19	1.36E-18	2.15E-18
l= 3	6.42E-28	5.93E-25	1.31E-22	1.51E-20	1.51E-19	6.78E-19	2.18E-18	3.47E-18
l= 4	8.04E-28	7.07E-25	1.57E-22	2.17E-20	2.39E-19	1.15E-18	3.67E-18	5.29E-18
l= 5	6.17E-28	9.77E-25	2.39E-22	3.04E-20	3.22E-19	1.52E-18	4.79E-18	6.86E-18
l= 6	3.32E-28	8.72E-25	2.59E-22	3.37E-20	3.41E-19	1.49E-18	4.34E-18	6.18E-18
n= 8	5.20E-28	3.84E-25	1.12E-22	2.93E-20	4.70E-19	3.08E-18	1.42E-17	2.74E-17
l= 0	4.14E-29	2.28E-26	2.64E-24	4.12E-22	6.90E-21	4.90E-20	2.45E-19	5.27E-19
l= 1	4.82E-29	2.62E-26	3.24E-24	6.20E-22	1.04E-20	7.59E-20	4.55E-19	1.07E-18
l= 2	1.92E-29	1.76E-26	5.95E-24	1.62E-21	2.54E-20	1.73E-19	8.47E-19	1.76E-18
l= 3	7.99E-29	5.28E-26	1.36E-23	3.24E-21	4.83E-20	2.99E-19	1.32E-18	2.58E-18
l= 4	1.50E-28	9.28E-26	1.93E-23	4.49E-21	6.94E-20	4.37E-19	1.85E-18	3.24E-18
l= 5	1.20E-28	8.20E-26	2.02E-23	5.20E-21	8.57E-20	5.74E-19	2.68E-18	5.08E-18
l= 6	4.97E-29	5.66E-26	2.61E-23	7.38E-21	1.18E-19	7.59E-19	3.45E-18	6.75E-18
l= 7	1.20E-29	3.35E-26	2.07E-23	6.31E-21	1.06E-19	7.15E-19	3.34E-18	6.41E-18
$\sigma_{ct,tot}$	8.93E-17	1.61E-16	2.87E-16	8.09E-16	1.48E-15	2.17E-15	2.67E-15	2.66E-15
$\sigma_{ex,de-ex}$								
n= 1	4.44E-64	1.40E-43	4.15E-31	1.45E-26	1.28E-24	3.31E-23	4.31E-21	7.23E-20
l= 0	4.44E-64	1.40E-43	4.15E-31	1.45E-26	1.28E-24	3.31E-23	4.31E-21	7.23E-20
n= 3	7.18E-18	2.03E-17	3.39E-17	5.49E-17	7.06E-17	9.96E-17	2.00E-16	3.03E-16
l= 0	2.19E-19	6.20E-19	1.03E-18	1.74E-18	3.19E-18	9.64E-18	3.19E-17	4.93E-17
l= 1	1.64E-21	4.58E-20	3.66E-19	2.80E-18	8.62E-18	2.16E-17	6.40E-17	1.02E-16
l= 2	6.96E-18	1.97E-17	3.25E-17	5.04E-17	5.88E-17	6.83E-17	1.04E-16	1.52E-16
σ_{ion}	1.28E-26	1.21E-23	1.92E-21	1.94E-19	2.44E-18	1.59E-17	9.21E-17	2.37E-16

Table 8: Cross sections (in units of 10^{-16} cm²) for state-specific and total charge transfer, excitation, de-excitation, and ionization for the $He^+(2s) + Be^{+4}$ collision system as a function of energy (in units of keV/u).

E(keV/u)	.30	.50	.70	1.00	1.50	2.00	3.00	5.00
σ_{ct}								
n= 2	5.99E-22	6.67E-21	2.08E-20	5.41E-20	1.22E-19	1.89E-19	3.32E-19	6.77E-19
l= 0	2.99E-22	3.32E-21	1.03E-20	2.67E-20	5.99E-20	9.19E-20	1.57E-19	2.95E-19
l= 1	3.00E-22	3.35E-21	1.05E-20	2.73E-20	6.20E-20	9.70E-20	1.75E-19	3.82E-19
n= 3	6.84E-17	1.66E-16	2.70E-16	4.14E-16	6.04E-16	7.40E-16	9.08E-16	1.03E-15
l= 0	1.84E-17	4.12E-17	6.21E-17	8.71E-17	1.15E-16	1.33E-16	1.58E-16	1.85E-16
l= 1	1.28E-17	4.24E-17	7.85E-17	1.32E-16	2.03E-16	2.52E-16	3.06E-16	3.43E-16
l= 2	3.71E-17	8.28E-17	1.29E-16	1.95E-16	2.86E-16	3.56E-16	4.45E-16	5.06E-16
n= 4	8.12E-17	1.45E-16	2.02E-16	2.88E-16	4.80E-16	6.52E-16	9.31E-16	1.28E-15
l= 0	2.03E-18	7.22E-18	1.46E-17	2.55E-17	4.34E-17	5.91E-17	8.63E-17	1.22E-16
l= 1	2.42E-17	4.35E-17	5.76E-17	7.79E-17	1.23E-16	1.62E-16	2.27E-16	3.25E-16
l= 2	3.81E-17	5.79E-17	7.77E-17	1.05E-16	1.64E-16	2.07E-16	2.57E-16	2.97E-16
l= 3	1.69E-17	3.68E-17	5.23E-17	7.94E-17	1.50E-16	2.24E-16	3.61E-16	5.41E-16
n= 5	1.91E-16	2.23E-16	2.32E-16	2.27E-16	2.15E-16	2.06E-16	1.99E-16	2.00E-16
l= 0	1.91E-18	1.59E-18	1.66E-18	1.98E-18	2.53E-18	3.10E-18	4.30E-18	6.79E-18
l= 1	1.93E-18	2.33E-18	2.92E-18	3.66E-18	5.33E-18	7.19E-18	1.08E-17	1.62E-17
l= 2	9.91E-18	8.71E-18	9.03E-18	1.04E-17	1.29E-17	1.56E-17	2.08E-17	2.86E-17
l= 3	5.10E-17	5.55E-17	6.06E-17	6.03E-17	5.63E-17	5.32E-17	5.02E-17	4.83E-17
l= 4	1.26E-16	1.55E-16	1.58E-16	1.51E-16	1.37E-16	1.27E-16	1.13E-16	1.00E-16
n= 6	1.14E-18	5.19E-18	1.14E-17	2.20E-17	3.83E-17	5.19E-17	7.22E-17	9.89E-17
l= 0	2.09E-20	7.23E-20	1.52E-19	3.14E-19	5.75E-19	8.26E-19	1.34E-18	2.63E-18
l= 1	1.53E-20	7.98E-20	1.93E-19	4.16E-19	8.84E-19	1.44E-18	2.69E-18	5.54E-18
l= 2	7.60E-20	2.77E-19	5.88E-19	1.20E-18	2.27E-18	3.32E-18	5.38E-18	9.81E-18
l= 3	2.01E-19	8.79E-19	1.95E-18	3.67E-18	6.08E-18	7.91E-18	1.04E-17	1.34E-17
l= 4	3.52E-19	1.60E-18	3.46E-18	6.52E-18	1.11E-17	1.47E-17	1.97E-17	2.49E-17
l= 5	4.75E-19	2.28E-18	5.06E-18	9.82E-18	1.74E-17	2.37E-17	3.27E-17	4.26E-17
n= 7	7.19E-20	5.72E-19	1.78E-18	4.73E-18	1.10E-17	1.73E-17	2.78E-17	4.06E-17
l= 0	2.15E-21	1.27E-20	3.61E-20	9.78E-20	2.28E-19	3.58E-19	5.77E-19	8.70E-19
l= 1	1.63E-21	1.41E-20	4.31E-20	1.10E-19	2.56E-19	4.01E-19	6.31E-19	8.97E-19
l= 2	5.60E-21	3.60E-20	1.03E-19	2.76E-19	6.45E-19	1.02E-18	1.66E-18	2.50E-18
l= 3	1.15E-20	8.91E-20	2.78E-19	7.28E-19	1.63E-18	2.48E-18	3.76E-18	5.15E-18
l= 4	1.81E-20	1.45E-19	4.50E-19	1.18E-18	2.66E-18	4.09E-18	6.32E-18	8.66E-18
l= 5	1.86E-20	1.52E-19	4.76E-19	1.26E-18	2.93E-18	4.64E-18	7.51E-18	1.09E-17
l= 6	1.43E-20	1.23E-19	3.96E-19	1.08E-18	2.63E-18	4.31E-18	7.36E-18	1.16E-17
n= 8	2.97E-21	3.79E-20	1.48E-19	4.81E-19	1.39E-18	2.51E-18	4.81E-18	8.37E-18
l= 0	8.84E-23	6.40E-22	2.29E-21	7.40E-21	2.02E-20	3.52E-20	6.51E-20	1.14E-19
l= 1	5.29E-23	8.95E-22	3.16E-21	8.57E-21	2.24E-20	3.70E-20	6.09E-20	8.70E-20
l= 2	2.16E-22	2.13E-21	7.40E-21	2.33E-20	6.79E-20	1.24E-19	2.39E-19	4.28E-19
l= 3	2.98E-22	3.74E-21	1.50E-20	4.68E-20	1.23E-19	2.06E-19	3.53E-19	5.46E-19
l= 4	3.72E-22	5.19E-21	2.09E-20	6.88E-20	1.96E-19	3.50E-19	6.49E-19	1.07E-18
l= 5	5.12E-22	6.95E-21	2.67E-20	8.68E-20	2.55E-19	4.68E-19	9.06E-19	1.56E-18
l= 6	7.14E-22	9.10E-21	3.48E-20	1.11E-19	3.20E-19	5.83E-19	1.14E-18	2.06E-18
l= 7	7.21E-22	9.20E-21	3.76E-20	1.28E-19	3.84E-19	7.10E-19	1.40E-18	2.51E-18
$\sigma_{ct,tot}$	3.42E-16	5.40E-16	7.17E-16	9.56E-16	1.35E-15	1.67E-15	2.14E-15	2.66E-15
$\sigma_{ex,de-ex}$								
n= 1	4.03E-30	1.67E-26	2.44E-25	1.88E-24	2.00E-23	7.85E-23	4.54E-22	4.95E-21
l= 0	4.03E-30	1.67E-26	2.44E-25	1.88E-24	2.00E-23	7.85E-23	4.54E-22	4.95E-21
n= 3	5.49E-17	5.62E-17	6.33E-17	7.70E-17	9.10E-17	1.04E-16	1.38E-16	2.20E-16
l= 0	1.95E-18	2.45E-18	3.25E-18	4.95E-18	7.85E-18	1.18E-17	2.13E-17	3.98E-17
l= 1	2.48E-19	7.87E-19	1.53E-18	2.96E-18	7.33E-18	1.38E-17	3.05E-17	6.72E-17
l= 2	5.27E-17	5.29E-17	5.85E-17	6.91E-17	7.58E-17	7.89E-17	8.62E-17	1.13E-16
σ_{ion}	1.17E-20	1.44E-19	5.94E-19	2.22E-18	7.75E-18	1.68E-17	4.33E-17	1.15E-16

Table 9: Cross sections (in units of 10^{-16} cm²) for state-specific and total charge transfer, excitation, de-excitation and ionization for the $He^+(2s) + B^{+5}$ collision system as a function of energy (in units of keV/u).

E(keV/u)	.05	.10	.20	.50	1.00	2.00	5.00	10.00
σ_{ct}								
n= 2	2.26E-36	1.09E-30	6.49E-27	9.45E-24	3.40E-22	5.70E-21	8.21E-20	3.13E-19
l= 0	1.13E-36	5.46E-31	3.24E-27	4.70E-24	1.68E-22	2.78E-21	3.84E-20	1.33E-19
l= 1	1.13E-36	5.47E-31	3.25E-27	4.75E-24	1.72E-22	2.91E-21	4.37E-20	1.80E-19
n= 3	9.05E-26	1.36E-20	7.74E-20	7.35E-19	4.69E-18	2.33E-17	1.07E-16	2.19E-16
l= 0	2.74E-26	4.53E-21	2.53E-20	2.16E-19	1.18E-18	4.89E-18	2.02E-17	4.34E-17
l= 1	3.97E-27	6.79E-21	3.56E-20	1.91E-19	1.06E-18	6.50E-18	3.38E-17	7.47E-17
l= 2	5.91E-26	2.32E-21	1.64E-20	3.28E-19	2.45E-18	1.20E-17	5.34E-17	1.01E-16
n= 4	1.37E-15	2.10E-15	2.87E-15	3.55E-15	3.56E-15	3.17E-15	2.32E-15	1.66E-15
l= 0	2.66E-16	3.83E-16	4.63E-16	4.46E-16	3.86E-16	3.29E-16	2.09E-16	1.08E-16
l= 1	2.21E-16	4.92E-16	8.23E-16	1.07E-15	1.00E-15	8.37E-16	6.15E-16	4.21E-16
l= 2	3.93E-16	6.03E-16	8.56E-16	1.12E-15	1.08E-15	8.29E-16	5.72E-16	5.50E-16
l= 3	4.93E-16	6.18E-16	7.28E-16	9.17E-16	1.09E-15	1.17E-15	9.26E-16	5.83E-16
n= 5	1.33E-16	1.67E-16	1.96E-16	1.98E-16	2.32E-16	3.49E-16	7.55E-16	1.17E-15
l= 0	3.28E-19	1.78E-18	2.75E-18	5.23E-18	8.49E-18	1.67E-17	3.83E-17	4.42E-17
l= 1	2.63E-17	2.94E-17	2.91E-17	2.06E-17	2.27E-17	4.21E-17	1.11E-16	1.47E-16
l= 2	5.62E-17	5.96E-17	5.82E-17	4.46E-17	4.50E-17	6.34E-17	1.61E-16	2.95E-16
l= 3	4.01E-17	4.62E-17	5.77E-17	6.00E-17	7.08E-17	9.64E-17	1.41E-16	2.37E-16
l= 4	9.82E-18	3.02E-17	4.85E-17	6.71E-17	8.52E-17	1.30E-16	3.04E-16	4.44E-16
n= 6	2.18E-16	3.36E-16	3.61E-16	3.10E-16	2.42E-16	1.87E-16	1.70E-16	2.04E-16
l= 0	2.72E-18	2.61E-18	2.12E-18	1.71E-18	1.61E-18	2.21E-18	5.06E-18	7.38E-18
l= 1	3.70E-18	3.54E-18	3.09E-18	3.02E-18	3.14E-18	4.29E-18	9.58E-18	1.48E-17
l= 2	9.27E-18	9.89E-18	9.44E-18	8.43E-18	8.42E-18	1.03E-17	1.73E-17	2.57E-17
l= 3	5.00E-17	4.88E-17	4.27E-17	3.69E-17	2.77E-17	2.28E-17	2.66E-17	3.73E-17
l= 4	9.55E-17	1.10E-16	1.17E-16	9.94E-17	7.44E-17	5.32E-17	4.06E-17	4.24E-17
l= 5	5.65E-17	1.61E-16	1.87E-16	1.61E-16	1.27E-16	9.39E-17	7.09E-17	7.63E-17
n= 7	3.96E-17	5.92E-17	6.92E-17	8.41E-17	9.11E-17	1.09E-16	2.32E-16	5.59E-16
l= 0	1.86E-18	2.77E-18	3.22E-18	3.69E-18	3.39E-18	3.46E-18	9.52E-18	1.68E-17
l= 1	1.86E-18	2.78E-18	3.28E-18	4.14E-18	4.93E-18	7.19E-18	2.32E-17	4.58E-17
l= 2	3.15E-18	4.68E-18	5.43E-18	6.60E-18	7.90E-18	1.16E-17	3.41E-17	8.05E-17
l= 3	1.10E-17	1.64E-17	1.89E-17	2.14E-17	2.00E-17	1.89E-17	3.49E-17	1.06E-16
l= 4	1.35E-17	2.01E-17	2.34E-17	2.73E-17	2.65E-17	2.54E-17	2.90E-17	7.65E-17
l= 5	6.92E-18	1.04E-17	1.24E-17	1.59E-17	1.85E-17	2.39E-17	4.35E-17	5.68E-17
l= 6	1.32E-18	2.01E-18	2.60E-18	5.16E-18	9.71E-18	1.86E-17	5.81E-17	1.76E-16
n= 8	1.52E-24	3.07E-22	1.69E-20	6.71E-19	3.95E-18	1.38E-17	4.51E-17	8.32E-17
l= 0	2.16E-26	5.92E-24	3.68E-22	1.49E-20	7.54E-20	2.67E-19	1.14E-18	2.06E-18
l= 1	2.55E-26	5.91E-24	3.90E-22	2.23E-20	1.79E-19	6.48E-19	1.73E-18	3.45E-18
l= 2	6.04E-26	1.44E-23	9.17E-22	3.88E-20	2.29E-19	8.51E-19	3.16E-18	6.42E-18
l= 3	1.69E-25	3.44E-23	1.84E-21	7.52E-20	4.12E-19	1.30E-18	4.52E-18	8.69E-18
l= 4	3.49E-25	5.96E-23	2.94E-21	1.09E-19	6.39E-19	2.18E-18	6.50E-18	1.17E-17
l= 5	4.55E-25	7.85E-23	3.60E-21	1.27E-19	7.12E-19	2.44E-18	7.72E-18	1.38E-17
l= 6	3.13E-25	6.32E-23	3.29E-21	1.26E-19	7.47E-19	2.65E-18	8.84E-18	1.65E-17
l= 7	1.23E-25	4.48E-23	3.51E-21	1.58E-19	9.57E-19	3.44E-18	1.15E-17	2.06E-17
$\sigma_{ct,tot}$	1.76E-15	2.66E-15	3.50E-15	4.14E-15	4.14E-15	3.86E-15	3.68E-15	4.00E-15
$\sigma_{ex,de-ex}$								
n= 1	2.02E-71	1.73E-49	1.71E-28	2.55E-25	6.78E-24	7.11E-23	2.23E-21	5.38E-20
l= 0	2.02E-71	1.73E-49	1.71E-28	2.55E-25	6.78E-24	7.11E-23	2.23E-21	5.38E-20
n= 3	3.17E-23	2.98E-21	6.63E-20	1.04E-18	4.20E-18	1.93E-17	1.53E-16	4.49E-16
l= 0	1.08E-24	1.33E-22	4.51E-21	1.18E-19	7.21E-19	4.69E-18	3.68E-17	8.79E-17
l= 1	1.77E-25	6.86E-23	3.94E-21	1.24E-19	8.53E-19	6.82E-18	6.46E-17	1.88E-16
l= 2	3.05E-23	2.78E-21	5.79E-20	8.02E-19	2.63E-18	7.78E-18	5.13E-17	1.73E-16
σ_{ion}	2.25E-33	6.76E-28	4.91E-24	1.28E-20	6.70E-19	1.09E-17	1.20E-16	3.50E-16

Cross-sections for ion production in $H^+ + H_2$ collisions calculated with the trajectory-surface-hopping method

A. Ichihara¹, O. Iwamoto, K. Yokoyama

Tokai research establishment,
Japan Atomic Energy Research Institute,
Tokai-mura, Ibaraki, Japan

Abstract. Cross sections for ion production occurring in the $H^+ + H_2$, $H^+ + D_2$, $D^+ + H_2$, and $D^+ + D_2$ collisions have been calculated in the center-of-mass collision energy range of $2.5 \leq E_{cm} \leq 8.0$ eV by using the conventional trajectory-surface-hopping method with the ab initio potential energy surfaces. The vibrational and rotational quantum numbers of reactant molecules have been taken in the range ($0 \leq v \leq 6$, $j=1$) for H_2 and ($0 \leq v \leq 8$, $j=1$) for D_2 , respectively, and the v dependence of cross sections has been evaluated. From the results it was found that the charge transfer reaction is enhanced remarkably as v increases. On the other hand, for other ion production by nuclear rearrangement or dissociation, the v dependence is much small compared with the charge transfer. The cross sections have been calculated with $j=5$ and 10 for the $H^+ + D_2$ collisions, and it has been confirmed that the j effect is secondary to the v effect. The vibrational state distribution of diatomic products for each collision system has been evaluated and tabulated.

1. Introduction

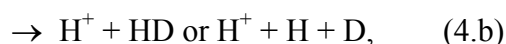
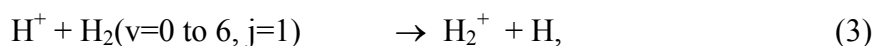
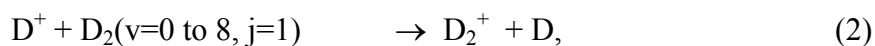
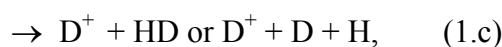
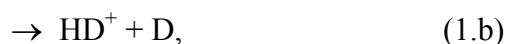
Ion-molecule reactions occurring in the H_3^+ system and its isotopic variants have been attracting the interest of both experimentalists and theorists. Accurate knowledge of these reactions is important for the analysis of collision phenomena taking place near the wall of fusion reactor. Neutral atoms and molecules are produced there because of the low temperature. These reactions are also fundamental to the development of gas diverter in which the hydrogen molecules are used as shock absorber.

On the bases of needs for the research and development of fusion reactor, we have compiled experimental cross sections for ion-molecule reactions occurring in hydrogen and helium species [1]. Also, we have calculated ion production cross sections for the $H^+ + H_2$ collisions within the framework of the conventional trajectory-surface-hopping (TSH) model [2–3]. It has been confirmed from the results that the calculated cross sections for the $H^+ + D_2(v=0)$, $D^+ + H_2(v=0)$, and $D^+ + D_2(v=0)$ systems, where v is the vibrational quantum number, give a good agreement with the experimental cross sections in the center-of mass collision energy range of $2.5 \leq E_{cm} \leq 8.0$ eV [2, 4, 5].

In the fusion reactor many hydrogen molecules may be in the vibrationally and rotationally excited states through collisions with other ions and neutral particles. Actually, in a low energy collision between H^+ and H_2 , a long-lived H_3^+ intermediate is created and the collision energy is converted to the energy to excite the vibrational state of H_2 . Therefore, collision data for the excited H_2 molecules are of great importance. However, it is difficult to measure cross sections with H_2 in a specific excited state. Thus we applied the TSH calculation in order to evaluate the ion production cross sections for excited molecules. As the TSH calculation could reproduce experimental cross sections for $v=0$, TSH is thought to be the most practical method to estimate absolute cross sections for the reaction of H^+ with the excited H_2 molecule, if the collision energy is high enough from the threshold [2, 6].

¹ E-mail: ichihara@ndc.tokai.jaeri.go.jp.

In this paper, we present the results for reactions:



where j is the rotational quantum number. We discuss the (v, j) dependence of cross section for each ion production. We also present the vibrational state (v') distribution of diatomic products, which is important when we consider the secondary reactions in the fusion reactor.

2. Computational method

Absolute cross sections have been calculated by the trajectory-surface-hopping (TSH) method of Tully and Preston [7] with the three-dimensional ab initio potential energy surfaces (ab initio PES's) [8, 9] in the center-of-mass collision energy range of $2.5 \leq E_{\text{cm}} \leq 8.0$ eV. The details of computational method are described in Refs [2, 7, 10].

Here, we mention only the characteristics of our TSH calculation. We evaluated the probability of surface hopping (nonadiabatic electronic transition) by using the formula established by Zhu and Nakamura (ZN) [11, 12], instead of the well-known Landau-Zener (LZ) formula [13–15], because the ZN formula is more accurate than the LZ formula. The hopping probability was evaluated in a trajectory calculation when a surface hop is possible under the conventional TSH description [7, 16]. 9000 to 30 000 trajectories were run for each combination of (E_{cm}, v, j) to obtain converged cross section. The vibrational and rotational (v', j') states of diatomic product were evaluated at the terminal point of each trajectory based on the procedure of Blais and Truhler [17], and the vibrational state distribution was derived from a set of trajectories. The rotational state distribution of products was not calculated, since the number of trajectories was insufficient to obtain the converged results.

3. Results and discussion

3.1. Comparison of the calculated total cross section with the experiment

The TSH cross sections for ion production from the $\text{H}^+ + \text{D}_2 (v=0, j=1)$, $\text{D}^+ + \text{D}_2 (v=0, j=1)$, and $\text{D}^+ + \text{H}_2 (v=0, j=1)$ collisions are shown in Figs.1 to 3, respectively. The experimental cross sections by the guided beam (GB) method are also shown in each figure. In the GB experiment at room temperature, most of reactant molecules are thought to be in the $(v, j)=(0, 1)$ state [5]. In Fig.1 the experimental cross sections have been determined with the estimated uncertainty of 20% [4], while they have been determined with the estimated uncertainty of 10% in Figs.2 and 3 [5]. It can be seen from Figs.1 to 3 that the TSH cross sections give a good agreement with the experimental cross sections in the calculated energy range, if the experimental uncertainty is

taken into account. In Figs.1 to 3, the energy dependence of cross section is well reproduced for every ion production. From above results it is expected that the TSH calculation is applicable to estimate absolute cross sections for the reaction of H^+ with H_2 in the excited states, where no experimental data is available.

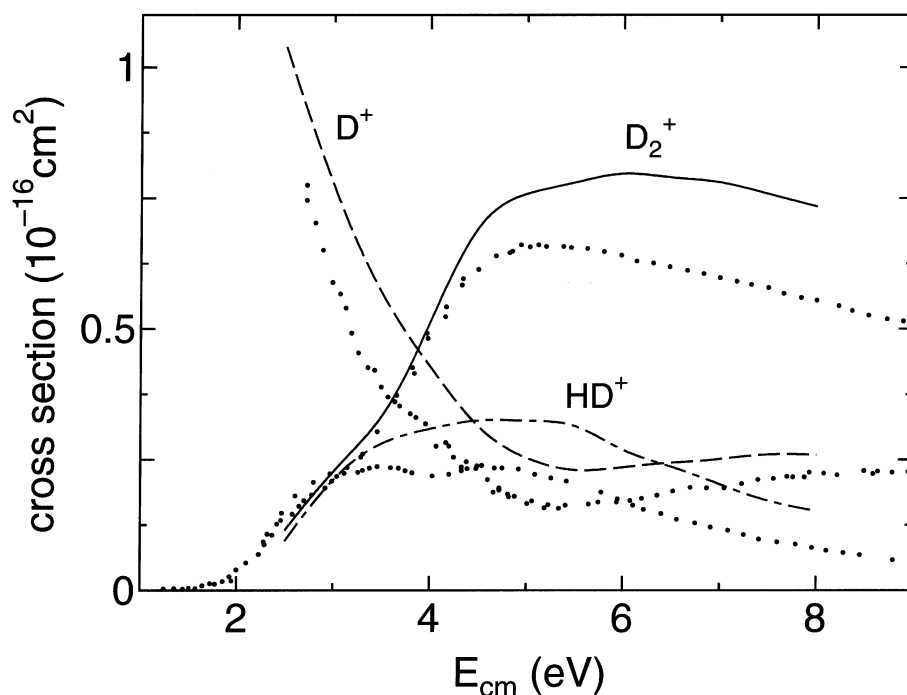


Fig.1. The cross sections for the production of D_2^+ , D^+ , and HD^+ ions from the $H^+ + D_2$ collisions. The cross sections are given as a function of the center-of-mass collision energy E_{cm} . The solid, dashed, and dash-dotted lines represent the TSH cross sections for the D_2^+ , D^+ , and HD^+ production from the $H^+ + D_2(v=0, j=1)$ collisions, respectively. The experimental results of Ochs and Teloj [4] are shown by dots in the figure.

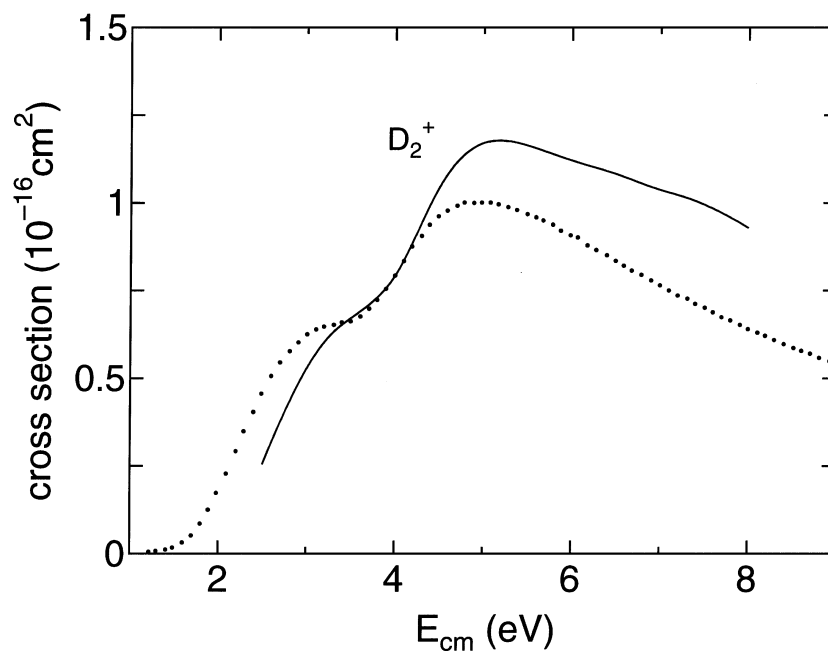


Fig.2. The cross sections for the reaction $D^+ + D_2 \rightarrow D_2^+ + D$. The cross sections are given as a function of the center-of-mass collision energy E_{cm} . The solid line represents the TSH cross section for the $D^+ + D_2(v=0, j=1)$ collisions. The experimental results of Schlier et al. [5] are shown by dots in the figure.

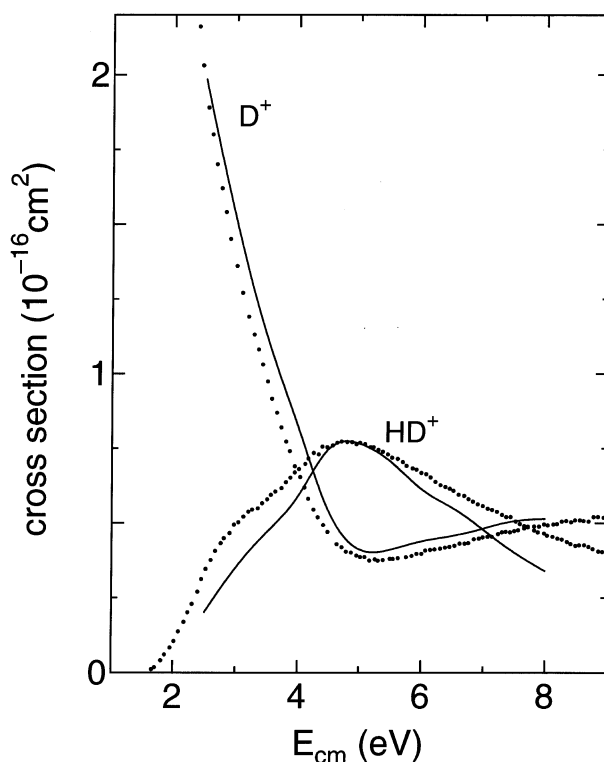


Fig.3. The cross sections for the production of HD^+ and D^+ ions from the $D^+ + H_2$ collisions. The cross sections are given as a function of the center-of-mass collision energy E_{cm} . The solid lines represent the TSH cross sections for the $D^+ + H_2(v=0, j=1)$ collisions. The experimental results of Schlier et.al [5] are shown by dots in the figure.

3.2. The (v, j) dependence of total cross sections

3.2.1. The $H^+ + D_2$ system

Figure 4 shows the cross sections for the reaction $H^+ + D_2(v=0 \text{ to } 8, j=1) \rightarrow D_2^+ + H$. It can be seen from Fig.4 that the D_2^+ production is enhanced remarkably as v increases up to $v=7$, and then becomes less dependent on v for $v \geq 7$.

The enhancement of the D_2^+ production (charge transfer) for $0 \leq v \leq 6$ can be explained from the characteristics of the ab initio potential energy surfaces (PES's) employed. Figure 5 shows the section of PES's at $R=5.29 \times 10^{-8}$ cm (10.0 bohr) in the isosceles triangle geometry, where R is the distance between H^+ and D_2 . PES's are given as a function of the internuclear distance (r) of D_2 . It can be seen from Fig.5 that the avoided crossing of two PES's appears at $r=1.32 \times 10^{-8}$ cm (2.5 bohr), where the electronic structure of PES in the ground state changes from $H^+ + D_2$ to $H + D_2^+$ drastically. It is known that the avoided crossing arises in the region ($r \approx 1.32 \times 10^{-8}$ cm, $R > 2.65 \times 10^{-8}$ cm (5.0 bohr)) in the three-dimensional PES's [8, 18]. In Fig.5 the D_2^+ production is induced when a trajectory running on the ground state PES reaches the avoided crossing point, because there which (upper or lower) PES is used for the subsequent trajectory calculation is determined in the conventional TSH model [2, 7]. From Fig.5 D_2 in the $v \geq 6$ state can take $r=1.32 \times 10^{-8}$ cm where the avoided crossing arises, so that the D_2^+ production becomes possible if D_2 is excited into the $v \geq 6$ vibrational state. Thus, if the reactant D_2 is in the vibrational excited state in advance, further vibrational excitation into the $v \geq 6$ state is brought about easily by the collision with H^+ . Therefore, the D_2^+ production is enhanced remarkably with the increase of v .

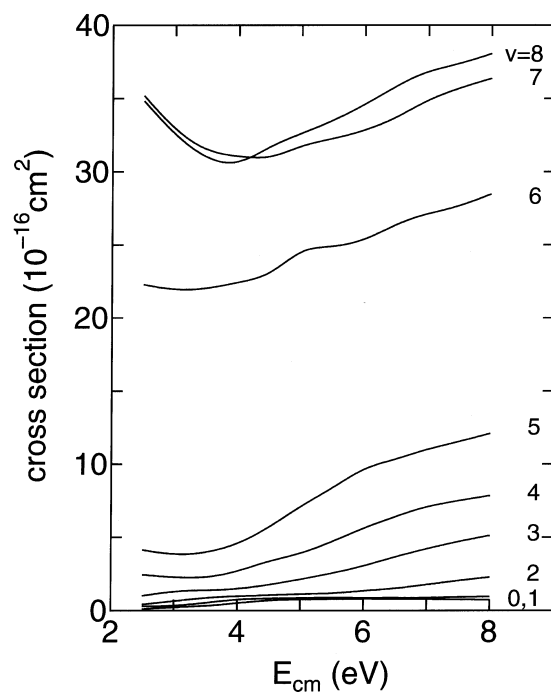


Fig.4. The TSH cross sections for the reaction $H^+ + D_2(v=0 \text{ to } 8, j=1) \rightarrow D_2^+ + H$. The cross sections are given as a function of the center-of-mass collision energy E_{cm} .

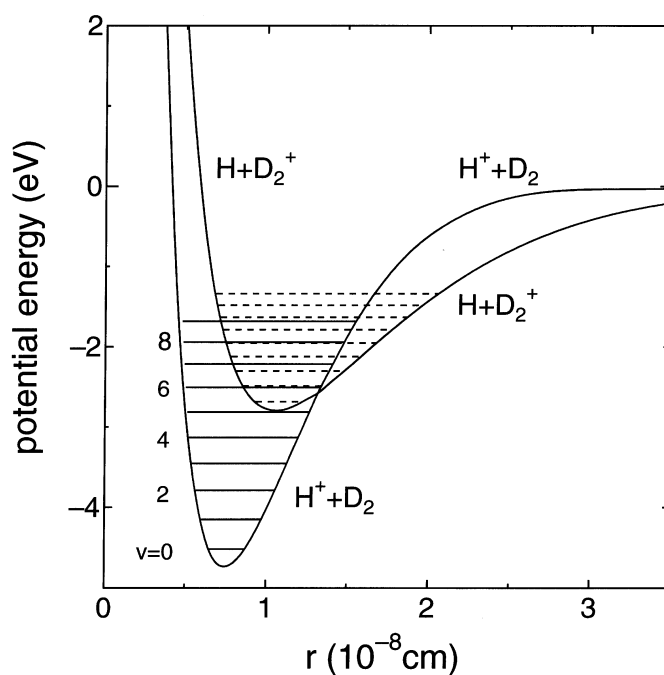


Fig.5. Section of the *ab initio* potential energy surfaces at $R=5.29 \times 10^{-8} \text{ cm}$ (10.0 bohr) in the isosceles triangle geometry. R is the distance from the mid point of deuteron pair to a proton. The potential curves are given as a function of the internuclear distance r between two deuterons. In the figure, the vibrational energy levels of D_2 and D_2^+ are shown by the solid and dotted lines, respectively.

From Fig.4 it is observed that the v dependence of the D_2^+ production cross section is small for $v \geq 7$. For $v \geq 7$, the production of D_2^+ is possible before H^+ comes near to D_2 , because the reactant D_2 can take $r \geq 1.32 \times 10^{-8} \text{ cm}$. It is thought that the increment of cross section between $v=6$ and

7 comes from the D_2^+ production (charge transfer) occurring before two reactants H^+ and D_2 approach. In Fig.4, however, the D_2^+ production is not enhanced any longer for $v \geq 7$.

Figure 6 shows the j dependence of the D_2^+ production cross section. As can be seen from Fig.6, the cross section increases appreciably as j becomes high. If D_2 is in the rotational excited state, the centrifugal force of the D_2 rotator contributes to the enlargement of the D-D bond length, and that should increase the D_2^+ production. From Figs.4 and 6 it is concluded that the vibrational excited state v has the primary effect on the D_2^+ production, and the rotational excited state j has the secondary effect.

Figure7 shows the cross sections for the reaction $H^+ + D_2 (v=0 \text{ to } 8, j=1) \rightarrow HD^+ + D$. It can be seen from Fig.7 that the HD^+ production is promoted at low collision energies E_{cm} below about 4 eV. In our TSH calculation for low collision energies, trajectories are trapped around the deep well of the ground state PES, and long-lived HD_2^+ intermediates are produced there. Then the H-D pair is formed when HD_2^+ decomposes. Thus, many HD^+ ions are formed via the HD_2^+ formation. As the formation of the HD_2^+ intermediate increases with the decrease of collision energy, the HD^+ production may be promoted at low collision energy.

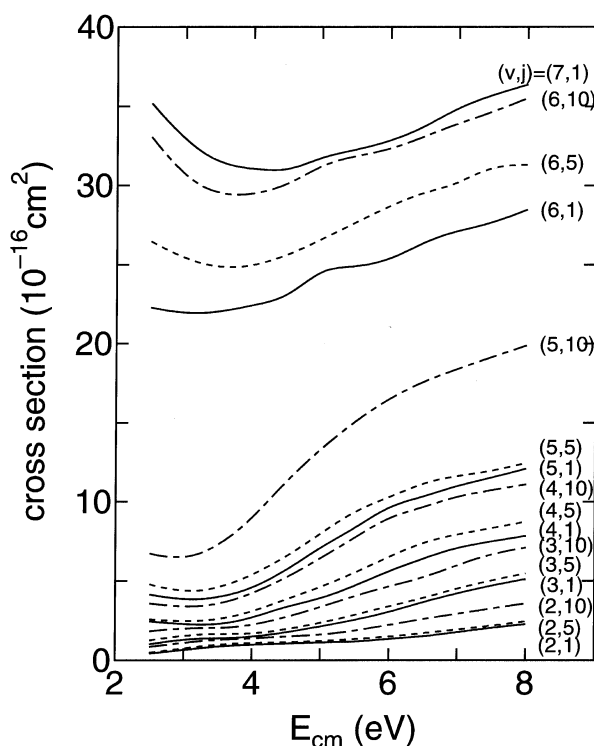


Fig.6. The dependence of the D_2^+ production cross section on the D_2 rotational excited state j . The TSH cross sections are given as a function of the center-of-mass collision energy E_{cm} . The solid, dotted, and dash-dotted lines represent the cross sections for $j=1, 5,$ and $10,$ respectively.

In the trajectory calculation, the HD^+ ion is produced if the H-D pair is formed on the ground state PES and the charge transfer is induced when two particles (H-D and D^+) recede. The HD^+ ion can be produced if the H-D pair has enough internal energy to take $r \geq 1.32 \times 10^{-8}$ cm [19]. From Fig.7 it is observed that the HD^+ production increases as v increases up to $v=6$ for E_{cm} below about 4 eV. Thus, for $v \leq 6$ and $E_{cm} < 4$ eV, the vibrational energy of D_2 contributes to the formation of the H-D pair which has enough internal energy to produce HD^+ .

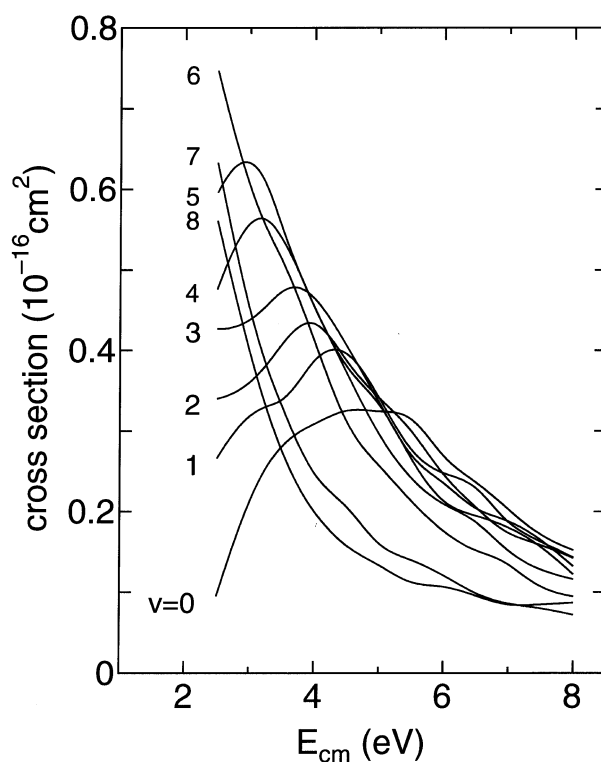


Fig.7. The TSH cross sections for the reaction $H^+ + D_2(v=0 \text{ to } 8, j=1) \rightarrow HD^+ + D$. The cross sections are given as a function of the center-of-mass collision energy E_{cm} .

It can be seen from Fig.7 that the cross section decreases with the increase of v for $v \geq 7$. The different v dependence of the HD^+ production between $v < 7$ and $v \geq 7$ may be related to the D_2^+ production. If $v \geq 7$, D_2^+ can be produced before H^+ approaches to D_2 . After D_2^+ is produced, H and D_2^+ are scattered by the repulsive wall of the excited state PES [8, 18]. Thus, the nuclear rearrangement (the H-D pair formation) may be interfered by the D_2^+ production taking place at the entrance of collision.

Figure 8 shows the cross sections for the production of D^+ ions from the $H^+ + D_2(v=0 \text{ to } 8, j=1)$ collisions. It can be seen from Fig.8 that for $v < 7$ and $E_{cm} < 4$ eV, the cross section decreases as v and E_{cm} increase. For $v < 7$ and $E_{cm} > 5$ eV, the cross section increases with the increase of v , while the cross sections are almost constant as a function of E_{cm} .

The D^+ ion can be produced from the reactions $H^+ + D_2 \rightarrow D^+ + HD$ (nuclear rearrangement) and $D^+ + H + D$ (dissociation). Therefore, for the collision energies below dissociation threshold, the production of the HD^+ and D^+ ions competes with each other. If the H-D pair does not have enough internal energy to take $r=1.32 \times 10^{-8}$ cm, only the D^+ ion is produced in our calculation. From Fig.7 and 8 it can be seen that the vibrational excited state of D_2 promotes the HD^+ production and reduces the D^+ production at the same time, if $v < 7$. On the other hand, if the collision energy is larger than the dissociation threshold, the D^+ ion can also be produced by dissociation. Fig.9 shows the contribution of dissociation to the D^+ production. In Fig.9, the cross section increases as E_{cm} increases. Thus, we can see from Figs.8 and 9 that for $E_{cm} < 4$ eV the nuclear rearrangement contributes to the D^+ production and the v dependence of the D^+ production is determined by that of nuclear rearrangement. Then, for $E_{cm} > 6$ eV, the dissociation contributes to the D^+ production, and the v dependence is determined mainly by the dissociation.

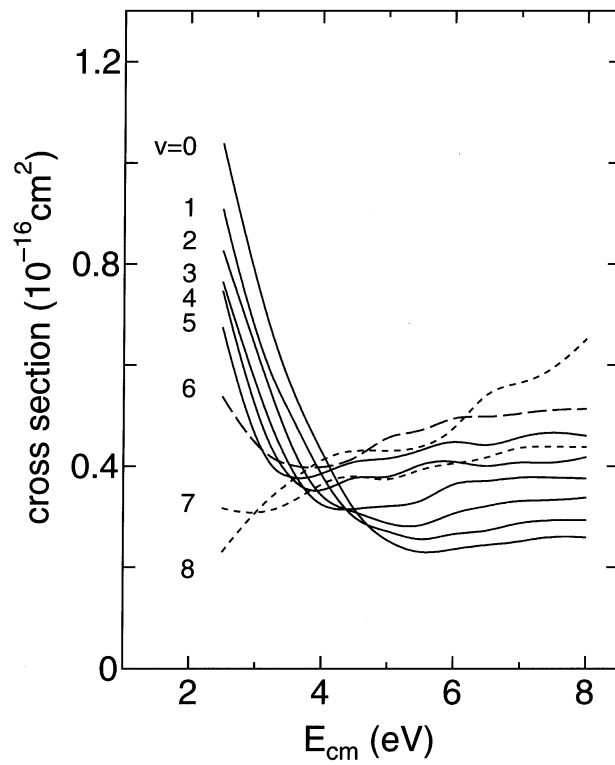


Fig.8. The TSH cross sections for the production of D^+ ions from the $H^+ + D_2(v=0 \text{ to } 8, j=1)$ collisions. The cross sections are given as a function of the center-of-mass collision energy E_{cm} .

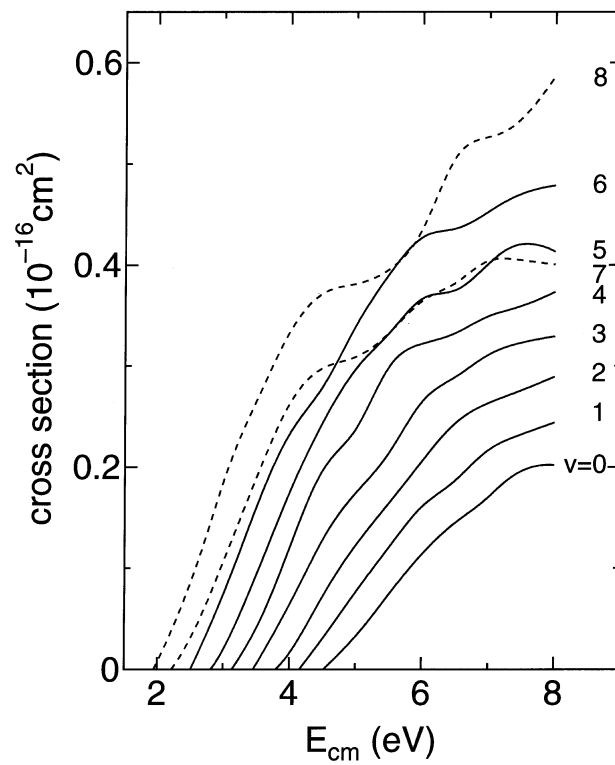


Fig.9 The contribution of dissociation to the production of D^+ ions from the $H^+ + D_2(v=0 \text{ to } 8, j=1)$ collisions. The TSH cross sections are given as a function of the center-of-mass collision energy E_{cm} .

In Fig.8, the D^+ production cross section shows the different E_{cm} and v dependence between $v < 7$ and $v \geq 7$. The different (E_{cm}, v) dependence should be related to the D_2^+ production, as the same with the HD^+ production. It is thought that the D_2^+ production at the entrance of collision reduces other reactions, and that causes the decrease of cross section between $v=6$ and 7 . For $v > 7$, the dissociation becomes more probable as can be seen in Fig.9, and the E_{cm} dependence of the D^+ production is determined by the E_{cm} dependence of dissociation.

In the production of HD^+ and D^+ ions from the $H^+ + D_2$ collisions, their j dependence has also been calculated. However, the j effect is smaller than the v effect for both cases. Since the v dependence of the D^+ and HD^+ production is very small compared with the D_2^+ production, the j dependence of the HD^+ and D^+ production is almost negligible.

3.2.2. The $D^+ + D_2$ system

Figure 10 shows the cross sections for the reaction $D^+ + D_2(v=0 \text{ to } 8, j=1) \rightarrow D_2^+ + D$. In this reaction D_2^+ can be produced both from the charge transfer and the charge transfer accompanied by nuclear rearrangement. Figure 11 shows the contribution of latter reaction to the D_2^+ production. It can be seen from Figs.10 and 11 that most of D_2^+ ions are produced by simple charge transfer. It can also be observed from Figs.4 and 10 that the charge transfer cross sections for the $H^+ + D_2$ and $D^+ + D_2^+$ collisions have similar v dependence. Moreover, the v dependence of cross section in Fig.11 is similar to that of the HD^+ production cross section for the $H^+ + D_2$ collisions in Fig.7.

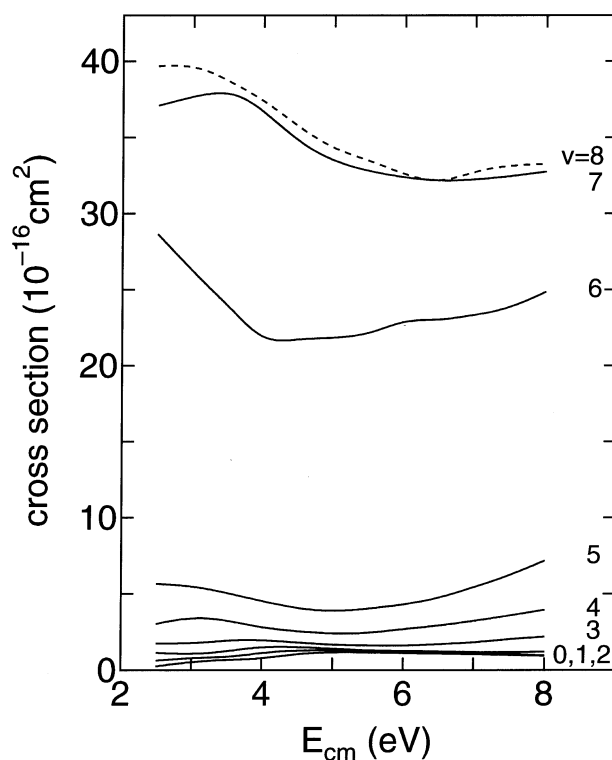


Fig.10. The TSH cross sections for the reaction $D^+ + D_2(v=0 \text{ to } 8, j=1) \rightarrow D_2^+ + D$. The cross sections are given as a function of the center-of-mass collision energy E_{cm} .

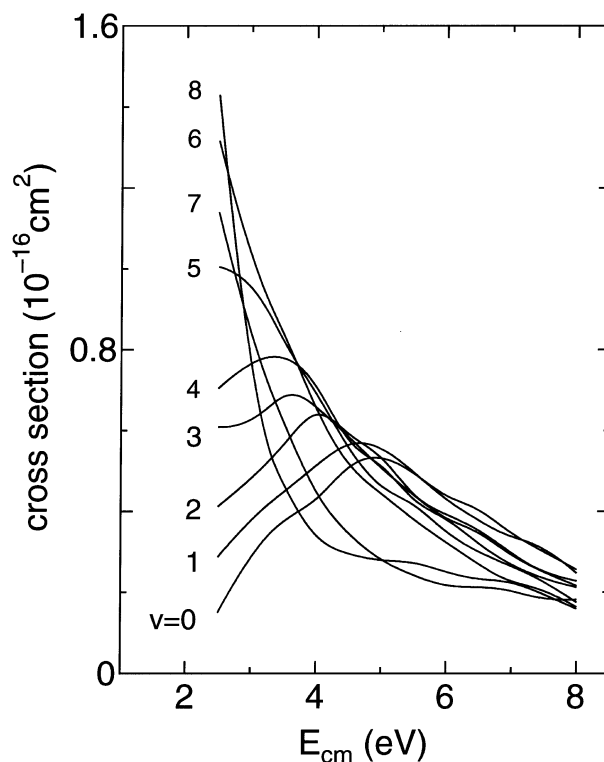


Fig.11. The contribution of the charge transfer reaction accompanied by nuclear rearrangement to the production of D_2^+ ions from the $D^+ + D_2(v=0 \text{ to } 8, j=1)$ collisions. The TSH cross sections are given as a function of the center-of-mass collision energy E_{cm} .

3.2.3. The $H^+ + H_2$ system

Fig.12 shows the cross section for the reaction $H^+ + H_2(v=0 \text{ to } 6, j=1) \rightarrow H_2^+ + H$. H_2^+ can be produced both from the charge transfer and the charge transfer accompanied by nuclear rearrangement. Fig.13 shows the contribution of latter reaction to the H_2^+ production. It can be seen from Figs.12 and 13 that most of H_2^+ ions are produced by simple charge transfer. While the D_2^+ production cross sections in Figs.4 and 10 increase rapidly with the increase of v up to 7, the H_2^+ production cross section dose not increase for $v>5$. This discrepancy is due to the different spacing of vibrational energy levels between H_2 and D_2 . The classical turning point of the H_2 vibration in the $v=4$ state appears on $r=1.32 \times 10^{-8}$ cm in our PES, which is located just on the avoided crossing seam [20]. Thus, the H_2^+ production cross section increases rapidly with the increases of v up to $v=5$ and then becomes almost independent of v for $v>5$. Also, if we take into account the difference of the vibrational levels between H_2 and D_2 , we can see that the (E_{cm}, v) dependence of cross section in Fig.13 is quite similar to that in Fig.11

3.2.4. The $D^+ + H_2$ system

Figures 14 and 15 indicate the cross sections for the production of HD^+ and D^+ ions from the $D^+ + H_2(v=0 \text{ to } 6, j=1)$ collisions, respectively. The (E_{cm}, v) dependence of cross section for the HD^+ production is similar to that for the H_2^+ production in Fig.13. Moreover, if we take into account the difference of the vibrational levels between H_2 and D_2 as in Section 3.2.3, we can see the D^+ production cross sections for the $D^+ + H_2$ and $H^+ + D_2$ collisions in Figs.8 and 15 have similar (E_{cm}, v) dependence. Fig.16 shows the contribution of dissociation to the D^+ production. It can be seen that the cross sections in Figs. 9 and 16 have similar (E_{cm}, v) dependence.

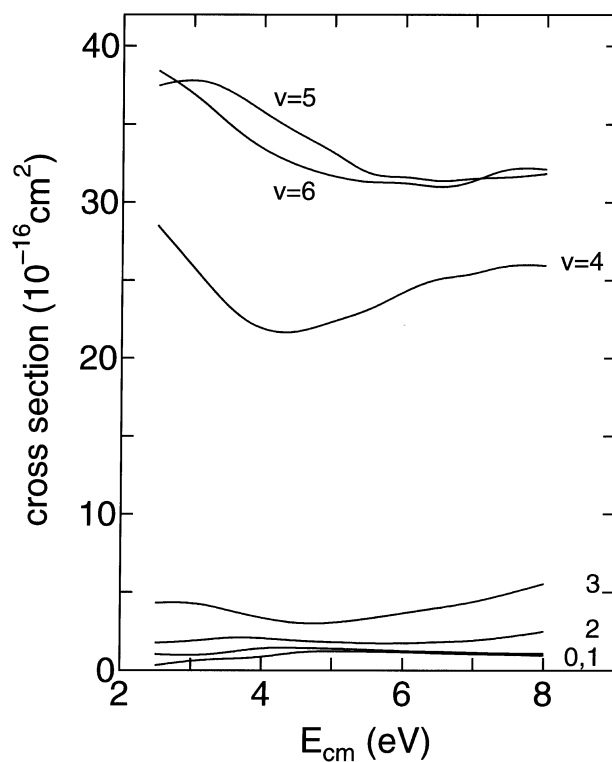


Fig.12. The TSH cross sections for the reaction $H^+ + H_2(v=0 \text{ to } 6, j=1) \rightarrow H_2^+ + H$. The cross sections are given as a function of the center-of-mass collision energy E_{cm} .

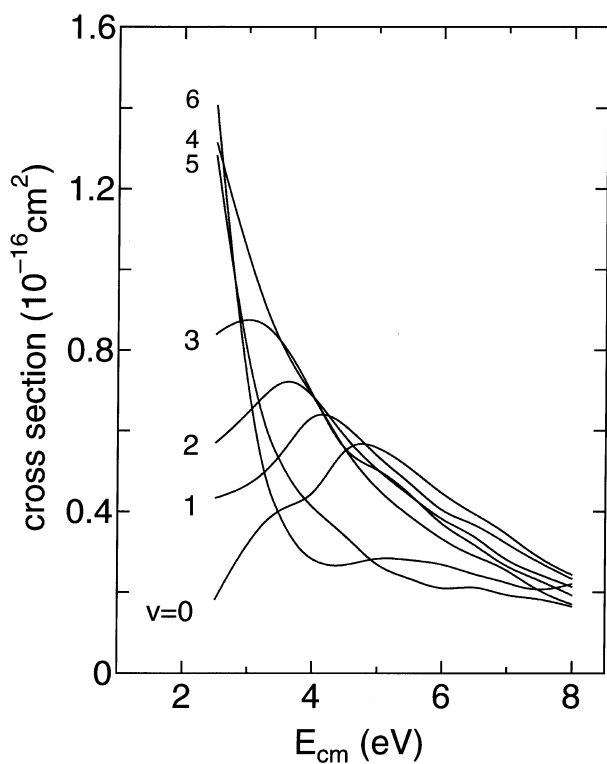


Fig.13. The contribution of the charge transfer reaction accompanied by nuclear rearrangement to the production of H_2^+ ions from the $H^+ + H_2(v=0 \text{ to } 6, j=1)$ collisions. The TSH cross sections are given as a function of the center-of-mass collision energy E_{cm} .

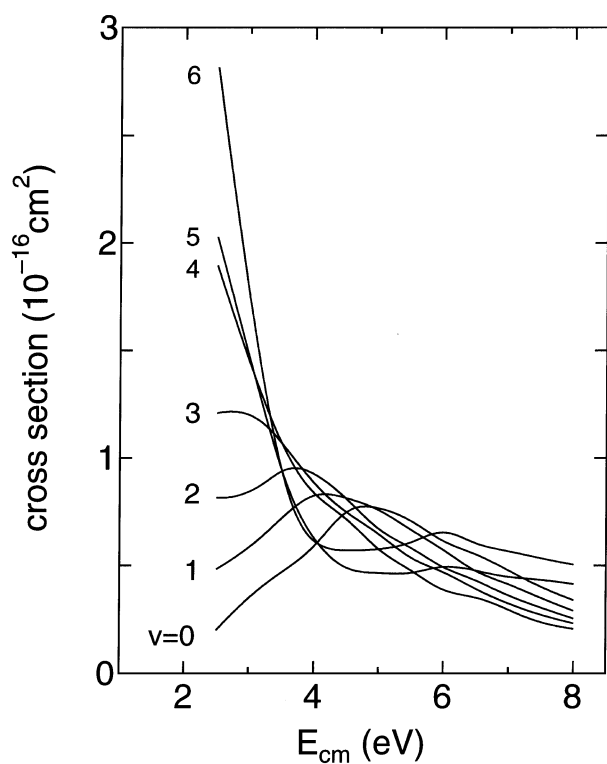


Fig.14. The TSH cross sections for the reaction $D^+ + H_2(v=0 \text{ to } 6, j=1) \rightarrow HD^+ + H$. The cross sections are given as a function of the center-of-mass collision energy E_{cm} .

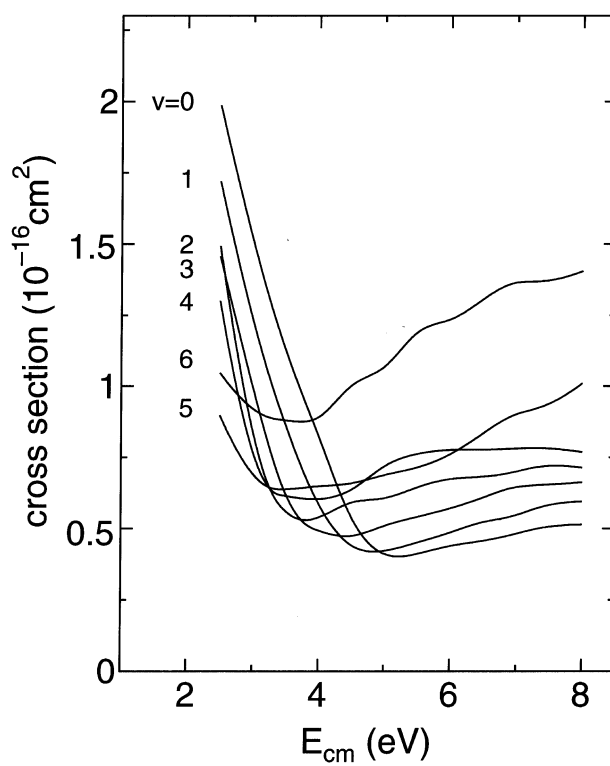


Fig.15. The TSH cross sections for the production of H^+ ions from the $D^+ + H_2(v=0 \text{ to } 6, j=1)$ collisions. The cross sections are given as a function of the center-of-mass collision energy E_{cm} .

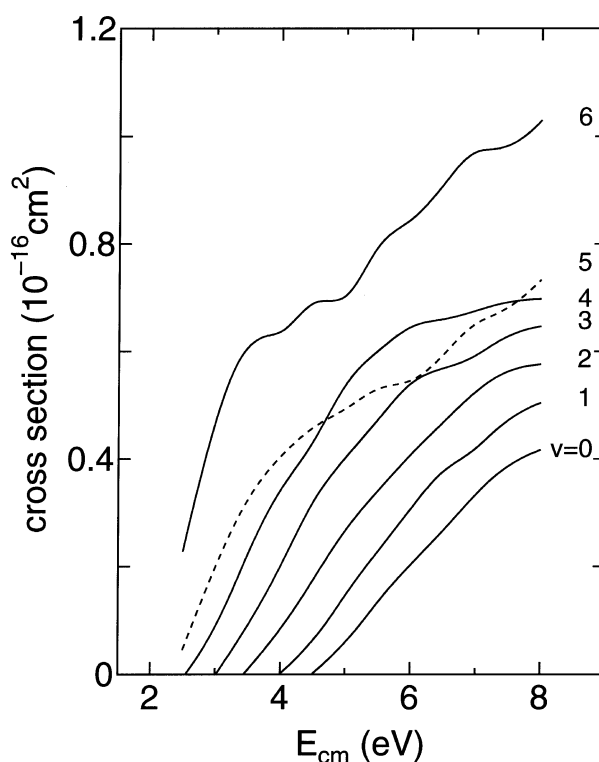


Fig.16. The contribution of dissociation to the production of H^+ ions from the $D^+ + H_2(v=0 \text{ to } 6, j=1)$ collisions. The TSH cross sections are given as a function of the center-of-mass collision energy E_{cm} .

3.3 Vibrational state distribution of diatomic products

To see the (E_{cm}, v) dependence of the vibrational state distribution of diatomic products, the results for the $H^+ + D_2$ collisions are shown in Figs.17 to 19 for a few representative cases. (The vibrational distribution of diatomic products for all collision systems for $j=1$ are tabulated in Appendix.) Fig.17 shows the vibrational distribution of product D_2^+ from the $H^+ + D_2(v=0, 2, 4, \text{ and } 6, j=1)$ collisions at $E_{cm}=3.0, 5.0, \text{ and } 7.0$ eV. From Fig.17 it can be seen that most of D_2^+ ions are found in the vibrational states in the range of $v'=0$ to 6 with a long tail for $v<6$. For $v=6$, a sharp peak appears at $v'=1$. In our calculation for $v\geq 6$, most of the produced D_2^+ ions have been found in a specific vibrational state v' whose energy level is close to the D_2 vibrational level v . We can see from Fig.5 that the $v'=1$ vibrational level of D_2^+ is located very close to the $v=6$ level of D_2 . Thus, most of D_2^+ ions have been found in the $v'=3$ state for $v=7$, and found in the $v'=4$ and 5 states for $v=8$.

Figures 18 and 19 show the vibrational state distribution of products HD^+ and HD , respectively. We should recognize that the absolute cross sections for $v\geq 2$ in Fig.18 and 19 are much smaller than those in Fig.17. In Fig.18, the HD^+ ions are formed with a broad vibrational (v') state distribution. This may come from that the HD^+ ions are produced via the H-D pair formation and there the H-D pairs have a broad distribution of internal energy. In contrast with the HD^+ production, in Fig.19, most of HD molecules are found in the $v'\leq 9$ vibrational states for every (E_{cm}, v) . This is because the HD production is reduced by the HD^+ production if the H-D pair is in the $v'\geq 5$ state.

It has been confirmed in our calculation that the (E_{cm}, v) dependence of vibrational distribution of each diatomic product for $j=5$ is similar to that for $j=1$.

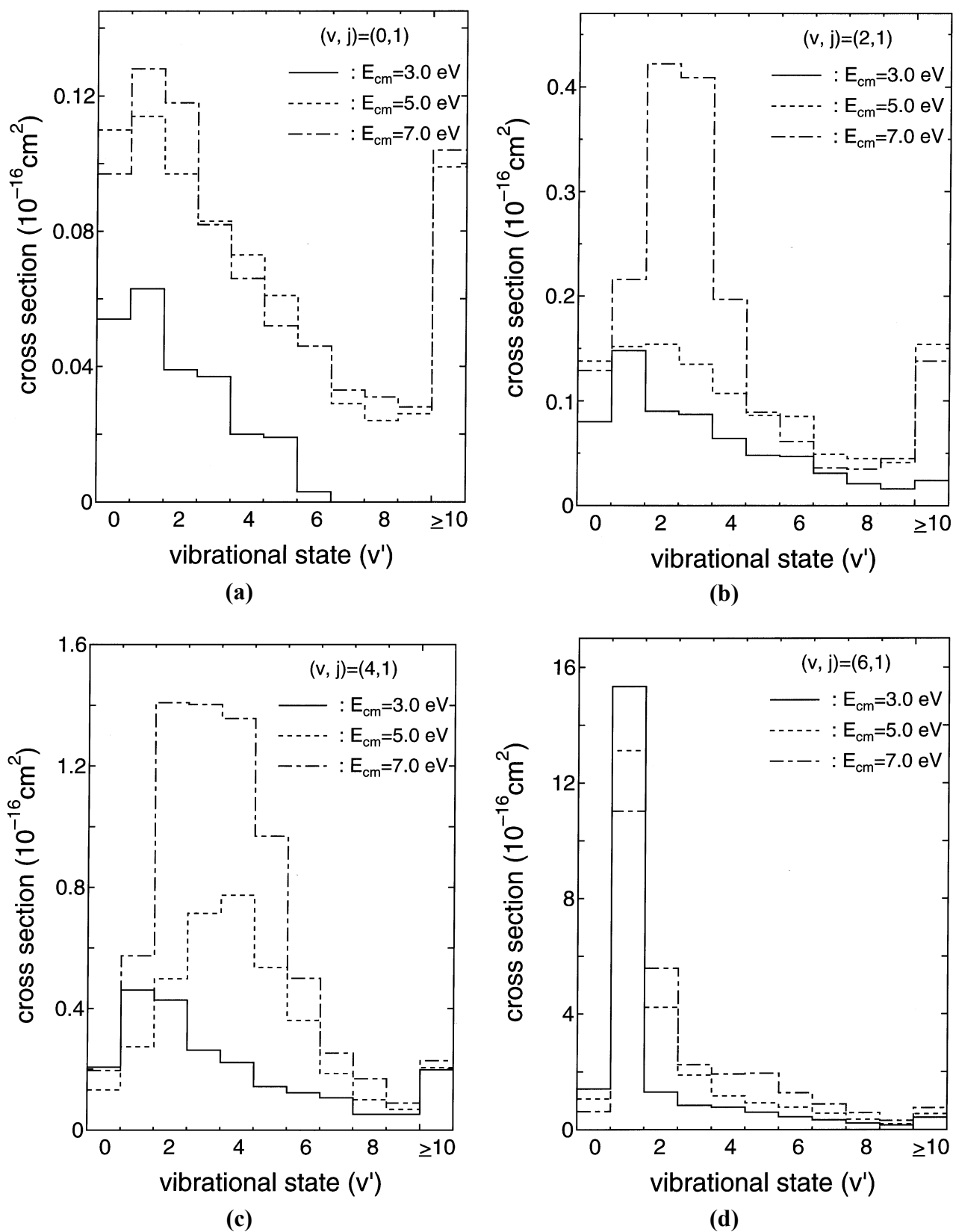


Fig.17. The TSH cross sections for the reaction $H^+ + D_2(v=0, 2, 4, \text{ and } 6, j=1) \rightarrow D_2^+(v') + H$. The cross sections are given as a function of the vibrational quantum number v' of D_2^+ . The results for $v=0, 2, 4, \text{ and } 6$ are shown in Figs.17(a) to (d). The solid, dotted, and dash-dotted lines in the figures represent the cross sections for the center-of-mass collision energies $E_{cm}=3.0, 5.0, \text{ and } 7.0$ eV, respectively. The cross sections for $v \geq 10$ are summed up and shown in the figures denoted as ≥ 10 .

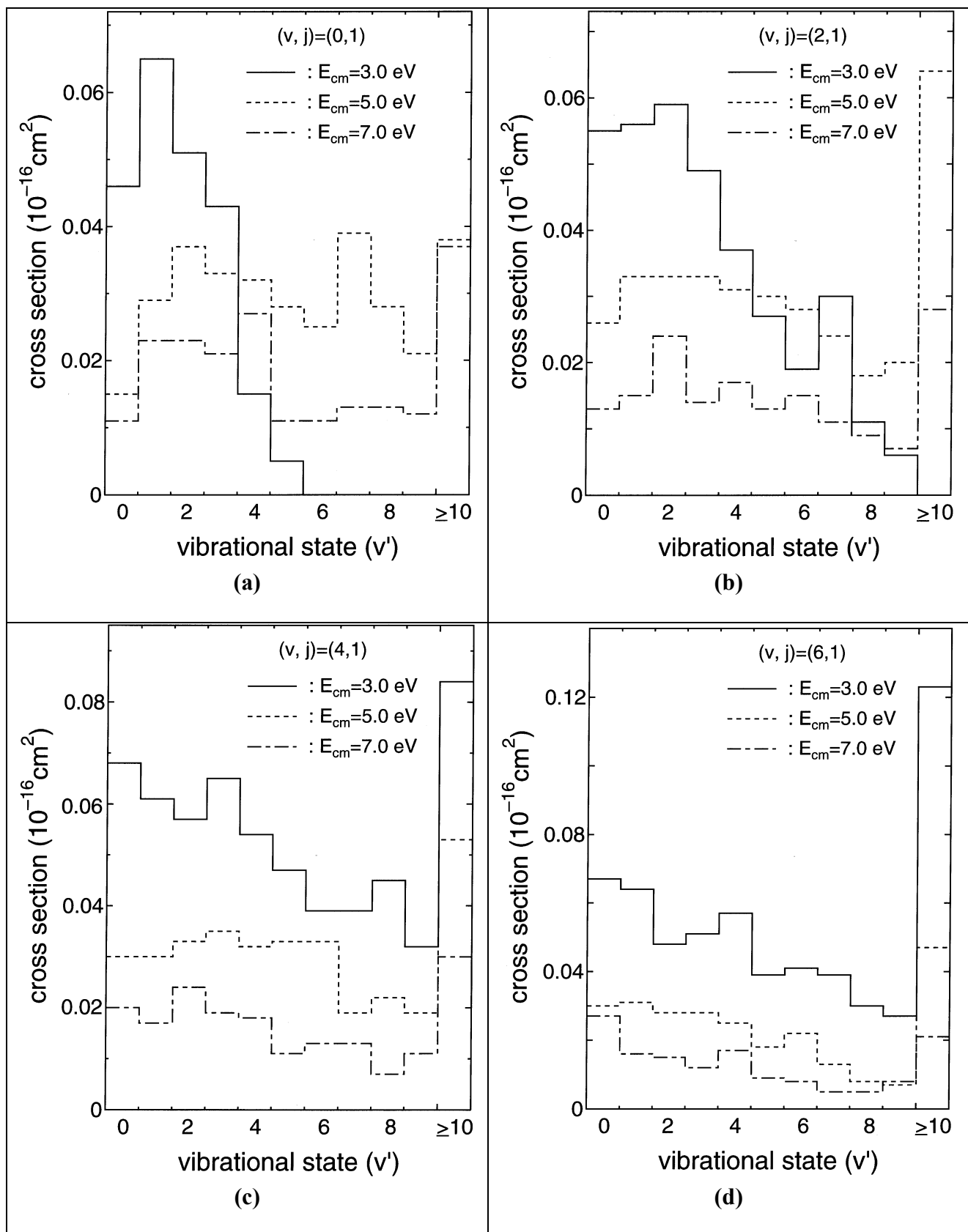


Fig.18. The TSH cross sections for the reaction $H^+ + D_2(v=0, 2, 4, \text{ and } 6, j=1) \rightarrow HD^+(v') + D$. The cross sections are given as a function of the vibrational quantum number v' of HD^+ . The results for $v=0, 2, 4, \text{ and } 6$ are shown in Figs.18(a) to (d). The solid, dotted, and dash-dotted lines in the figures represent the cross sections for the center-of-mass collision energies $E_{cm}=3.0, 5.0, \text{ and } 7.0 \text{ eV}$, respectively. The cross sections for $v' \geq 10$ are summed up and shown in the figures denoted as ≥ 10 .

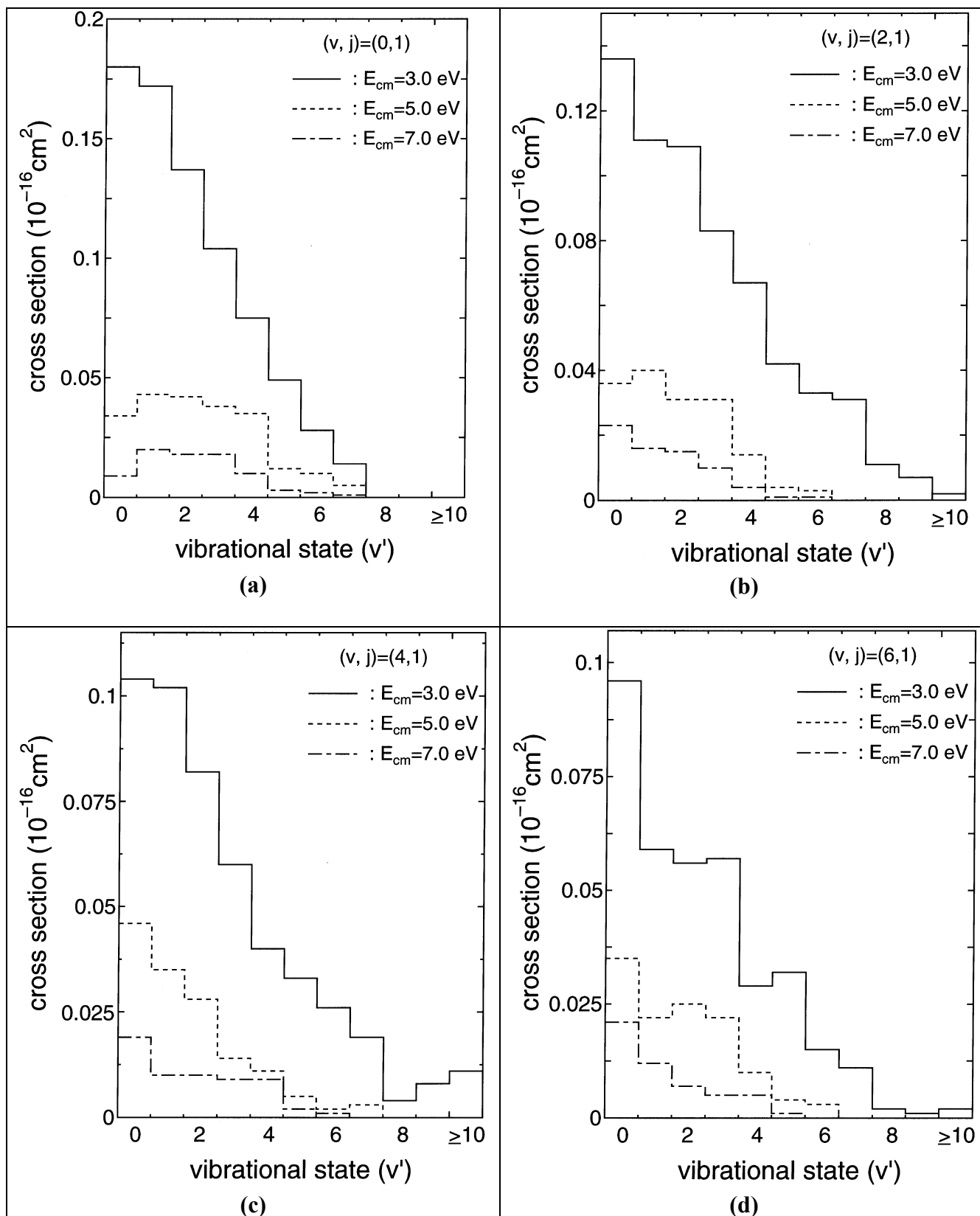


Fig.19 The TSH cross sections for the reaction $H^+ + D_2(v=0, 2, 4, \text{ and } 6, j=1) \rightarrow HD(v') + D^+$. The cross sections are given as a function of the vibrational quantum number v' of HD. The results for $v=0, 2, 4, \text{ and } 6$ are shown in Figs.19 (a) to (d). The solid, dotted, and dash-dotted lines in the figures represent the cross sections for the center-of-mass collision energies $E_{cm}=3.0, 5.0, \text{ and } 7.0 \text{ eV}$, respectively. The cross sections for $v' \geq 10$ are summed up and shown in the figures denoted as ≥ 10 .

4. Summary

We have presented the cross sections for ion production occurring in the $H^+ + H_2$ system and its isotopic variants in the center-of-mass collision energy range of $2.5 \text{ eV} \leq E_{\text{cm}} \leq 8.0 \text{ eV}$. The conventional TSH method with the ab initio PES's has been applied to calculate cross sections. The v dependence of cross section for each ion production have been evaluated with the vibrational quantum numbers in the range $0 \leq v \leq 8$ for D_2 and $0 \leq v \leq 6$ for H_2 , respectively. It has been found that the charge transfer reaction is enhanced remarkably as v increases. This enhancement has been explained from the characteristics of PES's. It has also been found that the v dependence of other ion production by dissociation or nuclear rearrangement is much small compared with charge transfer. For the $H^+ + D_2$ collisions, the j dependence of ion production has been evaluated with the rotational quantum numbers $j=1, 5, 10$. It has been confirmed that the j effect on the charge transfer reaction is secondary to the v effect. We have also presented the vibrational distribution of diatomic products, which should provide an important information for the analysis of recombination processes taking place in the fusion reactor.

REFERENCES

- [1] ICHIHARA, A., HAYAKAWA, S., SATAKA, M., and SHIRAI, T., JAERI-Data/Code **94-015** (1994), and related references therein.
- [2] ICHIHARA, A., SHIRAI, T., AND YOKOYAMA, K., J.Chem.Phys.**105**, 1857(1996). It should be noted that the square root of hopping coefficient E_c is given as a function of ΔE_0 in Fig.1 of the reference.
- [3] ICHIHARA, A., IWAMOTO, O., AND YOKOYAMA, K., JAERI-Research **98-056** (1998).
- [4] OCHS, G. AND, TELOY, E., J.Chem.Phys.**61**, 4930 (1974).
- [5] SCHLIER, Ch., NOWOTNY, U., AND TELOY, E., Chem.Phys.**111**, 401 (1987).
- [6] CHAPMAN, S., Adv.Chem.Phys.**82**, 423(1992).
- [7] TULLY, J.C. AND PRESTON, R.K. J.Chem.Phys.**55**, 562 (1971).
- [8] ICHIHARA, A. AND YOKOYAMA, K., J.Chem.Phys.**103**, 2109 (1995).
- [9] ICHIHARA, A., YOKOYAMA, K., AND IWAMOTO, O., JAERI Data/Code **98-031** (1998).
- [10] KARPLUS, M., PORTER, R.N., AND SHARMA, R.D., J.Chem.Phys. **43**, 3259 (1965).
- [11] ZHU, C. AND NAKAMURA, H., J.Chem.Phys.**102**, 7448 (1995).
- [12] ZHU, C. AND NAKAMURA, H., Comm.Atom.Mol.Phys.**32**, 249 (1996). The hopping probability was calculated using Eq.(3.7) of the reference with parameters defined by Eqs.(3.3) to (3.6).
- [13] LANDAU, L.D., Phys.Z.Sowjetunion **2**, 46 (1932).
- [14] ZENER, C., Proc.R.Soc.**A137**, 696 (1932).
- [15] STUCKELBERG, E.C.G., Helv.Phys.Acta **5**, 369 (1932).
- [16] The hopping probability was set to be unity if it was larger than 0.99 in order to terminate a trajectory calculation.
- [17] BLAIS, N.C. AND TRUHLAR, D.G., J.Chem.Phys.**65**, 5335 (1976).
- [18] BAUSCHLICHER, Jr., C.W., O'NEIL, S.V., PRESTON, R.K., SCHAEFER III, H.F., AND BENDER, C.F., J.Chem.Phys.**59**, 1286(1973).

- [19] The ab initio PES's are independent of the nuclear mass. The turning point of the HD vibration in the $v=5$ state appears at $r=1.35 \times 10^{-8}$ cm.
- [20] The turning point of the H_2 vibration in the $(v=4, j=1)$ state appears on the avoided crossing point in our PES. In this case the vibration velocity is zero at the point of avoided crossing, so that the hopping probability in Refs [11, 12] dose not converge to unity even if a proton is largely separated. Thus, for $v=4$, our TSH calculation dose not terminate with a finite value of the maximum impact parameter. To avoid this problem, we shifted the $v=4$ level to 0.01 eV upward artificially.

APPENDIX

The vibrational state distribution of ions and molecules produced from the $\text{H}^+ + \text{D}_2$, $\text{D}^+ + \text{D}_2$, $\text{H}^+ + \text{H}_2$, and $\text{D}^+ + \text{H}_2$ collisions is given in Tables 1 to 8. In Tables, the absolute TSH cross section (σ in 10^{-16}cm^2) and associated error estimate ($\Delta\sigma$ in 10^{-16}cm^2 , see Ref. [17]) are given as a function of the vibrational quantum number v' of diatomic product for each $(E_{\text{cm}} v)$, where E_{cm} is the center-of-mass collision energy in eV and v is the vibrational quantum number of reactant molecule. The cross sections for $v' \geq 10$ are summed up and given in Tables. The total cross section and associated error are also given in Tables for each $(E_{\text{cm}} v)$.

Table 1-1. Cross section ($\sigma, \Delta\sigma$ in 10^{-16}cm^2) for the reaction $H^+ + D_2(v, j = 1) \rightarrow H + D_2^+(v')$

See Text of Appendix for Explanation of Tables

E_{cm} (eV)	3.0		4.0		5.0		6.0		7.0		8.0	
v'	σ	$\Delta\sigma$	σ	$\Delta\sigma$	σ	$\Delta\sigma$	σ	$\Delta\sigma$	σ	$\Delta\sigma$	σ	$\Delta\sigma$
$v = 0$												
0	0.054	0.007	0.085	0.010	0.110	0.010	0.109	0.010	0.097	0.009	0.106	0.009
1	0.063	0.007	0.080	0.008	0.114	0.010	0.121	0.010	0.128	0.010	0.122	0.009
2	0.039	0.005	0.091	0.009	0.097	0.009	0.111	0.009	0.118	0.009	0.099	0.008
3	0.037	0.005	0.058	0.007	0.083	0.008	0.080	0.008	0.082	0.007	0.073	0.007
4	0.020	0.004	0.045	0.005	0.073	0.007	0.079	0.007	0.066	0.007	0.055	0.006
5	0.019	0.003	0.031	0.004	0.061	0.006	0.059	0.006	0.052	0.006	0.036	0.005
6	0.003	0.001	0.028	0.004	0.046	0.005	0.039	0.005	0.046	0.005	0.035	0.005
7	0.000	0.000	0.029	0.004	0.029	0.004	0.038	0.005	0.033	0.004	0.041	0.005
8	0.000	0.000	0.015	0.003	0.024	0.004	0.029	0.004	0.031	0.004	0.031	0.004
9	0.000	0.000	0.012	0.002	0.026	0.004	0.031	0.004	0.028	0.004	0.023	0.004
≥ 10	0.000	0.000	0.036	0.004	0.099	0.007	0.107	0.007	0.104	0.007	0.113	0.007
total	0.236	0.013	0.512	0.019	0.762	0.021	0.804	0.021	0.785	0.020	0.734	0.019
$v = 1$												
0	0.051	0.007	0.103	0.010	0.112	0.010	0.095	0.009	0.097	0.010	0.138	0.013
1	0.057	0.007	0.086	0.009	0.130	0.011	0.143	0.011	0.121	0.010	0.151	0.013
2	0.040	0.006	0.111	0.010	0.101	0.009	0.095	0.009	0.122	0.009	0.148	0.011
3	0.054	0.007	0.098	0.009	0.097	0.009	0.100	0.009	0.094	0.008	0.097	0.008
4	0.038	0.005	0.073	0.007	0.084	0.008	0.073	0.007	0.076	0.007	0.076	0.007
5	0.024	0.004	0.059	0.006	0.067	0.007	0.075	0.007	0.052	0.006	0.069	0.007
6	0.018	0.004	0.042	0.005	0.059	0.006	0.063	0.006	0.056	0.006	0.048	0.006
7	0.013	0.003	0.047	0.006	0.047	0.006	0.039	0.005	0.037	0.005	0.040	0.005
8	0.008	0.002	0.043	0.005	0.030	0.004	0.037	0.005	0.036	0.005	0.033	0.005
9	0.001	0.000	0.030	0.004	0.024	0.004	0.026	0.004	0.030	0.004	0.024	0.004
≥ 10	0.000	0.000	0.092	0.007	0.121	0.008	0.117	0.007	0.135	0.008	0.133	0.008
total	0.303	0.016	0.782	0.023	0.872	0.023	0.863	0.022	0.856	0.022	0.956	0.025
$v = 2$												
0	0.080	0.010	0.118	0.012	0.138	0.012	0.113	0.011	0.129	0.013	0.203	0.018
1	0.148	0.015	0.126	0.013	0.152	0.013	0.193	0.016	0.216	0.017	0.295	0.021
2	0.090	0.010	0.110	0.010	0.154	0.014	0.234	0.018	0.422	0.027	0.687	0.034
3	0.087	0.009	0.104	0.010	0.135	0.013	0.224	0.018	0.409	0.027	0.506	0.030
4	0.064	0.008	0.086	0.008	0.107	0.009	0.138	0.012	0.197	0.016	0.188	0.016
5	0.048	0.006	0.083	0.008	0.086	0.008	0.098	0.008	0.089	0.008	0.083	0.008
6	0.047	0.007	0.075	0.008	0.085	0.008	0.071	0.007	0.061	0.006	0.062	0.006
7	0.031	0.005	0.067	0.007	0.049	0.006	0.054	0.006	0.036	0.005	0.043	0.005
8	0.021	0.004	0.047	0.006	0.045	0.006	0.048	0.006	0.035	0.005	0.043	0.005
9	0.016	0.003	0.039	0.005	0.041	0.005	0.038	0.005	0.045	0.006	0.036	0.005
≥ 10	0.024	0.004	0.138	0.009	0.154	0.009	0.148	0.009	0.138	0.008	0.138	0.009
total	0.655	0.026	0.993	0.027	1.146	0.029	1.358	0.035	1.775	0.046	2.286	0.054

Table 1-2. Cross section ($\sigma, \Delta\sigma$ in 10^{-16}cm^2) for the reaction $H^+ + D_2(v, j = 1) \rightarrow H + D_2^+(v')$

See Text of Appendix for Explanation of Tables

E_{cm} (eV)	3.0		4.0		5.0		6.0		7.0		8.0	
v'	σ	$\Delta\sigma$	σ	$\Delta\sigma$	σ	$\Delta\sigma$	σ	$\Delta\sigma$	σ	$\Delta\sigma$	σ	$\Delta\sigma$
$v = 3$												
0	0.151	0.015	0.146	0.013	0.125	0.011	0.116	0.012	0.187	0.018	0.177	0.018
1	0.345	0.028	0.208	0.019	0.221	0.017	0.266	0.020	0.338	0.024	0.466	0.030
2	0.181	0.018	0.223	0.018	0.347	0.024	0.538	0.032	0.864	0.041	1.150	0.048
3	0.144	0.015	0.163	0.015	0.397	0.027	0.669	0.035	1.142	0.046	1.493	0.053
4	0.145	0.015	0.157	0.015	0.351	0.025	0.586	0.033	0.762	0.038	0.892	0.040
5	0.081	0.009	0.124	0.011	0.242	0.020	0.341	0.025	0.381	0.026	0.429	0.028
6	0.070	0.008	0.084	0.008	0.099	0.010	0.155	0.015	0.195	0.018	0.169	0.017
7	0.063	0.007	0.077	0.007	0.063	0.007	0.059	0.006	0.074	0.009	0.085	0.011
8	0.047	0.006	0.060	0.007	0.045	0.006	0.053	0.006	0.056	0.006	0.048	0.006
9	0.045	0.006	0.039	0.005	0.042	0.005	0.046	0.006	0.038	0.005	0.039	0.005
≥ 10	0.096	0.008	0.189	0.011	0.194	0.011	0.186	0.011	0.177	0.010	0.167	0.009
total	1.369	0.043	1.470	0.038	2.125	0.052	3.016	0.065	4.215	0.079	5.115	0.086
$v = 4$												
0	0.207	0.019	0.122	0.012	0.132	0.012	0.139	0.015	0.196	0.020	0.169	0.018
1	0.461	0.032	0.287	0.022	0.274	0.022	0.392	0.028	0.574	0.037	0.734	0.042
2	0.428	0.029	0.357	0.024	0.498	0.031	0.901	0.045	1.409	0.058	1.602	0.062
3	0.263	0.022	0.396	0.026	0.714	0.038	1.105	0.048	1.403	0.055	1.551	0.058
4	0.222	0.019	0.374	0.026	0.774	0.038	1.106	0.046	1.357	0.051	1.619	0.056
5	0.143	0.015	0.310	0.024	0.536	0.032	0.800	0.039	0.969	0.043	0.897	0.041
6	0.123	0.013	0.238	0.021	0.361	0.026	0.467	0.030	0.500	0.031	0.496	0.031
7	0.106	0.011	0.187	0.017	0.186	0.018	0.280	0.023	0.253	0.021	0.285	0.023
8	0.052	0.007	0.077	0.009	0.100	0.012	0.159	0.016	0.169	0.017	0.166	0.017
9	0.052	0.007	0.053	0.007	0.068	0.009	0.069	0.009	0.089	0.012	0.092	0.012
≥ 10	0.198	0.012	0.244	0.013	0.205	0.011	0.210	0.012	0.228	0.013	0.230	0.014
total	2.253	0.059	2.645	0.060	3.849	0.076	5.628	0.094	7.145	0.105	7.842	0.110
$v = 5$												
0	0.296	0.026	0.121	0.012	0.155	0.016	0.294	0.028	0.260	0.028	0.320	0.032
1	0.895	0.049	0.466	0.032	0.632	0.041	0.845	0.050	1.109	0.059	1.348	0.066
2	0.491	0.031	0.602	0.036	1.289	0.059	1.755	0.070	2.027	0.077	2.180	0.079
3	0.490	0.031	0.681	0.038	1.121	0.051	1.816	0.068	2.054	0.073	2.281	0.076
4	0.387	0.028	0.626	0.035	1.113	0.048	1.554	0.059	1.781	0.062	1.933	0.065
5	0.320	0.025	0.614	0.034	0.955	0.044	1.254	0.050	1.425	0.053	1.493	0.054
6	0.226	0.020	0.427	0.030	0.646	0.036	0.860	0.042	0.969	0.044	0.964	0.043
7	0.168	0.016	0.340	0.026	0.468	0.031	0.519	0.033	0.510	0.032	0.564	0.033
8	0.119	0.012	0.225	0.021	0.268	0.023	0.321	0.025	0.325	0.025	0.388	0.028
9	0.093	0.010	0.131	0.015	0.131	0.016	0.181	0.019	0.168	0.018	0.228	0.021
≥ 10	0.265	0.015	0.262	0.015	0.354	0.020	0.370	0.022	0.414	0.024	0.390	0.022
total	3.751	0.081	4.494	0.086	7.133	0.112	9.770	0.132	11.042	0.141	12.089	0.146

Table 1-3. Cross section ($\sigma, \Delta\sigma$ in 10^{-16}cm^2) for the reaction $H^+ + D_2(v, j = 1) \rightarrow H + D_2^+(v')$

See Text of Appendix for Explanation of Tables

E_{cm} (eV)	3.0		4.0		5.0		6.0		7.0		8.0	
v'	σ	$\Delta\sigma$	σ	$\Delta\sigma$	σ	$\Delta\sigma$	σ	$\Delta\sigma$	σ	$\Delta\sigma$	σ	$\Delta\sigma$
$v = 6$												
0	1.406	0.071	1.363	0.066	1.066	0.056	0.742	0.043	0.631	0.038	0.420	0.029
1	15.337	0.231	13.894	0.223	13.118	0.218	11.577	0.208	11.025	0.205	10.161	0.201
2	1.299	0.060	2.553	0.092	4.229	0.119	5.089	0.129	5.587	0.134	6.299	0.141
3	0.838	0.044	1.371	0.060	1.883	0.074	1.817	0.076	2.245	0.085	2.627	0.091
4	0.775	0.041	0.856	0.045	1.170	0.055	1.618	0.067	1.919	0.074	2.261	0.079
5	0.606	0.036	0.605	0.036	0.925	0.045	1.393	0.057	1.952	0.068	2.162	0.072
6	0.443	0.030	0.506	0.033	0.776	0.040	1.076	0.047	1.276	0.052	1.467	0.056
7	0.341	0.027	0.365	0.027	0.566	0.034	0.705	0.038	0.885	0.043	0.911	0.043
8	0.229	0.021	0.314	0.025	0.360	0.028	0.455	0.031	0.587	0.035	0.705	0.038
9	0.156	0.018	0.205	0.020	0.196	0.020	0.231	0.022	0.318	0.026	0.388	0.028
≥ 10	0.426	0.024	0.402	0.024	0.551	0.030	0.576	0.032	0.760	0.037	1.072	0.044
total	21.855	0.256	22.436	0.257	24.841	0.266	25.278	0.265	27.184	0.269	28.473	0.269
$v = 7$												
0	0.437	0.032	1.321	0.054	1.749	0.059	1.470	0.054	1.190	0.048	0.929	0.042
1	6.668	0.127	4.244	0.099	2.052	0.069	1.103	0.051	0.572	0.037	0.345	0.028
2	9.939	0.185	6.078	0.153	4.081	0.130	3.386	0.121	3.037	0.116	3.050	0.115
3	11.229	0.197	12.256	0.201	13.278	0.205	13.617	0.204	14.367	0.206	13.858	0.203
4	1.797	0.080	2.552	0.095	3.851	0.111	4.433	0.116	5.052	0.122	5.770	0.127
5	0.751	0.049	1.453	0.069	2.170	0.083	2.939	0.094	3.328	0.099	3.761	0.103
6	0.444	0.034	0.917	0.050	1.538	0.065	2.173	0.076	2.695	0.083	2.758	0.085
7	0.353	0.028	0.652	0.040	0.952	0.047	1.220	0.054	1.617	0.063	2.033	0.070
8	0.295	0.024	0.449	0.031	0.663	0.039	0.649	0.038	0.855	0.045	1.167	0.052
9	0.237	0.023	0.317	0.027	0.376	0.029	0.468	0.032	0.565	0.035	0.644	0.037
≥ 10	0.570	0.033	0.825	0.042	1.133	0.049	1.355	0.053	1.720	0.058	2.050	0.063
total	32.718	0.260	31.063	0.256	31.843	0.251	32.813	0.246	35.000	0.246	36.366	0.239
$v = 8$												
0	0.201	0.020	0.208	0.018	0.496	0.028	0.614	0.034	0.714	0.036	0.629	0.034
1	1.634	0.064	1.779	0.062	1.545	0.057	1.025	0.047	0.688	0.038	0.365	0.027
2	4.965	0.107	2.563	0.077	1.157	0.051	0.430	0.031	0.241	0.023	0.194	0.019
3	4.127	0.104	1.452	0.067	0.943	0.058	0.821	0.055	0.833	0.055	0.904	0.058
4	10.729	0.197	9.025	0.186	8.719	0.184	8.759	0.184	8.877	0.185	8.828	0.185
5	6.110	0.145	7.982	0.157	9.222	0.164	9.876	0.165	10.910	0.172	11.110	0.174
6	1.679	0.076	2.588	0.092	3.542	0.106	4.307	0.114	4.664	0.118	4.694	0.117
7	0.993	0.057	1.885	0.076	2.628	0.088	2.979	0.093	2.959	0.092	3.150	0.095
8	0.623	0.042	1.057	0.054	1.616	0.067	1.973	0.074	2.123	0.076	2.386	0.080
9	0.440	0.033	0.500	0.035	0.730	0.043	1.074	0.052	1.460	0.061	1.685	0.065
≥ 10	0.892	0.046	1.403	0.056	2.030	0.067	2.736	0.076	3.502	0.083	4.114	0.088
total	32.395	0.251	30.442	0.243	32.626	0.237	34.595	0.231	36.971	0.225	38.058	0.220

Table 2-1. Cross section ($\sigma, \Delta\sigma$ in 10^{-16}cm^2) for the reaction $H^+ + D_2(v, j = 1) \rightarrow D + HD^+(v')$

See Text of Appendix for Explanation of Tables

E_{cm} (eV)	3.0		4.0		5.0		6.0		7.0		8.0	
v'	σ	$\Delta\sigma$	σ	$\Delta\sigma$	σ	$\Delta\sigma$	σ	$\Delta\sigma$	σ	$\Delta\sigma$	σ	$\Delta\sigma$
$v = 0$												
0	0.046	0.006	0.041	0.006	0.015	0.003	0.014	0.003	0.011	0.003	0.014	0.003
1	0.065	0.007	0.042	0.006	0.029	0.004	0.021	0.004	0.023	0.004	0.015	0.003
2	0.051	0.006	0.041	0.005	0.037	0.005	0.038	0.005	0.023	0.003	0.018	0.003
3	0.043	0.006	0.045	0.006	0.033	0.004	0.025	0.004	0.021	0.004	0.015	0.003
4	0.015	0.003	0.033	0.005	0.032	0.005	0.020	0.003	0.027	0.004	0.011	0.002
5	0.005	0.002	0.030	0.005	0.028	0.004	0.021	0.003	0.011	0.002	0.014	0.003
6	0.000	0.000	0.024	0.004	0.025	0.004	0.022	0.003	0.011	0.002	0.011	0.002
7	0.000	0.000	0.024	0.004	0.039	0.005	0.021	0.003	0.013	0.003	0.011	0.002
8	0.000	0.000	0.011	0.003	0.028	0.004	0.017	0.003	0.013	0.003	0.009	0.002
9	0.000	0.000	0.009	0.002	0.021	0.004	0.010	0.002	0.012	0.003	0.005	0.002
≥ 10	0.000	0.000	0.008	0.002	0.038	0.004	0.055	0.005	0.037	0.004	0.031	0.004
total	0.225	0.013	0.308	0.014	0.323	0.013	0.263	0.011	0.203	0.010	0.152	0.009
$v = 1$												
0	0.065	0.008	0.050	0.007	0.022	0.004	0.020	0.004	0.019	0.004	0.016	0.003
1	0.072	0.008	0.049	0.006	0.029	0.004	0.027	0.004	0.014	0.003	0.021	0.004
2	0.049	0.007	0.036	0.005	0.034	0.005	0.029	0.004	0.023	0.004	0.016	0.003
3	0.049	0.006	0.043	0.005	0.027	0.004	0.020	0.003	0.018	0.003	0.017	0.003
4	0.048	0.007	0.030	0.004	0.036	0.005	0.026	0.004	0.014	0.003	0.016	0.003
5	0.030	0.005	0.034	0.005	0.029	0.004	0.026	0.004	0.012	0.002	0.008	0.002
6	0.014	0.004	0.038	0.005	0.031	0.005	0.012	0.002	0.012	0.002	0.010	0.002
7	0.006	0.002	0.039	0.006	0.026	0.004	0.018	0.003	0.009	0.002	0.007	0.002
8	0.000	0.000	0.023	0.004	0.029	0.005	0.012	0.003	0.015	0.003	0.006	0.002
9	0.000	0.000	0.016	0.003	0.016	0.003	0.011	0.003	0.006	0.002	0.006	0.002
≥ 10	0.000	0.000	0.041	0.005	0.064	0.006	0.044	0.005	0.037	0.005	0.020	0.003
total	0.334	0.017	0.399	0.016	0.342	0.014	0.245	0.011	0.178	0.010	0.143	0.009
$v = 2$												
0	0.055	0.007	0.045	0.006	0.026	0.005	0.016	0.003	0.013	0.003	0.017	0.004
1	0.056	0.007	0.029	0.005	0.033	0.005	0.034	0.005	0.015	0.003	0.018	0.004
2	0.059	0.008	0.052	0.006	0.033	0.005	0.026	0.004	0.024	0.004	0.010	0.003
3	0.049	0.007	0.034	0.005	0.033	0.005	0.024	0.004	0.014	0.003	0.011	0.002
4	0.037	0.006	0.042	0.006	0.031	0.005	0.025	0.004	0.017	0.003	0.017	0.003
5	0.027	0.005	0.034	0.005	0.030	0.005	0.014	0.003	0.013	0.003	0.011	0.003
6	0.019	0.004	0.046	0.006	0.028	0.004	0.018	0.003	0.015	0.003	0.009	0.002
7	0.030	0.005	0.029	0.005	0.024	0.004	0.014	0.003	0.011	0.003	0.009	0.002
8	0.011	0.003	0.035	0.005	0.018	0.004	0.016	0.003	0.009	0.002	0.008	0.002
9	0.006	0.002	0.030	0.005	0.020	0.004	0.012	0.003	0.007	0.002	0.008	0.002
≥ 10	0.000	0.000	0.074	0.007	0.064	0.006	0.042	0.005	0.028	0.004	0.024	0.004
total	0.349	0.017	0.451	0.018	0.340	0.014	0.242	0.012	0.167	0.010	0.142	0.009

Table 2-2. Cross section ($\sigma, \Delta\sigma$ in 10^{-16}cm^2) for the reaction $H^+ + D_2(v, j = 1) \rightarrow D + HD^+(v')$

See Text of Appendix for Explanation of Tables

E_{cm} (eV)	3.0		4.0		5.0		6.0		7.0		8.0	
v'	σ	$\Delta\sigma$	σ	$\Delta\sigma$	σ	$\Delta\sigma$	σ	$\Delta\sigma$	σ	$\Delta\sigma$	σ	$\Delta\sigma$
$v = 3$												
0	0.049	0.007	0.054	0.007	0.036	0.005	0.032	0.005	0.020	0.004	0.013	0.003
1	0.064	0.008	0.038	0.005	0.031	0.005	0.021	0.004	0.022	0.004	0.018	0.003
2	0.047	0.006	0.045	0.006	0.030	0.005	0.021	0.004	0.020	0.004	0.014	0.003
3	0.051	0.007	0.039	0.005	0.031	0.005	0.018	0.004	0.015	0.003	0.011	0.003
4	0.052	0.007	0.041	0.006	0.027	0.004	0.021	0.004	0.022	0.004	0.007	0.002
5	0.038	0.006	0.031	0.005	0.032	0.005	0.019	0.004	0.014	0.003	0.007	0.002
6	0.027	0.005	0.037	0.005	0.026	0.004	0.021	0.004	0.012	0.003	0.010	0.003
7	0.026	0.005	0.037	0.006	0.019	0.003	0.013	0.003	0.015	0.003	0.009	0.002
8	0.019	0.004	0.026	0.005	0.023	0.004	0.015	0.003	0.005	0.002	0.005	0.002
9	0.026	0.005	0.026	0.005	0.020	0.004	0.010	0.003	0.008	0.002	0.009	0.002
≥ 10	0.026	0.004	0.099	0.009	0.061	0.006	0.048	0.005	0.039	0.005	0.028	0.004
total	0.425	0.019	0.473	0.018	0.336	0.015	0.238	0.012	0.191	0.011	0.132	0.009
$v = 4$												
0	0.068	0.008	0.058	0.007	0.030	0.005	0.025	0.005	0.020	0.004	0.008	0.002
1	0.061	0.008	0.036	0.005	0.030	0.005	0.021	0.004	0.017	0.003	0.018	0.004
2	0.057	0.007	0.036	0.005	0.033	0.005	0.015	0.003	0.024	0.004	0.010	0.003
3	0.065	0.008	0.051	0.006	0.035	0.005	0.024	0.004	0.019	0.004	0.012	0.003
4	0.054	0.007	0.040	0.005	0.032	0.005	0.026	0.004	0.018	0.004	0.013	0.003
5	0.047	0.007	0.039	0.006	0.033	0.005	0.012	0.003	0.011	0.003	0.009	0.002
6	0.039	0.006	0.028	0.005	0.033	0.005	0.011	0.003	0.013	0.003	0.007	0.002
7	0.039	0.006	0.028	0.005	0.019	0.004	0.011	0.003	0.013	0.003	0.007	0.002
8	0.045	0.007	0.026	0.005	0.022	0.004	0.011	0.003	0.007	0.002	0.007	0.002
9	0.032	0.005	0.020	0.004	0.019	0.004	0.009	0.002	0.011	0.003	0.003	0.001
≥ 10	0.084	0.008	0.086	0.008	0.053	0.006	0.041	0.005	0.030	0.004	0.027	0.004
total	0.590	0.022	0.450	0.018	0.340	0.015	0.206	0.012	0.182	0.011	0.122	0.009
$v = 5$												
0	0.071	0.008	0.059	0.007	0.038	0.005	0.014	0.003	0.015	0.003	0.022	0.004
1	0.078	0.009	0.053	0.007	0.036	0.005	0.028	0.005	0.013	0.003	0.012	0.003
2	0.050	0.007	0.040	0.006	0.033	0.005	0.016	0.003	0.018	0.004	0.011	0.003
3	0.064	0.008	0.038	0.006	0.020	0.004	0.026	0.004	0.020	0.004	0.011	0.002
4	0.056	0.007	0.034	0.005	0.029	0.005	0.019	0.004	0.012	0.003	0.009	0.003
5	0.043	0.007	0.038	0.006	0.029	0.005	0.019	0.004	0.009	0.002	0.007	0.002
6	0.046	0.007	0.033	0.005	0.020	0.004	0.011	0.003	0.012	0.003	0.009	0.002
7	0.052	0.007	0.033	0.005	0.013	0.003	0.013	0.003	0.008	0.002	0.005	0.002
8	0.045	0.007	0.026	0.005	0.012	0.003	0.014	0.003	0.008	0.002	0.002	0.001
9	0.027	0.005	0.019	0.004	0.018	0.004	0.009	0.003	0.008	0.002	0.005	0.002
≥ 10	0.144	0.011	0.080	0.008	0.045	0.006	0.038	0.005	0.024	0.004	0.022	0.004
total	0.677	0.024	0.452	0.019	0.292	0.014	0.207	0.012	0.147	0.010	0.116	0.009

Table 2-3. Cross section ($\sigma, \Delta\sigma$ in 10^{-16}cm^2) for the reaction $H^+ + D_2(v, j = 1) \rightarrow D + HD^+(v')$

See Text of Appendix for Explanation of Tables

E_{cm} (eV)	3.0		4.0		5.0		6.0		7.0		8.0	
v'	σ	$\Delta\sigma$	σ	$\Delta\sigma$	σ	$\Delta\sigma$	σ	$\Delta\sigma$	σ	$\Delta\sigma$	σ	$\Delta\sigma$
$v = 6$												
0	0.067	0.008	0.055	0.007	0.030	0.005	0.027	0.005	0.027	0.005	0.014	0.003
1	0.064	0.008	0.040	0.006	0.031	0.005	0.022	0.004	0.016	0.004	0.015	0.004
2	0.048	0.007	0.033	0.005	0.028	0.005	0.014	0.003	0.015	0.003	0.007	0.002
3	0.051	0.007	0.059	0.007	0.028	0.005	0.014	0.003	0.012	0.003	0.009	0.003
4	0.057	0.007	0.047	0.007	0.025	0.005	0.013	0.003	0.017	0.004	0.011	0.003
5	0.039	0.006	0.031	0.006	0.018	0.004	0.010	0.003	0.009	0.003	0.008	0.002
6	0.041	0.006	0.027	0.005	0.022	0.005	0.013	0.003	0.008	0.002	0.003	0.001
7	0.039	0.006	0.025	0.005	0.013	0.003	0.012	0.003	0.005	0.002	0.005	0.002
8	0.030	0.005	0.020	0.004	0.008	0.003	0.009	0.003	0.005	0.002	0.003	0.002
9	0.027	0.005	0.017	0.004	0.007	0.002	0.011	0.003	0.008	0.003	0.005	0.002
≥ 10	0.123	0.011	0.060	0.007	0.047	0.006	0.030	0.005	0.021	0.004	0.015	0.003
total	0.586	0.023	0.413	0.019	0.258	0.014	0.174	0.012	0.141	0.010	0.095	0.008
$v = 7$												
0	0.075	0.009	0.039	0.006	0.030	0.006	0.023	0.005	0.015	0.004	0.015	0.004
1	0.051	0.008	0.020	0.004	0.021	0.005	0.008	0.003	0.015	0.004	0.013	0.003
2	0.038	0.007	0.032	0.006	0.018	0.004	0.015	0.004	0.012	0.003	0.009	0.003
3	0.026	0.005	0.025	0.005	0.015	0.004	0.017	0.004	0.005	0.002	0.012	0.003
4	0.016	0.004	0.026	0.005	0.012	0.003	0.013	0.004	0.005	0.002	0.001	0.001
5	0.029	0.006	0.025	0.005	0.006	0.002	0.015	0.004	0.007	0.003	0.004	0.002
6	0.034	0.006	0.011	0.003	0.007	0.003	0.006	0.002	0.005	0.002	0.002	0.001
7	0.046	0.008	0.010	0.003	0.013	0.004	0.008	0.003	0.004	0.002	0.008	0.003
8	0.025	0.006	0.011	0.004	0.006	0.002	0.006	0.002	0.005	0.002	0.000	0.000
9	0.015	0.004	0.005	0.002	0.002	0.001	0.001	0.000	0.003	0.001	0.000	0.000
≥ 10	0.079	0.009	0.033	0.006	0.023	0.005	0.011	0.003	0.009	0.002	0.007	0.002
total	0.433	0.022	0.237	0.015	0.153	0.012	0.122	0.011	0.084	0.008	0.072	0.008
$v = 8$												
0	0.085	0.011	0.029	0.006	0.028	0.005	0.030	0.005	0.019	0.004	0.030	0.004
1	0.046	0.008	0.025	0.005	0.016	0.004	0.013	0.003	0.018	0.004	0.025	0.005
2	0.044	0.007	0.024	0.005	0.013	0.004	0.013	0.003	0.010	0.003	0.008	0.003
3	0.026	0.006	0.015	0.004	0.024	0.005	0.006	0.002	0.007	0.002	0.005	0.002
4	0.028	0.006	0.018	0.004	0.013	0.003	0.008	0.003	0.004	0.002	0.003	0.002
5	0.025	0.006	0.011	0.004	0.010	0.003	0.006	0.002	0.004	0.002	0.001	0.001
6	0.026	0.006	0.008	0.003	0.006	0.002	0.008	0.003	0.002	0.001	0.002	0.002
7	0.017	0.005	0.012	0.004	0.002	0.001	0.004	0.002	0.002	0.001	0.001	0.001
8	0.018	0.005	0.011	0.004	0.006	0.003	0.010	0.003	0.001	0.001	0.004	0.002
9	0.012	0.003	0.012	0.004	0.003	0.001	0.002	0.001	0.005	0.002	0.003	0.001
≥ 10	0.064	0.008	0.032	0.006	0.013	0.003	0.009	0.003	0.009	0.003	0.005	0.002
total	0.390	0.022	0.196	0.015	0.135	0.011	0.109	0.010	0.081	0.008	0.087	0.008

Table 3-1. Cross section ($\sigma, \Delta\sigma$ in 10^{-16}cm^2) for the reaction $H^+ + D_2(v, j = 1) \rightarrow D^+ + HD(v')$

See Text of Appendix for Explanation of Tables

E_{cm} (eV)	3.0		4.0		5.0		6.0		7.0		8.0	
v'	σ	$\Delta\sigma$	σ	$\Delta\sigma$	σ	$\Delta\sigma$	σ	$\Delta\sigma$	σ	$\Delta\sigma$	σ	$\Delta\sigma$
$v = 0$												
0	0.180	0.012	0.071	0.007	0.034	0.005	0.021	0.004	0.009	0.002	0.004	0.001
1	0.172	0.012	0.086	0.008	0.043	0.005	0.037	0.005	0.020	0.004	0.018	0.003
2	0.137	0.010	0.079	0.007	0.042	0.005	0.026	0.004	0.018	0.003	0.013	0.003
3	0.104	0.009	0.050	0.006	0.038	0.005	0.020	0.003	0.018	0.003	0.013	0.003
4	0.075	0.007	0.056	0.006	0.035	0.005	0.010	0.002	0.010	0.003	0.004	0.001
5	0.049	0.006	0.027	0.004	0.012	0.002	0.005	0.002	0.003	0.001	0.004	0.002
6	0.028	0.005	0.024	0.004	0.010	0.003	0.003	0.001	0.002	0.001	0.001	0.001
7	0.014	0.003	0.017	0.004	0.005	0.002	0.000	0.000	0.001	0.001	0.000	0.000
8	0.000	0.000	0.009	0.002	0.000	0.000	0.000	0.000	0.000	0.000	0.000	0.000
9	0.000	0.000	0.002	0.001	0.000	0.000	0.000	0.000	0.000	0.000	0.000	0.000
≥ 10	0.000	0.000	0.007	0.002	0.000	0.000	0.000	0.000	0.000	0.000	0.000	0.000
total	0.759	0.023	0.429	0.016	0.220	0.011	0.122	0.008	0.082	0.007	0.057	0.006
$v = 1$												
0	0.151	0.011	0.083	0.008	0.046	0.006	0.021	0.004	0.022	0.004	0.013	0.003
1	0.119	0.010	0.092	0.008	0.039	0.005	0.025	0.004	0.017	0.003	0.011	0.002
2	0.099	0.009	0.055	0.006	0.040	0.005	0.020	0.003	0.011	0.002	0.012	0.003
3	0.091	0.008	0.052	0.006	0.038	0.005	0.018	0.003	0.006	0.002	0.007	0.002
4	0.066	0.007	0.033	0.005	0.013	0.003	0.010	0.002	0.009	0.003	0.003	0.001
5	0.058	0.007	0.021	0.004	0.012	0.003	0.004	0.002	0.003	0.001	0.004	0.001
6	0.023	0.004	0.020	0.004	0.006	0.002	0.005	0.002	0.000	0.000	0.000	0.000
7	0.019	0.004	0.009	0.003	0.002	0.001	0.001	0.001	0.001	0.001	0.000	0.000
8	0.014	0.003	0.008	0.003	0.000	0.000	0.000	0.000	0.000	0.000	0.000	0.000
9	0.001	0.000	0.002	0.001	0.000	0.000	0.000	0.000	0.000	0.000	0.000	0.000
≥ 10	0.000	0.000	0.001	0.001	0.000	0.000	0.000	0.000	0.000	0.000	0.000	0.000
total	0.640	0.021	0.376	0.016	0.196	0.011	0.103	0.008	0.068	0.007	0.049	0.005
$v = 2$												
0	0.136	0.011	0.097	0.009	0.036	0.005	0.035	0.005	0.023	0.004	0.019	0.004
1	0.111	0.010	0.061	0.007	0.040	0.006	0.018	0.004	0.016	0.003	0.013	0.003
2	0.109	0.010	0.049	0.006	0.031	0.005	0.024	0.004	0.015	0.003	0.007	0.002
3	0.083	0.008	0.040	0.005	0.031	0.005	0.011	0.003	0.010	0.003	0.005	0.002
4	0.067	0.007	0.028	0.005	0.014	0.003	0.009	0.002	0.004	0.001	0.002	0.001
5	0.042	0.006	0.027	0.005	0.004	0.002	0.005	0.002	0.001	0.001	0.001	0.001
6	0.033	0.005	0.007	0.003	0.003	0.002	0.002	0.001	0.001	0.001	0.002	0.001
7	0.031	0.005	0.002	0.001	0.000	0.000	0.000	0.000	0.000	0.000	0.000	0.000
8	0.011	0.003	0.002	0.001	0.000	0.000	0.000	0.000	0.000	0.000	0.000	0.000
9	0.007	0.002	0.000	0.000	0.000	0.000	0.000	0.000	0.000	0.000	0.000	0.000
≥ 10	0.002	0.001	0.000	0.000	0.000	0.000	0.000	0.000	0.000	0.000	0.000	0.000
total	0.632	0.021	0.314	0.015	0.160	0.011	0.104	0.008	0.070	0.007	0.049	0.005

Table 3-2. Cross section ($\sigma, \Delta\sigma$ in 10^{-16}cm^2) for the reaction $H^+ + D_2(v, j = 1) \rightarrow D^+ + HD(v')$

See Text of Appendix for Explanation of Tables

E_{cm} (eV)	3.0		4.0		5.0		6.0		7.0		8.0	
v'	σ	$\Delta\sigma$	σ	$\Delta\sigma$	σ	$\Delta\sigma$	σ	$\Delta\sigma$	σ	$\Delta\sigma$	σ	$\Delta\sigma$
$v = 3$												
0	0.135	0.011	0.067	0.008	0.045	0.006	0.030	0.005	0.022	0.004	0.013	0.003
1	0.089	0.009	0.056	0.007	0.031	0.005	0.029	0.005	0.014	0.003	0.014	0.003
2	0.091	0.009	0.045	0.006	0.023	0.004	0.018	0.003	0.012	0.003	0.009	0.002
3	0.061	0.007	0.023	0.004	0.017	0.004	0.012	0.003	0.012	0.003	0.006	0.002
4	0.048	0.006	0.028	0.005	0.016	0.003	0.007	0.002	0.004	0.001	0.004	0.002
5	0.038	0.006	0.019	0.005	0.008	0.002	0.002	0.001	0.001	0.001	0.001	0.001
6	0.033	0.006	0.009	0.003	0.003	0.002	0.001	0.001	0.000	0.000	0.000	0.000
7	0.025	0.005	0.002	0.002	0.004	0.002	0.002	0.001	0.000	0.000	0.000	0.000
8	0.013	0.004	0.002	0.001	0.001	0.001	0.000	0.000	0.000	0.000	0.000	0.000
9	0.010	0.003	0.000	0.000	0.000	0.000	0.000	0.000	0.000	0.000	0.000	0.000
≥ 10	0.014	0.004	0.000	0.000	0.000	0.000	0.000	0.000	0.000	0.000	0.000	0.000
total	0.556	0.021	0.251	0.014	0.147	0.010	0.100	0.008	0.065	0.007	0.047	0.006
$v = 4$												
0	0.104	0.010	0.064	0.007	0.046	0.006	0.023	0.004	0.019	0.004	0.016	0.004
1	0.102	0.010	0.053	0.007	0.035	0.005	0.023	0.004	0.010	0.003	0.011	0.003
2	0.082	0.009	0.032	0.005	0.028	0.005	0.016	0.003	0.010	0.003	0.010	0.003
3	0.060	0.007	0.025	0.004	0.014	0.003	0.014	0.003	0.009	0.003	0.003	0.001
4	0.040	0.006	0.019	0.004	0.011	0.002	0.007	0.002	0.009	0.002	0.003	0.001
5	0.033	0.005	0.014	0.003	0.005	0.002	0.005	0.002	0.002	0.001	0.001	0.001
6	0.026	0.005	0.008	0.003	0.002	0.001	0.001	0.001	0.001	0.001	0.000	0.000
7	0.019	0.004	0.003	0.002	0.003	0.002	0.001	0.001	0.000	0.000	0.000	0.000
8	0.004	0.002	0.004	0.002	0.000	0.000	0.000	0.000	0.000	0.000	0.000	0.000
9	0.008	0.003	0.000	0.000	0.000	0.000	0.000	0.000	0.000	0.000	0.000	0.000
≥ 10	0.011	0.003	0.000	0.000	0.000	0.000	0.000	0.000	0.000	0.000	0.000	0.000
total	0.489	0.020	0.222	0.013	0.143	0.011	0.090	0.008	0.061	0.007	0.044	0.006
$v = 5$												
0	0.086	0.009	0.052	0.007	0.023	0.004	0.016	0.004	0.015	0.004	0.015	0.003
1	0.092	0.009	0.046	0.006	0.024	0.005	0.023	0.004	0.019	0.004	0.013	0.003
2	0.065	0.007	0.033	0.005	0.027	0.005	0.015	0.003	0.010	0.003	0.009	0.003
3	0.051	0.007	0.032	0.005	0.018	0.004	0.011	0.003	0.007	0.002	0.005	0.002
4	0.033	0.005	0.021	0.004	0.008	0.002	0.010	0.003	0.002	0.001	0.002	0.001
5	0.030	0.006	0.010	0.003	0.007	0.002	0.004	0.002	0.002	0.001	0.002	0.001
6	0.020	0.005	0.006	0.002	0.002	0.001	0.001	0.001	0.001	0.001	0.000	0.000
7	0.010	0.003	0.004	0.002	0.000	0.000	0.000	0.000	0.000	0.000	0.000	0.000
8	0.002	0.002	0.000	0.000	0.001	0.001	0.000	0.000	0.000	0.000	0.000	0.000
9	0.007	0.003	0.000	0.000	0.000	0.000	0.000	0.000	0.000	0.000	0.000	0.000
≥ 10	0.006	0.002	0.000	0.000	0.000	0.000	0.000	0.000	0.000	0.000	0.000	0.000
total	0.402	0.019	0.205	0.013	0.109	0.009	0.081	0.008	0.056	0.007	0.046	0.006

Table 3-3. Cross section ($\sigma, \Delta\sigma$ in 10^{-16}cm^2) for the reaction $H^+ + D_2(v, j = 1) \rightarrow D^+ + HD(v')$

See Text of Appendix for Explanation of Tables

E_{cm} (eV)	3.0		4.0		5.0		6.0		7.0		8.0	
v'	σ	$\Delta\sigma$	σ	$\Delta\sigma$	σ	$\Delta\sigma$	σ	$\Delta\sigma$	σ	$\Delta\sigma$	σ	$\Delta\sigma$
$v = 6$												
0	0.096	0.010	0.043	0.006	0.035	0.006	0.025	0.005	0.021	0.004	0.015	0.004
1	0.059	0.007	0.029	0.005	0.022	0.004	0.013	0.003	0.012	0.003	0.009	0.003
2	0.056	0.007	0.024	0.004	0.025	0.004	0.011	0.003	0.007	0.003	0.005	0.002
3	0.057	0.007	0.028	0.005	0.022	0.004	0.009	0.003	0.005	0.002	0.004	0.002
4	0.029	0.005	0.015	0.004	0.010	0.003	0.007	0.002	0.005	0.002	0.001	0.000
5	0.032	0.006	0.009	0.003	0.004	0.002	0.001	0.000	0.001	0.001	0.000	0.000
6	0.015	0.004	0.005	0.002	0.003	0.002	0.000	0.000	0.000	0.000	0.000	0.000
7	0.011	0.004	0.001	0.001	0.000	0.000	0.000	0.000	0.000	0.000	0.000	0.000
8	0.002	0.002	0.001	0.001	0.000	0.000	0.000	0.000	0.000	0.000	0.000	0.000
9	0.001	0.001	0.000	0.000	0.000	0.000	0.000	0.000	0.000	0.000	0.000	0.000
≥ 10	0.002	0.001	0.000	0.000	0.000	0.000	0.000	0.000	0.000	0.000	0.000	0.000
total	0.361	0.018	0.156	0.012	0.121	0.010	0.066	0.007	0.050	0.006	0.035	0.005
$v = 7$												
0	0.045	0.007	0.038	0.006	0.011	0.003	0.011	0.003	0.011	0.003	0.014	0.004
1	0.051	0.008	0.022	0.005	0.018	0.004	0.014	0.004	0.005	0.002	0.008	0.003
2	0.038	0.007	0.019	0.005	0.011	0.003	0.003	0.002	0.008	0.003	0.005	0.002
3	0.024	0.005	0.006	0.002	0.014	0.004	0.002	0.001	0.002	0.001	0.005	0.002
4	0.012	0.004	0.004	0.002	0.003	0.002	0.004	0.002	0.003	0.002	0.001	0.001
5	0.014	0.005	0.004	0.002	0.002	0.002	0.001	0.001	0.001	0.001	0.004	0.002
6	0.003	0.002	0.004	0.002	0.000	0.000	0.001	0.001	0.000	0.000	0.000	0.000
7	0.003	0.002	0.001	0.001	0.000	0.000	0.000	0.000	0.001	0.001	0.000	0.000
8	0.004	0.003	0.000	0.000	0.000	0.000	0.000	0.000	0.000	0.000	0.000	0.000
9	0.000	0.000	0.000	0.000	0.000	0.000	0.000	0.000	0.000	0.000	0.000	0.000
≥ 10	0.000	0.000	0.000	0.000	0.000	0.000	0.000	0.000	0.000	0.000	0.000	0.000
total	0.195	0.015	0.097	0.010	0.060	0.008	0.036	0.006	0.030	0.005	0.038	0.006
$v = 8$												
0	0.040	0.007	0.021	0.005	0.015	0.004	0.015	0.004	0.014	0.004	0.005	0.002
1	0.029	0.006	0.017	0.005	0.014	0.004	0.003	0.002	0.009	0.003	0.010	0.003
2	0.012	0.004	0.014	0.004	0.010	0.003	0.008	0.003	0.001	0.001	0.004	0.002
3	0.018	0.005	0.014	0.004	0.003	0.002	0.008	0.003	0.005	0.002	0.007	0.003
4	0.014	0.005	0.006	0.003	0.004	0.002	0.001	0.001	0.002	0.001	0.007	0.002
5	0.002	0.002	0.003	0.002	0.004	0.002	0.006	0.002	0.002	0.002	0.006	0.002
6	0.003	0.002	0.001	0.001	0.001	0.001	0.000	0.000	0.002	0.001	0.008	0.002
7	0.000	0.000	0.000	0.000	0.000	0.000	0.000	0.000	0.000	0.000	0.007	0.002
8	0.000	0.000	0.000	0.000	0.000	0.000	0.000	0.000	0.000	0.000	0.005	0.002
9	0.000	0.000	0.000	0.000	0.000	0.000	0.000	0.000	0.000	0.000	0.001	0.001
≥ 10	0.000	0.000	0.000	0.000	0.000	0.000	0.000	0.000	0.001	0.000	0.004	0.001
total	0.117	0.012	0.076	0.009	0.050	0.007	0.040	0.006	0.037	0.006	0.064	0.007

Table 4-1. Cross section ($\sigma, \Delta\sigma$ in 10^{-16}cm^2) for the reaction $D^+ + D_2(v, j = 1) \rightarrow D + D_2^+(v')$

See Text of Appendix for Explanation of Tables

E_{cm} (eV)	3.0		4.0		5.0		6.0		7.0		8.0	
v'	σ	$\Delta\sigma$	σ	$\Delta\sigma$	σ	$\Delta\sigma$	σ	$\Delta\sigma$	σ	$\Delta\sigma$	σ	$\Delta\sigma$
$v = 0$												
0	0.116	0.011	0.107	0.010	0.113	0.011	0.094	0.009	0.104	0.009	0.100	0.009
1	0.134	0.011	0.101	0.010	0.134	0.011	0.106	0.009	0.127	0.010	0.107	0.009
2	0.116	0.010	0.087	0.009	0.124	0.010	0.144	0.011	0.104	0.009	0.111	0.009
3	0.090	0.009	0.062	0.007	0.105	0.009	0.123	0.010	0.090	0.008	0.083	0.008
4	0.069	0.007	0.064	0.007	0.117	0.010	0.094	0.009	0.090	0.008	0.088	0.008
5	0.037	0.005	0.063	0.007	0.077	0.007	0.087	0.008	0.068	0.007	0.061	0.006
6	0.010	0.002	0.051	0.006	0.081	0.008	0.081	0.008	0.074	0.007	0.060	0.006
7	0.000	0.000	0.052	0.006	0.071	0.007	0.069	0.007	0.055	0.006	0.054	0.006
8	0.000	0.000	0.043	0.005	0.052	0.006	0.053	0.006	0.050	0.006	0.039	0.005
9	0.000	0.000	0.027	0.004	0.061	0.007	0.042	0.005	0.041	0.005	0.036	0.005
≥ 10	0.000	0.000	0.092	0.008	0.259	0.012	0.225	0.011	0.228	0.011	0.191	0.010
total	0.572	0.022	0.750	0.022	1.194	0.026	1.118	0.024	1.031	0.023	0.929	0.022
$v = 1$												
0	0.161	0.013	0.119	0.011	0.127	0.011	0.119	0.011	0.108	0.010	0.108	0.010
1	0.149	0.012	0.120	0.011	0.142	0.012	0.137	0.011	0.144	0.011	0.100	0.009
2	0.138	0.012	0.132	0.011	0.129	0.011	0.151	0.012	0.118	0.010	0.111	0.010
3	0.117	0.011	0.123	0.010	0.126	0.011	0.096	0.009	0.108	0.009	0.082	0.008
4	0.093	0.009	0.106	0.010	0.112	0.010	0.110	0.009	0.098	0.009	0.086	0.008
5	0.065	0.007	0.085	0.008	0.094	0.009	0.098	0.009	0.076	0.007	0.064	0.007
6	0.046	0.006	0.083	0.008	0.099	0.009	0.071	0.007	0.075	0.007	0.072	0.007
7	0.042	0.006	0.065	0.007	0.082	0.008	0.079	0.008	0.057	0.006	0.062	0.007
8	0.014	0.003	0.057	0.007	0.068	0.007	0.063	0.006	0.060	0.006	0.050	0.006
9	0.004	0.001	0.070	0.007	0.057	0.006	0.056	0.006	0.035	0.005	0.041	0.005
≥ 10	0.000	0.000	0.200	0.012	0.286	0.013	0.244	0.012	0.228	0.011	0.186	0.010
total	0.828	0.026	1.159	0.028	1.322	0.028	1.225	0.026	1.106	0.025	0.961	0.023
$v = 2$												
0	0.167	0.013	0.155	0.013	0.173	0.014	0.144	0.012	0.111	0.010	0.127	0.011
1	0.147	0.013	0.172	0.014	0.162	0.014	0.140	0.012	0.148	0.012	0.151	0.013
2	0.116	0.011	0.143	0.012	0.110	0.010	0.129	0.011	0.130	0.012	0.179	0.015
3	0.124	0.011	0.154	0.012	0.143	0.012	0.134	0.011	0.132	0.011	0.167	0.015
4	0.099	0.010	0.132	0.011	0.108	0.010	0.108	0.009	0.111	0.009	0.087	0.008
5	0.087	0.009	0.123	0.011	0.094	0.009	0.103	0.009	0.094	0.008	0.097	0.008
6	0.077	0.009	0.113	0.010	0.094	0.009	0.085	0.008	0.076	0.007	0.080	0.007
7	0.064	0.008	0.087	0.009	0.079	0.008	0.069	0.007	0.058	0.006	0.053	0.006
8	0.047	0.006	0.079	0.008	0.071	0.007	0.062	0.007	0.061	0.006	0.046	0.005
9	0.039	0.006	0.069	0.007	0.062	0.007	0.050	0.006	0.040	0.005	0.038	0.005
≥ 10	0.038	0.005	0.335	0.016	0.311	0.014	0.243	0.012	0.210	0.011	0.179	0.010
total	1.005	0.029	1.563	0.033	1.407	0.031	1.267	0.028	1.170	0.027	1.205	0.030

Table 4-2. Cross section ($\sigma, \Delta\sigma$ in 10^{-16}cm^2) for the reaction $D^+ + D_2(v, j = 1) \rightarrow D + D_2^+(v')$

See Text of Appendix for Explanation of Tables

E_{cm} (eV)	3.0		4.0		5.0		6.0		7.0		8.0	
v'	σ	$\Delta\sigma$	σ	$\Delta\sigma$	σ	$\Delta\sigma$	σ	$\Delta\sigma$	σ	$\Delta\sigma$	σ	$\Delta\sigma$
$v = 3$												
0	0.241	0.018	0.209	0.016	0.195	0.015	0.170	0.013	0.113	0.011	0.129	0.011
1	0.386	0.027	0.357	0.026	0.218	0.018	0.165	0.015	0.185	0.016	0.193	0.016
2	0.212	0.019	0.228	0.018	0.205	0.017	0.187	0.016	0.226	0.018	0.341	0.024
3	0.156	0.015	0.200	0.017	0.156	0.013	0.175	0.016	0.226	0.019	0.396	0.027
4	0.110	0.011	0.156	0.013	0.143	0.012	0.187	0.017	0.265	0.021	0.356	0.026
5	0.112	0.011	0.138	0.012	0.118	0.010	0.118	0.011	0.256	0.021	0.267	0.021
6	0.119	0.011	0.096	0.009	0.106	0.009	0.094	0.009	0.082	0.009	0.113	0.012
7	0.086	0.009	0.094	0.009	0.093	0.009	0.071	0.007	0.073	0.007	0.070	0.007
8	0.068	0.008	0.093	0.009	0.063	0.007	0.070	0.007	0.065	0.007	0.067	0.007
9	0.083	0.009	0.074	0.008	0.069	0.007	0.064	0.007	0.052	0.006	0.042	0.006
≥ 10	0.156	0.011	0.355	0.016	0.298	0.014	0.281	0.014	0.244	0.012	0.219	0.012
total	1.729	0.046	2.000	0.045	1.665	0.037	1.582	0.037	1.787	0.044	2.192	0.053
$v = 4$												
0	0.300	0.021	0.298	0.020	0.217	0.016	0.153	0.013	0.129	0.012	0.113	0.011
1	0.748	0.041	0.518	0.032	0.351	0.025	0.288	0.022	0.291	0.022	0.275	0.022
2	0.628	0.037	0.393	0.026	0.301	0.022	0.318	0.022	0.378	0.026	0.480	0.030
3	0.472	0.031	0.339	0.023	0.264	0.020	0.346	0.025	0.501	0.030	0.754	0.039
4	0.337	0.025	0.240	0.019	0.248	0.019	0.384	0.027	0.479	0.031	0.740	0.038
5	0.216	0.018	0.163	0.015	0.178	0.016	0.318	0.025	0.438	0.029	0.588	0.035
6	0.179	0.015	0.133	0.012	0.209	0.019	0.273	0.022	0.359	0.026	0.357	0.026
7	0.154	0.014	0.104	0.010	0.109	0.011	0.166	0.017	0.200	0.018	0.221	0.019
8	0.127	0.012	0.115	0.010	0.096	0.009	0.082	0.009	0.122	0.014	0.100	0.012
9	0.094	0.010	0.084	0.009	0.073	0.008	0.070	0.007	0.061	0.007	0.070	0.009
≥ 10	0.315	0.016	0.392	0.017	0.345	0.016	0.305	0.015	0.263	0.013	0.250	0.013
total	3.570	0.074	2.778	0.058	2.390	0.052	2.703	0.060	3.222	0.068	3.948	0.077
$v = 5$												
0	0.368	0.024	0.401	0.029	0.225	0.020	0.142	0.013	0.133	0.012	0.128	0.013
1	1.136	0.051	1.176	0.055	0.698	0.041	0.429	0.030	0.533	0.036	0.673	0.043
2	0.937	0.045	0.561	0.033	0.476	0.029	0.526	0.032	0.847	0.045	1.390	0.061
3	0.708	0.039	0.465	0.029	0.471	0.030	0.605	0.035	0.830	0.042	1.174	0.053
4	0.618	0.036	0.430	0.028	0.388	0.027	0.599	0.035	0.743	0.039	1.030	0.047
5	0.409	0.028	0.347	0.026	0.365	0.027	0.508	0.032	0.603	0.035	0.928	0.043
6	0.284	0.022	0.283	0.023	0.343	0.026	0.412	0.029	0.540	0.033	0.606	0.035
7	0.234	0.019	0.185	0.017	0.255	0.022	0.360	0.027	0.423	0.030	0.433	0.030
8	0.181	0.016	0.141	0.014	0.147	0.016	0.215	0.020	0.299	0.024	0.274	0.024
9	0.125	0.012	0.098	0.009	0.087	0.010	0.137	0.015	0.133	0.015	0.140	0.016
≥ 10	0.565	0.024	0.439	0.019	0.377	0.017	0.364	0.019	0.342	0.019	0.397	0.022
total	5.565	0.093	4.526	0.086	3.832	0.079	4.296	0.083	5.427	0.096	7.174	0.113

Table 4-3. Cross section ($\sigma, \Delta\sigma$ in 10^{-16}cm^2) for the reaction $D^+ + D_2(v, j = 1) \rightarrow D + D_2^+(v')$

See Text of Appendix for Explanation of Tables

E_{cm} (eV)	3.0		4.0		5.0		6.0		7.0		8.0	
v'	σ	$\Delta\sigma$	σ	$\Delta\sigma$	σ	$\Delta\sigma$	σ	$\Delta\sigma$	σ	$\Delta\sigma$	σ	$\Delta\sigma$
$v = 6$												
0	0.948	0.048	0.869	0.050	1.530	0.076	1.429	0.073	1.365	0.068	1.162	0.060
1	19.035	0.257	15.601	0.236	14.853	0.230	15.154	0.230	13.954	0.221	13.009	0.216
2	1.669	0.065	1.212	0.054	1.342	0.061	2.067	0.080	2.822	0.097	4.324	0.121
3	0.953	0.045	0.832	0.041	0.860	0.044	1.260	0.056	1.501	0.063	1.922	0.074
4	0.760	0.039	0.618	0.036	0.719	0.040	0.853	0.044	0.971	0.048	1.154	0.054
5	0.630	0.036	0.490	0.030	0.653	0.037	0.590	0.036	0.676	0.038	0.944	0.046
6	0.530	0.033	0.398	0.028	0.498	0.031	0.423	0.030	0.563	0.034	0.727	0.039
7	0.400	0.028	0.349	0.027	0.327	0.026	0.369	0.028	0.490	0.032	0.511	0.032
8	0.284	0.023	0.260	0.022	0.301	0.025	0.253	0.022	0.349	0.026	0.385	0.028
9	0.201	0.018	0.221	0.021	0.195	0.018	0.170	0.018	0.223	0.021	0.220	0.022
≥ 10	0.738	0.029	0.577	0.024	0.533	0.026	0.488	0.026	0.428	0.025	0.504	0.028
total	26.146	0.274	21.427	0.253	21.811	0.256	23.056	0.259	23.341	0.259	24.862	0.265
$v = 7$												
0	0.440	0.026	0.292	0.022	0.330	0.025	0.443	0.031	1.011	0.048	1.410	0.056
1	2.567	0.085	4.766	0.114	5.234	0.115	4.960	0.109	3.890	0.096	2.775	0.081
2	15.494	0.217	14.173	0.209	9.829	0.181	7.167	0.159	5.641	0.145	4.509	0.134
3	13.529	0.216	12.759	0.208	12.570	0.204	12.609	0.201	12.923	0.204	13.464	0.203
4	2.329	0.076	2.139	0.077	2.204	0.085	2.860	0.099	3.248	0.105	3.763	0.110
5	1.092	0.049	0.806	0.046	0.886	0.052	1.395	0.068	1.697	0.074	2.170	0.082
6	0.577	0.035	0.428	0.032	0.630	0.043	0.916	0.051	1.310	0.061	1.560	0.065
7	0.437	0.031	0.319	0.026	0.424	0.031	0.519	0.035	0.799	0.044	1.027	0.050
8	0.257	0.023	0.263	0.023	0.319	0.026	0.385	0.028	0.494	0.033	0.570	0.036
9	0.189	0.019	0.216	0.021	0.248	0.022	0.281	0.024	0.298	0.025	0.363	0.028
≥ 10	0.801	0.036	0.628	0.033	0.710	0.037	0.818	0.041	0.908	0.044	1.143	0.049
total	37.711	0.264	36.789	0.264	33.382	0.259	32.353	0.255	32.219	0.255	32.756	0.252
$v = 8$												
0	0.362	0.024	0.301	0.023	0.267	0.023	0.214	0.020	0.155	0.015	0.301	0.022
1	1.126	0.051	1.312	0.056	1.483	0.060	1.309	0.054	1.457	0.056	1.594	0.059
2	2.077	0.076	3.386	0.093	4.042	0.096	3.588	0.091	2.670	0.080	1.696	0.063
3	8.100	0.143	8.318	0.140	5.135	0.116	2.855	0.089	1.635	0.070	1.176	0.063
4	17.682	0.235	13.753	0.214	11.053	0.197	9.875	0.191	9.696	0.191	8.843	0.185
5	6.371	0.145	6.298	0.144	6.867	0.150	7.642	0.156	8.656	0.162	9.579	0.166
6	1.916	0.071	1.563	0.071	1.929	0.081	2.664	0.094	3.081	0.100	3.580	0.107
7	0.718	0.044	0.887	0.053	1.204	0.062	1.600	0.071	2.052	0.079	2.429	0.086
8	0.322	0.028	0.511	0.038	0.762	0.047	0.918	0.051	1.266	0.059	1.486	0.064
9	0.293	0.027	0.300	0.027	0.431	0.032	0.596	0.039	0.657	0.041	0.759	0.044
≥ 10	0.913	0.043	0.859	0.043	1.008	0.048	1.266	0.054	1.507	0.058	1.810	0.063
total	39.880	0.250	37.487	0.250	34.181	0.249	32.526	0.246	32.832	0.243	33.254	0.237

Table 5-1. Cross section ($\sigma, \Delta\sigma$ in 10^{-16}cm^2) for the reaction $H^+ + H_2(v, j = 1) \rightarrow H + H_2^+(v')$

See Text of Appendix for Explanation of Tables

E_{cm} (eV)	3.0		4.0		5.0		6.0		7.0		8.0	
v'	σ	$\Delta\sigma$	σ	$\Delta\sigma$	σ	$\Delta\sigma$	σ	$\Delta\sigma$	σ	$\Delta\sigma$	σ	$\Delta\sigma$
$v = 0$												
0	0.183	0.013	0.119	0.011	0.174	0.013	0.163	0.012	0.131	0.011	0.159	0.012
1	0.197	0.014	0.133	0.011	0.179	0.012	0.188	0.013	0.182	0.012	0.143	0.010
2	0.162	0.012	0.128	0.011	0.175	0.012	0.159	0.011	0.147	0.010	0.130	0.010
3	0.088	0.009	0.109	0.009	0.125	0.009	0.131	0.010	0.115	0.009	0.111	0.009
4	0.025	0.003	0.097	0.009	0.126	0.010	0.113	0.009	0.096	0.008	0.083	0.007
5	0.001	0.001	0.077	0.008	0.100	0.008	0.094	0.008	0.076	0.007	0.069	0.007
6	0.000	0.000	0.073	0.008	0.096	0.008	0.072	0.007	0.062	0.006	0.055	0.006
7	0.000	0.000	0.040	0.005	0.075	0.007	0.058	0.006	0.053	0.006	0.052	0.006
8	0.000	0.000	0.015	0.002	0.048	0.006	0.049	0.006	0.042	0.005	0.044	0.005
9	0.000	0.000	0.019	0.003	0.047	0.005	0.045	0.005	0.035	0.004	0.029	0.004
≥ 10	0.000	0.000	0.011	0.002	0.090	0.007	0.095	0.007	0.097	0.007	0.080	0.007
total	0.656	0.024	0.821	0.024	1.235	0.026	1.167	0.025	1.035	0.023	0.954	0.022
$v = 1$												
0	0.242	0.016	0.189	0.014	0.232	0.016	0.188	0.013	0.188	0.013	0.155	0.012
1	0.191	0.014	0.242	0.016	0.192	0.014	0.194	0.013	0.176	0.013	0.202	0.015
2	0.146	0.012	0.223	0.015	0.200	0.013	0.182	0.012	0.158	0.011	0.150	0.011
3	0.130	0.011	0.198	0.013	0.145	0.011	0.140	0.010	0.121	0.009	0.119	0.009
4	0.078	0.008	0.139	0.011	0.137	0.010	0.129	0.010	0.104	0.008	0.112	0.009
5	0.063	0.007	0.115	0.010	0.112	0.009	0.086	0.008	0.076	0.008	0.067	0.006
6	0.040	0.006	0.097	0.009	0.086	0.008	0.072	0.007	0.071	0.007	0.065	0.007
7	0.015	0.003	0.075	0.008	0.067	0.007	0.058	0.006	0.062	0.007	0.046	0.005
8	0.001	0.001	0.055	0.006	0.065	0.007	0.043	0.006	0.047	0.005	0.033	0.005
9	0.000	0.000	0.035	0.005	0.045	0.006	0.039	0.005	0.038	0.005	0.036	0.005
≥ 10	0.000	0.000	0.106	0.009	0.108	0.008	0.099	0.008	0.086	0.007	0.086	0.007
total	0.907	0.027	1.474	0.032	1.389	0.029	1.230	0.027	1.129	0.026	1.072	0.026
$v = 2$												
0	0.387	0.025	0.405	0.025	0.348	0.023	0.264	0.018	0.199	0.014	0.231	0.016
1	0.486	0.030	0.423	0.026	0.307	0.020	0.286	0.020	0.331	0.022	0.434	0.027
2	0.233	0.018	0.277	0.018	0.266	0.018	0.320	0.022	0.372	0.025	0.630	0.035
3	0.201	0.015	0.203	0.014	0.200	0.015	0.264	0.020	0.374	0.026	0.573	0.032
4	0.157	0.013	0.174	0.013	0.170	0.012	0.143	0.011	0.174	0.015	0.240	0.018
5	0.130	0.011	0.120	0.010	0.127	0.010	0.097	0.008	0.100	0.008	0.085	0.008
6	0.088	0.009	0.125	0.010	0.106	0.009	0.069	0.007	0.079	0.007	0.062	0.007
7	0.065	0.008	0.091	0.009	0.065	0.007	0.072	0.007	0.047	0.005	0.055	0.006
8	0.054	0.007	0.074	0.008	0.056	0.006	0.065	0.007	0.048	0.006	0.048	0.006
9	0.024	0.004	0.053	0.007	0.054	0.006	0.044	0.006	0.045	0.006	0.039	0.005
≥ 10	0.022	0.003	0.134	0.010	0.115	0.009	0.106	0.008	0.108	0.008	0.084	0.007
total	1.846	0.048	2.079	0.046	1.814	0.041	1.730	0.041	1.877	0.047	2.482	0.058

Table 5-2. Cross section ($\sigma, \Delta\sigma$ in 10^{-16}cm^2) for the reaction $H^+ + H_2(v, j = 1) \rightarrow H + H_2^+(v')$

See Text of Appendix for Explanation of Tables

E_{cm} (eV)	3.0		4.0		5.0		6.0		7.0		8.0	
v'	σ	$\Delta\sigma$	σ	$\Delta\sigma$	σ	$\Delta\sigma$	σ	$\Delta\sigma$	σ	$\Delta\sigma$	σ	$\Delta\sigma$
$v = 3$												
0	0.716	0.037	0.623	0.033	0.472	0.030	0.330	0.024	0.205	0.015	0.185	0.016
1	1.222	0.051	0.742	0.037	0.515	0.029	0.619	0.034	0.736	0.039	1.181	0.052
2	0.816	0.042	0.557	0.031	0.494	0.029	0.735	0.038	1.045	0.046	1.292	0.052
3	0.466	0.029	0.416	0.026	0.443	0.028	0.661	0.037	0.862	0.042	1.299	0.051
4	0.364	0.024	0.273	0.020	0.369	0.025	0.480	0.030	0.667	0.037	0.741	0.038
5	0.241	0.018	0.151	0.012	0.204	0.016	0.338	0.025	0.343	0.025	0.404	0.028
6	0.157	0.013	0.154	0.012	0.144	0.012	0.155	0.015	0.165	0.016	0.153	0.016
7	0.139	0.012	0.109	0.010	0.088	0.008	0.066	0.007	0.082	0.009	0.083	0.010
8	0.102	0.010	0.088	0.009	0.073	0.008	0.063	0.007	0.055	0.007	0.053	0.007
9	0.075	0.009	0.066	0.007	0.062	0.007	0.056	0.007	0.043	0.006	0.036	0.005
≥ 10	0.155	0.011	0.168	0.011	0.148	0.011	0.148	0.010	0.129	0.009	0.101	0.008
total	4.452	0.083	3.348	0.066	3.011	0.064	3.651	0.075	4.333	0.083	5.529	0.095
$v = 4$												
0	17.091	0.252	14.870	0.234	14.906	0.233	13.004	0.217	10.993	0.208	9.760	0.203
1	4.118	0.108	2.521	0.087	2.476	0.090	4.929	0.133	6.968	0.160	8.704	0.179
2	1.595	0.058	1.110	0.047	1.315	0.054	2.292	0.076	3.069	0.089	3.070	0.089
3	0.961	0.044	0.964	0.044	1.150	0.049	1.476	0.057	1.724	0.062	1.862	0.064
4	0.674	0.037	0.687	0.037	0.910	0.044	1.004	0.046	1.047	0.046	1.209	0.050
5	0.483	0.030	0.538	0.033	0.648	0.037	0.632	0.036	0.609	0.035	0.581	0.034
6	0.316	0.023	0.362	0.027	0.384	0.027	0.382	0.028	0.313	0.025	0.303	0.025
7	0.190	0.015	0.195	0.017	0.213	0.019	0.239	0.021	0.180	0.018	0.163	0.017
8	0.135	0.012	0.136	0.013	0.137	0.014	0.117	0.014	0.156	0.017	0.108	0.013
9	0.108	0.010	0.080	0.009	0.077	0.010	0.074	0.010	0.095	0.012	0.060	0.009
≥ 10	0.263	0.015	0.222	0.014	0.172	0.012	0.190	0.014	0.141	0.012	0.117	0.011
total	25.933	0.279	21.685	0.258	22.387	0.262	24.340	0.267	25.293	0.273	25.936	0.276
$v = 5$												
0	0.805	0.038	0.876	0.045	1.051	0.052	1.019	0.050	1.483	0.058	1.644	0.059
1	7.707	0.142	9.885	0.148	8.422	0.139	6.470	0.122	4.101	0.102	2.856	0.087
2	21.776	0.243	17.809	0.226	15.609	0.213	14.137	0.204	13.745	0.204	13.597	0.202
3	4.895	0.116	4.277	0.114	4.397	0.118	5.082	0.126	5.708	0.132	6.259	0.134
4	1.186	0.053	1.130	0.058	1.523	0.068	2.198	0.081	2.967	0.093	3.502	0.100
5	0.546	0.035	0.584	0.037	0.848	0.047	1.126	0.054	1.533	0.062	1.822	0.068
6	0.432	0.031	0.389	0.029	0.476	0.032	0.640	0.038	0.707	0.041	0.729	0.040
7	0.230	0.021	0.267	0.023	0.333	0.028	0.337	0.027	0.422	0.031	0.456	0.032
8	0.165	0.018	0.210	0.021	0.171	0.019	0.233	0.023	0.337	0.027	0.318	0.027
9	0.128	0.016	0.130	0.016	0.160	0.019	0.189	0.020	0.187	0.021	0.207	0.021
≥ 10	0.250	0.019	0.167	0.016	0.257	0.023	0.295	0.026	0.430	0.031	0.449	0.032
total	38.118	0.251	35.724	0.251	33.247	0.249	31.726	0.244	31.620	0.243	31.839	0.239

Table 5-3. Cross section ($\sigma, \Delta\sigma$ in 10^{-16}cm^2) for the reaction $H^+ + H_2(v, j = 1) \rightarrow H + H_2^+(v')$

See Text of Appendix for Explanation of Tables

E_{cm} (eV)	3.0		4.0		5.0		6.0		7.0		8.0	
v'	σ	$\Delta\sigma$	σ	$\Delta\sigma$	σ	$\Delta\sigma$	σ	$\Delta\sigma$	σ	$\Delta\sigma$	σ	$\Delta\sigma$
	$v = 6$											
0	0.673	0.037	0.490	0.032	0.388	0.028	0.292	0.023	0.344	0.023	0.452	0.026
1	1.503	0.060	1.220	0.053	1.318	0.052	1.502	0.054	1.636	0.057	1.450	0.054
2	3.372	0.092	4.571	0.101	4.215	0.096	2.756	0.080	1.655	0.063	0.948	0.049
3	12.302	0.179	8.460	0.156	4.862	0.126	3.547	0.112	2.835	0.103	2.695	0.101
4	14.012	0.210	12.320	0.198	12.640	0.199	13.195	0.200	13.673	0.202	13.989	0.202
5	2.897	0.094	3.380	0.104	3.853	0.111	4.685	0.120	4.815	0.121	5.606	0.127
6	0.995	0.056	1.359	0.066	2.044	0.079	2.646	0.089	2.993	0.094	2.968	0.093
7	0.516	0.038	0.634	0.043	0.996	0.054	1.153	0.057	1.352	0.062	1.637	0.067
8	0.311	0.028	0.377	0.032	0.528	0.037	0.543	0.038	0.717	0.043	0.825	0.046
9	0.210	0.023	0.232	0.025	0.293	0.028	0.354	0.031	0.452	0.033	0.491	0.035
≥ 10	0.313	0.025	0.278	0.025	0.476	0.034	0.646	0.039	0.793	0.044	1.041	0.049
total	37.104	0.241	33.322	0.240	31.614	0.237	31.319	0.232	31.266	0.229	32.102	0.223

Table 6-1. Cross section ($\sigma, \Delta\sigma$ in 10^{-16}cm^2) for the reaction $D^+ + H_2(v, j = 1) \rightarrow D + H_2^+(v')$

See Text of Appendix for Explanation of Tables

E_{cm} (eV)	3.0		4.0		5.0		6.0		7.0		8.0	
v'	σ	$\Delta\sigma$	σ	$\Delta\sigma$	σ	$\Delta\sigma$	σ	$\Delta\sigma$	σ	$\Delta\sigma$	σ	$\Delta\sigma$
$v = 0$												
0	0.094	0.011	0.132	0.012	0.093	0.010	0.086	0.010	0.082	0.009	0.093	0.010
1	0.120	0.012	0.068	0.008	0.078	0.009	0.095	0.010	0.094	0.009	0.116	0.011
2	0.066	0.008	0.054	0.007	0.072	0.009	0.082	0.009	0.086	0.009	0.088	0.009
3	0.033	0.006	0.050	0.007	0.074	0.009	0.091	0.009	0.063	0.008	0.073	0.008
4	0.011	0.003	0.044	0.007	0.061	0.008	0.057	0.007	0.054	0.007	0.053	0.006
5	0.000	0.000	0.034	0.005	0.049	0.007	0.050	0.007	0.052	0.006	0.039	0.005
6	0.000	0.000	0.017	0.004	0.036	0.005	0.029	0.005	0.028	0.004	0.040	0.005
7	0.000	0.000	0.015	0.003	0.033	0.005	0.026	0.004	0.034	0.005	0.027	0.004
8	0.000	0.000	0.010	0.002	0.027	0.004	0.027	0.004	0.030	0.005	0.028	0.004
9	0.000	0.000	0.003	0.001	0.021	0.004	0.019	0.004	0.019	0.004	0.020	0.004
≥ 10	0.000	0.000	0.002	0.001	0.036	0.004	0.044	0.005	0.054	0.006	0.050	0.005
total	0.325	0.019	0.429	0.020	0.581	0.022	0.607	0.022	0.597	0.021	0.627	0.022
$v = 1$												
0	0.221	0.017	0.121	0.012	0.109	0.011	0.119	0.012	0.128	0.012	0.134	0.012
1	0.229	0.017	0.105	0.011	0.117	0.012	0.139	0.012	0.123	0.011	0.130	0.012
2	0.126	0.012	0.086	0.010	0.128	0.012	0.128	0.012	0.107	0.010	0.110	0.010
3	0.075	0.009	0.078	0.009	0.115	0.011	0.086	0.009	0.074	0.008	0.101	0.009
4	0.060	0.008	0.068	0.009	0.081	0.009	0.073	0.008	0.066	0.007	0.057	0.007
5	0.032	0.005	0.061	0.008	0.060	0.007	0.063	0.007	0.064	0.007	0.051	0.006
6	0.013	0.003	0.040	0.006	0.053	0.007	0.063	0.007	0.046	0.006	0.042	0.006
7	0.008	0.002	0.037	0.005	0.038	0.006	0.037	0.005	0.035	0.005	0.033	0.005
8	0.001	0.001	0.020	0.004	0.030	0.005	0.030	0.005	0.029	0.005	0.023	0.004
9	0.000	0.000	0.030	0.005	0.030	0.005	0.020	0.003	0.023	0.004	0.026	0.004
≥ 10	0.000	0.000	0.036	0.005	0.063	0.007	0.052	0.006	0.058	0.006	0.062	0.007
total	0.766	0.029	0.683	0.025	0.823	0.027	0.811	0.026	0.753	0.025	0.769	0.024
$v = 2$												
0	0.423	0.028	0.359	0.025	0.350	0.026	0.296	0.023	0.215	0.019	0.157	0.015
1	0.462	0.030	0.435	0.030	0.318	0.025	0.207	0.018	0.220	0.018	0.192	0.016
2	0.193	0.017	0.197	0.018	0.150	0.014	0.175	0.015	0.181	0.016	0.217	0.019
3	0.103	0.012	0.110	0.012	0.122	0.012	0.123	0.012	0.131	0.012	0.145	0.014
4	0.087	0.010	0.105	0.011	0.093	0.010	0.087	0.009	0.084	0.008	0.100	0.010
5	0.080	0.010	0.092	0.010	0.059	0.008	0.086	0.009	0.064	0.007	0.070	0.007
6	0.050	0.008	0.067	0.008	0.067	0.008	0.049	0.006	0.043	0.005	0.061	0.007
7	0.015	0.003	0.043	0.006	0.051	0.007	0.044	0.006	0.047	0.006	0.041	0.006
8	0.012	0.003	0.043	0.006	0.044	0.006	0.029	0.004	0.032	0.005	0.023	0.004
9	0.013	0.003	0.031	0.005	0.043	0.007	0.018	0.004	0.030	0.005	0.027	0.004
≥ 10	0.006	0.002	0.056	0.006	0.080	0.008	0.076	0.007	0.064	0.007	0.072	0.007
total	1.445	0.048	1.537	0.047	1.377	0.043	1.191	0.038	1.111	0.036	1.104	0.035

Table 6-2. Cross section ($\sigma, \Delta\sigma$ in 10^{-16}cm^2) for the reaction $D^+ + H_2(v, j = 1) \rightarrow D + H_2^+(v')$

See Text of Appendix for Explanation of Tables

E_{cm} (eV)	3.0		4.0		5.0		6.0		7.0		8.0	
v'	σ	$\Delta\sigma$	σ	$\Delta\sigma$	σ	$\Delta\sigma$	σ	$\Delta\sigma$	σ	$\Delta\sigma$	σ	$\Delta\sigma$
$v = 3$												
0	0.618	0.035	0.556	0.034	0.526	0.034	0.459	0.031	0.359	0.027	0.254	0.022
1	1.006	0.049	1.198	0.052	0.864	0.042	0.461	0.029	0.422	0.028	0.442	0.029
2	0.746	0.040	0.798	0.041	0.478	0.030	0.457	0.030	0.454	0.029	0.574	0.034
3	0.526	0.034	0.389	0.027	0.316	0.024	0.317	0.024	0.395	0.028	0.517	0.032
4	0.321	0.025	0.241	0.021	0.169	0.016	0.274	0.023	0.343	0.026	0.403	0.028
5	0.189	0.018	0.118	0.013	0.106	0.011	0.130	0.013	0.219	0.020	0.235	0.021
6	0.127	0.014	0.073	0.008	0.081	0.009	0.064	0.008	0.072	0.009	0.111	0.013
7	0.076	0.010	0.077	0.008	0.070	0.008	0.060	0.007	0.056	0.007	0.052	0.006
8	0.072	0.010	0.045	0.006	0.050	0.007	0.033	0.005	0.041	0.007	0.041	0.006
9	0.036	0.006	0.038	0.006	0.033	0.005	0.031	0.005	0.037	0.006	0.027	0.004
≥ 10	0.054	0.006	0.107	0.010	0.092	0.009	0.102	0.009	0.077	0.008	0.087	0.008
total	3.770	0.082	3.642	0.079	2.787	0.067	2.388	0.062	2.476	0.064	2.742	0.068
$v = 4$												
0	20.477	0.270	17.872	0.258	14.664	0.240	13.943	0.231	14.497	0.230	13.888	0.225
1	4.953	0.124	4.395	0.113	3.011	0.091	2.121	0.078	2.334	0.087	3.595	0.112
2	1.628	0.061	1.322	0.054	0.995	0.046	1.004	0.046	1.196	0.052	1.718	0.065
3	1.049	0.048	0.910	0.045	0.783	0.040	0.751	0.040	0.977	0.047	1.130	0.050
4	0.686	0.039	0.681	0.038	0.534	0.034	0.685	0.038	0.798	0.042	0.784	0.041
5	0.420	0.030	0.409	0.028	0.415	0.029	0.541	0.034	0.536	0.034	0.613	0.037
6	0.242	0.021	0.181	0.017	0.254	0.022	0.281	0.024	0.339	0.026	0.340	0.027
7	0.198	0.019	0.105	0.011	0.135	0.014	0.114	0.014	0.166	0.018	0.200	0.020
8	0.120	0.015	0.079	0.009	0.057	0.008	0.107	0.014	0.120	0.014	0.117	0.014
9	0.064	0.009	0.060	0.008	0.064	0.008	0.065	0.009	0.063	0.010	0.058	0.009
≥ 10	0.143	0.014	0.167	0.013	0.161	0.012	0.133	0.011	0.128	0.011	0.140	0.012
total	29.981	0.298	26.180	0.285	21.074	0.263	19.744	0.253	21.154	0.258	22.582	0.263
$v = 5$												
0	0.893	0.038	0.818	0.037	0.691	0.038	0.768	0.043	1.001	0.050	0.798	0.045
1	5.128	0.119	5.880	0.128	8.391	0.143	9.132	0.145	8.113	0.138	6.784	0.127
2	22.581	0.245	22.385	0.245	20.369	0.237	17.945	0.227	16.253	0.218	15.407	0.213
3	3.745	0.105	4.585	0.114	4.403	0.112	4.655	0.118	4.626	0.120	4.946	0.125
4	1.074	0.049	1.342	0.053	1.379	0.057	1.348	0.061	1.558	0.069	2.084	0.080
5	0.630	0.036	0.623	0.035	0.552	0.034	0.603	0.038	0.760	0.045	1.003	0.052
6	0.389	0.029	0.319	0.025	0.305	0.026	0.364	0.028	0.458	0.032	0.495	0.034
7	0.247	0.022	0.189	0.020	0.221	0.021	0.231	0.022	0.337	0.028	0.330	0.027
8	0.192	0.019	0.151	0.017	0.133	0.017	0.163	0.019	0.170	0.019	0.237	0.023
9	0.110	0.014	0.134	0.016	0.072	0.012	0.101	0.014	0.112	0.016	0.115	0.016
≥ 10	0.228	0.020	0.177	0.018	0.153	0.016	0.160	0.017	0.155	0.018	0.221	0.022
total	35.216	0.255	36.603	0.251	36.669	0.249	35.472	0.251	33.544	0.250	32.421	0.248

Table 6-3. Cross section ($\sigma, \Delta\sigma$ in 10^{-16}cm^2) for the reaction $D^+ + H_2(v, j = 1) \rightarrow D + H_2^+(v')$

See Text of Appendix for Explanation of Tables

E_{cm} (eV)	3.0		4.0		5.0		6.0		7.0		8.0	
v'	σ	$\Delta\sigma$	σ	$\Delta\sigma$	σ	$\Delta\sigma$	σ	$\Delta\sigma$	σ	$\Delta\sigma$	σ	$\Delta\sigma$
	$v = 6$											
0	0.556	0.034	0.578	0.034	0.479	0.032	0.327	0.025	0.355	0.026	0.303	0.024
1	1.232	0.052	1.263	0.055	1.176	0.052	1.039	0.048	1.120	0.050	1.129	0.048
2	2.264	0.078	2.365	0.079	2.947	0.085	3.834	0.094	3.902	0.094	3.462	0.089
3	10.043	0.173	11.889	0.180	10.903	0.170	8.359	0.156	6.035	0.138	4.881	0.129
4	15.638	0.220	14.784	0.216	13.478	0.206	12.726	0.200	12.806	0.201	12.452	0.199
5	3.193	0.095	3.288	0.098	3.188	0.099	3.484	0.106	4.033	0.114	4.213	0.116
6	1.092	0.052	1.174	0.056	1.302	0.064	1.625	0.072	1.991	0.080	2.348	0.085
7	0.530	0.035	0.510	0.036	0.613	0.042	0.752	0.047	0.783	0.047	1.010	0.054
8	0.325	0.027	0.300	0.028	0.265	0.026	0.383	0.033	0.425	0.034	0.548	0.039
9	0.184	0.020	0.130	0.017	0.183	0.022	0.175	0.021	0.292	0.027	0.325	0.029
≥ 10	0.313	0.026	0.238	0.023	0.238	0.023	0.239	0.024	0.426	0.033	0.530	0.037
total	35.370	0.242	36.519	0.242	34.773	0.239	32.944	0.238	32.168	0.238	31.202	0.234

Table 7-1. Cross section ($\sigma, \Delta\sigma$ in 10^{-16}cm^2) for the reaction $D^+ + H_2(v, j = 1) \rightarrow H + HD^+(v')$

See Text of Appendix for Explanation of Tables

E_{cm} (eV)	3.0		4.0		5.0		6.0		7.0		8.0	
v'	σ	$\Delta\sigma$	σ	$\Delta\sigma$	σ	$\Delta\sigma$	σ	$\Delta\sigma$	σ	$\Delta\sigma$	σ	$\Delta\sigma$
$v = 0$												
0	0.095	0.009	0.071	0.008	0.077	0.008	0.069	0.007	0.062	0.007	0.047	0.006
1	0.092	0.009	0.090	0.009	0.084	0.008	0.067	0.007	0.054	0.006	0.034	0.005
2	0.071	0.008	0.079	0.008	0.088	0.008	0.066	0.007	0.051	0.006	0.032	0.005
3	0.058	0.007	0.071	0.007	0.072	0.007	0.062	0.007	0.039	0.005	0.034	0.005
4	0.029	0.004	0.065	0.007	0.075	0.007	0.052	0.006	0.042	0.006	0.036	0.005
5	0.013	0.002	0.049	0.006	0.065	0.007	0.064	0.007	0.038	0.005	0.025	0.004
6	0.002	0.001	0.047	0.006	0.061	0.006	0.041	0.005	0.031	0.004	0.021	0.003
7	0.000	0.000	0.027	0.004	0.049	0.006	0.026	0.004	0.027	0.004	0.026	0.004
8	0.000	0.000	0.018	0.003	0.040	0.006	0.035	0.005	0.027	0.004	0.011	0.002
9	0.000	0.000	0.023	0.004	0.037	0.005	0.025	0.004	0.026	0.004	0.019	0.003
≥ 10	0.000	0.000	0.030	0.004	0.126	0.009	0.096	0.007	0.082	0.007	0.055	0.005
total	0.360	0.017	0.571	0.019	0.774	0.022	0.603	0.019	0.478	0.017	0.339	0.014
$v = 1$												
0	0.120	0.011	0.099	0.010	0.081	0.009	0.080	0.008	0.064	0.007	0.045	0.006
1	0.090	0.009	0.121	0.010	0.096	0.009	0.057	0.007	0.046	0.006	0.029	0.005
2	0.091	0.009	0.098	0.009	0.086	0.008	0.065	0.007	0.049	0.006	0.032	0.005
3	0.088	0.009	0.086	0.008	0.080	0.008	0.068	0.007	0.046	0.006	0.026	0.005
4	0.051	0.007	0.095	0.009	0.072	0.007	0.049	0.006	0.036	0.005	0.018	0.003
5	0.050	0.007	0.074	0.008	0.064	0.007	0.034	0.005	0.024	0.004	0.020	0.004
6	0.045	0.006	0.069	0.008	0.044	0.006	0.043	0.006	0.026	0.004	0.021	0.004
7	0.023	0.003	0.036	0.005	0.042	0.005	0.039	0.005	0.025	0.004	0.013	0.003
8	0.013	0.002	0.039	0.006	0.034	0.005	0.032	0.005	0.026	0.004	0.013	0.003
9	0.001	0.000	0.034	0.005	0.048	0.006	0.024	0.004	0.018	0.003	0.017	0.003
≥ 10	0.000	0.000	0.099	0.008	0.119	0.009	0.085	0.007	0.057	0.005	0.054	0.006
total	0.572	0.022	0.852	0.024	0.766	0.022	0.577	0.019	0.417	0.016	0.290	0.014
$v = 2$												
0	0.109	0.011	0.133	0.012	0.068	0.008	0.077	0.009	0.058	0.007	0.049	0.007
1	0.115	0.011	0.107	0.010	0.071	0.008	0.060	0.007	0.038	0.005	0.039	0.006
2	0.108	0.010	0.109	0.010	0.082	0.008	0.036	0.005	0.044	0.006	0.016	0.003
3	0.099	0.009	0.082	0.008	0.060	0.007	0.045	0.006	0.033	0.005	0.023	0.004
4	0.081	0.009	0.087	0.009	0.073	0.008	0.041	0.005	0.026	0.004	0.022	0.004
5	0.076	0.008	0.066	0.007	0.052	0.006	0.041	0.006	0.025	0.004	0.018	0.004
6	0.063	0.007	0.054	0.007	0.040	0.005	0.042	0.006	0.032	0.005	0.010	0.002
7	0.047	0.007	0.057	0.007	0.038	0.006	0.026	0.004	0.019	0.003	0.015	0.003
8	0.035	0.006	0.040	0.006	0.029	0.005	0.022	0.004	0.016	0.003	0.015	0.003
9	0.029	0.005	0.041	0.006	0.028	0.005	0.022	0.004	0.015	0.003	0.008	0.002
≥ 10	0.047	0.005	0.164	0.011	0.112	0.009	0.072	0.007	0.048	0.005	0.039	0.005
total	0.808	0.026	0.939	0.026	0.655	0.022	0.483	0.018	0.355	0.016	0.254	0.013

Table 7-2. Cross section ($\sigma, \Delta\sigma$ in 10^{-16}cm^2) for the reaction $D^+ + H_2(v, j = 1) \rightarrow H + HD^+(v')$

See Text of Appendix for Explanation of Tables

E_{cm} (eV)	3.0		4.0		5.0		6.0		7.0		8.0	
v'	σ	$\Delta\sigma$	σ	$\Delta\sigma$	σ	$\Delta\sigma$	σ	$\Delta\sigma$	σ	$\Delta\sigma$	σ	$\Delta\sigma$
$v = 3$												
0	0.151	0.013	0.107	0.010	0.095	0.010	0.062	0.008	0.039	0.006	0.028	0.005
1	0.161	0.013	0.111	0.010	0.080	0.008	0.051	0.007	0.033	0.005	0.034	0.005
2	0.139	0.013	0.101	0.010	0.068	0.008	0.052	0.007	0.037	0.006	0.025	0.005
3	0.128	0.012	0.077	0.008	0.076	0.008	0.055	0.007	0.033	0.005	0.021	0.004
4	0.110	0.011	0.076	0.008	0.063	0.007	0.044	0.006	0.018	0.003	0.019	0.004
5	0.085	0.009	0.074	0.008	0.041	0.006	0.036	0.005	0.024	0.004	0.019	0.004
6	0.096	0.010	0.057	0.008	0.045	0.006	0.038	0.006	0.020	0.004	0.019	0.004
7	0.060	0.009	0.057	0.007	0.028	0.005	0.022	0.004	0.018	0.004	0.011	0.003
8	0.046	0.007	0.044	0.006	0.032	0.005	0.022	0.004	0.017	0.004	0.013	0.003
9	0.063	0.008	0.032	0.005	0.028	0.005	0.017	0.004	0.018	0.004	0.010	0.002
≥ 10	0.201	0.014	0.136	0.011	0.095	0.008	0.078	0.008	0.061	0.006	0.032	0.004
total	1.241	0.034	0.871	0.026	0.652	0.022	0.475	0.019	0.321	0.015	0.232	0.013
$v = 4$												
0	0.164	0.013	0.089	0.010	0.060	0.008	0.047	0.007	0.039	0.006	0.024	0.005
1	0.124	0.012	0.094	0.009	0.057	0.007	0.042	0.006	0.030	0.005	0.021	0.004
2	0.128	0.013	0.083	0.009	0.069	0.008	0.045	0.006	0.028	0.005	0.022	0.004
3	0.142	0.015	0.079	0.009	0.063	0.008	0.038	0.006	0.031	0.005	0.023	0.004
4	0.136	0.014	0.078	0.009	0.062	0.008	0.025	0.004	0.026	0.004	0.011	0.003
5	0.077	0.010	0.064	0.008	0.041	0.006	0.029	0.005	0.023	0.004	0.014	0.003
6	0.094	0.011	0.065	0.008	0.039	0.006	0.022	0.004	0.020	0.004	0.013	0.003
7	0.073	0.010	0.058	0.007	0.030	0.005	0.026	0.004	0.017	0.003	0.019	0.004
8	0.083	0.012	0.051	0.007	0.034	0.005	0.018	0.003	0.017	0.003	0.012	0.003
9	0.077	0.011	0.030	0.005	0.023	0.005	0.019	0.004	0.015	0.003	0.010	0.002
≥ 10	0.338	0.020	0.124	0.010	0.083	0.008	0.059	0.006	0.050	0.005	0.037	0.004
total	1.436	0.041	0.815	0.026	0.561	0.021	0.371	0.016	0.296	0.014	0.207	0.012
$v = 5$												
0	0.151	0.015	0.085	0.010	0.073	0.009	0.053	0.007	0.043	0.006	0.044	0.006
1	0.141	0.015	0.052	0.007	0.050	0.007	0.040	0.006	0.064	0.007	0.107	0.009
2	0.170	0.016	0.063	0.008	0.043	0.006	0.089	0.008	0.114	0.009	0.095	0.009
3	0.140	0.016	0.051	0.007	0.056	0.007	0.120	0.010	0.091	0.009	0.063	0.007
4	0.096	0.012	0.061	0.008	0.059	0.007	0.079	0.008	0.048	0.006	0.037	0.006
5	0.117	0.015	0.053	0.008	0.037	0.006	0.025	0.005	0.019	0.004	0.018	0.004
6	0.102	0.013	0.030	0.006	0.031	0.006	0.020	0.005	0.016	0.004	0.011	0.003
7	0.076	0.012	0.039	0.007	0.020	0.004	0.018	0.004	0.012	0.003	0.007	0.002
8	0.088	0.014	0.031	0.006	0.020	0.004	0.009	0.002	0.011	0.004	0.008	0.003
9	0.090	0.013	0.026	0.006	0.011	0.003	0.013	0.004	0.008	0.003	0.006	0.002
≥ 10	0.305	0.022	0.114	0.011	0.068	0.008	0.043	0.006	0.017	0.004	0.016	0.004
total	1.475	0.048	0.604	0.025	0.468	0.021	0.507	0.020	0.441	0.018	0.414	0.017

Table 7-3. Cross section ($\sigma, \Delta\sigma$ in 10^{-16}cm^2) for the reaction $D^+ + H_2(v, j = 1) \rightarrow H + HD^+(v')$

See Text of Appendix for Explanation of Tables

E_{cm} (eV)	3.0		4.0		5.0		6.0		7.0		8.0	
v'	σ	$\Delta\sigma$	σ	$\Delta\sigma$	σ	$\Delta\sigma$	σ	$\Delta\sigma$	σ	$\Delta\sigma$	σ	$\Delta\sigma$
	$v = 6$											
0	0.195	0.021	0.066	0.009	0.035	0.007	0.045	0.007	0.038	0.006	0.049	0.006
1	0.166	0.019	0.048	0.008	0.045	0.007	0.055	0.007	0.079	0.008	0.105	0.009
2	0.179	0.020	0.046	0.007	0.051	0.006	0.105	0.009	0.131	0.011	0.115	0.010
3	0.170	0.019	0.057	0.008	0.086	0.009	0.163	0.012	0.130	0.011	0.071	0.008
4	0.145	0.018	0.060	0.009	0.118	0.010	0.110	0.010	0.068	0.008	0.057	0.008
5	0.122	0.016	0.084	0.010	0.101	0.010	0.090	0.009	0.038	0.006	0.025	0.005
6	0.086	0.014	0.046	0.008	0.040	0.007	0.046	0.007	0.030	0.006	0.021	0.004
7	0.117	0.017	0.041	0.008	0.026	0.005	0.023	0.005	0.013	0.004	0.024	0.005
8	0.078	0.013	0.033	0.007	0.016	0.005	0.017	0.004	0.012	0.004	0.009	0.003
9	0.100	0.015	0.024	0.007	0.010	0.003	0.005	0.002	0.009	0.003	0.006	0.002
≥ 10	0.353	0.027	0.070	0.010	0.046	0.007	0.023	0.005	0.020	0.004	0.022	0.005
total	1.711	0.059	0.577	0.027	0.573	0.023	0.683	0.024	0.569	0.022	0.504	0.021

Table 8-1. Cross section ($\sigma, \Delta\sigma$ in 10^{-16}cm^2) for the reaction $D^+ + H_2(v, j = 1) \rightarrow H^+ + HD(v')$

See Text of Appendix for Explanation of Tables

E_{cm} (eV)	3.0		4.0		5.0		6.0		7.0		8.0	
v'	σ	$\Delta\sigma$	σ	$\Delta\sigma$	σ	$\Delta\sigma$	σ	$\Delta\sigma$	σ	$\Delta\sigma$	σ	$\Delta\sigma$
$v = 0$												
0	0.395	0.019	0.169	0.012	0.099	0.009	0.078	0.008	0.047	0.006	0.024	0.004
1	0.302	0.016	0.204	0.013	0.085	0.008	0.063	0.007	0.046	0.006	0.032	0.005
2	0.259	0.015	0.141	0.011	0.056	0.007	0.052	0.006	0.029	0.004	0.023	0.004
3	0.203	0.014	0.122	0.010	0.044	0.005	0.025	0.004	0.014	0.003	0.012	0.003
4	0.147	0.011	0.087	0.009	0.031	0.005	0.017	0.003	0.006	0.002	0.006	0.002
5	0.105	0.010	0.046	0.006	0.014	0.003	0.003	0.001	0.003	0.001	0.001	0.001
6	0.057	0.006	0.032	0.005	0.006	0.002	0.002	0.001	0.000	0.000	0.000	0.000
7	0.023	0.004	0.013	0.003	0.003	0.001	0.001	0.001	0.000	0.000	0.000	0.000
8	0.001	0.001	0.008	0.002	0.000	0.000	0.000	0.000	0.000	0.000	0.000	0.000
9	0.000	0.000	0.009	0.003	0.000	0.000	0.000	0.000	0.000	0.000	0.000	0.000
≥ 10	0.000	0.000	0.003	0.001	0.000	0.000	0.000	0.000	0.000	0.000	0.000	0.000
total	1.492	0.031	0.835	0.024	0.338	0.015	0.240	0.013	0.144	0.010	0.097	0.008
$v = 1$												
0	0.240	0.015	0.149	0.012	0.081	0.008	0.059	0.007	0.043	0.006	0.034	0.005
1	0.243	0.015	0.132	0.011	0.074	0.008	0.048	0.006	0.039	0.005	0.031	0.005
2	0.216	0.014	0.105	0.009	0.051	0.006	0.038	0.005	0.027	0.004	0.012	0.003
3	0.169	0.012	0.080	0.008	0.030	0.005	0.019	0.003	0.012	0.003	0.007	0.002
4	0.140	0.011	0.046	0.006	0.018	0.004	0.010	0.003	0.005	0.002	0.005	0.002
5	0.090	0.009	0.021	0.005	0.010	0.002	0.003	0.001	0.002	0.001	0.001	0.001
6	0.041	0.006	0.016	0.004	0.001	0.001	0.001	0.001	0.001	0.001	0.001	0.001
7	0.027	0.004	0.006	0.002	0.001	0.001	0.000	0.000	0.000	0.000	0.000	0.000
8	0.023	0.004	0.003	0.002	0.000	0.000	0.000	0.000	0.000	0.000	0.000	0.000
9	0.008	0.002	0.001	0.001	0.000	0.000	0.000	0.000	0.000	0.000	0.000	0.000
≥ 10	0.001	0.000	0.002	0.001	0.000	0.000	0.000	0.000	0.000	0.000	0.000	0.000
total	1.198	0.030	0.562	0.021	0.266	0.014	0.178	0.011	0.128	0.009	0.091	0.008
$v = 2$												
0	0.213	0.016	0.125	0.011	0.074	0.008	0.056	0.007	0.043	0.006	0.033	0.005
1	0.237	0.016	0.081	0.009	0.054	0.007	0.042	0.006	0.034	0.005	0.017	0.003
2	0.164	0.013	0.089	0.009	0.053	0.007	0.025	0.004	0.030	0.005	0.017	0.003
3	0.131	0.011	0.063	0.008	0.035	0.005	0.023	0.004	0.012	0.003	0.010	0.003
4	0.095	0.010	0.030	0.005	0.014	0.003	0.009	0.003	0.005	0.002	0.004	0.001
5	0.062	0.008	0.016	0.004	0.007	0.003	0.004	0.002	0.002	0.001	0.004	0.001
6	0.031	0.006	0.004	0.002	0.003	0.002	0.000	0.000	0.000	0.000	0.001	0.001
7	0.024	0.005	0.003	0.002	0.001	0.001	0.000	0.000	0.001	0.001	0.001	0.001
8	0.016	0.004	0.000	0.000	0.000	0.000	0.000	0.000	0.000	0.000	0.001	0.001
9	0.006	0.002	0.000	0.000	0.000	0.000	0.000	0.000	0.000	0.000	0.000	0.000
≥ 10	0.007	0.002	0.000	0.000	0.000	0.000	0.000	0.000	0.000	0.000	0.000	0.000
total	0.987	0.030	0.410	0.019	0.242	0.014	0.160	0.011	0.127	0.010	0.087	0.008

Table 8-2. Cross section ($\sigma, \Delta\sigma$ in 10^{-16}cm^2) for the reaction $D^+ + H_2(v, j = 1) \rightarrow H^+ + HD(v')$

See Text of Appendix for Explanation of Tables

E_{cm} (eV)	3.0		4.0		5.0		6.0		7.0		8.0	
v'	σ	$\Delta\sigma$	σ	$\Delta\sigma$	σ	$\Delta\sigma$	σ	$\Delta\sigma$	σ	$\Delta\sigma$	σ	$\Delta\sigma$
$v = 3$												
0	0.170	0.014	0.100	0.010	0.054	0.007	0.039	0.006	0.032	0.005	0.023	0.004
1	0.151	0.013	0.084	0.009	0.056	0.007	0.036	0.005	0.027	0.005	0.015	0.003
2	0.130	0.012	0.074	0.008	0.041	0.006	0.026	0.004	0.020	0.004	0.010	0.003
3	0.118	0.012	0.041	0.006	0.021	0.004	0.014	0.003	0.013	0.003	0.009	0.002
4	0.068	0.009	0.019	0.004	0.011	0.003	0.010	0.003	0.011	0.003	0.005	0.002
5	0.030	0.006	0.009	0.003	0.008	0.003	0.003	0.001	0.004	0.002	0.002	0.001
6	0.020	0.005	0.004	0.002	0.003	0.002	0.001	0.001	0.001	0.001	0.002	0.001
7	0.008	0.003	0.001	0.001	0.000	0.000	0.001	0.001	0.001	0.001	0.001	0.001
8	0.006	0.003	0.000	0.000	0.000	0.000	0.000	0.000	0.001	0.001	0.000	0.000
9	0.007	0.003	0.000	0.000	0.000	0.000	0.000	0.000	0.000	0.000	0.000	0.000
≥ 10	0.012	0.004	0.000	0.000	0.000	0.000	0.000	0.000	0.000	0.000	0.000	0.000
total	0.720	0.028	0.331	0.017	0.194	0.013	0.129	0.010	0.110	0.009	0.067	0.007
$v = 4$												
0	0.156	0.013	0.066	0.008	0.057	0.007	0.040	0.006	0.043	0.006	0.018	0.004
1	0.126	0.011	0.058	0.007	0.047	0.006	0.033	0.005	0.024	0.004	0.011	0.003
2	0.081	0.009	0.046	0.006	0.030	0.005	0.024	0.004	0.018	0.004	0.018	0.004
3	0.081	0.011	0.039	0.006	0.021	0.004	0.012	0.003	0.010	0.002	0.013	0.003
4	0.050	0.009	0.017	0.004	0.016	0.004	0.012	0.002	0.008	0.002	0.007	0.002
5	0.032	0.007	0.012	0.003	0.007	0.002	0.002	0.001	0.002	0.001	0.002	0.001
6	0.018	0.005	0.008	0.003	0.002	0.002	0.002	0.001	0.001	0.001	0.000	0.000
7	0.011	0.005	0.001	0.001	0.000	0.000	0.002	0.001	0.001	0.000	0.000	0.000
8	0.004	0.003	0.000	0.000	0.000	0.000	0.000	0.000	0.000	0.000	0.000	0.000
9	0.001	0.001	0.000	0.000	0.000	0.000	0.000	0.000	0.000	0.000	0.000	0.000
≥ 10	0.001	0.001	0.000	0.000	0.000	0.000	0.000	0.000	0.000	0.000	0.001	0.001
total	0.562	0.025	0.247	0.015	0.181	0.012	0.127	0.010	0.107	0.009	0.071	0.007
$v = 5$												
0	0.096	0.011	0.056	0.008	0.049	0.007	0.021	0.004	0.028	0.005	0.041	0.006
1	0.094	0.012	0.058	0.008	0.034	0.006	0.020	0.004	0.015	0.004	0.020	0.004
2	0.093	0.013	0.043	0.007	0.025	0.005	0.018	0.004	0.031	0.005	0.028	0.005
3	0.044	0.008	0.028	0.005	0.025	0.005	0.018	0.004	0.018	0.003	0.023	0.004
4	0.055	0.010	0.030	0.006	0.019	0.004	0.017	0.004	0.021	0.004	0.027	0.004
5	0.034	0.008	0.012	0.004	0.010	0.003	0.017	0.004	0.028	0.004	0.016	0.003
6	0.006	0.003	0.013	0.004	0.009	0.002	0.014	0.003	0.025	0.005	0.026	0.005
7	0.005	0.003	0.003	0.002	0.006	0.002	0.031	0.005	0.027	0.005	0.037	0.005
8	0.003	0.002	0.002	0.001	0.008	0.002	0.019	0.003	0.022	0.004	0.023	0.004
9	0.004	0.004	0.000	0.000	0.006	0.002	0.016	0.003	0.009	0.002	0.015	0.003
≥ 10	0.000	0.000	0.000	0.000	0.011	0.002	0.028	0.004	0.027	0.004	0.023	0.004
total	0.434	0.026	0.245	0.016	0.201	0.013	0.219	0.012	0.251	0.013	0.278	0.014

Table 8-3. Cross section ($\sigma, \Delta\sigma$ in 10^{-16}cm^2) for the reaction $D^+ + H_2(v, j = 1) \rightarrow H^+ + HD(v')$

See Text of Appendix for Explanation of Tables

E_{cm} (eV)	3.0		4.0		5.0		6.0		7.0		8.0	
v'	σ	$\Delta\sigma$	σ	$\Delta\sigma$	σ	$\Delta\sigma$	σ	$\Delta\sigma$	σ	$\Delta\sigma$	σ	$\Delta\sigma$
	$v = 6$											
0	0.059	0.009	0.038	0.007	0.039	0.007	0.038	0.006	0.037	0.006	0.057	0.008
1	0.078	0.012	0.028	0.006	0.026	0.005	0.028	0.005	0.025	0.004	0.023	0.004
2	0.080	0.013	0.026	0.006	0.022	0.004	0.019	0.004	0.030	0.005	0.042	0.006
3	0.065	0.011	0.024	0.005	0.025	0.005	0.024	0.004	0.028	0.005	0.029	0.005
4	0.043	0.009	0.018	0.004	0.023	0.004	0.028	0.005	0.025	0.004	0.029	0.005
5	0.034	0.009	0.016	0.004	0.024	0.004	0.031	0.005	0.040	0.006	0.036	0.006
6	0.014	0.005	0.009	0.003	0.023	0.004	0.029	0.005	0.047	0.006	0.031	0.005
7	0.011	0.005	0.012	0.003	0.030	0.005	0.045	0.006	0.045	0.006	0.036	0.005
8	0.002	0.002	0.019	0.004	0.046	0.006	0.041	0.006	0.030	0.005	0.029	0.005
9	0.004	0.002	0.018	0.003	0.044	0.006	0.035	0.005	0.030	0.005	0.025	0.005
≥ 10	0.002	0.001	0.034	0.004	0.065	0.006	0.066	0.007	0.055	0.007	0.037	0.005
total	0.392	0.027	0.243	0.015	0.367	0.017	0.384	0.017	0.391	0.017	0.375	0.017

Isotope effect on dynamics of a collinear He + H₂⁺ collision

Kunizo Onda

Faculty of Industrial Science and Technology,
Science University of Tokyo,
Oshamambe, Japan

Abstract. The accurate time-independent quantum mechanical method is applied to investigate a non-reactive vibrational transition, atom exchange reaction, and dissociation processes in a collinear He + H₂⁺(v_i) collision. We concentrate our consideration on clarifying isotope effect in dynamics of this collision system, in which the hydrogen atom is replaced by deuterium or tritium. We thus report the results of the collinear collisions of He + H₂⁺(v_i), HD⁺(v_i), DH⁺(v_i), HT⁺(v_i), and TH⁺(v_i). We have employed the most reliable interaction potential energy surface analytically fitted by Joseph and Sathyamurthy for this system. The energy dependence of the probabilities of the non-reactive vibrational transition, atom exchange reaction, and dissociation processes is investigated at the total energy from 4 to 10 eV and the dependence of these probabilities on the initial vibrational state of H₂⁺(v_i)($0 \leq v_i \leq 17$), HD⁺(v_i)($0 \leq v_i \leq 20$), or HT⁺(v_i)($0 \leq v_i \leq 21$) ion is also studied to understand isotope effect on this collision dynamics. We have found a remarkable isotope effect on dynamics of this collinear collision system.

1. Introduction

One of unresolved problems in a presently pursued fusion reactor such as the International Thermonuclear Experimental Reactor (ITER) is how we can efficiently exhaust thermal power and the He ash from the reactor region without degradation of the main plasma burning conditions. The enhancement of longitudinal plasma power and particle flows is considered to be a plausible solution of this problem in the reactor chamber periphery located outside the main plasma torus. This intense directional scrape-off plasma flow concentrates large heat and particle loads on the flux intercepting material surfaces in the divertor chamber. Atomic and molecular collision processes play crucial roles in exhausting enormous power flowed from edge or scrape-off layer (SOL) plasmas.

It is estimated [1] that gas temperature is in the range of several eV and number density of particles is in the order of $10^{21} \sim 10^{22} \text{ m}^{-3}$ at the most interesting part in gas divertor plasmas. Main components in the divertor chamber are H₂, H, He, their isotopic variations, their ions, and electrons. Hydrogen atoms in these relatively high density regions are easily recombined into molecular form on divertor plates. It is expected that newly formed hydrogen molecules can be in rotationally and vibrationally excited states, and are predominantly abundant in number density over any other molecules. Since hydrogen molecules and its molecular ions have no permanent electric dipole moment, radiative lifetime of rotationally and vibrationally excited states is known to be $10^5 \sim 10^6$ s. Hydrogen molecules with different mass combinations are considered to be a heteronuclear molecule. It is experimentally confirmed that they have very small permanent electric dipole moment in the order of $10^{-(4\sim 5)} \text{ D}$ (1 debye(D) = 10^{-18} e.s.u.). Therefore, radiative lifetime of them

becomes shorter. Even if these mass combinations are occurred as a matter of fact, it is highly probable that H_2 molecules and its molecular ions in vibrationally excited states collide with other atoms, molecules, or their ions in the divertor chamber.

As a molecule is rotationally and/or vibrationally excited higher, a size of the molecule becomes larger. It is expected that any cross section can be large for collision of molecules or their ions in rotationally and/or vibrationally excited states with any kind of particles. Therefore, it is highly desirable to investigate collision processes related to hydrogen molecules or its molecular ions in rotationally and/or vibrationally excited states. The energy range interested in gas divertor plasmas is specifically below about 10 eV for these collision processes. If the total energy is above the dissociation energy of molecules or molecular ions, collision induced dissociation processes must be properly taken into account in collision dynamics. This is still a challenging problem in a theoretical point of view.

The numerical method (referred to as paper I [2]) has been developed to investigate the atom-diatomic molecule collision dynamics, in which the non-reactive vibrational transition, atom exchange reaction, and dissociation processes actively compete with each other on the lowest electronic potential energy surface. This method has been numerically tested by applying to a collinear $\text{He} + \text{H}_2^+(v_i)$ rearrangement collisions (referred to as paper II [3]) at the total energy below the dissociation threshold of the H_2^+ ions. Our numerical results have nicely reproduced a fine structure obtained by Kouri and Baer [4] and Adams [5] using the semi-empirical diatomics-in-molecules (DIM) potential energy surface of Kuntz [6].

We have further studied this collision system by using the reliable potential energy surface (referred to the MTJS) provided by Joseph and Sathyamurthy [7], who have analytically fitted the *ab initio* potential energies calculated by McLaughlin and Thompson [8]. Sakimoto examined the isotope effect of this collision system at the total energy below and above the dissociation threshold [referred to as paper III [9] and IV [10], but the initial vibrational state investigated was limited to below $v_i = 6$ and the total energy surveyed was below 7 eV.

Onda and Sakimoto (referred to as paper V [11]) improved in efficiency of numerical calculations, and investigated the total energy and initial vibrational state dependence of the probabilities for the non-reactive vibrational transition, atom exchange reaction, and dissociation processes in a collinear $\text{He} + \text{H}_2^+(v_i)$ ($0 \leq v_i \leq 17$) collision. In Section 2, we very briefly describe our method, and selective results of the collinear $\text{He} + \text{H}_2^+(v_i)$ collision are presented and remarkable findings are pointed out in Section 3. In order to investigate isotope effect on dynamics of this collinear $\text{He} + \text{H}_2^+$ collision by extending the range of the total energy and by including the whole vibrational states as the initial vibrational states, we have studied $\text{He} + \text{HD}^+(v_i)$ ($0 \leq v_i \leq 20$), $\text{HT}^+(v_i)$ ($0 \leq v_i \leq 21$), $\text{DH}^+(v_i)$ ($0 \leq v_i \leq 20$), and $\text{TH}^+(v_i)$ ($0 \leq v_i \leq 21$) collisions at the total energy from 4 to 10 eV by considering all of the vibrational bound states. Representative results for these collision systems are presented and discussed in Section 4. Concluding remarks are mentioned in Section 5.

2. Theory

Since our numerical method is fully described in paper I [2] and V [11], we very briefly represent our method in this section. A collision system is composed of three atoms being a collinear configuration in the order of A-B-C having their masses of m_A , m_B , and m_C , respectively. Let r_{BC} (the BC internuclear distance) and $R_{A,BC}$ (the distance of A to the center of mass of BC) be the Jacobi coordinates corresponding to the A + BC arrangement; and let r_{AB} and $R_{C,AB}$ be the Jacobi coordinates to the AB + C arrangement. The mass-scaled coordinates are defined by using the Jacobi coordinates as follows: $R_\lambda = a_\lambda R_{A,BC}$, $r_\lambda = a_\lambda^{-1} r_{BC}$, $a_\lambda = (\mu_{A,BC}/\mu_{BC})^{1/4}$, $R_\nu = a_\nu R_{C,AB}$, $r_\nu = a_\nu^{-1} r_{AB}$, $a_\nu = (\mu_{C,AB}/\mu_{AB})^{1/4}$. Here μ_{BC} and μ_{AB} are the reduced masses of the molecule BC and AB, respectively, and $\mu_{A,BC}$ and $\mu_{C,AB}$ are those between the atom A and molecule BC and between the atom C and molecule AB, respectively. The Schrödinger equation in these mass-scaled Jacobi coordinates is written as

$$\left\{ -\frac{\hbar^2}{2\mu} \left(\frac{\partial^2}{\partial R^2} + \frac{\partial^2}{\partial r^2} \right) + V(R, r) - E_{tot} \right\} \Psi = 0. \quad (1)$$

Here the characteristic mass of the whole system is defined by $\mu = \{m_A m_B m_C / (m_A + m_B + m_C)\}^{1/2}$, and the coordinates (R, r) are either of (R_λ, r_λ) or (R_ν, r_ν) . The lowest electronically adiabatic potential energy surface is represented by $V(R, r)$, and the total energy E_{tot} is measured from the lowest bottom of the diatomic well.

The hyperspherical coordinates (ρ, ω) are defined by $\rho = (R^2 + r^2)^{1/2}$ and $\omega = \tan^{-1}(r_\kappa/R_\kappa)$ for $\kappa = \lambda$ or ν . Although ρ is independent of the arrangement, ω depends on the arrangement $\kappa = \lambda$ or ν . The range of ω is restricted from 0 to $\omega_{max} = \tan^{-1}(m_C/\mu)$. Equation (1) is to be solved in the two dimensional space within the range of $0 \leq \rho \leq \rho_{max}$ and $0 \leq \omega \leq \omega_{max}$, where ρ_{max} is the maximum values of ρ coordinate.

Substituting the total wave function in the following form into Eq. (1)

$$\Psi(\rho, \omega) = \rho^{-1/2} \psi(\rho, \omega), \quad (2)$$

we obtain two dimensional partial differential equation

$$\frac{\partial^2 \psi}{\partial \rho^2} + \frac{1}{\rho^2} \frac{\partial^2 \psi}{\partial \omega^2} + \frac{1}{\rho^2} W(\rho, \omega) \psi = 0, \quad (3)$$

where

$$W(\rho, \omega) = \frac{2\mu\rho^2}{\hbar^2} [E_{tot} - V(\rho, \omega)] + \frac{1}{4}. \quad (4)$$

We have defined a two dimensional grid with equally spaced points associated with the hyperspherical coordinates as described in paper I and V. Chebyshev polynomials of the second kind as pointed out by Muckerman [12] are chosen as the DVR basis function

$v_j(\omega)$, which satisfies the Kronecker delta property $v_j(\omega_i) = \delta_{j,i}$, at the grid points in the ω direction. The wave function is expanded in terms of these basis functions as follows:

$$\psi(\rho, \omega) = \sum_{j=1}^M \varphi(\rho, \omega_j) v_j(\omega). \quad (5)$$

Inserting this wave function into the wave equation (3) and making use of the Kronecker delta property of the DVR basis function, a set of coupled linear equations with respect to $\varphi(\rho, \omega_i)$ is derived as follows:

$$\left[\frac{d^2}{d\rho^2} + Q(\rho, \omega_i) \right] \varphi(\rho, \omega_i) = 0, \quad (6)$$

where

$$Q(\rho, \omega_i) = \frac{1}{\rho^2} \sum_{j=1}^M \{v_j''(\omega_i) + \delta_{j,i} W(\rho, \omega_i)\}, \quad \text{for } i = 1, 2, \dots, M. \quad (7)$$

Here $v_j''(\omega_i)$ are the values of the second derivative of the DVR basis function $v_j(\omega)$ with respect to ω at the i -th grid point.

Equation (6) reduces in the Numerov algorithm to the following three terms recurrence form in the matrix representation

$$[\mathbf{1} - \mathbf{T}_{n-1}] \varphi_{n-1} - [2\mathbf{1} + 10\mathbf{T}_n] \varphi_n + [\mathbf{1} - \mathbf{T}_{n+1}] \varphi_{n+1} = 0. \quad (8)$$

Here $\varphi_n = (\phi_1(\rho_n), \phi_2(\rho_n), \dots, \phi_M(\rho_n))^T$, $\mathbf{1}$ is the $M \times M$ unit matrix, and

$$\mathbf{T}_n = -\frac{h_\rho^2}{12} \mathbf{Q}(\rho_n, \omega), \quad (9)$$

is also an $M \times M$ matrix. Equation (8) is directly solved as described in paper V.

Since the mathematical treatment of the scattering wave functions in the asymptotic regions is described fully in paper I and further remarks with respect to the imposition of the boundary conditions on the scattering wave functions are stated in paper IV [10], we do not repeat such mathematical manipulations here. We only mention that the S-matrix and the reactant matrix are defined by the asymptotic analyses and are calculated numerically with sufficient accuracy.

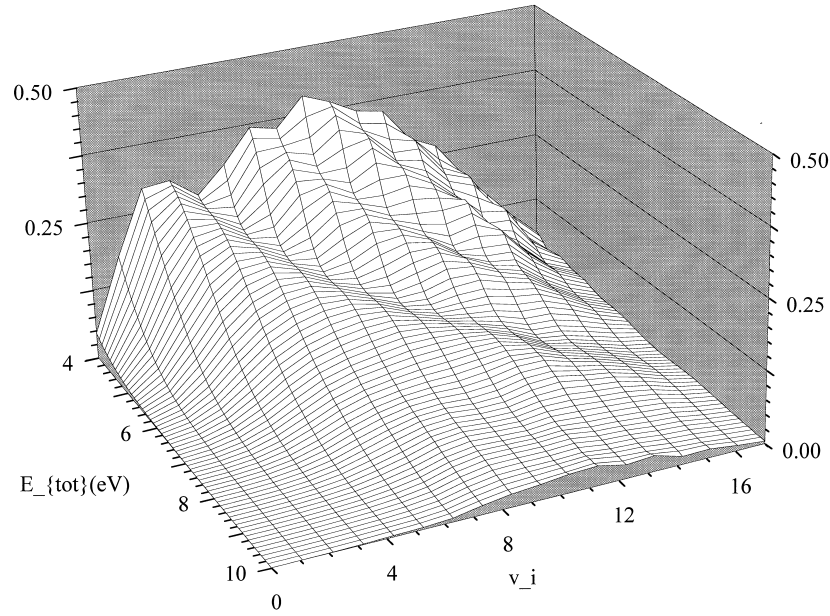


FIG. 1. Three dimensional surface plot of the probability of the total non-reactive vibrational transition summed over the reactant final vibrational states in $\text{He} + \text{H}_2^+(v_i)$ collinear collision as a function of both the initial vibrational state v_i and the total energy E_{tot} .

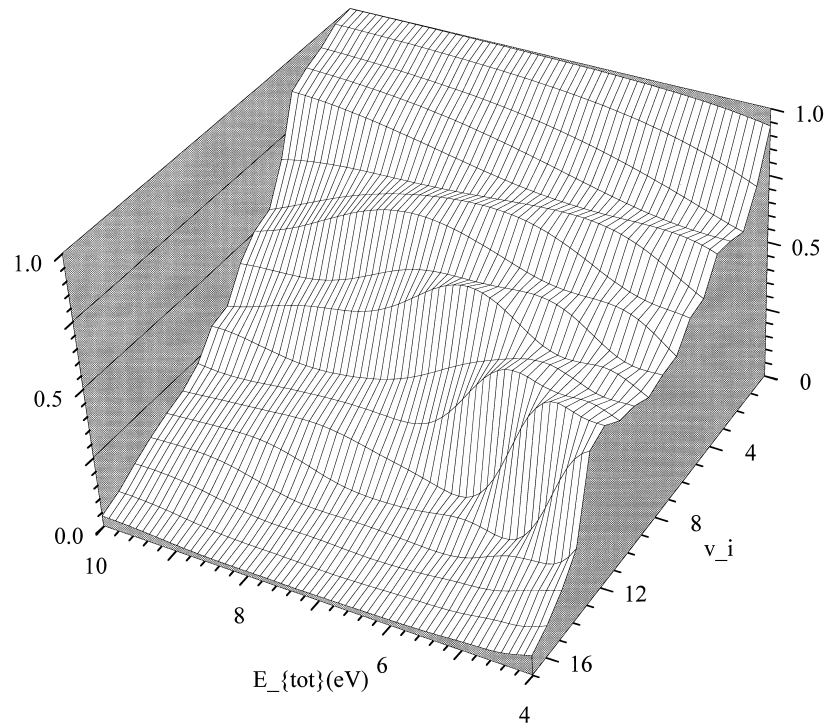


FIG. 2. Three dimensional surface plot of the probability of the total reaction summed over the product vibrational states in $\text{He} + \text{H}_2^+(v_i)$ collinear collision as a function of both the initial vibrational state v_i and the total energy E_{tot} .

3. Results of $\text{He} + \text{H}_2^+(v_i)$ collision

The method described in Section 2 is applied to a collinear $\text{He} + \text{H}_2^+(v_i)$ collision, and collision dynamics, in which non-reactive vibrational, reactive, and dissociative channels

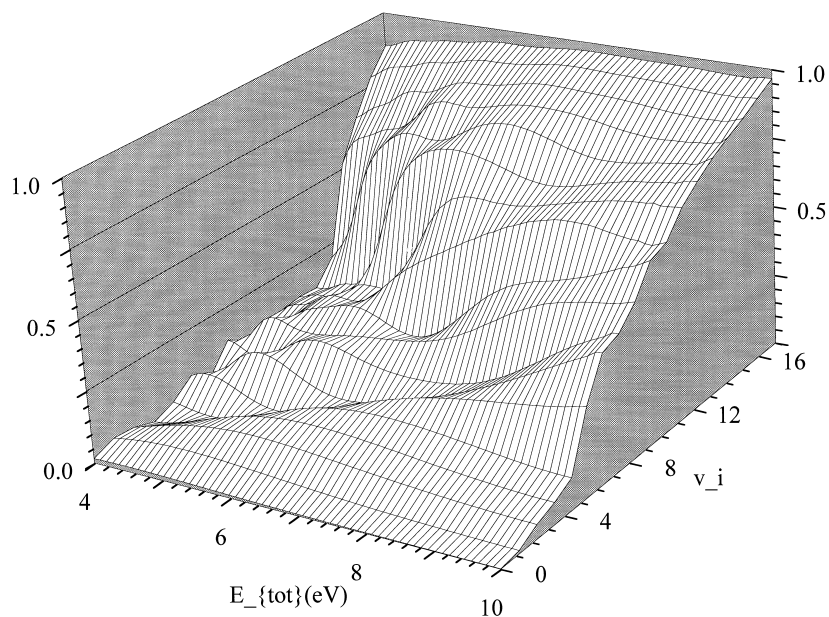


FIG. 3. Three dimensional surface plot of the total dissociation probability in $\text{He} + \text{H}_2^+(v_i)$ collinear collision as a function of both the initial vibrational state v_i and the total energy E_{tot} .

strongly couple with each other, is investigated by taking into account all of the vibrational states $0 \leq v_i \leq 17$ as the initial state at the total energy E_{tot} from 4 to 10 eV. The dissociation energy of this collision system is 2.787 eV measured from the lowest minimum of the diatomic well. In this report, the mass of a ^1H atom is 1.008 u (1 u being 1 universal atomic mass unit = one twelfth the mass of a ^{12}C atom) and that of He is 4.003 u as the normal mass, respectively.

A three dimensional surface plot of the probabilities of the total non-reactive vibrational transition summed over the reactant final vibrational states is displayed in Fig. 1, a surface plot of the probabilities of the total reaction summed over the product vibrational states is shown in Fig. 2, and the total dissociation probability is represented in Fig. 3 as a function of both the initial vibrational state v_i and the total energy E_{tot} . These three dimensional surfaces of the probabilities are useful to gain overall features as a function of both E_{tot} and v_i .

In order to understand a full detail of the collision dynamics, the probabilities shown in Figs 1–3 for each process are collectively plotted in Figs 4(a)–(e) as a function of E_{tot} for the total non-reactive vibrational transition (shown by a solid line), the total atom exchange reaction (a dashed line), and the total dissociation (a long-dashed line) from an indicated initial vibrational state of $v_i = 0, 4, 8, 12$, or 16, respectively.

The following characteristics are noticeable from Figs 1, 2, 3 and 4(a)–(e).

Non-reactive vibrational transitions have the probabilities larger than 0.1 for $2 \sim 3 \leq v_i \leq 13 \sim 14$ at the total energy below about 5~6 eV, and the internal energy stored in the vibrational mode is effective to enhance vibrational transitions for the initial vibrational states $v_i \leq 11 \sim 12$. The probabilities of the total non-reactive vibrational transition become smaller without any exception for all of the initial vibrational states as the total

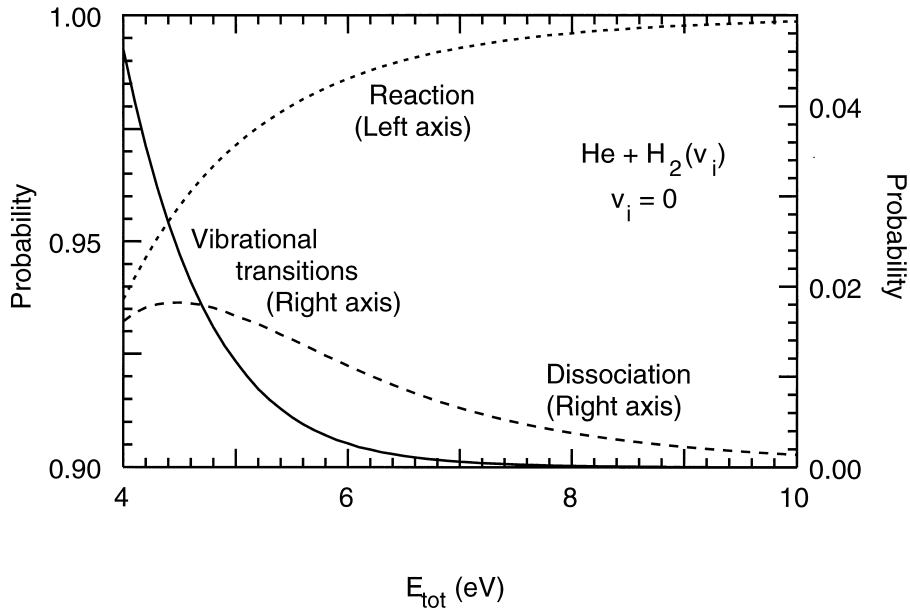


FIG. 4(a). The energy dependence of the probabilities of the total non-reactive vibrational transition (shown by a solid line with the letter of “vibrational transitions”), the total atom exchange reaction (shown by a dotted line with “reaction”), and the total dissociation (shown by a long dashed line with “dissociation”) in $\text{He} + \text{H}_2^+(v_i)$ collision with $v_i = 0$.

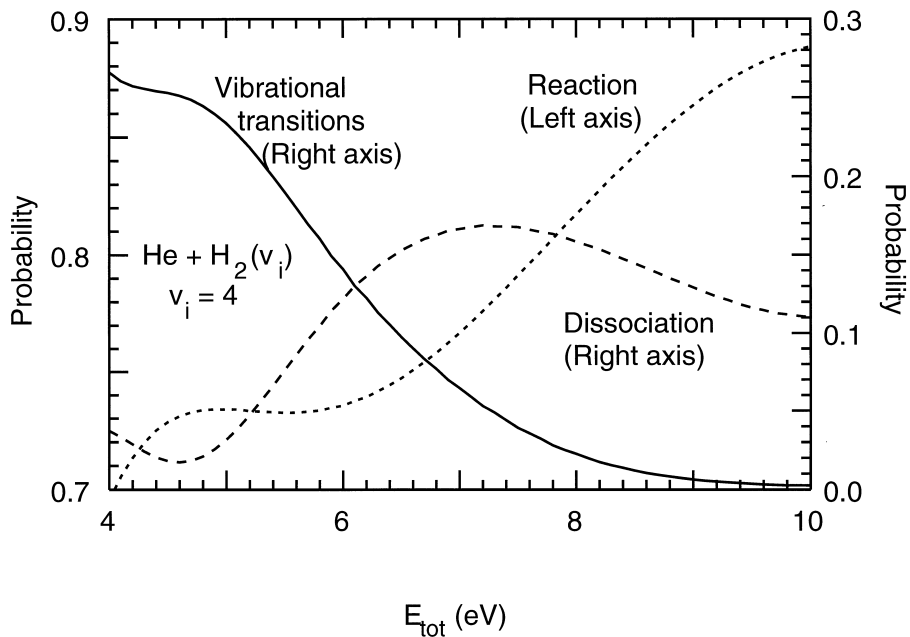


FIG. 4(b). The same as Fig. 4(a) except for $v_i = 4$.

energy is increased from 6 to 10 eV, and decrease for $v_i \leq 3$ monotonically with the increase of the total energy, but those for $v_i \geq 4$ oscillate as a function of E_{tot} .

Both the probabilities of the total non-reactive vibrational transition and dissociation are very small for $v_i \leq 4$, and the collision primarily proceeds to a formation of HeH^+ , even if the total energy is increased up to 10 eV, which is higher than 3 times of the dissociation energy of the H_2^+ ion. On the other hand, the collision proceeds predominantly

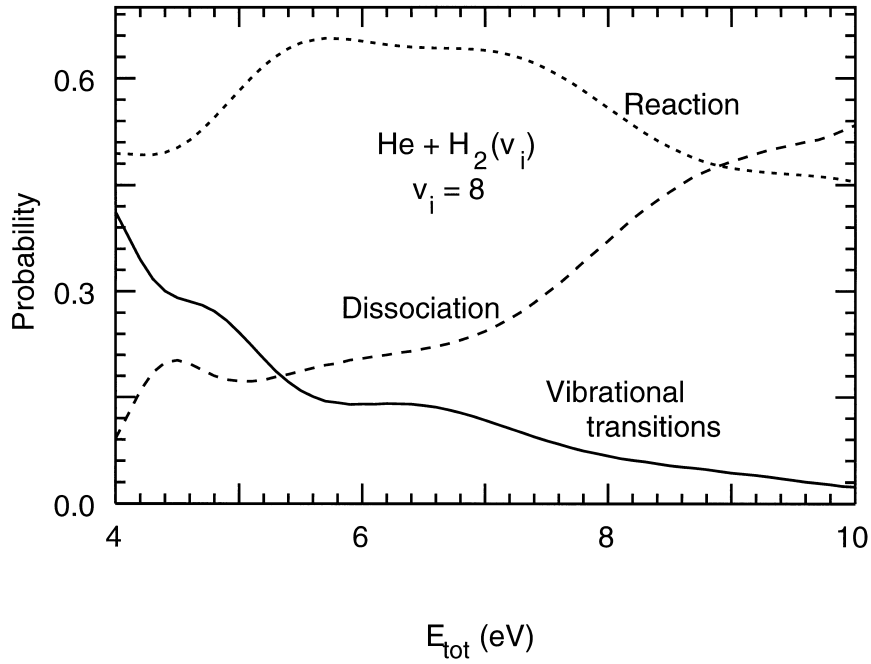


FIG. 4(c). The same as Fig. 4(a) except for $v_i = 8$.

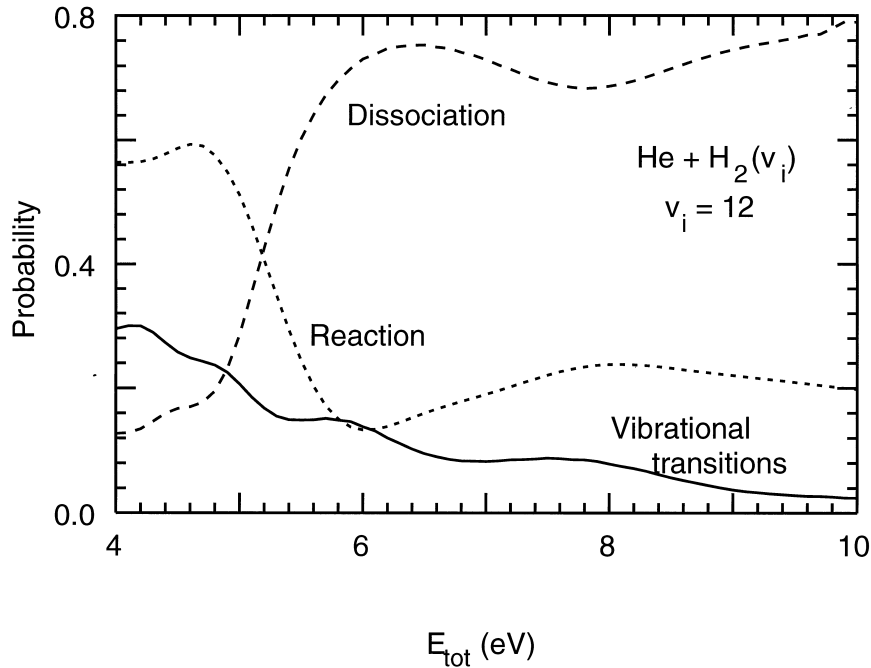


FIG. 4(d). The same as Fig. 4(a) except for $v_i = 12$.

to dissociation of the H_2^+ ion for $11 \sim 13 \leq v_i$ depending on the total energy. In both cases, it seems that the atom exchange reaction process is little influenced by the dissociation process or *vice versa*. Therefore, the probabilities of the reaction and dissociation processes depend weakly on E_{tot} in a wide range of the total energy of $4 \leq E_{tot} \leq 10$ eV. Since the probability of the total non-reactive vibrational transition is small at $E_{tot} \geq 6$ eV, the reaction or dissociation is the dominant process at this range of the total energy for all of the initial vibrational state v_i . It is probable that these results are caused by the nature

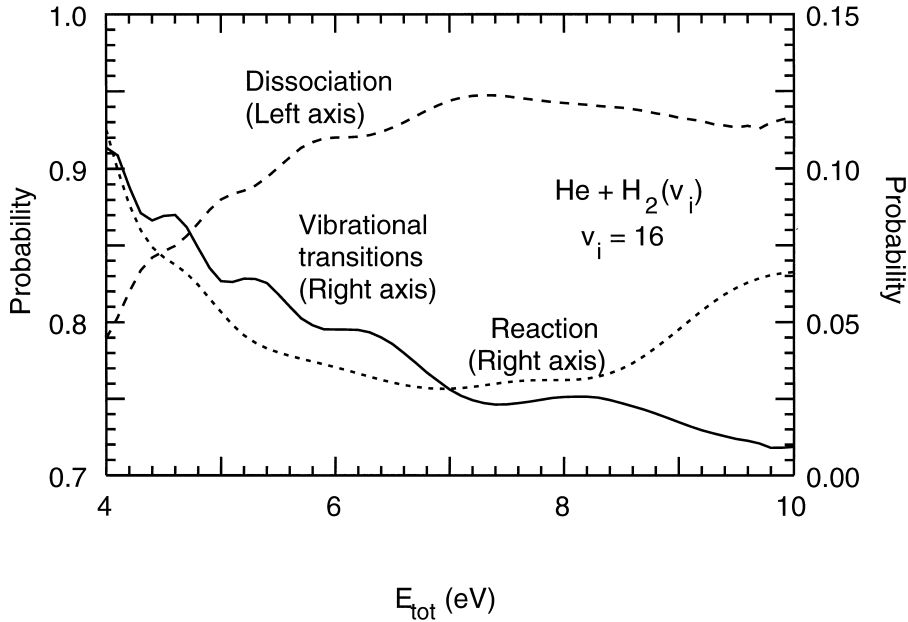


FIG. 4(e). The same as Fig. 4(a) except for $v_i = 16$.

of the interaction potential surface itself, or by a collinear arrangement of this collision system.

In cases of the initial vibrational states between above two extremes, that is, one of $5 \leq v_i \leq 10 \sim 12$, the probability of the atom exchange reaction is comparable in magnitude to that of the dissociation. Both the probabilities of the reaction and dissociation processes are undulatory and are almost anti-phase with each other as a function of E_{tot} as shown in Figs 2, 3, and 4(a)–(e). It is understood from these results that the atom exchange reaction channels actively couple with the dissociative ones.

Figure 3 clearly shows that the collision induced dissociation is more or less enhanced by effectively converting the internal vibrational energies into the energy required to break a molecular bond. Since Sakimoto in papers III [9] and IV [10] has shown for initial vibrational states $v_i \leq 6$ that this vibrational enhancement is not always seen in this collision system with different isotope mass combinations, we need to investigate further collision induced dissociation processes in this collision system with the isotope variations by taking into account all of the vibrational states. The results are presented in Section 4 below.

The probabilities of the reaction and dissociation processes obtained here are compared with those calculated by Dove *et al.* [13] in paper V [11] for the initial vibrational states $v_i = 0 - 1$. Dove *et al.* employed the same potential energy surface of the MTJS as ours and solved the collision dynamics by applying the quasiclassical trajectory (QCT) method. These results tell us that both results for the reaction and dissociation probabilities agree reasonably with each other.

As can be seen from Figs 3 and 4(a)–(e), the dissociation of the $\text{H}_2^+(v_i)$ ion is the predominant process for $v_i \geq 14$ at the total energy $E_{tot} \geq 4$ eV, and the total energy dependence

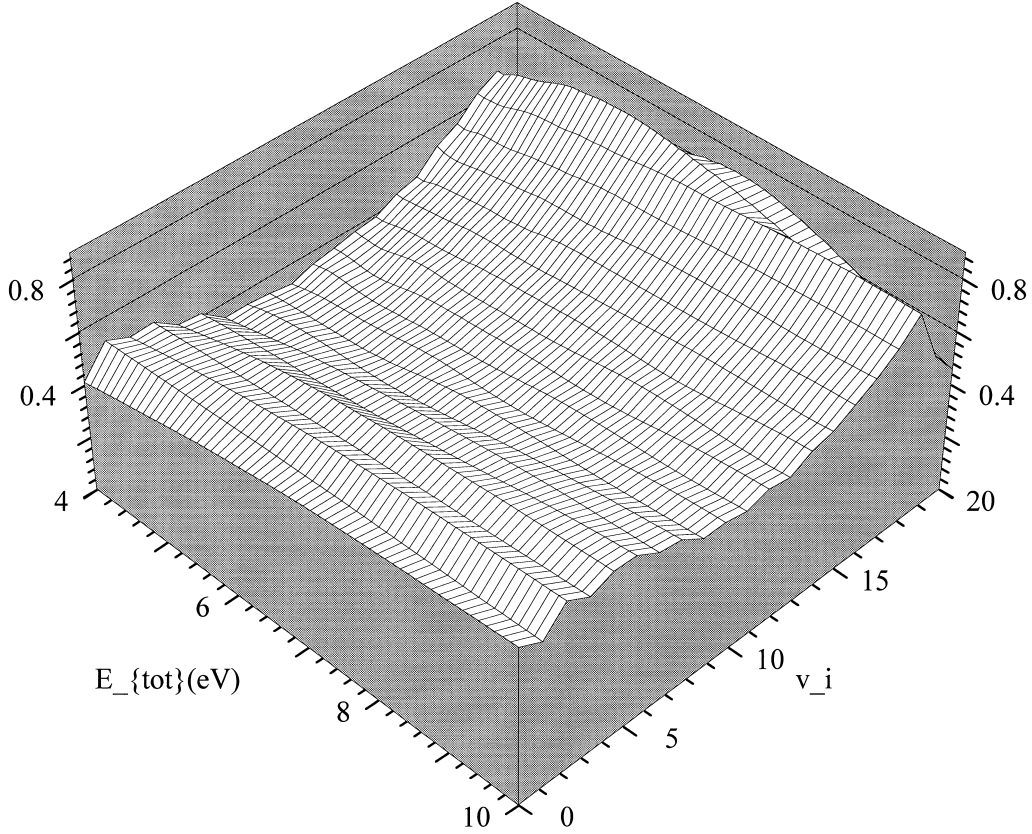


FIG. 5. Three dimensional surface plot of the probability of the total non-reactive vibrational transition summed over the reactant final vibrational states in $\text{He} + \text{HD}^+(v_i)$ collinear collision as a function of both the initial vibrational state v_i and the total energy E_{tot} .

of this probability is very weak for $v_i \geq 14$. Although the dissociation of the H_2^+ ion is the main process for the initial vibrational states in $10 \leq v_i \leq 13$ at the total energy $E_{tot} \geq 6$ eV, the atom exchange reaction channels actively couple with the dissociation channels and both the probabilities of the reaction and dissociation processes are undulatory as a function of E_{tot} .

4. Results of isotope variations on $\text{He} + \text{H}_2^+(v_i)$ collision system

It is a highly interesting subject to make clear from both points of view in a fundamental physics itself and an application to a gas divertor plasma physics whether different mass combinations cause any effect on dynamics in atomic and molecular elementary collision processes or not. Sakimoto investigated in paper III [9] an isotope effect on dynamics in the collinear $\text{He} + \text{H}_2^+(v_i)$ collision with different mass combinations, that is, in $^3\text{He} + \text{HT}^+(v_i)$, $^3\text{He} + \text{TH}^+(v_i)$, $^3\text{He} + \text{T}_2^+(v_i)$, and $^3\text{He} + \text{MuT}^+(v_i)$. Here, muon or mu meson is denoted by Mu. Energy dependence of the exchange and dissociation probabilities is investigated for $0 \leq v_i \leq 2$ at the total energy $E_{tot} \leq 7$ eV, and the dependence of the exchange and dissociation probabilities on the initial vibrational state v_i is studied for $0 \leq v_i \leq 6$ at $E_{tot} = 6$ eV. In paper IV [10], he studied $\text{He} + \text{Mu}_2^+$, $\text{He} + \text{H}_2^+$, $\text{He} + \text{D}_2^+$, $\text{He} + \text{T}_2^+$, $^3\text{He} + \text{T}_2^+$ as $\text{A} + \text{B}_2$ collision system, $\text{He} + \text{DH}^+$, $\text{He} + \text{TH}^+$, $^3\text{He} + \text{TH}^+$, He

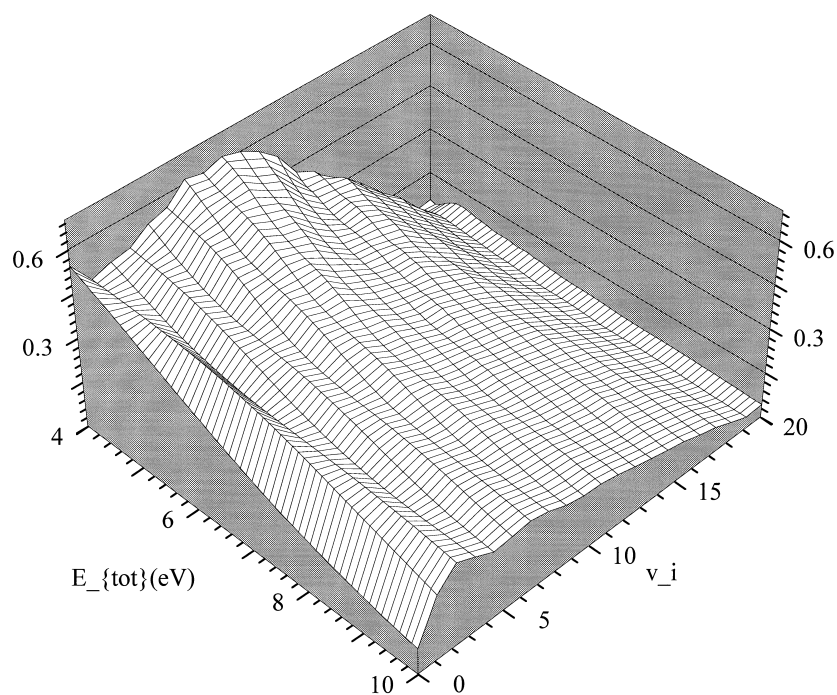


FIG. 6. Three dimensional surface plot of the probability of the total reaction summed over the product vibrational states in $He + HD^+(v_i)$ collinear collision as a function of both the initial vibrational state v_i and the total energy E_{tot} .

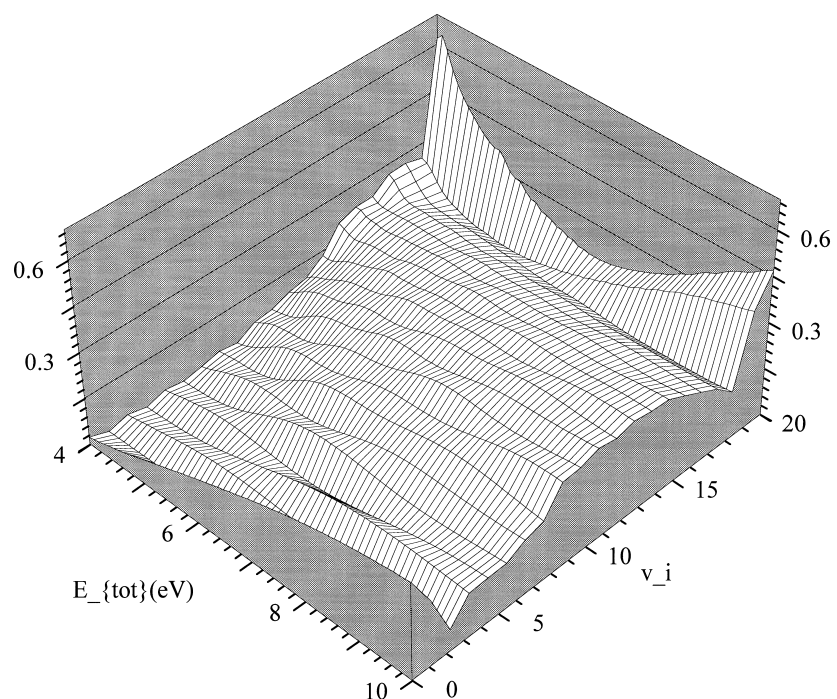


FIG. 7. Three dimensional surface plot of the total dissociation probability in $He + HD^+(v_i)$ collinear collision as a function of both the initial vibrational state v_i and the total energy E_{tot} .

+ HMu^+ as heavy-heavy-light (HHL) collision system, and $He + MuH^+$, $He + HT^+$, $^3He + HT^+$, $He + HD^+$ as heavy-light-heavy (HLH) collision system for $v_i = 0$ at the total energy $E_{tot} \leq 6$ eV. He found a remarkable isotope effect on these collision systems.

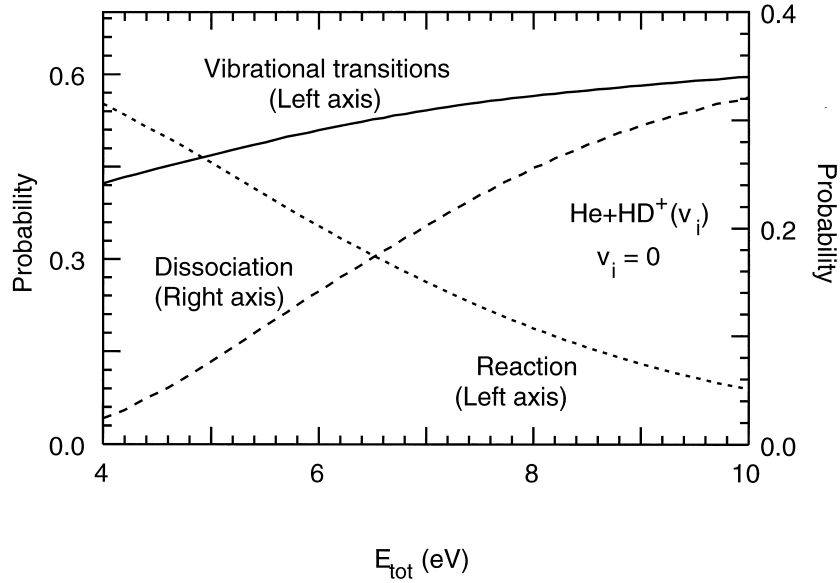


FIG. 8(a). The energy dependence of the probabilities of the total non-reactive vibrational transition (shown by a solid line with the letter of “vibrational transitions”), the total atom exchange reaction (shown by a dotted line with “reaction”), and the total dissociation (shown by a long dashed line with “dissociation”) in $\text{He} + \text{HD}^+(v_i)$ collision with $v_i = 0$.

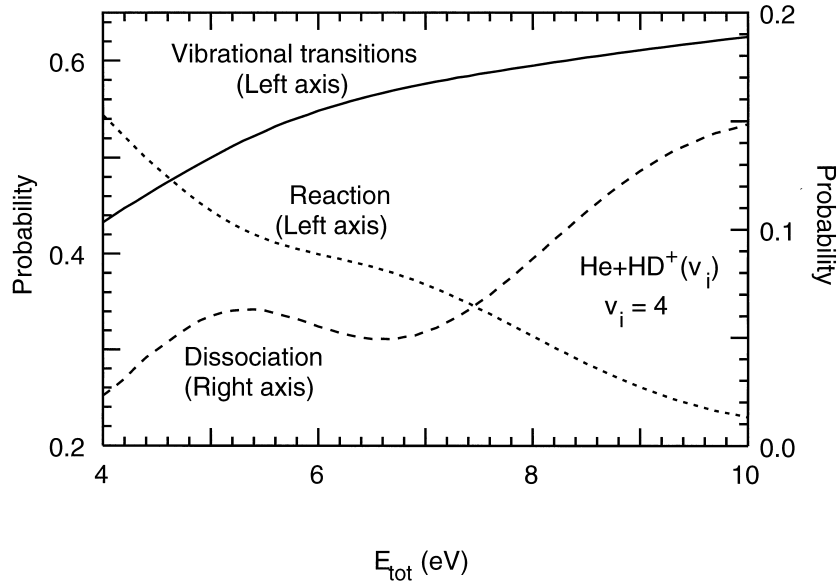


FIG. 8(b). The same as Fig. 8(a) except for $v_i = 4$.

We mention that a collinear collision of $\text{A} + \text{BC}$ is different from that of $\text{A} + \text{CB}$. The former arrangement produces AB as a reaction product, and the latter does AC .

In order to investigate further isotope effect on dynamics of the collinear $\text{He} + \text{H}_2^+$ collision, we have studied $\text{He} + \text{HD}^+(v_i)$ ($0 \leq v_i \leq 21$), $\text{HT}^+(v_i)$ ($0 \leq v_i \leq 22$), $\text{DH}^+(v_i)$ ($0 \leq v_i \leq 21$), and $\text{TH}^+(v_i)$ ($0 \leq v_i \leq 22$) collisions at the total energy from 4 to 10 eV by considering all of the vibrational bound states as an initial state. The normal mass of He is employed throughout this report. Representative results are presented in the following subsections.

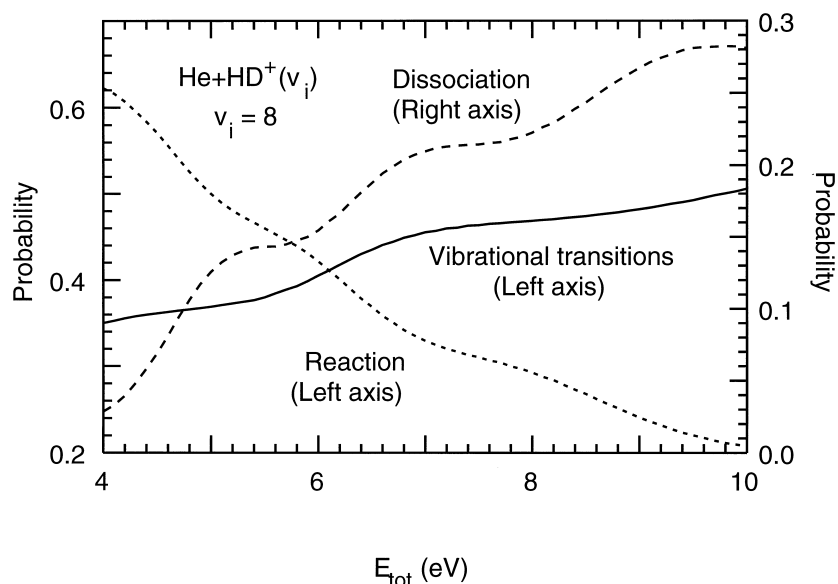


FIG. 8(c). The same as Fig. 8(a) except for $v_i = 8$.

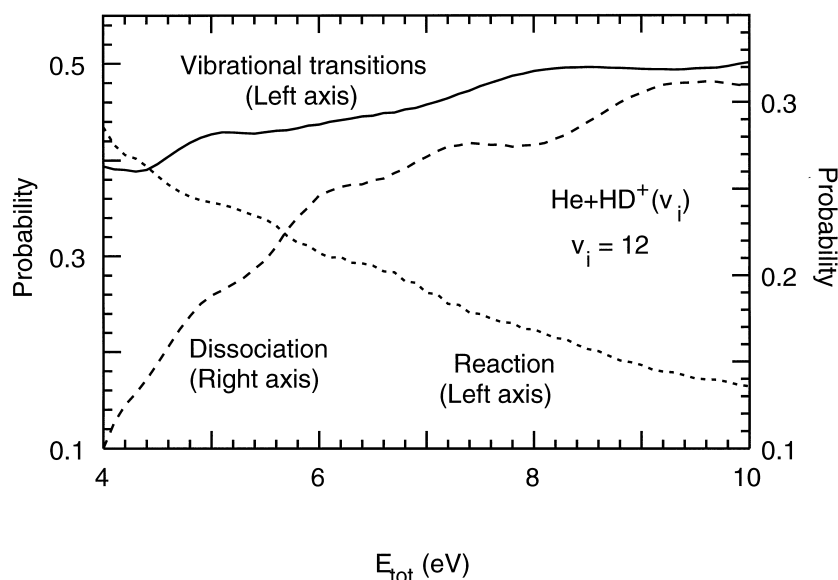


FIG. 8(d). The same as Fig. 8(a) except for $v_i = 12$.

4.1. He + HD⁺(v_i) collision

Three dimensional surface plots of the probabilities as a function of both E_{tot} and v_i are displayed in Figs 5–7 for the total non-reactive vibrational transition summed over the reactant final vibrational states, the total atom-exchange reaction summed over the product vibrational states, and the total dissociation, respectively.

The probabilities as a function of E_{tot} are collectively plotted in Figs 8(a)–(f) for the total non-reactive vibrational transition (shown by a solid line), the total atom-exchange reaction (a dashed line) and dissociation (a long dashed line) from an indicated initial vibrational state of $v_i = 0, 4, 8, 12, 16$ or 20 , respectively.

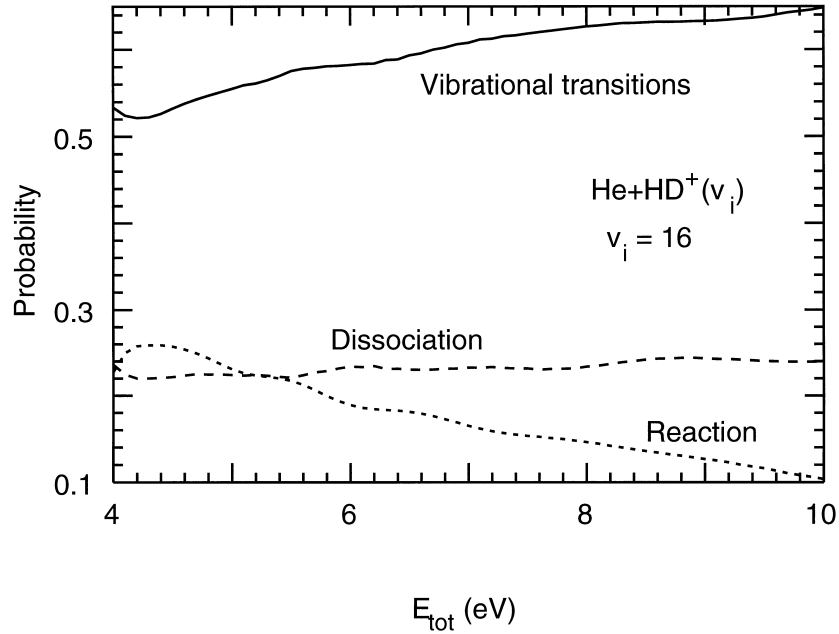


FIG. 8(e). The same as Fig. 8(a) except for $v_i = 16$.

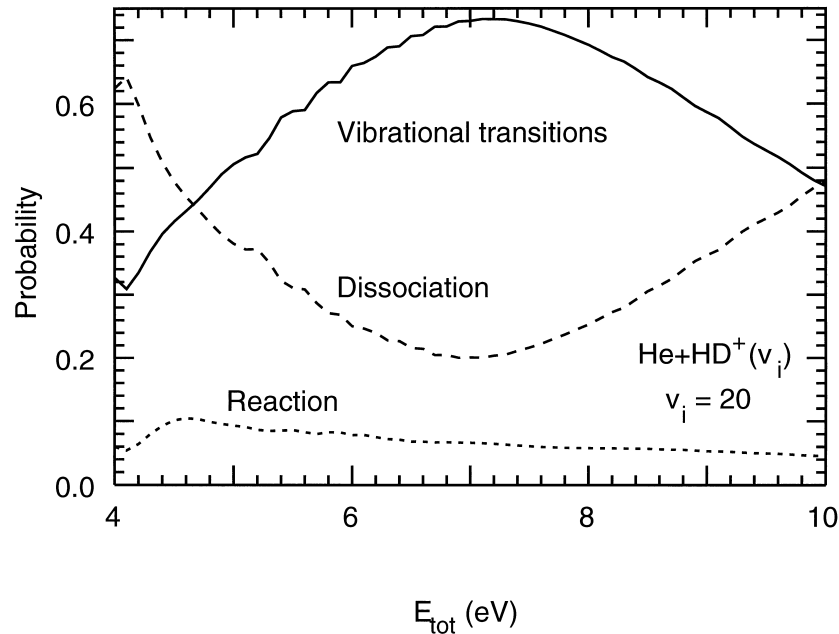


FIG. 8(f). The same as Fig. 8(a) except for $v_i = 20$.

The following characteristics are clearly seen from Figs 5, 6, 7, and 8(a)–(f).

Nearly all of the probabilities of the total non-reactive vibrational transition are larger than about 0.4 for all vibrational states of $0 \leq v_i \leq 20$ at the total energy of $4 \leq E_{tot} \leq 10$ eV. The non-reactive vibrational transitions dominate over the atom exchange reaction and dissociation processes for $0 \leq v_i \leq 3$ and $12 \leq v_i \leq 19$ at $4 \leq E_{tot} \leq 10$ eV. These probabilities moderately depend on the total energy except for the highest vibrational state $v_i = 20$.

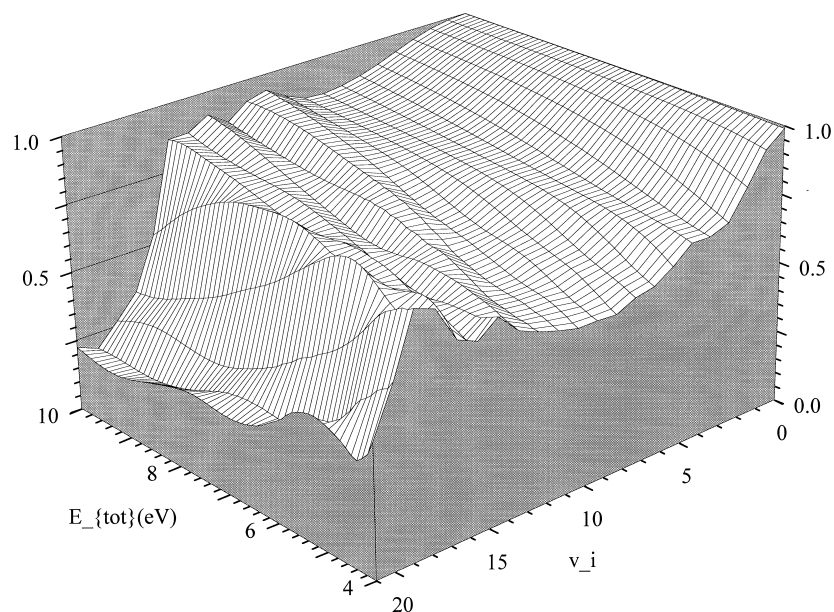


FIG. 9. Three dimensional surface plot of the probability of the total non-reactive vibrational transition summed over the reactant final vibrational states in $\text{He} + \text{HT}^+(v_i)$ collinear collision as a function of both the initial vibrational state v_i and the total energy E_{tot} .

Atom exchange reactions become the major processes for $4 \leq v_i \leq 11$ at the total energy $4 \leq E_{tot} \leq 6$ eV, and the magnitude of these probabilities is about 0.4 - 0.6. The reaction probability appreciably decreases as the increase of the total energy at $4 \leq E_{tot} \leq 6$ eV for $v_i \leq 14$, but becomes almost independent of E_{tot} for $v_i \geq 16$. If we closely consider these results from physical point of view, it is thought that the atom-exchange reactions are caused by mainly two different kinds of interactions on the potential energy surface (PES) depending on the initial vibrational states v_i .

The dissociation probability becomes larger as the total energy is increased from 4 to 10 eV, but dissociation in this collision system is more or less suppressed, and the values of these probabilities are less than 0.3 except for the highest vibrational state $v_i = 20$. The internal energy stored in the vibrational mode is effective to enhance the dissociation process for $3 \leq v_i \leq 12$ at $4 \leq E_{tot} \leq 10$ eV. Both the reaction and dissociation probabilities are comparable in magnitude to each other for the vibrational states of $12 \leq v_i \leq 19$ at the total energy of $4 \leq E_{tot} \leq 6$ eV, and are undulatory as a function of E_{tot} . These results tell us that the atom-exchange reaction channels actively couple with the dissociation ones.

These results are appreciably different from those obtained in $\text{He} + \text{H}_2^+$ system.

4.2. $\text{He} + \text{HT}^+(v_i)$ collision

A three dimensional surface plot is displayed in Fig. 9 for the probabilities of the total non-reactive vibrational transition summed over the reactant final vibrational states, a surface plot of the probabilities of the total reaction summed over the product vibrational

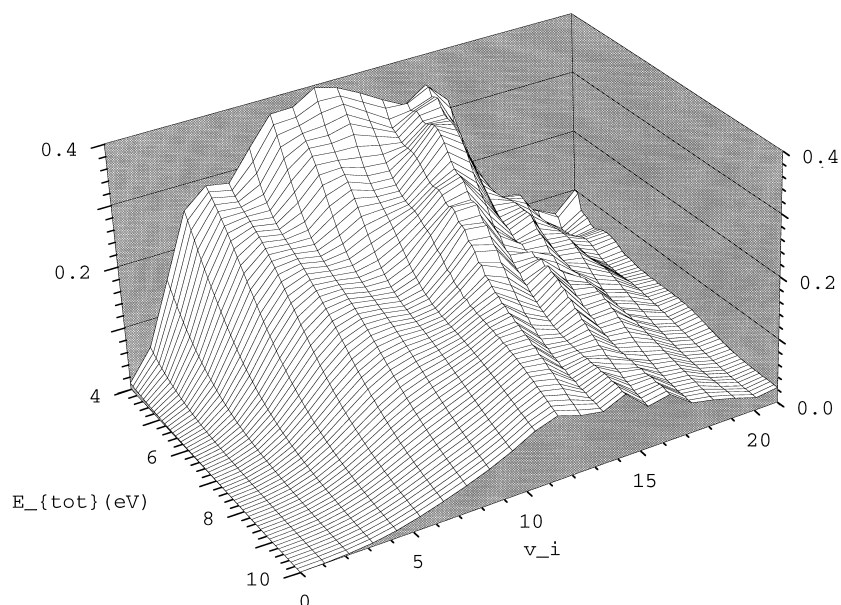


FIG. 10. Three dimensional surface plot of the probability of the total reaction summed over the product vibrational states in $He + HT^+(v_i)$ collinear collision as a function of both the initial vibrational state v_i and the total energy E_{tot} .

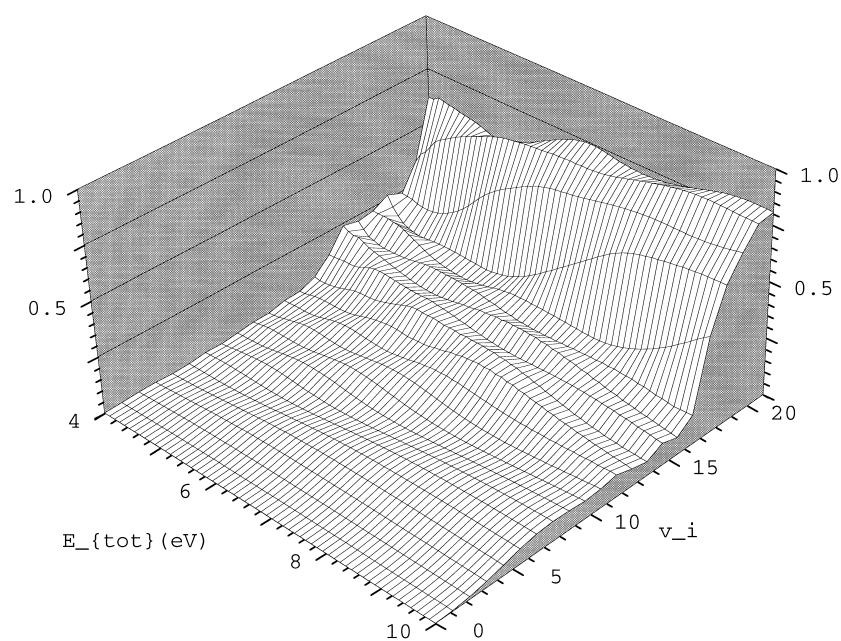


FIG. 11. Three dimensional surface plot of the total dissociation probability in $He + HT^+(v_i)$ collinear collision as a function of both the initial vibrational state v_i and the total energy E_{tot} .

states is shown in Fig. 10, and the total dissociation probabilities are represented in Fig. 11 as a function of both E_{tot} and v_i .

The probabilities are plotted as a function of E_{tot} in Figs 12(a)–(f) for the total non-reactive vibrational transition (shown by a solid line), the total atom-exchange reaction

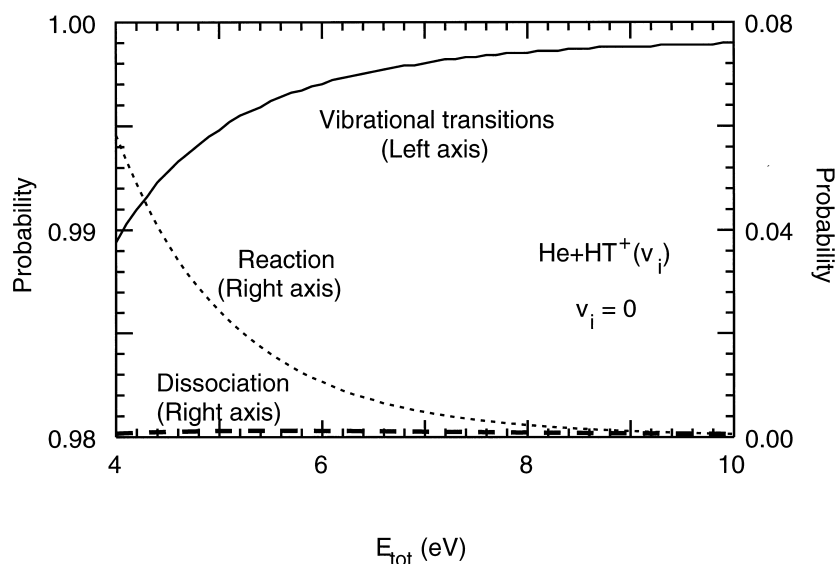


FIG. 12(a). The energy dependence of the probabilities of the total non-reactive vibrational transition (shown by a solid line with the letter of “vibrational transitions”), the total atom exchange reaction (shown by a dotted line with “reaction”), and the total dissociation (shown by a long dashed line with “dissociation”) in $\text{He} + \text{HT}^+(v_i)$ collision with $v_i = 0$.

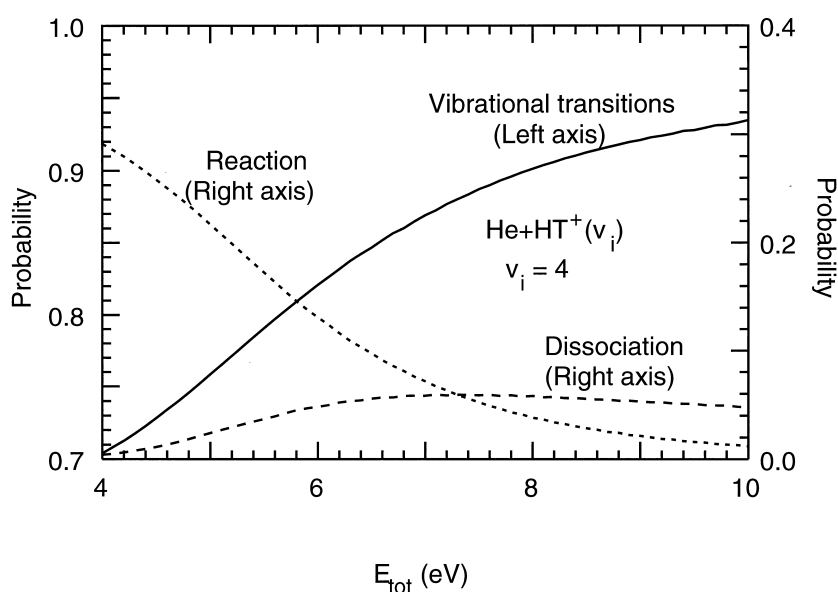


FIG. 12(b). The same as Fig. 12(a) except for $v_i = 4$.

(a dashed line), and the total dissociation (a long-dashed line) from an indicated initial vibrational state of $v_i = 0, 4, 8, 12, 16$, or 20 , respectively.

The followings are characteristic features seen from Figs 9, 10, 11, and 12(a)–(f).

The probabilities of the total non-reactive vibrational transition are larger than about 0.7 for $0 \leq v_i \leq 5$, and are larger than about 0.5 for $6 \leq v_i \leq 17$ at the total energy of $4 \leq E_{tot} \leq 10$ eV. The energy dependence of these probabilities for $0 \leq v_i \leq 17$ is different from that for $v_i \geq 18$. It seems that different kinds of interactions on the PES cause the non-reactive vibrational transitions depending on the initial vibrational states v_i .

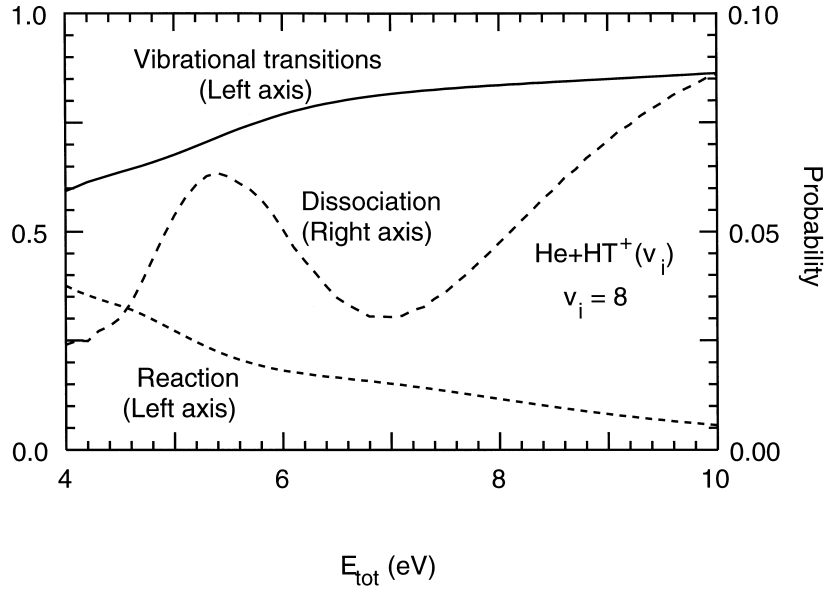


FIG. 12(c). The same as Fig. 12(a) except for $v_i = 8$.

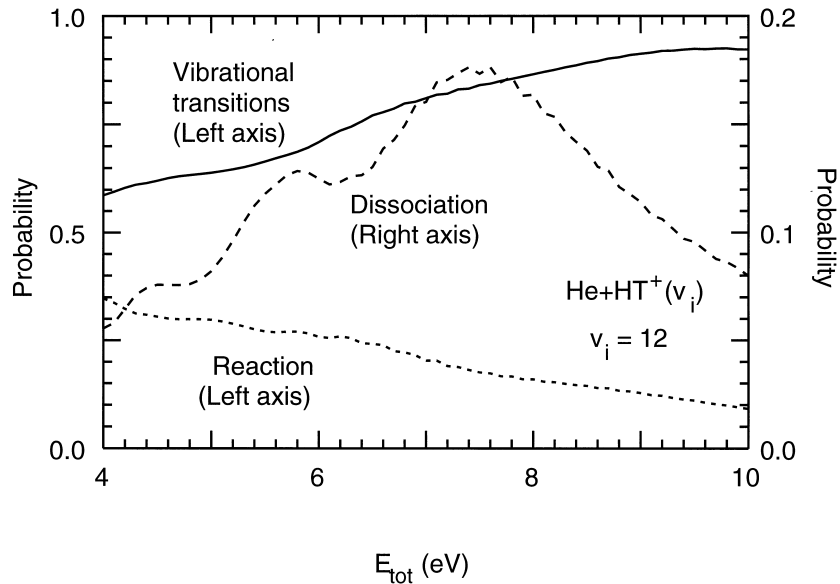


FIG. 12(d). The same as Fig. 12(a) except for $v_i = 12$.

For the initial vibrational states $v_i \geq 18$, the non-reactive vibrational transitions are the major processes at the total energy $E_{tot} \leq 8$ eV, but the dissociation becomes the major process at a higher total energy, that is, these two processes exchange its role in collision dynamics with the total energy. These results are considerably different from both the results obtained in $\text{He} + \text{H}_2^+$ and $\text{He} + \text{HD}^+$ collisions.

Exchange reaction processes are vibrationally enhanced for $0 \leq v_i \leq 12-14$ at $4 \leq E_{tot} \leq 10$ eV. The magnitude of these probabilities is smaller than about 0.1 for $0 \leq v_i \leq 2$. The energy dependence of these probabilities for $0 \leq v_i \leq 4$ is different from that for $v_i \geq 5$.

The magnitude of dissociation probabilities is less than 0.05 for $0 \leq v_i \leq 4$ at $4 \leq E_{tot} \leq 10$ eV. The collision energy is not effective to break the molecular bond for the initial

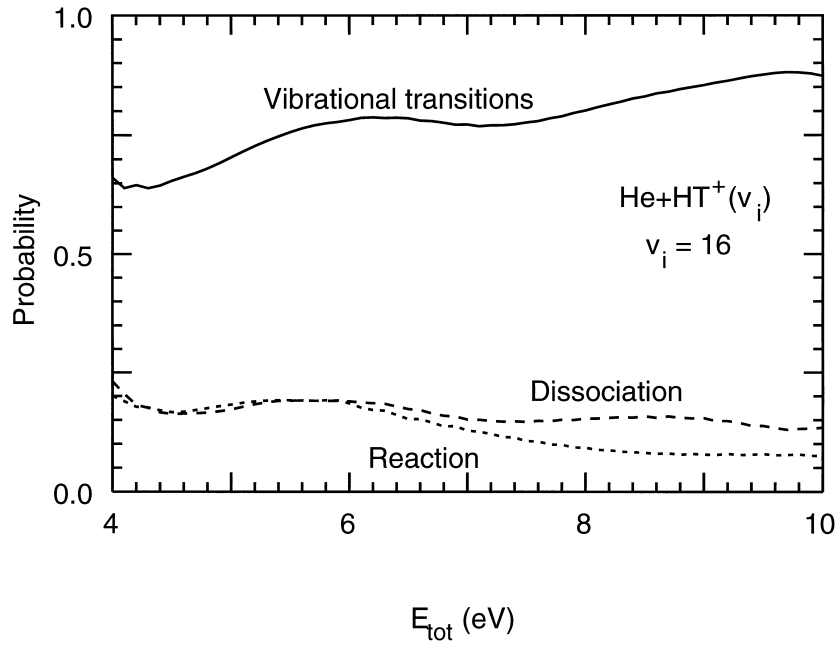


FIG. 12(e). The same as Fig. 12(a) except for $v_i = 16$.

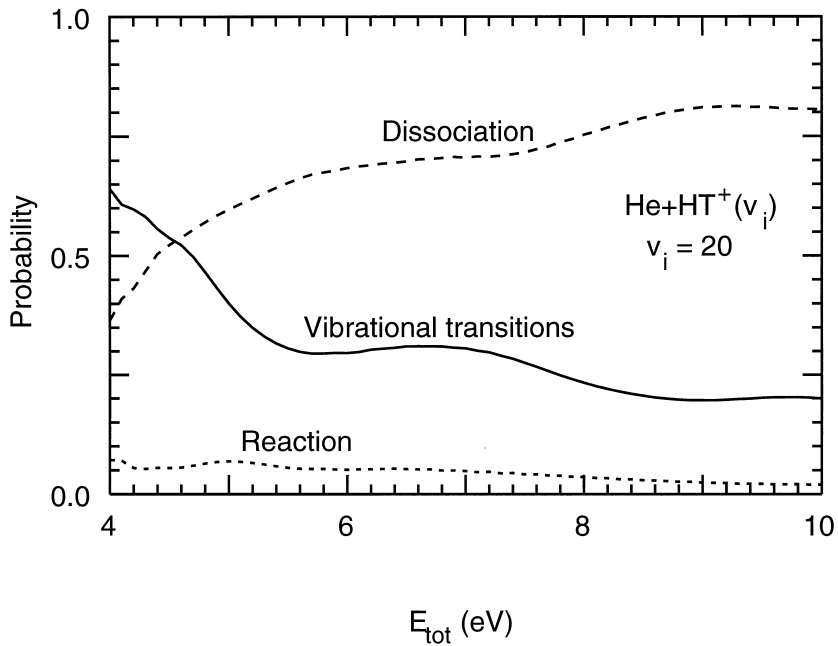


FIG. 12(f). The same as Fig. 12(a) except for $v_i = 20$.

vibrational states $v_i \leq 4$, even if the total energy is increased up to 10 eV, which is higher than 3 times of the dissociation energy of the HT^+ ion. Dissociation probabilities are gradually increased as the initial vibrational state is excited higher up to $v_i = 16$, and are abruptly increased to about 0.5 for the initial vibrational state $v_i \geq 17$. Both the probabilities of exchange reaction and dissociation are comparable in magnitude to each other for $8 \leq v_i \leq 16$.

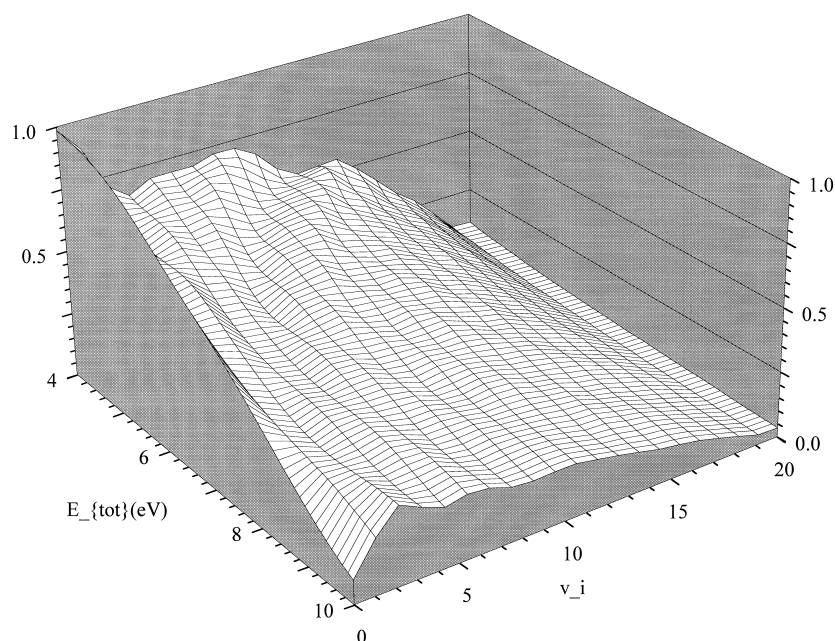


FIG. 13. Three dimensional surface plot of the probability of the total non-reactive vibrational transition summed over the reactant final vibrational states in $\text{He} + \text{DH}^+(v_i)$ collinear collision as a function of both the initial vibrational state v_i and the total energy E_{tot} .

For the initial vibrational states $0 \leq v_i \leq 2$, the exchange reaction and dissociation processes are almost completely suppressed at the energy $4 \leq E_{tot} \leq 10$ eV. These results are special in this mass combination.

As can be seen from Figs 4(a)–(d) and Figs 12(a)–(d), both the probabilities of the non-reactive vibrational transitions in $\text{He} + \text{H}_2^+$ collision and of the reaction process in $\text{He} + \text{HT}^+$ collision have very similar dependence on the total energy.

4.3. $\text{He} + \text{DH}^+(v_i)$ collision

In Figs 13–15, dependence of the probabilities on the total energy and the initial vibrational state is displayed for the total non-reactive vibrational transition summed over the reactant final vibrational states, for the total atom-exchange reaction summed over the product vibrational states, and for the total dissociation, respectively. These surface plots are quite different in shape from those shown in Figs 1–3 for $\text{He} + \text{H}_2^+$ collision, those shown in Figs 5–7 for $\text{He} + \text{HD}^+$, those shown in Figs 9–11 for $\text{He} + \text{HT}^+$.

The total energy dependence of the probabilities is plotted in Figs 16(a)–(f) for the total non-reactive vibrational transition (shown by a solid line), the total atom-exchange reaction (a dashed line) and the total dissociation (a long dashed line) from an indicated initial vibrational state of $v_i = 0, 4, 8, 12, 16$, or 20 , respectively.

Characteristic features are pointed out from Figs 13, 14, 15, and 16(a)–(f) in the followings.

The non-reactive vibrational transitions are the dominant processes for the initial vibrational states $v_i \leq 10$ at $4 \leq E_{tot} \leq 6 - 7$ eV, and for $11 \leq v_i \leq 13$ at $4 \leq E_{tot} \leq 5$ eV.

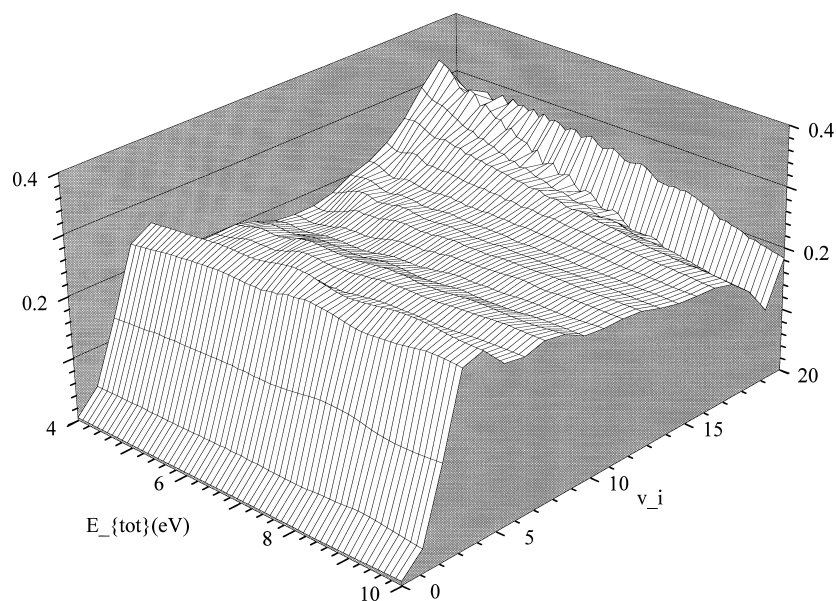


FIG. 14. Three dimensional surface plot of the probability of the total reaction summed over the product vibrational states in $He + DH^+(v_i)$ collinear collision as a function of both the initial vibrational state v_i and the total energy E_{tot} .

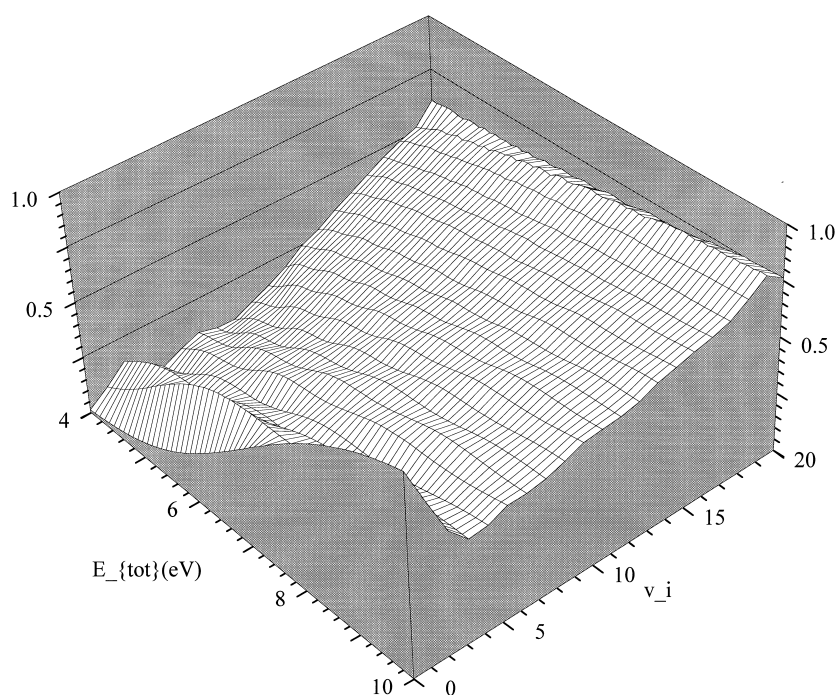


FIG. 15. Three dimensional surface plot of the total dissociation probability in $He + DH^+(v_i)$ collinear collision as a function of both the initial vibrational state v_i and the total energy E_{tot} .

The magnitude of these probabilities gradually decreases from 0.4 to 0.1 for the initial vibrational state $14 \leq v_i \leq 20$. The energy dependence for $v_i = 0$ is different from that for $1 \leq v_i \leq 13$ and the one for $v_i \geq 14$ at $4 \leq E_{tot} \leq 10$ eV. It seems that these processes depending on the initial vibrational states v_i are caused by different kinds of interactions on the PES.

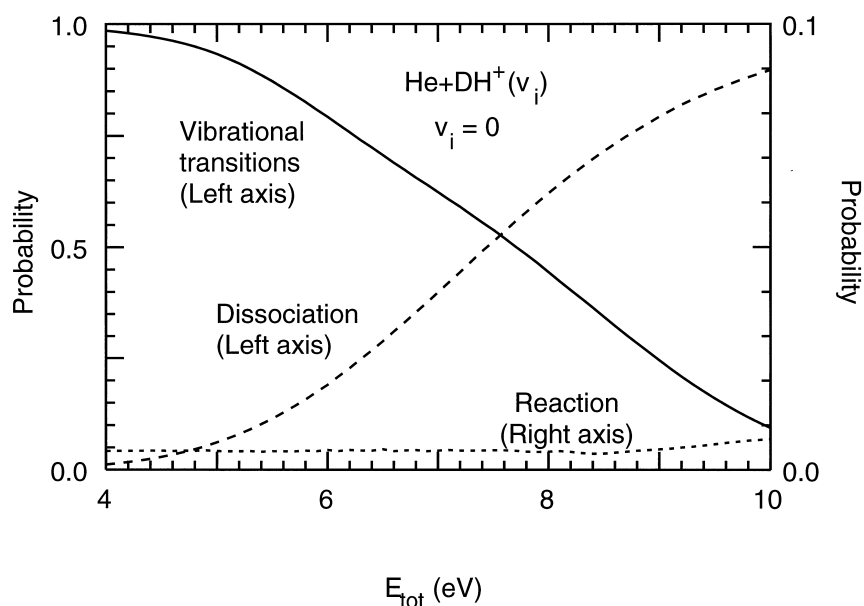


FIG. 16(a). The energy dependence of the probabilities of the total non-reactive vibrational transition (shown by a solid line with the letter of “vibrational transitions”), the total atom exchange reaction (shown by a dotted line with “reaction”), and the total dissociation (shown by a long dashed line with “dissociation”) in $\text{He} + \text{DH}^+(v_i)$ collision with $v_i = 0$.

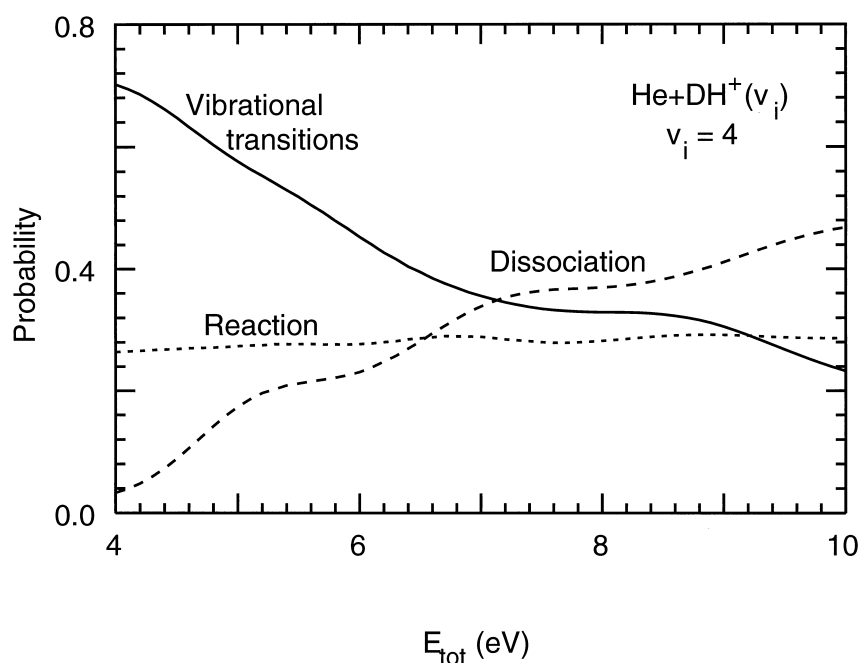


FIG. 16(b). The same as Fig. 16(a) except for $v_i = 4$.

For $0 \leq v_i \leq 2$, the magnitude of the reaction probabilities is less than about 0.05, and the reaction process is almost negligible. The reaction probability has the magnitude about 0.2 - 0.3 for $3 \leq v_i \leq 8$ and $17 \leq v_i$, and about 0.15 - 0.25 for $9 \leq v_i \leq 15$. Although these probabilities gradually increase with E_{tot} for $2 \leq v_i \leq 15$, they moderately decrease with E_{tot} for $16 \leq v_i$. This means that the collision dynamics caused by coupling among different channels is sensitive to the initial vibrational states v_i .

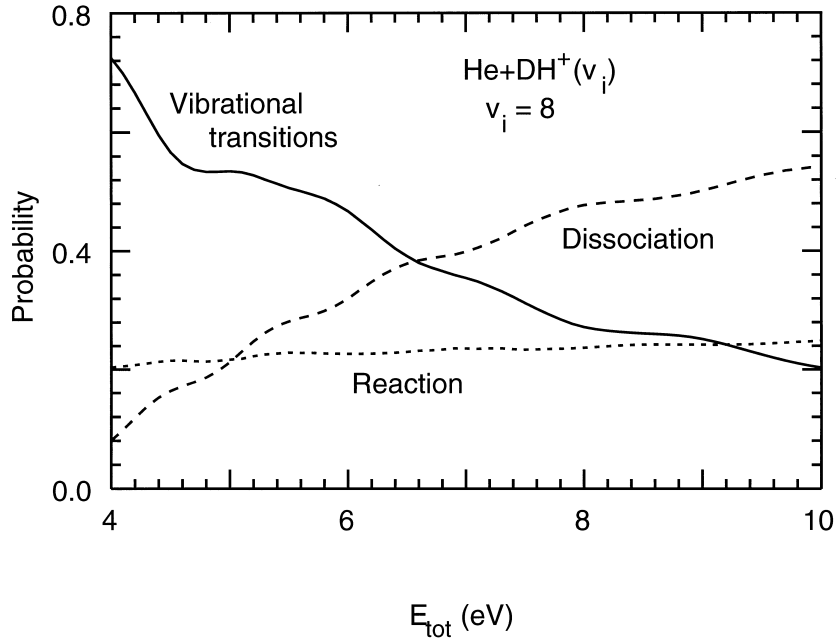


FIG. 16(c). The same as Fig. 16(a) except for $v_i = 8$.

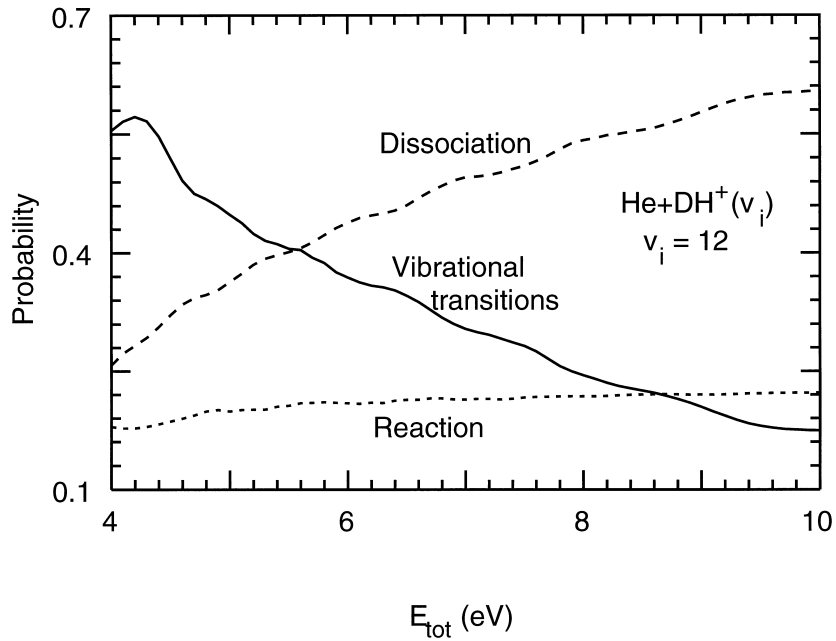


FIG. 16(d). The same as Fig. 16(a) except for $v_i = 12$.

The dissociation process dominates over the non-reactive vibrational transitions for $v_i \leq 10$ at $6 - 7 \leq E_{tot} \leq 10$ eV, for $11 \leq v_i \leq 13$ at $5 \leq E_{tot} \leq 10$ eV, and for $15 \leq v_i$ at $4 \leq E_{tot} \leq 10$ eV. Since both the probabilities of the total non-reactive vibrational transition and the total dissociation are undulatory as a function of E_{tot} for $0 \leq v_i \leq 17$, both the channels strongly couple with each other. For $v_i \geq 17$, the coupling between the dissociation and reaction channels becomes stronger, and these probabilities show weakly oscillatory patterns as a function of E_{tot} . The vibrational enhancement is clearly seen for almost all vibrational states except for $v_i \leq 1$ at $7 \leq E_{tot} \leq 10$ eV.

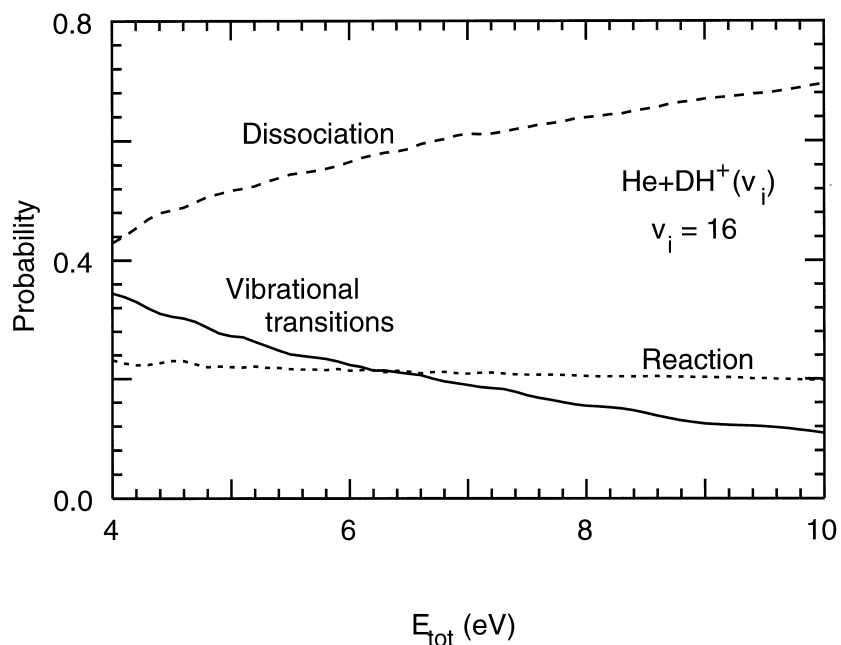


FIG. 16(e). The same as Fig. 16(a) except for $v_i = 16$.

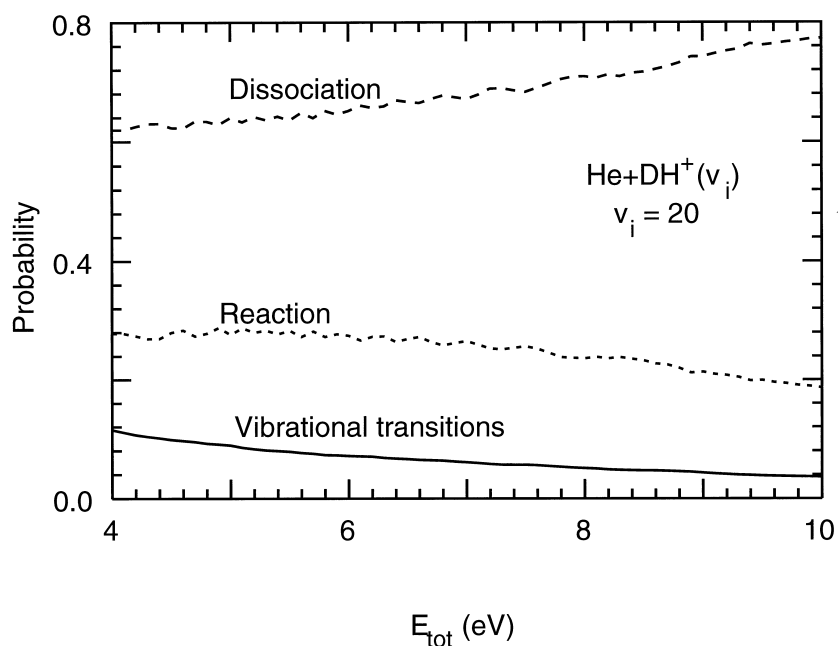


FIG. 16(f). The same as Fig. 16(a) except for $v_i = 20$.

4.4. He + TH⁺(v_i) collision

A three dimensional surface plot of the probabilities of the total non-reactive vibrational transitions summed over the reactant final vibrational states is displayed in Fig. 17, a surface plot of the probabilities of the total reaction summed over the product vibrational states is shown in Fig. 18, and the total dissociation probability is represented in Fig. 19 as a function of both the initial vibrational state v_i and the total energy E_{tot} . Although these three dimensional surfaces of the probabilities bear a certain similarity to those of

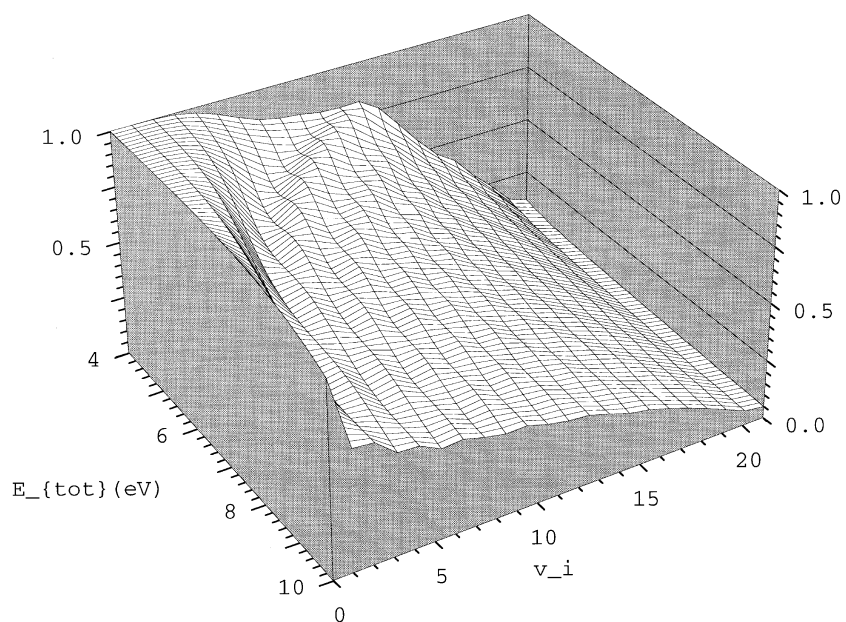


FIG. 17. Three dimensional surface plot of the probability of the total non-reactive vibrational transition summed over the reactant final vibrational states in $\text{He} + \text{TH}^+(v_i)$ collinear collision as a function of both the initial vibrational state v_i and the total energy E_{tot} .

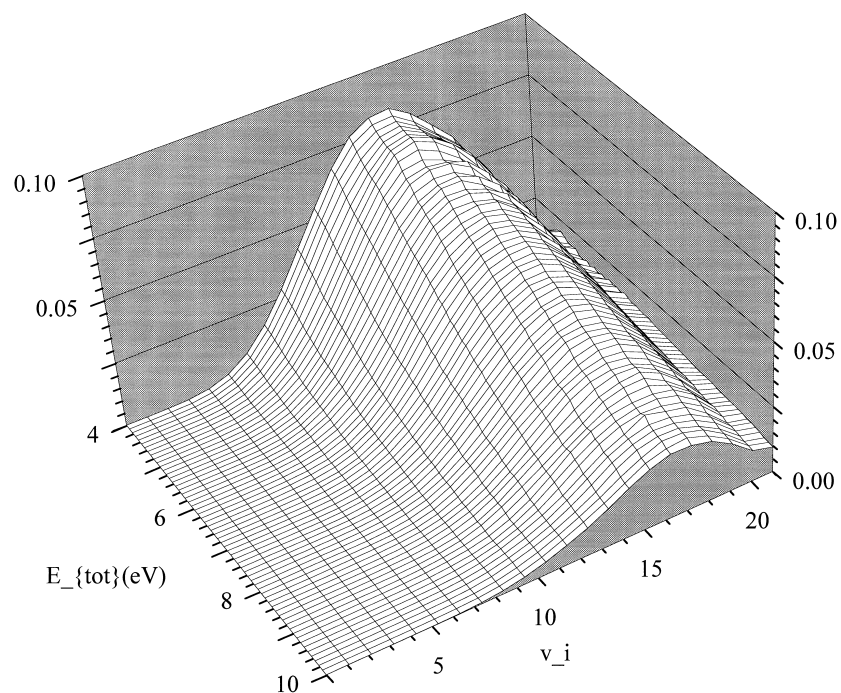


FIG. 18. Three dimensional surface plot of the probability of the total reaction summed over the product vibrational states in $\text{He} + \text{TH}^+(v_i)$ collinear collision as a function of both the initial vibrational state v_i and the total energy E_{tot} .

$\text{He} + \text{DH}^+$ collision in view of dependence on both E_{tot} and v_i , but they are quite different from those of $\text{He} + \text{H}_2^+$, HD^+ , HT^+ collisions.

The probabilities shown in Figs 17–19 for each collision process are plotted as a function of E_{tot} for the total non-reactive vibrational transition (shown by a solid line), the total

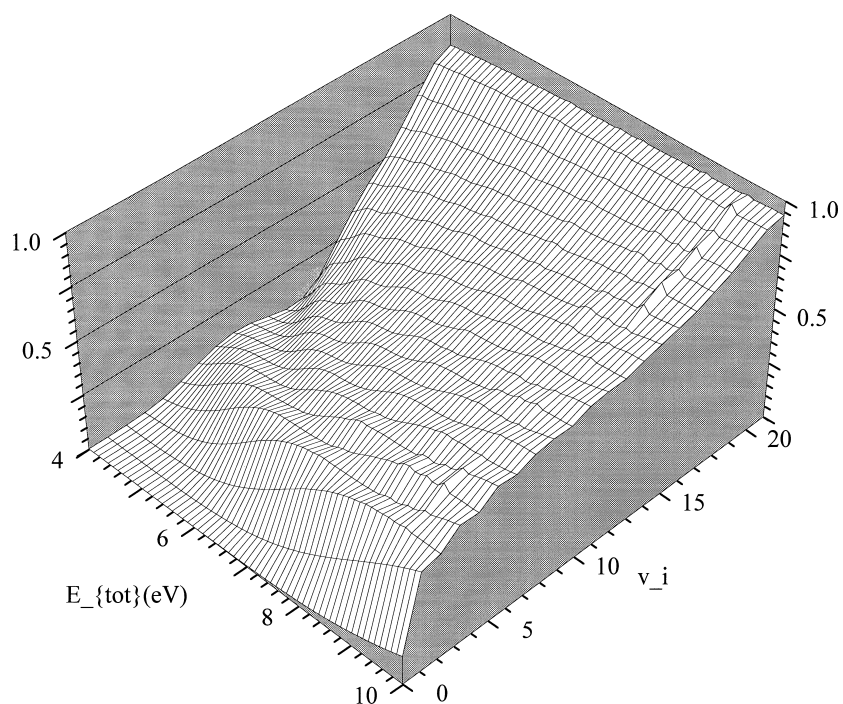


FIG. 19. Three dimensional surface plot of the total dissociation probability in $He + TH^+(v_i)$ collinear collision as a function of both the initial vibrational state v_i and the total energy E_{tot} .

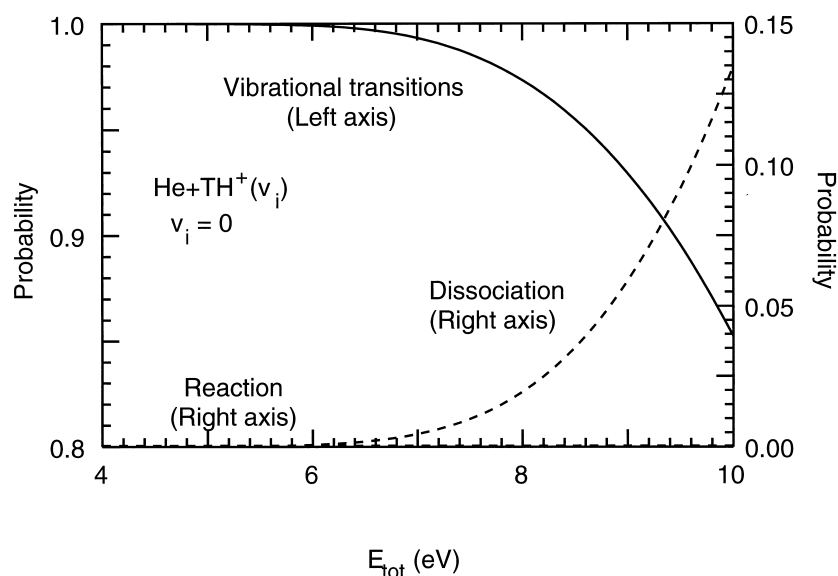


FIG. 20(a). The energy dependence of the probabilities of the total non-reactive vibrational transition (shown by a solid line with the letter of “vibrational transitions”), the total atom exchange reaction (shown by a dotted line with “reaction”), and the total dissociation (shown by a long dashed line with “dissociation”) in $He + TH^+(v_i)$ collision with $v_i = 0$.

atom exchange reaction (a dashed line), and the total dissociation (a long-dashed line) in Figs 20(a)–(f) from an indicated initial vibrational state of $v_i = 0, 4, 8, 12, 16,$ or $20,$ respectively.

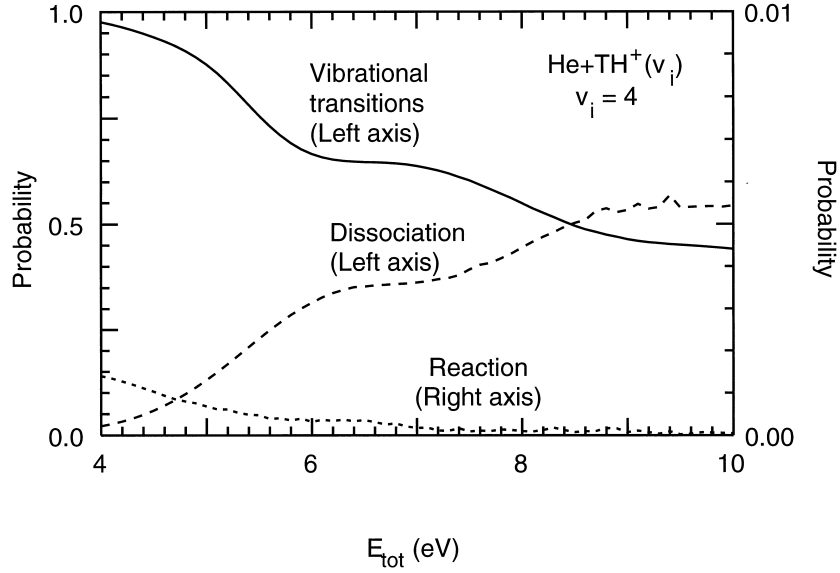


FIG. 20(b). The same as Fig. 20(a) except for $v_i = 4$.

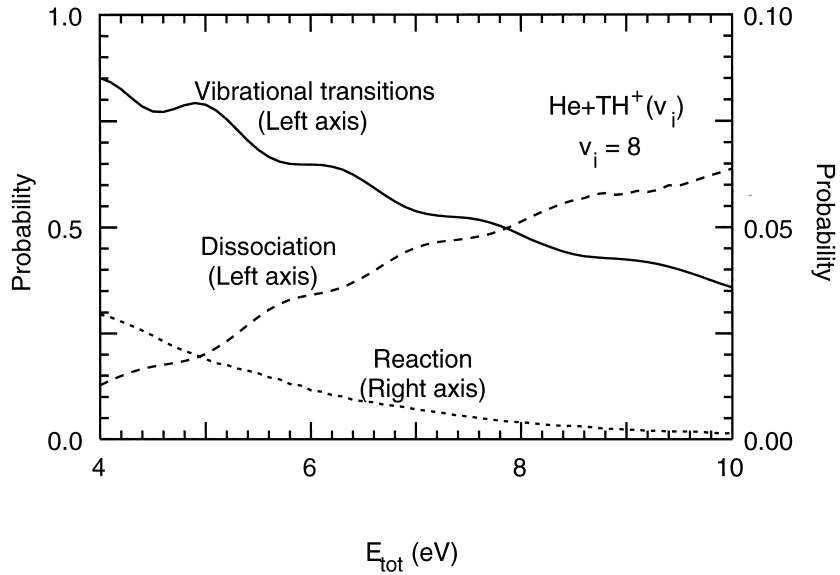


FIG. 20(c). The same as Fig. 20(a) except for $v_i = 8$.

The reaction probabilities are less than 0.03 for $0 \leq v_i \leq 8$ and $20 \leq v_i \leq 21$ at the total energy $4 \leq E_{tot} \leq 10$ eV, and have the magnitude of 0.03 - 0.08 for $9 \leq v_i \leq 19$ at the total energy $4 \leq E_{tot} \leq 8$ eV. The reaction process is really negligible for nearly all initial vibrational states. These results are special for this mass combination.

The non-reactive vibrational transitions are the major processes and the magnitude of these probabilities is larger than 0.5 for $0 \leq v_i \leq 8$ at the total energy $4 \leq E_{tot} \leq 10$ eV, and for $9 \leq v_i \leq 13$ at $6 \leq E_{tot} \leq 7$. The energy dependence of these probabilities changes in shape as a function of E_{tot} for mainly three groups of the initial vibrational state $v_i \leq 2$, $3 \leq v_i \leq 15$, and $16 \leq v_i$.

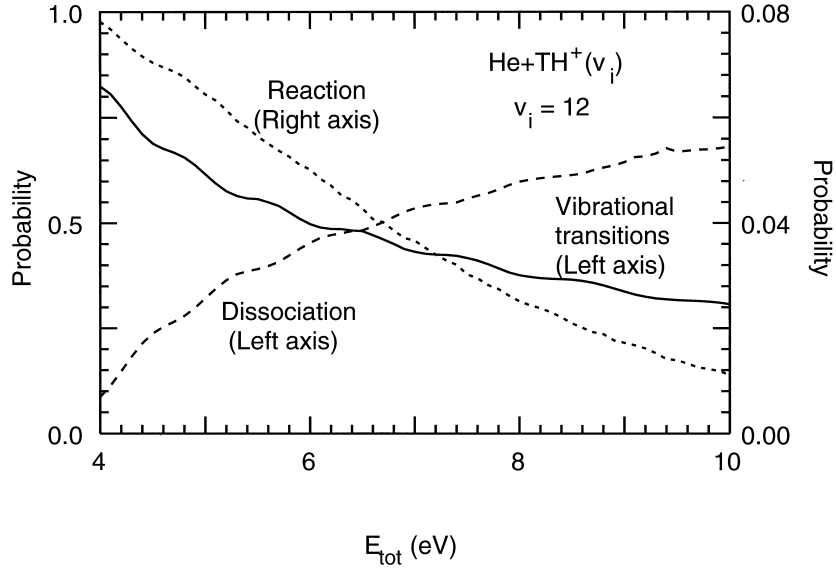


FIG. 20(d). The same as Fig. 20(a) except for $v_i = 12$.

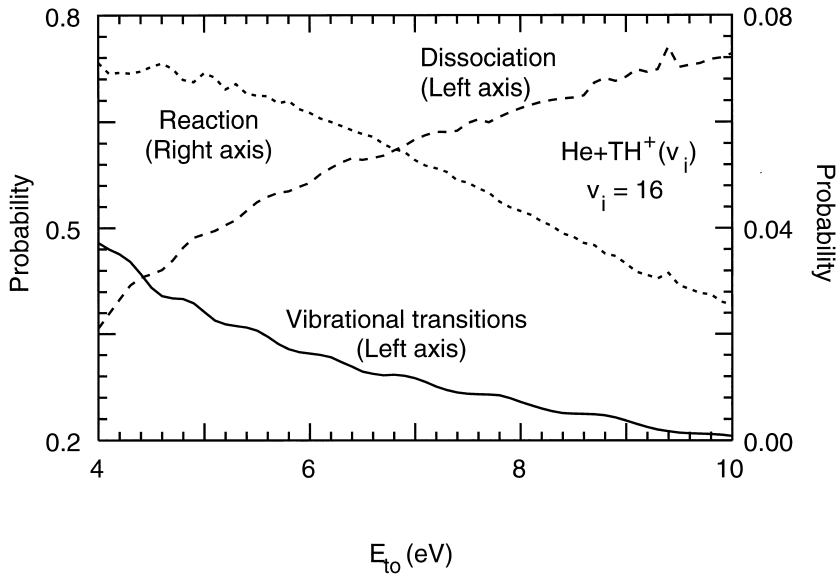


FIG. 20(e). The same as Fig. 20(a) except for $v_i = 16$.

The probabilities of the dissociation for the initial vibrational states $8 \leq v_i \leq 12$ become larger than those of the non-reactive vibrational transitions at $6 - 8 \leq E_{tot} \leq 10$ eV, and the dissociation process dominates over the non-reactive vibrational transitions for $15 \leq v_i$ at $4 - 5 \leq E_{tot} \leq 10$ eV. The internal energy stored in the vibrational mode is effective to enhance the dissociation for nearly all of the initial vibrational states v_i .

5. Concluding remarks

We have investigated quantum mechanically the collinear collisions of ${}^4\text{He} + \text{H}_2^+(v_i)$ system with different hydrogen isotopes and calculated the probabilities for the non-reactive

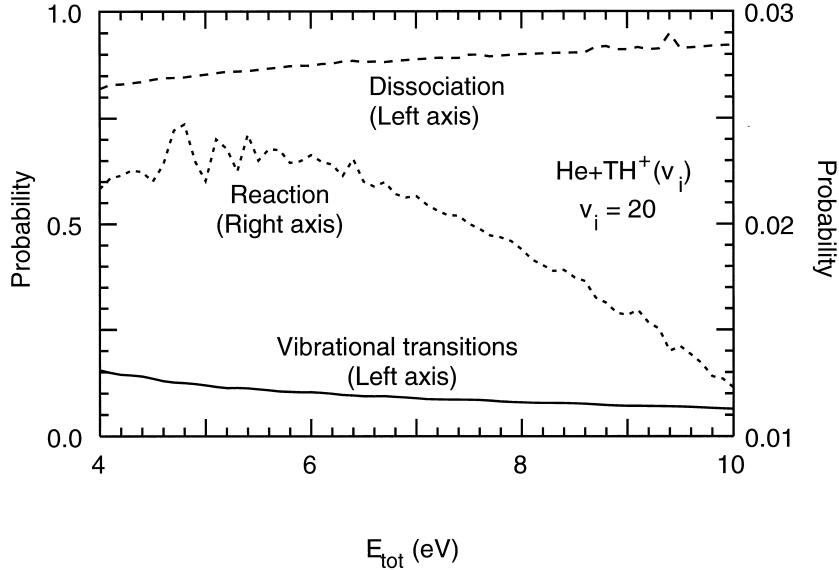


FIG. 20(f). The same as Fig. 20(a) except for $v_i = 20$.

vibrational transition, atom exchange reaction, and dissociation processes for all the initial vibrational states at a wide range of the total energy $4 \leq E_{tot} \leq 10$ eV.

Since the shapes of the potential energy surface (PES) are known to be different for different isotopes, the collision dynamics in the present collision system is expected to be varied depending on isotopes involved. Indeed, as seen in a series of Figs 1–20, a remarkable isotope effect has been demonstrated in the present calculations. As the collision dynamics depends on the initial vibrational state, the probabilities for the processes mentioned above have also calculated for the possible vibrational states.

Thanks to the reasonable accuracies in the electronically lowest PES [7, 8] and the established accuracies of the present calculation procedures, the present results are believed to be quite reliable for all the initial vibrational states investigated over the wide range of the total energy.

In the collinear $\text{He} + \text{HD}^+(v_i)$ collisions, the non-reactive vibrational transitions dominate over the reaction and dissociation processes for the initial vibrational states of $0 \leq v_i \leq 3$ and $12 \leq v_i \leq 19$ at the total energy over $4 \leq E_{tot} \leq 10$ eV. These results are appreciably different from those of the collinear $\text{He} + \text{H}_2^+(v_i)$ collisions. Thus, it is important to emphasize that the detailed studies for different isotopes are necessary to understand the present collinear collision dynamics as no simple interpolation or extrapolation seems work.

In paper V, we have discussed the results of the collinear $\text{He} + \text{H}_2(v_i)$ collision by considering the role of the interaction potentials on dynamics. It is highly desirable to analyze the results of the isotope variations of $\text{He} + \text{H}_2(v_i)$ collision system based on this physical point of view [14].

REFERENCES

- [1] D.E. Post, J. Nucl. Mater. **220–222**, 143 (1995).
- [2] K. Sakimoto, K. Onda, J. Chem. Phys. **100**, 1171 (1994).
- [3] K. Sakimoto, K. Onda, Chem. Phys. Lett. **226**, 227 (1994).
- [4] D.J. Kouri, M. Baer, Chem. Phys. Lett. **24**, 37 (1974).
- [5] J.T. Adams, Chem. Phys. Lett. **33**, 275 (1975).
- [6] P.J. Kuntz, Chem. Phys. Lett. **16**, 581 (1972).
- [7] T. Joseph, N. Sathyamurthy, J. Chem. Phys. **86**, 704 (1987).
- [8] D.R. McLaughlin, D. L. Thompson, J. Chem. Phys. **70**, 2748 (1979).
- [9] K. Sakimoto, Chem. Phys. Lett. **248**, 414 (1996).
- [10] K. Sakimoto, J. Chem. Soc. Faraday Trans., **93**, 791 (1997).
- [11] K. Onda, K. Sakimoto, J. Chem. Phys. **111**, 988 (1999).
- [12] J.T. Muckerman, Chem. Phys. Lett. **173**, 200 (1990).
- [13] J.E. Dove, M. E. Mandy, V. Mohan, N. Sathyamurthy, J. Chem. Phys. **92**, 7373 (1990).
- [14] K. Onda, in preparation.

Recombination of hydrogen on a carbon surface

M. Rutigliano, M. Cacciatore

CNR-Centro di Studio Chimica dei Plasmi,
Dipartimento di Chimica, University of Bari,
Bari, Italy

Gert D. Billing

Department of Chemistry,
H.C. Ørsted Institute, University of Copenhagen,
Copenhagen, Denmark

Abstract. A semi-classical model has been used to calculate energy accommodation and probabilities for recombination of hydrogen on a carbon surface. The information obtained is relevant for simulations of hot plasmas near a surface of carbon.

1. Introduction

A semi-classical theory for atom/molecule surface dynamics has been used to study recombination and dissociation reactions as well as diffusion processes on solid surfaces [1]. Such processes are important both from a fundamental as well as a technological point of view. Knowledge about the energy accommodation as well as the recombination and reaction processes on surfaces is crucial for the modeling of non-equilibrium kinetics as that relevant for understanding the behaviour of plasma chemistry, interstellar and atmospheric chemistry involving processes on for instance grains of carbon or ice crystals. Quantities as dissociative sticking, recombination and desorption are important ingredients for our understanding of the chemistry involved in such complex chemical processes occurring in hot plasmas and it is the purpose of the present paper to give data relevant for the hydrogen-carbon system. Previous calculations have considered recombination of hydrogen and deuterium on a copper surface [2, 3]. By combining recent progress in *ab initio* and here especially in density functional theory (DFT) for the calculation of the interaction potential with the methods developed for a dynamical treatment of surface processes it has become possible to obtain a detailed, i.e. at the molecular level, knowledge about mechanisms, final state distributions of molecules, energy accommodation etc.

2. Theory

The semi-classical model used in the present calculations is described in detail in Ref. [1] and numerous papers [4]. We shall therefore only briefly summarize the important points here.

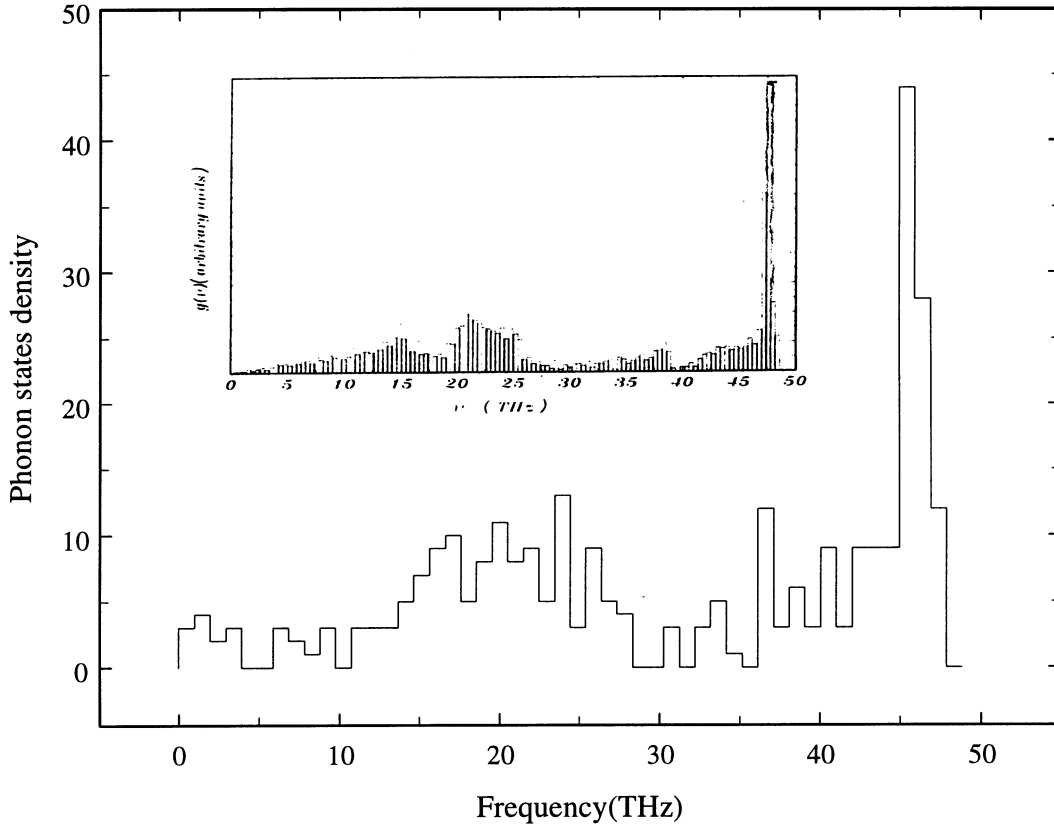


FIG. 1. Phonon frequency spectrum.

We assume that the dynamics of the gas-phase atom can be followed using classical trajectories, i.e. by solving the classical equations of motion using however an effective interaction potential consisting of three terms:

$$V_{eff} = V_{HH}(r) + V_{HH/C}(\{R_{ij}\}) + V_{add} \quad (1)$$

where the first term is the interaction potential between the two hydrogen atoms (usually taken as a Morse potential) and $r = R_{H-H}$ (the hydrogen bond distance). The next term is the intermolecular potential for the hydrogen-solid interaction with the solid atoms in their reference, i.e. equilibrium positions and R_{ij} denote atom-atom distances. The last term is a potential which depends upon the excitation processes occurring in the solid, i.e. it depends not only on the positions of the surface atoms but also upon the degree of phonon and electron excitation in the solid [5]. Thus this potential is time-dependent and couples the excitation processes in the solid to the motion of the gas-phase atoms in a selfconsistent manner. By including a distribution of phonon states according to the surface temperature, the last term also becomes a surface temperature dependent term. For details the reader is referred to refs. [1, 4].

The phonons are treated simply as a set of normal mode oscillators. We obtain the normal mode eigenvalues (the spectrum) and eigenvectors by diagonalizing the force constant matrix for a finite size crystal. Our previous calculations have shown that the quantities we are interested in converge with a crystal size of about a few hundred atoms.

Thus the effective hamiltonian can be written as

$$H_{eff} = \sum_{i=1,2} \frac{1}{2m_i} (p_{x_i}^2 + p_{y_i}^2 + p_{z_i}^2) + V_{eff} + E_{int}(t) \quad (2)$$

where the first term is the kinetic energy of the gas-phase atoms and the last term is the energy transferred to the solid, depending upon time (and surface temperature) only.

3. Phonon Dynamics

The interaction of hydrogen atoms with a model graphite surface has been examined according to the dynamical semi-classical method described in the previous section.

The graphite surface sample used in the scattering calculations has been modeled by repeating four times in 3D space the unit cell of the hexagonal graphite. The model crystal K62/62/62 consists of 186 carbon atoms displayed over three layers according to the appropriate lattice symmetry. The resulting lattice is used to model the phonon properties of the surface. In particular, to calculate the dynamical matrix associated with the vibrational normal modes of the lattice atoms we use the most important central and angular forces between the nearest and next-nearest neighbours in plane and out of plane carbon atoms recently obtained from semi-empirical calculations [6]. By numerical diagonalization of the force constant matrix the phonon eigenvalues and eigenvectors needed in scattering calculations are obtained.

The phonon frequency spectrum is shown in Fig. 1. The frequency range as well as the two peaks at 22 and 47 THz typical for graphite are well reproduced. As can be noticed, there is a general very good agreement between the obtained spectrum and the phonon density distribution of Ref. [6] shown in the inset on Fig. 1.

4. The H, H₂/Graphite interaction potential

We express the full atom/surface interaction as a sum of two terms

$$V_{int} = V_{H_2/C} F_S + V_{H/C} (1 - F_S) \quad (3)$$

where $V_{H/C}$ and $V_{H_2/C}$ are, respectively, the interaction potential between the atomic and molecular hydrogen in the gas-phase and the carbon atoms of the lattice sample. The F_S function is defined by

$$F_S = -0.5((\tanh(2.65R_{H-H} - 2.65)) - 1) \quad (4)$$

It smoothly switches the potential from one term to the other according to the interatomic separation R_{H-H} between the two hydrogen atoms.

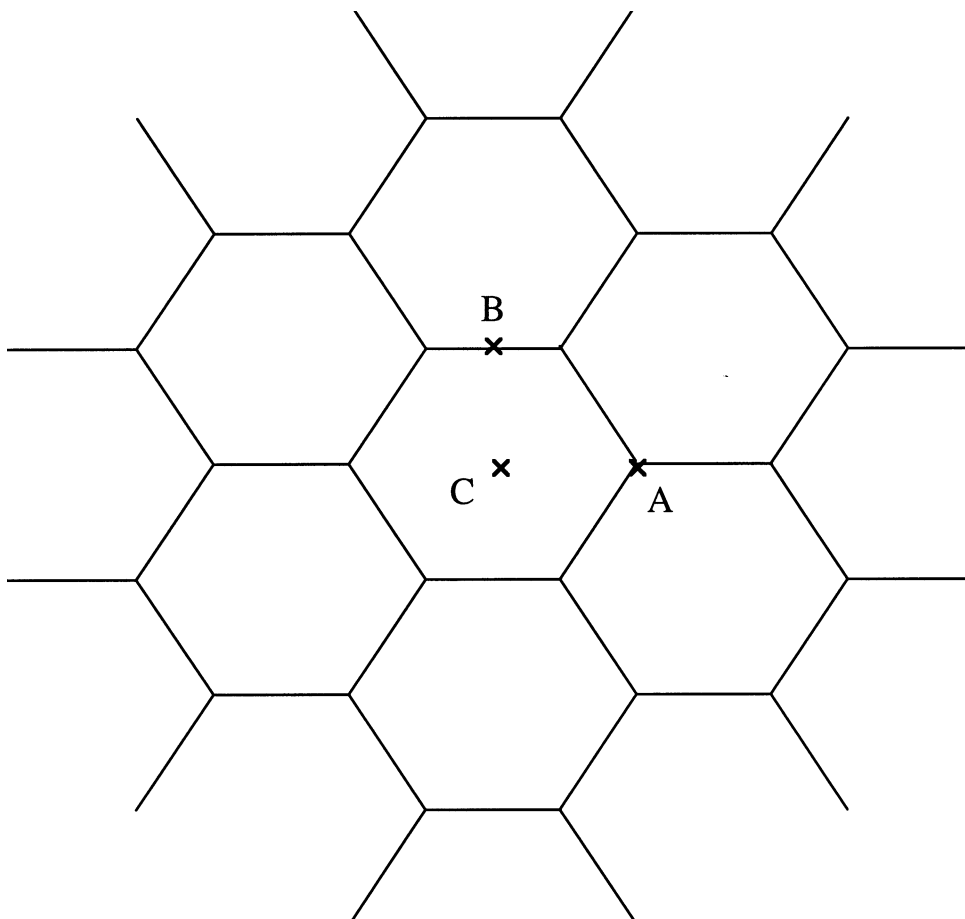


FIG. 2. The surface structure and the lattice points A, B and C.

The first term in 3 was modeled on the basis of ab initio binding energy calculations recently reported in the literature. For H_2 interacting with graphite we refer to the experimental results obtained from molecular beam experiments [7] subsequently confirmed in electronic structure calculations [8]. In these latter works it has been shown that, irrespective of the adsorption surface site, H_2 is physisorbed on graphite in the perpendicular geometry at a distance from the surface of about 2.8 \AA with a negligible adsorption energy of 51.55 meV .

In contrast to this atomic hydrogen is chemisorbed on graphite. This potential has been explored in several theoretical electronic structure calculations where different semiempirical electronic structure methods has been used to calculate the surface binding energy for a hydrogen atom interacting with carbon at different adsorption sites [9]. We refer in the present work to the most recent results reported by Fromherz et al. [9]. In this study the binding energies of hydrogen approaching the surface perpendicularly on top at three different sites were calculated as a function of the atom-surface distance.

It turns out that on site B, shown in Fig. 2, the hydrogen is physisorbed at a distance of about 1.5 \AA from the surface with a negligible adsorption energy of about 0.05 eV , but when the interaction occurs on top of a carbon atom according to site A of Fig. 2, the hydrogen is chemisorbed with a bonding energy of $\sim 1.3 \text{ eV}$ at a distance of $\sim 1.5 \text{ \AA}$ from the surface. On site C, at the centre of the hexagonal ring, the interaction is repulsive. We mention in passing that in recent DFT calculations performed on the same system

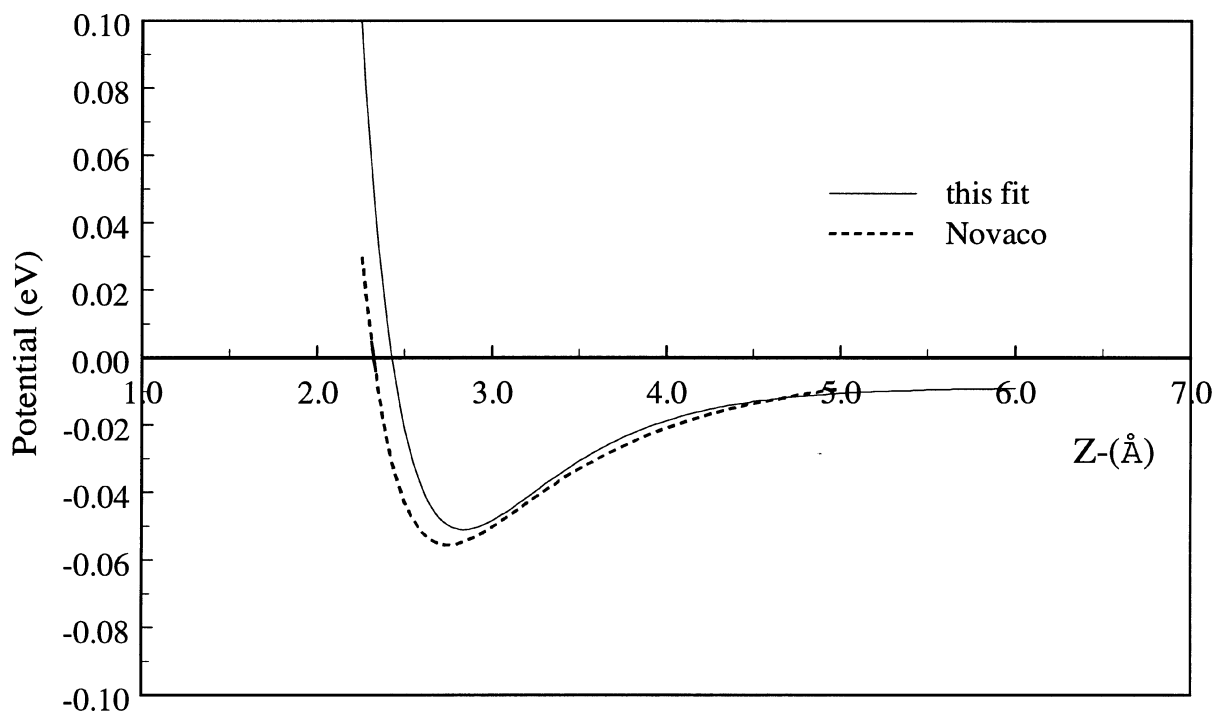


FIG. 3. Hydrogen molecule surface interaction as a function of the distance to the surface. The dashed line indicate data from Ref. [8].

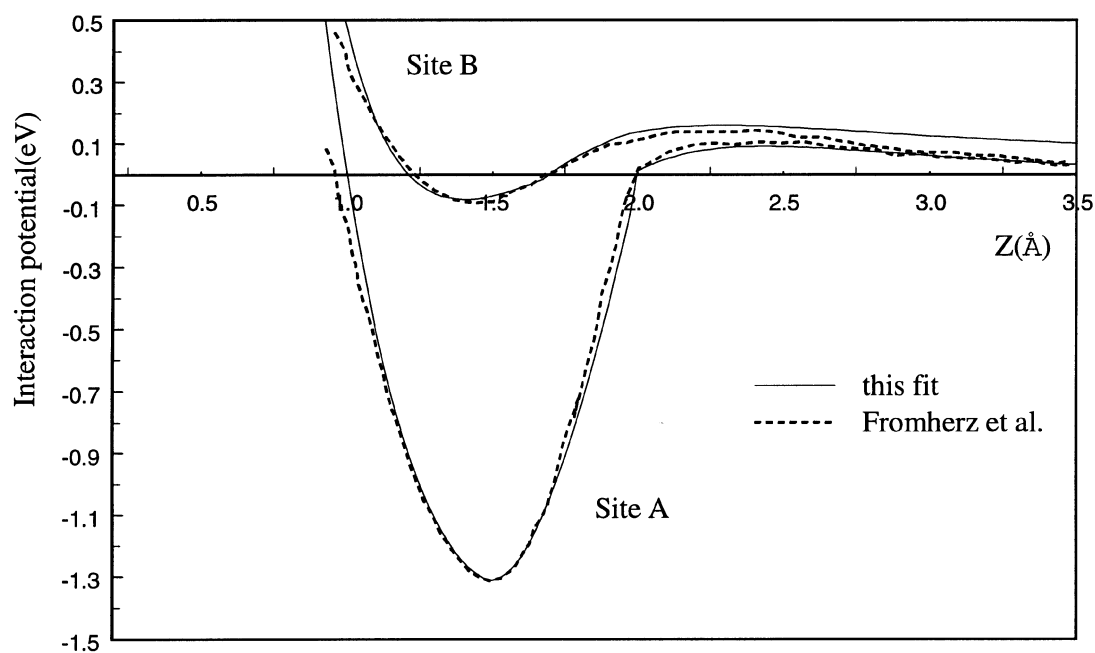


FIG. 4. Hydrogen atom surface interaction as a function of distance to the surface at sites A and B. Dashed lines indicate data from [9].

[10], appearing after the present work had started, the well depth obtained for site A is of ~ 0.63 eV, a factor of two lower with respect to the value calculated by Fromherz et al. and used in our work. A general agreement among the two works is found for the position of the well for site A as well as for the physisorption behaviour of hydrogen on the B site. Nevertheless, it is quite clear that a drastic reduction of the energy well depth in the atom/surface interaction potential will have consequences for the catalytic activity

Site A Perpendicular

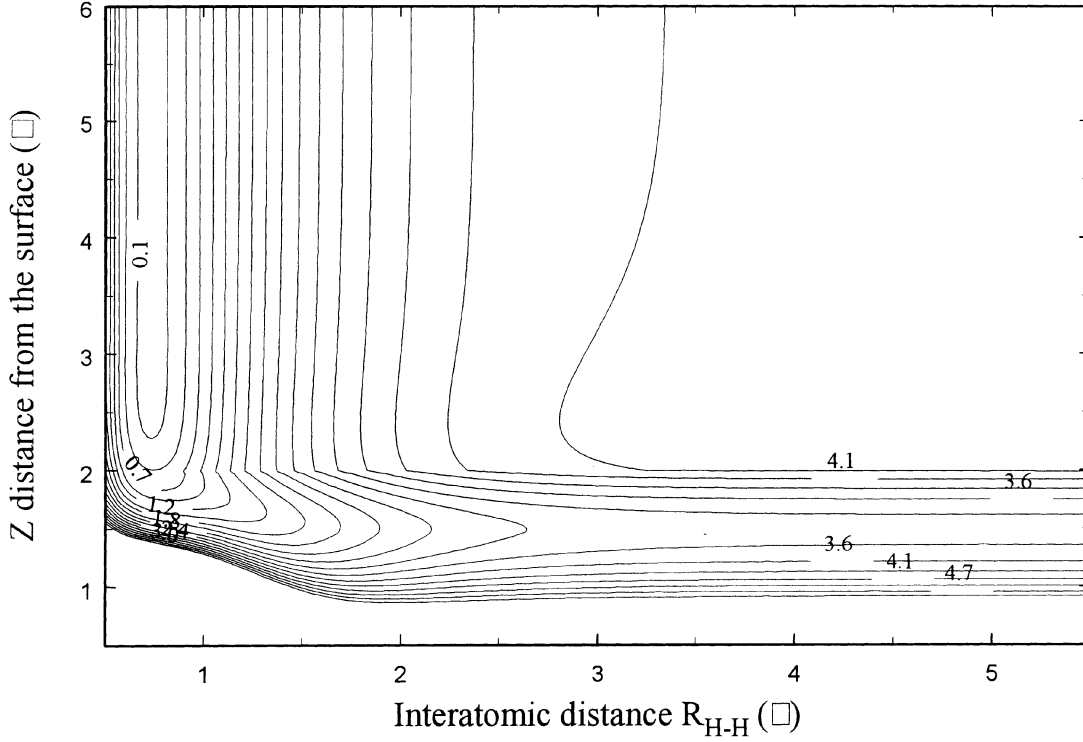


FIG. 5. Hydrogen-surface interaction (contour maps) at site A as a function of the center of mass distance from the surface and the hydrogen bond distance. Distances in Å and energies in units of eV.

of the surface. We assume for the atom and molecule/surface interactions the following parametric potentials:

$$V_{H_2/C} = \sum_{j=1}^2 \sum_{i=1}^N D \exp(-p(R_{ji} - 3.255)) (\exp(-p(R_{ji} - 3.255)) - 2.) - a \quad (5)$$

$$V_A = \begin{cases} \sum_{j=1}^2 \sum_{i=1}^N a \exp(-b(R_{ji} - 2.185)) (\exp(-b(R_{ji} - 2.185)) - 2.) + q & Z \leq 1.48 \\ \sum_j \sum_i a_1 \exp(-b(R_{ji} - 2.12)) (\exp(-b(R_{ji} - 2.12)) - 2.) + q_1 & 1.48 < Z_H \leq 1.98(4) \\ \sum_j \sum_i -a_2 \exp(-b_2(R_{ji} - 2.8)) (\exp(-b_2(R_{ji} - 2.8)) - 2.) & Z_H > 1.98 \end{cases} \quad (6)$$

$$V_B = \begin{cases} \sum_j \sum_i a \exp(-b(R_{ji} - 1.63)) (\exp(-b(R_{ji} - 1.63)) - 2.) + q & Z_H \leq 1.68 \\ \sum_j \sum_i a_1 \exp(-b_1(R_{ji} - 2.7)) (\exp(-b_1(R_{ji} - 2.7)) - 2.) + q_1 & Z_H > 1.68 \end{cases} \quad (7)$$

$$V_C = 0.07 \exp(-2.05(R_{ji} - 2.)) \quad (8)$$

Table 1. Potential parameters for the interaction $V_{H_2/C}$

D(eV)	p(\AA^{-1})	a ₁ (\AA)	a(eV)
3.287(-3)	1.985	3.255	2.375(-5)

Table 2. Potential parameters for the interaction V_A

a(eV)	b(\AA^{-1})	q(eV)	a ₁ (eV)	q ₁ (eV)	a ₂ (eV)	b ₂ (\AA^{-1})
0.284	1.096	1.350(-2)	0.795	4.940(-2)	1.040(-2)	1.733

Table 3. Potential parameters for the interaction V_B

a(eV)	b(\AA^{-1})	q(eV)	a ₁ (eV)	b ₁ (\AA^{-1})	q ₁ (eV)
0.079	2.700	1.000(-3)	9.200(-3)	1.6	2.0(-4)

where V_A , V_B and V_C are the interaction potentials for surface sites A, B and C respectively. R_{ji} is the separation distance between the hydrogen atom j in the gas-phase and the lattice atom i of the surface. N is the total number of surface carbon atoms. It should be noticed that we for simplicity have used the hydrogen-atom potential for site A in the present calculations. A more elaborate procedure would use switching functions of the type described above in order to distinguish between the sites. Since this calculation would involve the introduction of further at present undetermined parameters we have not considered this aspect here.

The potential parameters for the H_2 /surface interaction were fitted to the experimental potential determined in Ref. [7]. Similarly, the fitting parameters for the H/surface potentials were obtained so as to reproduce the main features of the theoretically predicted potentials for these interaction sites [9]. Figs 3, 4 show the one-dimensional $V_{H_2/C}$ and $V_{H/C}$ potentials as a function of the distance from the surface. A comparison between the calculated and the reference potentials is also shown. Fig. 5 shows the energy contour plot of the complete molecule/surface potential $V_{int} + V_{H_2}$ for hydrogen interacting with the carbon surface at site A as a function of the bond distance and the distance from the surface to the center of mass of the molecule (Z). We notice that V_{H_2} denote the intramolecular Morse potential of the free molecular hydrogen. From the displayed PES we see that there is no energy barrier for H_2 formation. The potential parameters for the best fit are given in Tables 1–3.

5. Trajectory calculations

Making use of the semiempirically determined PES, which however should be considered acceptable as qualitative only, also due to the insufficient or contrasting data available for the H/graphite interaction, the semiclassical dynamics of hydrogen impinging on a

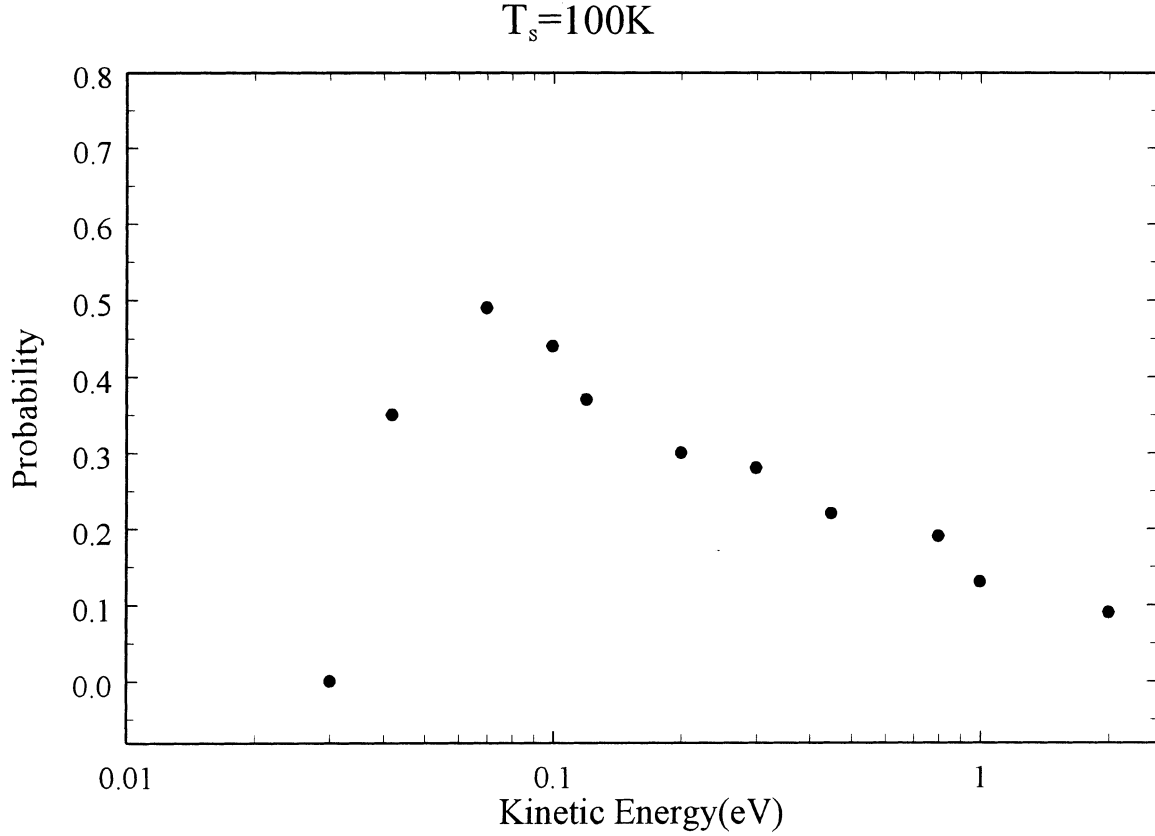
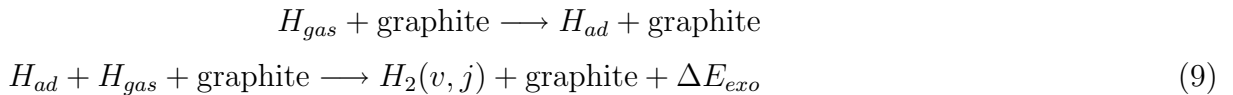


FIG. 6a. Recombination probability as a function of incident kinetic energy at surface temperature 100 K.

graphite surface was then developed aiming at determining at least some of the most basic features of the processes taking place at the surface. We in particular focus on the H_2 formation after hydrogen atom adsorption at the surface. As it is well known, this process can occur through two mechanisms. In the ‘direct’ Eley-Rideal mechanism the recombination takes place through two steps: first a hydrogen atom is chemisorbed, then the ad-atom, possibly scattered from the surface, reacts with the atom approaching the surface from the gas-phase to form molecular hydrogen in a specific vibrational and rotational state:



According to the Langmuir-Hinshelwood mechanism the reaction occurs between two adsorbed hydrogen atoms which migrate on the surface and then recombine.



The dynamics and the energetics of two reactions are substantially different and so the macroscopic conditions (surface coverage, surface temperature, gas pressure and temperature, etc.) under which one of the two processes can be preferentially activated. In particular, in the L-H mechanism the nuclear motion of both adsorbed atoms occurs through

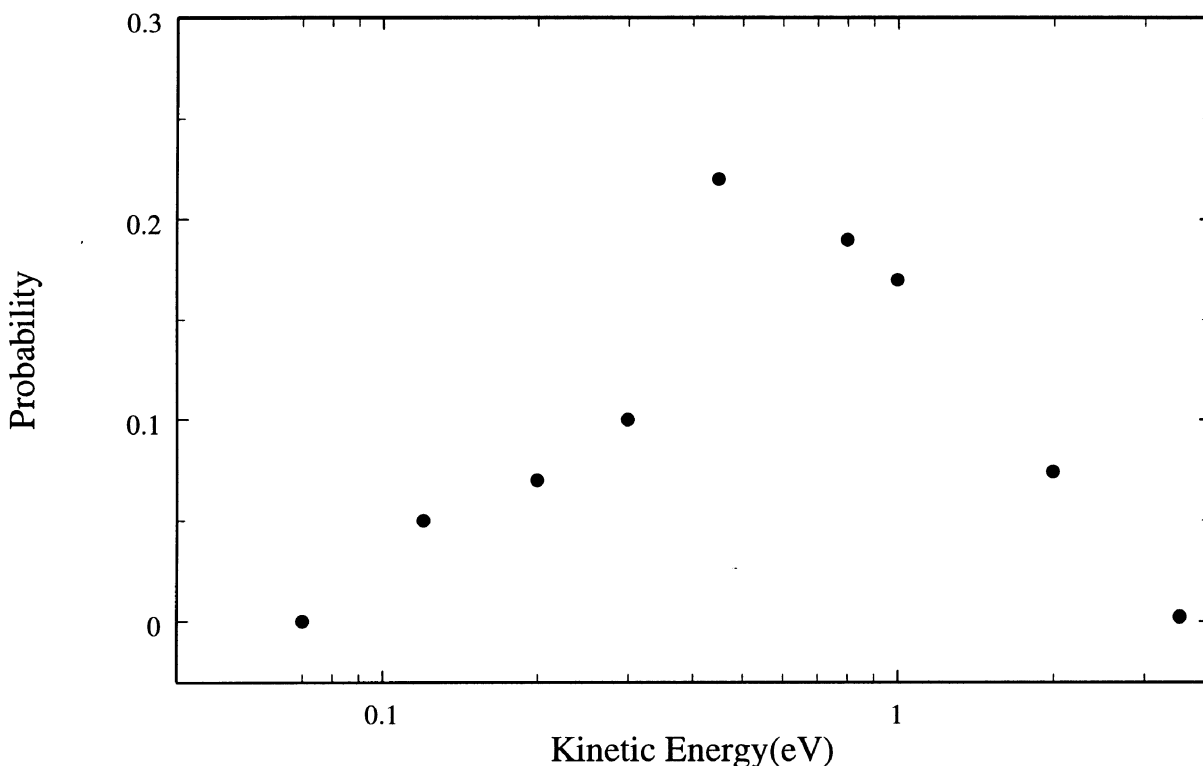


FIG. 6b. Same as Fig. 6a but for surface temperature 500 K.

a diffusive process across the surface between adjacent surface sites until the minimum energy path to reaction is found. Consequently, the simulation of such complex reaction mechanism would require the knowledge of the full topology of the interaction potential, in particular the height and position of the energy barriers from site to site. For the case under study this information is, at the moment, not available yet (although the recent calculations by Sidis et al.[10] show the existence of a large lateral energy barrier, of about 0.3 eV, that would prevent the diffusion of the chemisorbed atom along the surface plane). Therefore, the rate determining step of the E-R recombination reaction was considered in the present study aiming at determining the most important feature of the surface process. We in particular focus on two fundamental aspects, that is, reaction probabilities and energy flow pathways between the graphite surface and the reaction products. In the simulation we assume that H_{ad} is chemisorbed on site A at the equilibrium distance of 1.5 Å from the surface and in thermal equilibrium at the surface temperature T_S , while the hydrogen atom in the gas phase strikes the graphite surface at a given kinetic energy perpendicularly with respect to the surface plane (polar angles $(\theta, \varphi)=(0,0)$). For each impact energy of H_{gas} a batch of about 2000 trajectories were computed.

Fig. 6a shows the calculated E-R recombination probability $P_{E-R}(E_{kin})$ at $T_S=100$ K as a function of the kinetic energy of the impinging atom. In Fig. 6b the same probability is shown for a surface temperature of 500 K. We notice that higher surface temperature decreases the probability for recombination through the E-R mechanism. The higher surface temperature increases the probability that one of the atoms leave the surface without reacting.

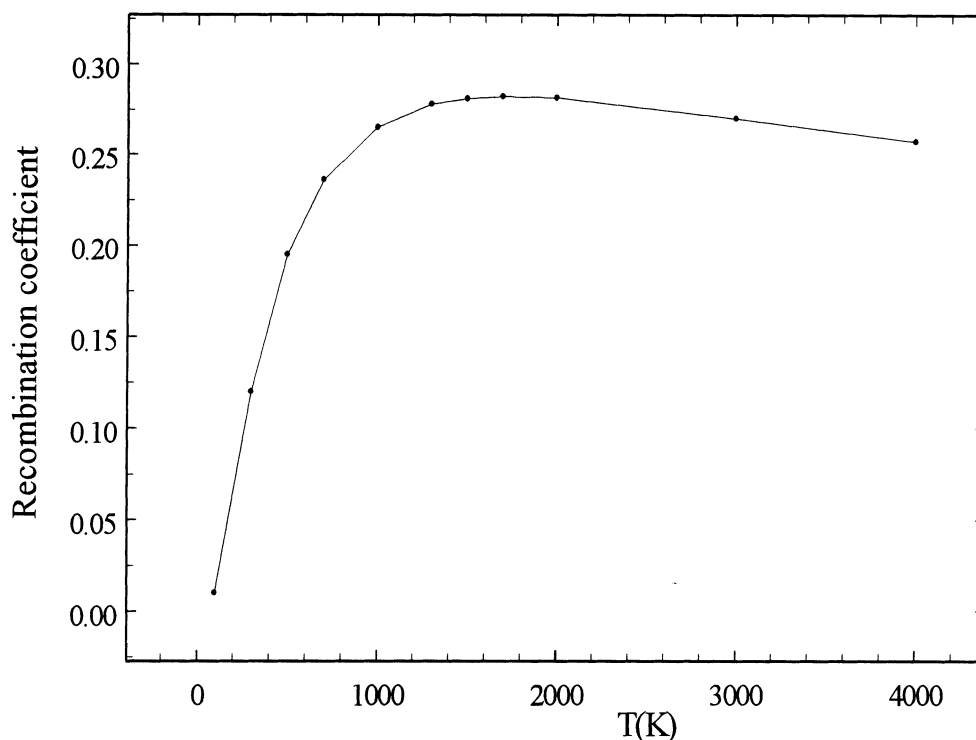


FIG. 7. Recombination probability as a function of the temperature of the incident atoms. The surface temperature is 100 K.

Fig. 7 shows the recombination coefficient $\gamma(T_{gas}, T_S)$ obtained from the calculated probabilities and assuming that a flux of hydrogen atoms hits the surface with a Maxwellian translational energy distribution at a given temperature T_{gas} . The recombination coefficient increases with the kinetic energy. The reason for this is that at low kinetic energy the amount of energy available to the incoming atom is too small for the molecule to be formed before the interaction with the phonons of the solid has trapped the atom (see also Fig. 10).

The analysis of the energy distribution in the reactive collisions shows that, as expected due to the release of the hydrogen binding energy, the desorbing H_2 molecules are formed in the low-lying vibrationally excited states up to $v=4$. However, the product molecules were found to be formed for the largest fraction in the $v=0$ and $v=1$ states, that is only a small fraction of the exothermic energy released in the reaction is shared among the internal state of the newly formed molecules. Indeed, a consistent part, $\sim 1.5eV$, of exothermicity ΔE_{exo} is acquired from the adsorbed hydrogen atom to escape from the chemisorption well. A non-negligible fraction of the reaction energy is also dissipated to the vibrational motions of the surface atoms (see Figs 8, 9). The vibrational population distributions of H_2 calculated at the various impact energies are reported in Figs 8, 9.

The recombination reaction is not the only possible surface process: the interaction of hydrogen with graphite can in fact lead to the activation of several other processes including the following adsorption and adsorption/desorption processes considered in the molecular dynamics simulation:

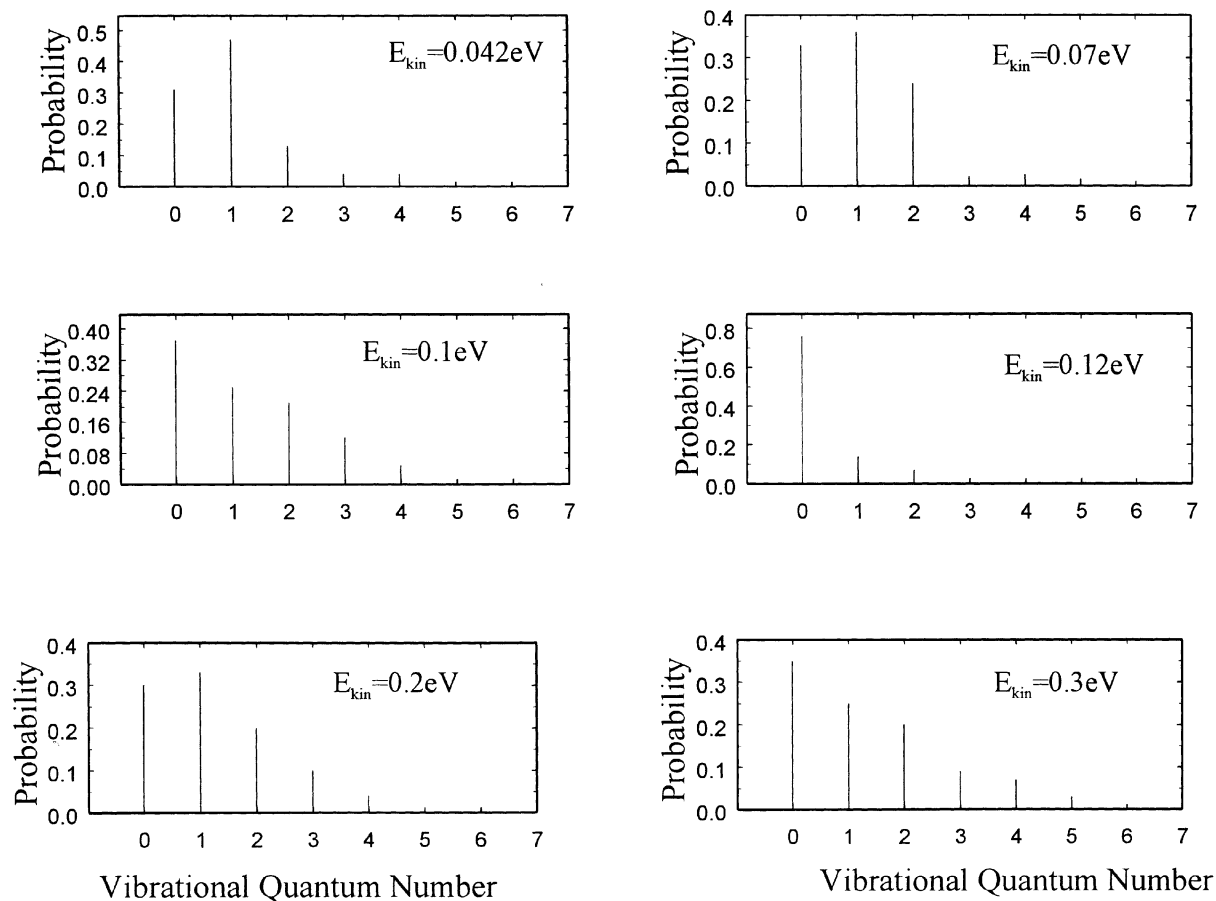


FIG. 8. Population of vibrational excited hydrogen in the recombination processes for kinetic energies 0.042 eV to 0.30 eV.

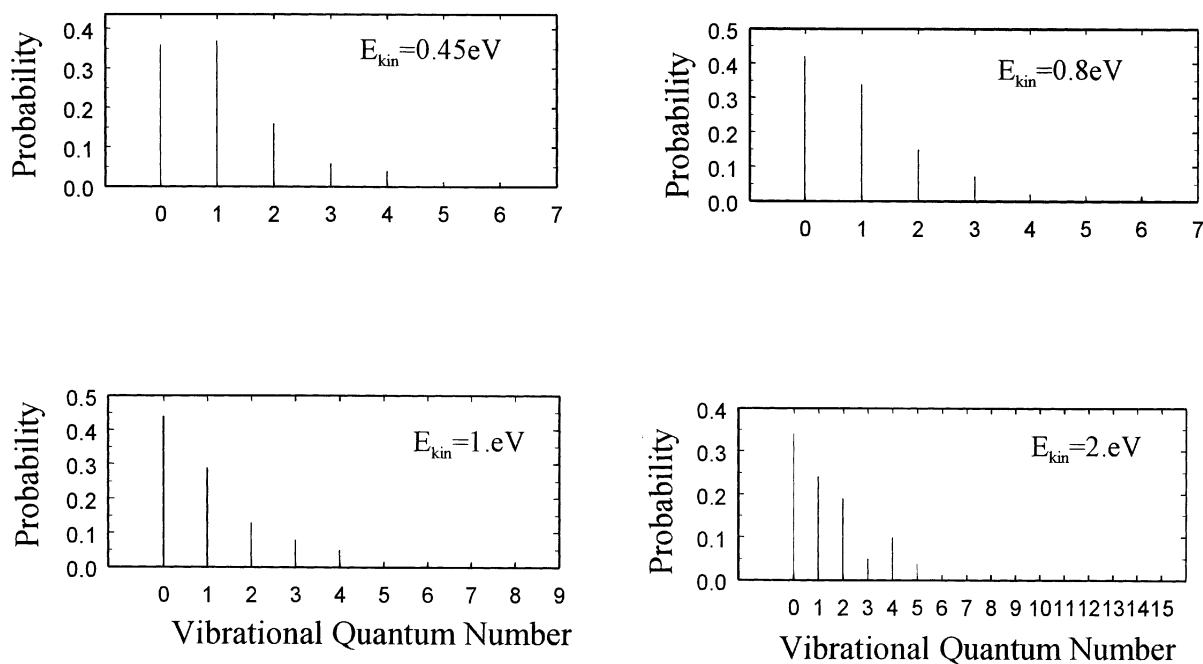


FIG. 9. Same as Fig. 8 but for energies 0.45 eV to 2 eV.

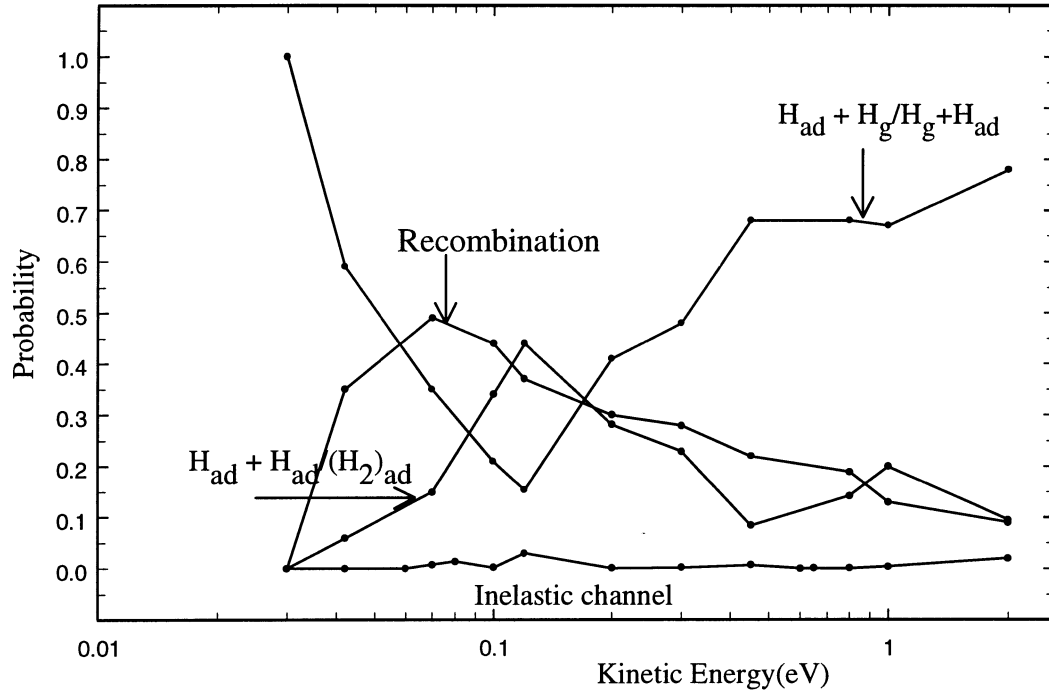
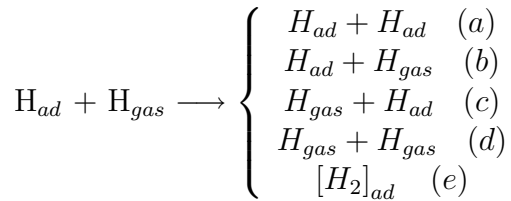


FIG. 10. Probability for recombination, adsorption of both atoms, one atom and scattering of both atoms (inelastic) as a function of kinetic energy. The surface temperature is 100K.



The last channel, that is the trapping of molecular hydrogen at the surface, is very unlikely due to the weak physisorption nature of the H_2 /graphite interactions. Instead, of great importance are, also with respect to surface damage and performance of the plasma walls in fusion devices, processes (a)–(c) where both or one of the two hydrogen atoms are adsorbed at the surface. (By adsorption it is here understood the process that the available total energy of the hydrogen atom after interaction with the surface is less than the energy needed to escape from the surface). In the simulation we treat these processes as inelastic collisions, that is reactions of H_{ad} with the surface carbon atoms to form hydrocarbons are not considered here. Nevertheless, the relative importance of processes (a)–(c) with respect to H_2 formation in the gas-phase can be an indication of the efficiency of the surface damage reactions observed in real experiments. In Fig. 10 we report the probabilities for the reactive (recombination) and non-reactive surface processes. We notice that the recombination probability is large for kinetic energies around 0.05 to 0.2 eV. This is in contrast to the findings for recombination on a copper surface and can be explained by the weaker hydrogen-carbon bond as compared with the H-H interaction. On copper the strong hydrogen-copper bond prevents efficient recombination on that surface, hence the recombination probability is small (a few per cent) [2]. Thus on carbon the mobility is increased and thereby the probability that a recombination can occur before the criterion for adsorption is met. The process is as mentioned denoted adsorbed if the available energy, i.e. the kinetic energy + the binding energy of a hydrogen molecule is smaller than the energy transfer to the phonons E_{int} + the effective surface binding potential V_{eff} . However,

on a longer time-scale the adsorbed atoms might recombine through the L-H mechanism and form adsorbed hydrogen molecule, which on a longer time-scale could diffuse and reach a "hot" spot and desorb through phonon-assisted desorption. To include this latter process would as discussed above require a site-dependent potential energy surface. We notice that there is a considerable probability for adsorption, a process which is connected with energy transfer to the surface, i.e. heating of it will take place.

6. Summary

By using a well established and documented method [1], which is able to include the most important dynamical aspects of the many-body system, we have been able to calculate quantities relevant for hydrogen recombination on a carbon surface. Thus we have investigated the effect of the incoming kinetic energy, the dependence with surface temperature and the role of adsorption and recombination. Also the final state distribution of the scattered molecules has been obtained. From the available data it is straightforward to obtain rate constants for recombination to specific final vibrational states [2]. These rates are important for the modeling of non-equilibrium plasmas near solid surfaces or in containers consisting of carbon.

REFERENCES

- [1] G.D. Billing, "Dynamics of molecule surface interactions", Wiley, New York, 2000.
- [2] B.F. Hansen, G.D. Billing, *Surf. Sci. Lett.* **373**, 333 (1997).
- [3] G.D. Billing, *Plasma Physics Reports*, **25**, 28 (1999).
- [4] See e.g., G.D. Billing, *Chem. Phys.* **70**, 223 (1982); *Comp. Phys. Rep.* **12**, 383 (1990); *J. Phys. Chem.* **99**, 15378 (1995).
- [5] G.D. Billing, *J. Chem. Phys.* **112**, 335 (2000).
- [6] L. Lang, S. Doyen-Lang, A. Charlier and M.F. Charlier *Phys. Rev. B* **49** (1994) 5672.
- [7] L. Mattera, F. Rosatelli, C. Salvo, F. Tommasini, U. Valbusa, G. Vidali, *Surf. Sci.* **93** (1980) 515.
- [8] D. Novaco, J.P. Wroblewski, *Phys. Review B* **39** (1989) 11364.
- [9] T. Fromherz, C. Mendoza, F. Ruetter, *Mon. Not. R. Astron. Soc.* **263** (1993) 851 and references therein.
- [10] L. Jeloica, V. Sidis, *Chem. Phys. Lett.* **300** (1999) 157.

Above surface neutralization of highly charged ions interacting with a metal surface

M.N. Mirakhmedov, R.A. Salimova

Arifov Institute of Electronics,
Tashkent, Uzbekistan

Abstract. Neutralization of highly charged ions at their approaching a metal surface is investigated using the Monte-Carlo method. The electron exchange processes between highly charged ions and the conduction band of metal are considered within framework of the classical overbarrier model. The results of calculations of neutralization of $\text{Ar}^{(10-18)+}$ on Au surface have shown that a substantial part of neutralization energy can be transferred to electrons of the conduction band via both resonant loss of electrons into empty states of the conduction band and emission of captured electrons into vacuum by the promotion mechanism. As a result of the losing of the most of captured electrons over these channels the highly charged ions approach to the surface still being in charged states. The results of calculations satisfactorily describe the dependencies of total slow electron yield on highly charged ions initial velocity.

1. Introduction

At the research of neutralization of highly charged ions (HCI) at solid surface information on redistribution of energy released at the neutralization between various involved particles is most important. Such information can be obtained by investigation of spectra of both Auger- and radiative transitions occurring at the neutralization of HCI.

The advent of high-current low-energy sources for highly charged ions allowed a detailed investigation of the HCI neutralization near the surface. Auger electron [1–3] and X ray [2, 4–6] spectra have been measured. In Auger spectra both the peaks formed as a result of above surface Auger neutralization of ion and the peak formed after ion penetration under the surface were found [7]. Additional information obtained experimentally allowed to refine the notions about the processes occurring during neutralization. A detailed theoretical analysis of above surface HCI neutralization based on a classical overbarrier model (CBM) for the description of electronic transitions between metal and HCI has been developed in reference [8]. By the solution of the rate equations made up within the framework of this model [8, 9] and by Monte Carlo calculation [10] made with the same assumptions as in ref.[9] a qualitative picture of the HCI neutralization at approaching a metal surface was obtained. The present notions about above surface neutralization of the HCI [11–13] conform to the results of these works.

A more detail information on released energy redistribution can be obtained by the calculation of spectra of both Auger- and radiative transitions occurring at the neutralization of HCI. The spectra of Auger- and radiative transitions in inner shells of ions $\text{Ar}^{(10-18)+}$ neutralized at the metal surface were calculated in ref. [14]. The results of calculations satisfactorily describe the origin of peaks in the experimental K-Auger spectra in the case of neutralization of Ar ions [15,16]. The calculated spectra allow estimating the energy of neutralization evolved at transitions both in inner shells and in outer shells. If it is taken into account that in outer shells Auger-transitions occur mainly with small energy ($\sim 10\text{--}20$ eV), the comparison of energy evolved in the outer shells with the experimental total electron emission yield indicates clearly, that only a part of the neutralization energy is spent in Auger emission process and the

essential its part being transferred to the electronic subsystem of metal by another way. For both better insights into this phenomenon and its quantitative description it is necessary to consider of the processes occurring at neutralization of HCI in detail.

From our point of view this complex process could be investigated in many details via simulating by a Monte-Carlo method. In this connection we developed the code where the neutralization of HCI approaching the metal surface are calculated with a Monte-Carlo method. In the present work a brief description of methods used in this code is given as well as the results of some calculations for the neutralization of $Ar^{(10-18)+}$ at the surface of gold and C^{6+} at the surface of graphite are presented.

2. Method of simulation

The charge of nucleus, its mass, the initial configuration of the electronic shell and the initial energy of HCI as well as the work function and the depth of the conduction band of metal are given as an input data of the code. On this data the code calculates the charge state of an ion, the critical distance on which the potential barrier is lowered up to the Fermi level of metal so that resonant electron capture from the conduction band can occur, and speed at which the ion with the given initial energy approaches this distance, being accelerated by the field of the image charge. The configuration of electron shells of the ion during further approaching the surface is determined by the several competing processes, namely: resonant electron capture; resonant electron loss at the shifting of the levels with electrons above the Fermi level under the action of both the image charge and the screening by captured electrons; Auger-transitions into the deeper shells; electron emission at the promotion of levels with electrons above the vacuum level.

For each configuration of the electronic shell of the ion formed at some distance above the surface the condition of the promotion in vacuum being tested and the electrons having negative binding energy are removed consequently. For the formed configuration the rates for each of the three rest channels are calculated and the lifetime of the configuration is determined with the expression

$$t_1(R) = 1 / [I_{tc}(R) + I_{tl}(R) + I_{ta}(R)] \quad (1),$$

where $I_{tc}(R)$, $I_{tl}(R)$, $I_{ta}(R)$ are the total rates of the processes of resonant capture, resonant loss and Auger and radiative transitions respectively. Further, with the Monte-Carlo procedure, surviving this configuration at the approaching the surface is run. The ions approach the surface by small steps. The length of a step is a smaller value of dr_1 and dr_2 , where $dr_1 = 0.1 v(R) t_1(R)$ is the distance covered by the ion at speed $v(R)$ for one tenth of the life time of the configuration, $dr_2 = 0.1 \Delta R_c$ is one tenth of the distance ΔR_c on which the barrier is lowered enough to capture next electron. The probability that the configuration decays on a given step is determined by the expression

$$Pd = [1 - \exp(-t_f / t_1)] \quad (2),$$

where t_f is the time necessary for the ion to fly over of the given step. If a due trial the configuration turns out to survive the next trial is performed, approaching the ion on one step.

After several such steps, a number of which is set in the code as a parameter, the lifetime of the configuration for the new distance between the ion and the surface is recalculated, taking into account both the lowering of the potential barrier and the promotion of the levels. If the decay of the configuration occurs on any step, the respective changes in the configuration are made in accordance with channel as well as the life time for the new configuration is recalculated. Further the fate of the new configuration is determined on next step and so on, nearly up to the ion-surface collision.

At the calculation of the life time the rates of all energy possible Auger-transitions as well as the rates of resonant capture and resonant loss for all shells of the ion for which necessary energy conditions are fulfilled are taken into account. In the case of the decay of the configuration all necessary changes in it are made taking into account their probabilities by a Monte Carlo method.

The electron exchange processes between the approaching HCI and the metal surface are considered in terms of classical overbarrier model [8]. Below we shall shortly note the basic points of the model used in our code. Atomic units are used unless otherwise stated.

(1) Approaching a metal surface the ion is accelerated under the action of the field of the image charge. Classical image potential is

$$U = -q / 4R \quad (3),$$

where q is the charge of the ion, R is the distance between the metal surface and the ion. In such a case the ion, with mass m and with speed v_0 being at the distance R_0 , approaching the distance R gets speed

$$v = (v_0 + q^2 / 2m (1 / R - 1 / R_0))^{1/2} \quad (4).$$

The time of flight t_f can be determined by the expression

$$t_f = [y (y^2 + a^2 / b^2)^{1/2} / b] - [y_0 (y_0^2 + a^2 / b^2)^{1/2} / b] + a^2 / b^2 \ln (| (y_0 + (y_0^2 + a^2 / b^2)^{1/2}) / (y + (y^2 + a^2 / b^2)^{1/2}) |) \quad (5),$$

where $b^2 = v_0^2 - q^2 / 2mR$, $a^2 = q^2 / 2m$, $y = \sqrt{R}$, $y_0 = \sqrt{R_0}$, m is the ion mass.

(2) The level of a saddle of the potential barrier between the metal and projectile U_0 will be expressed as [8]

$$U_0 = - (8q + 2)^{1/2} / (2R) \quad (6).$$

From eq.(6) one can find the critical distance R_c on which the barrier lowers to the Fermi level and resonant electron capture can occur.

$$R_c = (8q + 2)^{1/2} / 2W \quad (7),$$

where W is the work function of metal. With decreasing the ion charge the critical distance, on which the capture of next electron can occur, decreases.

The probability of the resonant capture is determined with the expression

$$I_c(n, R) = \sigma(R) j(n, R) \quad (8),$$

where n is the principal quantum number, $j(n, R)$ is the number of electrons of the conduction band falling on to the unit of area for the unit of time, are determined as

$$j(n, R) = \int_{\max(U_0, -i(n-1/2))}^{\min(-W, -i(n+1/2))} \nu(\varepsilon) d\varepsilon \quad (9),$$

$$\begin{aligned} \text{where } i(n+1/2) &= (q_n^2) / 2(n+1/2)^2 - (q-1/2) / (2R), \\ i(n-1/2) &= (q_n^2) / 2(n-1/2)^2 - (q-1/2) / (2R), \end{aligned} \quad (10)$$

$i(n \pm 1/2)$ is the binding energy of electrons in the shells with quantum numbers of $n \pm 1/2$ which are estimated in the hydrogen like approximation, q_n is the effective charge of a nucleus for an electron in the shell with the quantum number n which are determined using Slater's rules.. Fractional values of the principal quantum number were used to count the broadening of the levels. The second terms in expression (10) take into account the amendment to the electron binding energy coming from the promotion of levels under the action of the image charge. In our calculations $\nu(\varepsilon) d\varepsilon$ is the number of electrons in the conduction band, falling onto unit of the surfaces area for the unit of time with the normal component of kinetic energy laying within the interval from ε to $\varepsilon + d\varepsilon$ and $\nu(\varepsilon) d\varepsilon$ is estimated as [17]

$$\nu(\varepsilon) d\varepsilon = 4\pi m_e (-W - \varepsilon) d\varepsilon / h^3 \text{ cm}^{-2} \text{ s}^{-1} \quad (11),$$

where m_e is the electron mass.

The cross section of the saddle of the barrier is estimated as [8]

$$\sigma(R) = \pi \{ [R * (i)]^2 - R^2 \} \quad (12),$$

where $R^*(i) = (8q(R) + 2)^{1/2} / (2i)$ is the critical distance on which become possible the electron capture from the conduction band to the level with the binding energy of i .

(3) At the rising of a level above the Fermi one back electron transition from the ion into empty levels of the conduction band of metal, resonant ionization, can occur. The rate of the resonant ionization process is determined by the expression

$$I_1(n, R) = f(n) P(n, R) \quad (13),$$

where $f(n) = q_n^2(R) / (2\pi n^3)$ is the frequency of the rotation of electron being on the hydrogen like orbit with the effective charge $q_n(R)$ and the principal quantum number n , $P(n, R)$ is the probability of collision of the electron with the plane in the area of the saddle point of the barrier, estimated as

$$P(n, R) = [R^*(i) - R] / R^*(i) \quad (14).$$

(4) At the approaching of ion the levels occupied by electron promote under the action both field of the image charge, and screening by other captured electrons. At the rising of a level with electrons above the level of vacuum the electrons leave the ion, leading to emission resulting from the promotion.

(5) The captured electrons can fill the inner shells of the ion by Auger transitions. For the simulating of these transitions the code simulating [16] cascades of Auger- and radiative transitions was used. For the Auger - and radiative transitions in inner shells the rates of diagram transitions [18,19] were used taking into account the amendments for configuration imperfection by statistical scaling procedure[20], i.e. the rate of transitions was considered to be proportional to the number of combinations of electrons and vacancies giving the same transitions. The rates of Auger-transitions in outer shells ($n > 4$) are estimated using the approximation formula [8]

$$I_a(n_1 - n_2 n_2) = 5,06 \cdot 10^{-3} / (n_2 - n_1)^{3.46} \quad (15)$$

And as

$$I_a(n_1 - n_2 n_3) = I_a(n_1 - n_2 n_2) / [5(n_3 - n_2)] \text{ for } n_3 > n_2 \quad (16)$$

where n_1, n_2, n_3 are the principal quantum numbers, $I_a(n_1 - n_2 n_3)$ is the rate of auger transition combining a $n_1 - n_2$ transition with ionisation of a second electron from n_3 shell in configurations with empty n_1 shell and with one electron in each of n_2 and n_3 shells, $I_a(n_1 - n_2 n_2)$ is the same but with ionisation of a second electron from n_2 shell. For other numbers of vacancies and electrons in these shells the rates are corrected by statistical scaling procedure.

The code allows to calculate the number of electrons captured and lost by the highly charged ion on various channels for various distances between the ion and the surface, and also to see

the evolution of the population of various shells of the ion approaching the surface, in the dependence on initial energy and charge of the ion, as well as the depth of the conduction band and the work function of metal.

3. Calculated results and discussions

Making use the code described above we have carried out calculations for the case of Ar HCI approaching a gold surface (the work function is 5,1 eV, the width of the conduction band is 5,4 eV). In fig. 1 the results obtained for the case of neutralization of Ar^{12+} approaching the

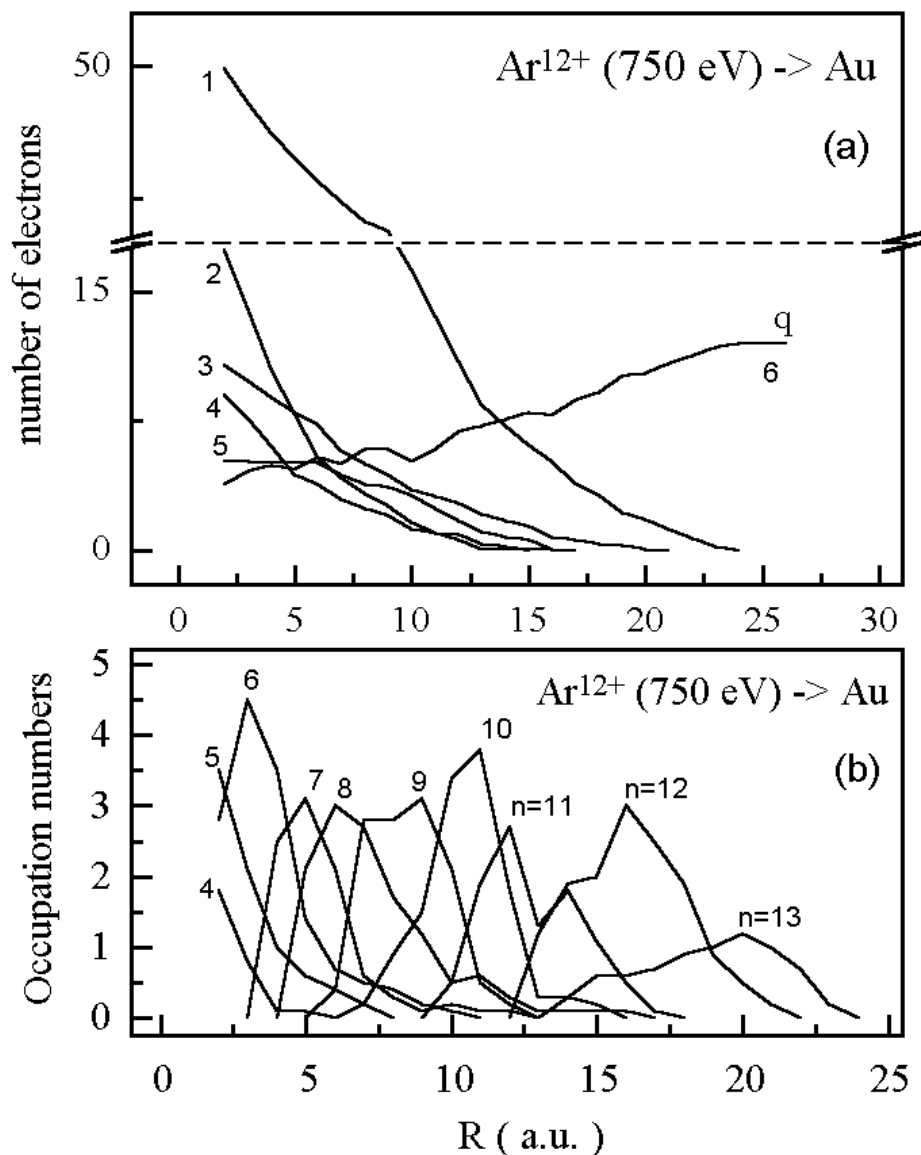


Fig. 1. Simulated above surface neutralization of a 750 eV Ar^{12+} on gold surface. (a) Evolution of ion charge and number of various transitions in highly charged ion vs projectile surface distance: (1) resonant capture; (2) resonant ionisation; (3) electron emission in the result of promotion of levels; (4) electron emission at Auger-transitions; (5) Auger loss of electrons; (6) the ion charge. (b) Population of various shells of highly charged ion with principal quantum numbers $n=4-13$ vs projectile surface distance.

surface of gold with the initial energy 750 eV are presented which can be compared with the results got in [9] by the solution of the rate equations. In fig. 1(a) we show evolutions of the ion charge, the number of captured electrons, the number of resonant lost electrons, the number of Auger-electrons both emitted into vacuum and lost into empty states of conduction band and the number of electrons promoted into vacuum versus projectile surface distance. It is seen that in the course of neutralization a considerable part of electrons captured by HCI proceed into the free part of the conduction band by the resonant ionization and emitted into vacuum as a result of promotion of levels. These electrons can gain the considerable part of the neutralization energy. In the given case about 31% of captured electrons transfer into empty states of the conduction band as a result of Auger lost and resonant ionisation, about 33% of electrons are emitted into vacuum at Auger transitions and about 21% of that are promoted into vacuum. In fig. 1(b) the evolution of population of various shells of the ion approaching the surface is shown. It is seen, that before hitting the surface, at the distance of about 2 a.u., electrons begin to populate the N-shell of the ion. Whereas, at the modelling of the similar case by the solution of the rate equations in ref [9], at the distance of 2 a.u. above the surface electrons begin populate the shells with the principal quantum number $n=8$.

The calculations show that a fraction of captured electrons promoted into vacuum considerably grows with increasing of the projectile charge state. For example, that is seen in fig. 2, where evolution of ion charge and number of various electronic transitions in ions are presented versus projectile surface distance for the case of neutralization of Ar^{18+} with the initial energy 750 eV. In this case about 17% of captured electrons transfer into empty states of the conduction band, only about 8% of electrons are emitted into vacuum at Auger transitions and nearly 71% of electrons are promoted into vacuum.

From figures 1 and 2, one can see that projectile approach the surface still being in charged states.

The calculations also have been performed for the case of impact of C^{6+} on graphite surface. In these calculations energy of levels in HCI have been estimated more correctly using Hartree-Fock method. An evolution of ion charge and number of various electronic transitions occurring in ions versus projectile surface distance got in these calculations are presented in fig. 3.

The obtained picture of above surface neutralization of C^{6+} on graphite is qualitatively similar to the picture got for impact Ar^{q+} on Au.

Thus, the results obtained in these calculations give a picture of the above surface neutralization of HCI, differing from the picture obtained in calculations [9,10]. The main differences are as follows:

- (1) Our calculations show that the number of electrons promoted into vacuum is comparable and in the case of high charges can considerably exceed the number of electrons emitted via Auger-transitions.
- (2) From our calculations it follows, that at HCI's approaching the metal surface electrons have time to populate much deeper shells, than as it was found in ref. [9].
- (3) The modelling by a Monte-Carlo method in this work shows that HCI approaching to the metal surface have not enough time to be completely neutralized.

These results could be explained by the essential promotion of the outer shell levels of the ion occupied by electrons at its neutralization and approaching the surface.

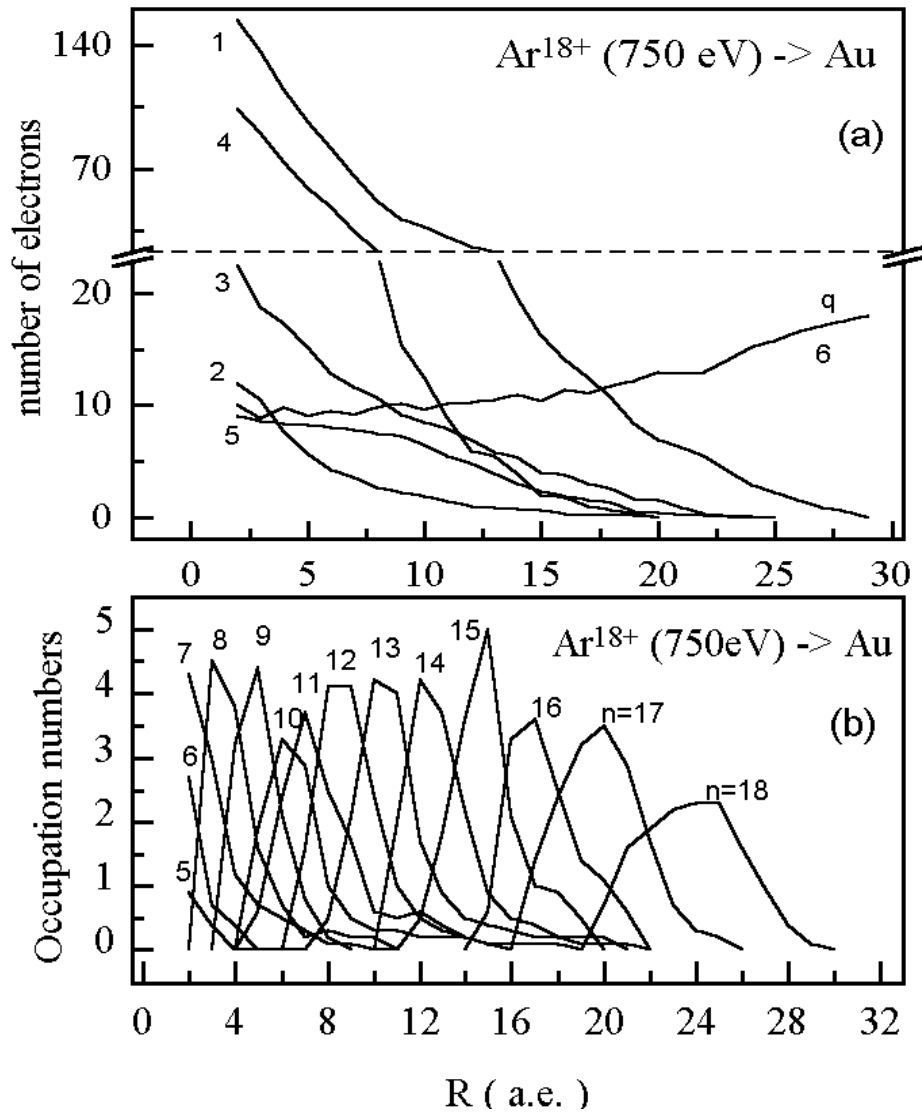


Fig. 2. Simulated above surface neutralization of a 750 eV Ar^{18+} on gold surface. (a) Evolution of ion charge and number of various transitions in highly charged ion vs projectile surface distance: (1) resonant capture; (2) resonant ionisation; (3) electron emission in the result of promotion of levels; (4) electron emission at Auger-transitions; (5) Auger loss of electrons; (6) the ion charge. (b) Population of various shells of highly charged ion with principal quantum numbers $n=5-18$ vs projectile surface distance.

As a result a significant number of captured electrons are transferred into the empty states of the conduction band and emit into vacuum and the filling of the deeper shells begin.

The differences between our results and the results obtained in references 9 and 10 are explained, apparently, by different suppositions made in calculations. Some indications to that can be found by examination of the presented in ref. [9] results. For example, in calculations in agreement with the CBM the ion is assumed to be not neutralized before reaching the critical distance corresponding to its charge state (see expr.7). In our calculations this condition is controlled for all event of neutralization of ion approaching the surface. However, presented in ref. [9] evolution of ion charge state versus projectile surface distance not always satisfies the condition $R(q') \leq R_c(q)$ at $q' < q$.

For example the initial Ar^{12+} become neutral at $R=13$ a.u. before reaching the critical distance for single charged ion $R_c(1)=8.4$ a.u.

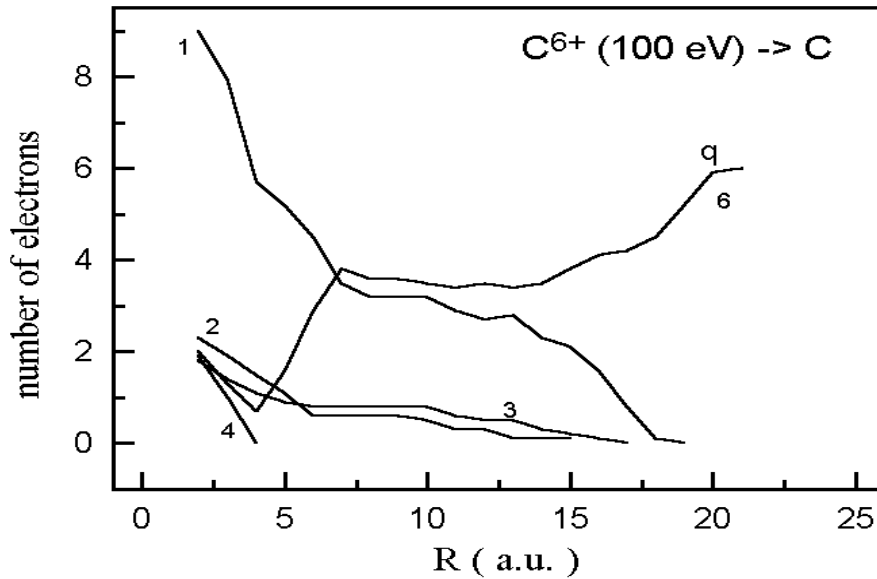


Fig. 3. Simulated above surface neutralization of a 750 eV Ar^{18+} on gold surface. (a) Evolution of ion charge and number of various transitions in highly charged ion vs projectile surface distance: (1) resonant capture; (2) resonant ionisation; (3) electron emission in the result of promotion of levels; (4) electron emission at Auger-transitions; (6) the ion charge.

Moreover, our estimations of the energy levels (see expr.10) show that if we take into account not only screening by inner shell electrons but as well as a mutual screening of the electrons being in the same shell the promotion of electrons into vacuum have to happen earlier at the bigger distance from the surface than it follows from the presented in ref. [9] evolution of population of ion shells by electrons. The neglecting of a mutual screening of electrons being in the same shell in calculations made in ref. [9, 10] is probably the main cause of the above noted differences in the results.

By the described above code the dependencies of the slow electron yield versus initial velocity of Ar^{q+} ($q=10-18$) approaching an Au surface have been calculated. At calculation of total slow electron yields the contribution of a third channel of electron emission (in addition to auto ionization AI and promotion of levels Pr), the so-called “peeling off mechanism” PO [8], has been taken into consideration. Over this channel all exited electrons with larger Rydberg radii $r = n^2 / q_n$ than the screening length within the solid $\lambda = v_F / \omega_p$ of the metal (ω_p surface plasmon frequency; $\lambda \approx 3$ a.u. for a gold) are emitted at touchdown of the projectile with a surface.

Some results of calculations are presented in fig.4. One can see from the figure that performed classical trajectory Monte Carlo calculations satisfactorily explain a character of dependencies of total slow electron yield versus HCI initial velocity. The calculations show that the decreasing of the electron yield with increasing of projectile velocity at low velocities and levelling at higher velocities is explained by changing of the relative contributions of the different channels into electron emission versus HCI velocity. The main part of emitted electrons at low projectile velocities are formed as a result of Auger transitions of captured electrons, while with increasing of projectile velocity a promotion of levels with electrons into vacuum begins to give the main contribution into electron emission. The contribution of “peeling off mechanism” into yield of slow electrons is relatively small.

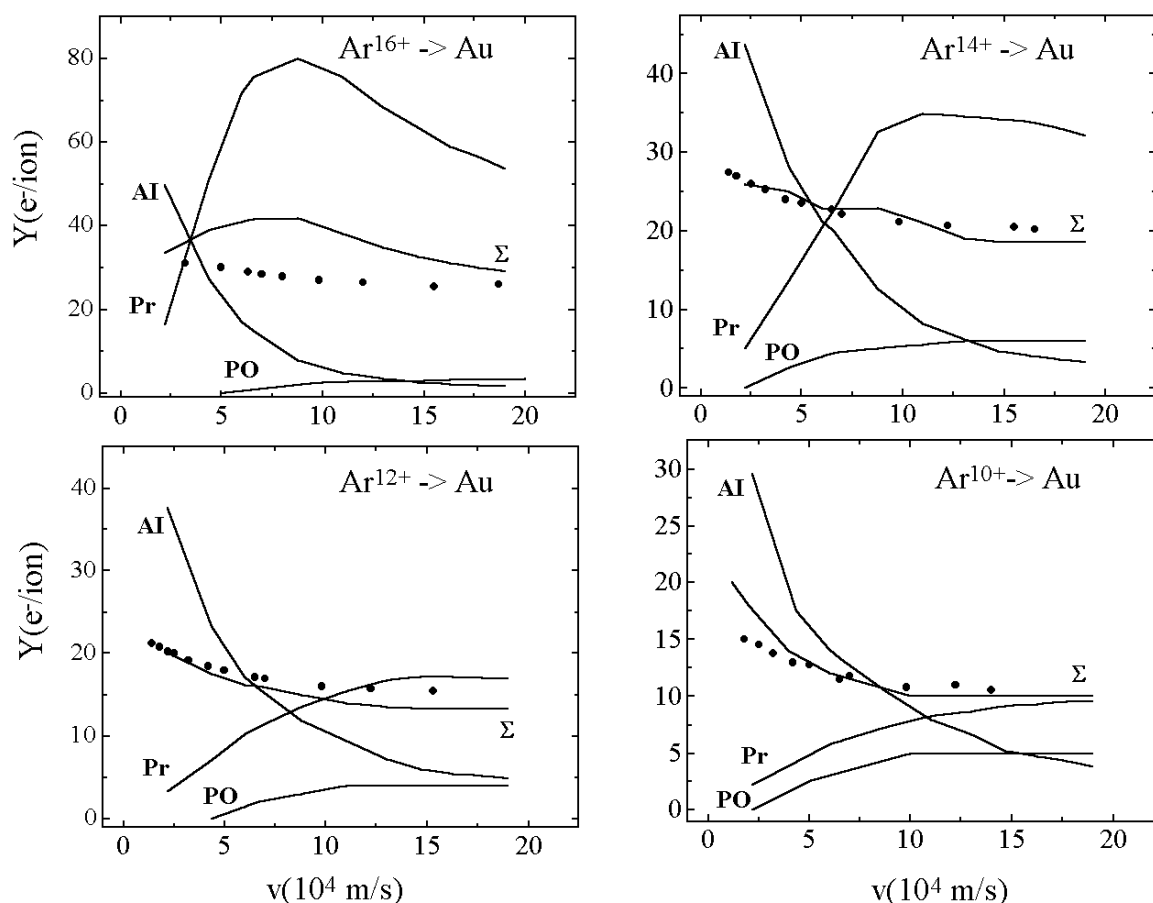


Fig. 4. Calculated total slow electron emission yields (Σ) for impact of Ar^{q+} ($q=10, 12, 14, 16$) on gold vs. projectile velocity, in comparison with measured slow electron yields (full symbols; data from [21]). Individual contributions of different channels into electron emission are separately indicated: (AI) emission at Auger-transitions; (Pr) emission in the result of promotion of levels; (PO) emission by “peeling off mechanism”. The calculated total electron yields derived under assumptions that 50% of emitted from the projectile electrons are absorbed by the Au surface: $\Sigma = 0.5 (AI + Pr + PO)$.

The results obtained in calculations satisfactorily agree with the experimental data for the projectile charges $q < 16$ and somewhat worse for the higher charges with one fitting parameter taking into account the fraction of electrons absorbed by surface.

4. Conclusion

An above surface part of neutralization of highly charged ions approaching a metal surface has been investigated by Monte Carlo simulation considering the electronic exchange between surface and HCI in terms of classical overbarrier model.

The results of calculations of neutralization of $Ar^{(10-18)+}$ on Au surface have shown that in consequence of promotion of levels occupied by electrons under the action both the image charge field and screening by other captured electrons the considerable portion of the captured electrons is transferred into the empty states of the conduction band and emit into vacuum. The number of electrons participating in these transitions can be comparable and even in the case of high charges can significantly exceed the number of electrons emitted via Auger transitions and over these channels can be released substantial part of neutralization energy.

As a result of the losing of the most of captured electrons on these channels HCI approach a metal surface still being in charged states.

The results of calculations satisfactorily describe the dependencies of total slow electron yield on highly charged ions initial velocity. The calculations show that the main part of emitted electrons at low projectile velocities are formed as a result of Auger transitions of captured electrons, while with increasing of projectile velocity a promotion of levels with electrons into vacuum begins to give the main contribution into electron emission. The contribution of “peeling off mechanism” into yield of slow electrons is relatively small.

REFERENCES

- [1] S.T.de ZWART, Abstracts, Groningem(1987).
- [2] H.J. ANDRA, A. SIMIONOVICI, T. LAMY, A. BRENAC, G. LAMBOLEY, J.J. BONNET, A. FLEURY, M. BONNEFOY, M. CHASSEVENT, S. ANDRIAMONJE, A. PESNELLE, Z. Phys. D21 (1991) 135.
- [3] L. FOLKERTS, I.G. HUGHES, F.W. MEYER, Abstracts of XVIII ICPEAC, (Aarhus, 1993) 770.
- [4] E.D. DONETS, Nuclear Instr. And Methods B 9 (1985) 522.
- [5] J.P. BRIAND, L. de BILLY, P. CHARLES, S. ESSABAA, P. BRIAND, R. GELLER, J.P. DESCLAUX, S. BLIMAN, C. RISTORY, Phys.Rev.Lett 65 (1990) 159.
- [6] J.P. BRIAND, D. SCHNEIDER, M. CLARK, V. DECAUX, Nuclear Instr. and Methods B 87 (1994) 138.
- [7] F.W. MEYER, S.H. OVERBARY, C.C. HAVENER, P.A. ZEIJLMANS van EMMICHOVEN, D.M. ZEHNER, Phys.Rev.Lett 13 (1991) 723.
- [8] J. BURGDORFER, P. LERNER, F.W. MEYER, Phys.Rev. A 44 (1991) 5674.
- [9] H. KURZ, F. AUMAYR, C. LEMELL, K. TOGLHOFER, H.P. WINTER, Phys.Rev. A 48 (1993) 2182.
- [10] H. KURZ, F. AUMAYR, C. LEMELL, K. TOGLHOFER, HP. WINTER, Phys.Rev. A 48 (1993) 2192.
- [11] F. AUMAYR, H.P. WINTER, Comments At.Mol.Phys. 29 (1994) 275.
- [12] A. ARNAU, F. AUMAYR, P.M. ECHNIQUE, M. GREThER, W. HEILAND, J. LIMBURG, R. MORGENSTERN, P. RONCIN, S. SCHIPPERS, R. SCHUCH, N. STOLTERFOHT, P. VARGA, T.J.M. ZOUROS, H.P. WINTER, Surface Science reports 27 (1997) 113.
- [13] H. WINTER, F. AUMAYR, J.Phys. B 32 (1999) R1.
- [14] M.N. MIRAKHMEDOV. Abstracts of VIII Intern. Conf. on the Physics of HCI,(Japan, 1996).
- [15] M.N. MIRAKHMEDOV. Abstracts of XIX ICPEAC, (Canada, 1995).
- [16] M.N. MIRAKHMEDOV, Nuclear Instr. and Methods B 98 (1995) 429.
- [17] L.N. DOBRETsov, M.V. GOMOYUNOVA. Emission electronics (1966) p.64.
- [18] M.H. CHEN, B. GRASEMANN, H.MARK, Atom. Data Nucl. Data Tables 24 (1979) 13.
- [19] J.H. SCOTFIELD, Atom. Data Nucl. Data Tables 14 (1974) 121.
- [20] F.P. LARKINS, J.Phys. B 4 (1971) L29.
- [21] H. KURZ, F. AUMAYR, K. TOGLHOFER, R. MANN, H.P. WINTER, Phys.Rev.Lett. 69 (1992) 1140.

Some features of scattering, sputtering and ion emission in hyperthermal energy range

V. Kh. Ferleger, U. Kh. Rasulev, I.A. Wojciechowski

Arifov Institute of Electronics,
Tashkent, Uzbekistan

Abstract. In this paper known experimental data on scattering, sputtering and ion emission of atomic particles escaping from a surface under its bombardment by atoms of hypethermal energies are analyzed. The dependence of the energy losses by a scattering hyperthermal particle on the initial energy and the angles of incidence and of reflection appears to be well described by the following model: the particle is being single-scattered by a certain complex of surface atoms forming an effective mass. Presumably, the result serves as evidence in favor of the non-binary nature of the hyperthermal collisions. It is shown that the observed features of the ion emission are determined in general by the behavior of the subthreshold sputtering coefficient, which in turn is described by a universal empirical formula.

1. Introduction

The features of interaction of hyperthermal (HT) particles with solid surfaces, i.e. particles with bombarding energies lying within the range of (1–30) eV presently are the least studied. The reason is that until very recently all attempts to obtain unidirectional and unienergetic beams of HT particles failed. Absence of reliable experimental data in the hyperthermal energy range has been a serious obstacle on the way to solve a number of the fundamental problems of particle-matter interaction. Knowing the features of the emission HT processes is also necessary for solving a number of applied tasks including the problem of a “first wall” of a fusion reactor as majority of particles sputtered from a “first wall” into the plasma are hyperthermal.

Let us discuss, for example, the question of the limits of applicability of the binary collision approximation (BCA) for a description of particle-solid interaction. BCA is the model according to which an elementary event of particle-solid interaction is a collision between two “free” (unbound) atoms described by the cross section as if in the gas phase [1, 2]. Within the framework of the model the backscattering of an impinging particle by a solid target is reduced to a sequence of its binary collisions with the target atoms. In the case of sputtering the collisions between target atoms are considered in a similar way. The BCA, because of its simplicity, is widely employed in analytical theories based on approximate solution of the kinetic Boltzmann equation. The use of the BCA made it possible to derive simple analytical formulas for integral- and differential characteristics of scattering of light ions by solid surfaces [3] as well as to create the analytical theory of sputtering in the linear cascade regime [1].

The both formulae obtained in ref. [3] and the computer simulation methods based on the BCA are in good agreement with the wide set of the experimental data on scattering in the initial energy range of $E_0 \geq 1$ keV where the applicability of the model is well justified. On the other hand it seems to be clear that the BCA is not the particularly good approach for particles having energies comparable with the binding energy of target atoms (several eV) [1, 2]. However, there are several quite different points of view on the exact position of the energetic boundary of the BCA applicability for particle-solid scattering [4–8].

For instance, Veksler in ref. [5] while analyzing the measured angle and energy distributions of heavy ions Cs^+ , Rb^+ and K^+ scattered by heavy targets (W, Mo) concluded that for the high energy tails of the distributions in question the contribution of non-binary collision is already noticeable when $E_0 \approx 300$ eV. But Tongson and Cooper in ref. [8] studied the energy distributions of light ions He^+ and Ne^+ scattered by the Cu surface did not find any deviation from the BCA at $E_0 \geq 20$ eV.

The question of the limits of applicability of the BCA for sputtering is even more complex and more important because the approximation is one of the basic assumptions of the linear cascade theory [1]. The point is that, even at $E_0 \geq 1$ keV, the majority of cascade recoils have energies lying in the HT range where the applicability of the BCA is questionable. In ref. [1] Sigmund remarks that the low energy collisions in solids cannot be solely binary ones; but he does not share point of view of the authors of ref. [9] that non-binary collisions contribute to sputtering significantly. He argued, first, that the possibility of a collision with several target atoms simultaneously could be taken into consideration within the framework of the BCA with the perturbation theory and, second, that the binding forces of the target atoms influence the scattering processes inside matter at the energies less than 10 eV only. Thus the deviations from the BCA cannot substantially change the results of the linear cascade theory. Actually, the results are in good agreement with the majority of the experimental data on sputtering coefficients and energy spectra of sputtered atoms (apart from lightest ones) at $E_0 \geq 1$ keV.

However, it should be noted that all the attempts to use the linear cascade theory for the description of sputtering of cluster particles were unsuccessful [10, 11]. In fact, there is a great discrepancy between the calculated and measured cluster yields as a function of the number of atoms in a cluster as well as of the energy distributions of sputtered clusters [12, 13]. Up until now, the reasons of such discrepancy are not clear.

At first glance, it seems that unlike the atomic sputtering, the mechanism of the cluster emission at $E_0 \sim$ keV may be determined by some nonlinear sputtering regime, like thermal spike (ref. [14]). Nevertheless, as it is shown by both the measurement [13] and the simulation [15], the fraction of sputtered bound atoms is up to 50% of the total sputtering yield, under conditions when a thermal spike contribution is negligible.

Among other problems requiring additional experimental data in the HT region one can single out the problems of the sub-threshold sputtering [1, 16, 17] and of the charge state formation of scattered and sputtered particles in the region of transition from the thermal equilibrium (where the Saha formula is valid) [18] to the non-equilibrium conditions [2, 19].

Some progress in studying the HT particle–solid surface interaction was achieved in 80th, when the effective supersonic sources of HT particles based on the aerodynamic acceleration in a flow of light carrier gas were developed [20]. By now, a certain amount of experimental data pertaining to the problem under consideration is accumulated. Summarizing, the data indicate the following:

- practically all the emission phenomena observed at $E_0 \geq 1$ keV take place in the HT energy range as well, although with essentially lower yields;
- the threshold energies of sputtering and secondary ion emission are somewhat less than those obtained by the extrapolation method [1];

- the nature of the majority of the features is non-trivial and some of them are not even explained qualitatively. Some features of HT scattering, sputtering and ion emission are under investigation in the present article.

2. Elastic scattering of HT atoms.

Experimental investigation of Ag, Kr and Xe HT-atom scattering on the single crystal surfaces Ge(110), GaAs(110) and Ag(110) was performed in ref. [21]. The scattering scheme is shown in figure 1, where θ_i and θ_r are the angles of incidence and of reflection correspondingly, both with respect to the surface normal, E_0 is the initial energy of the bombarding atom, E is the final energy of a scattered atom. It was found that the average energy losses of the scattered particles ΔE are quite large and both the scattered atom normal velocity component and the tangential one are not conserved. Also, it was established that ΔE can be calculated using the simple empirical formula:

$$\Delta E = kE_0 \cos^2[(\theta_i + \theta_r)/2], \quad (1)$$

where k is the coefficient of proportionality which does not depend on the type of the bombarded target within the limit of the measurement's assurance [21], decreasing as the bombardment atom mass decreases. According to the data of ref. [21] $k(\text{Xe}) = 1$, $k(\text{Kr}) = 0.92$, $k(\text{Ar}) = 0.63$.

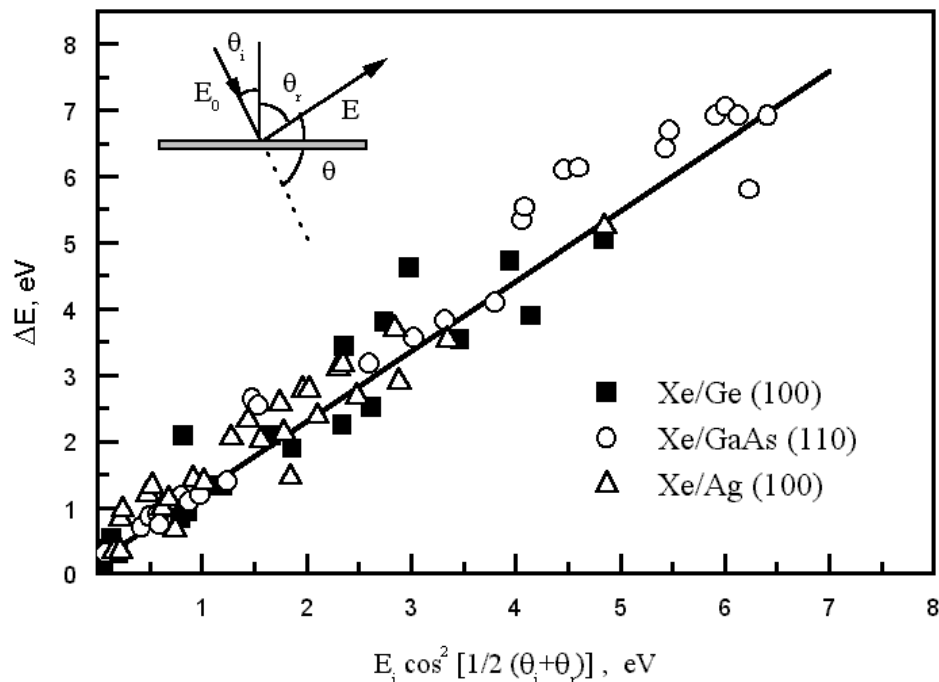


Figure 1: Energy losses of scattered hyperthermal Xe, on data of ref. [21]. Scheme of scattering is shown in the left upper corner.

The molecular dynamics simulations performed in ref. [22] under the conditions of the experiment of ref. [21] gave the angle distributions of scattered atoms being in reasonable agreement with the measured ones, but the simulations do not corroborate the result of

formula (1). It is conceivable that the reason of such a discrepancy lies in the choice of the interaction potential function in [22] leading to the mostly binary picture of HT-collisions.

It is interesting to note that formula (1) may be easily derived from the well-known formula describing the energy of elastic single scattered atom written for the case when the bombarding atom mass (m) is less than the mass (M) of the target particle:

$$E(\theta) = E_0 \left[\frac{\nu \cos \theta + \sqrt{1 - \nu^2 \sin^2 \theta}}{1 + \nu} \right]^2, \quad (2)$$

where θ is the polar scattering angle, $\nu = m/M$ is the mass ratio of the colliding particles. If the vectors of the velocities of the bombarding- and scattered atom and the vector of the normal to the surface are in the same plane then:

$$\theta = \pi - (\theta_i + \theta_r) \quad (3)$$

Let us assume that some surface structure with the effective mass $M = M_e$ ($M_e \gg m$, i.e. $\nu \ll 1$) plays the role of the target for the impinging particle. Then, disregarding the terms of order of ν^2 one can obtain using (2) and (3):

$$\Delta E = (4m/M_e)E_0 \cos^2[(\theta_i + \theta_r)/2] \quad (4)$$

Comparing the formulae (1) and (4), one has:

$$k = 4m/M_e \quad (5)$$

Thus k decreases with *decreasing* the bombarding atom mass in agreement with ref. [21], but the measured rate of decrease is somewhat slower than $k \sim m$. This means that M_e in (5) is in fact a function of m . If we take $k(\text{Xe}) = 1$ according to the results of ref. [21] then the effective mass of the surface structure is 524 a.u. This value of M_e is approximately equal to the total mass of $n = 5$ silver atoms and $n \approx 7$ atoms for other surfaces. Effective masses obtained with eq. (4), and k values measured in ref. [21] as well as n values are presented in Table 1.

Table 1. Effective masses obtained with EQ. (4) and n values

	Xe	Kr	Ar
M_e	524	365	254
n	4.9	3.4	2.3

Therefore, HT particle-surface collisions with energy losses calculated with formula (4) have the non-binary nature.

The attempts to treat the low energy particle-surface collisions as the particle's single scattering on some surface structures with effective masses have fairly long history. Veksler

in ref. [5, 6] introduced the effective mass in the energy range (100–300) eV. Within his approach M_e is determined by a number of surface atoms participating in simultaneous collisions with the bombarding heavy ion, but its real value depends on both the angle of incidence and the form of the ion-atom interaction potential. As a result the model appeared to be too complicated and has not been developed any further.

The effective mass approach was used in several papers [23, 24] on particle-surface scattering at the extremely low (thermal) bombarding energies in the framework of the “hard cube” scattering model. In terms of the model the “hard cube” is some surface structure with the mass M_e which can only move along the direction normal to a surface under impinging particle hits.

In spite of the fact that M_e was introduced in a number of different manners, using the data from ref. [5, 6, 23, 24] and the results of the present work one may observe that as a tendency M_e decreases as the bombarding particle energy increases. Thus, by the results of ref. [24] at thermal energies, $M_e \approx 760$ a.u. ($n = 4.2$) for the system of Ar \rightarrow W; by the ref. [21] at $E_0 \leq 5.5$ eV, $M_e = 254$ a.u. ($n = 2.3$) for Ar \rightarrow Ag and by ref. [5] at $E_0 = 260$ eV, $M_e = 144$ a.u. ($n = 1.5$) for K⁺ \rightarrow Mo.

Our opinion is that the approaches based on the introduction of effective mass are no more than a rough qualitative description of the true non-binary collective nature of low energy particle-surface collisions. However, the intervals of energies and masses of bombarding particles where deviations from the BCA become essential are still not determined precisely, even after the studies of ref. [21].

It should be also noted that the physical meaning of the effective mass is not clear enough. Refining the molecular dynamics simulations is paramount for a progress in the area.

Nevertheless, let us assume that M_e itself is the mass of a certain group of atoms which acquires its momentum from a particle moving either in the vacuum or in the matter. Then presence of such “effective mass”, moving as a whole, may prove to be important paradigm for the problems of cluster formation in sputtering. One cannot exclude the possibility that the physical reason for the correlation of moment of several atoms that leads to the effective emission of small clusters is the collective, non-binary nature of the low energy particle collisions.

3. Sputtering and ion emission

Peculiarities of positive ion emission for a number of particles sputtered from Ag, Ge, InP, GaAs targets bombarded with HT Xe atoms with the energies $E_0 < 20$ eV were studied in ref. [25]. The following has been established:

- only the elements with relatively low ionization potentials, $4.3 \text{ eV} < I < 6 \text{ eV}$, were detected as the positively charged sputtered ions;
- the yields of the ion emission were fairly large $Y(\text{In}^+) \sim 10^{-3}$, $Y(\text{Ga}^+) \sim 2 \cdot 10^{-4}$;
- the threshold energies for sputtered ion formation were $E_t \approx 6 \text{ eV}$ in all the cases under investigation, being somewhat greater than the sublimation energies of the corresponding surfaces but significantly less than the sputtering thresholds known from literature [26];

- at $E_0 > E_t$, the yield of ion emission drastically increases with E_0 increasing and may be described by a simple empirical formula $Y \sim (E_0 - E_t)^n$, with $n = 2.5-3.5$.

It was noted in ref. [25] that in some cases very small currents of scattered Xe^+ ions (Xe atom's ionization potential is 12.1 eV) were also observed. But neither the threshold energy for Xe ion formation nor the dependence $Y(E_0)$ were measured. In ref. [27] mercury ions were detected during the process of bombardment of the slightly oxidized platinum surface by Hg neutral atoms ($I = 10.44$ eV). Two processes determine the features of ion emission observed in ref. [25]: sputtering and charge state formation of particles leaving the surface. These processes thoroughly studied at $E_0 > 1$ keV [1, 28, 29] were conjectured to be independent, having different values of E_t and different dependencies of their main characteristics (sputtering coefficient, probabilities of ionization etc.) on bombarding particle's energy.

In the HT energy range where the work [25] pioneered there was practically nothing known about the features of sputtering and charge state formation. So it was important to determine, to the very least, which of the two processes chiefly determines the values of the threshold energies and the form of the curves $Y(E)$. It is the belief of the authors of ref. [25] that the main process here is the charge state formation. Namely, the following mechanism of the sputtered ion formation was assumed. The bombarding Xe^0 atom scattered as Xe^+ and simultaneously knocks on a neutral target atom A^0 . Then, the charge exchange process $\text{Xe}^+ + \text{A}^0 \rightarrow \text{Xe}^0 + \text{A}^+$ occurs. The only reason in favor of such a complicated picture was that the measured value of E_t was close to the Xe atom ionization energy near the surface, $E_t \approx I' \sim I - e\phi - \Delta E \approx 6$ eV. Here $I = 12.1$ eV is the ionization potential of Xe in vacuum, $e\phi \approx 5$ eV is the surface's work function, $\Delta E \approx 1$ eV is the value of the atomic level promotion near the surface. In order to test the plausibility of such a picture, the special experiment was carried out where Kr ions were used instead of Xe as bombarding particles. The approach is suggested by the fact that the ionization potential of Kr is greater than that of Xe by 2 eV. Therefore, if Kr is being used, the threshold energy must increase. However, the actual measurements gave the opposite result, namely, the threshold energy fell down to 3.9 eV.

Let us show that the observed peculiarities of HT ion emission can be consistently explained within a simple model based on the ideas similar to those describing the ion emission in the interval of $E_0 > 1$ keV [2, 28]. The yield of the ion emission of sputtered particles can be written as:

$$Y(E_0) = Q \cdot S(E_0) \cdot P^+(E_0), \quad (6)$$

where $S(E_0)$ is the sputtering coefficient in the sub-threshold region described by the empirical dependence derived in ref. [30]:

$$S(E_0) = 0.75M_0\gamma^{5/3}f(E_0), \quad (7)$$

where $\gamma = 4M_0m(M_0 + m)^{-2}$, m is the mass of the bombarding atom, M_0 is the mass of the target atom,

$$f(E_0) = 8.5 \cdot 10^{-3} (E_0 / E_t)^{1/4} [(E_0 - E_t) / E_0]^{7/2}. \quad (8)$$

Other empirical formulae for $S(E_0)$ may be found in the literature (ref. [31]). Our choice of $S(E_0)$ as in ref. [30] is because in that case the form of the function $f(E_0)$ resembles the dependence $Y(E_0) \sim (E_0 - E_t)^n$ observed experimentally in ref. [25].

The value of $P^+(E_0)$ in formula (6) has the physical meaning of the probability of ionization of the sputtered particles averaged over all trajectories of sputtering. If we assume that in the HT range the conditions of charge state formation of sputtered particles are still far from the thermal equilibrium in particle-surface system then the $P^+(E_0)$ function can be written in the form of [2, 19, 28]:

$$P^+(E_0) = \exp[-\nu_0 / \nu_{\perp}(E_0)], \quad (9)$$

where parameter ν_0 describes the efficiency of the electron exchange processes in the particle-solid system, $\nu_0 \sim (I - e\phi)$ is independent of E_0 in the adiabatic models like the model of ref. [19]. Thus, the dependence of P^+ on E_0 is determined by the function $\nu_{\perp}(E_0)$, i.e. by the dependence of the normal to a surface component of the sputtered particle velocity on the bombarding atom energy. The specific form of the function $\nu_{\perp}(E_0)$ is given by the mechanism of sputtering. Therefore, in the linear cascade regime, when the form of sputtered particle energy distribution does not depend on E , $\nu_{\perp}(E_0) \sim \text{const}$. In the primary knock-on regime [1], $\nu_{\perp}(E_0) \sim E_0^{1/2}$. In ref. [25] the energy distribution of sputtered In^+ ions was measured at $E < 15.5$ eV for the case of $\text{Xe} \rightarrow \text{InP}$. It has been found that the energy yielding the maximum of In^+ ion distribution increase approximately linearly as a function of E_0 . The same conclusion follows from the assumption that the energy $\Delta E \sim E_0$, lost by a HT-particle in the collision with the effective mass is partially transferred to the sputtered atom.

Finally, $P^+(E_0)$ reads:

$$P^+(E_0) = \exp(-\alpha / E_0^{1/2}). \quad (10)$$

Formulae (9) and (10) have the same forms independent of the initial charged state of the sputtered particle. If the sputtered particle was located on the surface being completely or partially ionized $P^+(E_0)$ may be interpreted as the probability of the initial charge conservation, i.e. the probability that the neutralization neither by electron tunneling nor by Auger transition would occur.

The meaning of Q in the formula (6) is the normalized probability for an atom of the given type to be present on the surface. For homogeneous surfaces $Q = 1$, for the heterogeneous $Q < 1$. We shall disregard any changes of Q resulting from HT sputtering. Let us now analyze most typical experimental data in the framework of the given model.

3.1. K^+ ion emission from the Ag surface

It is well known that alkaline atoms of K and Na exist within most materials as impurities. As the ionization potential of K ($I = 4.54$ eV) is less than the work function of the Ag surface

($e\phi = 4.72$ eV) then $P^+ \approx 1$ and practically all K must escape as K^+ . That means that the measured $Y(E_0)$ dependencies practically coincide with $S(E_0)$, i.e. it is described by formula (8).

It is easy to see in figure 2 that the curve calculated with $E_t = 6.1$ eV is in good agreement with the experimental one.

3.2. In^+ ion emission from the InP surface

The In^+ ion emission features were experimentally studied in ref. [25] in details. In this case not only $Y(E_0)$ but also the absolute value of ion yield ($Y = 2 \cdot 10^{-3}$ at $E_0 = 16$ eV) and the energy distribution of the sputtered ions were measured.

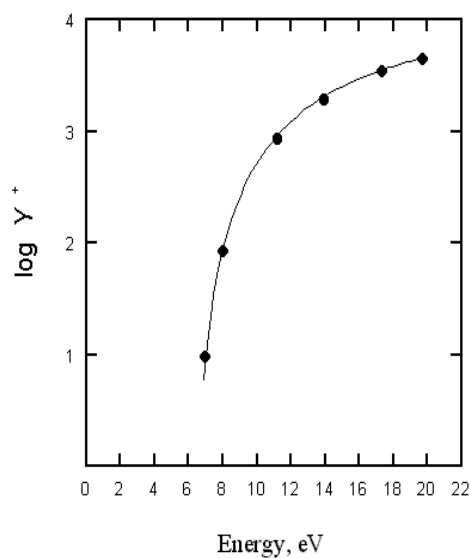


Figure 2. Dependence of the yields of K^+ ions sputtered from the Ag surface on energy of bombarding Xe atoms. Dots are the experimental data of ref. [25], the curve was calculated with eqs. (6)–(10).

In figure 3 the solid line is the dependence $Y(E_0)$ calculated with the formulae (6)–(10) with $E_t = 6.2$ eV and $\alpha = 29.75$ eV^{1/2}. The value of the parameter α which gives the best agreement with the experimental data as well as the data of ref. [25] on the energy distribution allow us to estimate the value of ν_0 in the formula (9). At $\nu_{\perp} = (2E_m / m)^{1/2} \sin \psi$, where E_m is the maximum of the energy distribution, ψ is the angle of emergence measured from the surface ($\psi = 48^\circ \pm 6^\circ$ according to [25]), we get $\nu_0 \approx 0.5 \cdot 10^6$ cm/s. Such a value of ν_0 is typical for non-metallic surfaces as well as for metal surfaces covered by electropositive adsorbates [28].

This value of α (or ν_0) results in the correct within the order of magnitude value of the absolute ion emission yield $Y \approx 0.7 \cdot 10^{-3}$ at $Q = 0.5$.

The results obtained for K and In HT-ion emission show that the form of the measured dependencies $Y(E_0)$ is mainly determined by the function of $S(E_0)$ described by the universal empirical formula (8) for the sputtering coefficient.

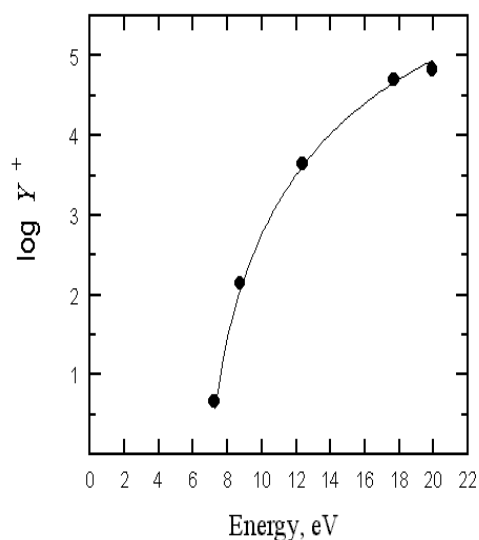


Figure 3. The same as in figure 2 but for In^+ ions sputtered from the InP surface.

In addition, it seems to be reasonable that the ion emission threshold energies practically coincide with the sputtering threshold. Actually, according to ref. [25] the difference between the values of E_t for K and In emissions is only about 0.1 eV.

On the other hand the obtained results indicate that the empirical formula (8) is also a good approximation in the HT energy region. It gives reasonable results both for metal- and semiconductor targets. Earlier it has been shown [30] that formula (8) is applicable to any mass of bombarding particles, from hydrogen to xenon.

It is not clear at present whether the formula (8) is just a very effective empirical approximation for the experimental data or it expresses some general law of sub-threshold sputtering for light and heavy particles. According to the contemporary concepts the mechanisms of subthreshold sputtering for light and heavy bombarding particles are quite different: the primary knock on mechanism for light particles and some mechanism similar to evaporation for heavy ones [16, 17].

However it is difficult to believe that such different events may be described uniformly with a simple formula. In our opinion the main contribution in sub-threshold sputtering may be given by the mechanism of the vibrational energy exchange between neighboring surface atoms which are vibrationally excited due to collisions with the bombarding particle. A non-cascade sputtering mechanism of that kind was suggested in ref. [32] for cluster formation in sputtering of nonmetallic targets. The process of vibrational energy exchange between the target particles was described in ref. [32] in terms of the theory of unimolecular reactions [33] but some other approaches cannot be excluded.

It is essential that the mechanism of ref. [32], first, does not depend on the mode of the vibrational excitation of sample atoms and therefore it may be similar for light and heavy

bombarding atoms. Second, the mechanism implies the following expression for the sputtering yield:

$$Y \sim (E^* - U)^{(s-1)/a}, \quad (11)$$

where E^* is the total vibrational energy of the excited atomic complex, U is the binding energy of a surface atom, $s = 3n - 6$, n is the number of atoms in the complex, $a = 1 \div 2$ [33]. Under the natural assumptions $E^* \sim E_0$, $U \sim E_t$, formula (11) becomes similar to formula (8). Third, the mechanism leads to the Maxwellian type energy spectrum of the sputtered atoms [34] in agreement with the experiments in the subthreshold region [1, 25].

In general the mechanism suggested in ref. [32] is similar to so called slow thermal sputtering [35], but unlike in [35] it neither assumes thermal equilibrium nor involves the notion of temperature. And, finally, if we plug in formula (11) $(s-1)/a = 3.5$ (to satisfy (8)) or $(s-1)/a = 2.5$ (in accordance with ref. [25]) then for the number of atoms in the excited complex we get $n = 3-5$.

It is interesting to note that this value of n is close to the number of atoms that form the effective mass in the case of HT particle-surface scattering. Apparently, the effective mass's kinetic energy $\Delta E \sim E_0$, which the former acquires after the HT scattering may be partially transformed into the vibrational energy of its atoms.

As the number of the vibrationally excited atoms is non large the time of energy exchange between them is relatively small too, $t \leq 10^{-11}$ s. This fact gives a possibility to apply the model of ref. [32] developed for insulators only to metals and semiconductors.

3.3. Hg^+ ion emission

In ref. [27] the emission yield of Hg ions escaping from a slightly oxidized Pt surface bombarded by HT Hg neutral atoms was measured. The shape of the curve $Y(E_0)$ was about the same as for sputtered ions in ref. [1], but the value of threshold energy was significantly smaller, $E_t \approx 3.5$ eV. At Hg atom ionization potential $I = 10.44$ eV and the surface work function $e\phi \leq 6$ eV the energy gap between the atomic and the Fermi levels $\Delta\varepsilon \geq 4.44$ eV.

So, it is difficult to reconcile the measured value of E_t with the energy conservation law. If the E_t value is not an experimental artifact, then, in our opinion the observed Hg^+ ions are not formed by ionization of scattered Hg atoms, but mainly by desorption of Hg particles from the bombarding beam, which were adsorbed on the surface in the state of partial or total ionization. It is conceivable that Hg adatoms form little islands on the Pt surface with a structure close to that of metallic mercury. Then $E_t = 3.5$ eV is the threshold energy of desorption without ionization. Within this assumption the dependence $Y(E_0)$ shown in figure 4 was calculated at $a = 21.93$ eV^{1/2} by formulae (6)–(10). Assuming Hg atom coverage on the Pt surface $Q = 10^{-2}$, the absolute value of $Y(E_0) = 2 \cdot 10^{-6}$ at $E_0 = 8.2$ eV measured in ref. [27] was obtained.

To test the accuracy of the approach it is interesting to study the Hg ion emission in experimental conditions that would allow to separate the contributions from scattered and desorbed particles in Hg ion emission. It can be done, for instance, by the method of “moving target” developed in ref. [36].

4. Summary

Though few experiments investigating the peculiarities of HT scattering, sputtering and ion emission were performed, some information of fundamental importance can be already extracted from the measured data. In particular, it has been established that the regularities of energy loss observed experimentally during HT scattering may serve as evidence in favor of non-binary of atomic HT collisions. If this conclusion is confirmed, in the scattering theory for medium and heavy atoms it is necessary to take into account the contribution of the non-binary collisions, at least for the energies $E_0 < 20$ eV.

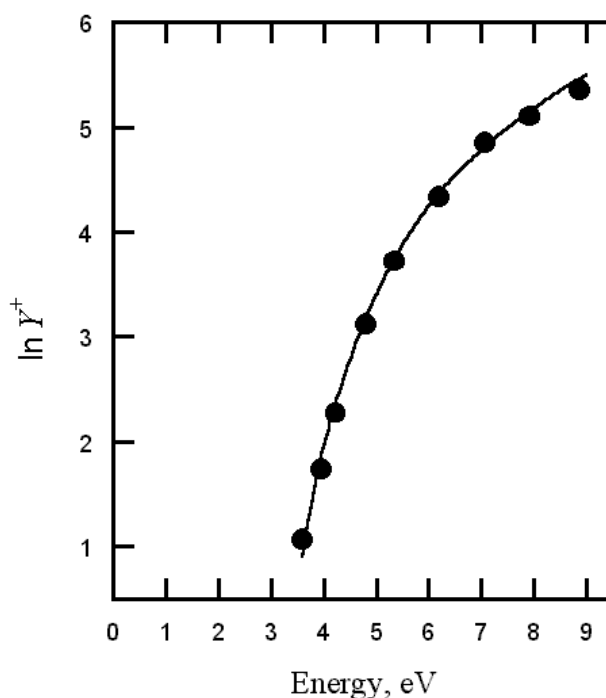


Figure 4. Dependence of the yield of Hg^+ ions scattered from the Pt surface on energy of bombarding Hg atoms. Dots are the experimental data of ref. [27], the curve was calculated with eqs. (6)–(10).

It is shown that the general empirical formula of ref. [30] for subthreshold sputtering is quite good approximation for the HT region. The fact may be considered as an evidence in favor of its fundamental nature connected with some subthreshold sputtering law common for different bombarding particles.

On the other hand the experimental data known for the HT energies do not allow to understand the features of charge state formation in the region of transition from thermal equilibrium conditions (when at the given value of $(I - e\phi)$ the ionization probability is determined by the surface temperature) to non equilibrium ones (when the probability is determined by the particle velocity component normal to the surface). To answer this question it is necessary to perform direct measurements of ionization probability as a function of the final particle energy and the temperature of a surface. Such measurements are related to detection of both charged and neutral particles.

ACKNOWLEDGEMENT

Financial support by the IAEA, Research Contract № 8613/R, the FPGI AN of the Republic of Uzbekistan, grant № 23–98, is gratefully acknowledged.

REFERENCES

- [1] SIGMUND, P., in *Sputtering by Particle Bombardment*, V.1, (BEHRISH, R., Ed), Springer, Heidelberg, 1981, 363.
- [2] PARILIS, E.S., KISHINEVSKY, L.M., TURAEV, N.YU., BAKLITZKY, B.E., UMAROV, F.F., FERLEGER, V.KH., NIZHNAYA, S.L., in *Atomic Collisions on Solid Surfaces*, North Holland, 1993, 664.
- [3] REMIZOVICH, V.S., RYAZANOV, M.I., TILININ, I.S., *Zh. Eksp. Teor. Fiz.* **79** (1980) 448. (in Russian)
- [4] KARPUSOV, D.S., YURASOVA, V.E., *Izv. AN SSSR, ser. Fiz.* **35** (1971) 393. (in Russian)
- [5] VEKSLER, V.I., *Zh. Eksp. Teor. Fiz.* **49** (1965) 90. (in Russian)
- [6] VEKSLER, V.I., EVSTIFEEV, V.V., *Izv. AN SSSR, ser. Fiz.* **37** (1973) 2570. (in Russian)
- [7] ANDERSEN, H.H., SIGMUND, P., *Kgl. Danske Videnskab. Selskab. Mat. Fys. Medd.* **34** (1966) 15.
- [8] TONGSON, L.L., COOPER, C.B., *Surf. Sci.* **52** (1975) 263.
- [9] GAY, W.L., HARRISON, D.E., *Phys. Rev.* **135** (1964) 1780.
- [10] HERHARD, W., *Z. Phys.* **B22** (1975) 31.
- [11] HARING, R.A., ROOSEDAAL, H.E., ZALM, P.C., *Nucl. Instr. and Meth.* **B28** (1987) 205.
- [12] COON, S.R., CALAWAY, W.F., PELLIN, M.J., WHITE, J.M., *Surf. Sci.* **298** (1993) 161.
- [13] WAHL, M., WUCHER, A., *Nucl. Instr. and Meth.* **B94** (1994) 36.
- [14] SIGMUND, P., CLAUSSEN, C.J., *Appl. Phys.* **52** (1981) 990.
- [15] COLLA, TH.J., URBASSEK, H.M., WUCHER, A., et al., *Nucl. Instr. and Meth.* **B143** (1998) 284.
- [16] BEHRISH, R., MODERLECHER, G., SCHLERZER, B.M., ROBINSON, M.T., *Appl. Phys.* **18** (1979) 391.
- [17] WINDAWI, H.M., *Surf. Sci.* **55** (1976) 573.
- [18] RASULEV, U.KH., ZANDBERG, E.YA., *Prog. Surf. Sci.* **28** (1988) 181.
- [19] BLANDIN, A., NOURTIER, A., HONE, D.W., *J. Phys.* **37** (1976) 369.
- [20] KOLODNEY, E., AMIRAV, A., *Chem. Phys.* **82** (1983) 269.
- [21] AMIRAV, A., CARDILLO, M.J., TREVOR, P.L., et al., *J. Chem. Phys.* **87** (1987) 87.
- [22] LIM, C., TULLY, J.C., AMIRAV, A., et al., *J. Chem. Phys.* **87** (1987) 1808.
- [23] LOGAN, R.M., STICKNEY, R.G., *J. Chem. Phys.* **44** (1966) 195.
- [24] ERIK, K., GRIMMELMANN, TULLY, J.C., CARDILLO, M.J., *Lett. Chem Phys.* **72(2)** (1980) 1039.
- [25] AMIRAV, A., CARDILLO, M., *Surf. Sci.* **198** (1988) 192.
- [26] ANDERSON, H.H., BAY, H., in *Sputtering by Particle Bombardment*, V.1, (BEHRISH, R., Ed), Springer, Heidelberg, 1981, 336.
- [27] DANON, A., VARDI, A., AMIRAV, A., *Phys. Rev. Lett.* **65** (1990) 2038.
- [28] CHEREPIN, V.T., VASILIEV, M.A., in *Secondary Ion-Ion Emission of Metals and Alloys*, Naukova Dumka, Kiev, 1982, 400. (in Russian)
- [29] VEKSLER, V.I., in *Secondary Ion Emission of Metals*, Nauka, Moscow, 1978, 240. (in Russian)

- [30] BOHDANSKY, J., ROTH, J., BAY, H.L., J. Appl. Phys. **51** (1980) 2861.
- [31] YAMAMURA, Y., in Proceedings International Ion Engineering Congress, Kyoto, 1983, 1.
- [32] KING, B.V., ZIV, A.R., LIM, S.H., TSONG, I.S.T., Surf. Sci. **167** (1986) 18.
- [33] FORST, W., Theory of Unimolecular Reactions, Atomic Press, New York, 1983, 256.
- [34] LIN, S.H., TSONG, I.S.T., ZIV, A.R., SZYMONSKI, M., LOXTON, C.M., Phys. Scr. **T6** (1983) 106.
- [35] KELLY, R., Rad. Eff. **32** (1977) 259.
- [36] BELYKH, S.F., EVTUKHOV, R.N., REDINA, I.W., FERLEGER, V.KH., Nucl. Instr. and Meth. **B 59–60** (1991) 72.

The nonelastic sputtering of ionic crystals under electron, cesium and multiple charged ions bombardment

B.G. Atabaev, Sh.S. Radzhabov, R. Dzhabbarganov, N.G. Saidkhanova

Arifov Institute of Electronics,
Tashkent, Uzbekistan

Abstract. Emission of negative charged cluster ions in sputtering of LiF, NaF and KBr with cesium ions of kinetic energy ranging from 0.1 keV to 0.3 keV has been investigated. An analysis of the experimental data allows the conclusion about the mechanism of direct cluster ejection from the defect mediated ionic crystals. It has been shown, that molecular ion emission from LiF, KCl depends slightly on the initial charge and energy of primary multicharged ions. Also, the mass and charge characteristics of desorbed positive particles under electron bombardment of KCl, KBr, LiF, CsI crystals depending on energy of beam and sample temperature have been investigated. It was assumed that multicharged ions desorption from ionic crystals surface is assumed to results in a "Coulomb explosion" mechanism.

1. Introduction

In recent studies on the impact of slow multiply charged ions on insulator surfaces, a dramatic increase of the yields for sputtering and secondary ion emission with projectile charge state has been observed for certain target species, e.g. for LiF and SiO. In contrast to the well established process of kinetically induced sputtering, the ejection of targeted atoms and ions due to the potential energy of ions is largely unexplored. Currently available experimental evidence and theoretical considerations strongly favour a so-called "defect-mediated desorption" model over an explanation involving a "Coulomb explosion" mechanism [1].

The present work is aimed at the extensive experimental study of secondary positive and negative ion emission from crystals KCl, LiF, NaF and KBr bombarded with positive multicharged ions (MCI) of Ar and single charged cesium ions and electrons of energies varied within the range of 0.1-3 keV to clarify the mechanism of the formation of secondary positive and negative ions ejected from the ionic crystals.

2. Experimental

Ions with different charge multiplicity were produced by electron impact gas ionization in a longitudinal magnetic field. The ion intensity I with maximum charge $q = 6$ at the target was $\sim 10^{-10}$ A. The ions were separated by m/q with a combined technique: with a V in mass-filter and time of flight in the drift space. To remove the neutral particles from the primary beam, the ion gun was declined by $\sim 2^\circ$ relative to the target direction with the following electrostatic ion beam deviation. The electrostatic lenses placed before the target are used allow for the decrease of each charge primary ion energy up to ~ 80 eV without a significant intensity loss. A monopole mass-spectrometer MH-7304 was used to analyze the sputtered ions and residual gas by mass and charge. To provide the identical bombardment conditions all charge ion energies and beam densities were set the same. The difference in the mass-spectra compared was determined then by the bombardment ion energy: $\Sigma eV - q(W + \chi)$, here eV is the atomic i -th electron ionization potential, ΔW is the crystal band gap, χ is the electron affinity. The technique involved the irradiation of the sample surface by ions with different q separately and the deposition of a graphite replica for the transmission electron microscopy study.

3. Results of the calculations

In order to obtain new information concerning the mechanisms of both atomic and cluster emission in sputtering and the formation of their charge state, the experimental studies have been carried out.

In particular, the mass spectra of negative charged and neutral sputtered species and the dependencies of the cluster ions yields on both the temperature of the target and the energy of the primary ions have been measured. The coefficients of ionization were determined employing the method described in ref. [2]. The following negative charged species were detected in the mass spectra obtained for sputtering of LiF, NaF and KBr: F_n^- ($n=1-4$), Br_n^- ($n=1-3$), H^- , C^- , CH^- , CH_2^- , C_2^- , C_2H^- , $C_2H_2^-$, O_2^- , OH^- , O_2H^- , Cl^- , K^- , FO^- , BrO^- , $Li_mF_n^-$, $Na_mF_n^-$, $K_mBr_n^-$, etc. The features of the mass spectra measured at the different target temperatures are as follows: ions of Li, Na and K can be detected after the target temperature reaches 200°C , the numbers of constituents n and m in F_n^- , Br_n^- , $Li_mF_n^-$, $Na_mF_n^-$, $K_mBr_n^-$ clusters increase with increasing the target temperature, the dependence of the yield of the clusters of given size (n, m) on the target temperature is a linear one (figure 1).

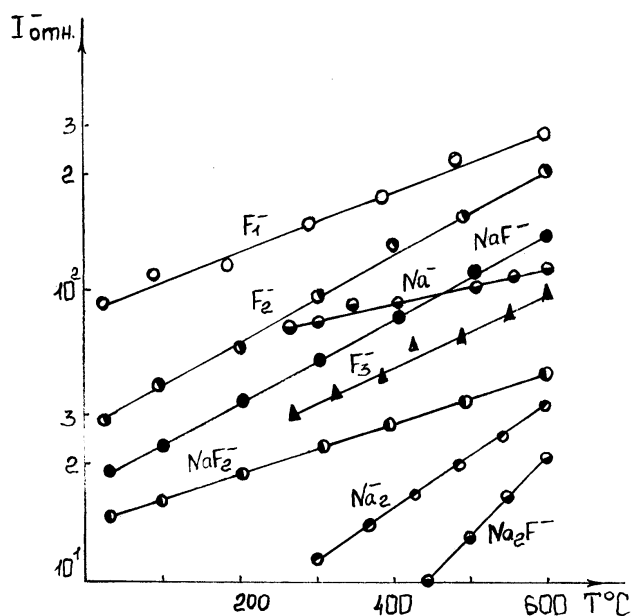


FIG. 1. Dependence of the yield of secondary negative charged cluster ions of Na, F and NaF on the target temperature under bombardment with cesium ions.

The examination of temperature dependencies of the yields of the ions, the anions, the cations and their clusters lead us to the conclusion that at low target temperatures the elastic cascade mechanism contributes mainly to the sputtering process. With increasing the temperature the contribution of the creation of F-H pairs and their diffusion and coalescence on surface becomes more pronounced.

The specific peculiarity of the cluster formation process at the bombardment of the ionic crystals with cesium ions made it possible: to reveal the existence of the threshold energies of the bombarding beam below which the yield of n -atomic cluster ion drops abruptly, and to study the features of the formation of negative charged clusters near the

threshold energies: $F^- = 80$ eV, $F_2^- = 90$ eV, $F_3^- = 350$ eV, $F_4^- = 750$ eV, $Li^- = 120$ eV, $Li_2^- = 150$ eV, $LiF^- = 210$ eV, $LiF_2^- = 130$ eV, $Li_2F_2^- = 350$ eV, $LiF_3^- = 370$ eV, $LiF_4^- = 510$ eV, $Na^- = 1000$ eV, $Na_2^- = 1350$ eV, $NaF^- = 750$ eV, $NaF_2^- = 1200$ eV, $Br^- = 80$ eV, $Br_2^- = 120$ eV, $Br_3^- = 650$ eV, $KBr^- = 820$ eV, $KBr_2^- = 1200$ eV, $K^- = 950$ eV, $K_2^- = 1400$ eV.

In sputtering of ionic crystals a large yield of negative halogen ions has been detected, corroborating the model of Koval' [3] based on the fact that tunnel resonance transitions are impossible in ionic crystals. Owing to that the probability of survival for negative halogen ions is close to unity, their yield depending on the electron affinity of a halogen atom. Our experimental data indicating the absence of dependence of normalized cluster ions yields on the primary ion energy corroborate the model of direct emission [4, 5].

The above presented results on the temperature and energy dependencies of the yields of the negative charged clusters sputtered from the ionic crystal surface can be interpreted as follows. At the room temperatures the concentrations of Schottky defects and interstitial are fairly low. Therefore in the case of the low energy bombardment (< 100 eV) the cluster yield is negligible. The increase of the cluster yield with increasing both the primary ion energy and the target temperature results from increasing the concentration of Schottky defects and interstitial as a result, more F^- , Br^- , Li^- , Na^- and K^- ions take the position of the defects promoting the cluster formation process.

In our work the energy dependencies of surface erosion and emission of positive ions under bombardment of KCl, LiF crystals by multicharged argon ions ($q = 1-6$, with energy from 0.08 keV to 3.0 keV) were presented. It was shown, that emission of ions and surface layer by layer erosion stimulated by desorption of neutral and charged particles were increased with the increase in charge or potential energy of multicharged ions. This experiment can be explained by a "Coulomb repulsion" mechanism [6].

The atomic and molecular ion emission data for the most abundant target isotopes are plotted as a function of the bombarding beam q and E_0 . The latter has the charge threshold and appears at $q = 2$ for KCl, LiF. The emission dependence on q and E_0 are found to be similar

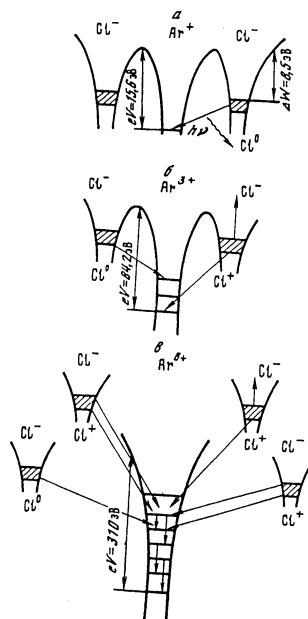


FIG. 2. Auger neutralization diagrams of the Ar (a), Ar^{3+} (b) and Ar^{6+} (c) ions on the KCl surface.

for M^+ and X^+ ions. The experimental data on LiF bombardment with $q=1,2$ and those obtained in [7] show that the bombarding ion potential energy contribution, depending on its charge, influence the lattice atom ionization in different ways. Figure 2 demonstrate the approximate diagrams of the Ar^+ , Ar^{3+} and Ar^{6+} Auger neutralization during interaction with the KCl crystals surface.

With Ar^+ (15.6 eV), the part of potential energy is spent on transition of Cl^- into the neutral Cl^0 and the remaining energy is carried away by a photon. With Ar^{3+} (84.2 eV), its neutralization energy goes to both the neutral Cl^0 and double ionized Cl^+ generation. As a result, the weakening of bonds between the target surface atoms occurs at the ion incidence site, promoting their sputtering. The atoms may be removed due to bombarding ion kinetic energy transfer and the target atoms evaporation at the target temperature [8].

With Ar^{6+} irradiation (310 eV), the ionized Cl^+ part increases. As a result the microscopic charged region is forms at the surface composed of Cl^+ and K^+ cations, existing initially in the crystal. Double charged cations were not discovered in the mass-spectra. In this case additional yield of these components as ions will be determined by the Coulomb repulsion forces. The surface ion desorption from alkali halides under electron impact proceeds in a similar way [9]. The peculiarities of M^+ and X^+ emission are discovered with primary ion q and E_0 change. With $q \leq 3$, when their potential energy is not large, the cation and anion yield is determined mainly by the bombarding ion kinetic energy and increases linearly in the investigated range. With transition to the ions $q \geq 4$, when the MCI potential energy begins to prevail over the potential energy in the initial E_0 region, the M^+ and X^+ yield weakly depends on E_0 in that energy region. In the large energy E_0 region the secondary particle yield plots approach each other, and this is most prominent with LiF and KCl. Similar dependences were observed in the electron emission study under the action of MCI [10]. This is due to the potential energy contribution decrease as a result of the neutralization process displacement into the sample depth, and the secondary ion yield due to the decreased inelastic processes. On the other hand, probably, the MCI penetration conditions into the crystal lattice are improved due to the neutralization conditions and their decreased dimensions.

As experiments show, molecular ion emission from LiF, KCl depends slightly on the initial ion charge and energy, probably mostly due to the bond decay between crystal molecule components during MCI neutralization and cation and anion transition to the weak and antibound state.

By using the electron-stimulated desorption (ESD) method, the mass and charge characteristics of desorbed positive particles under electron bombardment of KCl, KBr, LiF, CsI crystals depending on energy of beam and sample temperature were investigated. The multicharged ion yields from KCl, KBr with $q = 1-3$, $q = 2$ for LiF and $q = 5$ for CsI were established. Obviously single charged ions desorption is occurs from ionization of outer energy levels and multicharged ions result from inner levels ionization of L (KCl, KBr), K(LiF), M(CsI) with excitation of Auger electrons.

The correlation between threshold of sputtered molecular and multicharged ions was found. The emission of multicharged ions is defined by ionization of inner levels of Cl and F. The yield of K^{2+} , Cl^{2+} , Cl^{3+} ions due to the formation of vacancies in core level of $1s$. The threshold of yield K^{3+} appears about ~ 300 eV that close to value of energy ionization of core level $K2p$ (~ 297 eV).

The threshold energy of emission Cs and I ions appears ~ 170 eV. In figure 3 the mass spectra of desorbed single and multicharged ions from CsI crystals under electron bombardment are shown. The atom with vacancies in the inner core is considered in multiple excitation state [11]. It may be assumed that multicharged ions desorption from ionic crystals surface results in the "Coulomb explosion" mechanism.

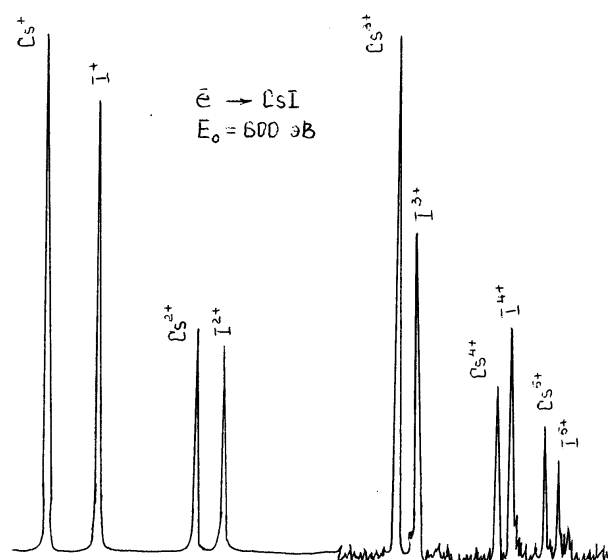


FIG. 3. The mass spectra of desorbed single and multicharged ions from CsI crystals under electron bombardment.

Using the target current spectra (TCS) of KCl and KBr films on Si(111) an intensive structure in the energy region corresponding to the bandgap was discovered. One group of peaks was induced by electron and ion irradiation and vanished at high temperatures. From the evolution of the TCS maximum intensities the defect concentration changes caused by electron and ion irradiation were estimated.

Financial support by the IAEA, Research Contract N8613/R is gratefully acknowledged.

REFERENCES

- [1] HAYDERER, G., SCHMID M., VARGA, P., WINTER H.P., AUMAYR, F. Phys. Rev. Lett., **83**, (1999) 3948.
- [2] AYUKHANOV, A.H., TURMASHEV, E. Zh. Tehn. Fiz., **47** (1977) 1234 (in Russian).
- [3] KOVAL, A.G. Radiotekhnika i electronica, **47** (1992) 2055 (in Russian).
- [4] BENNINGHOVEN, A. Surf.Sci., **35** (1973) 427.
- [5] STAUDENMAIR, G. Radiat.Eff., **13** (1972) 31.

- [6] ATABAEV, B.G., RADJABOV, SH.S., AKHMADZHONOVA, M.KH. Nucl. Instr. and Meth. in Phys. Res., **98** (1995) 462.
- [7] VARGA, P., DIEBOLID, U., WUTTE, D. Nucl. Instr. Meth., **B58** (1999) 417.
- [8] KELLY, R. Ion Sputtering Thermal and Electron Collision Processes, Mir, Moskow, (1980) 194 (in Russian).
- [9] VASUE, T., ICHIMIYA, Surf. Sci., **186** (1987) 191.
- [10] RADZHABOV, SH.S., RAKHIMOV, R.R., ABDUSALAMOV, D. Izv. Akad. Nauk. SSSR, Ser. Fiz., **43** (1976) 2543.
- [11] PARILIS, E.S. Auger effect, Fan, Tashkent, (1969) 191 (in Russian).

Contents of previous volumes of Atomic and Plasma–Material Interaction Data for Fusion

Volume 1 (1991)

R. Behrisch: Particle bombardment and energy fluxes to the vessel walls in controlled thermonuclear fusion devices	7
W. Eckstein: Reflection	17
K.L. Wilson, R. Bastasz, R.A. Causey, D.K. Brice, B.L. Doyle, W.R. Wampler, W. Möller, B.M.U. Scherzer, T. Tanabe: Trapping, detrapping and release of implanted hydrogen isotopes	31
W. Eckstein, J. Bohdansky, J. Roth: Physical sputtering	51
J. Roth, E. Vietzke, A.A. Haasz: Erosion of graphite due to particle impact	63
E.W. Thomas: Particle induced electron emission	79
H. Wolff: Arcing in magnetic fusion devices	93
J.B. Whitley, W.B. Gauster, R.D. Watson, J.A. Koski, A.J. Russo: Pulse heating and effects of disruptions and runaway electrons on first walls and divertors	109
R.K. Janev, A. Miyahara: Plasma-material interaction issues in fusion reactor design and status of the database	123

Volume 2 (1992)

W.L. Wiese: Spectroscopic data for fusion edge plasmas	7
S. Trajmar: Electron collision processes with plasma edge neutrals	15
G.H. Dunn: Electron–ion collisions in the plasma edge	25
H. Tawara, Y. Itikawa, H. Nishimura, H. Tanaka, Y. Nakamura: Cross-section data for collisions of electrons with hydrocarbon molecules	41
M.A. Cacciatore, M. Capitelli, R. Celiberto: Dissociative and energy transfer reactions involving vibrationally excited H ₂ /D ₂ molecules	65
R.A. Phaneuf: Assessment of ion–atom collision data for magnetic fusion plasma edge modelling	75
T. Tabata, R. Ito, T. Shirai, Y. Nakai, H.T. Hunter, R.A. Phaneuf: Extended scaling of cross-sections for the ionization of H, H ₂ and He by multiply charged ions	91
P. Reinig, M. Zimmer, F. Linder: Ion–molecule collision processes relevant to fusion edge plasmas	95
X. Bonnin, R. Marchand, R.K. Janev: Radiative losses and electron cooling rates for carbon and oxygen plasma impurities	117

Volume 3 (1992)

H.P. Summers, M. von Hellermann, F.J. de Heer, R. Hoekstra: Requirements for collision data on the species helium, beryllium and boron in magnetic confinement fusion	7
F.J. de Heer, R. Hoekstra, A.E. Kingston, H.P. Summers: Excitation of neutral helium by electron impact	19
T. Kato, R.K. Janev: Parametric representation of electron impact excitation and ionization cross-sections for helium atoms	33
W. Fritsch: Helium excitation in heavy particle collisions	41

F.J. de Heer, R. Hoekstra, H.P. Summers: New assessment of cross-section data for helium excitation by protons	47
M. Anton, D. Detleffsen, K.-H. Scharfner: Heavy ion impact excitation of helium: Experimental total cross-sections	51
H.B. Gilbody: Review of experimental data on electron capture and ionization for collisions of protons and multiply charged ions with helium atoms and ions	55
R. Hoekstra, H.P. Summers, F.J. de Heer: Charge transfer in collisions of protons with helium	63
R.K. Janev: Cross-section scaling for one- and two-electron loss processes in collisions of helium atoms with multiply charged ions	71
A.A. Korotkov: Sensitivity of neutral helium beam stopping in fusion plasmas to atomic collision cross-sections	79
K.A. Berrington, R.E.H. Clark: Recommended data for electron impact excitation of Be ⁹⁺ and B ⁹⁺ ions	87
D.L. Moores: Electron impact ionization of Be and B atoms and ions	97
M.S. Pindzola, N.R. Badnell: Dielectronic recombination rate coefficients for ions of the Be and B isonuclear sequences	101
R.A. Phaneuf, R.K. Janev, H. Tawara, M. Kimura, P.S. Krstic, G. Peach, M.A. Mazing: Status and critical assessment of the database for collisions of Be ⁹⁺ and B ⁹⁺ ions with H, H ₂ and He	105
P.S. Krstic, M. Radmilovic, R.K. Janev: Charge exchange, excitation and ionization in slow Be ⁴⁺ + H and B ⁵⁺ + H collisions	113

Volume 4 (1993)

R.K. Janev, J.J. Smith: Cross sections for collision processes of hydrogen atoms with electrons, protons and multiply charged ions	1
1. Electron impact processes	1
2. Proton impact processes	41
3. Collision processes with He ²⁺	83
4. Collision processes with highly charged ions	123

Volume 5 (1994)

W.B. Gauster, W.R. Spears and ITER Joint Central Team: Requirements and selection criteria for plasma-facing materials and components in the ITER EDA design ...	7
D.E. Dombrowski, E.B. Deksnis, M.A. Pick: Thermomechanical properties of Beryllium ...	19
T.D. Burchell, T. Oku: Material properties data for fusion reactor plasma-facing carbon-carbon composites	77
T. Tanabe: High-Z candidate plasma facing materials	129
R.F. Mattas: Recommended property data for Mo, Nb and V-alloys	149
S.J. Zinkle, S.A. Fabritsiev: Copper alloys for high heat flux structure applications	163
A. Hassanein, I. Konkashbaev: Erosion of plasma-facing materials during a tokamak disruption	193
H.-W. Bartels, T. Kungugi, A.J. Russo: Runaway electron effects	225
M. Araki, M. Akiba, R.D. Watson, C.B. Baxi, D.L. Youchison: Data bases for thermo-hydrodynamic coupling with coolants	245

Volume 6 (1995)

F.J. de Heer, I. Bray, D.V. Fursa, F.W. Blik, H.O. Folkerts, R. Hoekstra, H.P. Summers: Excitation of He($2^{1,3}S$) by electron impact	7
V.P. Shevelko, H. Tawara: Spin-allowed and spin-forbidden transitions in excited He atoms induced by electron	27
P. Defrance: Recommended data for electron impact ionization of noble gas ions	43
M. Stenke, K. Aichele, D. Hathiramani, G. Hofmann, M. Steidl, R. Völpel, E. Salzborn: Electron impact ionisation of Tungsten ions	51
A. Müller: Dielectronic recombination and ionization in electron-ion collisions: data from merged-beams experiments	59
V.P. Shevelko, H. Tawara: Multiple ionization of atoms and positive ions by electron impact	101
M.S. Pindzola, D.C. Griffin, N.R. Badnell, H.P. Summers: Electron-impact ionization of atomic ions for ADAS	117
W. Fritsch: Theoretical studies of slow collisions between medium-Z metallic ions and neutral H, H ₂ , or He	131
R.K. Janev: Excitation of helium by protons and multiply charged ions: analytic form of scaled cross sections	147
M. Gargaud, R. McCarroll: Electron capture from H and He by Al ⁺²³ , Si ^{+23,4} , Ar ⁺⁶ and Ti ⁺⁴ in the eV to keV energy range	163
D.R. Schultz, P.S. Krstic: Inelastic processes in 0.1-1000 keV/u collisions of Ne ^{q+} (q=7-10) ions with atomic hydrogen	173
H. B. Gilbody: Charge transfer and ionization studies involving metallic species	197
R. Hoekstra, J.P.M. Beijers, F.W. Blik, S. Schippers, R. Morgenstern: Fusion related experiments with medium-Z, multiply charged ions	213
M. Druetta, D. Hitz, B. Jettkant: Charge exchange collisions of multicharged Ar ^{5,6+} , Kr ^{5,6+} , Fe ^{7,8+} and Ni ¹⁷⁺ ions with He and H ₂	225
C. Cisneros, J. De Urquijo, I. Alvarez, A. Aguilar, A.M. Juarez, H. Martinez: Electron capture collision processes involving multiply-charged Si, Ni, Ti, Mo, and W ions with H, H ₂ and He targets	247

Volume 7/A (1998)

A.A. Haasz, J.A. Stephens, E. Vietzke, W. Eckstein, J.W. Davis and Y. Hirooka: Particle induced erosion of Be, C and W in fusion plasmas. Part A: Chemical erosion of carbon-based materials	1
1. Introduction	9
2. Erosion data derived from Tokamaks	13
3. Carbon-based materials: selected collection of chemical erosion data	23
4. Comprehensive set of chemical erosion data from various laboratories	63

Volume 7/B (1998)

W. Eckstein, J.A. Stephens, R.E.H. Clark, J.W. Davis, A.A. Haasz,

E. Vietzke, and Y. Hirooka: Particle induced erosion of Be, C and W in fusion plasmas.

Part B: Physical sputtering and radiation-enhanced sublimation 1

- 1. Introduction 9
- 2. Physical sputtering of elemental targets and compounds: data collection 17
- 3. Radiation-enhanced sublimation: data collection 115

Volume 8 (2001)

P.S. Krstic and D.R. Schultz: Elastic and related transport cross sections for collisions among isotopomers of H^+ and H , $H^+ + H_2$, $H^+ + He$, $H + H$, and $H + H_2$.

Part A: Introduction and theory 1

Part B: Ion-neutral collision systems 77

Part C: Neutral-neutral collision systems 413